FACULTY OF SCIENCE
UNIVERSITY OF COPENHAGEN

PhD thesis

Helle Astrid Kjær

Continuous chemistry in ice cores

-Phosphorus, pH and the photolysis of humic like substances

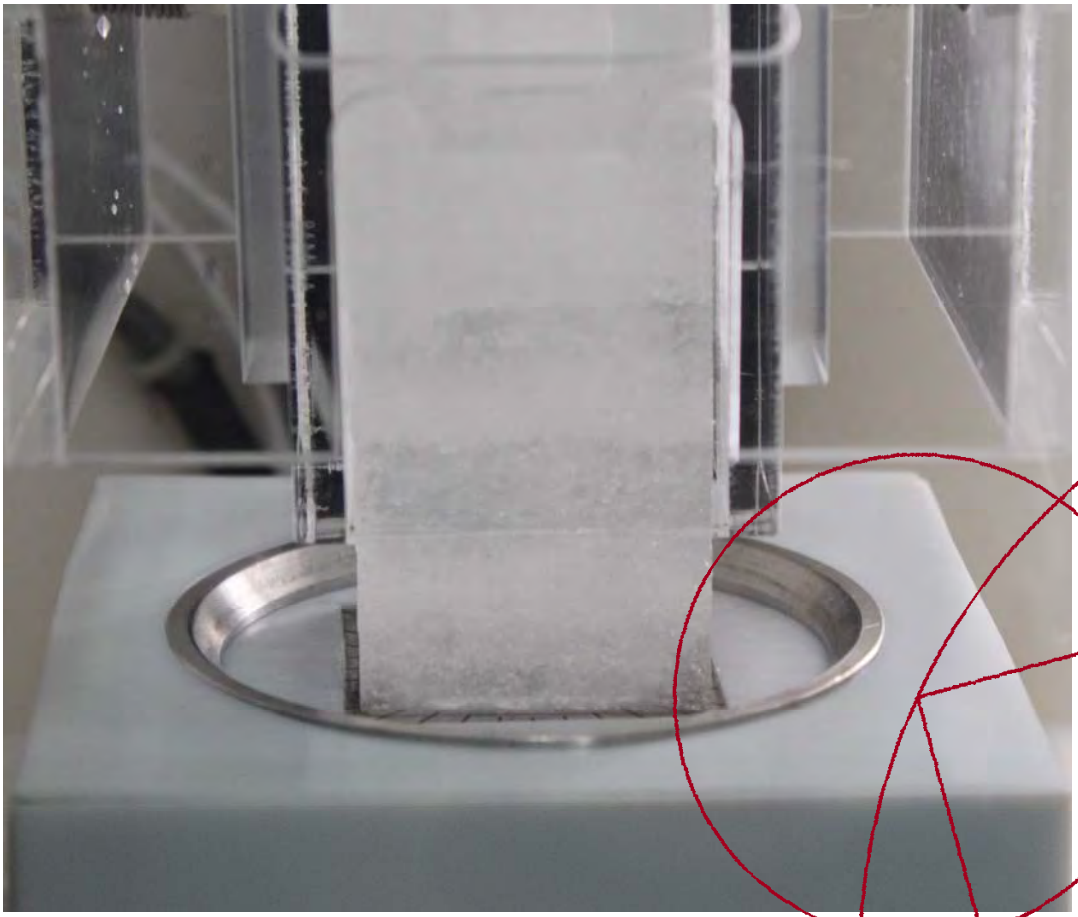

Academic supervisors: Anders Svensson and Matthew S. Johnson
This thesis has been submitted to the PhD School of The Faculty of Science, University of Copenhagen, 1. July 2014

Abstract

Ice cores provide high resolution records of past climate and environment. In recent years the use of continuous flow analysis (CFA) systems has increased the measurement throughput, while simultaneously decreasing the risk of contaminating the ice samples. CFA measurements of high temporal resolution increase our knowledge on fast climate variations and cover a wide range of proxies informing on a variety of components such as atmospheric transport, volcanic eruptions, forest fires and many more. New CFA methods for the determination of dissolved reactive phosphorus (DRP) and pH are presented as part of this thesis.

Phosphorus is an essential nutrient for the biosphere. The phosphorus is cycled mainly via hydrology, but some biological systems, such as the remote oceans and old forests are dependent on atmospheric deposition of phosphorus. The flux of phosphorus to the ocean is suggested to have increased during the glacial and in recent times there is clear evidence of increased phosphorus load in waters as a result of increased fertilizer use, waste treatment and other human influences. To investigate if atmospheric deposition of P, too has changed over time a CFA method was developed for the continuous determination of dissolved reactive phosphorus (DRP) by means of a reaction with molybdenum blue. The concentration of DRP in polar ice is low and thus the method relies on enhancing the limit of detection by increasing the absorption length by means of a 2.5 metre Liquid Waveguide Capillary Cell. The method was applied to a firn core from the North East Greenland Ice Stream (NEGIS) and to glacial sections of the Greenland NEEM ice core. In the NEGIS firn core concentrations were about 2.7 nM PO_4^{3-} and there was no evidence of any recent anthropogenic impact during the past 300 years. Sources of DRP to the NEGIS site were found to be dust as well as a secondary source-likely of biological origin. The DRP deposited at the NEEM site during the last glacial maximum was 14 times higher than the DRP deposited at present at the NEGIS site. The study of the NEEM ice core sections also included determination of total P. The ratio between DRP and total P reveal large changes in the soluble fraction of P over time, with low solubility in cold glacial periods.

The second part of the thesis continues in the track of CFA ice core measurements: A high resolution optical method has been developed using the dyes chlorophenol red and bromophenol blue for the determination of pH in ice cores. pH controls many chemical processes and equilibria. Hence pH data are important for the proper interpretation of data for the various proxies found in the ice. Further, determination of the acidity can be used to identify layers originating from volcanic eruptions, crucial for cross-dating ice cores and relevant for climate interpretations. The method includes a heat bath to minimize the acidifying effect of CO_2 both from the laboratory and from the ice itself. While for acidic ice the method finds similar concentrations of H^+ as are deduced from the ionic budget, for more alkaline ice there seems to be an acidifying effect of the CO_2, causing the indicator method to err towards lower pH. The pH method was applied on the NEGIS firn core where it proved an improvement over both conventional ECM and DEP, which require density corrections. Further the method successfully identified volcanic eruptions as well as the underlying anthropogenic signal related to the industrial pollution

peaking in the 1970's. The pH method was also applied on the Antarctic RICE ice core and proved useful, contrary to both the ECM and melt water conductivity obtained for the ice ore, to determine a volcanic eruption record.

The third part of the thesis is a theoretical review to determine if photolysis of pyruvic acid is a likely source of in situ production of CO_2 in ice cores. While CO_2 records from Antarctica show similar trends with decreased CO_2 concentrations during the glacial, excess peaks of CO_2 are observed in parts of the Greenland CO_2 records as a result of *in situ* production of CO_2. The source of the *in situ* production is debated. One proposed source is the photolysis of pyruvic acid or other carboxylic acids. Large uncertainties remain on parameters involved in the study of photolysis as a source of in situ CO_2. The concentration of organic substances in Greenland ice is poorly known due to their low levels and the fact that only a few studies evaluate the concentrations of specific organic compounds. Light does not penetrate deep into the ice due to scattering by individual snow grains at the very surface and by air bubbles in the upper part of the ice. However light is produced *in situ* by Cherenkov radiation from cosmic rays. As part of this thesis the penetration of light on surface layers of snow at NEEM was determined andthe 1/e depth was found as a function of wavelength. Further, by computational chemistry hybrid density functional methods (DFT), the four most common conformers of pyruvic acid were investigated in both gas, water and ice using the DFT model CAM-B3LYP with dielectric medium methods. A decrease of the energy difference between the second and third most common conformers of pyruvic acid was found. The study serves as a basis of future studies of the photolytic production of CO_2 from pyruvic acid and other β-carbonyl humic-like substances found in glacial ice.

Resumé

Målinger i iskerner giver detaljerede oplysninger om klimaet. De Grønlanske iskerner indeholder klimadata om de sidste ca. 110.000 år, mens de Antarktiske iskerner kan gå op til 800.000 år tilbage i tiden. Traditionelt har man målt indholdet af urenheder i isen ved at skære den i stykker og måle hvert stykke for sig. Men jo mere isen berøres, jo større er sandsynligheden for forurening. Derfor måler man nu helst isen kontinuert og benytter den såkaldte "Continuous Flow Analysis" (CFA) metode. Sådanne CFA målinger giver detaljeret information om fortidens klima og kan blandt andet give information om vind, vulkaner, skovbrande med flere.

To nye CFA metoder er udviklet som del af denne Ph.D. afhandling. Den ene måler opløst reaktivt Fosfor (DRP), den anden surheden pH.

Fosfor (P) er et essentielt stof for biosfæren. Den primære del af den globale tranport af P foregår i vand, men der er dele af det globale biologiske system, som er afhængige af at ny P deponeres via atmosfæren. For eksempel er både gamle skove og det åbne hav afhængige af P deponeret fra atmosfæren. Under istiden mener man at niveauet af P i havene har været højere end i dag, og i nyere tid er der observeret en menneskeskabt stigning af P i floder og søer. En CFA metode, der benytter reaktionen mellem molybdænblåt og P, er som del af dette studie udviklet for iskerner for at undersøge, om der også er sket sådanne ændringer i den atmosfæriske circulation af P. I iskerner er koncentrationen af P meget lav og detektionsgrænsen øges derfor v.h.a. en 2.5 meter lang absorptionscelle. DRP koncentrationer blev målt både i en firnkerne fra den nordøstgrønlandske isstrøm (NEGIS) og i en iskerne fra nord-vest Grønland (NEEM). Vi fandt ingen menneskabt ændring i NEGIS firn kernen, som havde et gennemsnitsniveau på 2.7 nM PO_4^{3-}. Vi fandt, at den primære kilde til DRP var støv, men at der også findes en anden signifikant kilde – muligvis af biologisk oprindelse. Under istiden var niveauet af DRP deponeret på isen 14 gange højere end det, vi ser idag, og vi observerer, at den opløselige del af P er højere i varme perioder end i kolde.

Den anden del af denne afhandling beskæftiger sig med pH-målinger af iskernevand. En CFA metode, der benytter sig af pH indikatorerne Klorphenol rÃ¸dt og Bromphenol blåt er udviklet som del af dette arbejde. pH målinger i isen er vigtige, da mange kemiske processer styres af pH. Derudover kan pH målt i isen bruges til at finde vulkanske lag. Disse vulkanske lag bruges til at datere isen. Mængden af CO_2 i vandet mindskes ved at varme systemet op; dette fordi CO_2 både fra laboratoriet og også fra isen selv, kan ændre pH. Vi fandt, at lave pH-værdier bestemt ved indikatormetoden var i overensstemmelse med pH bestemt ved at opstille et ion-budget, mens indikatormetodens høje pH-værdier pga. CO_2'ens forsurende virkning var for lave og altså lavere end pH bestemt udfra ion-balancen. Metoden, der er udviklet her, var bedre end ECM og DEP på firnkernen NEGIS, hvor de konventionelle metoder er afhængige af en densitetskorrektion. Signalet fra NEGIS kernen viser et fald i pH frem til 1970'erne, hvorefter pH igen stiger. Metoden identificerer også nemt de forventede vulkanske lag. Målinger blev også foretaget af den Antarktiske iskerne RICE. Her var hverken den traditionelle ECM eller den ofte målte smeltevands-konduktivtet brugbare til at indentificere vulkaner, og pH metoden var endog meget vigtig for at få etableret vulkanske referencelag.

CO_2'en målt i grønlandske iskerner er højere end den, man måler i Antarktiske. Derfor mener man, at der bliver dannet CO_2 inde i den grønlandske is. I den tredje del af denne afhandling evalueres der på, hvorvidt karboksylsyren pyrodruesyres fotolyse er involveret i de processer, der danner CO_2 inde i iskerner og fortstyrrer det klimatiske CO_2 signal. Da der kun er lavet ganske få målinger af organske syrer i isen, er der meget store usikkerheder på deres koncentrationer. Solens lys rækker ikke fra overfladen ned i de dybder hvor photolysen af pyrodruesyre skal foregå hvis den skal være årsag til de ekstra høje CO_2 målinger fra Grønlandsk is. Det lys der findes i isen kommer fra Cherenkov stråling, der dannes når kosmiske sråler trænger dybt ned i isen. I denne afhandling blev lysgennemtrængningen i sne ved NEEM målt for forskellige bølgelængder. Derudover gjorde vi et forstudie af pyrodruesyres forskellige kemisk former i vand og is. Til dette studie blev kvantekemisk computer modellering (DFT/CAM-B3LYP) benyttet. Vi fandt at både den anden og tredje mest sandsynlige struktur af pyrodruesyre blev endnu mere sandsynlige i vand og is. Studiet danner base for fremtidige studier, der vil kigge nærmere på exitationsspektret for pyrodrue syre og andre karboksylsyrer i vand og is.

Preface

The work of this Ph.D. was carried out in multiple environments; In the autumn heat at the National Institute for Polar Research (Tokyo, Japan), in the New Zealand winter at the Antarctic Research Centre, Wellington University, as well as in the winter at the Desert Research Institute in Nevada, USA, not to mention here at University of Copenhagen where I have experienced all seasons.

While each of these places is unique both in terms of climate and culture and provided great company, my heart was lost to the Arctic long ago. And earlier still I found my great interest in ice cores while doing a small project in High School. My physics teacher had contact to Anders Svensson at the Centre for Ice and Climate. Anders provided me with a small record of $\delta^{18}O$ from a section of the NGRIP ice core. No one had looked at the $\delta^{18}O$ results from that particular section prior to me and I was hooked. The riddle of the climate intrigued me and still does.

Further, as part of the high school project, I was invited to take part in a symposium about the NGRIP ice core. I sat in an auditorium for a full day understanding only very little, but I was very intrigued. More importantly I found that the people at the symposium shared great stories about both the science and the ice core drilling operations.

People at the Centre for Ice and Climate still share great stories about life on the ice. But I have found during the work of this thesis that people working with ice cores generally are great at telling stories, whether in Japan, New Zealand, USA, Denmark or on the Greenland ice sheet.

Without all your stories, knowledge, great cooperation and your capability to set aside different nationalities and scientific backgrounds the interdisciplinary work presented in this Ph.D. would not have been completed (it would not even have been started). Thank you!

Helle Astrid Kjær
Copenhagen, June 2014

Acknowledgements

I would like to acknowledge my supervisors; associate professor Anders Svensson and professor Matthew Johnson, who supported me with their great knowledge. But also associate professor Paul Vallelonga has been an invaluable collaborator, very much so in the laboratory, but also when discussing science.

This work could not have been carried out without the help of colleagues both at the Centre for Ice and Climate and the Copenhagen Centre for Atmospheric Research, but I certainly also could not have finished this thesis without the help from colleagues in continuous flow analysis laboratories at the Desert Research Institute (Reno, Nevada, USA), the National Institute for Polar Research (Tokyo, Japan), and at the Antarctic Research Centre (Wellington University, New Zealand).

I am grateful to Mathilde Thorn Poulsen and Trine Schmidt Jensen for their preliminary studies of dye-based pH detection, as well as Catalin Tibuleac, Magnus E. L. Kristensen, Maria Arvanti, Marius Simonsen and Camilla Marie Jensen for their help running the Copenhagen CFA.

I would especially like to acknowledge Peter Neff, who provided the ECM data for the RICE ice core, James Lee and Thomas Blunier for the methane comparison work for that ice core as well as all the hard working CFA people, who worked 12 hour shifts to obtain the RICE ice core data.

Furthermore I thank Joe McConnell for running an amazing laboratory and the great scientists working hard in it. Especially I thank Daniel Pasteris, Michael Sigl, Olivia Maselli and Rachael Rhodes.

Professor Kumiko Goto-Azuma at the National Institute for Polar Research (Tokyo, Japan), Remi Dallmeyr and Hironobu Yamada are acknowledged for their invaluable help in making the NEEM measurements happen. I am also grateful for the work of Motohiro Hirabayashi (NIPR) and Jacobo Gabrieli at Institute for Dynamics of Environmental Processes, IDPA-CNR, Venice, Italy, regarding IC and ICP-MS measurements, respectively.

I would like to thank professor Nozomu Takeuchi from Hokkaido university, Japan for the opportunity to work with the high concentration DRP samples from the Gregoriev glacier, Inner Tienshan, Kyrgyzstan. Additionally, I would like to thank Jun Uetake from the National Institute for Polar Research, Tokyo, Japan for facilitating the contact as well as for handling the transport of the Gregoriev glacier samples.

I also thank professor Natalie Mahowald, Earth and Atmospheric Sciences, Cornell University, New York, USA for providing the model output for atmospheric phosphorus deposition at the NEGIS firn site.

Further thanks to the Alfred Wegener Institute for polar and marine research (AWI) for supporting the retrieval of the NEGIS firn core. I would also like to thank Trine Ebbensgaard Strømfeldt for measurements of Mg and K performed on the NG00S6 firn core.

Finally I would like to thank Kristian Kjær, Mikkel Riber Bojsen, Astrid Schmidt and Paul Vallelonga for proofreading.

Part of the data is genrated as part of the RICE project. The RICE project is supported by an international collaboration between New Zealand, USA, Denmark,

United Kingdom, Germany, Australia, Italy and China. I thank all the people involved in the RICE logistics, fieldwork, sampling and analytical programmes.

Part of the data presented is part of the NEEM ice core drilling programme. NEEM is directed and organized by the Center of Ice and Climate at the Niels Bohr Institute and US NSF, Office of Polar Programs. It is supported by funding agencies and institutions in Belgium (FNRS-CFB and FWO), Canada (NRCan/GSC), China (CAS), Denmark (FIST), France (IPEV, CNRS/INSU, CEA and ANR), Germany (AWI), Iceland (RannIs), Japan (NIPR), Korea (KOPRI), The Netherlands (NWO/ALW), Sweden (VR), Switzerland (SNF), United Kingdom (NERC) and the USA (US NSF, Office of Polar Programs).

CONTENTS

1. ICE CORES AND CONTINUOUS FLOW ANALYSIS – AN INTRODUCTION

Ice cores provide a high resolution archive of past climatic and environmental conditions. Ice cores contain proxies for many different parts of the earth system; water isotopes tell about past temperatures, gases entrapped in the ice reveal the atmosphere of the past and impurities can inform on a variety of components such as sea ice, atmospheric transport, biosphere productivity, forest fires and many more.

Ice cores from Greenland reach back beyond the last glacial period, while their Antarctic counterparts extend up to 800.000 years (yrs) back. Ice cores from both polar regions are as thick as 3 km and thus the temporal resolution in ice core records is high compared to other palaeoclimatic archives such as sediment cores, where a few metres often cover much longer periods.

Continuous flow analysis is one of the methods used to extract information of the impurity content in ice cores. The method provides a rapid determination of mainly ions, while contamination risks are decreased by splitting the sample stream into a clean inner sample stream and a potentially contaminated outer stream. The resolution of such a continuous flow analysis system can be less than 1 cm and thus individual annual layers can be recognized 60.000 yrs back in time and even longer in the 'warm' glacial interstadials, where precipitation was increased as compared to the glacial stadials.[1]

1.1 Ice cores-a climate archive

Ice cores provide a high resolution climate archive. As the snow precipitates onto the large ice caps of Greenland and Antarctica, it remains in its frozen condition if it falls in the dry snow zone. As more and more precipitation accumulates, layers start to compact. If however the snow falls below the dry snow zone, it melts away in part or fully during summer. Thus a build up takes place in the cold central zone, while mass is lost from the margins causing the ice to flow from the center to the margins.

The flow and the weight of above lying snow cause the annual layers deposited to stretch, creating thinner and thinner layers with depth as shown in figure 1.1. Thus the best place for drilling an ice core reaching far back in time is on the ice divide. Here, ideally, layers are flat because stretching occurs laterally in all directions and as there is no melting, even in summer, layers are preserved.

Several parameters, however, complicate the flow. Geothermal heat can cause melting conditions in the bottom of the ice removing the oldest ice layers. The

[1] Part of this chapter is adapted from chapter 1 and 2 of my masters thesis [*Kjær*, 2010].

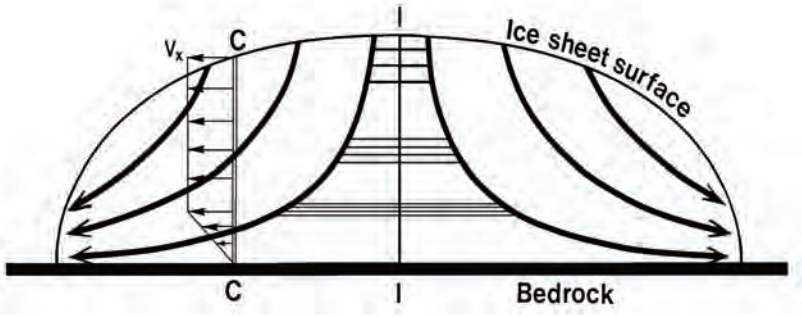

Fig. 1.1: The figure illustrates how the ice flows from the deposition site towards the edges of the ice sheet, making the ice divide (I) an ideal place for drilling, since the deposited snow stays, and flow lines are undisturbed. However bottom melting and bed structures can complicate this picture.

topography of the bottom, with obstacles, boulders and changes in roughness, can change flow patterns and create bumps that penetrate high into the ice. The change in flow, due to the obstacles, can cause folding of ice strata with different ages, causing a mixed climate signal in the very deep ice. Moreover, the geology is not the only cause of folding. Recent evidence from the NEEM ice core and high resolution radar measurements suggest that in Greenland, folding takes place as well in the boundary between the last interglacial ice (the Eemian) and the above lying glacial ice. Difference in rheology of the warm interglacial ice with large ice crystals vis-a-vis the glacial ice with smaller crystal sizes is suggested to be the cause [*Dahl-Jensen et al.*, 2013]. Further, the ice divide positions have changed over time as a result of ice extent and subsequent changes in flow patterns. For Greenland there is evidence that during the last glacial maximum (LGM) the Greenland ice sheet extended onto the outer shelf in Greenland and models find a much smaller extent during the Eemian than at present [*Evans et al.*, 2009; *Kelly and Long*, 2009; *Paterson and Cuffey*, 2010].

As climate has changed over time so have precipitation rates and temperature. This also affects the climate signals recorded in the ice. Precipitation rates affect the rate at which gases are entrapped in the ice and also influence the chemicals deposited by changing the ratios of wet and dry deposition. Changes in temperature can cause melt layers, again affecting the lock in depth of gases [2], but may also modify the chemistry by concentrating some ions, and finally severe melting may altogether remove entire years or redeposit them in deeper crust layers, making the dating of the ice difficult. Fortunately melt layers are relatively easily recognized as layers containing little or no gas.

Ice cores are, however, still the only records to provide direct evidence of gases in the past atmosphere [*EPICA community members*, 2004] and are also a great archive in which preserved annual layers can be determined continuous up to 60.000 yrs back [*Svensson et al.*, 2008].

In Figure 1.2 some deep drillings reaching back to the Eemian in Greenland

[2] The depth at which gases are trapped in the ice. More about this in section 9.1.

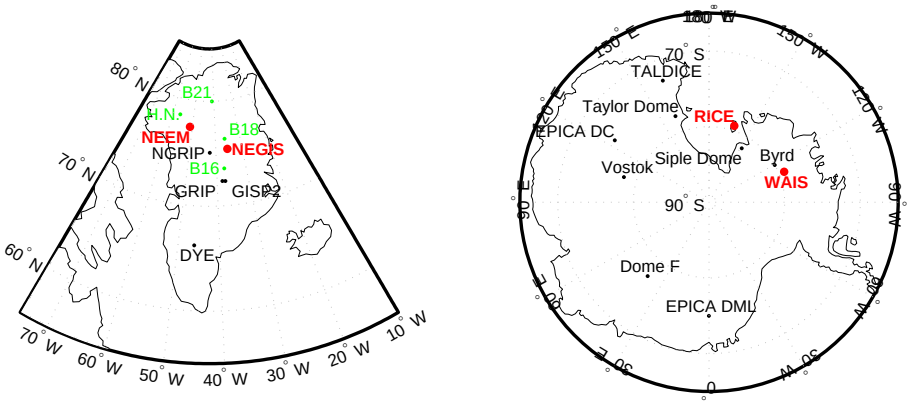

Fig. 1.2: Positions of deep ice cores (black) together with ice cores from which dissolved reactive phosphorus and/or colorimetric acidity (red) has been measured. Also shown are a few shallow cores (green) mentioned within this thesis.

and up to 8 glacial cycles back in Antarctica are shown together with ice cores investigated in this thesis.

1.1.1 Information from polar ice cores

Before ice cores were studied, climate was believed to have been relatively stable over time. Ice cores allows for high resolution climate determinations further back in time than conventional paleo-records and have provided evidence of a highly variable climate, containing rapid fluctuations happening within only a few decades.

Ice cores span a wide range of time scales. The oldest ice core extracted is the Antarctic Dome C, which spans the last 800.000 yrs. In Greenland the oldest cores span back to the Eemian lasting from 130.000 B.P. to 110.000 B.P. In Figure 1.3 the climate record as observed in the Greenland ice core NGRIP is shown.

Ice cores show evidence of a rapid changing climate. From Greenland ice cores evidence of rapid changes between warm glacial interstadials (GI's, also called Dansgaard-Oeschger, DO, events) and glacial stadials (GS) is observed and related to temperature changes exceeding 10 °C. Some of the GI/GS events are related to the Heinrich events. Heinrich events are found in marine sediment cores as a result of increased discharge (ice bergs) from the Laurentide ice sheet. Less pronounced and anti correlated temperature variations are observed in the Antarctic. *Stocker* [1998]; *Stocker and Johnsen* [2003] suggest that this anti-correlation between the two hemispheres is caused by changes in the ocean circulation, termed the "bipolar sea saw".

As an example of rapid changes in the climate system both *Steffensen et al.* [2008] and *Thomas et al.* [2009] find that the polar atmospheric circulation shift 1 to 3 years prior to the initiation of the glacial interstadial (GI) warmings. Based

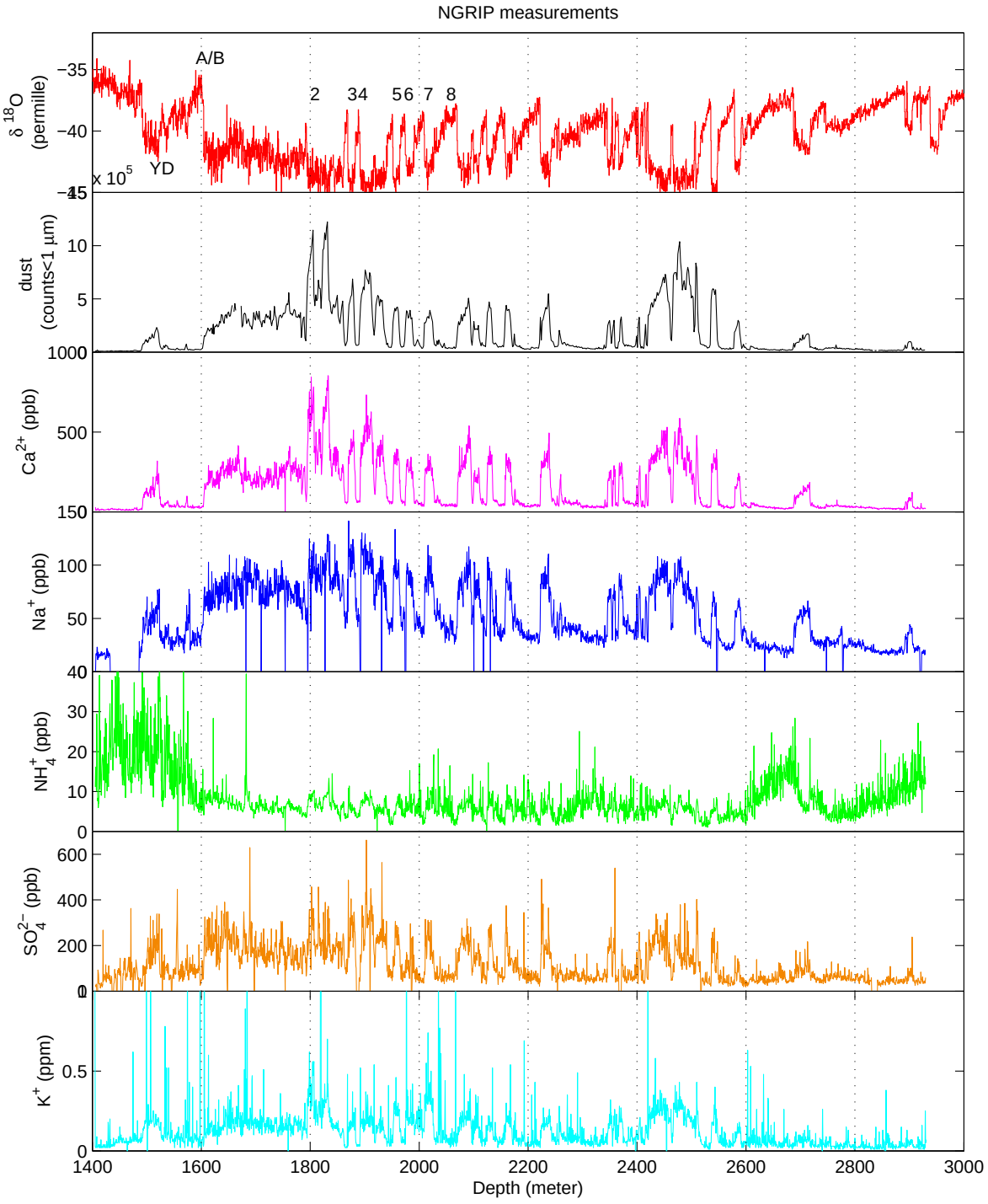

Fig. 1.3: Measurements from the Greenland North-GRIP ice core. Top: δ^{18}O, which is a proxy for temperature. Then dust (black) and Ca^{2+} (pink), which are proxies of dust. In blue Na^{+}, a sea salt proxy. NH_4^+ is a tracer for biogenic land sources (green). In orange SO_4^{2-}, which has various sources including volcanic eruption and finally K^+, which represents a mixture of dust and sea salt and possibly also some biogenic signal such as forest fire. The period covers the last glacial. YD denotes the younger dryas and A/B is the Bølling-Allerød warm period. The numbers denote periods of glacial inter-stadials, more than 8 are present, but the rest are not numbered here [*NGRIP*, 2004; *Ruth et al.*, 2003b].

on evidence from multiple proxies they suggest that the atmospheric loading and dustiness from East Asia (determined by insoluble dust and dust related ions) is the first to change followed by snow accumulation (determined by the annual cycles of e.g. ions), the moisture source conditions (determined by deuterium excess), and finally the atmospheric temperature in Greenland (determined by δO^{18}) [*Steffensen et al.*, 2008; *Thomas et al.*, 2009]. It is possible to obtain such a precise order of events only because multiple proxies are determined in high resolution in ice cores. In the following paragraphs some proxies from ice cores and their interpretation are explained.

Water isotopes are related to the **temperature** gradient between the evaporation and condensation site. The water isotopes are measured relative to a standard of mean ocean water (SMOW) and the $\delta^{18}O = \frac{^{18}O/^{16}O_{sample}}{^{18}O/^{16}O_{SMOW}} - 1$ and δD (similarly defined) are thus to a first order linearly correlated with temperature at the precipitation site [*Dansgaard*, 1964]. The difference between the two water isotopes, the deuterium excess (D_{ex}) [*Craig*, 1961] is driven by the humidity and temperature at the site of evaporation and rapid changes in source regions can thus be inferred from the D_{ex} [*Masson-Delmotte et al.*, 2005; *Johnsen et al.*, 1989]. Furthermore the water isotopes can be calibrated with borehole temperatures. The ice works as an insulator and thus the temperature at the site is preserved albeit smoothed in the ice. The ice temperature can be determined by a thermistor in the borehole after the drill liquid has reached thermal equilibrium with the ice [*Johnsen et al.*, 1995; *Dahl-Jensen et al.*, 1998]. From these direct temperatures and the water isotopes we know from ice cores that the last glacial period ended 11.711 kyr BP and that temperatures in Greenland during the Last glacial maximum were about 20 °C lower than at the present. Multiple lines of evidence also suggest that the last interglacial, the Eemian, was warmer than the present interglacial [*Dahl-Jensen et al.*, 2013]. Furthermore by comparing isotopes from multiple drill sites changes in the ice cap elevation can be inferred [*Vinther et al.*, 2009].

Dust consists of wind borne minerals. These affect climate both directly and indirectly: Direct by scattering and absorption of solar radiation. Indirectly by changing cloud properties, which then affect the radiation budget. Another indirect effect is the fertilizing of the ocean by nitrate, phosphorus and iron, increasing the primary production, which in turn draws down CO_2 and thus affects climate. Dust is regularly determined in ice cores and insoluble dust transported to the ice is a combination of **wind, soil moisture, source area, vegetation cover, transport time** affected by rain out [*Steffensen*, 1997; *Ruth et al.*, 2003]. During the glacial the dust load in the ice cores from both hemispheres increases [*Legrand and Mayewski*, 1997; *Steffensen*, 1997; *Ruth et al.*, 2003]. During the LGM the mean dust flux to Antarctica was 10-15 times higher than during the Holocene, while a 15-20 times higher dust flux was observed in Greenland ice cores [3] [*Fischer et al.*, 2007; *Maher et al.*, 2010]. As an example in the Holocene ice non-soluble dust concentrations of 33 μg/kg were found in the Greenland ice core GRIP, and concentration levels of 0.72 μeq/kg Ca^{2+}, while the last glacial maximum had insoluble particle concentrations

[3] Concentration of insoluble dust determined in the Greenland NGRIP ice was about 80-100 times higher during the LGM as compared to recent Holocene ice, while for the Antarctic ice core Vostok, a 30 to 35 times concentration change of insoluble dust was found

of 7600 μg/kg nonsoluble particles and 31.02 μeq/kg Ca^{2+} [4] [*Steffensen*, 1997]. The cause of the increase is suggested to be a mixture of increased transport due to stronger winds, reduced precipitation causing both drier source areas and increasing transport times, as well as larger source areas [*Fischer et al.*, 2007]. Increased winds and shorter transport times in glacial stadials as compared to glacial interstadials are further supported by a 10% increase in the amount of large dust particles [*Ruth et al.*, 2003]. For Greenland ice cores the glacial provenance of dust is East Asia (the Takla Makan) [*Biscaye et al.*, 1997; *Svensson et al.*, 2000; *Bory et al.*, 2002; 2003], while in the Holocene mineral dust deposited in Greenland is suggested to possibly have secondary sources, such as for example North America [*Lupker et al.*, 2010]. The Antarctic dust originates from Patagonia, with some extra local sources during the Holocene [*Grousset et al.*, 1992; *Basile et al.*, 1997; *Delmonte et al.*, 2007; 2008]. **Calcium** arrives with dust in the Greenland spring [*Whitlow et al.*, 1992], while the Calcium signal in coastal Antarctica is a mixture of both a summer peak of crustal origin and a marine peak in winter time from sea salts. Thus depending on the proximity to the ocean calcium determined in Antarctic ice cores is a proxy for either dust or sea salt [*Legrand and Mayewski*, 1997].

Sea salts determined in ice cores are enhanced in winter time. One would expect sea salt concentrations to be high when the ocean is nearby and not when sea ice covers the ocean. However the high sea salt concentrations in cold periods may be explained by stronger winds or brine or frost flowers forming in newly produced sea ice. Both brine and frost flowers have increased amounts of salt relative to seawater [*Kreutz*, 2007]. Sea salts are enhanced in ice cores in cold periods and are similarly with dust anti correlated to $\delta^{18}O$. The increase in sea salt flux during the glacial is however much smaller than that observed for dust; the salt flux increases by a factor 3 in both Greenland and Antarctica. It is speculated that open sea ice leads and thus newly formed sea ice formation of frost flowers is increased during the glacial and could explain the Antarctic change in sea salt concentrations [*Fischer et al.*, 2007], while for Greenland the cyclonic activity is believed to explain the major part of the increase, making increased frost flowers a minor effect [*Fischer et al.*, 2007].

While sodium and chloride are regarded as being of pure sea salt origin [*Herron*, 1982; *Herron and Langway Jr*, 1985; *Röthlisberger et al.*, 2000; *Bigler et al.*, 2011] other sea salts are masked by other sources [*Legrand and Mayewski*, 1997]. By assuming that either sodium or chloride originates from sea salt only and using the ratio of one of these pure sea salt proxies to the proxy of interest, the non sea salt part (nss) is often determined and used for further analysis. Species which have a partial sea salt signal are for example, Ca^{2+} (7%), SO_4^{2-}(12%), Mg^{2+}(51%) and K^+(27%), where the percentages relate to the sea salt fraction in the Greenland Renland ice core [*Hansson*, 1994; *Kreutz*, 2007].

Another proxy related to sea ice is methansulfonic acid (MSA) [*Abram et al.*,

[4] eq is the equivalent weight of a substance needed to react with one mole of hydrogen ions or one mole of electrons. Basically the equivalent weight of an element is its molar weight times its valence. When a compound is given in mol the weight can be obtained by multiplying with the molar weight of the compound in question. Thus 0.72 μeq/kg Ca^{2+}, which has charge 2 and a molar weight of 40 g/mol, is the same as 0.36 μmol/kg=14.4μg/kg.

2007]. Methansulfonic acid is a product of the atmospheric oxidation of dimethyl sulfate (DMS) produced by phytoplankton. Thus both DMS and MSA relate to the primary production in the oceans. However the correlation to sea ice is explained by the primary production taking place near the sea ice edge as well as due to increased biological activity within brine channels in sea ice [*Legrand and Mayewski*, 1997; *Kreutz*, 2007]. However a recent review about MSA as a sea ice proxy *Abram et al.* [2013] shows that the ice core site selection is crucial if aiming for a sea ice record of past time periods as there are other sources of MSA than just those of the biology related to sea ice. Contrary to both sea salt and dust, the MSA concentration is diminished during the glacial in the Antarctic Siple Dome record. This is surprising as other Antractic ice cores show evidence of increased ocean fertilization by iron, which is suggested to enhance primary production in the southern ocean [*Saltzman et al.*, 2006; *Hiscock et al.*, 2013; *Spolaor et al.*, 2013]. The difference is suggested to be caused by different groups of phytoplankton behaving differently both in terms of iron fertilization and DMS production and thus it seems that DMS is not necessarily a simple record of ocean biosphere productivity [*Saltzman et al.*, 2006]. In the Greenland GISP2 record as well, DMS was lower during glacial times and again the cause is speculated to have been related to differences in phytoplankton speciation [*Saltzman et al.*, 1997].

Another chemical species often measured in ice cores and strongly associated with the **biosphere** is **ammonium**. NH_4^+ is believed to show both soil and vegetation emissions as well as biomass burning and thus the annual peak in Greenland ice cores occurs in summer time [*Legrand and Mayewski*, 1997]. Ammonium is among the very few species which drop to low values in the glacial. NH_4^+ drops by a factor of 5 in Greenland ice cores. It is suggested that the minimum NH_4^+ content found in the period 21 kyr-18 kyr B.P. is caused by the maximum extent of the Laurentide ice sheet, inhibiting soil and vegetation emissions over large parts of North America [*Legrand et al.*, 1992; *Fuhrer et al.*, 1996]. **Biomass burning** events show up as peaks far exceeding the background concentration of ammonium. Another biomass burning proxy is **vanillic acid** and also K^+ peaks peaks are speculated to be related to biomass burning [*Hansson*, 1994; *McConnell et al.*, 2007]. Several organic acids are also proposed to originate from biomass burning and vegetation emissions, however often secondary aerosols are produced during transportation of organics complicating the interpretation [*Legrand et al.*, 1992]. Organic acids as tracers for the biosphere are discussed further in section 10.

As discussed above sulphuric acid not only originates from sea salt, but also from primary production. Sulphuric acid shows peaks both in spring and summer [*Legrand and Mayewski*, 1997]. To further complicate matters the non-sea salt sulphuric acid signal observed in ice cores is also influenced by **volcanic eruptions** causing large peak increases far above the baseline [*Zielinski et al.*, 1996; *Kreutz*, 2007; *Sigl et al.*, 2013] and furthermore recent **anthropogenic changes** in the atmospheric load of sulphuric acid are observed with one increase from 1850 peaking in 1910 and a second one from 1950 to the 1970's followed by a slow decrease onwards until today. The pattern is explained by the industrialisation in North America and Europe [*Herron*, 1982; *Neftel et al.*, 1985]. NOx (NO_3^-) is another proxy showing a similar increase due to increased industrial processes and fossil fuel use [*Neftel et al.*, 1985]. Though

nitrate clearly shows evidence of anthropogenic impacts, its underlying signal is speculated to originate from multiple sources including oxidation of ammonia and N_2O [*Herron*, 1982] and extraterrestrial lightnings [*Herron and Langway Jr*, 1985; *Legrand and Kirchner*, 1990]. There are many other proxies also showing an increase in recent time as a result of anthropogenic impact; It has for example been observed that the amount of heavy metal (Pb) increased until it became obligatory for cars to have exhaust filters and Pb was removed in gasoline, while black carbon increased seven fold (in Greenland) during the industrial revolution [*Schwikowski et al.*, 2004; *Kreutz*, 2007; *McConnell et al.*, 2007;b].

For any climatic story to be inferred from ice cores it is of crucial importance that the **dating of the ice** be accurate, especially if ice cores from different sites are to be compared. In Greenland **annual layers** can be identified up to 60.000 yrs BP [*Svensson et al.*, 2008]. Further back in time annual layers are also identified in some of the warm GI periods, when the precipitation is increased as compared to the cold GSs [*Vallelonga et al.*, 2012]. As an example the Greenland timescale, GICC05, is based on annual layer counting back to 60 kyr BP, and the maximum counting error of the chronology ranges from 4% in the warm GI periods to 7% in GS [*Andersen et al.*, 2006]. In the deeper ice flow models, such as the Dansgaard-Johnsen flow model – also known as the kink model [*Dansgaard and Johnsen*, 1969], are used to estimate the layer thinning and thus the age of the ice core at depth. Another method that works deeper in the ice is the relative amount of oxygen over nitrogen molecules in the air to the local summer insolation. The method of O_2/N_2 has been used to date Antarctic ice cores 360.000 yrs of age [*Kawamura et al.*, 2007]. Using this method to date older ice might be impossible due to diffusion removing the difference between the two gases [*Bereiter et al.*, 2014].

Besides the annual layer counting, **reference layers** such as layers with deposited volcanic material (eg. identified by sulphate, acidity or tephra) [*Svensson et al.*, 2008] and cosmogenic isotopes, such as ^{10}Be and ^{36}Cl are used to for example transfer the Greenland time scale GICC05 based on high resolution data to Antarctic records where the annual signal cannot be resolved because of limited precipitation. ^{10}Be and ^{36}Cl are produced from the interaction of the cosmic rays with the atmosphere and thus represents a global signal [*Beer et al.*, 1990].

Time scales can also be transferred between ice cores by aligning layers of rapid transitions, such as for Greenland the change from GS's to GI's [*Svensson et al.*, 2008]. Further, methane is a global gas with a relatively short atmospheric lifetime and is also used to cross date ice cores [*Chappellaz et al.*, 1993].

1.2 Continuous flow analysis (CFA)

Conventional chemical analysis of ice cores relies on complicated and time consuming cleaning procedures. Continuous flow analysis offers high temporal resolution combined with reduced handling of the core, minimizing the time consumption as well as the contamination risks.

Several such continuous flow analysis (CFA) systems have been developed in the recent decade after the pioneering work of Sigg et al. [1994]. The CFA method for ice cores was initially a system developed for measuring concentrations of ions. The

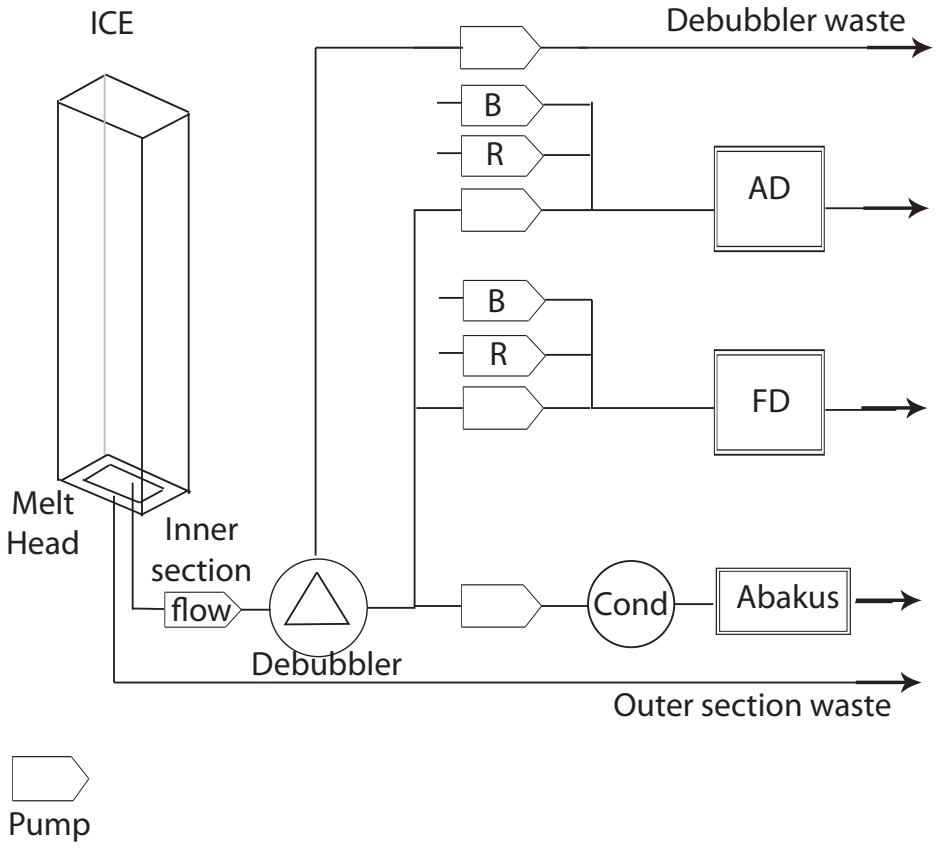

Fig. 1.4: Schematic of a continuous flow analysis (CFA) system. The ice is melted and the melt water split in an inner and an outer flow. The inner flow goes through a debubbler and is split into various detection lines. Conductivity (cond.) and dust (Abakus) are measured. To other lines a reagent (R) and in some cases a buffer (B) are added before determination by absorption (AD) or florescence (FD) techniques.

most recent systems, however, also add semi-discrete analysis systems [Osterberg et al., 2006; McConnell et al., 2002] and continuous determination of gases[Federer et al., 2009; Stowasser et al., 2012; Rhodes et al., 2013; Chappellaz et al., 2013] and water isotopes [Gkinis et al., 2011] using cavity ring-down spectrometers.

This section introduces CFA and CFA techniques for the determination of various chemical species. Further the specific CFA systems used as part of this project are introduced and differences between them are discussed (section 1.2.4).

1.2.1 Key components in a CFA system

A CFA system generally consists of a melt head, which continuously melts the ice splitting it into two (or more[*McConnell et al.*, 2002]) streams; an inner part used for analysis of highly sensitive chemical compounds and an outer part going to waste or to non sensitive systems (eg. water isotopes). A schematic illustration of a simple CFA system for determining ion concentrations is shown in figure 1.4.

The liquid from the inner part is debubbled to remove air from the water and

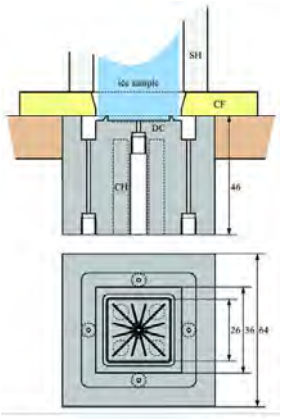

Melt heads.

(a) Copenhagen type melt head

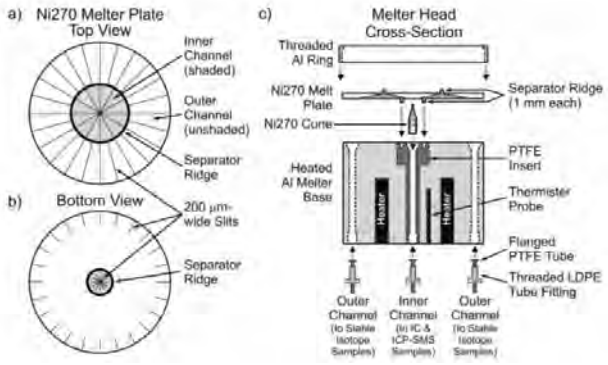

(b) NIPR and AWI type melt head

Fig. 1.5: (a) The melting device used in the Copenhagen set-up [Bigler et al., 2011]. (b) The melt system used at NIPR, Japan and at AWI, Germany [Osterberg et al., 2006; Dallmeyr et al., 2014]. Note that the inner and outer parts are separated in both systems to avoid contamination and that both melt heads have narrow slits to prevent capillary effects in the ice smoothing the signal. Figures are from Bigler et al. [2011] and Osterberg et al. [2006].

make the flow steady. In some systems the air is used for continuous determination of gases (eg. methane[*Stowasser et al.*, 2012; *Rhodes et al.*, 2013; *Chappellaz et al.*, 2013]), while in other systems it discarded.

After the removal of gas the clean water flow sample is split into different detection lines. For the determination of ions each line typically has a flow rate of 1 mL/min. These low flow rates are necessary because of the small quantities of ice available. Dust and conductivity are measured directly in the water stream, while different ions are measured after adding reagent and buffer using either an absorption or a fluorescence method [*Sigg et al.*, 1994; *Röthlisberger et al.*, 2000; *Kaufmann et al.*, 2008]. In some cases part of the water stream is collected in bottles for discrete samples, while in other situations semi-discrete methods are implemented [*Osterberg et al.*, 2006]. Also continuous methods, not based on simple absorption and fluorescence techniques, have recently been developed, such as methods for detecting black carbon (BC)[*McConnell et al.*, 2007] and total organic carbon (TOC) [*Federer et al.*, 2008].

In the following the key components of a CFA system is explained and examples from different systems are provided and in appendix C an outreach article on CFA intended for Danish high school kids (in Danish) co-written with David Baslev-Clausen can be found.

Melt head

The melt head should provide a non reactive chemical surface, and have a design, which ensures that as little mixing as possible occurs and at the same time avoids contamination from the outer part of the core. A schematic of a melting device can be found in figure 1.5.

The ice is placed in a core holder above of the melt head and pressed down by its own weight and sometimes also by additional load. The melt head is heated to temperatures between 15 and 48 °C depending on the number of analytes and on the desired time resolution [*Sigg et al.*, 1994; *Röthlisberger et al.*, 2000; *Kaufmann et al.*, 2008].

The melt unit can be made from many different materials and have many different shapes. It is important that the melt head is chemically inert; however there is a trade off to costs and heat transfer of the material used. Early melt heads by *Sigg et al.* [1994] and *Röthlisberger et al.* [2000] used a melt head made in aluminium and surface coated with PTFE, while *Kaufmann et al.* [2008] made a chemical inert surface by electroless nickel plating a copper melt head 5 μm and covering it with a layer of 2 μm gold. The Copenhagen system employs different melt heads depending on the purpose of the study.

The melt stream is split in an outer and an inner part by a barrier of 0.5 to 1 mm height on the melt head. The suction in the inner section is less than the amount actually melted in the inner section, thus creating an overflow of about 10% to the outer section. This is beneficial for avoiding contamination of the inner part. Conversely, of course, there is a need to preserve as much water as possible for measurements.

The square of the inner melt section is from 10 x 10 mm^2 to 26 x 26 mm^2. The melt head used at the Desert Research Institute in Reno operates with two inner sections, where the inner most section is used for high purity ICP-MS determination and the second inner ring is used for conventional CFA systems such as dust, conductivity, ammonium and nitrate [*McConnell et al.*, 2002].

Recent melt heads have more than one hole holes for the water to be sucked through from the outer part of the sample. Multiple tubes reduce the mixing on the melt head, however this at the same time requires that the length of the tubes and suction on the tubes be similar, because they are often assembled further down the line.

For firn melting it is important to keep a relative high suction and melt rate because of capillary forces in the ice dragging the water back into the ice during melting and thus diminishing the temporal resolution of the measurements. To avoid this smoothing of the signal, melt heads with several radial narrow slits are used to make the capillary force in the melt head larger than those in the ice[*Röthlisberger et al.*, 2000; *Osterberg et al.*, 2006; *Bigler et al.*, 2011].

Melting speed sensor

The melt speed is determined by the power to the melt head (controlling the temperature) and to a second degree by the overlying weight on the ice. Conventionally the melt speed is measured by an optical encoder (eg. Baumer electric [*Sigg et al.*, 1994]). This encoder measures the movement of a string that is attached to the above lying load and as the ice melts the position of the line shortens. This kind of encoder has been used in multiple CFA systems including the Copenhagen and the Bern systems [*Röthlisberger et al.*, 2000; *Bigler et al.*, 2011].

Though such a system works to great precision it is not ideal, if one wants to stack ice pieces continuously. Sections of ice vary in lengths and in order to gain

high throughput and in order to obtain high resolution continuous gas measurements often when one ice sample of eg. 55 cm (called a bag) is almost melted the next is added on the top. However this requires the load to be moved away and thus there is no depth control during the addition of the new sample.

Alternatively a laser can be used to determine the melt speed. A laser positioned in the top of the freezer shines down upon the ice, or the load and the time for the reflectance to come back is recorded [*Dallmeyr et al.*, 2014]. However determining the melt speed by laser has disadvantages as well, such as reflections and refractions from the core holder and potential misalignments after addition of new samples causing the reflected signal to not reach the instrument. Both these errors are typically only temporary and depending on the exact laser system used to determine the melt speed results can be steady. New developments into image recognition as a means for determining melt speed are currently being undertaken ans is used at the Desert Research Institute, Reno, Nevada (personal communication Paul Vallelonga). The idea is that as ice is "striped" by annual layers in recent periods and by dust events during the glacial using image pattern recognition could provide the melt rate by simply following specific patterns found in the ice. While also laser systems, similar to encoder melt speed detection, are affected when stacking, camera melt speed recordings would not be disturbed by stacking of cores, because such a camera would not look on the top of the core, but rather on the side of a core.

Debubbler

Another central unit of a CFA detection system is the debubbler used to remove from the water stream the about 10% air naturally found in ice. In early systems, the air sample was not used and thus an "open" pipette type debubbler was applied (Figure 1.6, left). An example of a simple open debubbler is a modified pipette tip. By having the sample stream (still mixed with air) dripping into the pipette and a suction on the lower narrow part of the pipette, the air is released to the ambient atmosphere and the air is removed from the water sample. To such an open pipette type debubbler a lid (with holes) may be applied to shield against contamination from the laboratory.

However recent developments in gas determination modules, such as cavity ring down spectroscopy (eg. Picarro [5]), has called for sealed debubblers [*Kaufmann et al.*, 2008; *Bigler et al.*, 2011]. This type of debubbler can also be made in a pipette design, however with the difference to the open debubblers that they are sealed with an air tight lid, and that the gas has a flow line as well. They can be designed as flat triangular cells as done by *Bigler et al.* [2011], see Figure 1.6 right, with one inlet and two outlets (one for the water and one for the gas). *Bigler et al.* [2011] found that an equilateral triangular cell with side length 10 mm and depth of 2 mm gave good results and also had a very small mixing volume, a mere 90 μL.

Clearly also the mixing volume of conventional debubblers (pipette types) can be limited by optimizing flow rates. The mixing in a sealed debubbler is controlled by the volume of the cavity of the debubbler. However in the open debubblers the volume can vary with the air content of the ice affecting the mixing of the sample.

[5] More on this device below.

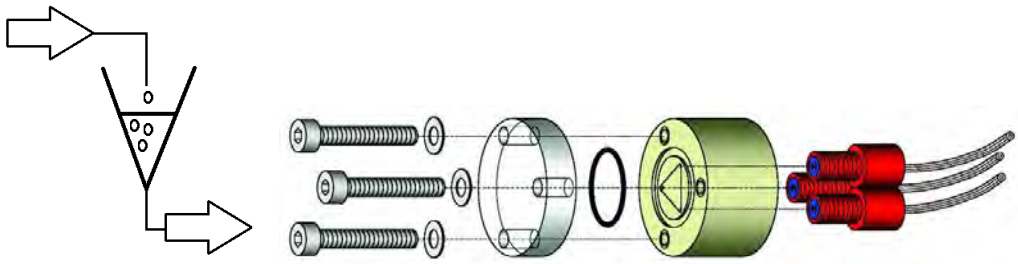

(a) Open debubbler (b) Sealed debubbler

Fig. 1.6: Debubblers used to separate the approximate 10% gas naturally found in the ice from the water stream used for analysis. *(a) illustrates an open pipette type debubbler as used by [Dallmeyr et al., 2014], while (b) show the debubbler used in the Copenhagen CFA set up [Bigler et al., 2011] the figure is from Bigler et al. [2011].*

In order to avoid this temporal difference in the mixing the newly developed CFA system at NIPR, Tokyo, Japan has an open type debubbler unit on top of a scale. The scale controls an extra waste line attached to the bottom sample flow stream and this extra waste is pumping fast, when water level in the debubbler is high and slowly when water level is low, thus attempting a stable water volume in the debubbler [*Dallmeyr et al.*, 2014]. Also *Breton et al.* [2012] work with a variable flow speed from the debubbler in that case it is however done to ensure all water is used and as a result the mixing as well as the dispersion in the system varies with time – something to take into account when later analysing the signal as it changes the time it takes for the sample to reach the detection unit.

1.2.2 Individual detection methods for CFA systems

After splitting water and gas sample at the debubbler unit the samples are analysed for multiple environmental and climate proxies using a variety of detection systems. Two of the measurements almost always performed are dust and conductivity measurements. These are non-destructive methods and thus the water sample can be used for determination of other chemical species too. Traditionally chemical species are determined continuously using fluorescence or absorption techniques. Newer developments for total organic carbon and black carbon also provide truly continuous detection systems and ring down spectroscopy instruments are available for water isotopes and methane. Furthermore semi-continuous ICP-MS set-up are used to determine many elements "on line" and discrete sampling based on CFA systems avoids time consuming rinsing of discrete samples prepared directly from the ice. The following section present CFA determination methods of some climate and environment related proxies. This is not to be seen as a complete compilation of all methods available to ice core CFA systems, but is rather a brief introduction to the general ideas behind some of the determination methods.

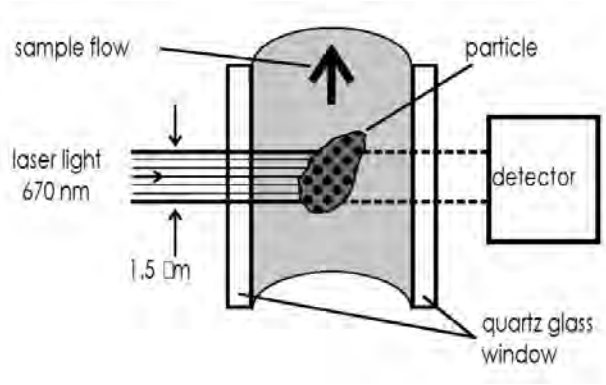

Fig. 1.7: Detection cell of the Abakus laser sensor. Figure from Ruth et al. [2003].

Conductivity

The melt water electrolytic conductivity (MWEC) gives a bulk signal of all the major ions. In Greenland ice cores it often resembles the dust signal, because the Ca^{2+} ion is the most predominant, while in coastal Antarctic ice cores it follows the sea salt signal as Cl^-, Na^+ are dominant. The conductivity further indicates volcanic eruptions as the SO_2 from these increases the conductivity [*Röthlisberger et al.*, 2000]. The conductivity can be determined in very high time resolution. Further the instrumentation is cheap and the method non-destructive and thus a conductivity cell in front of multiple other detection units can be used to align various detection techniques post determination and thus enhance depth control.

Dust detection

Insoluble mineral dust particles are measured by an attenuation principle, typically using a so-called Abakus (Klotz GmbH, Germany) [*Ruth et al.*, 2003; 2008; *Lambert et al.*, 2012]. In Figure 1.7 the principle of detection is illustrated. The water stream that enters the Abakus has to go through a narrow channel and in theory only one dust particle at the time can enter the channel. A laser (670 nm) is mounted orthogonal to the flow and a detector sits on the opposite side of the flow. The particles are detected by counting the number of times the laser signal shuts off due to a particle blocking the light. A precise flow is needed to transfer the results in [particle counts/sec] obtained by the Abakus into [particle counts/cm] for that purpose a flow meter is normally positioned right after or just prior to the Abakus. The size distribution of the insoluble particles is determined by detecting the scattered light and using a comprehensive algorithm made by comparing Abakus measurements to a Coulter counter[6]. However, as geometric shadowing is only dominant for particles larger than 7μM, but the mode distribution is smaller in ice, *Kettner* [2014] found evidence that transfer algorithms between the scatter found in the Abakus and the Coulter counter are not similar over time nor between different Abakus instruments.

[6] A Coulter counter is a discrete and more precise way of measuring particles and their size distribution based on the electrical impedance of the particles as they pass through an orifice.

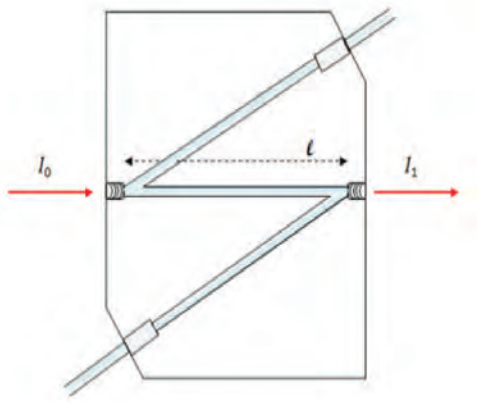

Fig. 1.8: The figure show an example of a flow through absorption cell [Nielsen, 2009].

Ions

As mentioned above, after the addition of a reagent and sometimes a buffer the concentration of ions can be determined by absorption or fluorescence techniques.

Absorption detection methods all have in common that the fluid concentration of the species in question is measured by the absorption of light. The fluid is led into a waveguide of length l and the intensity of incoming light (I_0) is absorbed so only a smaller fraction makes it through (I). Figure 1.8 illustrates such a waveguide. Absorbance (Abs) is given by the Beer-Lambert equation:

$$-\ln(\frac{I}{I_0}) = \sigma \cdot N \cdot l \tag{1.1}$$

where N is the number of absorbing molecules (molecules/cm^3), σ is the cross section of light absorption by a single particle (cm^2) and l is the path length (cm). We can also write:

$$-\ln(\frac{I}{I_0}) = \varepsilon'' \cdot l \cdot c \tag{1.2}$$

where the molar concentration c (M=moles/liter) is given by c= $N/N_A \cdot 1000$ cm^3/L, where $N_A = 6.02214 \cdot 10^{23} mol^{-1}$ is Avogadros constant and where ε'' is the wavelength dependent molar absorptivity to base e (in M^{-1}cm^{-1}). Conversely $\sigma = (\varepsilon''/N_A) \cdot 1000$ cm^3/L. In the chemical literature one usually finds:

$$-\log_{10}(\frac{I}{I_0}) = \varepsilon \cdot l \cdot c = Abs \tag{1.3}$$

in terms of ε, the wavelength dependent molar absorptivity to base 10 (in M^{-1}cm^{-1}), where $\varepsilon = \varepsilon''/\ln(10)$ and $\sigma = (\varepsilon \cdot \ln(10)/N_A) \cdot 1000$ [cm^3/L].

Note that an increase in length of the cell provides a better limit of detection.

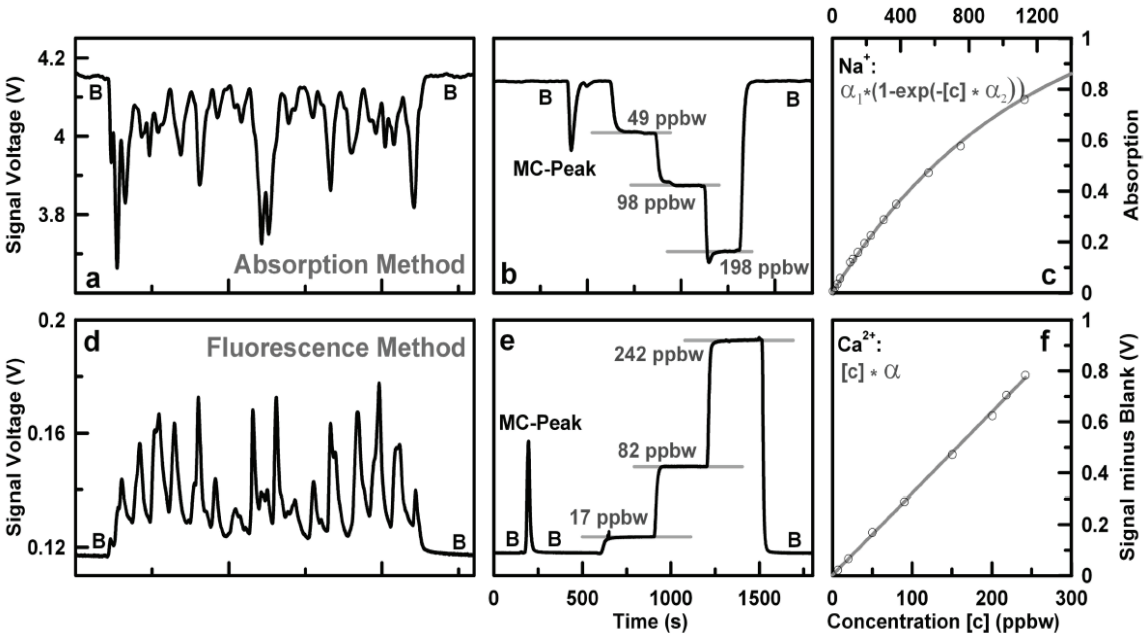

Fig. 1.9: The top row shows absorbance (a,b,c) and the bottom row (d,e,f) shows floures-ence. a) and d) is examples of raw signals measuring a 110 cm ice core. B denotes blank-sample without the species of interest. b) and e) is example of standards used for calibration. c) and f) show typical calibration series. Figure from Kaufmann et al. [2008].

The combined factor of $\varepsilon \cdot l$ can be determined using standards of known concentration. The absorption is found by the difference between detected light in a sample without the chemical substance to be determined (eg. MilliQ water, Millipore) and a sample (eg. natural ice) with the species we want to determine. Thus concentration can be found using equation 1.1. It should be noted, however that the Beer Lambert linear relationship between absorption and concentration breaks down at high concentrations (>0.01 M). Further in the case shown in Figure 1.9 the relation between absorption and concentration is exponential and does thus not follow the linear relationship from Beer Lambert. The exponential relationship for Na^+ is caused by the use of an immobilized enzyme reactor in the set up.

Examples of ions measured in ice cores using a CFA absorption method are Ca^{2+}[*Sigg et al.*, 1994], Na^+ [*Röthlisberger et al.*, 2000], NO_3^-[*Röthlisberger et al.*, 2000] and SO_4^{2-} [*Bigler et al.*, 2007; *Röthlisberger et al.*, 2000].

Also **fluorescence detection techniques** are often applied to determine ion concentrations. The technique relies on the molecule in question being excited by photons to a higher energy state. When the molecule again decays to the ground state a photon is emitted. The emitted photons, will have a different energy than the absorbed photons and thus the detection can be done at a different wavelength from the wavelength used to excite the molecule. The emission intensity is often detected using an optical filter to ensure only the emitted light is detected. Similar to the absorption methods a set of standards are run to create a, in the case of fluorescence, linear calibration between concentration and emission intensity subtracted

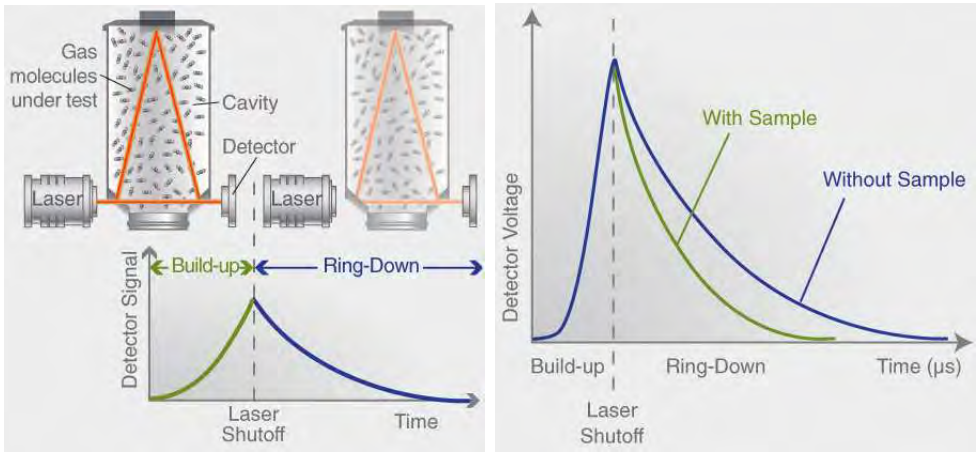

(a) (b)

Fig. 1.10: Cavity Rings Down Spectrocopy. Figure from Picarro [2014] website.

the intensity causing the excitation (Figure 1.9(f)).

Examples of the fluorescence method is presented in figure 1.9 (bottom). H_2O_2[*Sigg et al.*, 1994], HCHO [*Sigg et al.*, 1994], Ca^{2+}[*Röthlisberger et al.*, 2000] and NH_4^+ [*Sigg et al.*, 1994] are all species that can be determined using fluorescence techniques.

For more information on the specific absorption and fluorescence detection methods I will refer to the original articles [*Sigg et al.*, 1994; *Röthlisberger et al.*, 2000; *Bigler et al.*, 2007] or for a summary on the techniques used as part of the Danish CFA system to the thesis of Ernesto Kettner chapter 2 [*Kettner*, 2014].

Cavity ring down spectrometers

Cavity ring down spectrometers (CRDS), *eg.* from Picarro Instruments, have made possible the continuous measurements of CH_4 [*Stowasser et al.*, 2012; *Rhodes et al.*, 2013; *Federer et al.*, 2009; *Chappellaz et al.*, 2013], CO_2, and water isotopes [*Gkinis et al.*, 2010; 2011]. Nearly every small molecule has a unique near infra-red spectrum and thus in theory the concentration of any molecule can be determined by looking at the absorption at a wavelength specific for the molecule in question. However the absorption is normally slight and thus difficult to determine in standard absorption cells. In CRDS (see Figure 1.10) a laser beam of a specific wavelength enters a triangular cavity. In the corners of the cavity mirrors reflect the light making the actual path length exceed km length, while keeping the internal sample volume (the cavity) small. The mirrors are slightly transmissive. When a photodetector reaches a certain threshold the laser is shut off. If the cavity is empty the time it takes the light intensity to reach zero is dependent only on how much is transmitted through the mirrors. However with the cavity containing, *eg.* methane, the time it takes to "ring down" is also dependent on the absorption and thus will occur faster. The difference between the ring downs is thus dependent on the concentration of the molecule in question [*Picarro*, 2014; *Stowasser et al.*, 2012].

Other CFA techniques applied on ice cores

Black carbon can be determined continuously using a single particle soot photometer SP2 (*eg.* Droplet Measurement Technologies, Boulder, Colorado). Light absorbing particles, such as black carbon, are heated to the point of incandescence by an Nd:YAG[7] laser. The incandescence can be correlated to the mass of black carbon using proxies of soot, such as Aquadag or fullerene soot. Further similar to the scatter measurements in the Abakus, single light scattering is also determined in the SP2 and thus also particle sizes and individual particles of black carbon mixing state can be inferred [*McConnell et al.*, 2007]. Black carbon shows a clear annual cycle in the ice and high resolution of the method (single particles are detected) makes it possible for finding annual layers at depths comparable to conventional CFA absorption and fluorescence techniques.

Inductively Coupled Plasma Mass Spectrometry (ICP-MS), which determines concentrations of specific elements and **Ion Chromatography (IC)** are useful for obtaining concentrations of multiple species in the same sample. Unfortunately some of these conventional chemistry determination techniques can not be implemented in a CFA system in a truly continuous way. However CFA systems are often used with an **autosampler** to collect clean discrete samples for later analysis in IC [*Traversi et al.*, 2002; *Cole-Dai et al.*, 2006] or ICP-(SF)MS (or other detection techniques) minimizing time consuming cleaning processes [*Kaufmann et al.*, 2008; *Osterberg et al.*, 2006].

The main problem for many instruments is the time it takes to determine concentrations of a sample. To deal with this in some CFA systems multiple instruments are implemented and by using a switch valve the sample is led first to one instrument then to the other and this way improving the resolution by a factor 2. This kind of split set up was for example used for the fast IC detections in the NEEM ice core optimizing resolution from 8 cm to 4 cm.

Some ICP-MS systems can also work in a continuous set up, though there is a trade-off between the concentration levels that can be resolved and the time available for the sample to be determined. Such a CFA ICP-MS set up is used at the Desert Research Institute in Reno, Nevada [*McConnell et al.*, 2002]. Some issues with ICP-MS systems using quadrupole-based mass analyzers (ICP-QMS) are the ppt range isobaric interference between two different elements or molecular species with the same mass-to-charge ratio. Oxides can cause isobaric interferences as well [*McConnell et al.*, 2002]. The isobaric interferences are not a problem for sector field ICP-SFMS systems as they rely on both electrical and magnetic focussing.

1.2.3 Dispersion in the CFA system

Within the CFA system some dispersion is unavoidable (see Figure 1.11). The dispersion is not necessarily similar for individual detection units and is influenced by reaction time (mixing length), absorption cell length among others. Though dispersion can to some degree be limited by optimizing the set up. The dispersion in relation to the melt head itself is unavoidable. As in the worst case the dispersion may erase the annual layer signal (important for dating) and causes faulty

[7] Neodymium-doped Yttrium Aluminum Garnet

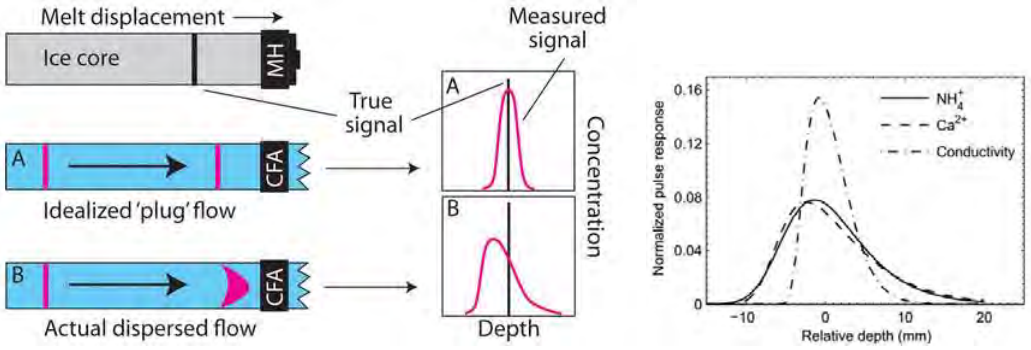

Fig. 1.11: Dispersion in the CFA system. 1.11(a) illustrates the difference between idealized plug flow dispersion and the true dispersion seen in the signal. 1.11(b) show the dispersion observed in a CFA system for NH_4^+, Ca^{2+} and Conductivity. Figures are from Breton et al. [2012] and Rasmussen et al. [2005] respectively.

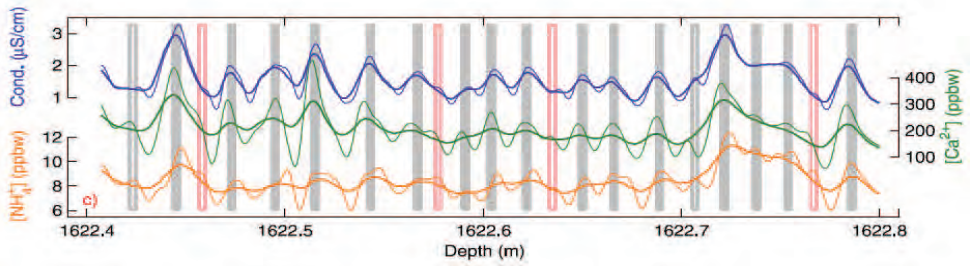

Fig. 1.12: The figure show an example of original (thick lines) and deconvoluted (thin lines) data. Figure from Rasmussen et al. [2005].

conclusions on leads and lags a correction is necessary. **Deconvolution** of the data can restore annual signals [*Rasmussen et al.*, 2005] as shown in Figure 1.12 and in some cases more detailed studies following individual liquid parcels (δ-peaks or step functions) and their dispersion through the system are undertaken [*Breton et al.*, 2012].

In the case of most of the above mentioned CFA detection methods, some standard calibration is performed. This calibration essentially provides a step function, which is adequate to make a filter, which can be used to de-convolute the data. The standards used for calibration are, however not introduced at the same position as the ice. Hence only restoration of details lost through mixing coming in the part after standard introduction can be accounted for [*Rasmussen et al.*, 2005]. Though a deconvolution using a filter as suggested by *Rasmussen et al.* [2005] obtains much of the original signal the method by *Rasmussen et al.* [2005] does assume that the peak position does not change as a parcel moves through the CFA system. This is not the case as mixing in the fluid or vessel due to gravitational changes, variable velocity field in the tube with higher velocities in the center and lower velocities at the edge due to friction etc. cause the flow to behave in a non ideal way.

In order to correct for the non ideal flow *Breton et al.* [2012] have developed an algorithm to track the dispersion of a parcel of water (**parcel tracking algorithm**).

This algorithm does not do a better job in deconvoluting the data, but optimizes the method by *Rasmussen et al.* [2005] by adding a third filter allowing for variable peak position in the dispersed and original flow. However the parcel tracking algorithm requires more information about the specific CFA system in question than needed for deconvolution and obtaining the data necessary to run the parcel tracking algorithm is a time consuming task involving measurements of the dispersed peak multiple places in the CFA system.

1.2.4 CFA systems used as part of this thesis

Four CFA systems were used for measurements performed as part of this PhD project; the CFA-Copenhagen [*Bigler et al.*, 2011] was used for the NEGIS firn core (pH and PO_4^{3-}), CFA-Copenhagen-NZ for the determination of the RICE ice core (pH), CFA-NIPR [*Dallmeyr et al.*, 2014] for the continuous determination of dissolved reactive phosphorus as well as collections of discrete samples for determination of total phosphorus (ICP-MS) and phosphate (IC) and finally the CFA-Bern system was used in 2010 to determine acid labile phosphorus. Table 1.1 shows technical details of the four CFA systems. Further for completeness the CFA system used at the Desert Research Institute, DRI, Reno, Nevada CFA system [*McConnell et al.*, 2002] is also included as I had the opportunity to work with the system in February 2012 as part of the WAIS campaign.

The North East Greenland Ice Stream (NEGIS) firn core melting campaign took place in Copenhagen. The **Copenhagen CFA system** [*Bigler et al.*, 2011] was set up to determine pH, PO_4^{3-}, NH_4^+, Na^+, dust (with an ABAKUS), and conductivity. The goal in the Copenhagen system is to achieve very high temporal resolution. To do this the melt speed and flow is kept low, but still sufficient that all detection units get enough water. The Copenhagen CFA system measures 55 cm [8] ice pieces at a time and it takes approximately 35 minutes. The mean melting speed is about 1.5 cm/min. Standards for calibration were measured after every 4th ice piece of 55 cm. The Copenhagen CFA stick is 34 x 34 mm large and is divided in two sections. The inner section used for detection is 26 x 26 mm.

A modified version of the Copenhagen CFA system, **CFA-Copenhagen-NZ**, was applied in New Zealand for the determination of pH, Ca^+, melt water conductivity, and dust in the Roosevelt Island Climate Evolution (RICE) ice core. Further to this system was attached a methane detection system (Picarro), and many discrete samples were obtained for high resolution determination using ICP-MS and IC. Because of the discrete sampling, the melt rate had to be higher than used for the determination of the NEGIS firn core and 4 times 100 cm pieces were measured in between calibrations to avoid losing a lot of the methane sample, as a result of long response times in the instrument when changing from measuring ice core sample air to ambient air.

The **Japanese CFA-NIPR system** [*Dallmeyr et al.*, 2014] evolved during the campaign. It differs from the other systems by having an open debubbler, where the volume is controlled by a weight and by the melt rate being determined by a laser

[8] The length of a piece of ice depend mainly on the boxes used for transport and is referred to as a bag. For the NEEM ice core a bag is 55 cm. For the RICE ice core a bag was 100 cm.

Tab. 1.1: Comparison between different CFA systems used to determine colorimetric acidity and phosphate as part of this thesis. The table show the difference between the Bern CFA system[*Kaufmann et al.*, 2008] used for the NEEM deep ice core in Greenland, which is optimized for many species, the Copenhagen CFA system [*Bigler et al.*, 2011] used for the NEGIS firn core, which is optimized for high resolution. The Japanese CFA-NIPR system [*Dallmeyr et al.*, 2014] that was also used for sections of the NEEM ice core. Also shown is information on the modified CFA-Copenhagen system used during the measurement campaign on the RICE ice core in New Zealand as well as on the Desert Research Institute CFA-DRI system[*McConnell et al.*, 2002] used on the Antarctic WAIS ice core.

CFA system		**Bern**	**Copenhagen**	**Copenhagen-NZ**	**NIPR**	**DRI**
Melt head	*material*	Copper, electroless nickel (5μm), gold coated (2μm)	Aluminium	Copper, gold coated (3μm)	Aluminium, Nickel coated(3 mm)	Aluminium, Nickel coated
Inner section	*side length*	24 mm	26 mm	26 mm	20 mm	1st 14 mm, 2nd 23 mm
	suction holes	one central	one central	one central	4	1st one central, 2nd two concentric
Outer section	*side length*	36 mm	34 mm	34 mm	34 mm	40 mm
	suction holes	4 concentric	4 concentric	4 concentric	1	4 concentric
Melt speed		3.5 cm/min	1.5 cm/min	3.2 cm/min	1.6 cm/min	5.5 cm/min
Overflow		20 %	10 %	10%	10%	-
Sample length		110 cm	55 cm	100 cm	55 cm	100 cm
Measuring time	*per sample*	32 min	36 min	31 min	35 min	18 min
Inner sample flow rate		15.2 mL/min	6.7 mL/min	16.8 mL/min	6.5 mL/min	-
Debubbler		sealed	sealed (90 μL)	sealed (90 μL)	open 400 μL	sealed
Melting speed sensor		optical encoder	optical encoder	optical encoder	laser	optical tracking
Load			200 g	200 g	750 g	-
Conductivity		Yes	Yes	Yes	Yes (multiple)	Yes (multiple)
Dust particles		Yes	Yes	Yes	Yes	Yes
Total air content		Yes	No	No	No	-
Continuous species		BC, Na^+, NH_4^+, SO_4^{2-}, Ca^{2+}, NO_3^-, H_2O_2, HCHO, δO^{18}, δD	Na^+, NH_4^+, SO_4^{2-}	pH, Ca^{2+}, δO^{18}, δD	PO_4^{3-}, δO^{18}, δD	BC, TOC, PDA, NH_4^+, NO_3^-, δO^{18}, δD
Discrete samples		Yes, also semi discrete ICP-MS x 2	No	Yes	Yes	Semi discrete ICP-MS x 2
Gases		Yes (methane)	No	Yes (methane)	No	Yes

instead of an optical decoder. This causes the melt rate to be better controlled. The melt head differs from the Copenhagen and Bern melt heads. The melt head used in the NIPR CFA system is circular and similar to that used by University of Maine [*Osterberg et al.*, 2006]. The system was set up to determine dust (ABAKUS), conductivity in several places in the system (used also to align the signals), continuous $\delta^{18}O$, δD, as well as collection of discrete samples for determination by IC and ICP-MS. Further the system was attached to an on-line ICP-MS, however with poor results. During the campaign for determination of dissolved reactive phosphorous (DRP) in the NEEM ice core, the melt rate was kept low to enhance the resolution. 55 cm was measured at a time, with standards of PO_4^{3-} run in between. More on the Japanese CFA set-up is presented in appendix D.

The **Bern CFA system** [*Röthlisberger et al.*, 2000; *Kaufmann et al.*, 2008] has been used in multiple ice core campaigns, and was used in the field at the NEEM site, Greenland for continuous determination of ionic species as well as for collections of discrete samples. Doing CFA in the field minimizes the risk of contamination and decreases the number of samples broken during transport [*Röthlisberger et al.*, 2000]. The Bern set-up used for the NEEM ice core during the field campaign in 2010 was constructed for the detection of many chemical species rather than for achieving high temporal resolution. In the Bern set-up used at NEEM 110 cm ice was melted in about 32 minutes and standards were run after every 4th sample of 110 cm. The Bern system measures 7 different ions (excluding phosphate) as well as total air content, dust, conductivity, black carbon and some gases. Further the water from the outer part is divided in 6 samples and used for IC measurements, tephra measurements and others. The melt head used at NEEM is the melt head by *Bigler et al.* [2011], with a chemical inert surface and 6 concentrically positioned drain holes for the inner part as well as six for the outer part.

The Desert Research Institute **(DRI) CFA system**, Reno, Nevada is another system set up for the determination of multiple species and thus the sample requirement is high and temporal resolution low. The system differs from other CFA systems by including a third ring on the melt head, thus separating the sample in an ultra pure inner sample, a pure middle sample and a potentially contaminated outer sample. The DRI-CFA system measures only a few conventional CFA species (middle stream), but include continuous determination using ICP-MS (inner sample) and semi continuous IC (4 IC instruments); also the system includes continuous determination of total organic carbon (TOC, inner sample) using an on-line instrument purchased from Sievers, and Black Carbon (BC, inner sample).

REFERENCES ICE CORES AND CONTINUOUS FLOW ANALYSIS

Abram, N. J., R. Mulvaney, E. W. Wolff, and M. Mudelsee (2007), Ice core records as sea ice proxies: an evaluation from the Weddell Sea region of Antarctica, *Journal of Geophysical Research: Atmospheres (1984–2012)*, *112*(D15).

Abram, N. J., E. W. Wolff, and M. A. Curran (2013), A review of sea ice proxy information from polar ice cores, *Quaternary Science Reviews*, *79*, 168–183.

Andersen, K. K., A. Svensson, S. J. Johnsen, S. O. Rasmussen, M. Bigler, R. Röthlisberger, U. Ruth, M.-L. Siggaard-Andersen, J. Peder Steffensen, D. Dahl-Jensen, et al. (2006), The Greenland ice core chronology 2005, 15–42ka. part 1: constructing the time scale, *Quaternary Science Reviews*, *25*(23), 3246–3257.

Basile, I., F. E. Grousset, M. Revel, J. R. Petit, P. E. Biscaye, and N. I. Barkov (1997), Patagonian origin of glacial dust deposited in East Antarctica (Vostok and Dome C) during glacial stages 2, 4 and 6, *Earth and Planetary Science Letters*, *146*(3), 573–589.

Beer, J., A. Blinov, G. Bonani, R. Finkel, H. Hofmann, B. Lehmann, H. Oeschger, A. Sigg, J. Schwander, T. Staffelbach, et al. (1990), Use of 10Be in polar ice to trace the 11-year cycle of solar activity.

Bereiter, B., H. Fischer, J. Schwander, and T. Stocker (2014), Diffusive equilibration of N_2, O_2 and CO_2 mixing ratios in a 1.5-million-years-old ice core, *The Cryosphere*, *8*(1), 245–256.

Bigler, M., A. Svensson, J. P. Steffensen, and P. Kaufmann (2007), A new continuous high-resolution detection system for sulphate in ice cores, *Annals of Glaciology*, *45*(1), 178–182.

Bigler, M., A. Svensson, E. Kettner, P. Vallelonga, M. E. Nielsen, and J. P. Steffensen (2011), Optimization of high-resolution continuous flow analysis for transient climate signals in ice cores, *Environ. Sci. Technol.*, *45*(10).

Biscaye, P., F. Grousset, M. Revel, S. Van der Gaast, G. Zielinski, A. Vaars, and G. Kukla (1997), Asian provenance of glacial dust (stage 2) in the Greenland ice sheet project 2 ice core, Summit, Greenland, *Journal of Geophysical Research: Oceans (1978–2012)*, *102*(C12), 26,765–26,781.

Bory, A. J.-M., P. E. Biscaye, and F. E. Grousset (2003), Two distinct seasonal Asian source regions for mineral dust deposited in Greenland (NorthGRIP), *Geophysical Research Letters*, *30*(4).

Bory, A.-M., P. E. Biscaye, A. Svensson, and F. E. Grousset (2002), Seasonal variability in the origin of recent atmospheric mineral dust at NorthGRIP, Greenland, *Earth and Planetary Science Letters*, *196*(3), 123–134.

Breton, D. J., B. G. Koffman, A. V. Kurbatov, K. J. Kreutz, and G. S. Hamilton (2012), Quantifying signal dispersion in a hybrid ice core melting system, *Environmental science & technology*, *46*(21), 11,922–11,928.

Chappellaz, J., T. Bluniert, D. Raynaud, J. M. Barnola, J. Schwander, and B. Stauffert (1993), Synchronous changes in atmospheric ch4 and Greenland climate between 40 and 8 kyr BP.

Chappellaz, J., C. Stowasser, T. Blunier, D. Baslev-Clausen, E. Brook, R. Dallmayr, X. Fain, J. Lee, L. Mitchell, O. Pascual, et al. (2013), High-resolution glacial and deglacial record of atmospheric methane by continuous-flow and laser spectrometer analysis along the NEEM ice core, *Climate of the Past*, *9*(6).

Cole-Dai, J., D. M. Budner, and D. G. Ferris (2006), High speed, high resolution, and continuous chemical analysis of ice cores using a melter and ion chromatography, *Environmental science & technology*, *40*(21), 6764–6769.

Craig, H. (1961), Standard for reporting concentrations of deuterium and oxygen 18 in natural waters, *Sciences*, *133*, 1833–1834.

Dahl-Jensen, D., K. Mosegaard, N. Gundestrup, G. D. Clow, S. J. Johnsen, A. W. Hansen, and N. Balling (1998), Past temperatures directly from the Greenland ice sheet, *Science*, *282*(5387), 268–271.

Dahl-Jensen, D., M. Albert, A. Aldahan, N. Azuma, D. Balslev-Clausen, M. Baumgartner, A.-M. Berggren, M. Bigler, T. Binder, T. Blunier, et al. (2013), Eemian interglacial reconstructed from a Greenland folded ice core, *Nature*, *493*(7433), 489–494.

Dallmeyr, R., H. Kjær, K. Goto-Azuma, M. Takata, S. Schupbach, P. Vallelonga, t. Segawa, and H. Yamada (2014), High resolution continuous flow analysis system for polar ice cores, *unpublished*.

Dansgaard, W. (1964), Stable isotopes in precipitation, *Tellus*, *16*(4), 436–468.

Dansgaard, W., and S. Johnsen (1969), A flow model and a time scale for the ice core from Camp Century, Greenland, *Journal of Glaciology*, *8*, 215–223.

Delmonte, B., J. Robert Petit, I. Basile-Doelsch, E. Jagoutz, and V. Maggi (2007), 6. Late quaternary interglacials in East Antarctica from ice-core dust records, *Developments in Quaternary Sciences*, *7*, 53–73.

Delmonte, B., P. Andersson, M. Hansson, H. Schöberg, J. R. Petit, I. Basile-Doelsch, and V. Maggi (2008), Aeolian dust in East Antarctica (EPICA-Dome C and Vostok): Provenance during glacial ages over the last 800 kyr, *Geophysical Research Letters*, *35*(7).

EPICA community members (2004), Eight glacial cycles from an Antarctic ice core, *Nature*, (431), 623–628.

Evans, J., C. Cofaigh, J. A. Dowdeswell, and P. Wadhams (2009), Marine geophysical evidence for former expansion and flow of the Greenland Ice Sheet across the north-east Greenland continental shelf, *Journal of quaternary science*, *24*, pp. 279–293.

Federer, U., P. R. Kaufmann, M. A. Hutterli, S. Schupbach, and T. F. Stocker (2008), Continuous flow analysis of total organic carbon in polar ice cores, *Environmental science & technology*, *42*(21), 8039–8043.

Federer, U., P. R. Kaufmann, M. A. Hutterli, D. Buiron, T. Blunier, H. Fischer, and T. F. Stocker (2009), A new method for high-resolution methane measurements on polar ice cores using continuous flow analysis, *Environmental science & technology*, *43*(14), 5371–5376.

Fischer, H., M.-L. Siggard-Andersen, U. Ruth, and R. W. E. Röthlisberger (2007), Glacial-interglacial changes in mineral dust and sea-salt records in polar ice cores: Sources, transport, and deposition, *Rev. Geophys.*, *45*(1).

Fuhrer, K., A. Neftel, M. Anklin, T. Staffelbach, and M. Legrand (1996), High-resolution ammonium ice core record covering a complete glacial inter-glacial cycle, *J. Geophys. Res.*, *101*(D2), 4147–4164.

Gkinis, V., T. J. Popp, S. J. Johnsen, and T. Blunier (2010), A continuous stream flash evaporator for the calibration of an IR cavity ring-down spectrometer for the isotopic analysis of water, *Isotopes in environmental and health studies*, *46*(4), 463–475.

Gkinis, V., T. J. Popp, T. Blunier, M. Bigler, S. Schüpbach, E. Kettner, and S. J. Johnsen (2011), Water isotopic ratios from a continuously melted ice core sample, *Atmospheric Measurement Techniques*, *4*(11), 2531–2542.

Grousset, F. E., P. E. Biscaye, M. Revel, J.-R. Petit, K. Pye, S. Joussaume, and J. Jouzel (1992), Antarctic (Dome C) ice-core dust at 18 kyr BP: Isotopic constraints on origins, *Earth and Planetary Science Letters*, *111*(1), 175–182.

Hansson, M. E. (1994), The Renland ice core. A northern hemisphere record of aerosol composition over 120.000 years, *Tellus*, (46B).

Herron, M. M. (1982), Impurity sources of F^-, Cl^-, NO_3^- and SO_4^{2-} in Greenland and Antarctic precipitation, *Journal of Geophysical Research: Oceans (1978–2012)*, *87*(C4), 3052–3060.

Herron, M. M., and C. C. Langway Jr (1985), Chloride, nitrate, and sulfate in the Dye 3 and Camp Century, Greenland ice cores, *Geophysical Monograph Series*, *33*, 77–84.

Hiscock, W. T., H. Fischer, M. Bigler, G. Gfeller, D. Leuenberger, and O. Mini (2013), Continuous flow analysis of labile iron in ice-cores, *Environmental science & technology*, *47*(9), 4416–4425.

Johnsen, S., W. Dansgaard, and J. White (1989), The origin of arctic precipitation under present and glacial conditions, *Tellus B*, *41*(4), 452–468.

Johnsen, S. J., D. Dahl-Jensen, W. Dansgaard, and N. Gundestrup (1995), Greenland palaeotemperatures derived from GRIP bore hole temperature and ice core isotope profiles, *Tellus B*, *47*(5), 624–629.

Kaufmann, P. R., U. Federer, M. A. Hutterli, M. Bigler, S. Schüpbach, U. Ruth, J. Schmitt, and T. F. Stocker (2008), An improved continuous flow analysis system for high-resolution field measurements on ice cores, *Environ. Sci. Technol.*, *42*(21), 8044–8050.

Kawamura, K., F. Parrenin, L. Lisiecki, R. Uemura, F. Vimeux, J. P. Severinghaus, M. A. Hutterli, T. Nakazawa, S. Aoki, J. Jouzel, et al. (2007), Northern hemisphere forcing of climatic cycles in Antarctica over the past 360,000 years, *Nature*, *448*(7156), 912–916.

Kelly, M. A., and A. J. Long (2009), The dimensions of the Greenland ice sheet since the last glacial maximum, *Pages NEWS*, *17*.

Kettner, E. (2014), Highly resolved paleoclimatic aerosol records: Continuous flow analysis and the potential of flow cytometry for the characterisation of aeolian dust in polar ice cores.

Kjær, H. A. (2010), Phosphate in ice cores-finding a method for continuous detection of phosphate in ice cores.

Kreutz, K. (2007), Ice core records: Glaciochemistry, *Encyclopedia of Quaternary Science. Elsevier, Oxford*, pp. 1192–1198.

Lambert, F., M. Bigler, J. P. Steffensen, M. Hutterli, and H. Fischer (2012), Centennial mineral dust variability in high-resolution ice core data from Dome C, Antarctica, *Clim. of the Past*, *8*(2), 609–623.

Legrand, M., and P. A. Mayewski (1997), Glaciochemistry of polar ice cores: A review, *Reviews of Geophysics*, *35*, 219–143.

Legrand, M., M. De Angelis, T. Staffelbach, A. Neftel, and B. Stauffer (1992), Large perturbations of ammonium and organic acids content in the summit-Greenland ice core. Fingerprint from forest fires?, *Geophysical research letters*, *19*(5), 473–475.

Legrand, M. R., and S. Kirchner (1990), Origins and variations of nitrate in south polar precipitation, *Journal of Geophysical Research: Atmospheres (1984–2012)*, *95*(D4), 3493–3507.

Lupker, M., S. Aciego, B. Bourdon, J. Schwander, and T. Stocker (2010), Isotopic tracing (Sr, Nd, U and Hf) of continental and marine aerosols in an 18th century section of the Dye-3 ice core (Greenland), *Earth and Planetary Science Letters*, *295*(1), 277–286.

Maher, B. A., J. M. prospero, D. Mackie, D. Gaiero, P. P. Hesse, and Y. Balkanski (2010), Global connections between aeolian dust, climate and ocean biogeochemistry at the present day and last glacial maximum, *Earth-science reviews*, *99*, pp. 61–97.

Masson-Delmotte, V., J. Jouzel, A. Landais, M. Stievenard, S. J. Johnsen, J. White, M. Werner, A. Sveinbjornsdottir, and K. Fuhrer (2005), GRIP deuterium excess reveals rapid and orbital-scale changes in Greenland moisture origin, *Science*, *309*(5731), 118–121.

McConnell, J. R., G. W. Lamorey, S. W. Lambert, and K. C. Taylor (2002), Continuous ice-core chemical analyses using inductively coupled plasma mass spectrometry, *Environ. Sci. Tech.*, *36*(1), 7–11.

McConnell, J. R., R. Edwards, G. L. Kok, M. G. Flanner, C. S. Zender, E. S. Saltzman, J. R. Banta, D. R. Pasteris, M. M. Carter, and J. D. W. Kahl (2007a), 20th-century industrial black carbon emissions altered arctic climate forcing, *Science*, *317*, 1381.

McConnell, J. R., R. Edwards, G. L. Kok, M. G. Flanner, C. S. Zender, E. S. Saltzman, J. R. Banta, D. R. Pasteris, M. M. Carter, and J. D. W. Kahl (2007b), Microparticle and trace element studies, *Elsevier*, pp. 1207–1211.

Neftel, A., J. Beer, H. Oeschger, F. Zürcher, and R. Finkel (1985), Sulphate and nitrate concentrations in snow from south Greenland 1895–1978.

NGRIP (2004), NGRIP unpublished data.

Nielsen, M. E. (2009), Early holocene and eemian impurity profiles from the NGRIP ice core, *Master thesis, Copenhagen University*.

Osterberg, E. C., M. J. Handley, S. B. Sneed, P. A. Mayewski, and K. J. Kreutz (2006), Continuous ice core melter system with discrete sampling for major ion, trace element, and stable isotope analyses, *Environmental science & technology*, *40*(10), 3355–3361.

Paterson, W. S. B., and K. M. Cuffey (2010), *The physics of glaciers*, Elsevier, fourth edition.

Picarro (2014), Cavity Ring-Down Spectroscopy (CRDS), http://www.picarro.com.

Rasmussen, S. O., K. K. Andersen, S. J. Johnsen, M. Bigler, and T. McCormack (2005), Deconvolution-based resolution enhancement of chemical ice core records obtained by continuous flow analysis, *Journal of Geophysical Research: Atmospheres (1984–2012)*, *110*(D17).

Rhodes, R. H., X. Faïn, C. Stowasser, T. Blunier, J. Chappellaz, J. R. McConnell, D. Romanini, L. E. Mitchell, and E. J. Brook (2013), Continuous methane measurements from a late Holocene Greenland ice core: Atmospheric and in-situ signals, *Earth and Planetary Science Letters*, *368*, 9–19.

Röthlisberger, R., M. Bigler, M. Hutterli, S. Sommer, B. Stauffer, H. G. Junghans, and D. Wagenbach (2000), Technique for continuous high-resolution analysis of trace substances in firn and ice cores, *Environ. Sci. Tech.*, *34*(2), 338–342.

Ruth, U., D. Wagenbach, J. P. Steffensen, and M. Bigler (2003a), Continuous record of microparticle concentration and size distribution in the central Greenland NGRIP ice core during the last glacial period, *J. Geophys. Res.: Atmospheres*, *108, D3*, 4098.

Ruth, U., D. Wagenback, J. P. Steffensen, and M. Bigler (2003b), Continuous record of microparticle concentration and size distribution in the central Greenland NGRIP ice core during the last glacial period, *Journal of geophysical research*, *108*(D3).

Ruth, U., C. Barbante, M. Bigler, B. Delmonte, H. Fischer, P. Gabrielli, V. Gaspari, P. Kaufmann, F. Lambert, V. Maggi, et al. (2008), Proxies and measurement techniques for mineral dust in Antarctic ice cores, *Environmental science & technology*, *42*(15), 5675–5681.

Saltzman, E., P.-Y. Whung, and P. A. Mayewski (1997), Methanesulfonate in the Greenland ice sheet project 2 ice core, *Journal of Geophysical Research: Oceans (1978–2012)*, *102*(C12), 26,649–26,657.

Saltzman, E. S., I. Dioumaeva, and B. D. Finley (2006), Glacial/interglacial variations in methanesulfonate (MSA) in the Siple Dome ice core, West Antarctica, *Geophysical research letters*, *33*(11).

Schwikowski, M., C. Barbante, T. Doering, H. W. Gaeggeler, C. Boutron, U. Schotterer, L. Tobler, K. Van de Velde, C. Ferrari, G. Cozzi, et al. (2004), Post-17th-century changes of european lead emissions recorded in high-altitude alpine snow and ice, *Environmental science & technology*, *38*(4), 957–964.

Sigg, A., K. Fuhrer, M. Anklin, T. Staffelbach, and D. Zurmuehle (1994), A continuous analysis technique for trace species in ice cores, *Environ. Sci. Tech.*, *28*(2), 204–209.

Sigl, M., J. R. McConnell, L. Layman, O. Maselli, K. McGwire, D. Pasteris, D. Dahl-Jensen, J. P. Steffensen, B. Vinther, R. Edwards, R. Mulvaney, and S. Kipfstuhl (2013), A new bipolar ice core record of volcanism from WAIS Divide and NEEM and implications for climate forcing of the last 2000 years, *J. of Geophys. Res.: Atmospheres*, *118*(3), 1151–1169.

Spolaor, A., P. Vallelonga, J. Gabrieli, M. Roman, and C. Barbante (2013), Continuous flow analysis method for determination of soluble iron and aluminium in ice cores, *Analytical and bioanalytical chemistry*, *405*(2-3), 767–774.

Steffensen, J. P. (1997), The size distribution of microparticles from selected segments of the Greenland ice core project ice core representing different climatic periods, *Analyst*, *120*, 187–191.

Steffensen, J. P., K. K. Andersen, M. Bigler, H. B. Clausen, D. Dahl-Jensen, H. Fischer, K. Goto-Azuma, M. Hansson, S. J. Johnsen, J. Jouzel, et al. (2008), High-resolution Greenland ice core data show abrupt climate change happens in few years, *Science*, *321*(5889), 680–684.

Stocker, T. F. (1998), The seesaw effect, *Science*, *282*(5386), 61–62.

Stocker, T. F., and S. J. Johnsen (2003), A minimum thermodynamic model for the bipolar seesaw, *Paleoceanography*, *18*(4).

Stowasser, C., C. Buizert, V. Gkinis, J. Chappellaz, S. Schuepbach, M. Bigler, X. Fain, P. Sperlich, M. Baumgartner, A. Schilt, et al. (2012), Continuous measurements of methane mixing ratios from ice cores, *Atmospheric Measurement Techniques*, *5*(5), 999–1013.

Svensson, A., P. E. Biscaye, and F. E. Grousset (2000), Characterization of late glacial continental dust in the Greenland ice core project ice core, *J. Geophys. Res.*, *105*(D4), 4673–4556.

Svensson, A., K. K. Andersen, M. Bigler, H. B. Clausen, D. Dahl-Jensen, S. M. Davies, S. J. Johnsen, R. Muscheler, F. Parrenin, S. O. Rasmussen, R. Röthlisberger, I. Seierstad, J. P. Steffensen, and B. M. Vinther (2008), A 60 000 year Greenland stratigraphic ice core chronology, *Clim. Past.*, *4*(1), 47–57.

Thomas, E. R., E. W. Wolff, R. Mulvaney, S. J. Johnsen, J. P. Steffensen, and C. Arrowsmith (2009), Anatomy of a Dansgaard-Oeschger warming transition: High-resolution analysis of the North Greenland Ice Core Project ice core, *Journal of Geophysical Research: Atmospheres (1984–2012)*, *114*(D8).

Traversi, R., S. Becagli, E. Castellano, A. Migliori, M. Severi, and R. Udisti (2002), High-resolution fast ion chromatography (FIC) measurements of chloride, nitrate and sulphate along the EPICA Dome C ice core, *Annals of Glaciology*, *35*(1), 291–298.

Vallelonga, P., G. Bertagna, T. Blunier, H. A. Kjær, T. J. Popp, S. O. Rasmussen, J. P. Steffensen, C. Stowasser, A. Svensson, E. Warming, et al. (2012), Duration of Greenland stadial 22 and ice-gas Δage from counting of annual layers in Greenland NGRIP ice core, *Climate of the Past Discussions*, *8*(4), 2583–2605.

Vinther, B. M., S. L. Buchardt, H. B. Clausen, D. Dahl-Jensen, S. J. Johnsen, D. Fisher, R. Koerner, D. Raynaud, V. Lipenkov, K. Andersen, et al. (2009), Holocene thinning of the Greenland ice sheet, *Nature*, *461*(7262), 385–388.

Whitlow, S., P. Mayewski, and J. Dibb (1992), A comparison of major chemical species seasonal concentration and accumulation at the South Pole and Summit, Greenland, *Atmospheric Environment. Part A. General Topics*, *26*(11), 2045–2054.

Zielinski, G. A., P. A. Mayewski, L. D. Meeker, S. Whitlow, and M. S. Twickler (1996), A 110.000-yr record of explosive volcanism from the GISP2 (Greenland) ice core, *Quat. Res.*, *45*, 109–118.

Part I

PHOSPHORUS AND PHOSPHATE DETECTION IN FIRN AND ICE

Phosphorus is an important nutrient for the global biosphere and potentially limits primary productivity [*Redfield*, 1958]. However whether it is the main limiting nutrient is generally not agreed upon, though recent studies show evidence of co-limitation of both P and N in 30% of the global systems and that most systems respond with an increase in production when either nutrient is added[*Elser et al.*, 2007; *Harpole et al.*, 2011].

The phosphorus cycle is relatively simple as the gaseous phase of P is limited and short-lived. Phosphorus bearing rocks are eroded by physical and chemical weathering, which produces soils and provides both soluble and insoluble P to rivers. The rivers transport the P to lakes and oceans, where it is taken up by the biosphere. Through burial and sedimentation of organic and mineral matter the P falls to the bottom and tectonic uplift will once again start the phosphorus cycle [*Ruttenberg*, 2003; *Filippelli*, 2002]. The global transport of P is dominated by water transport, but although the atmospheric input is small, it can cause primary production in some environments and thus is not irrelevant in ocean sites far from the coast and upwelling zones. Also tropical forests are dependent on atmospheric transport. In such environments the atmospheric transport provides 50% of new P added, while riverine flux supports the other half.

In recent times the global phosphorus cycle has been disturbed by anthropogenic impacts [*Filippelli*, 2002]. Waste, fertilizers and changes in land use enhance the flux of P especially to rivers. The biological systems are severely impacted by this increase of P and elevated phosphorus concentrations have caused eutrophication in lakes and coastal areas [*Ruttenberg*, 2003]. A few modelling studies have investigated the impact on the atmospheric transport of P of this anthropogenic increase [*Mahowald et al.*, 2008; *Kanakidou et al.*, 2012]. They find that the anthropogenic part of atmospheric P is now in the order of 10%. A study of P from a polar ice core confirms an increase since 1950 [*Edwards et al.*, 2007]. More on the global phosphorus cycle and its impacts can be found described in chapter 2.

In glacial times the so-called sea shelf hypothesis describes a change in the global P cycle; as the sea level is lowered P previously deposited on the shelf areas is once again introduced to the global cycle and thus increased P in the glacial periods are expected and there is evidence of increased primary production during periods of low sea level [*Falkowski et al.*, 1998].

In this part of the thesis a method for the continuous determination of dissolved reactive phosphorus (DRP) in ice cores is presented in chapter 3. Initial studies for the method were presented in my masters thesis. The method was published in Environmental Science & Technology [*Kjær et al.*, 2013]. The paper presents first DRP results from a Greenland shallow firn core from the North East Greenland Ice Stream (NEGIS) covering the recent century. We find that the major source is dust, but with clear evidence of secondary sources. No anthropogenic impact was observed in the NEGIS firn core.

To investigate changes in the glacial DRP deposition pattern the method was applied to glacial sections of the NEEM ice core. During this experiment the method was further validated against other methods; ion chromatography for the determination of PO_4^{3-} and total P using ICP-SFMS. We found that the method developed in this study detects a smaller soluble fraction than the PO_4^{3-} concentration found

by IC, but our method is advantageous when it comes to resolving features in the ice as well as for analysis time. We find evidence of increased P and PO_4^{3-} transport during the recent glacial cold periods and we find that the soluble fraction changes over time. The study constitutes chapter 4 and is in preparation for submission to Global Biogeochemical Cycles.

A few samples from the Tiashan mountains, Kyrgyzstan were analysed for DRP and further strengthen our finding of increased P during glacial periods. The Tienshan mountain area is likely influenced by local effects of wind and erosion and thus to a higher degree represents changes in local conditions. Results from the Tienshan mountains are presented in chapter 5.2. The chapter further includes a more detailed analysis of subannual variations observed in the NEGIS firn core and an outlook including suggestions for future work using the DRP method.

2. PHOSPHORUS IN THE CLIMATE SYSTEM

Phosphorus is an important nutrient for the global biosphere. Recent studies suggest that P and N are equally limiting across different biological systems [Harpole et al., 2011], while the general understanding is that N is more important for the ocean primary production and in terrestrial ecosystems, while P governs the production in freshwater systems and in old forests [Schindler, 1977; Vitousek and Howarth, 1991; Howarth and Marino, 2006].

The atmospheric transport of P account for only a small fraction of the global P cycle. Though small, the atmospheric deposition governs the production in remote oceans and in tropical forests atmospheric P accounts for 50% of the renewal of P [Vitousek and Farrington, 1997; Richardson et al., 2004]. Semiarid regions such as the grasslands of the Sahel and central Asia are highly affected by the atmospheric deposition arriving from nearby deserts [Okin et al., 2004].

As the vapour pressure of P is negligible, the atmospheric transport of P occurs as particulates or in sea spray. The global atmospheric flux to the surface ocean is 0.02-0.05 T mol P/yr, while the flux to land is about a factor 10 higher related to the short atmospheric residence time [Ruttenberg, 2003].

Atmospheric P is believed to be influenced by anthropogenic changes and now 10% is from anthropogenic impact e.g.. waste, land use change and fertilizers [Mahowald et al., 2008; Kanakidou et al., 2012]. But also in the past changes have occurred in the P cycle such as the reintroduction of P from exposed shelves during glacial periods [Falkowski et al., 1998] and there is speculation as to redistribution by megafauna [Doughty et al., 2013; Daufresne, 2013].

2.1 Effect of nutrients on the global biosphere

Phosphorus is part of DNA, RNA and ATP and is thus essential for all life. Phosphorus constitutes 3% of dry mass of living cells.

In the oceans orthophosphates are taken up by photosynthetic organisms at the base of the food web and marine phytoplankton on average has molar ratios of 106C:16N:1P (the Redfield ratio) [*Redfield*, 1958].

Thus phosphorus is also an important nutrient for primary production. Exactly how important is generally not agreed upon and evidence of N limitation of ocean primary production is often found. Further in some systems primary production is limited by micro nutrients such as iron, potassium or sulphate.

In traditional studies of nutrient limitation Liebigs law of minimum is often applied. It states that a system is always limited by one component only [*Harpole et al.*, 2011]. Thus several studies over time have investigated the effect of adding P or N to different biogenic systems.

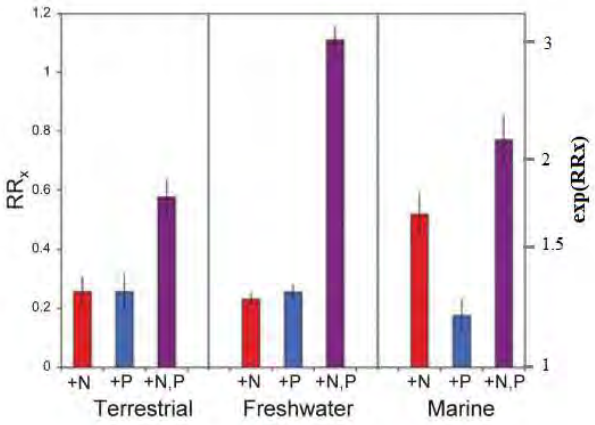

Fig. 2.1: The response of autotrophs to the single enrichment of P (blue) and of N (red) as well as the effect when adding both (purple) in different ecosystems. RR_x is the natural logarithmic value of the biosphere in the experiment where nutrients are added relative to a control. Thus a 0.5 value indicates a 1.6 times higher production when nutrients are added, while 1 indicate a 2.7 fold increase. The Figure is adapted from Elser et al. [2007] and is based on 1069 studies.

Early studies found that N was the main limiting nutrient in ocean and terrestrial ecosystems, while P was limiting in freshwater systems mainly [*Schindler*, 1977; *Vitousek and Howarth*, 1991; *Howarth and Marino*, 2006]. However recent evidence from [*Elser et al.*, 2007] based on combining studies from 653 freshwater, 243 marine and 173 terrestrial experiments, find that the response in the ecosystem to N and P perturbations is surprisingly uniform, with a positive synergistic effect [*Elser et al.*, 2007] (see Figure 2.1).

Elser et al. [2007] found that autotrophs increase to addition of either P or N in both freshwater and terrestrial systems is about 1.3, while the combination of both nutrients increase production by a factor 1.8 for terrestrial and almost 3 for freshwater. They find that the response in marine systems is small for P, but yet of a significant size, though the response of marine systems to N is much larger at about 1.6. The combined effects of N and P in the marine web amount to more than a doubling of primary production. [*Elser et al.*, 2007]. For comparison, increasing CO_2 by the expected amount for the coming 100-200 years was found to only increase the ocean primary production by ∼20% [*Hein and Sand-Jensen*, 1997; *Engel et al.*, 2005]. In all systems synergistic effects of increasing N and P were found, suggesting that Liebigs law does not always apply.

Biological systems can be limited by more than one nutrient and/or micro nutrient for several reasons:

- Nutrients can be biochemically substitutable within the same enzyme [*Harpole et al.*, 2011]
- Different enzymes may have the same catalytic function but need different elements [*Harpole et al.*, 2011]
- A biochemical function can depend on more than one element[*Harpole et al.*,

2011]

- A biological community can consist of multiple species limited by different nutrients or by each other and thus the system can either be synergistically co-limited (eg. one species is limited by P, the other by N) or serially co-limited (one species blooms due to increased nutrients then after some time the next, because it forages on the first species)[*Harpole et al.*, 2011].

Harpole et al. [2011] using a subset of the studies used by *Elser et al.* [2007] found that 28% of 641 studies show co-limitation of both N and P (Figure 2.2) and contrary to *Elser et al.* [2007] found that the effect of P and N is equal over different biological systems, including the oceans.

2.1.1 Influence of phosphorus on the ocean primary production

The Redfield ratio (P:N:C:O_2 = 1:16±1 : 117±14 : 170 ±10) is the mean molar ratio found in primary organisms of the ocean [*Redfield*, 1958]. This is due to the photosynthetic fixation of carbon and nutrients (N,P):

$$106CO_2 + 64H_2O + 16NH_3 + H_3PO_4 + h\nu \rightarrow C_{106}H_{179}O_{68}N_{16}P + 106O_2 \quad (2.1)$$

A similar ratio is found in ocean water and after a perturbation in either P, C, N and O in the ocean concentrations return to these concentrations through self regulating feedback processes [*Redfield*, 1958]. If e.g. an increase of P occurs, two things can happen; Either, if nitrogen fixation is limited (e.g. no Fe), the PO_4^{3-} can deviate above the Redfield ratio causing N to be the limiting nutrient, while if N and P are coupled by the responsive nitrogen fixation, negative feedbacks on organic and calcium bind P stabilizing both N and P concentrations [*Lenton and Watson*, 2000]. Decreases in P can quickly remove anoxia through combined decreases of PO_4^{3-} and NO_3^-, while increases of P may also rapidly increase anoxia [*Lenton and Watson*, 2000]. Thus the P concentration, though perhaps in most areas not as dominant as N, is an important constraint on the ocean biosphere.

It is believed that P limits ocean primary productivity on geological time scales. This is so because P supply to the ocean is governed by weathering and riverine flux, while N is always abundant in the atmosphere (N_2) and can become bioavailable through N-fixing photosynthetic organisms.

Whether phosphorus is in fact a limitation of the ocean primary production today, is a subject of debate [*Ruttenberg*, 2003; *Falkowski et al.*, 1998]. Traditional studies find that N limits ocean primary productivity [*Ruttenberg*, 2003; *Elser et al.*, 2007], while more recent studies find that such a simplistic mechanism involving response to only one nutrient is unlikely. Recent studies also to a larger degree consider differences in geographic distribution of nutrient limitation.

Elser et al. [2007] observe a significant variance in the response to P and N between various ecosystems. The response to N is stronger in the marine hard benthic and pelagic communities, while the response to P and N is almost equal for marine soft benthos [*Elser et al.*, 2007].

The oligotrophic gyres in the western North Atlantic and subtropical North Pacific are believed to be currently P limited [*Ammerman et al.*, 2003; *Karl et al.*,

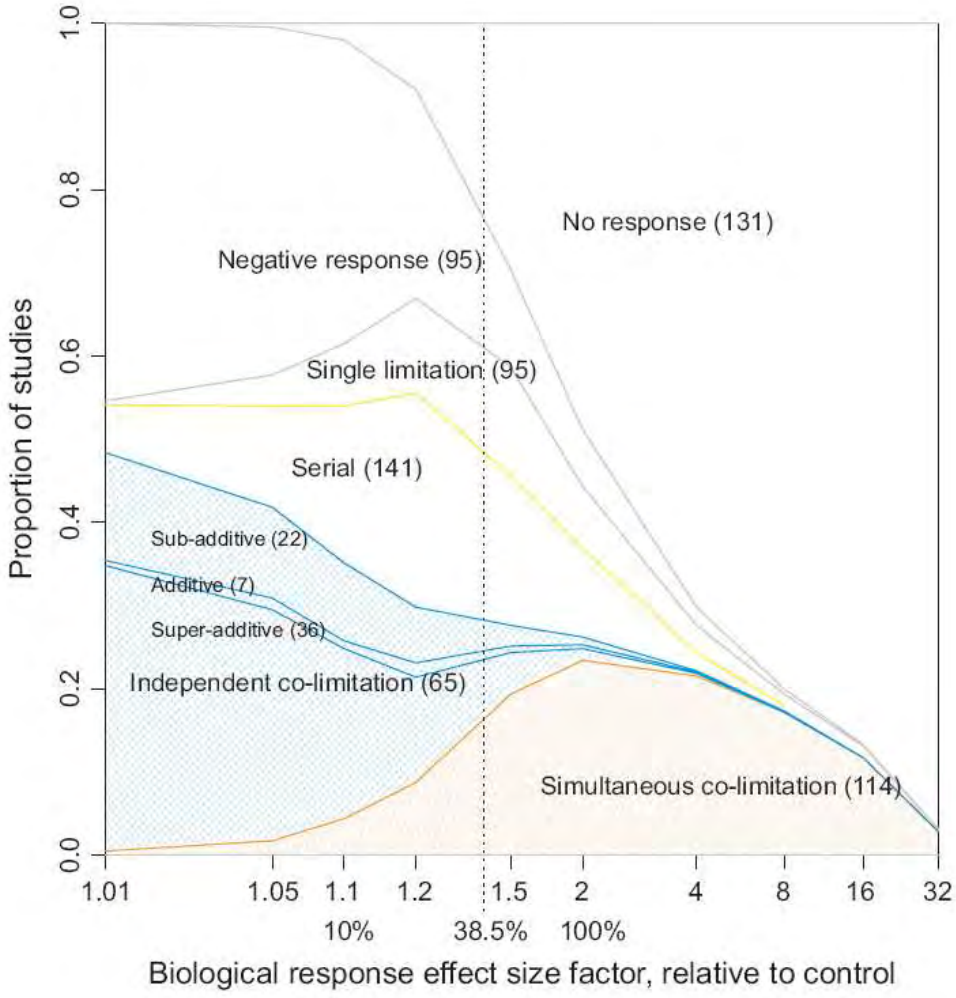

Fig. 2.2: Proportion of 641 studies that showed simultaneous co-limitation of P and N (orange region), independent effects of P and N (blue region), and serial limitation of N and P (yellow region) as a function of the relative response factor (similar to RR_x in Figure 2.1). Other responses to P and N include limitation of only each of them or a negative or no response to the addition of the nutrients (grey). Numbers in parenthesis indicate the number of studies within each category. The Figure is from Harpole et al. [2011].

2001; *Wu et al.*, 2000], while seasonal limitation of P has been observed in the area of Louisiana shelf (Gulf of Mexico), Eel river shelf (California), upper Chesapeake bay (USA) and regions of the Baltic sea; and other areas where P limitation is suggested include the Mediterranean sea, Florida Bay, Shark bay (Australia), Trondheim and Oslo fjords in Norway according to *Ruttenberg* [2003] and references therein. Thus evidence of P limitation also in the ocean is widespread.

A new branch of the nutrient limitation studies involves investigations of whether the phosphorus or nitrogen concentration determined is also bioavailable. This branch has evolved from new measurement techniques pushing the limits of detection. Evidence on bioavailable P and N potentially alter conclusions reached from determination of total P and N in ocean water.

The atmospheric transport of P to the oceans is small compared to the total budget of the ocean [*Ruttenberg*, 2003]. Nevertheless the atmospheric transport can be a significant source of nutrients to the remote oceans.

Also knowledge on turnover rates in the open ocean is important in order to estimate the limitation of various nutrients. Dissolved inorganic phosphorus (DIP) has turnover times from weeks to months, total dissolved organic phosphorus (DOP) from 20-300 days, while bioavailable DOP is removed in just 1-4 days. The turnover is faster at coastal sites where production is larger ([*Ruttenberg*, 2003; *Filippelli*, 2002] and references therein).

2.1.2 Influence of phosphorus on the terrestrial biosphere

Terrestrial photosynthesis also causes fixation of carbons and nutrients and is more efficient in the drawdown of CO_2 than the marine system. Despite the variation between individual plants the findings seems robust [*Ruttenberg*, 2003]. The terrestrial photosynthetic process proceeds according to:

$$830CO_2 + 600H_2O + 9NH_3 + H_3PO_4 + h\nu \rightarrow C_{830}H_{1230}O_{604}N_9P + 830O_2 \quad (2.2)$$

The soluble part of total P is kept low in terrestrial environments as various soil constituents, especially ferric iron and aluminium hydroxides, adsorb P.

The study by *Elser et al.* [2007], summarising the results of others, finds the response to P is stronger than that of N in forest and shrub land, while the response to an increase in N is stronger in wetlands and in tundra [*Elser et al.*, 2007]. They also find that fire volatilizes N and leaves behind P [*Elser et al.*, 2007], so that after a fire systems are more prone to be N limited.

Atmospheric P turnover times in soils, a measure of the time from when P atom is deposited from the atmosphere to when it is removed from a system again, is a good estimate of whether the biological system is dependent on atmospheric deposition or not [*Okin et al.*, 2004], though the turnover is also affected by other removal mechanisms. Thus a short turnover time indicates that a system is not P dependent. *Okin et al.* [2004] investigated the global P turnover time. The results are shown in Figure 2.3. They find the soil turnover times for atmospherically deposited P range between 10^2 to 10^5 yrs. The variation in the turnover depends both on new deposition and on the soil P concentration [*Okin et al.*, 2004]. Hence

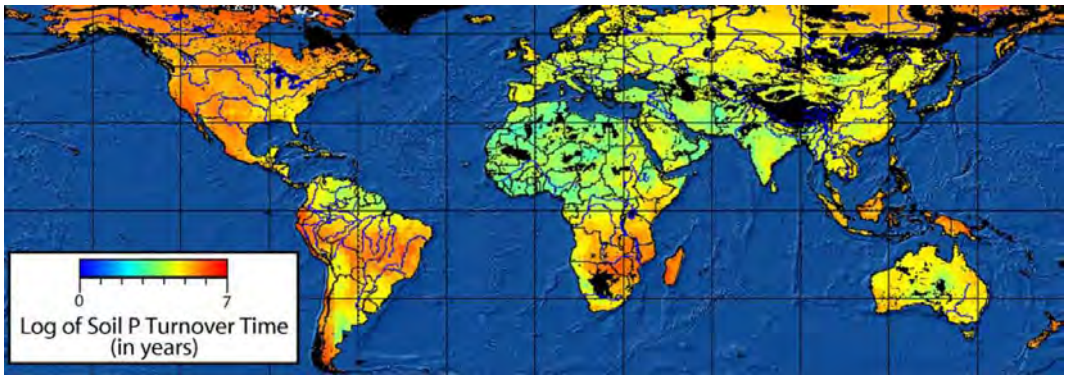

Fig. 2.3: Estimated values of soil P turnover time with respect to inputs of P on desert dust. Note log scale. Black areas have little to no soil development: ice, shifting sand, and rock. The Figure is from Okin et al. [2004].

once deposited the atmospheric P remains important in the local environment for a significant period of time.

Short turnover times are found for dust borne P in e.g. Europe as the P content is renewed by atmospheric deposition of North Africa aeolian dust [*Okin et al.*, 2004], while North America has long turnover times. The shortest turnover times are found in the desert regions, as P is often transported away due to the arid conditions. Though the high P deposition does not affect the biosphere in the desert themselves, the semiarid regions such as the grasslands of the Sahel and central Asia are highly sensitive to P deposition.

Okin et al. [2004] also find an east-west trend in the P turnover time for North America and suggest that the eastern North American forest long term productivity is mediated by atmospheric P originating from the North African deserts. However they also observe a north-south trend with long turnover time in the north due to glacially deposited material or glacial exposed bedrock increasing the local source.

In tropical forests the P recycling is very efficient and almost all P is tied up in the biomass leaving the soil extremely depleted in phosphorus [*Ruttenberg*, 2003] and thus tropical forests are P limited [*Elser et al.*, 2007].

Tropical forests and other old forests are believed to be limited equally by phosphorus from atmospheric transport and phosphorus from water sources as the soil becomes depleted of nutrients over time [*Vitousek and Farrington*, 1997; *Vitousek et al.*, 2010; *Menge et al.*, 2012]. This effect to some extent varies geographically as in the polar regions, glacial deposition have given rise to new nutrients; however *Elser et al.* [2007] find no effect of latitude on the terrestrial P. Despite this lack of confirmation on large data sets evidence of P limitation are seen in large parts of tropical forests [*Vitousek and Farrington*, 1997; *Richardson et al.*, 2004].

A study by *Chadwick and Goldstein* [2004] on Hawaian soils finds that the oldest islands are 100% dependent on the atmospheric deposition of P, while the younger islands are to a higher degree dependent on the parent rock (Figure 2.4). *Okin et al.* [2004] reach a similar conclusion from a model study. Notice that volcanic ash tend to have greater P sorption as compared to other soil types. This is caused by the high loads of amorphous material in volcanic soils [*Jones and Gislason*, 2008].

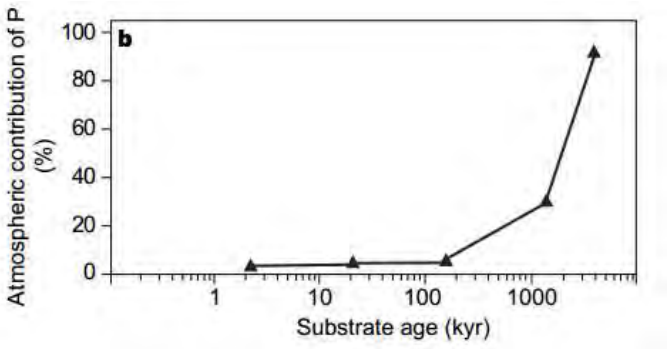

Fig. 2.4: The global atmospheric flux of P is more important for old soils. Figure from *Chadwick et al.* [1999].

2.1.3 Influence of phosphorus on freshwater systems

In general freshwater lakes are believed to be P limited and increasing the load of P can cause significant increases in the primary production [*Schindler*, 1977; *Carpenter et al.*, 1998].

Redox-dependent P retention in sediments, denitrification, watershed land use patterns, and internal food web structures can affect both N and P supply in freshwater systems [*Elser et al.*, 2007].

The classic view is that the re-oxidation/re-precipitation of ferric oxyhydroxides controls whether sediments release P [*Ruttenberg*, 2003]. However it has also been shown that bacteria can directly take up and release phosphate as a function of redox changes [*Ruttenberg*, 2003]. To what extent the two functions control P in waters is not resolved.

In a review *Bennett et al.* [2001] find that the increased use of fertilizer in recent periods significantly enhances the P load in lakes and watersheds. Thus the P concentration in lakes varies significantly based on its proximity to human settlements. However, even lakes close to human settlement in some cases show very low P concentrations; the total P concentration in Lake Superior, USA is in some areas below 1 ppb [*Field and Sherrell*, 2003]. *Elser et al.* [2007] find that the response to P is stronger in lakes and find an almost equal response to P and N in streams [*Elser et al.*, 2007]. Some lakes have been found to be limited by the atmospheric deposition of P, for example Lake Tahoe (Calfornia/Nevada) [*Jassby et al.*, 1994].

In rivers a phosphate buffer mechanism is evident; the sorption equilibrium with suspended material controls the amount of dissolved inorganic phosphorus (DIP) [*Ruttenberg*, 2003]. The sorption is either controlled by a thermodynamic equilibrium with the calcium phosphate mineral (e.g. the Mississippi river) or by a thermodynamic equilibrium between DIP and a solid solution of ferric phosphate hydroxide (e.g. the Amazon river). This buffer mechanism can keep the DIP levels in rivers, streams and estuaries rather constant and can also function as a buffer for human introduced fertilizers and other anthropogenic pollution sources.

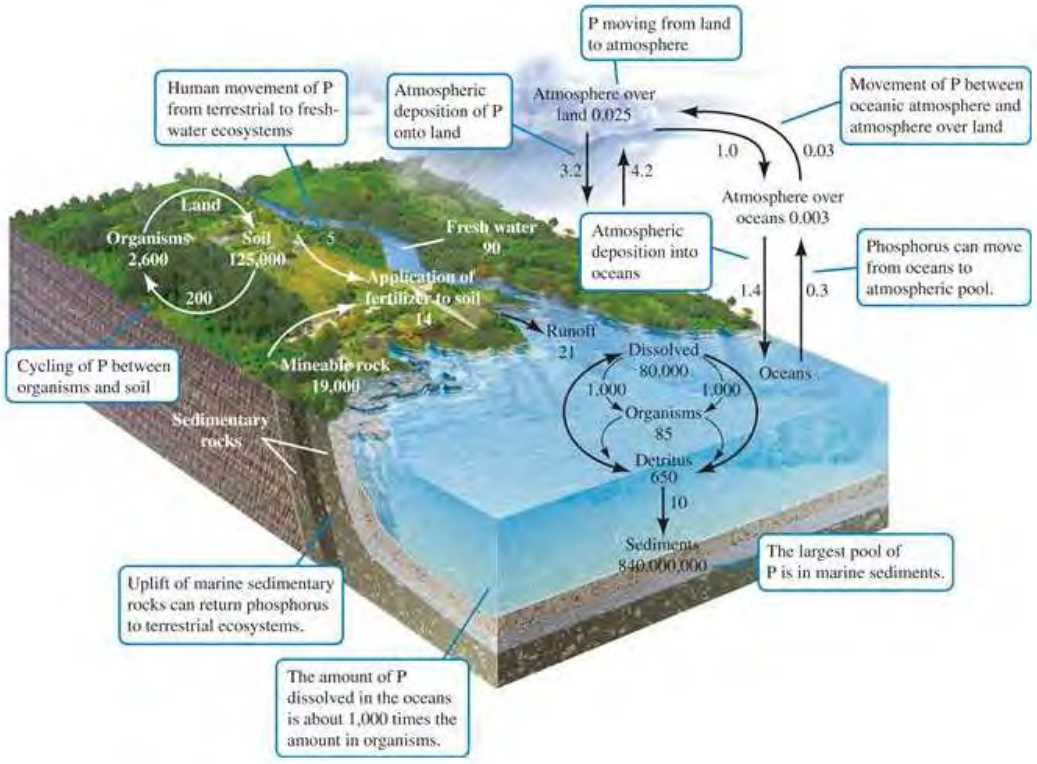

Fig. 2.5: The global phosphorus cycle. P fluxes are in Tg P/yr. The Figure is from *Biology-forums.com* [2014] and fluxes are based on *Schlesinger* [1991].

2.2 The global cycle of Phosphorus

The global phosphorus cycle is shown in Figure 2.5. The phosphorus cycle is relatively simple as phosphorus has only a negligible gaseous phase.

Phosphorus bearing rocks, eg. apatite ($Ca_{10}(PO_4)_6X_2$, where X can be F^{-1}, OH^{-1} or Cl^{-1} and Ca^{2+} can be substituted by a number of other positive ions), are eroded by physical and chemical weathering, which produce soils and provide both soluble and insoluble P to rivers. The rivers transport the P to lakes and oceans, where it is taken up by the biosphere. Through burial and sedimentation of organic and mineral matter the P falls to the bottom and tectonic uplift will once again start the phosphorus cycle [*Filippelli*, 2002; *Ruttenberg*, 2003].

Organic P is processed by microbes to inorganic P and the microbes also mobilize chemically fixed P. P can be chemically fixed by reactions with Ca^{2+}, Mg^{2+}, Fe^{2+} and others. Both very high (fixation as calcium phosphates) and very low pH (fixation by hydrous oxides of Fe, Mg and Al) cause P fixation, the highest amount of available P is found between pH 6 and 7. Though the content of P in most soils is large due to chemical fixation only a fraction is available to the biosphere.

In sea water the distribution of P species is as shown in Figure 2.6; about 42 % is present as $MgHPO_4$, 29% HPO_4^{2-} (free), 15% $NaHPO_4^-$, 8% $CaPO_4^-$, 4.7% $CaHPO_4$, while minor amounts of H, Mg, and Na and Ca bound phosphate and free phosphate are also found.

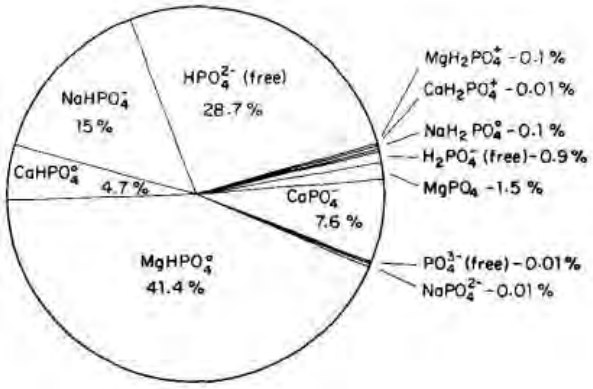

Fig. 2.6: Calculated speciation of PO_4^{3-} in sea water of 34.8 ppt salinity at 20 °C and a pH of 8.0 (Atlas, 1975).

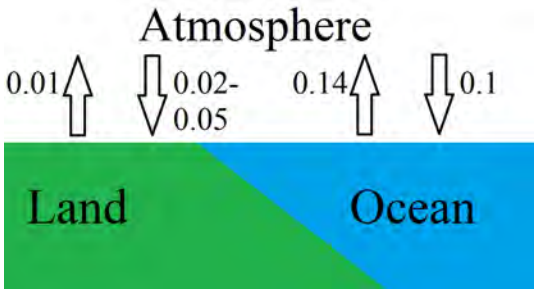

Fig. 2.7: The global atmospheric fluxes in Tmol/yr P as described in *Ruttenberg* [2003].

2.2.1 Atmospheric transport of Phosphorus

Though the majority of the P cycle (shown in Figure 2.5) takes place as transport in water the atmospheric transportation to biosphere systems on land is not unimportant for the reasons discussed above.

The gaseous phase of P, phosphine, in the natural environment is not very well studied. However it is believed that for the atmospheric global P cycle it can be neglected, as it is a rather short lived gas destroyed by hydroxyl radicals during day and only exists in low concentrations near sources (pg/m^{-3} to ng/m^{-3})[*Glindemann et al.*, 2005; *Zhang et al.*, 2010]. It should be mentioned however that *Zhu et al.* [2007] found evidence of longer lifetimes during Antarctic summer conditions, when clouds were present. However for the studies presented in this thesis the gaseous phase of P has been neglected as is often done and the atmospheric transport of P is assumed simple with transfer in the air taking place as particulates or as sea spray.

The global atmospheric flux to the surface ocean is 0.02-0.05 Tmol/yr P [*Ruttenberg*, 2003], while the flux to land is about a factor of 10 higher due to the short atmospheric residence time of just 80 hours [*Ruttenberg*, 2003].

However, not much is known about the atmospheric transport of phosphorus [*Mahowald et al.*, 2008], and often it is assumed that phosphorus and changes in the dust transport are identical [*Mahowald et al.*, 2008]. Assuming the atmospheric P transport from dust involves use of the crustal value 700 ppm. However, there is significant variation of the crustal value and values of up to 1300 ppm are used as

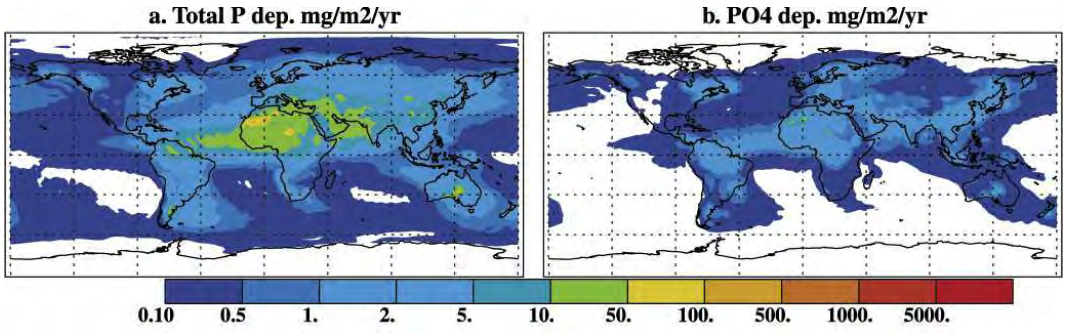

Fig. 2.8: Total P and phosphate deposition as modelled by *Mahowald et al.* [2008].

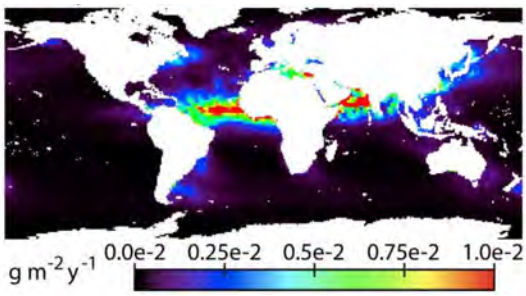

Fig. 2.9: Total oceanic P deposition as modelled by *Okin et al.* [2011]. The results are based on natural deposition from *Mahowald et al.* [2008] combined with dust deposition from *Luo et al.* [2008] using a crustal value of 700 ppm. The Figure is from *Okin et al.* [2011].

the mean amount depending on the study [*Mahowald et al.*, 2008; *Okin et al.*, 2004; 2011]. In Figure 2.10 concentrations of P in different types of soil and the global soil distribution are presented.

Furthermore model calculations unfortunately place wide limits only on the atmospheric transport of dust to remote oceans and the uncertainty on the dust deposition over the oceans today is about an order of magnitude [*Mahowald et al.*, 2005; 2009]. Results from two studies employing dust deposition to determine the deposition of P and PO_4^{3-} are shown in Figures 2.8 and 2.9. Both Figures show the significance of Saharan dust over the Atlantic as well as a high concentration near largely populated areas as a result of fossil fuel and biomass combustion.

Using dust transport to constrain P transport (Figure 2.8), *Mahowald et al.* [2008] found that in present times the atmospheric transport of P to the oceans is 0.32 Tg/yr, a small fraction of the total global P cycle. 0.13 Tg/yr of the atmospheric contribution to the oceans is deposited in the Atlantic ocean, 0.073 Tg/yr in the Indian ocean, 0.067 Tg/yr in the Pacific and 0.032 Tg/yr in the Southern Ocean [*Okin et al.*, 2011]. [*Mahowald et al.*, 2008] find that the inorganic phosphorus (IP) fraction of the total P deposited to the oceans is 0.24 Tg/yr, with 14% associated with anthropogenic release.

The concentrations of total phosphorus fluxes are not enough to constrain the effect of P on the biosphere. Information on the solubility or the bioavailable fraction is also important and changes in these could have occurred over time as source and

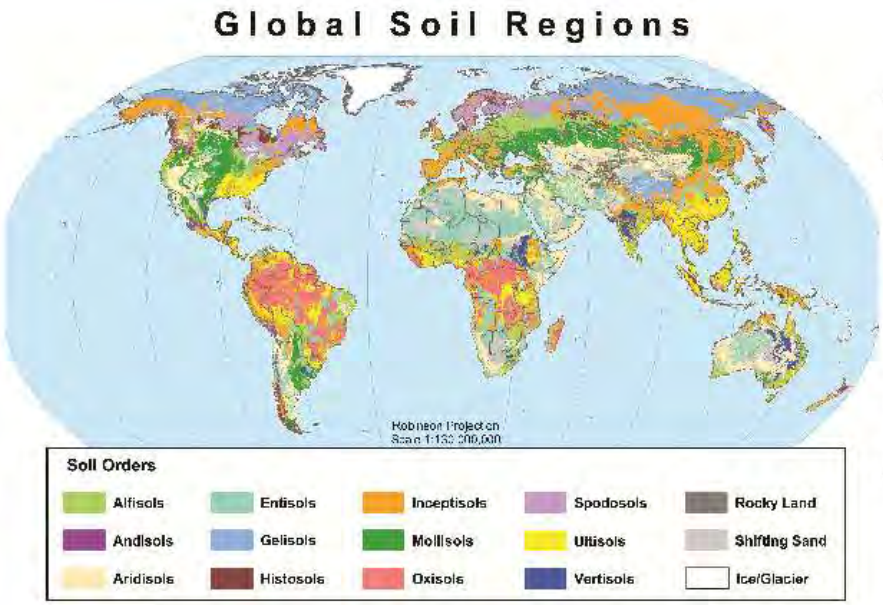

Soil Order	Total P Top 20 cm, kg/ha
Alfisol	613
Andisol	1039
Entisol	1369
Gelisol	982
Histosol	1076
Inceptisol	841
Mollisol	1101
Oxisol	354
Spodosol	410
Ultisol	515
Vertisol	1906

Fig. 2.10: The table show concentration of P in different types of soil by *Okin et al.* [2004] and references therein. The map show the global distribution of soil types [*US Department of Agriculture Natural Resources Conservation Service*, 2005].

transport patterns vary. Information about the solubility of P is limited [*Okin et al.*, 2011], however, a recent study finds that today the atmospheric transport of soluble organic P ranges from 20-83% (0.35 Tg P/yr) of atmospheric total soluble phosphorus [*Kanakidou et al.*, 2012], with 6% associated with anthropogenic sources. The dissolved organic fraction was found to constitute 30-50% of the P available to the ocean biosphere in the North Pacific [*Bjorkman and Karl*, 2003]. *Zamora et al.* [2013] found that the solubility was very dependent on source, with the ratio of soluble reactive phosphorus to total phosphorus varying between 8% and 18% for dust sources, while up to 98% was soluble reactive phosphorus when sea salt was the source. An intermediate solubility was found in precipitation originating from biomass burning.

A study found that organic phosphorus supports 25% of the annual production in the subtropical North Atlantic [*Lomas et al.*, 2010]. The amount of aeolian dust released in the water column was approximately 10%, while the remaining 90% sank to the bottom [*Mahowald et al.*, 2008; *Wallmann*, 2010]. Thus both the amount of soluble phosphorus arriving from the atmosphere and the amount of soluble phosphorus that is bioavailable are not well constrained.

The annual variability of P deposition is also poorly constrained. A study found that dry deposition to the subtropical north Atlantic was 2 to 10 times higher in summer than during other seasons [*Zamora et al.*, 2013], but generally information is scarce.

All in all the the data provide wide limits on the amount of P transported in the atmosphere to the open ocean today and provide even wider limits on the the amount available to the biosphere.

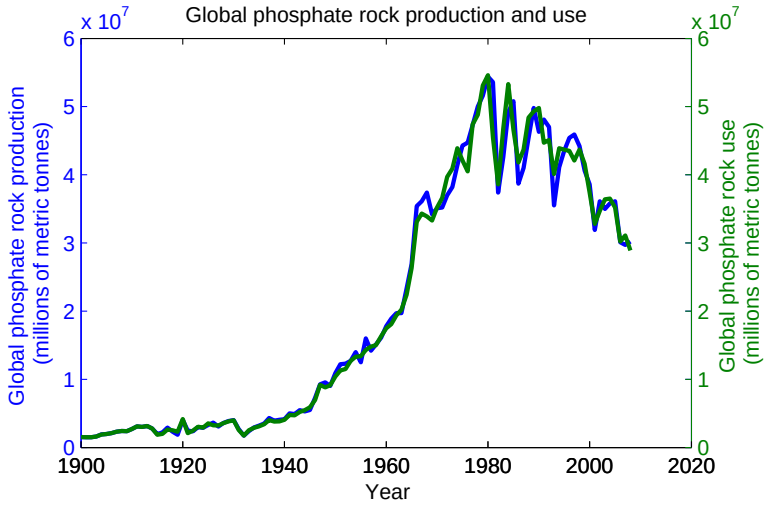

Fig. 2.11: Global production and use of phosphate rock increased rapidly from 1940 to 1980 and shows a more decreasing trend in the last 30 years. The data is from *Survey* [2010].

2.2.2 Changes in the P cycle over time

Recent increases in the concentration of atmospheric P as a result of increased anthropogenic impact have been suggested [*Mahowald et al.*, 2008; *Kanakidou et al.*, 2012]. Changes in the transport of Phosphorus and phosphate as a result of sea level variations; the so-called sea shelf nutrient hypothesis are believed to enhance the flux of P to the ocean in glacial times [*Filippelli et al.*, 2007], while past grazing by mega fauna and more recently grazing from livestock is also suggested to influence the cycle of P [*Neff et al.*, 2008; *Doughty et al.*, 2013; *Daufresne*, 2013; *Metcalfe et al.*, 2014]. Finally it has been suggested that on longer geological time scales P could be the most limiting nutrient [*Filippelli*, 2008], however evidence of any changes over time in the atmospheric P cycle are scarce.

Anthropogenic impact

Every year 14 million metric tons of phosphorus is used to fertilize fields. P fertilizer is mainly extracted from apatite [*Schlesinger*, 1991; *Tiessen*, 1995]. The trend of using fertilizers was rapidly increasing until the 1980's when concern of eutrophication caused regulation and a slight decrease in the use of fertilizers resulted [*Diaz and Rosenberg*, 2008; *Oelkers and Valsami-Jones*, 2008].

Other sources of anthropogenic P and PO_4^{3-} include urban and industrial waste disposal, deforestation and increased cultivation, which both increase soil erosion [*Ruttenberg*, 2003; *Mahowald et al.*, 2008].

Detergents were a large source of P to the environment between 1940 and 1970 as they contained up to 7% P, but today detergents have a low content of P [*Filippelli*, 2008; *Tiessen*, 1995]

The atmospheric P cycle has been amplified in recent times by +400% as a result of anthropogenic impact [*Elser et al.*, 2007], while the riverine P flux has been increased by 50% [*Ruttenberg*, 2003]. *Goll et al.* [2014] find that increased weathering

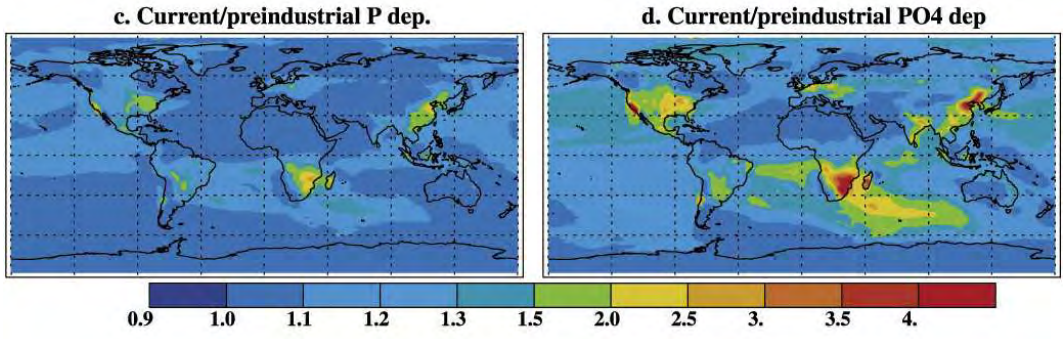

Fig. 2.12: The ratio between the current and the pre-industrial deposition of total P and phosphate deposition as modelled by *Mahowald et al.* [2008]. The Figure is from *Mahowald et al.* [2008].

between 1850 and 2005 AD caused a +12 % increase in P run off, further causing increased CO_2 consumption and and a -0.02 $W/m^2/^\circ K$ response was estimated.

Neff et al. [2008] found increased dust deposition over the western United States and also found during the 19th century that the western settlement of the United States increased the atmospheric dust load by 500% as a result of livestock grazing. They suggest that this would also cause a 5 fold increase in inputs of K, Mg, Ca, N and P to alpine ecosystems.

Though the rate of change is significant *Mahowald et al.* [2008] estimate that the anthropogenic part of the atmospheric cycle is on the order of 10% of the total cycle (see figure 2.12). However the atmospheric aerosols from human impact are often smaller and more soluble than natural aerosols causing the impact of anthropogenic changes to be more widespread than natural occurring changes [*Mahowald et al.*, 2008].

Shelf nutrient hypothesis

Phosphorus is believed to have been the limiting nutrient for ocean primary productivity in past times [*Falkowski et al.*, 1998], either directly or through its effect on nitrogen fixation in combination with Fe [*Okin et al.*, 2011], and thus P is essential to estimate CO_2 drawdown.

It is hypothesised that the lowered sea level during the glacial periods might enhance transport of P to the oceans [*Filippelli et al.*, 2007; *Filippelli*, 2008] and sediment records from the Southern Ocean and the equatorial Pacific indicate a maximum in marine export production during the last deglaciation [*Filippelli et al.*, 2007] (see Figure 2.13). During glacial times the sea level is lower and the shelf is exposed. Thus weathering would enhance the transport of P and P compounds from the shelf to the ocean, reintroducing them into the ocean system where they would increase the biospheric productivity and thus the CO_2 drawdown [*Broecker*, 1982; *Kohfeld et al.*, 2005].

The effect would be strongest close to the shelf, where river run off would be responsible for the transportation of P. Recently it was suggested that due to this increased flux of P during the glacial, even today the oceanic P cycle is out of bal-

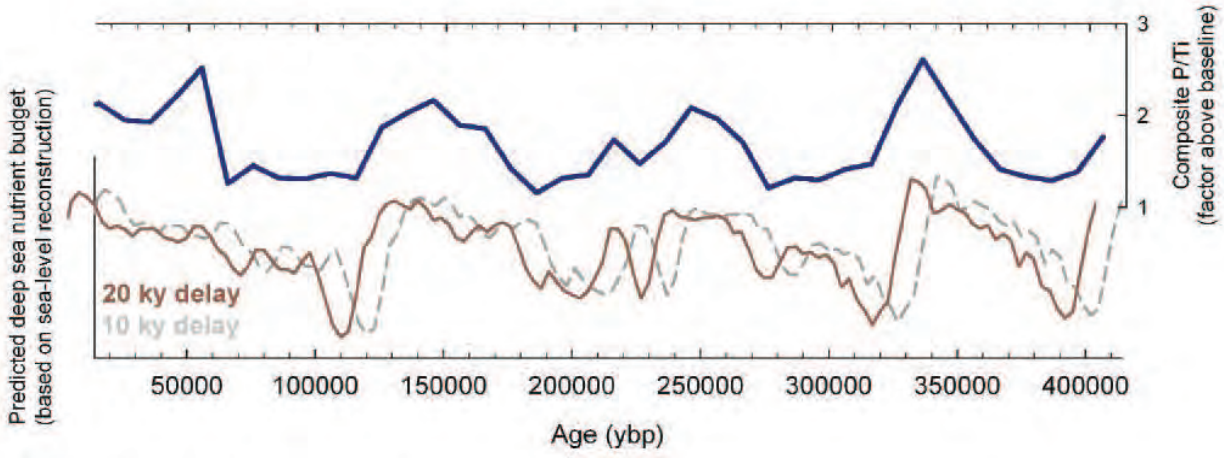

Fig. 2.13: Changes in the mass balance of phosphorus on glacial time scales deduced from the marine record of phosphorus burial (P/Ti) composed by individual cores from the equatorial pacific and southern ocean compared to a sea-level-based model (using the marine oxygen isotope record of ice volume) of phosphorus mass balance changes due to the redistribution of phosphorus from exposed continental margins during glacial sea level lowstands. The lag represents the response time in the ocean. The Figure is from *Filippelli et al.* [2007].

ance, with a net loss of more than 4.5 % P/kyr [*Wallmann*, 2010], however also huge uncertainty relates to the perturbation times of ocean P from recent published numbers of 10.000 to 60.000 yrs while most textbooks write numbers as high as 100.000 years. Clearly, the error on these numbers significantly impact any calculations of present net loss of P [*Tamburini and Fölimi*, 2009; *Lenton and Watson*, 2000].

Broecker and Henderson [1998] investigated termination II, in the Antarctic Vostok ice core, finding that the timing of CO_2 and dust changes do not support the shelf nutrient hypothesis unless it is also related to an increase in nitrogen fixation e.g. by Fe or P and due to the residence time of nitrogen in the ocean it could only cause a slow ramp up of CO_2.

Ushie and Matsumoto [2012] recently suggested that the shelf nutrients might not support a draw down of CO_2, but rather cause an increase of 20 ppm in the atmosphere. This is due to a decoupling between P and C, with P stored in the deep ocean and C stored in the upper ocean. Further because the C:P ratio in the continental margin sediments (C:P=200-800 [*Berner et al.*, 1993; *Ruttenberg and Goni*, 1997; *Ushie and Matsumoto*, 2012]) is higher than the redfield ratio in the oceans [*Redfield*, 1958; *Anderson and Sarmiento*, 1994], it would release CO_2.

In the open ocean large changes might not be caused by river run off. Here aeolian dust transport, which is increased during the glacial cold periods [*Svensson et al.*, 2000; *Ruth et al.*, 2003], could enhance the amount of P available to the biosphere. It is believed that the increase in aeolian dust in ice cores observed during the glacial is an effect of both transport, drier source areas and increased source area such as exposed shelves [*Ruth et al.*, 2003; *Svensson et al.*, 2000]. *Hood and Scott* [2008] investigated the P concentration in Alaskan watersheds and found increased loads of P in relation to run off from glaciers. They suggest that this could be caused

both by increased glacial deposition of P and by increased turbidity during run off events limiting sunlight and thus biosphere production leaving behind P.

A recent study investigating several marine cores does not find any significant change between burial rates in glacial and interglacial periods; however the response is not in consistent agreement between individual cores. Combining the effect from the marine cores they find a small decrease (8%) in the burial flux during the glacial, possibly as a result of longer residence times as the shelf is not ocean covered during the glacial [*Tamburini and Fölimi*, 2009]. The absence of any clear effect could be caused by redistribution of the ocean circulation patterns, the shelf nutrient hypothesis not being valid, or post depositional processes, causing a strong smoothing in any variation. In view of the short residence times of P in the ocean (10.000 yrs) it is likely that P perturbations could influence glacial transitions of CO_2, while the longest estimate (100.000 yrs) makes it highly unlikely that perturbations caused by the exposure of the shelf would have any short term effect.

Megafauna

Another suggestion for a change in the P cycle over time is the extinction of 97 mega fauna species during the late pleistoscene [*Doughty et al.*, 2013].

Animals can transport nutrients from nutrient rich places to nutrient poor regions. As an example, snow geese are responsible for 40% of the N and for 75% of the P influx to their wintering grounds in the Apache Reserve, New Mexico [*Kitchell et al.*, 1999]. Furthermore evidence that $\delta^{15}N$ found in leaves 500 metres from rivers corresponded to that found in fish, suggest that brown bears carry the fish inland [*Hilderbrand et al.*, 1999].

Similarly megafauna are believed to be important for the lateral distribution of nutrients. The deposition of dung causes dispersion of nutrients, while hot spots form where animals fall dead [*Doughty et al.*, 2013]. *Doughty et al.* [2013] estimate a decrease in the lateral movement of phosphorus of 98% following the Pleistocene extinction of Amazonian megafauna (decreasing the mean body mass for animals, larger than 10 kg, from 843 to 81 kg). They also state that though the decrease in lateral movement of phosphorus is most likely smaller on other continents it is still significant; *e.g.* the decrease in lateral movement of nutrients in Africa and Australia would be 18 and 45 %, with North America and Eurasia heavily impacted with a decrease of 90 % and 82 % of the lateral movement by fauna. They also suggest that the Amazon basin has not yet adjusted to the post-megafauna low nutrient supply and that this might also be the case for other continents. Similar conclusions of impact on lateral distribution of nutrients by the extinction of megafauna are found in other model studies [*Daufresne*, 2013; *Metcalfe et al.*, 2014].

The hypothesis of lateral distribution of nutrients by megafauna is new and given its nature, it is clearly difficult to quantitatively square it with observations.

2.3 Why determine P and PO_4^{3-} in ice?

As also explained in section 1.1 ice cores provide the opportunity for a high resolution climate archive covering down to 800000 yrs back. Thus the determination

of phosphorus in ice provides a record of past atmospheric phosphorus concentration and deposition rates far back in time, and further, evidence of changes in the phosphorus cycle, particularly in the atmospheric cycle, can be inferred from the ice. Thus by determining P in ice cores evidence of human impact in recent times, exposed shelves on glacial time scales on the global atmospheric P cycle could be constrained. The effect of lateral distribution by megafauna probably cannot be determined by means of ice core research, though it cannot be completely ruled out that the change in distribution of nutrients may also influence the atmospheric flux to the ice sheets.

Tockner et al. [2002] made measurements on melt water from a glacier in Switzerland and found that the concentrations of total dissolved phosphorus was 0.26 μM PO_4^{3-} when coming from snow and that glacier melt water had a concentration of 0.07 μM PO_4^{3-}. The concentration of total phosphorus was found to be 0.37 μM P for snow and for glacial run off 3.0 μM P, implying that the soluble fraction of phosphorus in snow is very high, while for the glacial run off very low for this particular glacier and that there might have been a change over time in P deposited on the glacier.

Concentrations of P in ice are low and therefore, finding a method capable of detecting phosphorus compounds in high resolution is challenging. Only two studies report P concentrations from Greenland ice cores. *Edwards et al.* [2007] find a mean concentration of 8.06 nM P in two shallow firn cores from Greenland covering from 1950 and onwards with an increase in the period 1990-2005 that is ascribed to an increase in forest fires. For that study an ICP-MS was set up in connection to a CFA system and thus the method provided semi continuous measurements. As part of my masters thesis the present author applying a molybdenum blue method in connection to a CFA on the Greenland ice core NEEM found acid labile dissolved reactive phosphorus (DRP_{acid}) concentrations between 4 and 616 nM PO_4^{3-} in the glacial [*Kjær*, 2010]. However what part of P these measurements exactly refer to is unclear as they were not filtered prior to the addition of the reagent molybdenum blue, which is required if aiming for the determination of phosphate using a molybdenum blue method.

Not only does the molybdenum blue method determine phosphate; it also detects the dissolved organic P [*Monaghan and Ruttenberg*, 1999]; and according to *Hudson et al.* [2000] true ortophosphate is 2 to 3 times lower. However during the investigations *Kjær* [2010] found that the molybdenum blue method was the only method that was applicable for determining the low concentrations expected in polar ice, and which could be implemented in a continuous flow analysis (CFA) system. A full discussion of other methods, their applicability to a CFA system and other advantages and disadvantages of these can be found in *Kjær* [2010] chapter 6.

As part of this thesis the molybdenum blue method previously selected [*Kjær*, 2010] was further optimized by displacing the filter to a position before the reagent in order to avoid acid labile phosphorus stuck on dust to contribute to the signal. Further different conventional filters were investigated and a white LED was chosen as the light source to make the apparatus easier to transport to remote locations, such as to the polar ice for larger drilling campaigns or to other laboratories around the world. The optimized version of the molybdenum blue method was published

in Environmental Science and Technology in *Kjær et al.* [2013] and is presented in the next chapter.

3. A CONTINUOUS FLOW ANALYSIS METHOD FOR DETERMINATION OF DISSOLVED REACTIVE PHOSPHORUS

Kjær, H. A., P. Vallelonga, A. Svensson, M. E. L. Kristensen, C. Tibuleac and M. Bigler[1]

Phosphorus (P) is an essential macronutrient for all living organisms. Phosphorus is often present in nature as the soluble phosphate ion PO_4^{3-} *and has biological, terrestrial and marine emission sources. Thus* PO_4^{3-} *detected in ice cores has the potential to be an important tracer for biological activity in the past. In this study a continuous and highly sensitive absorption method for detection of dissolved reactive phosphorus (DRP) in ice cores has been developed using a molybdate reagent and a 2 m liquid waveguide capillary cell (LWCC). DRP is the soluble form of the nutrient phosphorus, which reacts with molybdate. The method was optimized to meet the low concentrations of DRP in Greenland ice, with a depth resolution of approximately 2 cm and an analytical uncertainty of 1.1 nM (0.1 ppb)* PO_4^{3-}*. The method has been applied to segments of a shallow firn core from Northeast Greenland, indicating a mean concentration level of 2.74 nM (0.26 ppb)* PO_4^{3-} *for the period 1930-2005 with a standard deviation of 1.37 nM (0.13 ppb)* PO_4^{3-} *and values reaching as high as 10.52 nM (1 ppb)* PO_4^{3-}*. Similar levels were detected for the period 1771-1823. Based on impurity abundances, dust and biogenic particles were found the most likely sources of DRP deposited in North-east Greenland.*

3.1 Introduction

Ice cores provide an archive of past climate and environmental conditions in high temporal resolution. Greenland ice cores cover the last glacial cycle [*NGRIP members*, 2004], whereas Antarctic ice cores archive almost a million years of past climate [*EPICA community members*, 2004]. Past climate conditions can be reconstructed from the impurities in Greenland ice cores. Insoluble dust provides information on atmospheric transport patterns and dust source regions [*Ruth et al.*, 2003; *Svensson et al.*, 2000], sea salt components are related to the oceanic environment and wind speed [*de Angelis et al.*, 1997; *Fischer et al.*, 2007], sulphate concentration peaks often reflect volcanic activity [*Zielinski et al.*, 1996], and biogenic activity, such as

[1] This Chapter is reproduced with permission from Kjær et al., Continuous Flow Analysis Method for Determination of Dissolved Reactive Phosphorus in Ice Cores, *Environmental science & technology*, 47 (21), pp. 12325–12332, 2013. Copyright 2014 American Chemical Society. Co-authors are all from the Center for Ice and Climate, NBI, University of Copenhagen, Denmark except Matthias Bigler, who is at Climate and Environmental Physics, Physics Institute, University of Bern, Switzerland. Part of the initial work on the method was done as my master thesis, but the method was further optimized and implemented on firn and ice cores as part of this PhD.

forest fires [*Fuhrer et al.*, 1996; *McConnell et al.*, 2007] can be detected as well, as is the case for anthropogenic impacts [*McConnell et al.*, 2002]. Furthermore, there is a pronounced seasonality in the deposition of these impurities; insoluble dust is regularly deposited in the boreal spring, forest fire proxies in summer and sea salts in winter [*Legrand and Mayewski*, 1997].

Phosphorus (P) is an essential macronutrient for all living organisms, is present in DNA and is stored in bone matter. Earth's biological systems have been dependent on P since the beginning of life [*Filippelli*, 2008; *Paytan and McLaughlin*, 2007], and as a result P recycling is very efficient in earth's biological systems [*Tiessen*, 1995]. P is one of the limiting nutrients in ecosystems, although the degree of limitation is debated, from being a controlling factor to P being minor compared to other macro nutrients such as nitrate [*Falkowski et al.*, 1998; *Elser et al.*, 2007; *Worsfold et al.*, 2008]. However, over geological time scales P is believed to be the most important limiting nutrient in oceans [*Falkowski et al.*, 1998; *Paytan and McLaughlin*, 2007].

As P does not have a gaseous phase it can only be transported through the atmosphere as particulate matter or as PO_4^{3-}[*Graham and Duce*, 1982; *Baker et al.*, 2006; *Mahowald et al.*, 2008; *Paytan and McLaughlin*, 2007]. This, in theory, makes the quantification of PO_4^{3-}fluxes simple to interpret from ice cores in that no remobilization of a gaseous phase of phosphorus occurs.

Mahowald et al. [2008] evaluated global atmospheric emissions of P at 1.39 Tg P/yr, dominated by mineral dust (82%) with sea salt, primary biogenic particles, volcanoes, and anthropogenic sources such as coal combustion, gasoline and diesel engines as well as incinerators accounting for the remainder. For PO_4^{3-}(globally 0.24 Tg P/yr), the water soluble part of total P, mineral dust accounts for only 48% of the global atmospheric transport, biogenic particles account for 38%, volcanism accounts for 1.3% and sea salt merely 2%, while anthropogenic activity is believed to account for about 14 %. In some countries of mid- and high-latitude Europe (Finland, Norway, Belgium), there is evidence of a high fraction of P in coarse aerosols ($> 1\mu$m) of biogenic origin [*Mahowald et al.*, 2008]. Although atmospheric transport only accounts for a small part of the P cycle, it is important for nourishing primary production in the remote ocean [*Paytan and McLaughlin*, 2007; *Mahowald et al.*, 2008]. *Kanakidou et al.* [2012] *Kanakidou et al.* [2012] found that of the soluble phosphorus transported to the ocean, between 20% and 83% (mean 35%) had biogenic origin, with only 10% originating from human activities.

Very little information on the amount of P and PO_4^{3-}in the Arctic exists and even less information is available on concentrations in glaciers. *Edwards et al.* [2007] [*Edwards et al.*, 2007] measured P in snow and firn from the Greenland ice sheet using high resolution inductively coupled plasma mass spectrometry and found average P concentrations of 8.06 nM (0.25 ppb) over the last 50 years. They found a dramatic increase in P during the period 1990-2005 and attributed this to increased forest fire burning. Analysis of run off from small glaciers in Argentina and the Swiss Alps indicates P concentrations between 10 nM and 4700 nM [*Chillrud et al.*, 1994; *Tockner et al.*, 2002]. The bioavailable fraction of P was found to be low, 0.2 % to 4.3 % of total P, in another study looking at glaciofluvial sediments in France, Pakistan, Svalbard and Sweden [*Hodson et al.*, 2004]. Thus a method for the detection of phosphate in ice should be able to resolve nM levels.

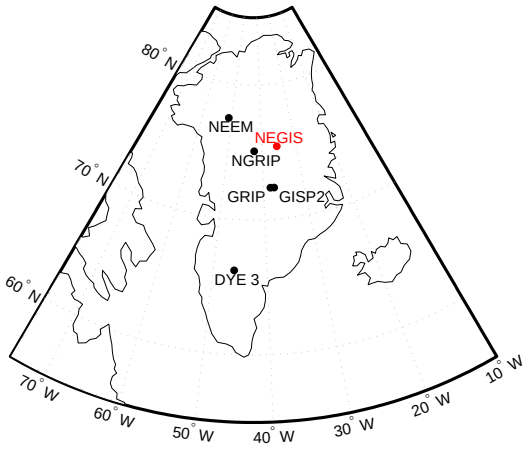

Fig. 3.1: Location of the NEGIS firn core.

The cycling of P is suggested to vary greatly over glacial-interglacial cycles [*Mahowald et al.*, 2008; *Filippelli*, 2008]. In glacial times sea level changes have exposed continental shelf areas allowing P deposited on shelves to be re-introduced to the atmospheric cycle. This so-called shelf nutrient hypothesis has been observed in marine records [*Filippelli*, 2008; *Delaney*, 2000; *Elderfield and Rickaby*, 2000]. In the Holocene a general trend of increasing mineral P has been observed as a sign of cooling conditions in alpine regions, but several short-lived changes have also been observed [*Filippelli et al.*, 2006]. In recent times, the natural cycling of PO_4^{3-} has been impacted by anthropogenic activities, such as the use of P as a fertilizer [*Schlesinger*, 1991; *Tiessen*, 1995; *Diaz and Rosenberg*, 2008; *Oelkers and Valsami-Jones*, 2008; *Filippelli*, 2008] and forest fire burning [*Filippelli*, 2008; *Paytan and McLaughlin*, 2007; *Bolin et al.*, 1981].

In this study, a novel method for the continuous detection of dissolved reactive phosphate (DRP)[*Worsfold et al.*, 2005] in ice cores is presented together with first results reported for polar ice; sections of a shallow ice core obtained at the North East Greenland Ice Stream (NEGIS, 75.38°N, 35.56°W, see Figure 3.1). Reactive phosphorus is defined here as the fraction of phosphate that after filtering reacts with molybdate, which is essentially the soluble inorganic phosphate fraction. This method differs from *Kjær et al.* [2011] in that the sample is now filtered for particles before the addition of reagent. The method presented here has the potential to reveal past variations and concentration levels of PO_4^{3-}(DRP) and to resolve the relative importance of the various speculated emission sources of PO_4^{3-}.

3.2 Dissolved reactive phosphorus detection in a CFA-set up

Continuous Flow Analysis (CFA) has recently become a preferred method for determination of insoluble dust and chemical impurities in ice cores, because of the high resolution as well as improved contamination control and the great sample

throughput provided by the method [*Bigler et al.*, 2011; *Kaufmann et al.*, 2008].

A dissolved reactive phosphorus (DRP) detection system suited to CFA has been adapted from the molybdenum blue method by *Murphy and Riley* [1958] that was later optimized by *Zhang et al.* [1999] and *Zhang and Chi* [2002]. The DRP detection system is described in Figure 3.2 and Table 3.1. The system detects the dissolved reactive phosphate after filtering. The non-reactive part of dissolved P (does not react with molybdate blue), which is believed mainly to be the organic part, is most likely not detected [*Worsfold et al.*, 2005].

A 12-molybdophosphoric acid is formed from the reaction of PO_4^{3-}in the sample with molybdate in an acidic solution in the presence of potassium antimony tartrate. The 12-molybdophosphoric acid is subsequently reduced by ascorbic acid to a phosphomolybdenum blue complex. The absorbance of the phosphomolybdenum blue complex is measured at 710 nm by a 2000S spectrometer, with the sample illuminated by a DT-MINI-2GS deuterium tungsten halogen light source (both Ocean Optics, Dunedin FL, USA). The system was also successfully tested using a LED light source specifically tuned to the absorption wavelength of 710 nm (Roithner LaserTecknik, Vienna, Austria). To enhance the limit of detection (LOD), absorbance was measured in a two metre liquid waveguide capillary cell (LWCC, Ocean Optics, Dunedin FL, USA) [*Gimbert and Worsfold*, 2007; *Páscoa et al.*, 2012] with an inner volume of 0.5 mL as reported by *Zhang and Chi* [2002]. A spectrometer integration time of 800 ms was used. Unlike the method reported by *Zhang and Chi* [2002], air segmentation of the sample stream was not employed here.

Various flow rates, mixing lengths, detection wavelengths, spectrum integration, and filter types were tested and optimized for the detection of low PO_4^{3-}concentrations. We found that exchanging the filter once a week, was sufficient to avoid clogging.

3.2.1 Reagents and standards

All samples and reagents were stored in polypropylene bottles . All reagents used were of analytical grade. The reagents are similar to those described in *Zhang and Chi* [2002] except for the stock ammonium molybdate, for which a higher concentration was used. Stock antimony potassium tartrate solution was prepared by dissolving 0.3 g of antimony potassium tartrate in 100 mL of deionized water. The solution was stored in a dark bottle at 4 °C. Ammonium molybdate reagent solution was prepared daily by dissolving 0.37 g of ammonium molybdate in 25 mL of 5N H_2SO_4 solution, then adding 5 mL stock antimony potassium tartrate solution and diluting to 100 mL with milliQ water. Ascorbic acid buffer solution was prepared daily by dissolving 0.5 g of ascorbic acid and 7 g of sodium dodecyl sulfate in 100 mL of milliQ water. Standards (79, 40, 20, 8.4, 4.2 nM PO_4^{3-} ±5%) were prepared by a two step dilution of a 1μg/L stock solution of PO_4^{3-}using purified water from a milliQ system. The phosphate content of the MilliQ water was below the analytical detection limit of 1.1 nM.

Tab. 3.1: DRP CFA detection system parameters

Flow rates:	
Sample	1.7 mL/min
Reagent	0.15 mL/min
Buffer	0.15 mL/min
LWCC detector	1.8 mL/min
Debubbler waste	0.20 mL/min
Particle filter pore size	0.2 μm
Reagent mixing length	3.5 m
Reagent mixing temperature	65 °
Absorption path length (LWCC)	200 cm
Absorption wavelength	710 nm
Spectrometer integration time	800 ms
Combined uncertainty	1.1 nM (0.1 ppb)
Linear range	<105 nM (10 ppb)
Response time (5-95%)	18s (<53 nM)
	40s (>53 nM)

3.2.2 Flow rates and mixing

The reagent flow rate was varied between 0.07 and 0.35 mL/min to find the optimal mixture between reagent and sample, with the best sensitivity found at a flow rate of 0.15 mL/min. Optimal flow rates, used to analyse the shallow firn core, were found to be 1.7 mL/min for sample, 0.15 mL/min for reagent and buffer. Mixing of the reagent and sample were found to be optimized using 3.5 m of PFA tubing of 1/16" outer diameter 0.5 mm internal diameter, in a 65 °C heat bath (see supplementary material Figure 3.6). When the mixing length was less than 200 cm small air bubbles formed in the flow path, which entered the flow cell and caused anomalous signal absorption. Longer tubing increases the backpressure in the mixing coil, preventing micro bubbles from forming. To avoid bubbles formed in the mixing coil to enter the LWCC a debubbler was implemented just prior to the cell, the waste flow from the debubbler was set to 0.2 mL/min resulting in a flow of 1.8 mL/min through the cell.

Phosphate samples are usually filtered to remove particles, thus ensuring that only the soluble $PO_4^{3-}$is detected, while the acid labile fraction is not. Furthermore, it is important that insoluble particles are removed from the sample stream before they enter the LWCC where they interfere with the absorption signal. The continuous nature of the CFA system requires that the filter can function for reasonably long periods of time without clogging yet being of sufficiently small volume to avoid excessive sample mixing. Commercial syringe filters with a pore size of 0.2 μm (Minisart, NML and LGG, polyethylene, Th. Geyer, 9055541 and 9049101) were found sufficient in removing solid particles and was placed on the sample line prior to mixing with reagent and buffer (see supplementary material Figure 3.7).

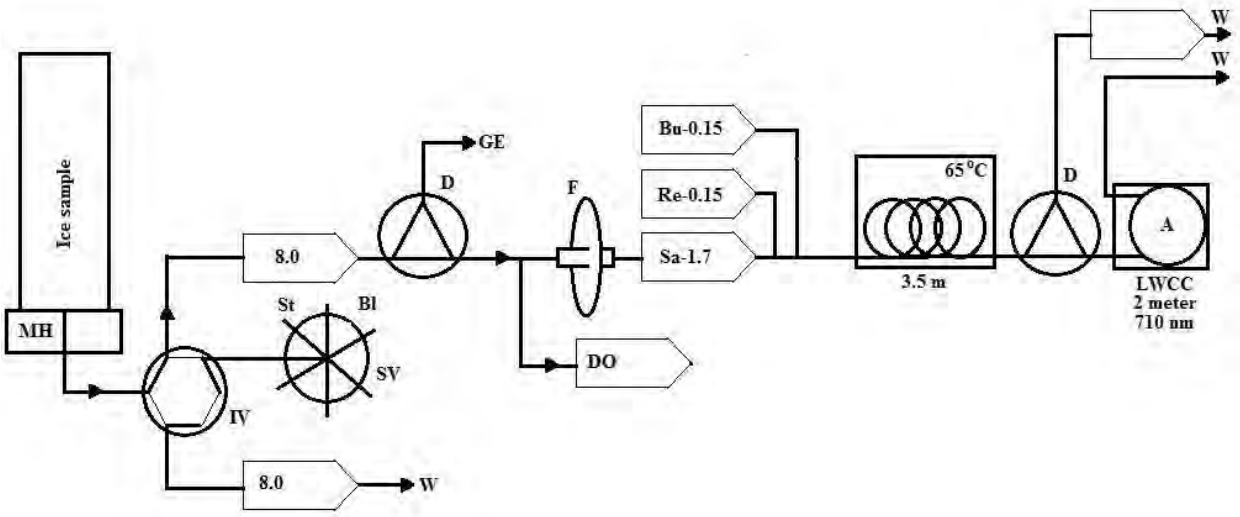

Fig. 3.2: The continuous flow setup for detection of dissolved reactive phosphorus. Ice is melted on a melt head (MH) in a freezer kept at -20 °C. An injection valve (IV) in combination with a selection valve (SV) for standards (St) and blank (Bl) allows for running either. The sample line is de-bubbled (D) to remove the air bubbles naturally occurring in the ice or firn and the gas (GE) is used for gas extraction measurements. The water line is split into various analytical channels (DO), and the PO_4^{3-}line which is the only one shown here. The water is filtered (F) to avoid interferences and the sample (Sa) is mixed with reagent (Re), buffer (Bu) then passed through a 3.5 m heated (65 °C) mixing coil before a second debubbler (D) removes any remaining air. Absorption (A) at 710 nm is measured in a 2 m Liquid Waveguide Capillary Cell (LWCC) after which the line goes to waste (W). Peristaltic pumps are represented by arrow boxes with flow rates(in mL/min) indicated by the number within the box.

3.2.3 Linearity and response time

A linear relationship between PO_4^{3-} and absorption was found below 105 nM (Figure 3.3). The 5% to 95% signal response times for concentrations in the linear range were 40 seconds for concentrations above 53 nM, and 18 seconds for standards below 53 nM. This corresponds well to the theoretical time required for replacement of water in the 2 meter LWCC. We attribute the longer response time at higher concentrations >53 nM)to increased staining of the flow cell and tubing, corresponding to an enhanced memory effect at higher phosphate concentrations.

3.3 Greenland firn core measurements

The optimized DRP detection system was connected to the CFA system in Copenhagen [*Bigler et al.*, 2011] to demonstrate the method on a firn core from the North East Greenland Ice Stream (NEGIS, 75.38°N, 35.56°W). The position of the firn core is shown in Figure 3.1.

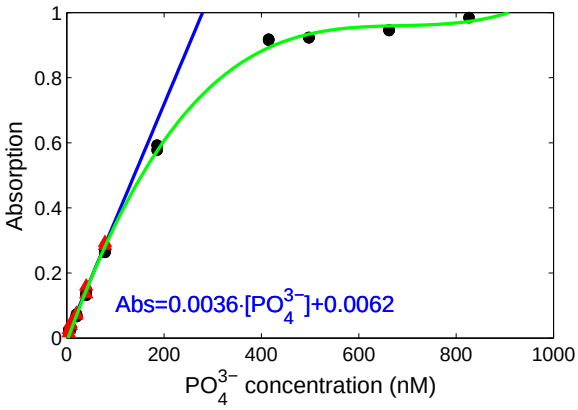

Fig. 3.3: Relation between $PO_4^{3-}$and absorption. Red triangles with a blue linear fit represent the four lower standards used in this study to determine concentrations from measured signal absorption. The black circles with green fit show that the technique is non-linear above concentrations of 105 nM.

The Copenhagen CFA set-up is optimized for high resolution measurements in ice and firn core samples with a cross-sectional area of 35 mm x 35 mm. Measurements of two sections of the firn core, from 3.3 m to 20.0 m and 38.0 to 46.0 m depth, are shown in Figures 3.4 and 3.5 respectively. The samples were dated using annual layer counting of Na^+ winter peaks[*Fischer et al.*, 2007; *Rasmussen et al.*, 2006; *Legrand and Mayewski*, 1997] together with volcanic reference points. The top section (3.3 m to 20.0 m) was found to cover the interval 1930 to 2005 yr AD. The deeper section (38.0 to 46.0 m) covers three volcanic eruptions; the Tambora eruption (1815), deposited on the icesheet in 1816 AD, was found at a depth of 39.1 metres, acid from an unknown eruption deposited in 1810 AD was found at 40.1 metres depth and markers of the 1783 AD eruption of Laki at a depth of 44.3 meter.

The mean DRP concentration level in the two sections were very similar; 2.78 nM (0.26 ppb) $PO_4^{3-}$with a standard deviation (σ) of 1.45 nM for the younger section, while the older section had levels of 2.71 nM $PO_4^{3-}$with a σ of 1.26 nM. There was no clear annual DRP signal detected in the sections reported here, but strong concentration variability was observed in both the sections. As anticipated the average concentration of DRP is lower than the reported value of 8 nM (0.25 ppb) for total P in Greenland firn [*Edwards et al.*, 2007].

Spikes larger than 6.5 nM PO_4^{3-}corresponding to the mean concentration plus 3σ were found in both the upper and lower firn sections reported here.

3.3.1 Uncertainties

All measurements conducted on the NEGIS firn core were calibrated using a linear fit between absorption and PO_4^{3-}standards of 20, 8.4 and 4.2 nM PO_4^{3-}±5% (Figure 3.3). These standard concentrations covered the level of DRP found in the NEGIS firn core. The standards are precise to ±5% corresponding to an uncertainty of ∼ 0.1 nM PO_4^{3-}at the level detected in the NEGIS firn core. The uncertainty on the

Tab. 3.2: Estimated sources for DRP in the NEGIS firn core. The anthropogenic estimate is based on *Mahowald et al.* [2008].

Sources	DRP fraction (%)
Dust	4-100
Biogenic	4-38
Anthropogenic	0-10
Sea salt	0.3
Volcanoes	0

linear fit introduces an additional uncertainty of $\sim$ 0.2 nM PO_4^{3-}(see Figure 3.4 and 3.5 top).

Since the response time (5 to 95 % signal) is about 20 s, any response shorter than 20 s can be attributed to instrument noise, thus a 30 s smoothing was applied to the raw data. The standard deviation on the smoothed baseline introduces an uncertainty of 0.8 nM PO_4^{3-}. The total combined uncertainty of the technique is therefore $\sim$1.1 nM PO_4^{3-}.

3.3.2 Sources of dissolved reactive PO_4^{3-}

Several impurity records were obtained from the NEGIS firn core along with the DRP detection, including insoluble dust particles using an Abakus laser particle counter (Klotz, Germany), electrolytic melt water conductivity, and Na^+, and NH_4^+ concentrations [*Bigler et al.*, 2011]. No consistently strong correlation between DRP and these other species was found in the investigated sections, the greatest correlation being with insoluble dust for the younger section (r=0.43), while the older section had somewhat lower correlation (r=0.34).

We find that mineral dust and biospheric emission sources are sufficient to account for the DRP concentration levels observed in Greenland firn, with the major transport mechanism for DRP related to dust, as the correlation between insoluble dust and DRP is higher than for other species detected in the NEGIS firn core. DRP is enhanced during volcanic eruptions, however not to a level higher than other peaks in the record. No correlation of extreme spikes to NH_4^+ was observed and thus we do not see evidence of a relation to forest fires. We further investigated the possibility that some of the high peaks observed are caused by the use of incendiary bombs with high P loads during the Iraq war, 2004 and the Korean war 1953, the lack of other war episodes deems this however unlikely.

Dust

To investigate whether insoluble dust is a source and/or transport mechanism for DRP, the theoretical upper limit of $PO_4^{3-}$from a dust source ($PO_{4\mathrm{dust}}^{3-}$) was determined using the following assumptions: 1) Typical continental crust contains 1080 mg P/kg dust [*Lide*, 2012] with higher estimates for rock dust reaching 3030 mg P/kg dust, 2) all of the phosphate in atmospheric dust can be dissolved in precipitation [*Nenes et al.*, 2011], and 3) the relationship between the number of particles

determined by the Abakus and the weight of the dust particles can be approximated by $\log_{10}$(CCmassconcentration) =(0.9084±0.03090)·$\log_{10}$(Abakuscounts)−(1.3276± 0.1076), as found by *Lambert et al.* [2012] where the Abakus counts are given in counts/mL and the CC mass concentration, which is the coulter counter determined weight, is given in ng/g. Using the mean level of dust present in the section of the NEGIS core (312 μg/kg), the greatest contribution of phosphorus that could arrive from a dust source is found to be 9.5 nM P. However, the amount of soluble P compared to total P was found by *Hodson et al.* [2004] to be between 0.2% and 3.4% in glaciofluvial sediments making a likely estimate of PO^{3-}_{4dust} closer to the order of 0.1 nM. However others suggest that the solubility of total inorganic P can be much higher (>80%) in cases of acidic emissions to the atmosphere, such as during volcanic eruptions and also increased during anthropogenic emissions for example SO_2 and NO_x [*Nenes et al.*, 2011]. Another value for the mass of dust deposited to Greenland in the recent times is 46 μg/kg ice detected in the GRIP ice core [*Steffensen*, 1997] leading to a P level of 1.6 nM, or 4.5 nM P if using the high estimate of P content in dust. Thehigh level of PO^{3-}_{4dust} found when assuming all P in dust can be released indicate that the upper limit of dust is sufficient to explain the entire level of DRP found in the NEGIS firn core. The lower more reasonable estimates calls for additional emission sources of P.

In the older section (1771-1823 AD, Figure 3.5) all extreme DRP spikes coincide with dust levels exceeding three standards deviations (>$3.6{\cdot}10^4$ counts), suggesting that high levels of DRP in the older section are related to high levels of dust. Another 2 dust events exceeding $3.6{\cdot}10^4$ counts are found in the deeper section, which correlate with smaller spikes in DRP.

In the recent period 1930-2005, only two of the seven DRP extreme peaks are associated with high dust events (8.46 and 18.42 metres depth). This finding is contrary to data from the older period. In the recent period, however, a further 13 extreme dust peaks are observed to occur simultaneously with minor DRP peaks.

Primary biogenic particles

One third of the soluble phosphorus in aerosols is expected to have a biogenic origin [*Mahowald et al.*, 2008]. Primary biogenic particles are associated with coarse K and Mg compounds [*Mahowald et al.*, 2008]. In ice, however both Mg and K are expected to have a mixture of sources, sea salts, dust, and forest fires [*Legrand and Mayewski*, 1997; *Kehrwald et al.*, 2012]. Neither Mg nor K were determined in the NEGIS firn core, thus to investigate a biogenic source levels of non sea salt(nss) Mg and nssK are only available from a NGRIP shallow core (NG01S6) covering the period 1968 to 1997. The mean nssK level in that shallow core is 0.1 μeq/L and the mean nssMg level is 0.09 μeq/L. The ratio of DRP as detected in the NEGIS firn core to both nssK and nssMg is in the order of 10^{-2}, thus in the order of the ratio of P/K and P/Mg in rock dust (10^{-1} to 10^{-2}) and above the ratio in sea salt (10^{-4} to 10^{-5}). For biogenic aerosols the ratio is in the order of 10^{-1} to 10^{-2} [*Graham et al.*, 2003] and it thus also corresponds to the ratio found in Greenland firn cores. Using the concentration of K in NGRIP shallow core NG01S6 and the ratio for biogenic particles between P and K, the corresponding PO^{-3}_{4bio} concentration is in the order of 1 to 0.1 nM P assuming that all K and Mg relates to biogenic particles, that all

biogenic P is soluble, and that the levels of K and Mg are similar at the NEGIS and NGRIP sites. On the basis of these assumptions, biogenic particles are a potential source of DRP in firn.

Sea salt

An evaluation, similar to that of dust, can be made of the potential amount of PO_4^{3-}arriving from a marine seasalt source ($ssPO_4^{3-}$) using the ratio between phosphorus (0.088 ppm) and Na^+ (10800 ppm) in sea water [*Turekian*, 1968] together with the Na^+ concentration detected in the section of the NEGIS firn core assuming that sea salt is the the only source of Na^+[*Legrand and Mayewski*, 1997]. The mean Na^+ concentration found in the depth between 3.3 and 20.0 meters is about 25 ppb giving a $ssPO_4^{3-}$ concentration of 0.007 nM P. Further, no correlation was observed between DRP and Na^+ in this section of the NEGIS core (corr=0.04). A sea salt source for the DRP detected at the NEGIS site thus seems negligible.

Volcanoes

Greenland ice cores contain acids deposited from volcanic events [*Sigl et al.*, 2013; *Arfeuille et al.*, 2013] and several of these were detected in the NEGIS firn core as an increase above the background level of conductivity. Volcanoes identified in the firn include Tambora (1815 yr AD, deposited 1816), an unknown eruption (1810 AD) and the 1783 AD Laki eruption. In Figure 3.5 DRP and conductivity for the three volcanoes are shown. The level of DRP follows the increase in conductivity during all three eruptions, but not to a level higher than background, thus it is unlikely that the $PO_4^{3-}$is emitted from volcanic sources, instead it is more likely that volcanism alters the pH and thus the solubility [*Nenes et al.*, 2011].

Anthropogenic emissions

An increase in anthropogenic sources of DRP was anticipated since the use of fertilizers globally have risen from 9 Tg P in 1960 to 40 Tg P by 2000 [*Vance et al.*, 2003]. Furthermore a rise in P could result from increased use of coal, oil and gasoline engines as well as incinerators [*Mahowald et al.*, 2008]. Finally an increase in the soluble fraction of P could occur due to changed acidity in the atmosphere as a result of introduced levels of NO_x and SO_2 [*Nenes et al.*, 2011]. In the NEGIS record no sign of anthropogenic impact was observed in the mean levels between the two periods investigated. However only ∼10% of total DRP is expected to be due to anthropogenic emissions[*Mahowald et al.*, 2008], suggesting an anthropogenic contribution on the order of $\sim$ 0.3 nM PO_4^{3-}(close to the level of uncertainty on the data).

Biomass burning

Not all of the high DRP spikes correlate with high events of dust. For example, the spikes in 2004, 1975, 1974, 1953, and 1949 AD do not (Figure 3.4). We speculate that the origin of the high spikes in DRP could be forest fires.

Spikes of NH_4^+ in ice records are often associated with biomass burning[*Fuhrer et al.*, 1996], but none of the extreme spikes in DRP coincide with extreme spikes of NH_4^+ (not shown here).

Incendiary weapons (white phosphorus)

We also consider the possibility that the origin of modern DRP spikes could be incendiary weapons, which are used in warfare to initiate fires, and often contain high loads of white phosphorus (P_4). The incendiary bombs were used during the first and second World Wars[*United states government*, 1946] as well as in the Korean (1953) [*Volkovskiy*, 2000], and Vietnam wars [*Neilands*, 1970], and in conflicts in Lebanon (1982 and 2006) [*Human Rights Watch*, 2009]. In the last decade they have been used in Iraq (2004) [*Iraq Analysis Group*, 2005], Somalia (April 2007), Gaza (2008 and 2009), and Afghanistan (2009) [*Human Rights Watch and Harvard Law Schools's International Human Rights Clinic*, 2011].

Some of the DRP spikes in the firn could be due to emissions from white phosphorus bombs; in 1953 70,000 tonnes of napalm mixture containing on the order of 160 g of phosphorus per kg, was used during the Korean war [*Volkovskiy*, 2000] and in 2004 18 tonnes of incendiary bombs were used in Iraq. This could regionally enhance the P level up to 3700 times and correspond to 0.8 % of global P fluxes. However, the absence of similar spikes during other significant periods of incendiary weapons use, eg. during the Vietnam [*Neilands*, 1970] and WWII [*United states government*, 1946], suggest that the use of incendiary weapons may represent only a local enhancement of P emissions.

While some DRP spikes do correspond to periods of incendiary weapons use, other war episodes do not show enhanced DRP concentrations. Particularly for conflicts on the Asian continent, it may be of interest to study DRP in local glaciers.

In this study a method for the detection of DRP in ice cores has successfully been implemented on a shallow firn core from Greenland. The method is capable of detecting the low DRP concentration levels and resolve annual variations of DRP as found in polar ice. Phosphorus is suggested to be the ultimate limiting nutrient to biological productivity in glacial times[*Filippelli*, 2008]. Applying the method described in this paper on larger sections of ice cores to investigate changes in the atmospheric transport of P over glacial times could help increase knowledge and constrain the suggested past variations of the atmospheric P fertilization to the far ocean [*Mahowald et al.*, 2008; *Filippelli*, 2008].

3.3.3 Aknowledgement

This work is supported by the Center of Ice and Climate at the Niels Bohr Institute. Further thanks to the Alfred Wegener Institute for polar and marine research (AWI) for supporting the retrieval of the NEGIS firn core. We would also like to thank Trine Ebbensgaard Strømfeldt for measurements of Mg and K performed on the NG00S6 firn core.

3.3.4 supplementary information

Temperature investigations, tests of filters and an example of a standard run, can be found in the supplementary material.

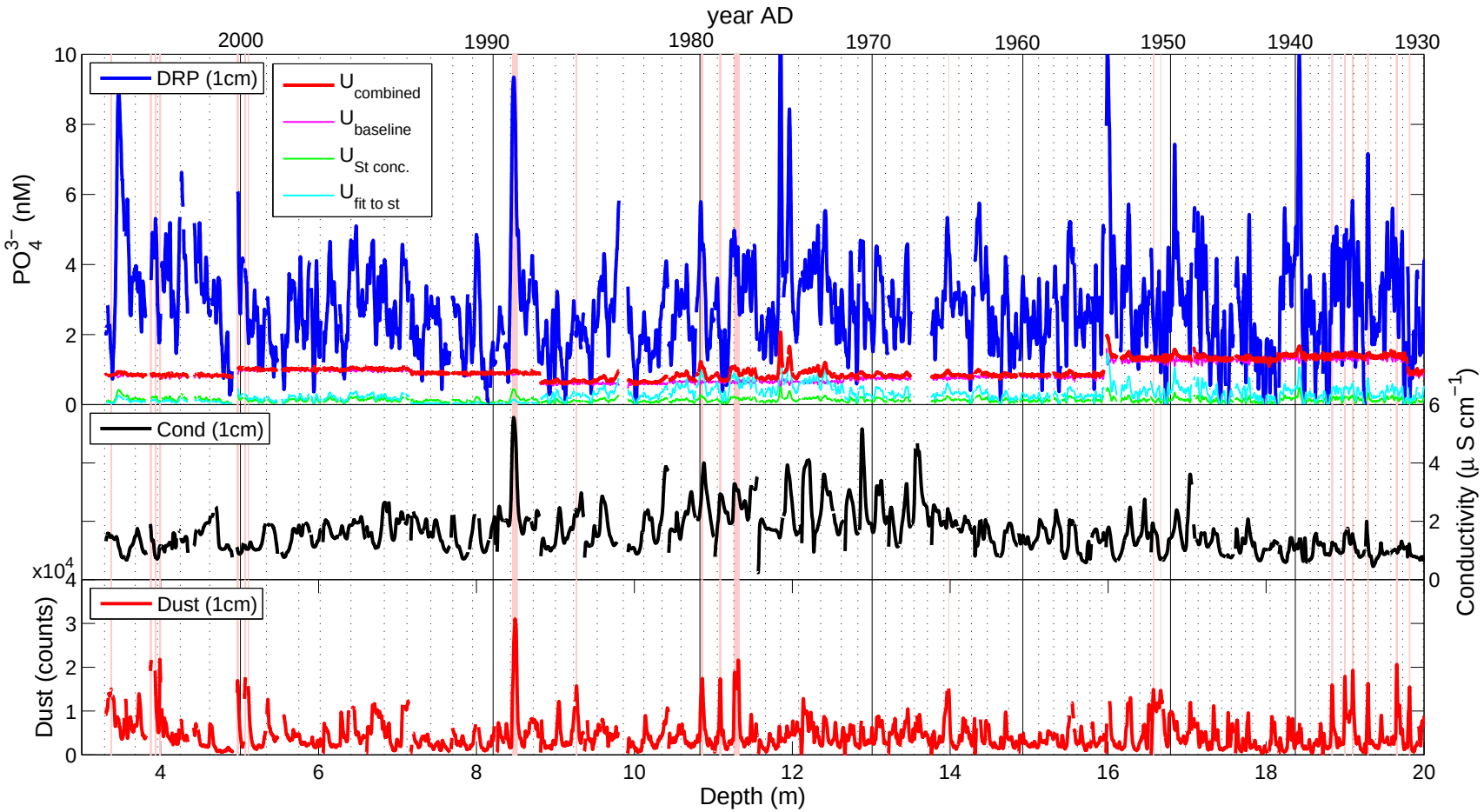

Fig. 3.4: Top: DRP concentration on a depth scale with 1 cm smoothing as detected in the North East Greenland Ice Sheet (NEGIS) firn core (blue) together with the uncertainty (U) budget for DRP; magenta shows the uncertainty arising from the noise on the baseline, green from precision when preparing standards, cyan from the uncertainty on the fit used, and red is the combined uncertainty. Middle: Conductivity with a 1 cm smoothing. Bottom: Dust with a 1 cm smoothing. Vertical red bars indicate peaks of dust exceeding three standard deviations from the mean. Dotted vertical lines are annual layers as determined from Na^+ peaks.

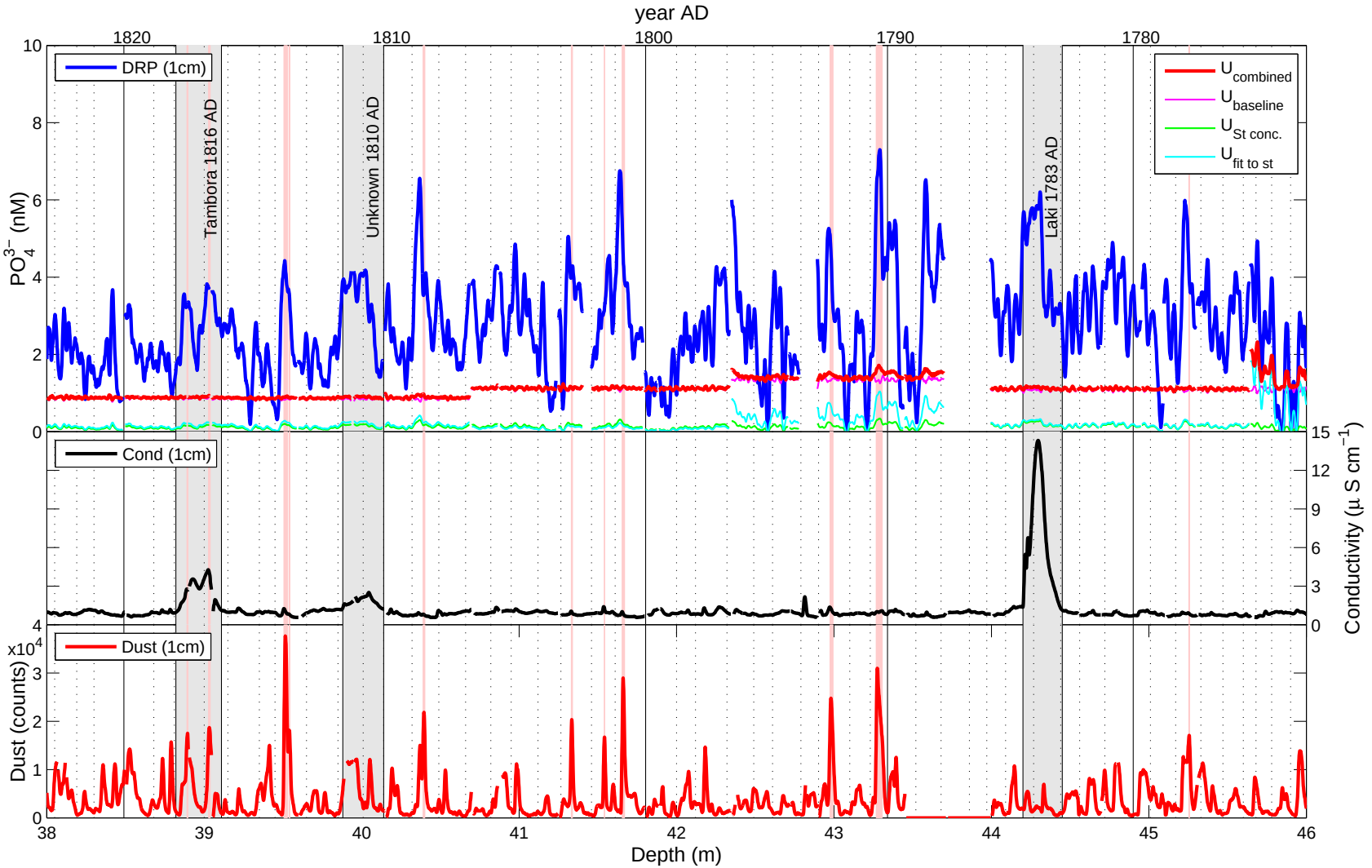

Fig. 3.5: Top: Calibrated DRP concentration on a depth scale applied a 1 cm smoothing as detected in the North East Greenland Ice Sheet (NEGIS) firn core (blue) together with the uncertainty (U) on the detected DRP; magenta shows the uncertainty arising from the noise on the baseline, green from precision when preparing standards, cyan from the uncertainty on the fit used, and red is the combined uncertainty. Middle: Conductivity applied a 1 cm smoothing. Grey vertical bars indicate the Tambora eruption 1816 AD, an unknown eruption in 1810 AD and the Laki eruption 1783 AD. Bottom: Dust applied a 1 cm smoothing. Vertical red bars indicate peaks of dust exceeding three standard deviations from the mean. Dotted vertical lines are annual layers as determined from Na^+ peaks.

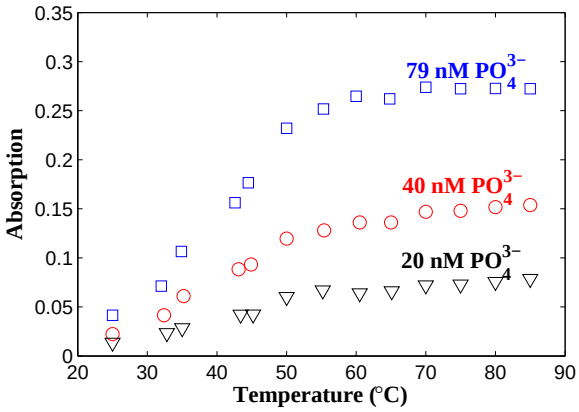

Fig. 3.6: Light absorption as a function of temperature for three different PO_4^{3-}standards; 79 nM (blue), 40 nM (red) and 20 nM (black). Standards were prepared for each temperature by repeated dilution from a solution of 1 μg/L PO_4^{3-}.

3.4 *Supplementary material for: A continuous flow analysis method for determination of dissolved reactive phosphorus in ice cores*

3.4.1 Temperature

The sensitivity of the method was increased by heating the mixed reagents to 65 °C, although sample heating increases the risk for interferences resulting from the production of precipitates of silicate and arsenate [*Zhang and Chi*, 2002; *Gimbert and Worsfold*, 2007; *Nollet*, 2007; *Ma et al.*, 2009]. Such interferences are possible, as these ions react with molybdenum blue to create the same blue colour as the reaction with PO_4^{3-}. However, silicates are not present in ice cores in quantities great enough to interfere and arsenate is probably not present in quantities large enough to perturb the DRP measurements. It has been reported that thiosulfate preferentially reacts with arsenate, and could therefore remove any potential for arsenate interferences [*Zhang and Chi*, 2002].

The sensitivity to changes in mixing coil temperature was also investigated. The 3.5 m long mixing coil was immersed in a heat bath and heated from 25 to 85 °C (Figure 3.6). Flow rates were maintained at 1.02 mL/min for the sample and 0.08 mL/min for buffer and reagent. The signal integration time was 300 ms. A strong increase in sensitivity was observed for temperatures up to 50 °C, so the mixing coil temperature was maintained at 65 °C.

3.4.2 Filtration

Phosphate samples are usually filtered to remove particles, thus ensuring that only the soluble $PO_4^{3-}$is detected, while the acid labile fraction is not. Furthermore, it is important that insoluble particles are removed from the sample stream before they enter the LWCC where they interfere with the absorption signal. The continuous nature of the CFA system requires that the filter can function for reasonably long

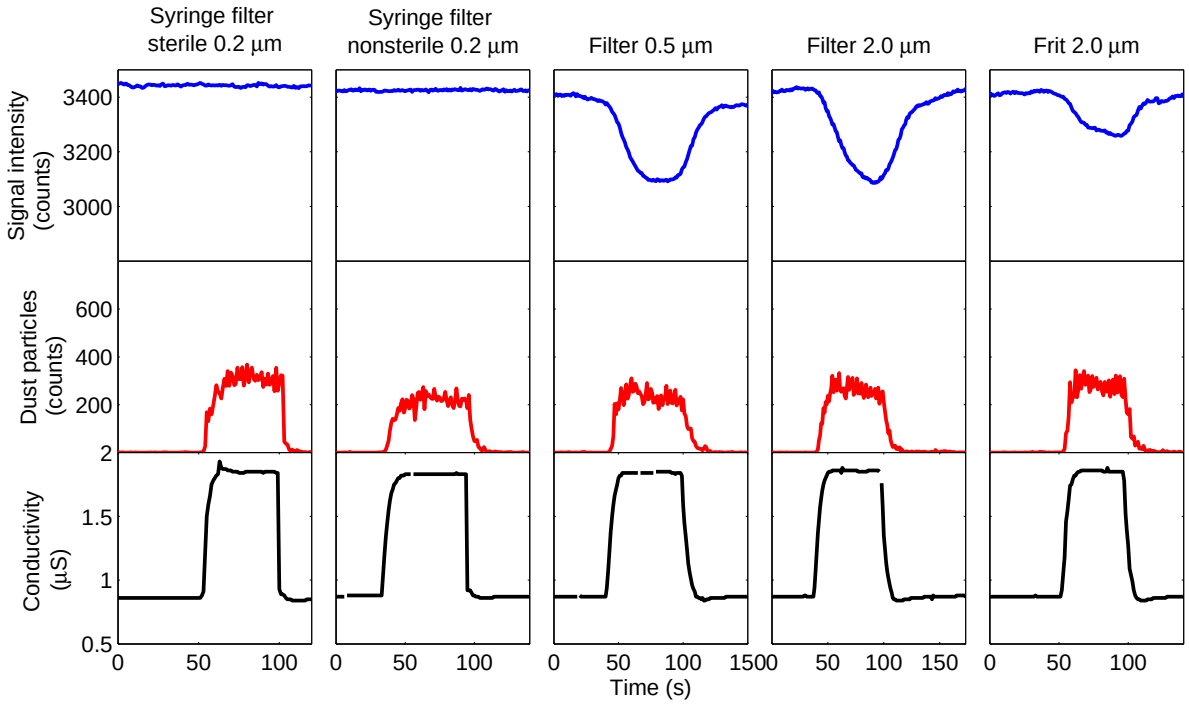

Fig. 3.7: Demonstration of the efficiency of filters, starting from left: Sterile syringe filter, Non-sterile syringe filter, 0.5 μm in-line filter, 2.0 μm in-line filter and a 2.0 μm frit-in-ferrule. Top: Absorption cell signal intensity for a filtered bulk snow sample. Note that molybdate was not added in this test and thus any absorption would be caused by particulate interference and not by PO_4^{3-}. Middle: Dust particles (red) counts detected using an ABAKUS laser particle counter. Bottom: Melt water conductivity (black). Both dust and conductivity were detected before filtering.

periods of time without clogging yet being of sufficiently small volume to avoid excessive sample mixing.

Filters were tested by introducing a bulk sample of melted ice core water through a conductivity meter, then an ABAKUS insoluble dust detector and finally through the filter into the LWCC, adding buffer and reagent but not molybdate. With this set-up, any absorption would be due to particle scattering in the LWCC rather than formation of molybdate complexes. Different types of filters were tested including an 2.0 μm frit-in-ferrule in PCTFE (Polychlorotrifluoroethylene) material and two in-line PEEK (organic polymer thermoplastic) filters of 0.5 μm and 2.0 μm pore size (IDEX-Health and Science, P372x, A701 and A702, respectively). All these filters were found to be ineffective for removing the particles (Figure 3.7, right). Commercial syringe filters with a pore size of 0.2 μm were also tested; one sterile (Minisart, NML) and one nonsterile (LGG, polyethylene) type, with diameters of 25 mm and 26 mm respectively (Th. Geyer, 9055541 and 9049101)(Figure 3.7, left). These two filters were capable of removing particulates from the sample stream, with minimal disruption to the flow rate.

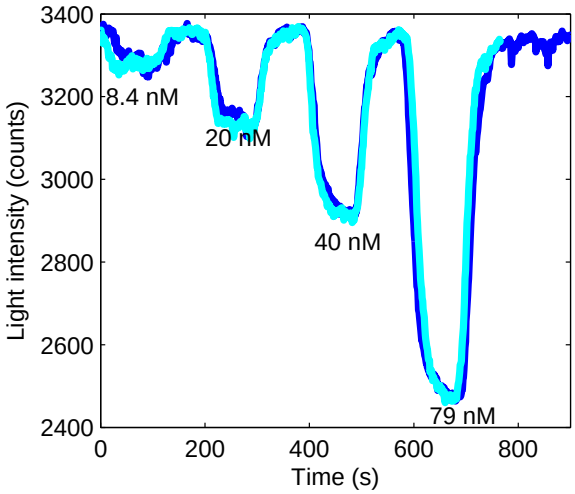

Fig. 3.8: Two PO_4^{3-}standard runs of four different concentrations.

3.4.3 Equipment used

Uncolored low density polypropylene bottles used were from Nalgene Corp., Rochester NY, USA. All reagents used were of analytical grade, purchased from Merck (Darmstadt, Germany). Stock solution of $PO_4^{3-}$was bought at Merck, Darmstadt, Germany and the milliQ system used is from Millipore Corporation, MQ advantage A10, 18.2 MΩ/cm.

3.4.4 Example of Standard runs

Two standard runs are presented in Figure 3.8. The standards were remade between the two runs.

3.4.5 Uncertainties

The precision of the standards were determined by the accuracy of the pipettes, which was determined to be 0.9%. Further we found that the precision of dispensing the milliQ varied by up to 6%. In combination after making a double dilution the maximum difference between the highest concentration possible and lowest possible, with these uncertainties on the pipetting and diluting yields 4.65% uncertainty on the standard concentrations used for determining calibrations for the NEGIS firn core.

The uncertainty of the linear fit delta_a was determined in the following way $\delta_\alpha = (\sqrt{\frac{\sum(c-\alpha\cdot abs)^2)}{n-1}} \cdot \frac{\sqrt{\sum abs^2}}{\sum abs^2})$, where α is the linear coefficient, c is the concentration in nM and abs is the absorption $(-\log_{10}(\frac{I}{I_0}))$. This is valid assuming that the fit goes through the zero point. The DRP concentration was then determined using the difference between $\alpha + \delta_\alpha$ and $\alpha - \delta_\alpha$ as the linear coefficient. The uncertainty from the baseline was determined by calculating the difference between using the

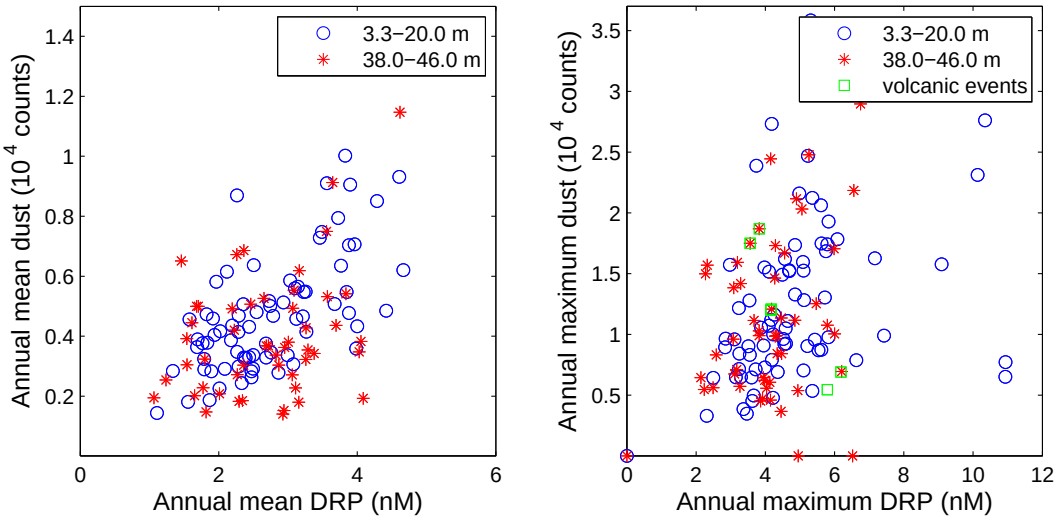

Fig. 3.9: Dust against DRP for the two sections of firn; 3.3 to 20 meters depth (blue) and 38 to 46 meters depth (red): Left for annual means and right for maximum annual peaks as well as for extreme values during volcanic events. Notice difference in scales between the two plots.

baseline I_0 to determine the absorption and the baseline minus three times the standard deviation ($I_0 - 3 \cdot \sigma(I_0)$).

3.4.6 DRP correlations

The correlation between DRP and dust is (r=0.45). Weaker correlations were found for Na (0.15), $\delta^{18}O$ (0.04) and conductivity (0.3). Figure 3.9 shows DRP annual levels and annual maximum values against similar for dust.

4. GREENLAND ICE CORES CONSTRAIN GLACIAL ATMOSPHERIC FLUXES OF PHOSPHORUS

Kjær, H. A., R. Dallmayr, J. Gabrieli, K. Goto-Azuma, M. Hirabayashi, P. Vallelonga and A. Svensson[1]

Phosphorus is a limiting nutrient for primary productivity although little is known about past atmospheric fluxes to the open ocean. In this study phosphate and phosphorus concentrations have been determined in the North Greenland Eemian Ice Drilling Project (NEEM) ice core for selected periods during the last glacial. Phosphate was determined continuously using a molybdenum blue spectroscopic absorption method and discretely by ion chromatograph (IC). Total P was determined discretely using inductively coupled plasma sector field type mass spectrometer (ICP-SFMS). For the last glacial period, we found concentrations between 3 and 62 nM PO_4^{2-} *and 7 to 929 nM P. We find glacial atmospheric fluxes of phosphorus were 4 to 11 times higher than the past century, with the highest input during the cold glacial stadials (GS). Changes in P and* PO_4^{3-} *fluxes between mild glacial inter stadials (GI) and GS correlate positively with dust variability. For the very high phosphate and phosphorus loads during last glacial maximum, the relationship between phosphate and dust is weaker than in GIs and milder GSs, suggesting either secondary phosphate sources or multiple dust sources. Based on crustal abundances, we find that dust inputs are sufficient to account for all P deposited during all periods investigated except the LGM. Sea salts contributing* 10^{-3} *nM P and land biogenic emissions are minor sources. The soluble fraction of P is larger in the mild GIs as compared to the dust rich GSs.*

4.1 Introduction

Phosphorus is an important nutrient for the biosphere, and is believed to have been the limiting nutrient for ocean primary production the past [*Falkowski et al.*, 1998] either directly or through its effect on nitrogen fixation [*Okin et al.*, 2011]. Thus knowing the P load to the ocean is essential to estimating primary productivity [*Redfield*, 1958; *Lenton and Watson*, 2000] and CO_2 draw down. The atmospheric transport of P to the oceans is small compared to the total P budget of the ocean, however concentrations of nutrients are often heavily depleted in the surface ocean

[1] This Chapter is intended for publication in Global BioGeoChemical Cycles. Co-authors R. Dallmayr and K. Goto-Azuma are from the National Institute for Polar Research, Tokyo, Japan and co-author J. Gabrielli is from Institute for Dynamics of Environmental Processes, IDPA-CNR, Venice, Italy. Remaining co-authors are from Center for Ice and Climate, NBI, University of Copenhagen

due to uptake by primary production. In sections of the remote ocean where nutrients are not resupplied by upwelling or from rivers, atmospheric transport is an important source of nutrients to the surface [*Mahowald et al.*, 2008].

The oceans are not the only biological systems dependent on P. In a review including 653 freshwater, 243 marine and 173 terrestrial experiments it was found that although N limitation is stronger in marine systems, N and P are of equal importance in terrestrial and freshwater systems and that there is a strong synergistic effect in all systems [*Elser et al.*, 2007]. Based on a subset of 641 experiments, it was found that 28% of the experiments were co-limited by P and N, and with similar effects of N and P across systems including marine habitat [*Harpole et al.*, 2011]. Although most terrestrial systems get their nutrient supply from water flow or from the soil, old forests are believed to be equally limited by phosphorus from atmospheric transport and phosphorus from water sources as the soil becomes depleted of nutrients over time [*Vitousek and Farrington*, 1997; *Vitousek et al.*, 2010; *Menge et al.*, 2012].

Little is known about the atmospheric transport of phosphorus, with estimates of global P deposition ranging from 0.54 Tg P/yr [*Krishnamurthy et al.*, 2010] to 1.15 Tg/yr [*Mahowald et al.*, 2008]. Furthermore, many poorly constrained assumptions are invoked in calculating dust-related changes in phosphorus transport: The crustal abundance of P varies from in the order of 300 ppm and up to 1300 ppm invoking a large uncertainty in the P content of atmospheric dust ([*Okin et al.*, 2011] and references therein). Additionally the atmospheric transport of dust to the remote oceans is poorly constrained in models and the present day dust deposition over the oceans differers from observations by an order of magnitude [*Mahowald et al.*, 2009]. Dust-based estimates of the atmospheric transport of P to the oceans are about 0.32 Tg/yr, only a small fraction of the total global P cycle, with 0.13 Tg/yr deposited in the Atlantic ocean, 0.073 Tg/yr in the Indian ocean, 0.067 Tg/yr in the Pacific and 0.032 Tg/yr in the Southern ocean [*Mahowald et al.*, 2008; *Okin et al.*, 2011].

Total phosphorus fluxes are insufficient to constrain the effect of P on the biosphere, due to the importance of solubility, speciation, chemical form (inorganic, organic, colloidal) and other parameters that control the bioavailability of such nutrients. It has been estimated that only 10% of the aeolian dust present in the water column is released, while the remaining 90% sinks to the bottom [*Mahowald et al.*, 2008; *Wallmann*, 2010]. Although limited information is available, one study found contemporary atmospheric fluxes of soluble organic P to the oceans range from 20-83% (0.35 Tg P/yr) of atmospheric total soluble phosphorus [*Kanakidou et al.*, 2012]. Other studies find approximately 16% of the total P deposition to the global oceans to be bioavailable [*Krishnamurthy et al.*, 2010] For specific ocean basins, it is estimated that the dissolved organic fraction forms 30-50% of the P available to the ocean biosphere in the North Pacific [*Bjorkman and Karl*, 2003] and that the organic phosphorus supports 25% of the annual production in the subtropical North Atlantic [*Lomas et al.*, 2010].

The influence of coastal shelves and complementary nutrients has led to much disagreement regarding the glacial-interglacial changes in oceanic productivity and P availability. The shelf nutrient hypothesis [*Broecker*, 1982; *Filippelli*, 2008] proposes that the lower sea level during glacial periods could have enhanced P trans-

port to the oceans. Sediment records from the sub-Antarctic Southern ocean and the equatorial Pacific indicate a maximum in marine export production during the last deglaciation [*Jaccard et al.*, 2013; *Filippelli et al.*, 2007] and recently it was suggested that the oceanic P cycle is even today out of balance with a net loss of more than 4.5 % per kyr [*Wallmann*, 2010]. Other studies suggest that the effect of the continental shelves on primary production is less important [*Ushie and Matsumoto*, 2012]. Records of paleoproductivity are scarce and the temporal resolution is often low. It is generally agreed upon that the sub Antarctic zone of the Southern ocean experienced higher primary production export [*Jaccard et al.*, 2013], but for other oceans the evidence is contradictory [*Maher et al.*, 2010]. For the Pacific ocean the export production during the glacial as compared to present day has been reported as greater [*Kohfeld et al.*, 2005], equal [*Anderson et al.*, 2008; *Ziegler et al.*, 2008; *Tamburini and Fölimi*, 2009] and lower [*Amo and Minagawa*, 2003; *Paytan et al.*, 2004; *Loubere and Richaud*, 2007; *Zhang et al.*, 2007]. The interpretation is complicated by changes in ocean currents, up-welling zones, position of production zones, mixing layer depth and deposition of non-organic material [*Tamburini and Fölimi*, 2009; *Maher et al.*, 2010].

Ice cores provide valuable information on large scale climate and environmental processes, such as atmospheric transport and source region variability [*Fuhrer et al.*, 1996; *Svensson et al.*, 2000; *Ruth et al.*, 2003; *Fischer et al.*, 2007] as well as detailed process information such as past iron fluxes to the ocean and dust-iron solubility changes [*Vallelonga et al.*, 2013; *Hiscock et al.*, 2013; *Spolaor et al.*, 2013], besides the well recognized records of temperature proxies and greenhouse gases [*EPICA community members*, 2004; *NGRIP members*, 2004]. Aeolian dust transport, which is increased during the glacial cold periods [*Svensson et al.*, 2000; *Ruth et al.*, 2003], is expected to enhance the amount of P available to the biosphere. The observed increase in aeolian dust in ice cores in glacial periods is believed to result from more efficient transport mechanisms and drier source areas[*Ruth et al.*, 2003; *Svensson et al.*, 2000].

Only two studies have reported P or PO_4^{3-} from ice cores. *Kjær et al.* [2013] used a molybdenum blue spectroscopic absorption method to find dissolved reactive phosphorus (DRP) with a mean concentration level of 2.74 nM PO_4^{3-} in a shallow Greenland firn core (NEGIS, 75.38°N, 35.56°W) covering the recent century, and 8.06 nM P was found using inductively coupled plasma sector field mass spectroscopy (ICP-SFMS) in two other Greenland shallow firn cores (D4, 71.4°N, 44°W and Basin 9, 65°N, 44.9 °W) covering the period since 1950 AD [*Edwards et al.*, 2007].

In this study we constrain the late glacial transport of phosphate and total P based on the North Greenland Eemian Ice Drilling Project (NEEM, 77.45 N 51.06 W, see Figure 4.1) ice core [*Dahl-Jensen et al.*, 2013]. Phosphate was detected continuously in selected ice core sections using a molybdenum blue method [*Kjær et al.*, 2013] and discretely by ion chromatograph (IC). Total P was determined on discrete samples using ICP-SFMS, and the acid labile fraction DRP_{acid} was determined using an unfiltered continuous molybdenum blue method [*Kjær et al.*, 2011].

Combining these analytical techniques, we provide the first evaluation of phosphate solubility and changes in the glacial atmospheric fluxes of the Northern Hemisphere over the last glacial period.

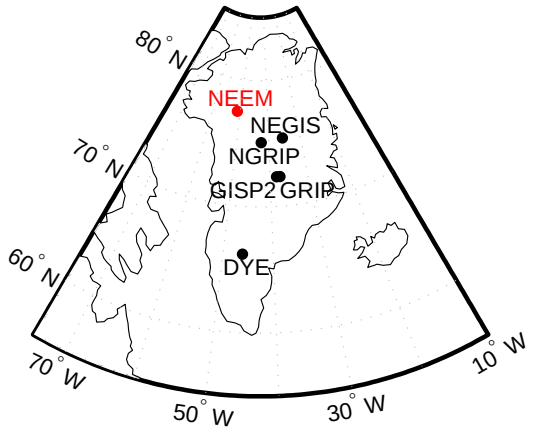

Fig. 4.1: Location of the NEEM ice core.

4.2 Methods

Several methods for the determination of phosphate and phosphorus were applied to replicate sections of the NEEM ice core. These involved discrete sample determination of total P using ICP-SFMS, IC for determination of PO_4^{3-} and continuous flow analysis (CFA) of dissolved reactive phosphorus (DRP) using a molybdenum blue method [*Kjær et al.*, 2013]. A summary of the methods is presented in Table 4.1. Ice core sections were drilled in 2009 and sampled in 2010 and 2013.

In 2010, 1.1 m long ice core sections were melted on site in the NEEM camp and determined for DRP_{acid}, the acid labile phosphorus, using a modified version of the DRP technique by *Kjær et al.* [2013]. Discrete samples integrating the 1.1 m samples were collected for later analysis. While the continuous detections were performed at the NEEM field site, the discrete samples were frozen and transported to the National Institute for Polar Research (NIPR), Tokyo, Japan for determination using IC and to IDPA-CBR, Venice, Italy for P detection using ICP-SFMS.

In 2013 55 cm pieces from the NEEM ice core were melted continuously using the recent build continuous flow analysis system (CFA) at NIPR, Tokyo, Japan and determined for DRP[*Kjær et al.*, 2013]. Further discrete samples were collected from the CFA system for every 5 to 9 cm. These discrete samples were later analysed for phosphate by IC and total phosphorus by ICP-SFMS in the same manner as the samples collected in 2010.

4.2.1 Continuous analysis methods

Melted NEEM samples were analysed continuously using a molybdenum blue (MB) reagent determination method. The primary difference between the 2010 and 2013 analyses is the position of a 0.2 μm particle filter, respectively located after and before the addition of MB reagent. The location of the filter after the acidic reagent in the 2010 NEEM continuous flow analysis (CFA) system allowed acid labile reactive phosphorus (DRP_{acid}) to be leached from insoluble dust particles [*Kjær et al.*, 2011], whereas the 2013 NIPR CFA set-up ensured that only the water-soluble reactive

Tab. 4.1: Methods used for the NEEM study.

Label	Compound determined	Concentration given in	Detection method	Sample Type	Laboratory	Collection Year	Detection Year	LOD	References
A1	total P	P	ICP-SFMS	discrete	NRC, Italy	2010	2014	1.6 nM P (50 ppt)	
A2		P		discrete	NRC, Italy	2013	2014	1.6 nM P (50 ppt)	
B1	acid labile P	PO_4^{3-}	DRP_{acid}	continuous	NEEM	-	2010	1.1 nM PO_4^{3-}(120 ppt)	[*Kjær et al.*, 2011]
C1	phosphate	PO_4^{3-}	IC	discrete	NIPR, Japan	2010	2011	1.0 nM PO_4^{3-}(110 ppt)	
C2		PO_4^{3-}		discrete	NIPR, Japan	2013	2013		
D1	water labile P	PO_4^{3-}	DRP	continuous	NIPR, Japan	-	2013	1.1 nM PO_4^{3-} (120 ppt)	[*Kjær et al.*, 2013]

phosphorus (DRP) fraction was determined [*Kjær et al.*, 2013]. Due to the use of slower liquid flow rates the DRP_{acid} system had greater dispersion [*Breton et al.*, 2012] of up to 0.5 m and a longer reaction time.

Both continuous methods (DRP and DRP_{acid}) were calibrated using PO_4^{3-} standards diluted from a concentration of 1g/L stock solution.

Insoluble dust particle concentrations were also determined continuously using an ABAKUS instrument (Klotz, Germany, [*Bigler et al.*, 2011]).

4.2.2 Discrete samples

During the 2010 NEEM CFA campaign discrete samples integrating 1.1 metre sections (2 bags) were collected in pre-cleaned 100 mL polypropylene (PP, Asone, Japan) bottles for analysis by Ion Chromatograph (IC) and 10 mL polyethylene (PE, Nalgene Corp, USA) bottles for analysis by ICP-SFMS. Phosphate concentrations were measured by IC in 2011 and total P was measured by ICP-SFMS in 2014.

Discrete samples were also collected during the 2013 NIPR CFA campaign using a Gilson FC204 fraction collector kept in a plastic hood with HEPA filtered flow. Each sample integrated either 5 cm, intended for cations only or 9 cm if intended for analysis of both cations and anions. The samples were transferred to polypropylene bottles after each 55 cm (1 bag) of ice was melted on the CFA system. Immediately after collection some samples were analysed by IC, while others were immediately frozen and analysed within two weeks. Some of these discrete samples were also, within 1 week of IC determinations, remelted and re-analysed for DRP using the molybdenum blue method [*Kjær et al.*, 2013]. In February 2014 the samples were sent to Venice, Italy, for determination of total P by ICP-SFMS.

Phosphate was determined discretely by ion chromatograph, using a Dionex DX500. AS11-HC and CS 14 columns were used for the determination of anions and cations respectively. No filtering or other pretreatments applied. For a 5 ppb (52.6 nM) PO_4^{3-} standard the repeatability of the IC measurements was about 1.5 %. The approximate detection limit of ion chromatograph was 110 ppt (1.0 nM). Blank values (milliQ water-stored in a similar way to samples) were below the PO_4^{3-} detection limit for the IC.

Total phosphorus concentrations were determined using ThermoScientific Element2 inductively coupled plasma sector field mass spectroscopy (ICP-SFMS) with an APEX2 (ESI, Omaha, USA) sample introduction system. The recovery of samples ranged from 102 to 108% with a precision of 3-4 %. The limit of detection (LOD) for total P was 30 ppt (1.0 nM) in medium resolution (MR) and 50 ppt (1.6 nM) P in high resolution (HR).

4.2.3 Method inter-comparison

There is no certified reference material available for phosphorus or phosphate in the concentration range or matrix material suitable for polar ice, therefore we have used diluted phosphate concentration standards (Merck) as means of inter-comparing the methods described here. Phosphate standards used to calibrate the DRP system ranged in concentration from 79 nM to 4.2 nM and were treated similarly to ice

samples. The standards were prepared in September 2013 for the NIPR CFA campaign and immediately measured for DRP, then later for IC (November 2013) and ICP-SFMS (February 2014). The standard concentrations determined by IC were found to be higher than expected, by +5 to 10 % for the 79 nM standard and by 100% for one of the 4.2 nM standards (9.5 nM PO_4^{3-}). For the ICP-SFMS analyses, the 79 nM standards were comparable to expected values (74.4-81.1 nM P), while the same low concentration standard of 4.2 nM standard showed similar results to the IC determination (10.6 nM P). This suggests that at least one of the standards was contaminated with approximately 5 nM P in the process of freezing, storage and remelting. Such a level of contamination is not significant for glacial stadial samples, but the low concentrations of phosphate found in glacial interstadials are comparable to this level of contamination. These results indicate the importance of determining phosphate immediately after melting ice core samples, and a potential bias induced by refreezing and re-analysing low concentration samples.

4.3 Results

Table 4.2 show the minimum and maximum range of concentrations of total P determined by ICP-SFMS, DRP_{acid} and DRP using CFA methods and PO_4^{3-} determined by IC found in the NEEM samples obtained both in 2010 and 2013. These results are also shown in Figure 4.2 along with insoluble particle concentrations. Note that the discrete samples collected during the 2010 NEEM CFA campaign do not usually correspond to the same depth range as those reported for the continuous data or 2013 CFA campaign. The samples collected in 2010 include adjacent 55 cm sections of ice located either above or below those sampled in 2013. As expected, the various phosphate fractions are consistently lower than total phosphorus, but vary greatly according to the analytical method used. The lowest concentrations were consistently determined by the CFA-DRP technique. Insoluble particle (dust) concentrations follow those observed in other Greenland ice cores [*Ruth et al.*, 2003].

4.3.1 Comparison of analytical methods

Correlations (Table 4.3) between the different methods of detecting P species is high (r>0.83) although the absolute concentrations vary greatly. Usually the lowest concentrations were determined by CFA-DRP (PO_4^{3-}), then IC (PO_4^{3-}), then DRP_{acid} (PO_4^{3-}) and the highest concentrations were consistently found for total P determined by ICP-SFMS. We expected total P determined by ICP-SFMS concentrations to be highest as the technique measures P in ionic forms other than phosphate, as well as P present in insoluble dust. Also we observed that DRP_{acid} concentrations were higher than PO_4^{3-} determined by both IC and DRP; the ratios of IC and DRP to DRP_{acid} are 0.53 $\pm$0.43 and 0.17 $\pm$0.16 respectively. This is probably due to the acid reagent in the MB method leaching acid-labile P from insoluble dust particles. The fraction of acid-released P from dust particles may depend on the type of dust. We find that the ratio of acid-labile phosphorus (DRP_{acid}) to total P is close to 1 (0.96 $\pm$0.6). Only for glacial stadial 8 is the DRP_{acid} signal consistently greater than total P determined by ICP-SFMS. In this section of the

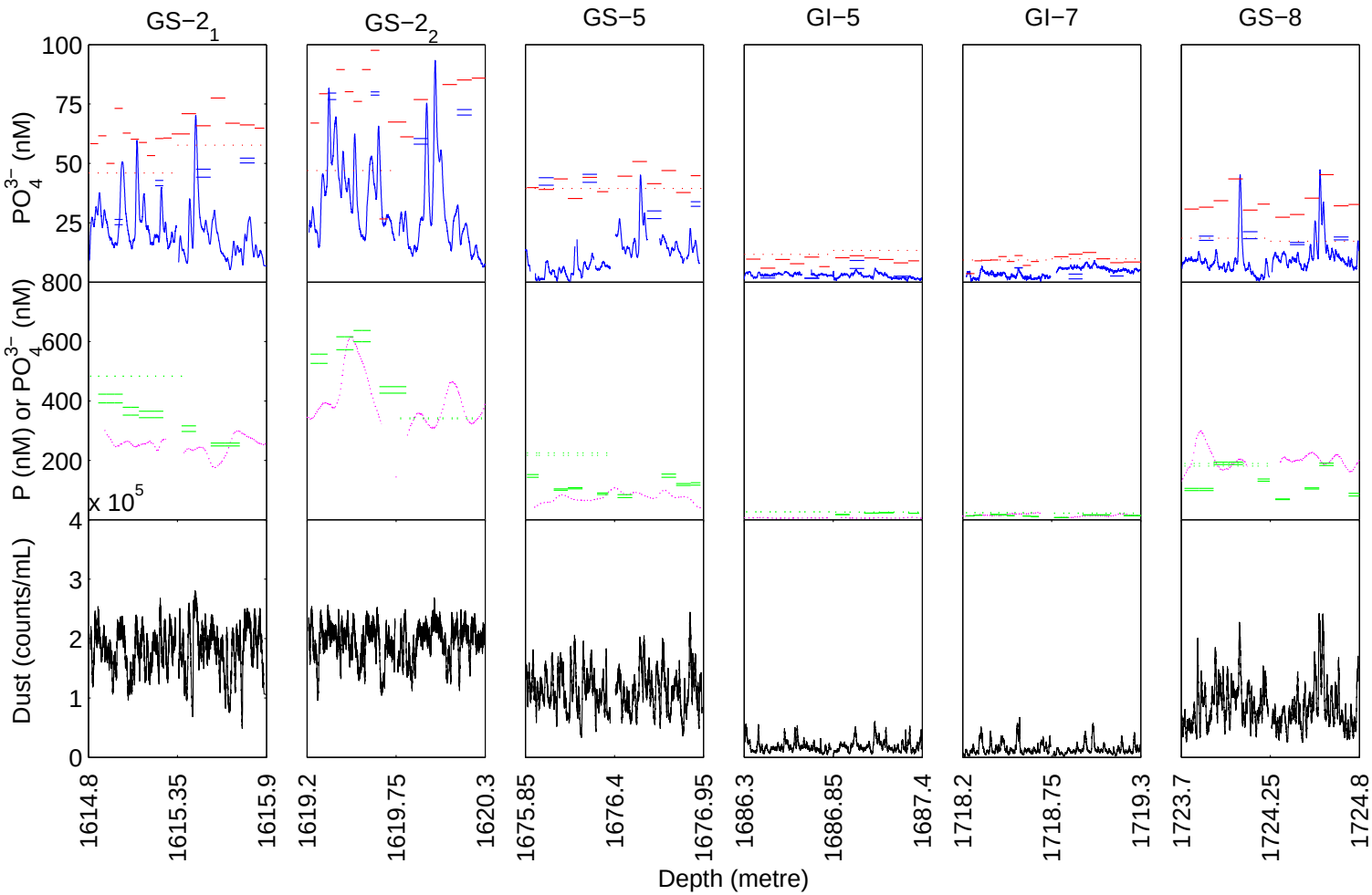

Fig. 4.2: Comparison of phosphorus and phosphate determinations for 6 climatic periods during the previous glacial. Top: IC-PO_4^{3-} (red) and DRP-PO_4^{3-} (blue). PO_4^{3-} as detected using IC (red), dotted lines represent double bag means (2010 samples), while full lines represent data from 2013 also shown in the top is continuous DRP using CFA (blue) and discrete samples detected using CFA also shown in blue. Middle: ICP-SFMS-P (green) and DRP$_a$*cid*-PO_4^{3-} (magenta). For ICP-SFMS-P dotted lines represent double bag means (2010 samples), while full lines represent data from 2013. Bottom: Insoluble dust particles (black) as determined using on 2013 samples.

Tab. 4.2: Concentrations, fluxes and solubilities of phosphorus and phosphate observed in the NEEM glacial ice. The sample ages were determined from the GICC05 time scale [*Rasmussen et al.*, 2013]. The letters refers to the type of measurements used, while the number following to the year the sample was obtained (see Table 4.1), as an example A2 is ICP-SFMS with the sample obtained in 2013. Note that for B1, and C2 often the data represent also the following and previous 0.55 m, if so values are noted with a star. Note that results from each detection method was not available for the entire time slice, thus estimates can vary relative to each other due to different temporal sections represented. Also shown are values for the recent ∼100 yrs (Holocene) as observed in other Greenland ice cores [*Edwards et al.*, 2007; *Kjær et al.*, 2013].

Climate interval	**GS2.1**	**GS2.2**	**GS5**	**GI5**	**GI7**	**GS8**	Holocene
Age (GICC05) (kyr)	25.17-25.31	25.70-25.84	31.24-31.36	32.27-32.34	35.17-35.24	35.52-35.64	1900-2004 AD
Depth(metre)	1614.80-1615.90	1619.20-1620.30	1675.85-1676.95	1686.30-1687.40	1718.20-1719.30	1723.70-1724.80	
Bag(#)	2937-2938	2945-2946	3048-3049	3067-3068	3125-3126	3135-3136	
Insoluble particles (# x 10^4/mL)	4.88-28.08	9.58-26.88	3.35-24.40	0.01-6.11	0.15-6.72	2.51-24.22	
Concentrations							
A1 (nM P)	483-484*	340-929*	217-225	26-27*	22-24*	181-189*	
A2 (nM P)	248-423	427-637	75-154	17-24	7-17	68-194	8.06
B1 (nM PO_4^{3-})	176-302	284-616	42-108	4-9	5-25	129-300	
C1(nM PO_4^{3-})	46-62*	47*	39	12-13*	9-10*	17-19*	
C2 (nM PO_4^{3-})	27-78	27-105	35-51	6-11	4-13	27-45	
D1 (nM PO_4^{3-})	22	32	11	3	4	10	2.74
Fluxes							
A2 (P nmol yr^{-1} m^{-2})	2.87	4.67	1.09	0.34	0.22	1.31	
B1 (PO_4^{3-} nmol yr^{-1})	2.02	3.40	0.66	0.10	0.24	1.94	
C2 (PO_4^{3-} nmol yr^{-1})	0.50	0.65	0.38	0.14	0.14	0.32	
D1(PO_4^{3-} nmol yr^{-1})	0.18	0.29	0.10	0.05	0.06	0.09	
Solubilities							
C2/A2 (%)	18	14	36	41	64	25	
D1/A2 (%)	6	6	9	13	27	7	34

Tab. 4.3: Pearson correlations between the different detections of P and PO_4^{3-} as well as correlations to dust in 5 or 9 cm resolution dependent on the available discrete samples.

	IC	DRP	ICP-SFMS	DRP_{acid}	Dust
IC	1	0.88	0.90	0.87	0.97
DRP		1	0.94	0.91	0.87
ICP-SFMS			1	0.83	0.90
DRP_{acid}				1	0.93

ice core, it may be that the presence of acid-labile P from insoluble dust collected on the filter and therefore biased the DRP_{acid} signal to a level greater than that of total P.

Effect of dust and freezing of samples

A significant deviation between the concentration levels of DRP determined continuously via CFA and PO_4^{3-} detected by IC (a ratio of 0.34 $\pm$0.14) was also observed. The concentration levels between the two techniques varied by as much as 76 nM, with greater differences for higher concentrations of dust (see Figure 4.3). The excess PO_4^{3-} determined by IC as compared to the continuous DRP technique correlates linearly with dust by r =0.89. Thus, after compensating for the effect of phosphate from soluble dust, the IC values can be corrected to match the ones detected by DRP or vice versa.

The relation between the excess phosphate detected by the IC could be explained by the fact that IC samples were unfiltered, while particles were filtered from the DRP sample soon after melting (<60 s) thereby quickly removing dust from the sample.

A previous study of DRP determination found that the filtration of surface water samples on 0.2 μm cellulose acetate membranes decreased DRP concentrations by up to 2 nM for sample concentrations ranging from 4.8 to 71 nM [*Patey et al.*, 2010]. The same study found that freezing of unfiltered samples resulted in an increase of approximately 2.7 nM PO_4^{3-} to further investigate this effect, a few samples of the discrete samples collected during the 2013 campaign were later determined as discrete samples on the CFA-DRP set up (Figure 4.2, top graph blue horizontal lines). For climate periods with high dust loads (glacial stadials), most of the remeasured sample concentrations were elevated compared to the initial continuous detection of DRP, but remained below PO_4^{3-} concentrations determined by IC. In contrast similar concentrations were found in samples from glacial interstadial periods with low dust concentrations for both discrete and continuous DRP determinations, again, however the concentration of PO_4^{3-} by IC remained consistently higher. Thus we find that the IC technique exceed the PO_4^{3-} concentration observed with the discrete DRP concentrations, which simulate the continuous DRP, in glacial interstadials (warm periods) suggesting either a detection limit in the IC technique exceeding observations of PO_4^{3-} or an effect of the filter in the DRP method making it a different fraction of dissolved P determined in the DRP as compared to the IC method. For cold climate periods the continuous DRP concentrations are low compared to the

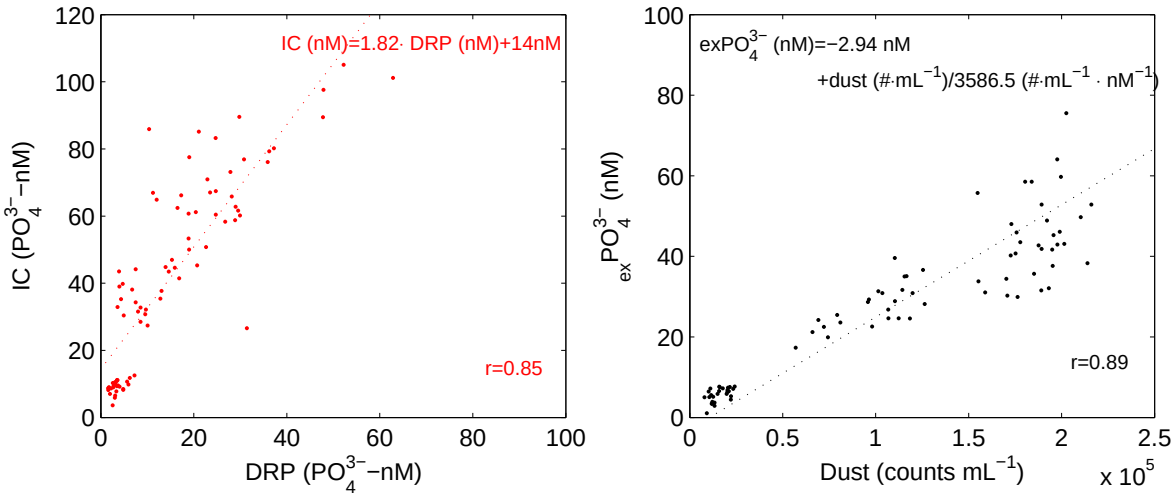

Fig. 4.3: Left) PO_4^{3-} determined using IC against CFA determined DRP. Right) Difference between DRP and IC determined PO_4^{3-} as a function of dust. Also shown is the linear fit and pearson correlations (r).

discrete DRP due to the limited time available for phosphate to be dissolved from dust between melting and analysis and again the difference between IC and discrete DRP could be explained by the filtering of the DRP derived PO_4^{3-}.

For the relation between the DRP discrete samples and the IC samples we do not observe any additional effect of freezing and remelting and the major effect of discrete vs continuous is a result of dust leaching in the water phase. However only limited numbers of discrete DRP samples (24 [2]) were evaluated, the problem of sample storage appears more significant for phosphate in sea water samples than for polar ice.

4.3.2 Influence of climatic changes on atmospheric P deposition

As shown in Table 4.2 and Figures 4.2, 4.4 and 4.5, significant variability is found in concentrations of P and PO_4^{3-} in the NEEM ice core glacial samples.

Phosphate and P concentrations are negatively correlated to temperature proxies δD and δO^{18} in the NEEM ice core. In the cold glacial stadials (GS) P and PO_4^{3-} concentrations are high. The concentrations determined using CFA-DRP are up to 93 nM PO_4^{3-} in the GS, while the GI has lower concentration between 0.6 nM and 9 nM PO_4^{3-}. The change in PO_4^{3-} from GI to GS is between a factor of 3 and 12, while total P changes by a greater amount, from a factor 5 to 39 (see Table 4.4). Similar factors of 15-20 were found for dust and dust proxies during changes from GI to GS for other deep Greenland ice cores [*Steffensen*, 1997; *Ruth et al.*, 2003; *Fischer et al.*, 2007; *Maher et al.*, 2010].

Using recent Holocene DRP data from the Greenland NEGIS firn core (2.74 nM

[2] 10 samples were kept frozen (GS2.1, GS8 and GI7 (top part)), 10 were kept melted (GS5 GI5, GI7 (deeper part)), 2 were frozen until IC measurements, then kept melted until DRP measurements (GS2.2 top part) and 2 were melted and then kept frozen (GS2.2 bottom part).

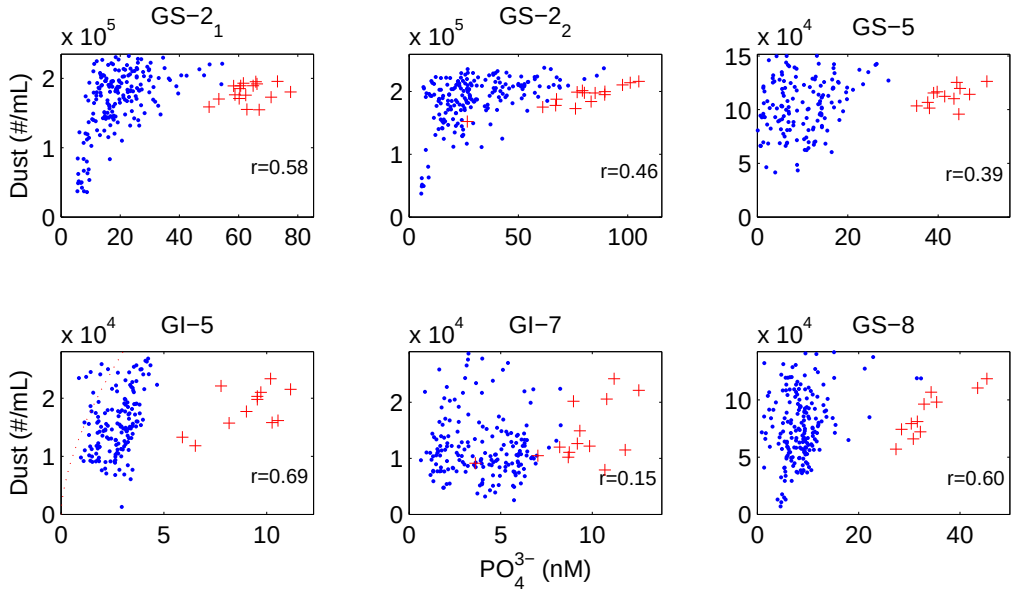

Fig. 4.4: Dust (counts/mL) as a function of PO_4^{3-} for 6 climatic periods as determined using DRP-CFA (blue) and IC (red). GS denote glacial stadial and GI glacial interstadial. Numbers indicate pearson correlation between insoluble dust and DRP in the respective period. Please note that the DRP and dust both have been smoothed by a 1 cm filter for this comparison.

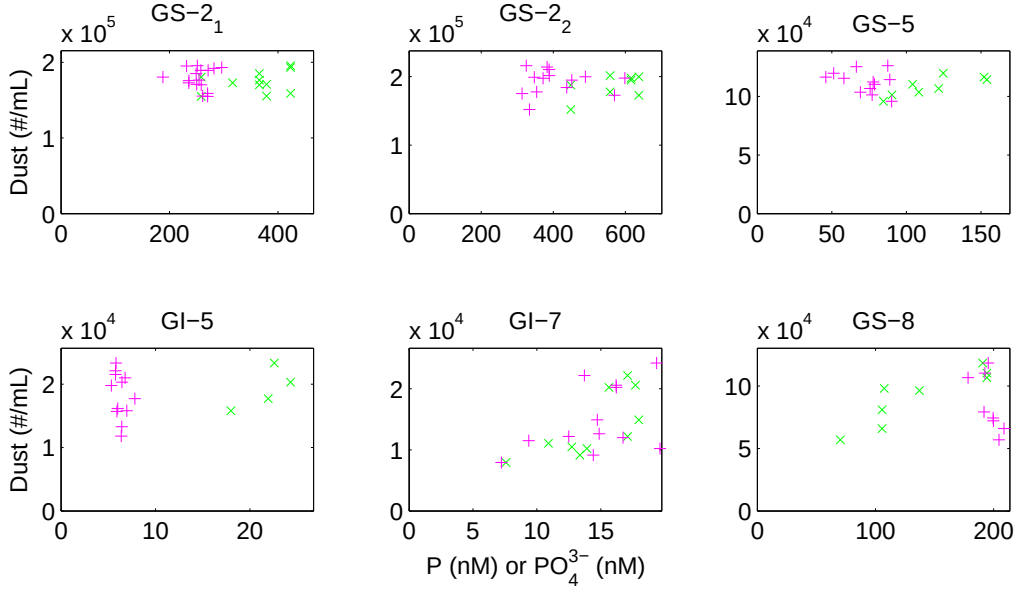

Fig. 4.5: Dust (counts/mL) as a function of PO_4^{3-} or P for 6 climatic periods as determined using DRP_{acid}-CFA (magenta) and ICP-SFMS (green). GS denote glacial stadial and GI glacial interstadial.

Tab. 4.4: The rate of change in deposition between Glacial interstadial (GI) and glacial stadials (GS) shown for the four different methods used in this study. Also shown for ICP-SFMS and DRP is the ratio between Holocene estimates found by *Edwards et al.* [2007] and *Kjær et al.* [2013] respectively (Hol) and last glacial maximum (LGM) represented by $GS2_2$. Note that results from each detection method was not available for the entire time slice, thus estimates of the ratio can vary relative to each other due to different temporal sections represented.

	ICP-SFMS P		$CFA\text{-}DRP_{acid}$		$IC\text{-}PO_4^{3-}$		CFA-DRP	
	flux	conc.	flux	conc.	flux	conc.	flux	conc.
GS/GI	3-21	5-39	3-34	5-76	3-5	4-8.8	2-6	3-12
Hol/LGM		∼70						∼14

PO_4^{3-} [*Kjær et al.*, 2013]) we find that DRP concentrations during the coldest glacial increased by a factor 14 (For concentrations see Table 4.4) suggesting that the land biosphere is not the main source for PO_4^{3-} found in the Greenland ice. The increase of PO_4^{3-} between the LGM and the Holocene is low compared to that of dust proxies in Greenland, which show concentration decreases of 80 to 100 times from the LGM to the Holocene [*Fischer et al.*, 2007]. The dust arrives in Greenland ice mainly from Chinese desert regions and estimated source changes of a factor 2-4 have been found in modelling studies, while a 2-12 times increase in transport mechanisms during the glacial is also suggested [*Fischer et al.*, 2007]. If the source region for P is also China, the combination of source and transport changes could account for the 14-fold increase in DRP.

Dust

We find that dust is the main source of total P in Greenland ice and that during the LGM, when the fluxes of dust were highest, up to 900 nM P could have originated from dust. In the GRIP and NorthGRIP Greenland ice cores approximately 8000-10000 μg dust/kg ice is observed [*Svensson et al.*, 2000; *Ruth et al.*, 2003], while the interglacial stadials show low concentrations in the order of 500 μg/kg. Using the method described by *Kjær et al.* [2013]; assuming all P in the dust is soluble and a mineral dust abundance of 3030 mg P/kg. The theoretical upper limit of P present in such dust (P_{dust}) is $\sim$ 900 nM. This is sufficient to explain total P concentrations observed in the NEEM ice core during the glacial stadials (Figure 4.5). The abundance ratio of P varies in different dust sources with the 3030 mg P/kg dust used here being in the high end compared to P concentration in surface soils (700-1300 ppm) [*Mahowald et al.*, 2008], which would yield P concentrations from dust of 220-420 nM P. Thus using crustal values P_{dust} can explain 40-75% of the 564 nM total P determined by ICP-SFMS. In the warm interglacial stadials P_{dust} is between 10 and 20 nM P using crustal abundances, and $\sim$ 50 nM using rock dust abundances and thus can explain all of the P found using ICP-SFMS in the NEEM ice.

We find high correlations between IC-determined dust species (Ca^{2+}, Mg^{2+}, K^+ and F^-) and PO_4^{3-} (IC), while the high resolution DRP has a lower correlation to insoluble dust, suggesting more complicated processes than simple dust transport,

such as a rain out effect or secondary sources. The IC PO_4^{3-} concentrations determined in 2013 correlate to other soluble dust species such as Ca^{2+}, Mg^{2+}, K^+ and F^- determined on the same samples by 0.94, 0.95, 0.97 and 0.94 (Pearson correlations) respectively. Though the IC results from NIPR 2013 are high resolution (5-9 cm ice) compared to many other discrete measurements performed normally on 55 cm ice pieces, correlation analysis of data that does not resolve annual pattern can only be given limited trust. We thus find that correlation between PO_4^{3-} other IC determined ions such as sea salt related Na^+ and Cl^- are also high (0.89 and 0.83), and that also the land biogenic species NH_4^+ [*Fuhrer et al.*, 1996] correlates by 0.83. NO_3^- is affected by post depositional effects [*Rothlisberger et al.*, 2002] and had a correlation of 0.65, and MSA, which is related to the ocean biosphere production [*Jaffrezo et al.*, 1994], was not correlated to PO_4^{3-} (r=0.01).

Although individual high peaks observed in the DRP record generally coincide with peaks in dust (Figure 4.2) and the P concentrations by ICP-SFMS and PO_4^{3-} (by IC) are strongly related to dust, the high resolution DRP data show that there is a decoupling of DRP and dust for high DRP concentrations especially during the last glacial maximum (LGM, GS2). DRP - dust correlations during different climatic periods are shown in Figure 4.4. The correlations are similar for all glacial stadials (r values from 0.4 to 0.6), but vary greatly between the two interstadials (r values of 0.15 and 0.7). This large variability may be due to a combination of factors such as: 1) Different sources of dust with variable soluble fractions of P, 2) different atmospheric transport mechanisms and 3) variations in the acidity of the atmosphere affecting the solubility during transport and post deposition by acid layers in the ice. Another consideration is that PO_4^{3-} binds to positively charged particles in the atmosphere due to its high negative charge. Thus an increase in dust could enhance the efficiency of PO_4^{3-} transport to the ice sheet independent of dust as a source.

Solubility

We find significant variability in the soluble fraction of P in the six different climatic periods (Table 4.2), which can't be directly inferred from the dust concentration alone. Similar cases of decoupling nutrient solubility (such as iron) dust concentrations have been found in other ice cores [*Vallelonga et al.*, 2013; *Hiscock et al.*, 2013; *Spolaor et al.*, 2013]. The ratio of PO_4^{3-} to P determined by ICP-SFMS was 38 $\pm$ 24 and 13 $\pm$ 13% for IC and DRP detection methods respectively in the NEEM ice (Table 4.2). Although it can't be excluded that the solubilities found here are influenced by the acids involved in the detection system, aerosols could also be significantly degraded during their transport to the Greenland ice, thus increasing the soluble fraction of P. We find that the soluble fraction of P is 2 to 4 times greater during glacial interstadials as compared to glacial stadials. In comparison *Kjær et al.* [2013] found DRP concentrations of 2.74 nM in the 100-year-old strata of the Greenland NEGIS firn core, while *Edwards et al.* [2007] found total P concentrations of 8 nM in another Greenland firn core. While care must be taken when comparing different ice cores, the soluble fraction (34%) calculated for late Holocene (post-industrialization) ice is greater than the range observed for the glacial.

Previous estimates of phosphorus solubility range between 0.02 % to 3.4 % for

atmospheric dry aerosols [*Hodson et al.*, 2004], however in precipitation the amount of soluble reactive phosphorus to total phosphorus varies between 8% and 18% for dust sources and up to 98% for marine salts. Precipitation originating from biomass burning has intermediate solubility [*Zamora et al.*, 2013]. Other studies have found solubilities of total inorganic P of up to >80% in cases of acidic emissions to the atmosphere (eg. volcanic eruptions) [*Nenes et al.*, 2011]. The acidity of the atmosphere, which can be evaluated in ice cores using electrical conductivity measurements and di-electrical profiling, is decreased during glacial periods due to high dust loads [*Taylor et al.*, 1993] and higher acidity concentrations are found in GIs as compared to GS periods [*Wolff et al.*, 1997]. This could explain why the soluble fraction of P found in the NEEM ice core is low during the GS's and higher during the GI. However other studies show increased volcanic activity in the period around 35 to 22 kyr B.P. [*Zielinski et al.*, 1996]. *Fischer et al.* [1998] reported sulphate and nitrate concentrations in Greenland ice, demonstrating high levels of atmospheric acids especially during the 20^{th} century. This supports the hypothesis that the changing acidity of the atmosphere, especially in recent times, influences the soluble fraction of total P, but is doesn't discount solubility changes due to source variability and transport processes.

Sea salt

The rate of change between concentrations of P in recent times and the observations of P found in the NEEM ice fit the change observed for the sea salt proxy Na^+ of 10 to 15 as determined from the Greenland GISP2 ice core [*Fischer et al.*, 2007]. To investigate if sea salt is a possible source of P during the glacial we use Na^+ and Cl^- data from IC and CFA data measurements of NEEM ice. Assuming that both ions originate only from sea salt and that the fraction between Cl^- and PO_4^{3-} in sea salt, $R^{Cl}_{seasalt} = 5.53 * 10^{-7}$ [*Gianguzza et al.*, 2002; *Concright et al.*, 2000] and $R^{Na}_{seasalt} = 8.14 * 10^{-7}$, we determine the concentration of salt-derived P during the glacial. The high resolution sea salt concentrations found using CFA in 2010 vary between 8.7 and 524 ppb Na^+ (0.4-22.8 μM), while the IC data obtained in 2013 vary between 17 to 214 ppb for Na^+ and 36 to 335 ppb for Cl^{-1}. Thus the sea salt derived PO_4^{3-} is on the order of 10^{-3} nM (pM concentrations) and therefore cannot explain the concentration levels found in the NEEM glacial ice.

In a multi-variable box model approach to the soft tissue carbon pump [*de Boer et al.*, 2010], the PO_4^{3-} level in the surface ocean at 70° N is estimated to change from a concentration of 49 ppb during interglacial to 80 ppb during glacial periods excluding atmospheric transport. However since Cl^- also doubles its concentration in surface sea waters (0.25 to 0.5 g/kg [*Adkins et al.*, 2002]) the higher levels of PO_4^{3-} in surface waters do not significantly increase the calculated contribution arriving from sea areas. Thus we conclude sea salt is not a major source of atmospheric P during the glacial.

4.4 Conclusion

In this study P and PO_4^{3-} concentrations have been determined for the first time in Greenland glacial ice. We studied sections covering between 35.6 and 25.2 kyr BP and find total P concentrations between 7 and 637 nM (fluxes of 0.22-4.67 nM yr^{-1} m^{-2}), with soluble PO_4^{3-} concentrations between 4 and 62 nM (fluxes of 0.05-0.65 nM yr^{-1} m^{-2}).

We find concentrations of both PO_4^{3-} and P increased by a factor 3-12 and 5-39 during the cold glacial stadials as compared to the milder glacial interstadials respectively. For DRP a 14-fold change was found between GS-2 and recent concentrations of the past 100 yrs [*Kjær et al.*, 2013]. Flux change ratios are 3.2-21 for total P, while fluxes of dissolved P vary by 1.6 to 6.4 times between glacial stadials and interstadials. Thus the rate of change for P is lower than that observed for dust, however the P concentrations fit the expected concentration determined from a dust input in the glacial interstadials, while for the LGM the dust derived P is just capable of explaining the load of total P in the NEEM ice. When using a lower resolution dataset (5-9 cm, IC and ICP-SFMS) we find significant correlation to other dust ions. If, however, using high resolution continuous measurements of insoluble dust and DRP the correlation is low. Furthermore there is a significant decoupling of DRP and insoluble dust during particularly during the LGM, which could indicate secondary P sources or multiple dust source regions. The level of sea salt-derived P is far lower than the P concentrations found in the NEEM ice and therefore are unlikely to be a significant source.

The mean soluble fraction of P varies from 13 to 38 % depending on the detection method used, with higher soluble fractions during the warm interglacial periods. We speculate that this could be caused by changes in source regions or by an increased acidity in glacial interstadials as compared to glacial stadials due to less carbonates in the atmosphere.

This study shows that the P and PO_4^{3-} concentrations found in the NEEM ice core fit those expected if dust is the main source, while the relative change between GS and GI's is lower than would be expected from a dust proxy. The variability between dust derived P and the levels of P and PO_4^{3-} reported here between different periods in the past glacial demonstrates the continued importance of observational data, for the specific nutrient in question, in order to accurately estimate the atmospheric nutrient supply to the oceans in past times and also show that relying on dust flux changes does not accurately resolve changes in P solubility.

Acknowledgement

The data presented is part of the NEEM ice core drilling programme. NEEM is directed and organized by the Center of Ice and Climate at the Niels Bohr Institute and US NSF, Office of Polar Programs. It is supported by funding agencies and institutions in Belgium (FNRS-CFB and FWO), Canada (NRCan/GSC), China (CAS), Denmark (FIST), France (IPEV, CNRS/INSU, CEA and ANR), Germany (AWI), Iceland (RannIs), Japan (NIPR), Korea (KOPRI), The Netherlands (NWO/ALW), Sweden (VR), Switzerland (SNF), United Kingdom (NERC) and the USA (US NSF, Office of Polar Programs).

5. ADDITIONAL RESULTS FROM THE DETERMINATION OF DRP IN ICE AND OUTLOOK

In this section the sub-annual deposition pattern of DRP obtained from the NEGIS DRP dataset is discussed. Fourier analysis revealed that similar sub annual investigation was impossible for the NEEM DRP dataset. The annual pattern of DRP found in the NEGIS firn core was compared to the pattern of other proxies found in the ice. Also comparisons to three observational stations (2 in Norway and 1 in Japan) was performed as well as a comparison to model output covering the NEGIS site from the model by Mahowald et al. [2008]. The annual peak in spring is coherent with dust from Asia, however additional DRP is deposited in late summer and early autumn as compared to dust suggesting secondary sources.

Further DRP is presented as determined in samples from the Gregoriev glacier in the Inner Tien Shan mountains, Kyrgyzstan. The samples had high concentrations of DRP beyond the linear calibration range, further black material was deposited in the debubbler during analysis and possibly also inside the absorption cell causing large uncertainties.

Finally an outlook and suggestions for further investigations using the novel DRP method developed for the determination of soluble P in ice cores is presented.

5.1 Sub-annual variability of DRP deposition in Greenland

The high resolution DRP concentration determined in the Greenland NEGIS firn core allows an investigation of the sub-annual variability. The main peak was observed in early spring and the minimum concentrations were found in late summer to early autumn following that observed for dust to some degree. An increase in the deposition relative to dust is observed in some periods of the year with the exact excess period varying between years. This variability could be caused by changes in precipitation patterns or by changes in the excess DRP source. The model results from Mahowald et al. [2008] suggest that the secondary peaks could be primary biogenic production if observed early in the season (May-Aug) or fossil fuel emissions if later in the season (Aug-Dec). However the uncertainty is significant due to the assumption of equal amounts of precipitation throughout the year. Further the change between subsequent years were assigned by the annual peak of sodium, which could also vary with time of year. Thus causing significant variability in the sub-annual DRP pattern between different time periods.

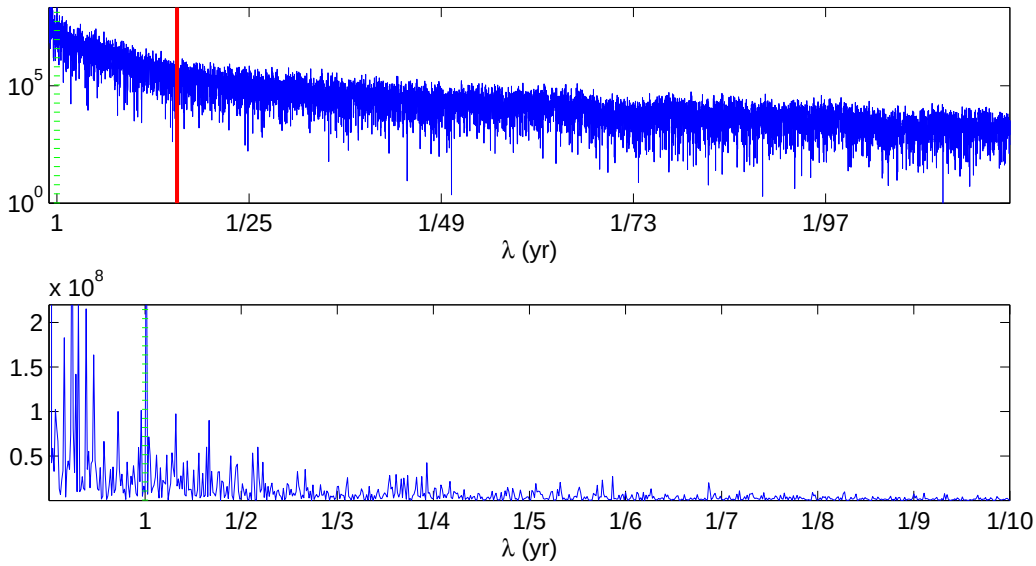

Fig. 5.1: Fourier analysis for DRP. Top on a y log scale, Bottom on a linear scale. Red dotted line show the cut off value chosen by eye and green line the annual peak. Note that the x-axis is given in years.

5.1.1 Sub-annual variability in the NEGIS firn core

To ascertain if the temporal resolution of the DRP measurements from the NEGIS firn core allows for subannual investigations, a Fourier analysis was performed (Figure 5.1). From the top graph in the figure it is not easy to identify the cut off. If however choosing the cut off where the signal equals 5 times the noise, where the noise is given as the mean for the data exceeding λ =1/25 year plus 3 times the standard deviation of that section. The cut off is found at λ =0.027 (1/37) yrs. A more reasonable estimate might be at 0.0625 (1/16) yr as chosen by eye and shown with full red line in Figure 5.1. The annual peak clearly shows up (bottom graph). Thus it is clear that the method is capable of resolving sub-annual layers at the NEGIS site. Smaller cycles of 0.6 yr, 3/4 yr, 1.38 yr, 2.14 yr and 3.94 yr also show up, possibly owing to breaks related to missing data.

To investigate the annual variability of DRP deposition on the Greenland ice, in sections (1775-1825 and 1925-2000) from the NEGIS firn a more practical approach was taken: Following the method by *Sommer et al.* [2000] , also used by *Bigler et al.* [2002], each year was split in 12 sub-annual periods (formal months) assuming equal accumulation throughout the year. The split between consecutive years was assigned using the annual peak in sodium, which is known to peak in February-March. Thus the peak in sodium was taken as March 1st.

Sub-annual deposition, following the formal months method, is shown in Figures 5.2 and 5.3. Figure 5.2 shows the annual variability of DRP when divided into 25 yr periods covering the sections detected (1775-1825 and 1925-2000) as determined in the NEGIS firn core as well as the standard deviation. Figure 5.3 shows the annual signal of DRP compared to that of other proxies determined in the NEGIS firn core.

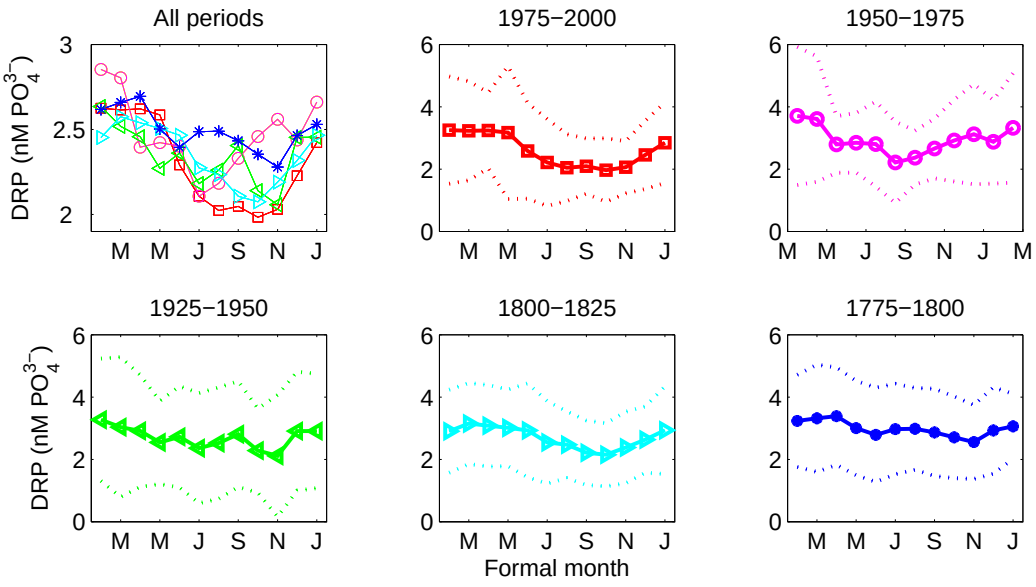

Fig. 5.2: The annual variability of DRP in the NEGIS firn core. Top left shows the mean for five 25 year periods, remaining plots show the 25 yr period mean as well as one standard deviation (dotted lines).

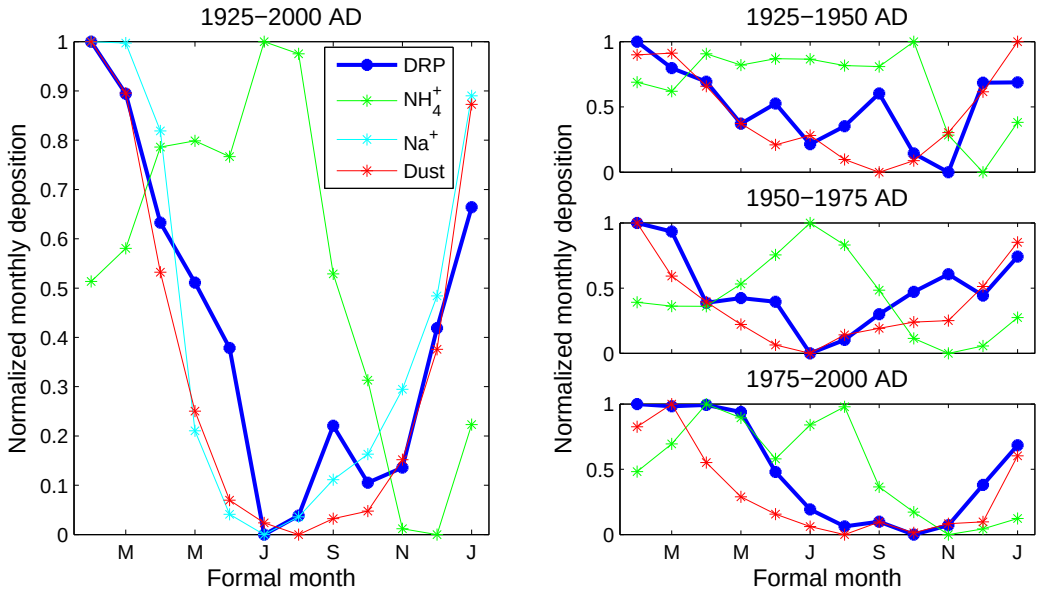

Fig. 5.3: The annual variability of DRP (blue), NH_4^+(green), Na^+ (cyan), dust (red) and MWEC (black) observed the NEGIS firn core. Left show the mean for the period 1925-2000 AD, while the three plots on the right show the same for 1925-1950 (top), 1950-1975 (middle) and 1975-2000 (bottom).

The annual peak of DRP is observed in formal month February and March. However as is evident when considering the standard deviation, the variability between years is significant.

A similar investigation of the annual deposition was not possible for the DRP obtained from the NEEM glacial section, as the temporal resolution was insufficient for resolving sub-annual layers. However as shown in Figure 5.4 the annual peak should be resolved in the warm glacial interstadials, however the annual peak does not show up in the Fourier analysis as a result of the timescale not being set by individual annual layers in other proxies, but merely transferred based on 0.5 metre GICC05 dating. For the cold stadials the annual peak (λ =1) falls outside the temporal resolution obtained with the DRP method. This is caused by precipitation rate being larger in the warm glacial stadials when the air holds increased moisture.

5.1.2 Discussion of the sub-annual variation in DRP deposition

The DRP deposition in the NEGIS firn core is greatest between formal months January to March (Figure 5.2), thus suggesting increased deposition from late winter to early spring. Such an increase in deposition could be caused either by an increase in the source area; by enhanced transport; or by decreased precipitation in that period in case DRP is dry and not wet deposited. Also the assumption of equal precipitation through the year may be faulty.

To evaluate if the annual signal found using the formal month approach can be trusted, the precipitation cycle from the nearest coastal meteorological station at Danmarkshavn in North East Greenland was compared to the assumption of equal precipitation through the year. In general the North East part of Greenland is expected to have higher precipitation rates in winter, where the circulation is dominated by a Baffin Bay low and a deep Icelandic low, causing the dominant wind pattern to blow towards the south east coast of Greenland, then bend and proceed northwards. In summer the weather is affected by south westerlies and westerlies causing the North East to receive only limited precipitation, as it lies in the shadow of the ice sheet [*Cappelen et al.*, 2001]. The precipitation pattern found at Danmarkshavn station follows this pattern. The minimum precipitation at Danmarkshavn occurs during late spring and summer (April, May and June) with an unexplained second minimum in December as shown in Figure 5.5.

Though the approach of comparing a coastal station to central Greenland is not straight forward, as the coastal station might be influenced significantly both by its proximity to the ocean as well as by local effects from mountains at the coast the general precipitation pattern at Danmarkshavn is not that different from the one expected for the North East Greenland in general.

Figure 5.6 shows the precipitation rate over the year using equal precipitation in each month, as well as the actual distribution of precipitation at Danmarkshavn. It is clear that some formal months, such as May, June and December, end up with precipitation from two months, while other formal months contain only half a month of precipitation, such as July, August and December. The DRP falls mainly as dry deposition and thus a month of little precipitation, e.g. May or June would reach higher concentrations of DRP as compared to months with large precipitation. Thus, as a result of increased dry deposition, the formal months May

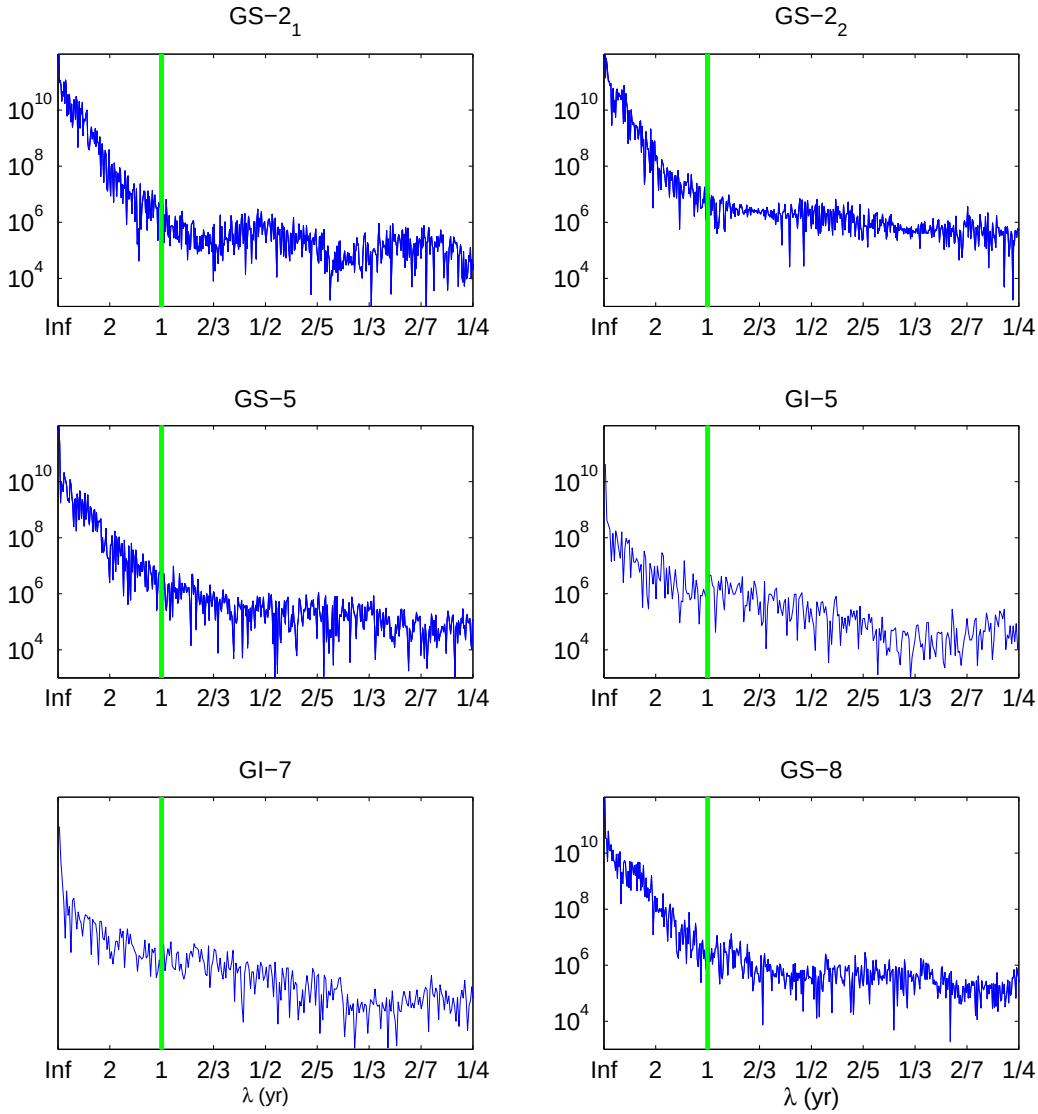

Fig. 5.4: Fourier analysis for DRP as determined in the NEEM ice core shown on a log y-scale. Green vertical line denotes the annual peak. Note that the x-axis is given in years.

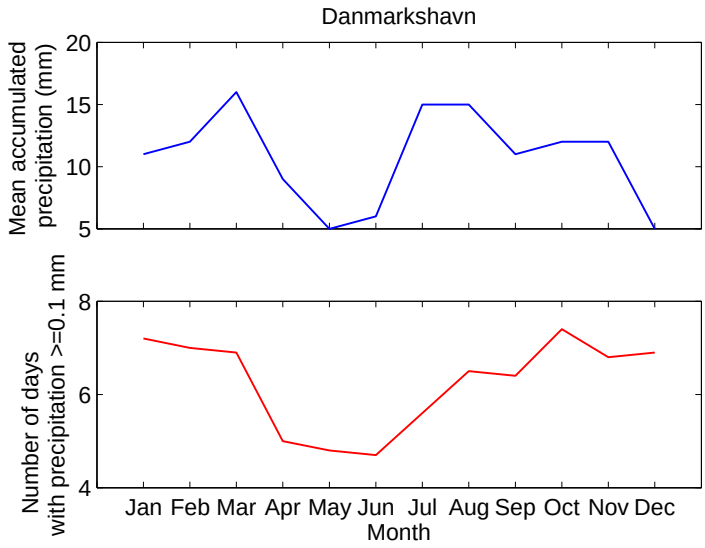

Fig. 5.5: The precipitation at Danmarkshavn, Greenland. Data from *Cappelen et al.* [2001].

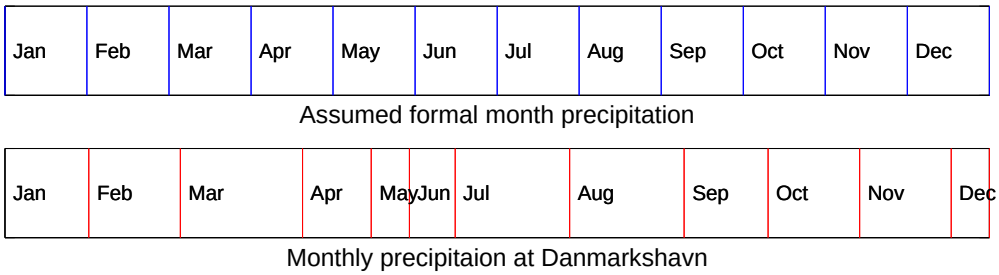

Fig. 5.6: The monthly precipitation at Danmarkshavn, Greenland compared to the assumed equal precipitation rate over the year attempted for the NEGIS sub annual analysis.

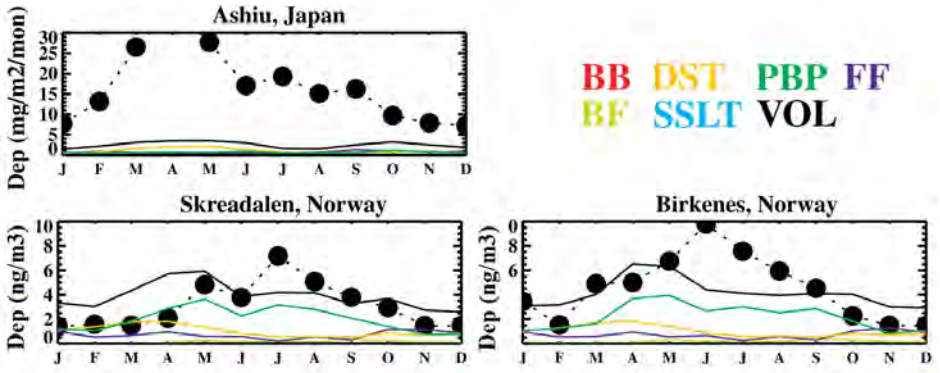

Fig. 5.7: Seasonal cycle of total phosphorus (TP) shown in ng m^{-3} for two Norwegian stations. Also shown is TP in mg m^{-2} $month^{-1}$ for Ashiu, Japan. The dots and dotted lines represent observations, while the solid lines are estimates from model simulations. The color scheme is as follows: BB, biomass burning, red; BF, biofuels, light green; FF, fossil fuels, purple; DST, dust, yellow; SSLT, sea salts, blue; PBP, primary biogenic particles, bright green; VOL, volcanics, black; and the total model estimate is also in black line. Figure modified from *Mahowald et al.* [2008].

and June, which represent both the actual months May and June but also April and July is expected to hold higher DRP concentrations if the precipitation pattern at NEGIS follows that of Danmarkshavn. DRP concentrations however show an increase in early spring (peak in March) and a decrease towards winter and thus the true sub-annual variation of DRP is possibly even stronger than shown in Figure 5.2.

As not much is known about the actual deposition mechanism of phosphorus, we also consider whether assuming only wet deposition would change the annual cycle. If phosphorus were deposited by wet deposition most phosphorus would be expected in March and August and a minimum of phosphorus would be expected in May and June. These real months correspond to the formal months March and April (March), August and part of September (August) and part of May and June (May and June). If expecting constant DRP sources and transport, the subannual variation would thus only be enhanced–also if wet deposition caused the signal. Thus independent of whether the deposition is dry or wet, the annual cycle of DRP is similar to what was found using the assumption of equal precipitation through the year. Therefore we may continue to a comparison of the sub annual variation of DRP concentration to other sites as well as to a discussion of sources based on the sub-annual variability.

The annual variability of P deposition has been only over a longer period of time determined at very few other places [*Mahowald et al.*, 2008]. *Mahowald et al.* [2008] gathered annual deposition from several stations around the world and found that the seasonal cycle is evident in many locations, with a maximum in summer and autumn for deposition in mid latitudes and a smaller seasonal variations in the tropics. The cause of the subannual variation was however not clear. Contrary to *Mahowald et al.* [2008], a study by *Zamora et al.* [2013] finds that dry deposition to the subtropical north Atlantic was 2 to 10 times higher in summer than during

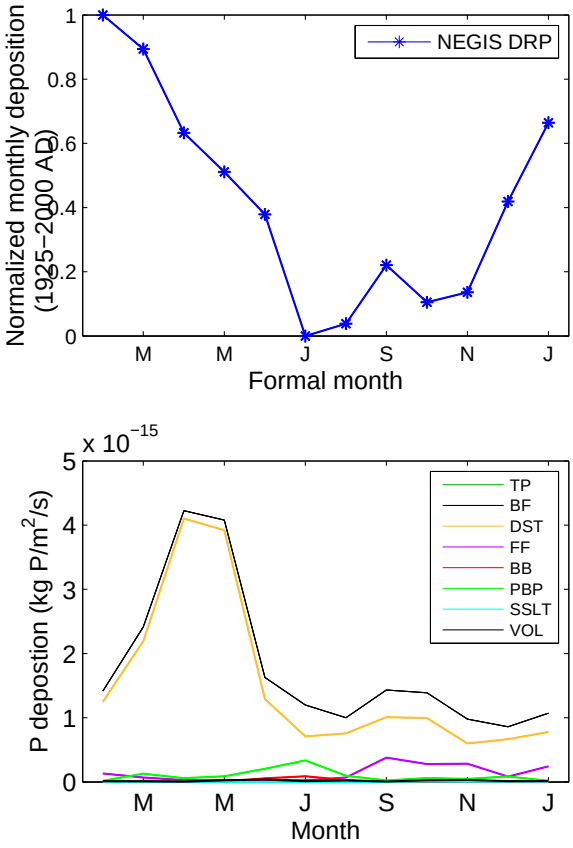

Fig. 5.8: Top) NEGIS annual DRP deposition (blue) for the period 1925-2000. Bottom) Seasonal cycle of total phosphorus (TP, black) based on the model by *Mahowald et al.* [2008] for the position closest to NEGIS; BB, biomass burning, red; BF, biofuels, light green; FF, fossil fuels, purple; DST, dust, yellow; SSLT, sea salts, blue; PBP, primary biogenic particles, bright green; VOL, volcanics, black; and the total model estimate is also in black (TP).

other periods, but generally information on the annual deposition of phosphorus is scarce. A few results of total P from the rural areas of Northern Norway (Skreadalen and Birkenes, Figure 5.7) show a summer peak (June, July), which is ascribed to primary biogenic particles. This could perhaps also explain the excess P relative to dust observed in the NEGIS firn core in early spring. However an earlier peak in March observed at the Norwegian stations is associated with the dust itself.

It is well known that dust in Greenland originates from East Asia (Taklamakan, Gobi desert) and it is expected that the annual peak in dust is a function of the source changes. *Bory et al.* [2002] find the spring deposition of dust originates from the Takla Makan desert, while the winter deposition could originate from multiple other deserts in the East Asian region. Thus the dust deposited in Greenland has travelled more than half around the world. Figure 5.7 shows the annual deposition for Japan. When the dust is transported from the Takla Mahan desert in China it is transported over Japan before it is transported towards Greenland [*Svensson et al.*, 2000; *Ruth et al.*, 2003]. The annual deposition of total phosphorus in Japan is largest in spring as a result of both anthropogenic (35%) and natural emissions from China, consistent with the peak observed of both dust and DRP found in spring at the NEGIS site.

In Figure 5.8 the *Mahowald et al.* [2008] model output for total P is compared to DRP determined in the NEGIS firn core. According to the model the annual peak of DRP should be observed in April and May, while the peak of DRP in the NEGIS firn core was observed earlier in the season. This discrepancy of deposition is either caused by the model not catching the annual deposition signal or by the assumption of equal precipitation shifting the peak season. Please note that the model by *Mahowald et al.* [2008] also does not catch the peak height found at the Japanese station or the peak position for the Norwegian stations. The cause of the mismatch is suggested to be the lack of aerosols larger than 10 μm in the model. Though incapable of determining the exact deposition over the year, the model does suggests that secondary sources to dust are a biogenic summer signal (May to September) and increased fossil fuel later in the season (September to December) at the NEGIS site. As in the NEGIS firn core DRP exceeds dust (1925-2000, Figure 5.3) in two periods, they could be a result of the sources suggested by the model findings.

In conclusion a shift in the annual cycle over time as a result of anthropogenic sources could not be identified. When averaging longer periods (1925-2000) dust and DRP show a very similar annual signal with some increase in DRP in May to June as well as in September relative to dust, this could be interpreted as a biogenic summer signal (May to September) or as a result of increased fossil fuel later in the season (September to December). However, when looking at shorter time sections the excess DRP deposition relative to dust does not appear in any specific section of the year. This lack of a consistent excess period could be caused by changes in the excess source over periods or to the fact that the entire analysis is based on the peak in sodium occurring at the same time every year. In conclusion the analysis performed here is limited by the lack of knowledge on precipitation both of the annual cycle, but also in changes over time, at the NEGIS site.

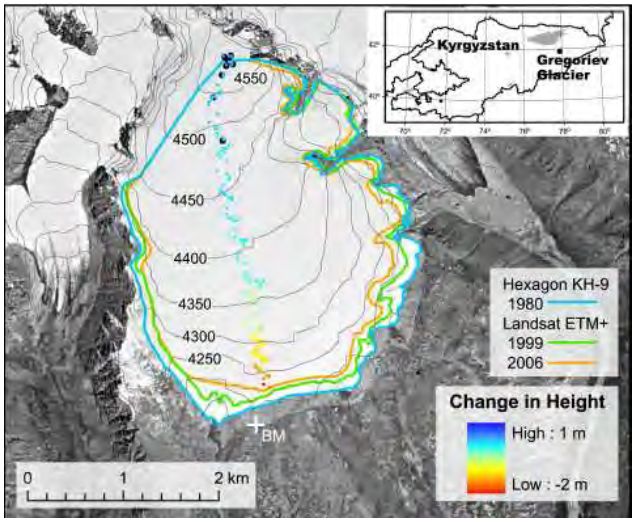

Fig. 5.9: Map showing the position and topography of the Gregoriev Glacier. Figure is from *Fujita et al.* 2011.

5.2 Dissolved reactive phosphorus (DRP) in samples from the Gregoriev Glacier at the Inner Tienshan mountains, Kyrgyzstan

DRP was determined in a few samples from the GGCI 2007 ice core, obtained from the Gregoriev glacier in Inner Tienshan mountains, Kyrgyzstan. The ice core was obtained by researchers from Hokkaido university and only a few discrete samples were measured for DRP by means of a setup similar to that described in section 3 and used also in section 4.

The samples cover a temporal range from 6 kyr AD to year 1960. DRP concentrations were from 123 nM and up to values higher than what can be detected by this method (∼600 nM PO_4^{3-}). Also the dust loads in this glacier were high and close to the detection limit of the ABAKUS dust counter. No consistent relation to dust, NH_4^+, Ca^+, Mg^+ or other tracers was observed.

5.2.1 Methods and Samples

In 2007 an ice core was obtained from the Gregoriev Glacier (GGCI), a flat-top glacier in the Inner Tienshan, Kyrgyzstan (Figure 5.9) [*Fujita et al.*, 2011]. Between 2005 and 2007 AD the temperature at the site varied between 0 and -30 °C. [*Fujita et al.*, 2011]. The ice retrieved was stored at Hokkaido university.

Discrete samples were sent in late 2013 from Hokkaido university to the National Institute for Polar Research (NIPR), Japan, in a frozen state, for determination of DRP. The samples were melted just prior to detection and were shaken to ensure mixing. The discrete samples were introduced to the continuous DRP detection system (see section 3 [*Kjær et al.*, 2013]) using a selection valve in a similar way as for the normal standards used for calibration. Each sample was introduced in the system for at least 3 minutes. After each sample the tube used to introduce the sample was washed in milliQ water and also milliQ water was left running through the sample line for at least 20 seconds to rinse it. Prior to the detection unit used

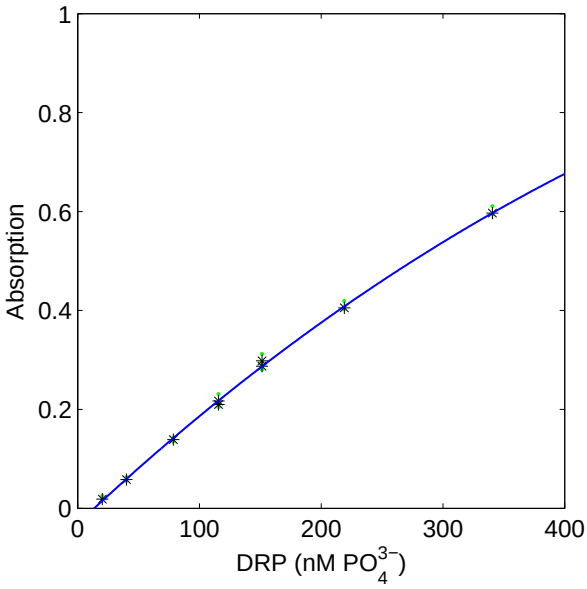

Fig. 5.10: Absorption as a function of DRP concentration used to calibrate the IGGS 2007 samples.

to analyse DRP, an ABAKUS was attached to provide dust counts. Standards used for calibration were prepared as described in section 3 but at higher concentrations to match the sample concentrations. These standards fall outside the linear range (Figure 5.10). Besides the standards shown in Figure 5.10 an additional standard of concentration 632 nM PO_4^{3-} was introduced.

5.2.2 Results and discussion of DRP determined in the Gregoriev glacier ice samples

Figure 5.11 shows the raw signal response to two ice samples from the Gregoriev glacier (GGCI). The return to baseline (milliQ) after a sample of GGCI is not very fast, nor is a stable concentration reached during a sample. The slow response after a sample could be 1) caused by slow wash out of blue coating in the line as a result of the high concentrations, 2) due to high loads of dust clogging the filter and thus changing the sample to reagent to buffer ratios or 3) due to coating accumulating inside the cell at a very inconvenient place such as just in front of the optical inlet or outlet. As shown in Figure 5.12 significant coating accumulated in the debubbler during the detection of these samples, and it seems likely that a similar coating deposited inside the absorption cell (the LWCC) may cause the lack of return to baseline by changing the LWCC's optical properties.

The slow response and lack of return to baseline combined with the fact that the range of samples outside the linear range of the method lead to significant uncertainty in the Gregoriev glacier ice DRP determination and thus the results presented in Table 5.1 provide just an upper and a lower estimate for the concentration range, based on high baseline low sample and low baseline high sample counts respectively.

Despite the limited samples and the significant uncertainty related to the DRP

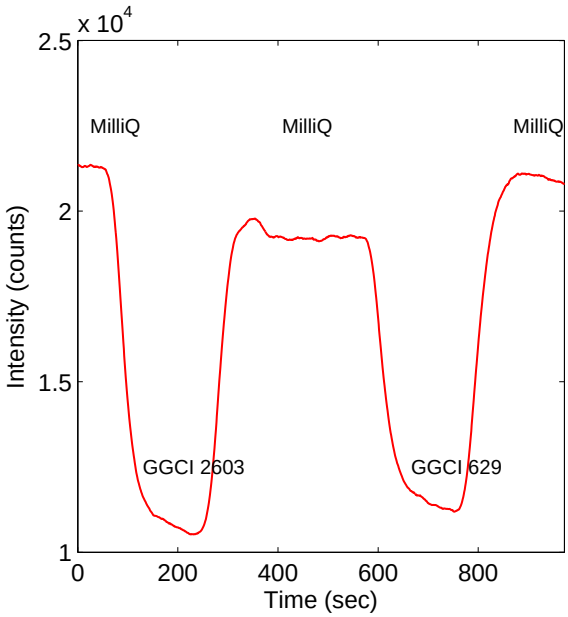

Fig. 5.11: Raw measurements of two GGCI 2007 samples measured for DRP in a semi discrete way with milliQ in between.

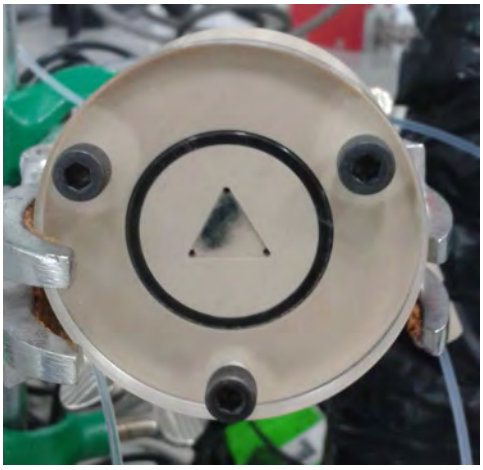

Fig. 5.12: During the determination of the samples from the Gregoriev glacier black material formed inside the debubbler.

Tab. 5.1: DRP as detected on the GGCI 2007 samples obtained at the Gregoriev glacier, Inner Tienshan, Kyrgyzstan. Also shown are age, depth, and the amount of dust in the samples (personal correspondence professor Takeuchi).

$\delta^{18}O$ ‰	Age yr AD	Sample #	Depth metre	min DRP nM	max DRP nM	Dust # x 10^4/mL
-14.04	-6035	2854	85.51-85.53	632	NP	1660
-11.06	-4278	2603	80.42-80.44	142	159	1261
-10.76	1913	629	34.86-34.91	123	143	5160
-8.46	1933	528	29.66-29.71	399	442	1335
-10.42	1960	336	20.06-20.11	143	178	829

determination, the results for DRP were compared to other proxies. However, no consistent relations to either dust, NH_4^+, Ca^+, Mg^+ or other tracers as detected by Nozomu Takeuchi (personal correspondence) were found (data not shown).

Unfortunately, I do not have access to much information on the samples and thus I have resigned from any interpretation of the concentrations determined. However, I expect that they are influenced by local conditions in the Gregoriev glacier and that concentrations could be influenced by snow bacteria, known to exist on the glacier (personal correspondence with professor Takeuchi).

5.3 Future work using the DRP method for continuous ice determination

For the study of dissolved reactive phosphorus in ice cores a CFA method for high resolution continuous measurements was developed. The method allows for the determination of sub-annual variations in Greenland firn and we find that DRP is deposited in the spring simultaneously with dust. However we also find that secondary sources influence the signal. We also studied the variability in the past 300 years from the NEGIS firn core and found no evidence of human impact and have concluded that while the main source was dust the secondary source was most likely of biological origin.

To obtain more knowledge on sources and the variability of DRP in Greenland ice, I suggest that firn cores covering the recent past should be analysed for DRP. Such cores could include the planned ice core from Renland, a site close to the coast of East Greenland, where an ocean or sea ice related signal could be expected. For resolving a potential anthropogenic impact, firn cores from the Southern part of Greenland, with high annual precipitation and a position closer to North America and Europe might exhibit a larger influence by humans. Also ice cores from the Alps are likely to show an anthropogenic imprint. However, it would also be valuable to determine DRP in Holocene sections older than 1700 AD, as the changes in transport of DRP related to humans might largely be a land use change occurring prior to the period investigated for the NEGIS firn core. However, if such ice indeed does have lower DRP than what was observed for the NEGIS firn core, then the method

might be incapable of resolving the signal as it could be below the limit of detection. To resolve the low signal, changing from the 2.5 (or 2) metre LWCC to a 5 metre LWCC would be required, with subsequent loss of temporal resolution.

We also succeeded in determining DRP in the Greenland NEEM ice core for the Glacial period. Filters had to be changed in between each 55 cm section measured in the cold glacial stadials, since otherwise insoluble particles would clog the filter. Thus the method currently requires that filters be changed frequently, and for each filter change additional time consuming calibrations must be performed. A way to avoid changing the filter that often would be to have multiple filters in series starting with larger filter sizes and ending with the 0.2 μm filter used for the studies of DRP presented here. This would increase the mixing and diminish the temporal resolution, and one should be aware that some of the particles stuck in the filters could leach over time and that increased back pressure could result. In Antarctic ice the concentration of insoluble particles is about 10 times smaller than found in Greenland. Thus measurements of DRP in Antarctic glacial samples are less likely to clog the filter and obtaining a full glacial record for Antarctic Inland ice cores could be easier than for ice cores from Greenland.

If DRP is to be determined in high concentration samples from smaller glaciers such as the Gregoriev glacier a number of optimizations should be considered:

1. Part of the high uncertainty on the concentrations is related to the concentrations being outside the linear range. Therefore changing to a shorter LWCC eg. of 1 metre would be beneficial. This would further decrease the response time. Such a change would however also increase the limit of detection (LOD), a compromise that does not influence the samples from the Gregoriev glacier where concentrations seem to be consistently high. However, if the sample concentration is highly variable a setup using to LWCC's of different length in series could be implemented to resolve both high and low concentration samples.

2. The black material observed in the debubbler should be removed from the sample stream before reaching the LWCC to prevent it from coating the cell, influencing the determination by blocking light. The black material could e.g. be removed by a second filter positioned right before the entrance to the LWCC.

3. The black material forms after the heat bath and thus it is probably related to the cooling after the heat bath, which changes the dissolution point. Possibly the formation of black material could be limited (or avoided) by reducing the heating of the samples. The temperature effect is significant for the LOD of the method. Yet since the ice concentrations in the ice samples from the Gregoriev glacier are high, it may be possible retaining the long LWCC and avoiding the heat bath, while the LOD would still be lower than the sample concentrations. Further, an increase of mixing could perhaps increase part of the response lost by less heating, however the cost would be slower response times. As samples are discrete, increasing the response time by up to a minute is not a severe draw down.

Further, if smaller filter sizes were added after determination of the DRP in the LWCC and the concentration of PO_4^{3-} were determined in a series of LWCC, each with a smaller filter size in front, additional knowledge of solubility as a function of size could be obtained. In theory, the smaller the size of the PO_4^{3-} complex the larger the bio-availability. Still, smaller filters are difficult to work with in a continuous system as they tend to clog fast. Moreover such a filter series solubility determination setup would only make sense for high concentration samples as concentrations would likely decrease for smaller filter sizes as compared to what is measured using the 0.2 μm filter.

In conclusion the DRP method is ready to be implemented on other ice cores increasing the knowledge of long-range atmospheric transport of soluble P to polar ices as well as its variability over time.

BIBLIOGRAPHY

Adkins, J. F., K. McIntyre, and D. P. Schrag (2002), The salinity, temperature, and $d^{18}O$ of the Glacial Deep Ocean, *Science*, *298*(5599), 1769–1773.

Ammerman, J. W., R. R. Hood, D. A. Case, and J. B. Cotner (2003), Phosphorus deficiency in the Atlantic: An emerging paradigm in oceanography, *Eos, Transactions American Geophysical Union*, *84*(18), 165–170.

Amo, M., and M. Minagawa (2003), Sedimentary record of marine and terrigenous organic matter delivery to the Shatsky Rise, western North Pacific, over the last 130 kyr, *Organic Geochemistry*, *34*(9), 1299–1312.

Anderson, L. A., and J. L. Sarmiento (1994), Redfield ratios of remineralization determined by nutrient data analysis, *Global Biogeochemical Cycles*, *8*(1), 65–80.

Anderson, R., M. Fleisher, Y. Lao, and G. Winckler (2008), Modern $CaCO_3$ preservation in equatorial Pacific sediments in the context of late-Pleistocene glacial cycles, *Marine Chemistry*, *111*(1), 30–46.

Arfeuille, F., D. Weisenstein, H. Mack, E. Rozanov, T. Peter, and S. Brönnimann (2013), Volcanic forcing for climate modeling: A new microphysics-based dataset covering years 1600-present, *Clim. Past. Discuss.*, *9*(1), 967–1012, doi:10.5194/cpd-9-967-2013.

Baker, A. R., T. D. Jickells, M. Witt, and K. D. Linge (2006), Trends in the solubility of iron, aluminium, manganese and phosphorus in aerosol collected over the Atlantic Ocean, *Mar. Chem.*, (98), 43–58.

Bennett, E. M., S. R. Carpenter, and N. F. Caraco (2001), Human impact on erodable phosphorus and eutrophication: a global perspective increasing accumulation of phosphorus in soil threatens rivers, lakes, and coastal oceans with eutrophication, *BioScience*, *51*(3), 227–234.

Berner, R. A., K. C. Ruttenberg, E. D. Ingall, and J.-L. Rao (1993), The nature of phosphorus burial in modern marine sediments, in *Interactions of C, N, P and S Biogeochemical Cycles and Global Change*, pp. 365–378, Springer.

Bigler, M., A. Svensson, E. Kettner, P. Vallelonga, M. E. Nielsen, and J. P. Steffensen (2011), Optimization of high-resolution continuous flow analysis for transient climate signals in ice cores, *Environ. Sci. Technol.*, *45*(10), doi:10.1021/es200118j.

Biology-forums.com (2014), Biology forums gallery. the phosphorus cycle, http://biology-forums.com/index.php?action=gallery;sa=view;id=2038.

Bjorkman, K., and D. M. Karl (2003), Bioavailability of dissolved organic phosphorus in the euphotic zone at Station ALOHA, North Pacific Subtropical Gyre, *Limnology and Oceanography*, *48*(3), 1049–1057.

Bolin, B., J. Crutzen, P. M. Vitousek, R. G. Woodmansee, E. D. Goldberg, and R. B. Cook (1981), SCOPE 21- the major biochemical cycles and their interactions-chap 1. Interactions of biochemical cycles, *Workshop on the interactions of biogeochemical cycles, 25-30 May 1981.*

Bory, A.-M., P. E. Biscaye, A. Svensson, and F. E. Grousset (2002), Seasonal variability in the origin of recent atmospheric mineral dust at NorthGRIP, Greenland, *Earth and Planetary Science Letters*, *196*(3), 123–134.

Breton, D. J., B. G. Koffman, A. V. Kurbatov, K. J. Kreutz, and G. S. Hamilton (2012), Quantifying signal dispersion in a hybrid ice core melting system, *Environmental science & technology*, *46*(21), 11,922–11,928.

Broecker, W. S. (1982), Glacial to interglacial changes in ocean chemistry, *Progress in Oceanography*, *11*(2), 151–197.

Broecker, W. S., and G. M. Henderson (1998), The sequence of events surrounding Termination II and their implications for the cause of glacial-interglacial CO_2 changes, *Paleoceanography*, *13*(4), 352–364.

Cappelen, J., B. V. Jørgensen, E. V. Laursen, S. L.S., and R. S. Thomsen (2001), Technical report 00-18, the observed climate of Greenland, 1958-99-with climatological standards normals, 1961-1990, *Danish Meterological Institute-ministry of transport*, pp. pp. 17–21.

Carpenter, S. R., J. J. Cole, J. F. Kitchell, and M. L. Pace (1998), Impact of dissolved organic carbon, phosphorus, and grazing on phytoplankton biomass and production in experimental lakes, *Limnology and Oceanography*, *43*(1), 73–80.

Chadwick, O., and R. Goldstein (2004), Control of dilation and collapse during weathering and soil formation on Hawaiian basalts, in *Proceedings of the Eleventh International Symposium on Water–Rock Interaction WR. Saratoga Springs, New York, NY. Routledge, London*, pp. 11–16.

Chadwick, O. A., L. Derry, P. M. Vitousek, B. J. Huebert, and L. O. Hedin (1999), Changing sources of nutrients during four million years of ecosystem development, *Nature*, *397*(6719), 491–497.

Chillrud, S. N., P. F. Temporetti, and H. F. Planas (1994), Chemical weathering of phosphate and germanium in glacial meltwater streams: Effects of subglacial pyrite oxidation, *Limnol. Oceanogr.*, *39*(5), 1130–1140.

Concright, M. E., W. W. Gregg, and S. Levitus (2000), Seasonal cycle of phosphate in the open ocean, *Deep-Sea Res Pt I*, *47*, 159–175.

Dahl-Jensen, D., M. Albert, A. Aldahan, N. Azuma, D. Balslev-Clausen, M. Baumgartner, A.-M. Berggren, M. Bigler, T. Binder, T. Blunier, et al. (2013), Eemian interglacial reconstructed from a Greenland folded ice core, *Nature*, *493*(7433), 489–494.

Daufresne, T. (2013), Palaeoecology: Megafauna as a nutrient pump, *Nature Geoscience*, *6*(9), 679–680.

de Angelis, M., J. P. Steffensen, M. Legrand, H. Clausen, and C. Hammer (1997), Primary aerosol (sea salt and soil dust) deposited in Greenland ice during the last climatic cycle: Comparison with east Antarctic records, *J. Geophys. Res.*, (102), 26,681–26,698.

de Boer, A. M., A. J. Watson, N. R. Edwards, and K. I. C. Oliver (2010), A multi-variable box model approach to the soft tissue carbon pump, *Clim. Past*, *6*(6), 827–841, doi:10.5194/cp-6-827-2010.

Delaney, P. (2000), Nutrients in glacial balance, *Nature*, *405*, 288–291.

Diaz, R. J., and R. Rosenberg (2008), Spreading dead zones and consequences for marine ecosystems, *Science*, *321*(5891), 926–929.

Doughty, C. E., A. Wolf, and Y. Malhi (2013), The legacy of the Pleistocene megafauna extinctions on nutrient availability in Amazonia, *Nature Geoscience*, *6*(9), 761–764.

Edwards, R., J. R. McConnell, and J. R. Banta (2007), Atmospheric Deposition of Iron and Phosphorus to Greenland over the 20th - Century, *AGU Fall Meeting Abstracts*, pp. B1154+.

Elderfield, H., and R. E. M. Rickaby (2000), Oceanic Cd/P ratio and nutrient utilization in the glacial Southern Ocean, *Nature*, *405*, 305–310.

Elser, J. J., C. E. Cleland, D. S. Gruner, W. S. Harpole, J. T. Ngai, E. W. Seabloom, J. B. Shurin, and J. E. Smith (2007), Global analysis of nitrogen and phosphorus limitation of primary producers in freshwater, marine and terrestrial ecosystems, *Ecol. Lett.*, *10*, 1135–1142.

Engel, A., I. Zondervan, K. Aerts, L. Beaufort, A. Benthien, L. Chou, B. Delille, J.-P. Gattuso, J. Harlay, C. Heemann, et al. (2005), Testing the direct effect of CO_2 concentration on a bloom of the coccolithophorid Emiliania huxleyi in mesocosm experiments, *Limnology and Oceanography*, *50*(2), 493–507.

EPICA community members (2004), Eight glacial cycles from an Antarctic ice core, *Nature*, (431), 623–628.

Falkowski, P. G., R. T. Barber, and V. Smetacek (1998), Biogeochemical controls and feedbacks on ocean primary production, *Science*, *281*(5374), 200–206, doi:10.1126/science.281.5374.200.

Field, M. P., and R. M. Sherrell (2003), Direct determination of ultra-trace levels of metals in fresh water using desolvating micronebulization and HR-ICP-MS: application to Lake Superior waters, *Journal of Analytical Atomic Spectrometry*, *18*(3), 254–259.

Filippelli, G. M. (2002), The global phosphorus cycle, *Reviews in mineralogy and geochemistry*, *48*(1), 391–425.

Filippelli, G. M. (2008), The global phosphorus cycle: Past, present, and future, *Elements*, *4*, 89–95.

Filippelli, G. M., C. Souch, B. Menounos, S. Slater-Atwater, A. J. Tomothy Jull, and O. Slaymaker (2006), Alpine lake sediment records of the impact of glaciation and climate change on the biogeochemical cycling of soil nutrients, *Quart. Res.*, *66*, 158–166.

Filippelli, G. M., J. C. Latimer, R. W. Murray, and J.-A. Flores (2007), Productivity records from the Southern Ocean and the equatorial Pacific Ocean: testing the glacial shelf-nutrient hypothesis, *Deep Sea Research Part II: Topical Studies in Oceanography*, *54*(21), 2443–2452.

Fischer, H., M.-L. Siggard-Andersen, U. Ruth, and R. W. E. Röthlisberger (2007), Glacial-interglacial changes in mineral dust and sea-salt records in polar ice cores: Sources, transport, and deposition, *Rev. Geophys.*, *45*(1).

Fuhrer, K., A. Neftel, M. Anklin, T. Staffelbach, and M. Legrand (1996), High-resolution ammonium ice core record covering a complete glacial inter-glacial cycle, *J. Geophys. Res.*, *101*(D2), 4147–4164.

Fujita, K., N. Takeuchi, S. Nikitin, A. Surazakov, S. Okamoto, V. Aizen, and J. Kubota (2011), Favorable climatic regime for maintaining the present-day geometry of the Gregoriev Glacier, Inner Tien Shan, *The Cryosphere*, *5*(3), 539–549.

Gianguzza, A., E. Pelizzetti, and S. Sammartano (2002), *Chemistry of marine water and sediments*, 5 pp., Springer.

Gimbert, L. J., and P. J. Worsfold (2007), Environmental applications of liquid-waveguide-capillary cells coupled with spectroscopic detection, *Trac. Trend Anal. Chem.*, *26*(9), 914–930.

Glindemann, D., M. Edwards, J.-a. Liu, and P. Kuschk (2005), Phosphine in soils, sludges, biogases and atmospheric implications – a review, *Ecological Engineering*, *24*(5), 457–463.

Goll, D. S., N. Moosdorf, J. Hartmann, and V. Brovkin (2014), Climate-driven changes in chemical weathering and associated phosphorus release since 1850: implications for the land carbon balance, *Geophysical Research Letters*.

Graham, B., P. Guyon, W. Maenhaut, P. E. Taylor, M. Ebert, S. Matthias-Maser, O. l. Mayol-Bracero, R. H. M. Godoi, P. Artaxo, F. X. Meixner, M. A. L. Moura, C. H. Rocha, R. Van Grieken, M. M. Glovsky, R. C. Flagan, and M. O. Andrea (2003), Composition and diurnal variability of the natural Amazonian aerosol, *J. Geophys. Res.*, *108*(D24), 4765.

Graham, W. F., and R. A. Duce (1982), The atmospheric transport of phosphorus to the western north Atlantic, *Atmos. Environ.*, *16*(5), 1089–1097.

Harpole, W. S., J. T. Ngai, E. E. Cleland, E. W. Seabloom, E. T. Borer, M. E. Bracken, J. J. Elser, D. S. Gruner, H. Hillebrand, J. B. Shurin, et al. (2011), Nutrient co-limitation of primary producer communities, *Ecology Letters*, *14*(9), 852–862.

Hein, M., and K. Sand-Jensen (1997), CO_2 increases oceanic primary production, *Nature*, *388*(6642), 526–527.

Hilderbrand, G., C. Schwartz, C. Robbins, M. Jacoby, T. Hanley, S. Arthur, and C. Servheen (1999), The importance of meat, particularly salmon, to body size, population productivity, and conservation of North American brown bears, *Canadian Journal of Zoology*, *77*(1), 132–138.

Hodson, A., P. Mumford, and D. Lister (2004), Suspended sediment and phosphorus in proglacial rivers: bioavailability and potential impacts upon the P status of ice-marginal receiving waters, *Hydrol. process.*, *18*, 2409–2422.

Hood, E., and D. Scott (2008), Riverine organic matter and nutrients in southeast Alaska affected by glacial coverage, *Nature geoscience*, *1*, pp. 583–587.

Howarth, R. W., and R. Marino (2006), Nitrogen as the limiting nutrient for eutrophication in coastal marine ecosystems: evolving views over three decades, *Limnology and Oceanography*, *51*(1), 364–376.

Hudson, J. J., W. D. Taylor, and D. W. Schindler (2000), Phosphate concentrations in lakes, *Nature*, *406*(6791), 54–56.

Human Rights Watch (2009), Rain of fire-Israel's Unlawful use of white phosphorus in Gaza, ISBN:1-56432-458-3, *Tech. rep.*

Human Rights Watch and Harvard Law Schools's International Human Rights Clinic (2011), Memorandum to convention on conventional weapons delegates the human suffering caused by incendiary munitions, *Tech. rep.*

Iraq Analysis Group (2005), Fire bombs in Iraq: Napalm by any other name, *Tech. rep.*

Jaccard, S., C. T. Hayes, A. Martínez-García, D. Hodell, R. F. Anderson, D. Sigman, and G. Haug (2013), Two modes of change in Southern Ocean productivity over the past million years, *Science*, *339*(6126), 1419–1423.

Jaffrezo, J.-L., C. I. Davidson, M. Legrand, and J. E. Dibb (1994), Sulfate and MSA in the air and snow on the Greenland ice sheet, *Journal of Geophysical Research: Atmospheres (1984–2012)*, *99*(D1), 1241–1253.

Jassby, A. D., J. E. Reuter, R. P. Axler, C. R. Goldman, and S. H. Hackley (1994), Atmospheric deposition of nitrogen and phosphorus in the annual nutrient load of Lake Tahoe (California-Nevada), *Water Resources Research*, *30*(7), 2207–2216.

Jones, M. T., and S. R. Gislason (2008), Rapid releases of metal salts and nutrients following the deposition of volcanic ash into aqueous environments, *Geochimica et Cosmochimica Acta*, *72*(15), 3661–3680.

Kanakidou, M., R. A. Duce, J. M. Prospero, A. R. Baker, C. Benitez-Nelson, F. J. Dentener, K. A. Hunter, P. S. Liss, N. Mahowald, G. S. Okin, M. Sarin, K. Tsigaridis, M. Uematsu, L. M. Zamora, and T. Zhu (2012), Atmospheric fluxes of organic N and P to the global ocean, *Global Biogeochem. Cy.*, *26*(3), doi:10.1029/2011GB004277.

Karl, D. M., K. M. Björkman, J. E. Dore, L. Fujieki, D. V. Hebel, T. Houlihan, R. M. Letelier, and L. M. Tupas (2001), Ecological nitrogen-to-phosphorus stoichiometry at station ALOHA, *Deep Sea Research Part II: Topical Studies in Oceanography*, *48*(8), 1529–1566.

Kaufmann, P. R., U. Federer, M. A. Hutterli, M. Bigler, S. Schüpbach, U. Ruth, J. Schmitt, and T. F. Stocker (2008), An improved continuous flow analysis system for high-resolution field measurements on ice cores, *Environ. Sci. Technol.*, *42*(21), 8044–8050.

Kehrwald, N., P. Zennaro, and C. Barbante (2012), Increasing fire activity in a warming climate? Ice core record insight from the present and last intergalcials, *Pages NEWS*, *21*(1), 16–17.

Kitchell, J. F., D. E. Schindler, B. R. Herwig, D. M. Post, M. H. Olson, and M. Oldham (1999), Nutrient cycling at the landscape scale: the role of diel foraging migrations by geese at the Bosque del Apache National Wildlife Refuge, New Mexico, *Limnology and Oceanography*, *44*(3), 828–836.

Kjær, H. A., A. Svensson, P. Vallelonga, E. Kettner, S. Schupbach, M. Bigler, J. P. Steffensen, and M. E. Hansson (2011), First continuous phosphate record from Greenland ice cores, *Clim. Past. Discuss.*, *7*(6), 3959–3989.

Kjær, H. A., P. Vallelonga, A. Svensson, M. E. L. Kristensen, C. Tibuleac, and M. Bigler (2013), Continuous flow analysis method for determination of dissolved reactive phosphorus in ice cores, *Environmental science & technology*.

Kohfeld, K. E., C. Le Quéré, S. P. Harrison, and R. F. Anderson (2005), Role of marine biology in glacial-interglacial CO_2 cycles, *Science*, *308*(5718), 74–78.

Krishnamurthy, A., J. K. Moore, N. Mahowald, C. Luo, and C. S. Zender (2010), Impacts of atmospheric nutrient inputs on marine biogeochemistry, *Journal of Geophysical Research: Biogeosciences (2005–2012)*, *115*(G1).

Lambert, F., M. Bigler, J. P. Steffensen, M. Hutterli, and H. Fischer (2012), Centennial mineral dust variability in high-resolution ice core data from Dome C, Antarctica, *Clim. of the Past*, *8*(2), 609–623, doi:10.5194/cp-8-609-2012.

Legrand, M., and P. A. Mayewski (1997), Glaciochemistry of polar ice cores: A review, *Reviews of Geophysics*, *35*, 219–143.

Lenton, T. M., and A. J. Watson (2000), Redfield revisited: 1. Regulation of nitrate, phosphate, and oxygen in the ocean, *Global biogeochemical cycles*, *14*(1), 225–248.

Lide, D. R. (2012), *CRC handbook of chemistry and physics*, 14-17 pp., CRC press.

Lomas, M. W., A. Burke, D. Lomas, D. Bell, C. Shen, S. T. Dyhrman, and J. W. Ammerman (2010), Sargasso Sea phosphorus biogeochemistry: an important role for dissolved organic phosphorus (DOP)., *Biogeosciences*, *7*(2).

Loubere, P., and M. Richaud (2007), Some reconciliation of glacial-interglacial calcite flux reconstructions for the eastern equatorial Pacific, *Geochemistry, Geophysics, Geosystems*, *8*(3).

Luo, C., N. Mahowald, T. Bond, P. Chuang, P. Artaxo, R. Siefert, Y. Chen, and J. Schauer (2008), Combustion iron distribution and deposition, *Global Biogeochemical Cycles*, *22*(1).

Ma, J., D. Yuan, M. Zhang, and Y. Liang (2009), Reverse flow injection analysis of nanomolar soluble reactive phosphorus in seawater with a long path length liquid waveguide capillary cell and spectrophotometric detection, *Talanta*, *78*, 315–320.

Maher, B. A., J. M. prospero, D. Mackie, D. Gaiero, P. P. Hesse, and Y. Balkanski (2010), Global connections between aeolian dust, climate and ocean biogeochemistry at the present day and last glacial maximum, *Earth-Sci. Rev.*, *99*, 61–97.

Mahowald, N., T. D. Jickells, A. R. Baker, P. Artaxo, C. R. Benietz-Nelson, G. Bergametti, T. C. Bond, Y. Ching, D. D. Cohen, B. Herut, N. Kubilay, R. Losno, C. Luo, W. Maenhaut, K. A. McGee, G. S. Okin, R. L. Siefert, and S. Tsukuda (2008), Global distribution of atmospheric phosphorus sources, concentration and deposition rates, and anthropogenic impact, *Global Biogeochem. Cy.*, *22*, GB4026.

Mahowald, N. M., A. R. Baker, G. Bergametti, N. Brooks, R. A. Duce, T. D. Jickells, N. Kubilay, J. M. Prospero, and I. Tegen (2005), Atmospheric global dust cycle and iron inputs to the ocean, *Global biogeochemical cycles*, *19*(4).

Mahowald, N. M., S. Engelstaedter, C. Luo, A. Sealy, P. Artaxo, C. Benitez-Nelson, S. Bonnet, Y. Chen, P. Y. Chuang, D. D. Cohen, et al. (2009), Atmospheric iron deposition: Global distribution, variability, and human perturbations, *Annual Review of Marine Science*, *1*, 245–278.

McConnell, J. R., G. W. Lamorey, S. W. Lambert, and K. C. Taylor (2002), Continuous ice-core chemical analyses using Inductively Coupled Plasma Mass Spectrometry, *Environ. Sci. Tech.*, *36*(1), 7–11, doi:10.1021/es011088z.

McConnell, J. R., R. Edwards, G. L. Kok, M. G. Flanner, C. S. Zender, E. S. Saltzman, J. R. Banta, D. R. Pasteris, M. M. Carter, and J. D. W. Kahl (2007), 20th-Century industrial black carbon emissions altered arctic climate forcing, *Science*, *317*, 1381.

Menge, D. N., L. O. Hedin, and S. W. Pacala (2012), Nitrogen and phosphorus limitation over long-term ecosystem development in terrestrial ecosystems, *PloS one*, *7*(8), e42,045.

Metcalfe, D. B., G. P. Asner, R. E. Martin, J. E. Silva Espejo, W. H. Huasco, F. F. Farfán Amézquita, L. Carranza-Jimenez, D. F. Galiano Cabrera, L. D. Baca, F. Sinca, et al. (2014), Herbivory makes major contributions to ecosystem carbon and nutrient cycling in tropical forests, *Ecology letters*, *17*(3), 324–332.

Monaghan, E., and K. Ruttenberg (1999), Dissolved organic phosphorus in the coastal ocean: Reassessment of available methods and seasonal phosphorus profiles from the Eel River Shelf, *Limnology and Oceanography*, *44*(7), 1702–1714.

Murphy, J., and J. P. Riley (1958), A single-solution method for the determination of soluble phosphate in sea water, *J. Mar. Biol. Ass. U.K.*, *37*, 9–14.

Neff, J., A. Ballantyne, G. Farmer, N. Mahowald, J. Conroy, C. Landry, J. Overpeck, T. Painter, C. Lawrence, and R. Reynolds (2008), Increasing eolian dust deposition in the western United States linked to human activity, *Nature Geoscience*, *1*(3), 189–195.

Neilands, J. B. (1970), Vietnam: Progress of the Chemical War, *Asian Survey*, *10*(3), pp. 209–229.

Nenes, A., M. D. Krom, N. Mihalopoulos, P. Van Cappellen, Z. Shi, A. Bougiatioti, P. Zarmpas, and B. Herut (2011), Atmospheric acidification of mineral aerosols: a source of bioavailable phosphorus for the oceans, *Atmospheric Chemistry and Physics*, *11*(13), 6265–6272, doi: 10.5194/acp-11-6265-2011.

NGRIP members (2004), High-resolution record of Northern Hemisphere climate extending into the last interglacial period, *Nature*, *431*, 147–151.

Nollet, L. M. L. (2007), *Handbook of Water Analysis-second edition*, 219-251 pp., CRC press.

Oelkers, E. H., and E. Valsami-Jones (2008), Phosphate mineral reactivity and global sustainability, *Elements*, *4*, 83–87.

Okin, G. S., N. Mahowald, O. A. Chadwick, and P. Artaxo (2004), Impact of desert dust on the biogeochemistry of phosphorus in terrestrial ecosystems, *Global Biogeochemical Cycles*, *18*(2).

Okin, G. S., A. R. Baker, I. Tegen, N. M. Mahowald, F. J. Dentener, R. A. Duce, J. N. Galloway, K. Hunter, M. Kanakidou, N. Kubilay, et al. (2011), Impacts of atmospheric nutrient deposition on marine productivity: Roles of nitrogen, phosphorus, and iron, *Global Biogeochemical Cycles*, *25*(2).

Páscoa, R. N., I. V. Tóth, and A. O. Rangel (2012), Review on recent applications of the liquid waveguide capillary cell in flow based analysis techniques to enhance the sensitivity of spectroscopic detection methods, *Analytica chimica acta*, *739*, 1–13.

Patey, M. D., E. P. Achterberg, M. J. Rijkenberg, P. J. Statham, and M. Mowlem (2010), Interferences in the analysis of nanomolar concentrations of nitrate and phosphate in oceanic waters, *Analytica Chimica Acta*, *673*(2), 109 – 116, doi:http://dx.doi.org/10.1016/j.aca.2010.05.029.

Paytan, A., and K. McLaughlin (2007), The oceanic phosphorus cycle, *Chem. Rev.*, *107*, 563–576.

Paytan, A., M. Lyle, A. Mix, and Z. Chase (2004), Climatically driven changes in oceanic processes throughout the equatorial Pacific, *Paleoceanography*, *19*(4).

Rasmussen, S., K. Andersen, A. M. Svensson, J. P. Steffensen, B. M. Vinther, H. B. Clausen, M.-L. Siggaard-Andersen, S. J. Johnsen, L. B. Larsen, D. Dahl-Jensen, M. Bigler, R. Röthlisberger, H. Fischer, K. Goto-Azuma, M. E. Hansson, and U. Ruth (2006), A new Greenland ice core chronology for the last glacial termination, *J. Geophys. Res.*, *111*, D06,102.

Rasmussen, S. O., P. Abbott, T. Blunier, A. Bourne, E. Brook, S. L. Buchardt, C. Buizert, J. Chappellaz, H. B. Clausen, E. Cook, D. Dahl-Jensen, S. Davies, M. Guillevic, S. Kipfstuhl, T. Laepple, I. K. Seierstad, J. P. Severinghaus, J. P. Steffensen, C. Stowasser, A. Svensson, P. Vallelonga, B. M. Vinther, F. Wilhelms, and M. Winstrup (2013), A first chronology for the NEEM ice core, *Climate of the Past Discussions*, *9*(3), 2967–3013, doi:10.5194/cpd-9-2967-2013.

Redfield, A. C. (1958), The biological control of chemical factors in the environment, *American scientist*, pp. 230A–221.

Richardson, S. J., D. A. Peltzer, R. B. Allen, M. S. McGlone, and R. L. Parfitt (2004), Rapid development of phosphorus limitation in temperate rainforest along the Franz Josef soil chronosequence, *Oecologia*, *139*(2), 267–276.

Rothlisberger, R., M. A. Hutterli, E. W. Wolff, R. Mulvaney, H. Fischer, M. Bigler, K. Goto-Azuma, M. E. Hansson, U. Ruth, M.-L. Siggaard-Andersen, et al. (2002), Nitrate in Greenland and Antarctic ice cores: a detailed description of post-depositional processes, *Annals of Glaciology*, *35*(1), 209–216.

Ruth, U., D. Wagenbach, J. P. Steffensen, and M. Bigler (2003), Continuous record of microparticle concentration and size distribution in the central Greenland NGRIP ice core during the last glacial period, *J. Geophys. Res.: Atmospheres*, *108, D3*, 4098, doi:10.1029/2002JD002376.

Ruttenberg, K. (2003), The global phosphorus cycle, *Treatise on geochemistry*, *8*, 585–643.

Ruttenberg, K., and M. Goni (1997), Phosphorus distribution, C:N:P ratios, and $\delta^{13}C_{OC}$ in arctic, temperate, and tropical coastal sediments: tools for characterizing bulk sedimentary organic matter, *Marine Geology*, *139*(1), 123–145.

Schindler, D. W. (1977), Evolution of phosphorus limitation in lakes, *Science*, *195*(4275), pp. 260–262.

Schlesinger, W. H. (1991), *Biochemistry, An analysis of global change*, Academic press.

Sigg, A., K. Fuhrer, M. Anklin, T. Staffelbach, and D. Zurmuehle (1994), A continuous analysis technique for trace species in ice cores, *Environ. Sci. Tech.*, *28*(2), 204–209.

Sigl, M., J. R. McConnell, L. Layman, O. Maselli, K. McGwire, D. Pasteris, D. Dahl-Jensen, J. P. Steffensen, B. Vinther, R. Edwards, R. Mulvaney, and S. Kipfstuhl (2013), A new bipolar ice core record of volcanism from WAIS Divide and NEEM and implications for climate forcing of the last 2000 years, *J. of Geophys. Res.: Atmospheres*, *118*(3), 1151–1169, doi:10.1029/2012JD018603.

Steffensen, J. P. (1997), The size distribution of microparticles from selected segments of the Greenland ice Core Project ice core representing different climatic periods, *Analyst*, *120*, 187–191.

Survey, U. G. (2010), Phosphorus statistics. In: Kelly TD, Mantos GR (compilers) Historic Statistics for Mineral and Mineral Commodities in the United States, *Tech. rep.*

Svensson, A., P. E. Biscaye, and F. E. Grousset (2000), Characterization of late glacial continental dust in the Greenland Ice Core Project ice core, *J. Geophys. Res.*, *105*(D4), 4673–4556.

Tamburini, F., and K. Fölimi (2009), Phosphorus burial in the ocean over glacial-interglacial time scales., *Biogeosciences*, *6*(4).

Taylor, K., C. Hammer, R. Alley, H. Clausen, D. Dahl-Jensen, A. Gow, N. Gundestrup, J. Kipfstuhl, J. Moore, and E. Waddington (1993), Electrical conductivity measurements from the GISP 2 and GRIP Greenland ice cores, *Nature*, *366*(6455), 549–552.

Tiessen, H. (1995), *Phosphorus in the global environment*, Springer.

Tockner, K., F. Malard, U. Uehlinger, and J. V. Ward (2002), Nutrients and organic matter in glacial river-foodplain system (Val Roseg, Switzerland), *Limnol. Oceanogr.*, *47*(1), 266–277.

Turekian, K. K. (1968), *Oceans*, Prentice-Hall.

United states government (1946), United states strategic bombing survey-summary report (Pacific war), *Tech. rep.*

US Department of Agriculture Natural Resources Conservation Service (2005), Global soil regions map, `http://www.nrcs.usda.gov/wps/portal/nrcs/detail/national/nedc/training/soil/?'cid$=$nrcs142p2\_054013`.

Ushie, H., and K. Matsumoto (2012), The role of shelf nutrients on glacial-interglacial CO_2: A negative feedback, *Global Biogeochemical Cycles*, *26*(2).

Vallelonga, P., C. Barbante, G. Cozzi, J. Gabrieli, S. Schüpbach, A. Spolaor, and C. Turetta (2013), Iron fluxes to Talos Dome, Antarctica, over the past 200 kyr., *Climate of the Past*, *9*(2).

Vance, C. P., C. Uhde-Stone, and D. L. Allan (2003), Phosphorus acquisition and use: critical adaptations by plants for securing a nonrenewable resource, *New Phytologist*, *157*(3), 423–447, doi:10.1046/j.1469-8137.2003.00695.x.

Vitousek, P. M., and H. Farrington (1997), Nutrient limitation and soil development: experimental test of a biogeochemical theory, *Biogeochemistry*, *37*(1), 63–75.

Vitousek, P. M., and R. W. Howarth (1991), Nitrogen limitation on land and in the sea: how can it occur?, *Biogeochemistry*, *13*(2), 87–115.

Vitousek, P. M., S. Porder, B. Z. Houlton, and O. A. Chadwick (2010), Terrestrial phosphorus limitation: mechanisms, implications, and nitrogen-phosphorus interactions, *Ecological Applications*, *20*(1), 5–15.

Volkovskiy, N. L. (Ed.) (2000), *The War in Korea 1950-1953*, 691-720 pp., Military Historical Library, Izdatel'stvo Poligon, Saint Petersburg.

Wallmann, K. (2010), Phosphorus imbalance in the global ocean?, *Global Biogeochemical Cycles*, *24*(4).

Wolff, E. W., J. C. Moore, H. B. Clausen, and C. U. Hammer (1997), Climatic implications of background acidity and other chemistry derived from electrical studies of the Greenland Ice Core Project ice core, *Journal of Geophysical Research: Oceans (1978–2012)*, *102*(C12), 26,325–26,332.

Worsfold, P. J., L. J. Gimbert, U. Mankasingh, O. N. Omaka, G. Hanrahan, P. C. Gardolinski, P. M. Haygarth, B. L. Turner, M. J. Keith-Roach, and I. D. McKelvie (2005), Sampling, sample treatment and quality assurance issues for the determination of phosphorus species in natural waters and soils, *Talanta*, *66*(2), 273 – 293, doi:10.1016/j.talanta.2004.09.006.

Worsfold, P. J., P. Monbet, A. D. Tappin, M. F. Fitzsimons, D. A. stiles, and I. D. McKelvie (2008), Characterisation and quantification of organic phosphorus and organic nitrogen components in aquatic system: A Review, *Anal. Chim. Acta*, *624*, 37–58.

Wu, J., W. Sunda, E. A. Boyle, and D. M. Karl (2000), Phosphate depletion in the western North Atlantic Ocean, *Science*, *289*(5480), 759–762.

Zamora, L., J. Prospero, D. Hansell, and J. Trapp (2013), Atmospheric P deposition to the subtropical North Atlantic: sources, properties, and relationship to N deposition, *Journal of Geophysical Research: Atmospheres*, *118*(3), 1546–1562.

Zhang, J., and J. Chi (2002), Automated analysis of nanomolar concentrations of Phosphate in natural waters with liquid waveguide, *Environ. Sci. Technol.*, *36*, 1048–1053.

Zhang, J., P. Wang, Q. Li, X. Cheng, H. Jin, and S. Zhang (2007), Western equatorial Pacific productivity and carbonate dissolution over the last 550 kyr: Foraminiferal and nannofossil evidence from ODP Hole 807A, *Marine Micropaleontology*, *64*(3), 121–140.

Zhang, J. Z., C. J. Fischer, and P. B. Ortner (1999), Optimization of performance and minimization of silicate interference in continuous flow phosphate analysis, *Talanta*, *49*, 293–304.

Zhang, R., M. Wu, Q. Wang, J. Geng, and X. Yang (2010), The determination of atmospheric phosphine in Ny-Ålesund, *Chinese Science Bulletin*, *55*(16), 1662–1666.

Zhu, R., D. Glindemann, D. Kong, L. Sun, J. Geng, and X. Wang (2007), Phosphine in the marine atmosphere along a hemispheric course from China to Antarctica, *Atmospheric Environment*, *41*(7), 1567–1573.

Ziegler, C. L., R. W. Murray, T. Plank, and S. R. Hemming (2008), Sources of Fe to the equatorial Pacific Ocean from the Holocene to Miocene, *Earth and Planetary Science Letters*, *270*(3), 258–270.

Zielinski, G. A., P. A. Mayeski, L. D. Meeker, S. Whitlow, and M. S. Twickler (1996), A 110.000-yr record of explosive volcanism from the GISP2 (Greenland) ice core, *Quat. Res.*, *45*, 109–118.

Part II

'PH' DETERMINED IN ICE USING AN OPTICAL DYE METHOD

Many chemicals change their properties when pH is changed. For example the soluble fraction of phosphorus changes with pH and the acidification of carbonates form CO_2 and is a reaction hypothesised to occur *in situ* in ice cores (and is further discussed in section 9.2.1).

Further determination of the acidity in ice can be used to identify volcanoes, crucial for cross-dating ice cores and is also relevant for climate interpretations. Furthermore the ionic budget in the ice will also depend on the concentration of H^+.

Chapter 6 discusses in more detail the relevance of determining the acidity in ice. Further, pH is defined in section 6.4 using Brønsted Lowry theory and section 6.4.3 continues with a review of pH and acidity determination methods, such as indicator dye methods and electrical probes. Section 6.4.4 describes existing methods used to identify or quantify acidity in ice cores, including Electrical Conductivity Measurements (ECM), DiElectric Profiling (DEP), titration, Melt Water Electrical Conductivity (MWEC) as well as continuous flow analysis (CFA) methods for both the determination of sulphate and determination of pH using electrical probes.

As part of this thesis, a method for the continuous determination of pH was developed. The method is based on indicator dye color changes, which are optically determined at two wavelengths. The method is thoroughly described in chapter 7, which is intended as a manuscript for the journal Environmental Science & Technology. In the manuscript the method is validated against H^+ as determined by the ionic budget and the manuscript also includes results from a North East Greenland ice stream (NEGIS) firn core. Further the method was implemented on the Antarctic RICE (Roosevelt Island Climate Evolution) ice core during a measurement campaign in New Zealand in 2013, where the top 500 metres of the RICE core were analysed. Preliminary results from the RICE ice core are presented in chapter 8 together with an outlook of the RICE data and the optical pH determination method.

6. MOTIVATION AND THEORY

Volcanic eruptions have a significant climatic impact e.g., the 1815 Tambora eruption caused the "year without a summer" [Robock, 2000]. Volcanic eruptions perturb the climate by large light absorbing ash particles and by injecting large quantities of sulphate into the stratosphere, with a residence time of about 1-2 years [Robock, 2000]. The overall effect on the troposphere is a general cooling, while in the stratosphere, the effect is a warming in the layer containing the sulphate particles.

In ice, volcanic eruptions can be identified either by detection of ash (tephra) layers or by recording sulphate or acidity, both deposited as a result of a volcanic eruption. Thus ice cores can provide an important record of past eruptions, which– together with other records– can be used to identify the climatic effect of volcanic eruptions.

Further the volcanic events are used extensively for dating ice cores. Precise dates can be assigned for recent volcanic eruptions and thus the dating of the ice is constrained by records of known volcanic eruptions. Further down in the ice, sequences of volcanic eruptions of unidentified origin are used to cross date ice cores. Thus the dating of ice cores from Antarctica, where precipitation is limited and annual signals can not be counted, can be constrained by the high annual precipitation counterparts from Greenland by identifying patterns of volcanic eruptions. Provided, however that the eruption be large enough to impact both hemispheres. Similar cross dating can also be used within one hemisphere [Seierstad et al., 2014].

Finally the acidity of the ice governs the ionic balance. Knowing the acidity content of the ice is thus critical for determining the chemical species originally deposited on the ice. Further acidity is expected to be important for the in in situ production of CO_2 as explained in section 9.2.1.

6.1 Volcanic indices and the impact of volcanic eruptions on climate

Volcanoes impact the climate in a variety of ways as shown in Figure 6.1 and Table 6.1. Thus, having a reliable record of volcanic eruptions is crucial when trying to understand excursions in climate records. Ice cores could potentially provide such a long term record of volcanic eruptions.

When a volcano erupts large quantities of gases and particles are emitted into the atmosphere. These include various chemical substances. Some stay in the atmosphere for long periods of time (e.g. CO_2 and N_2), others for an intermediate period of say two years (e.g. sulphurous compounds) and some only stay in the atmosphere for a short period, such as the ash particles and chloride. Thus the temporal effect of a volcanic eruption varies as does the effect on climate of these different substances [*Robock*, 2000].

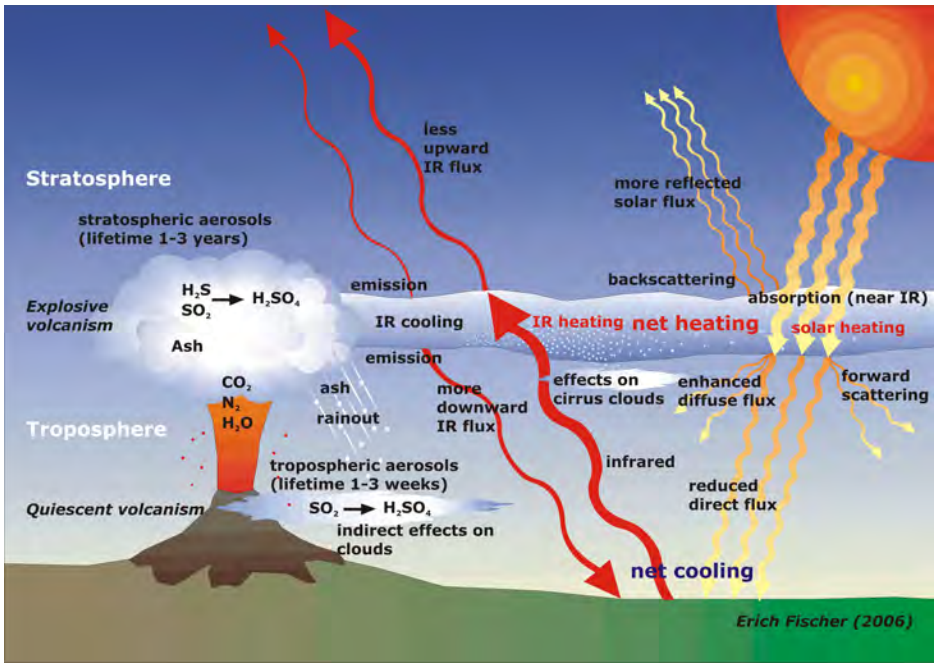

Fig. 6.1: Schematic diagram of the climatic impact of an explosive volcano. Figure from *Fischer* [2006], modified from *Robock* [2000].

While over geological timescale greenhouse gases partly originate from volcanoes, the short term effect is small. It is estimated that the mean amount of CO_2 outgased by a single volcano is about 100 times smaller than the current anthropogenic amount of CO_2 added to the atmosphere per year [*Myhre and Zhang*, 2013; *Robock*, 2000].

Ash particles present in the atmosphere during and shortly after an eruption can significantly influence the diurnal cycle by blocking ingoing and outgoing radiation. The ash particles are removed quickly ($\sim$ 4 days) from the atmosphere and though they locally significantly alter the environment by changing diurnal cycles and albedo and by introducing high loads of nutrients, the global effect is not pronounced.

The largest effect of volcanic eruptions is a cooling due to high loads of SO_2, which in the atmosphere react within weeks with OH^- and H_2O to form H_2SO_4 [*Robock*, 2000]. The amount of SO_2 from volcanic eruptions varies greatly. While explosive volcanoes tend to generate large quantities of debris that falls as ash, they do not necessarily contribute with the highest loads of SO_2. Further, the distribution of the SO_2 and thus the climatic effect is influenced by the wind pattern during the eruption. For example two volcanoes positioned just 2° latitude apart can have an effect up to 15° latitude apart due to the initial wind distribution[*Robock*, 2000].

The sulphate aerosols are small and the size scatters ingoing solar radiation, thus increasing the albedo, they reduce the solar energy influx and cause a net cooling of the troposphere. This net cooling also decreases evaporation and thus the precipitation rate is decreased–particularly in the tropics.

Sulphuric compounds from a volcanic eruption can make it to the stratosphere quickly; however there is also evidence that the sulphur can be lifted from the troposphere to the stratosphere over months [*Myhre and Zhang*, 2013]. In the stratosphere

Tab. 6.1: Effects of large explosive volcanoes on weather and climate. Table modified from *Robock*[2000].

Effect	**Mechanism**	**Begins**	**Duration**
Reduction of diurnal cycle	Blockage of shortwave and emission of longwave radiation	immediately	1-4 days
Reduced tropical precipitation	Blockage of shortwave radiation , reduced evaporation	1-3 months	3-6 months
Summer cooling of NH tropics and subtropics	Blockage of shortwave radiation	1-3 months	1-2 years
Stratospheric warming	stratospheric absorption of shortwave and longwave radiation	1-3 months	1-2 years
Winter warming of NH continents	stratospheric absorption of shortwave and longwave radiation, dynamics	1/2 year	one or two winters
Global cooling	Blockage of shortwave radiation	immediately	1-3 years
Global cooling from multiple eruptions	Blockage of shortwave radiation	immediately	10-100 years
Ozone depletion, enhanced UV	dilution, heterogeneous chemistry on aerosols	1 day	1-2 years

the sulphuric acid causes an absorption of near-IR at the sulphuric layer, causing a net increase of the temperature within the layer. Thus the sulphuric acid causes heating in the stratosphere and more so in the tropics than at the poles. This causes a change in the wind patterns in the stratosphere, which in turn affects the Northern Hemisphere winter warming, which is governed by advective effects [*Robock*, 2000].

Sulphate aerosols in the cold part of the stratosphere are involved in heterogeneous chemical reactions freeing chlorine, which destroys ozone. This in turns influences the amount of UV ingoing radiation that is harmful for living creatures. Thus also indirectly volcanoes are harmful for living creatures [*Robock*, 2000].

To estimate the strength of volcanic eruptions several indexes has been developed based on different datasets as well as different approaches. These include the dust veil index (DVI)[*Lamb*, 1970] based on information about historical eruptions, optical phenomena, radiation measurements (1983 onwards), temperature and volume of ejecta estimates. The DVI index was challenged due to its use of temperature data, making the argument somewhat circular, however recent methods where temperature is not included reach similar DVI strengths [*Robock*, 2000]. The DVI index is scaled so the 1883 AD eruption of Krakatau has a DVI of a 1000.

Another often used index is the volcanic explosivity index (VEI), which is based on geological evidence and thus the index does not include any information about the sulphur load of the eruption. However a VEI of 3 is stated to have possible stratospheric injection, 4 definitely has stratospheric injection and a VEI of 5 has significant stratospheric injection. However, while the St. Helens eruption in 1980 had a VEI of 5 it had little stratospheric impact[*Robock*, 2000].

Other indexes are the Mitchell index and the Sato index. The Mitchell index is similar to the DVI index, with the difference that the Mitchell index includes some additional smaller eruptions. The Sato index is based on newer measurements such

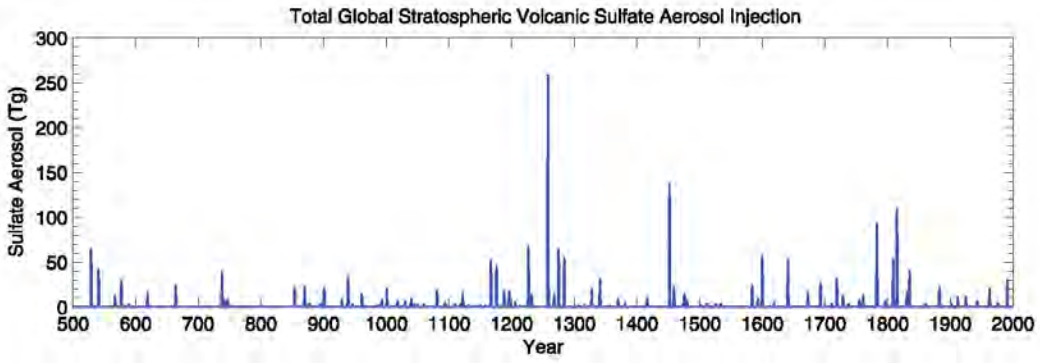

Fig. 6.2: Global volcanic eruptions and their strength since 500 AD based on the ice core volcanic index (IVI). Figure from *Gao et al.* [2008].

as those obtained from satellites. The Sato index is given in optical depth at a wavelength of 0.55 μm [*Robock*, 2000].

Finally an ice core volcanic index (IVI) based on acidity or sulphate measurements has been developed (see Figure 6.2)[*Gao et al.*, 2008]. The natural position of the ice cores used to provide such information makes the IVI influenced more by high latitude eruptions. The latitudinal effect can be corrected for if the eruptions are unambiguously identified [*Robock*, 2000]. The advantage of the IVI is that in high resolution it can inform on past eruptions. As an example the Toba eruption at 74 kyr BP was thought to be just one large eruption, but in both Greenland and Antarctic records the Toba eruption is identified as 9 acidity peaks[*Svensson et al.*, 2013].

6.1.1 Cross dating ice cores using volcanic eruptions

Volcanic eruptions can be identified in ice cores when acidity or sulphate is determined. Further, when ash (tephra) is present, unique identifications of specific volcanic eruptions can be performed by analysing the ash composition and comparing it to ash, which is known to originate from a specific volcano (e.g. [*Davies et al.*, 2008]).

Figure 6.3 shows two acid peaks identified in a Greenland ice core (B20). Section 6.4.4 will have more information about how acid and sulphate is determined in ice cores.

The records of sulphate, acidity and similar volcanic compounds, are extensively used to cross date ice cores. As mentioned in section 1.1 ice cores are dated with high accuracy using the fact that annual cycles can be determined 60.000 yr back in Greenland ice [*Svensson et al.*, 2008]. This method for of accurately determining the exact age of volcanic eruptions can be used to constrain the age of another ice core if the same eruption is found. By using such reference layers, the GICC05 time scale [*Andersen et al.*, 2006; *Svensson et al.*, 2006; *Rasmussen et al.*, 2013] has been extended to cover almost all of the Greenland deep ice cores [*Seierstad et al.*, 2014]. Using the volcanic eruptions to provide one time-scale for several ice cores allow for detailed investigations of the differences between other high resolution climate parameters determined in the ice cores. Such well dated ice records are

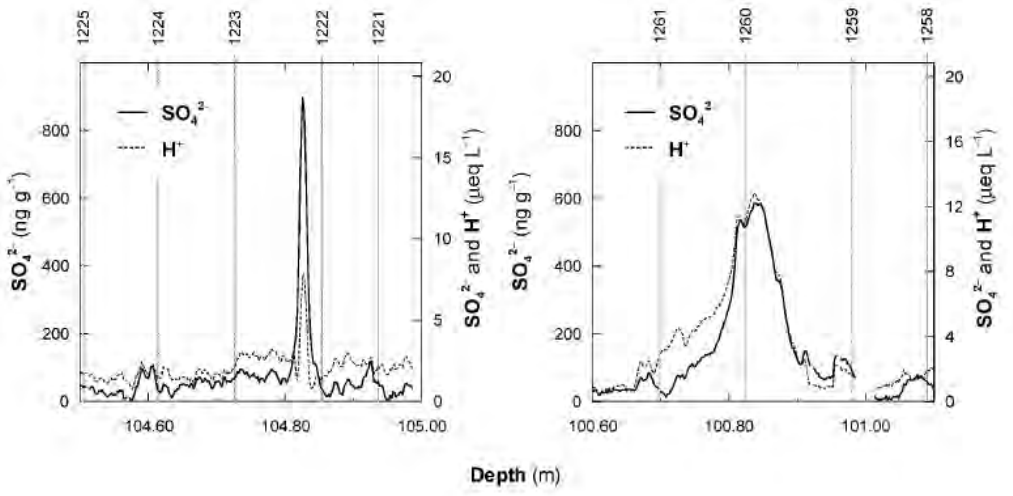

Fig. 6.3: Examples of SO_2^{3-} and H^+ as determined in the Greenland B20 ice core. Left) short-pulse feature, possibly from Hekla (AD1222) or Reykjaneshryggur (AD1223); right) unknown source (AD1259) with bipolar occurrence. Figure adapted from *Bigler et al.* [2002].

for example crucial for understanding changes in height between core sites, which can be inferred from $\delta^{18}O$, providing knowledge on the shape of the ice sheet over time [*Vinther et al.*, 2009] or may provide knowledge about precipitation differences between ice cores sites over time [*Seierstad et al.*, 2014].

6.2 Anthropogenic changes in rain acidity

While precipitation naturally has a pH of 5.6 when in equilibration with CO_2, in the late 1960's and early 1970's awareness of rain with a pH of about 4, and with individual precipitation events with a pH of 2.1 emerged, especially in England, America and Scandinavia [*Likens and Bormann*, 1974]. As an example the H^+ content in precipitation increased 200 fold between 1956 and 1974 in Scandinavia [*Likens and Bormann*, 1974].

It was recognized that the acid rain was caused by increases in SO_4^{3-}, NO_x and ozone and was of anthropogenic origin [*Likens and Bormann*, 1974; *Bhargava and Bhargava*, 2013]. Sources of SO_2 are combustion of burnable waste, coal and fossil fuels in thermal plants and smelters, while the natural sources are ocean and volcanic eruptions [*Singh and Agrawal*, 2008; *Bhargava and Bhargava*, 2013]. While SO_2 is the current larger cause of acid rain, combustion of natural gas in power stations, industrial emission and vehicle exhaust increase NO_x also affecting the acidity. The natural sources of NO_x are lightning, volcanic eruptions and biological processes [*Likens and Bormann*, 1974]. The acid is transported far from the source and thus the environmental effect of acid rain occurs far from the sources ($>$ 1000km). Coal combustion increases the sulphuric acid content released to the atmosphere. Since 1850 AD the sulphuric acid was neutralized and precipitated out by co-emission of basic particles causing a local soot problem. Contrary when sulphuric acid is released by fossil fuel burning, prevalent since the 1950's, it is not neutralized and

thus it causes more severe regional acid rain problems [*Likens and Bormann*, 1974].

The consequences of acid rain are numerous; it affects water chemistry, leaching of nutrients, the availability of heavy metals, and thus food chains. The acidity also erodes buildings and statues. Even in remote areas as the Arctic, SO_2 is involved in producing Arctic Haze[*Barrie et al.*, 1985; *Law and Stohl*, 2007; *Quinn et al.*, 2007].

Soil acidification causes acid induced leaching of nutrients, which can eventually cause a decrease in the nutrient level in the soil, affecting biological growth rates. However the soil acidity is also effected by other processes e.g. vegetation cover changes [*Krug et al.*, 1983; *Singh and Agrawal*, 2008], making it difficult to distinguish the effect of acid rain from other processes. Besides the effect on nutrients an increase in the availability of heavy metals is also observed in acid soils [*Likens and Bormann*, 1974; *Bhargava and Bhargava*, 2013]. These heavy metals are toxic to plants and also have negative effects further up in the food chain[*Likens and Bormann*, 1974; *Bhargava and Bhargava*, 2013]. Acid rain also affects forest trees. Both by direct tissue damage and through the soil changes. Especially boreal forests are affected. Also crops are affected by acid rain and are reported to reduce CO_2 fixation when subjected to acid waters [*Singh and Agrawal*, 2008].

Water systems are less well buffered than soil and thus acid rain more severely affects water bodies. The acidity of the water influences on all parts of living systems in the water, whether phytoplankton, amphibians or fish [*Likens and Bormann*, 1974; *Singh and Agrawal*, 2008; *Bhargava and Bhargava*, 2013]. The species are to varying degree affected by the acidity and the ecological system changes with pH. The numbers of phytoplankton and snails decrease in lakes with a pH below 5.5, zooplankton disappears below pH 5 and below a pH of 4 the embryos of several fish species fail to mature [*Singh and Agrawal*, 2008].

Humans (and other larger mammals) are affected by acid rain directly by eye and skin irritation, through water intake, but also indirectly through an increased content of heavy metals in food, potentially causing severe diseases.

Marble and limestone buildings and statues, as well as carbonate rich concrete, deteriorate and form Ca^{2+}, HCO_3^- and SO_4^{2-} in the presence of acid waters [*Likens and Bormann*, 1974; *Singh and Agrawal*, 2008; *Bhargava and Bhargava*, 2013]. Corrosion of steel buildings and railway tracks occurs more than twice as fast in polluted areas and replacements are costly to society [*Singh and Agrawal*, 2008].

Following the awareness and concern about the many consequences of pollution the US Clean Air Act was introduced in the 1970's, however not with a particular focus on acid rain. Starting with emission controls of SO_2, the European Convention on Long-range Transboundary Air Pollution (CLRTAP) protocols on emission, reductions were agreed upon by various European countries in the early 1980s and later expanded to also include NO_x and volatile organic compounds (VOC's) [*Milieu Ltd and the Center for Clean Air Policy*, 2004]. In the 1980's the Acid Rain Program was initiated in the US to investigate the effect of acid rain and based on this program clean air legislation to control emissions of NO_2 and SO_2 were introduced in the US in the 1990's (see Figure 6.4) [*Milieu Ltd and the Center for Clean Air Policy*, 2004; *Singh and Agrawal*, 2008; *Smith et al.*, 2011]. These regulations have resulted in a return to more natural pH values in rain. In Europe in the period between 1982 and 1999 the reduction of SO_2 was about 65%, while the USA reduced

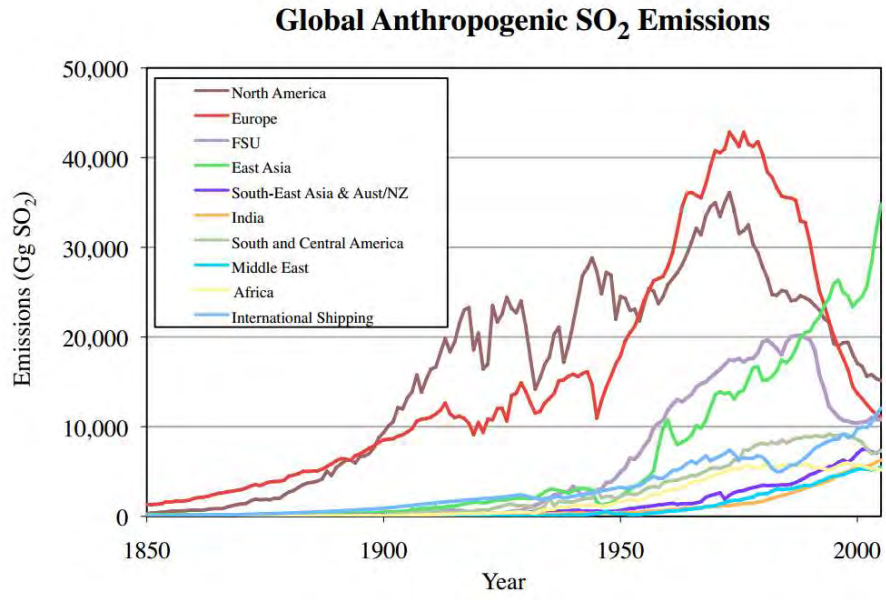

Fig. 6.4: SO_2 emissions from different countries based on emission and consumption data as found by *Smith et al.* [2011]. Figure from *Smith et al.* [2011].

the SO_2 emission by 40% [*Singh and Agrawal*, 2008]. In Asia sulphur emissions were decreasing, but are now again rising and cause significant health problems especially in larger cities in China and India [*Singh and Agrawal*, 2008; *Smith et al.*, 2011].

As mentioned above, the impact of the acid pollution is widespread and has effected even remote places such as the Arctic, where the Arctic haze phenomenon [*Barrie et al.*, 1985; *Law and Stohl*, 2007; *Quinn et al.*, 2007] was recognized as early as the 1950s. The Arctic haze forms as a consequence of pollution; primarily sulphate mixtures and particulate organic matter. The Arctic haze occurs during late winter/early spring when pollution from the south is strongest due to the prevailing wind systems. Partly due to studies of the Arctic haze phenomenon it was recognized that anthropogenic pollution in the form of aerosols spreads much further than was earlier the belief [*Quinn et al.*, 2007]. The anthropogenic imprint related to SO_4^{3-} and NO_x sources is also recognized in the Greenland B18 and B20 ice core records of SO_2^{3-} (see Figure 6.5).

6.3 Ionic balance and in situ production of carbonates

Ions can be detected in ice and provide information about past climate and environmental conditions. The ionic balance is the balance between cations and anions. However one should also be aware of post depositional effects. These effects include volatilization of e.g. organic acids in connection with the sublimation and condensation of snow. As a result lower concentrations of volatile species are observed in snow pack than in the snow fall. Molecular diffusion within the snow and ice also influence the record post deposition and finally also chemical reactions can change the ion records. Thus it is crucial that the acidity in the snow and ice is known with high precision.

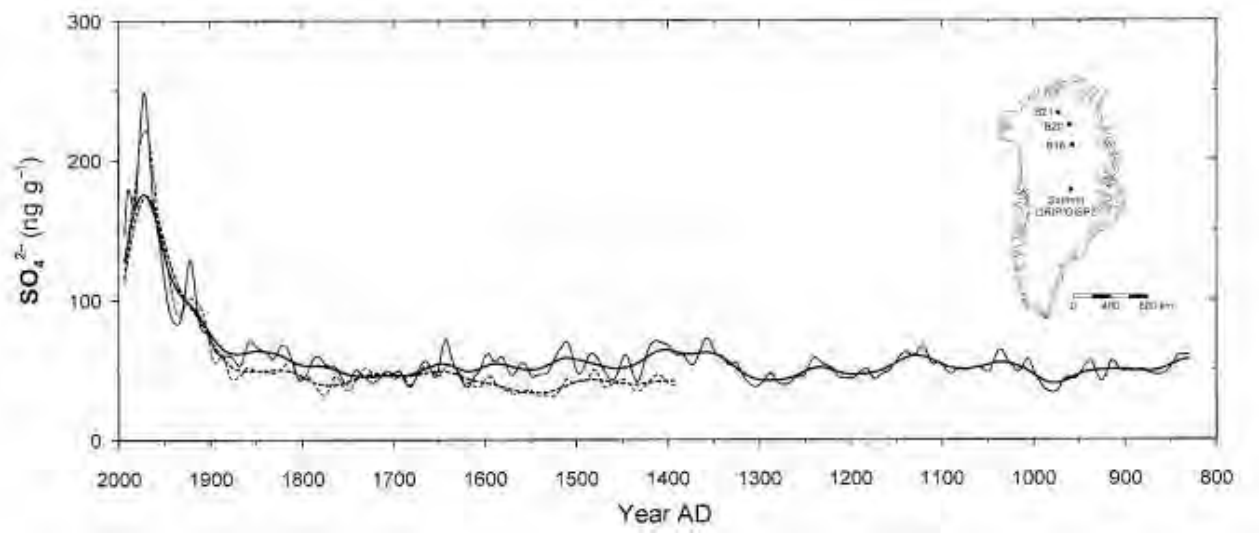

Fig. 6.5: SO_2^{3-} filtered with a low pass filter of 30 yrs (thin lines) or 100 yrs (thick lines) based on the Greenland ice cores B18 (dashed lines) and B20 (full lines). Figure modified from *Bigler et al.* [2002].

The cations and anions should balance, thus ΔC should be 0 in equation 6.1. Clearly knowing the concentrations of multiple ions as well as the concentration of H^+ is crucial to investigate the ionic balance. More information about the ionic balance in ice is presented in section 6.4.4.

$$\begin{aligned} \Delta C = {} & Na^+ + NH_4^+ + K^+ + H^+ + 2 \cdot Ca^{2+} + 2 \cdot Mg^{2+} \\ & -F^- - Cl^- - NO_3^- - 2 \cdot SO_4^{2-} - CH_3SO_3^- - HCOO^- - CH_3COO^- \end{aligned} \tag{6.1}$$

Iizuka et al. [2008; 2012] investigated the relationship between the ion balance and the salt inclusions in the Greenland GRIP and the Antarctic Dome Fuji ice cores. They observed that the dominant compounds were dependent only on the ionic balance and the sequence of chemical reactions. Changes related to the acidic environment of the Holocene versus the reductive environment of the glacial as well as between coastal and continental sites effect the salt inclusions observed in the ice. Employing the method by *Iizuka et al.* [2008], *Iizuka et al.* [2012] found that the dust adhered sulphate stayed constant over the glacial and the interglacial periods, while the salt derived sulphate correlated inversely with temperature in the Antarctic Dome Fuji ice core.

Another example where knowledge of the acidity in ice cores is crucial is for determining the cause(s) of the observed *in situ* production of CO_2 and as will be further discussed in section 9.2.1, acidification carbonates is one of the expected causes.

To summarize: The reasons for investigating the pH in ice cores are numerous varying from investigations of climatic impacts by volcanoes and anthropogenic changes, knowing the atmospheric acidity over longer time scales as well as to constrain the ionic budget and derive the exact sea salt compositions or determine the cause of in situ CO_2 contributions within the ice core records.

Tab. 6.2: Alternative definitions of acids and bases.

Model	**Acid**	**Base**	Example
Arrhenius	causes excess H^+ in water	causes excess OH^- in water	Ammonia(g) does not act as a base when added to HCl(g)
Brønsted-Lowry	H^+ donor	OH^- donor	Ammonia acts as a base both when added to water and to HCl(g)
Lewis	electron pair acceptor	electron pair donor	Zn^{2+} is seen as an acid

6.4 pH definition and determination

In this section an introduction to pH and acidity is given intended as a theoretical background for understanding the methods used for determining acidity in water samples and in ice cores.

6.4.1 Theoretical definitions related to pH

This section is based mainly on literature from Masterton et al. [2011a] and Hites and Raff [2012].

There are many different definitions of acids and bases. The main ones referred to are the Arrhenius, Brønsted-Lowry and Lewis theories.

The Brønsted-Lowry theory is most commonly used. In **Brønsted-Lowry theory** an acid is a proton (H^+ ion) donor, while a base is a proton (H^+ ion) acceptor. In an acid-base reaction a proton is transferred from an acid to a base. Thus Brønsted-Lowry theory can be applied only if the reactions involve proton transfers [*Masterton et al.*, 2011a]. In the **Arrhenius** definition an acid is a substance that produces excess H^+ in water, while a base is a substance producing excess OH^- in water. The Arrhenius definition is a subset of the Brønsted-Lowry as there is only a limited number of acids and bases that strictly fulfil the Arrhenius definition. While the Brønsted-Lowry theory applies only if a proton transfer is involved, the **Lewis acid-base model** has removed this restriction. A Lewis acid accepts an electron pair and a Lewis base donates an electron pair in an acid-base reaction. Thus while the Lewis model does not significantly change the number of species acting as a base from the Brønsted-Lowry theory, it greatly increases the number of species considered acids, eg. the substance that accepts an electron pair can equally well be a proton and a cation, such as Zn^{2+}. From here on I will refer to the definition of Brønsted-Lowry theory when mentioning acids and bases, while more concepts are introduced.

The species formed when a proton is removed from an acid is called the conjugate base of that acid. In equation 6.2 B^- is the conjugate base of the acid HB and similarly A^- is the conjugate base for the acid HA. Also recall that the equilibrium

constant (K) in that case is given as $K = \frac{[HA(aq)][B^-(aq)]}{[HB(aq])][A^-(aq)]}$, where the square brackets refer to molar concentration units (moles per liter).

$$HB(aq) + A^-(aq) \leftrightarrows HA(aq) + B^-(aq) \tag{6.2}$$

Further a species that can both accept a proton as well as donate one is **amphiprotic**. Water, H_2O, thus shows amphiprotic behaviour and the equilibrium constant (K_w) at 25°C is $1 \cdot 10^{-14}$. A water solution containing more [H^+] ($> 1.0 \cdot 10^{-7}$M) than [OH^-] is acidic, while a water solution containing more [OH^-] than [H^+] is basic (alkaline).

$$H_2O \leftrightarrows H^+ + OH^- \tag{6.3}$$

$$K_w = [H^+][OH^-] = 1 \cdot 10^{-14} \tag{6.4}$$

Sørensen defined pH (the 'power of the hydrogen ion'). Thus if pH>7 the water sample is basic and if pH<7 the sample is acidic:

$$\mathrm{pH} = -\log_{10}([H^+]) \tag{6.5}$$

In the Brønsted-Lowry theory acids and bases are further subdivided into strong acids and bases, weak acids and bases, and species that does not form water solutions. Strong bases are bases that are stronger proton acceptors than the OH^- ion, and similarly strong acids are stronger proton donors than the H_3O^+ ion. Weak acids and bases are weaker than the H_3O^+ ion and OH^- ion respectively, but stronger than the H_2O molecule. Species that do not form a water solution are naturally weaker acceptors (donors) than the water molecule.

Strong bases and acids are completely ionized in water, making it relatively easy to determine the pH in solutions. Strong acids and bases are e.g. HCl and H_2SO_4. Strong bases are the hydroxides of group 1 and 2, such as NaOH. Because strong acids and bases are completely ionized in water they are strong electrolytes, as an example the combination of HCl and NaOH forms NaCl.

$$\mathrm{HCl\ (aq)} + H_2O \leftrightarrows H_3O^+(aq) + Cl^-(aq) \tag{6.6}$$

$$\mathrm{NaOH\ (aq)} + H_2O \leftrightarrows H_2O + OH^-(aq) + Na^+(aq) \tag{6.7}$$

The pH of a **Weak acid** is more difficult to determine as the weak acid is not completely dissociated. This clearly makes the electrolytic properties of weak acids and bases weaker. If in equation 6.10, HB represents a weak acid, less than 1% of HB will usually be converted to the ion B^-. The acid equilibrium constant, K_a, is thus larger for stronger acids.

$$HB(aq) + H_2O \leftrightarrows H_3O^+(aq) + B^-(aq) \tag{6.8}$$

$$HB(aq) \leftrightarrows H^+(aq) + B^-(aq) \tag{6.9}$$

$$K_a = \frac{[H^+][B^-]}{HB} \tag{6.10}$$

For the carbonic acid (H_2CO_3) K_a is $4.4 \cdot 10^{-7}$, while its conjugate base (HCO_3^-) has $K_b = 2.3 \cdot 10^{-8}$. The hydrogen carbonate ion (HCO_3^-) has a K_a of $4.7 \cdot 10^{-11}$ and its conjugate base (CO_3^{2-}) has $K_b = 2.1 \cdot 10^{-4}$. Thus carbonic acid is a stronger acid than the hydrogen carbonate ion. Since K_a is usually a very low number, in the literature $pK_a = -log_{10}(K_a)$ is often given. K_a is often known to only ±5%. However if either the K_a or K_b is known its conjugate can easily be found because $K_w = K_a \cdot K_b$.

Two types of weak acids exist. One is the cations such as the ammonium ion, with NH_3 as the conjugate base (see equation 6.11).

$$NH_4^+ + H_2O \leftrightarrows NH_3 + H_3O^+ \tag{6.11}$$

The other type of weak acids are molecules containing an ionizable hydrogen ion, such as nitrous acid (HNO_2).

Polyprotic acids are acids that contain more than one ionizable H^+ ion. Thus the acid will ionize in steps, with a separate equilibrium constant for each step. The anion formed in one step will produce another H^+ in the next step. Thus with each successive step the equilibrium constant decreases; the acid becomes weaker. An example of a polyprotic acid is **carbonic acid**, it is diprotic as it takes two steps to form the CO_3^{2-} ion. The calibration constants are $K_{a1} = 4.4 \cdot 10^{-7}$ and $K_{a2} = 4.7 \cdot 10^{-11}$. Thus based on these two equilibrium constants the **pH of a water sample with access to the ambient CO_2** in the laboratory can be determined. First we need to find out how much of the gaseous CO_2 that gets dissolved in water. This can be determined using Henry's law (eq. 6.13).

$$CO_2(air) \leftrightarrows CO_2(water) \tag{6.12}$$

$$K_H = \frac{[CO_2]}{P_{CO_2}} = 10^{-1.47}(\mathrm{M/atm}) \tag{6.13}$$

Here P_{CO_2} is the partial pressure of CO_2 in the atmosphere. For an atmospheric CO_2 concentration of 390 ppm the atmospheric partial pressure is $390 \cdot 10^{-6}$ atm $= 10^{-3.41}$ atm. The term $[CO_2]$ represent all CO_2 dissolved in the water whether in form of CO_2 or in form of H_2CO_3[1]. Please note that in the literature often $CO_{2(aq)}$ is also called $H_2CO_3\star$ and in some textbooks it is referred to as H_2CO_3. Thus we can determine the amount of dissolved CO_2 as $K_H P_{CO2} = 10^{-1.47} 10^{-3.41} = 10^{-4.88}$.

When $[CO_2]$ reacts with water bicarbonate is formed.

$$CO_2(aq) + H_2O \leftrightarrows H^+(aq) + HCO_3^-(aq) \tag{6.14}$$

$$K_{a1} = \frac{[H^+][HCO_3^-]}{[CO_2]} = 4.4 \cdot 10^{-7} = 10^{-6.35} \tag{6.15}$$

Through rearranging and using Henrys law we can now estimate the concentration of bicarbonate.

$$[H^+][HCO_3^-] = K_{a1}[CO_2] \tag{6.16}$$

$$= K_{a1} K_H P_{CO_2} \tag{6.17}$$

$$= 10^{-11.23} \tag{6.18}$$

[1] At 25 °C the dissolved CO_2 is 99.85% of the sum.

However as mentioned above bicarbonate further dissociates and forms carbonate and additional acid.

$$\mathrm{HCO_3^-} \leftrightarrows \mathrm{CO_3^{2-}} + \mathrm{H^+} \tag{6.19}$$

$$K_{a2} = \frac{[\mathrm{H^+}][\mathrm{CO_3^{2-}}]}{[\mathrm{HCO_3^-}]} = 4.7 \cdot 10^{-11} = 10^{-10.33} \tag{6.20}$$

By combining with equation 6.18 we further obtain:

$$[\mathrm{H^+}][\mathrm{CO_3^{2-}}] = K_{a2}[\mathrm{HCO_3^-}] \tag{6.21}$$

$$= \frac{K_{a2}K_{a1}K_H P_{CO_2}}{[\mathrm{H^+}]} \tag{6.22}$$

$$= \frac{K_3 P_{CO_2}}{[\mathrm{H^+}]} \tag{6.23}$$

$$= \frac{10^{-18.15}10^{-3.41}}{[\mathrm{H^+}]} \tag{6.24}$$

$$= \frac{10^{-21.56}}{[\mathrm{H^+}]} \tag{6.25}$$

We also know that if in equilibrium there should also be charge balance or electroneutralitry; $[\mathrm{H^+}]$=$[\mathrm{HCO_3^-}]$+2$[\mathrm{CO_3^{2-}}]$+$[\mathrm{OH^-}]$. Substituting this into equation 6.25 and eliminating all variables we obtain.

$$[\mathrm{H^+}] = \frac{10^{-11.23}}{[\mathrm{H^+}]} + 2\frac{10^{-21.56}}{[\mathrm{H^+}]^2} + \frac{10^{-14}}{[\mathrm{H^+}]} \tag{6.26}$$

$$[\mathrm{H^+}]^3 = 10^{-11.23}[\mathrm{H^+}] + 10^{-21.26} \tag{6.27}$$

It is directly evident that the last term ($[\mathrm{OH^-}]$) is smaller (by $10^{2.77} \sim 600$ times) than the first term on the right ($[\mathrm{HCO_3^-}]$) and can thus be dropped and we arrive at equation 6.27 after recalling that $2 = 10^{0.30}$ and multiplying with $[\mathrm{H^+}]^2$.

Further we can neglect the last term in equation 6.27 as for acidic samples it will be small.[2] Finally we arrive at equation 6.30 and find that the pH of water in equilibrium with an atmosphere containing 390 ppm $\mathrm{CO_2}$ is 5.62.

$$[\mathrm{H^+}]^2 = K_{a1}K_H P_{CO_2} = 10^{-6.35}10^{-1.47}10^{-3.41} = 10^{-11.23} \tag{6.28}$$

$$[\mathrm{H^+}] = (K_{a1}K_H P_{CO_2})^{1/2} = 10^{-5.62} \tag{6.29}$$

$$\mathrm{pH} = -\log_{10}[\mathrm{H^+}] = 5.62 \tag{6.30}$$

Solid salts, ionic solids containing a cation other than $\mathrm{H^+}$ and an anion other than $\mathrm{OH^-}$, also act as a base or an acid. In order to determine whether a salt acts as a base or an acid one needs to investigate whether the cation acts as an acid and how strong an acid and similarly for the anion.

[2] For a pH of 6 $10^{-21.26}$ is more than a 1000 times smaller than $10^{-23}[\mathrm{H^+}] = 10^{-17.2}$ and $[\mathrm{H^+}]^3 = 10^{-18}$.

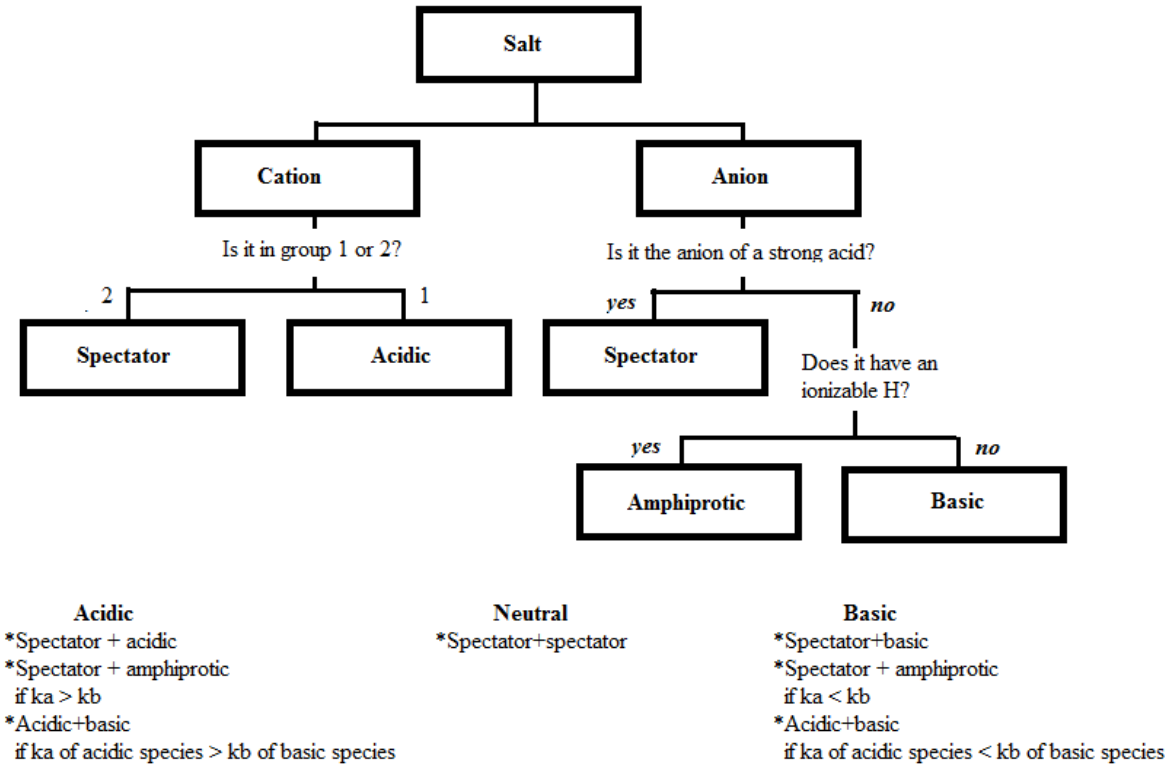

Fig. 6.6: Flow chart to determine whether salts behave like an acid or a base.

It is suggested that to classify an ion as an acid or a base it should change the pH by more than 0.5 pH units in a 0.1 M solution. If this definition is used the cations from strong bases such as the alkali metal ions (eg. Na^+ and K^+) and heavier alkaline earth cations (eg. Ca^{2+} and Ba^{2+}) are spectator ions; ions that are both a reactant and a product in a chemical reaction. A flow chart can be used to determine whether a salt is an acid or a base (see Figure 6.6).

A **buffer** contains close to equal amounts of a weak acid (HB) and its conjugate base (B^-). Such a buffer is highly resistant to changes in pH brought about even from strong acids or bases as it has a very high equilibrium constant (pK_a) and a pH close to pK_a. For any buffered system the *Henderson-Hasselbach* equation (6.31) is valid, and because the two species of HB and B^- are present in the same solution, the ratio of their concentration is also their mole (n) ratio.

$$\begin{aligned} [\mathrm{H}^+] &= K_a \cdot \left(\frac{n_{HB}}{n_{B^-}}\right) \\ [\mathrm{H}^+] &= K_a \cdot \left(\frac{[HB]}{[B^-]}\right) \\ \mathrm{pH} &= pK_a + \log_{10}\left(\frac{[B^-]}{[HB]}\right) \end{aligned} \tag{6.31}$$

Thus for a buffer the pH depends mainly on the equilibrium constant K_a and only to a limited degree on the ratio of concentrations, because the concentration of both the weak acid and the conjugate base is similar making $\log_{10}\left(\frac{[B^-]}{[HB]}\right) \sim 0$ and thus the pH$\sim$ pK$_a$.

6.4.2 CO_2, temperature and ice

As mentioned above CO_2 can alter the pH of water since both carbonic acid and hydrogen carbonate act as weak acids.

As the CO_2 concentration varies from laboratory to laboratory and also varies over the time spend in individual laboratories it could significantly alter sample pH of non buffered water samples. Ice cores contain very low impurity concentrations and thus are essentially unbuffered ultra pure water samples very prone to pH changes due to the CO_2. Furthermore the CO_2 content within the ice has changed over time,[3] which could also cause the pH of an ice core sample to alter over the cause of a measurement run, even if the sample is not exposed to ambient air. Thus for pure water, such as rain water and ice core samples the term acidity is often used instead of pH. Acidity is defined as:

$$acidity = [\mathrm{H^+}] - [\mathrm{HCO_3^-}] - 2[\mathrm{CO_3^{2-}}] - [\mathrm{OH^-}] \tag{6.32}$$

and thus removes the part of pH changed by CO_2 [*Pasteris et al.*, 2012]. While the definition is straight forward, actually finding the effect on pH of CO_2 requires precise knowledge of the CO_2 concentration in the sample, which in theory is governed mainly by the CO_2 around the sample, however the exact composition of the ice could effect the CO_2 dissolution, eg. if the ice contain buffering components.

While the CO_2 contribution can be determined using equations 6.15 to 6.30 if the pH and the partial pressure is known, it should be noted that Henry's laws constant is temperature (T) dependent[*Millero et al.*, 2006; *Harned and Davis Jr*, 1943].

$$\begin{aligned} pK_{HM}(T) &= 0.034 \cdot \exp\left(2400K\left(\frac{1}{T} - \frac{1}{298.5K}\right)\right) \\ pK_{HH}(T) &= \frac{-2622.38}{T} - 0.0178471 * T + 15.5873 \end{aligned} \tag{6.33}$$

The suffix M and H relate to *Millero et al.* [2006] and *Harned and Davis Jr* [1943] approximations respectively. Thus to know the amount of CO_2 in the sample, and thus the acidity, not only the CO_2 concentration of the ambient air or in the sample, but also the temperature should be known with high precision.

Further the dissociation constants are temperature dependent [*Millero et al.*, 2006; *Harned and Scholes Jr*, 1941; *Harned and Davis Jr*, 1943]. The autoprotolysis constant K_w is temperature dependent as well, albeit only to a minor degree as compared to K_{a1} and K_{a2}. Again the suffix M and H relate to *Millero et al.* [2006] and *Harned and Scholes Jr* [1941]; *Harned and Davis Jr* [1943] approximations respectively, but as shown in Figure 6.7, left column the difference between the two approximations are minor.

[3] see Section 9.1

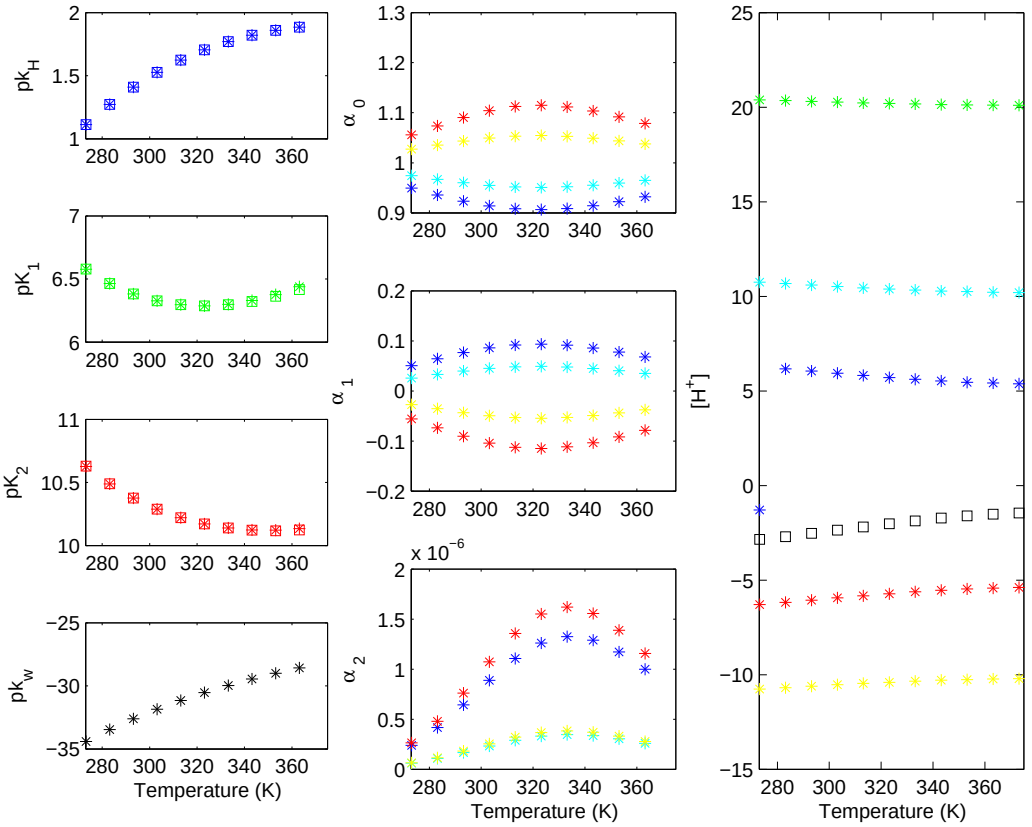

Fig. 6.7: CO_2 solubility as a function of absolute temperature. The left column shows dissociation constants related to the dissolution of CO_2 in water, the stars are the approximation to temperature by *Millero et al.* [2006] and squares are *Harned and Scholes Jr* [1941]; *Harned and Davis Jr* [1943]. The middle column plots α_0, the ionization fraction of H_2CO_3, α_1, the ionization fraction of HCO_3^- and α_2, the ionization fraction of CO_2^{2-} for fixed concentrations of $[H^+]$ (10 μM (cyan), 5 μM (blue), -5 μM (red) and -10 μM (yellow)) and the right column shows the ΔH^+ concentrations relative to pure water for a fixed acidity of 10 μM (cyan), 5 μM (blue), 0 μM (black), -5 μM (red) and -10 μM (yellow).

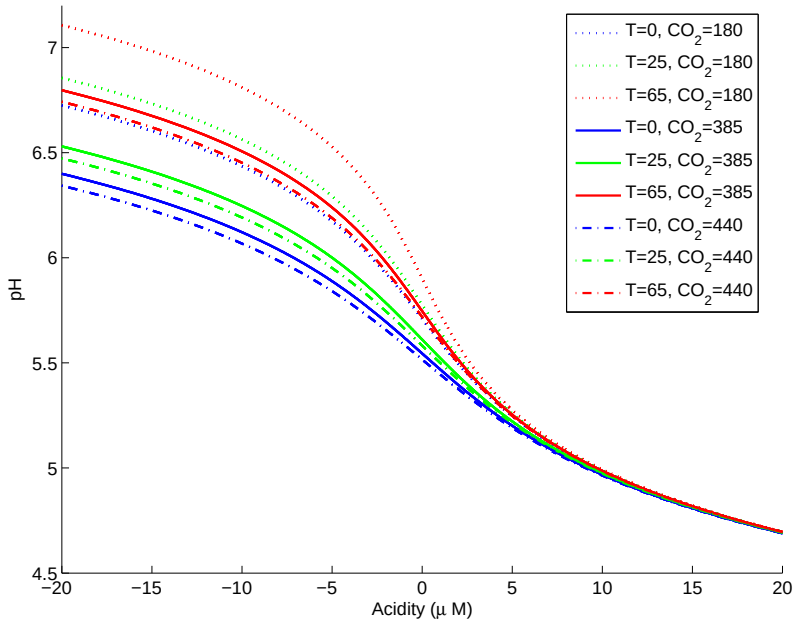

Fig. 6.8: pH as a function of acidity, shown for temperatures of 0°C (blue), 25°C (green) and 65°C (red), as well as for 180 ppm (dotted), 385 ppm (full) and 440 ppm (dash-dotted) CO_2.

$$pK_{a1M} = -126.34048 + \frac{6320.813}{T} + 19.568224 \cdot \ln(T) \tag{6.34}$$

$$pK_{a2M} = \frac{3404.71}{T} + 0.032786 * T - 14.8435 \tag{6.35}$$

$$pK_{a1H} = -90.18333 + \frac{5143.692}{T} + 14.613358 \cdot \ln(T) \tag{6.36}$$

$$pK_{a2H} = \frac{2902.39}{T} + 0.02379 * T - 6.4980 \tag{6.37}$$

Equation 6.32 can be rewritten as shown in equation 6.38 [*Pasteris et al.*, 2012], where α are ionisation fractions (Figure 6.7, second column) and dependent of dissociation constants and the pH. α_0 is the ionization fraction of H_2CO_3, α_1 is the ionization fraction of HCO_3^- and α_2 is the ionization fraction of CO_2^{2-}. Thus as shown in Figure 6.8 the effect of CO_2 is significant for alkaline liquids, it is also evident that increasing temperature cause less CO_2 to be dissolved in the liquid.

$$acidity = [H^+] - \frac{K_H P_{CO_2}}{\alpha_0}(\alpha_1 + 2\alpha_2) - \frac{K_w}{[H^+]} \tag{6.38}$$

$$\alpha_0 = \left(1 + \frac{K_{a1}}{[\mathrm{H}^+]} + \frac{K_{a1}K_{a2}}{[\mathrm{H}^+]^2}\right)^{-1} \tag{6.39}$$

$$\alpha_1 = \left(1 + \frac{[\mathrm{H}^+]}{K_{a1}} + \frac{K_{a2}}{[\mathrm{H}^+]}\right)^{-1} \tag{6.40}$$

$$\alpha_2 = \left(1 + \frac{[\mathrm{H}^+]}{K_{a2}} + \frac{[\mathrm{H}^+]^2}{K_{a1}K_{a2}}\right)^{-1} \tag{6.41}$$

6.4.3 Determination of pH

pH can be determined using a variety of methods. pH can be determined by means of a pH meter, which translates the ion concentration into an electrical signal, which, when calibrated to known pH standards, can be read directly on a display. Another way to measure pH is by the use of a pH sensitive indicator dye. Such an indicator changes its color with pH and by suitable photometry the pH is found. Finally pH can be determined by titration.

pH meter

A pH meter is a high-resistance voltmeter calibrated by buffered pH standards, allowing pH to be read rather than voltage [*Masterton et al.*, 2011c].

A pH-meter consists of both a glass electrode (also called the measuring electrode) and a reference electrode. The potential between them is proportional to pH. Figure 6.9 shows schematics of typical pH-meters. However a pH meter can also be assembled as just one probe where the glass electrode, reference electrode, and temperature-compensation electrode are integrated into one unit. Both the reference and the measuring electrode typically consist of a highly conductive material such as Ag coated with AgCl. The reference electrode is in an internal solution e.g. KCl.

The measuring electrode determines the electrochemical potential between a known liquid inside the glass electrode and an unknown liquid outside (the sample). The thin glass membrane allows the small hydrogen ions to penetrate. Thus the glass electrode measures the electro-chemical potential of hydrogen ions. Note that the instrument does not measure a current but an electrical voltage, yet a small leakage of ions from the reference electrode is needed, forming a conducting bridge to the glass electrode. A pH meter is thus not ideal for moving liquids of low conductivity [*Anthoni*, 2005].

The relationship between concentration of the ions and voltage is given by the Nernst equation (see equation 6.43).

$$E = E^\circ - \frac{RT}{nF}\ln(Q) \tag{6.42}$$

$$E = E^\circ - \frac{RT}{nF}\ln\left(\frac{[\text{ions outside the cell}]}{[\text{ions inside the cell}]}\right) \tag{6.43}$$

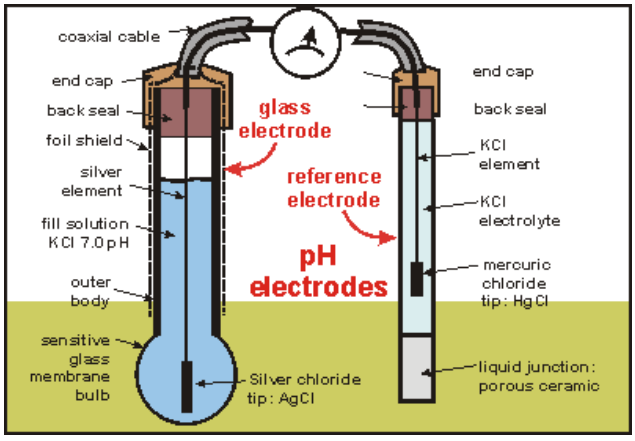

Fig. 6.9: Schematics of typical pH meters. Figure is from *Anthoni* [2005].

E is the cell voltage and $E°$ is the standard voltage and is given as the difference between the voltage for the reduction and oxidation half reactions measured when all ions and molecules in solution are at a concentration of 1 M and all gases at 1 atm. n is the number of moles changed in the reaction; and Q is the reaction coefficient, with products in the numerator and reactants in the denominator. In the special case that the reaction is at equilibrium the reaction quotient is constant and equal to the equilibrium constant (K). R (8.31 J/mol·K) is the gas constant, T the temperature and F is the Faraday constant ($9.648{\cdot}10^4$ J/mol · V)[*Masterton et al.*, 2011c].

Thus if E is measured and T is known, it will be possible to determine the concentration of specific ions such as H^+ in a concentration and determine the pH [*Masterton et al.*, 2011c].

Indicator dye

An acid base indicator is derived from a weak acid (HIn), where the weak acid and its conjugate base (In^-) have different light absorption properties (colors). Thus the color depends on the ratio between the weak acid and its conjugate base, which is related to the H^+ concentration as shown in equation 6.45, assuming that the indicator is added in a small enough quantity to not change the pH [*Masterton et al.*, 2011b].

$$HIn(aq) \rightleftarrows H^+(aq) + In^-(aq) \tag{6.44}$$

$$K_a = \frac{[H^+][In^-]}{[HIn]} \Longleftrightarrow \frac{[HIn]}{[In^-]} = \frac{[H^+]}{K_a} \tag{6.45}$$

Typically an indicator works over a range of 2 pH units with the color change occurring when $[H^+] \sim K_a$. When outside this range either the acid with its color will dominate or the conjugate base with its color dominates. For the indicator dye bromophenol blue the color change is from yellow at low pH to blue at high pH, while chlorophenol red changes from yellow to violet when increasing the pH [*Masterton*

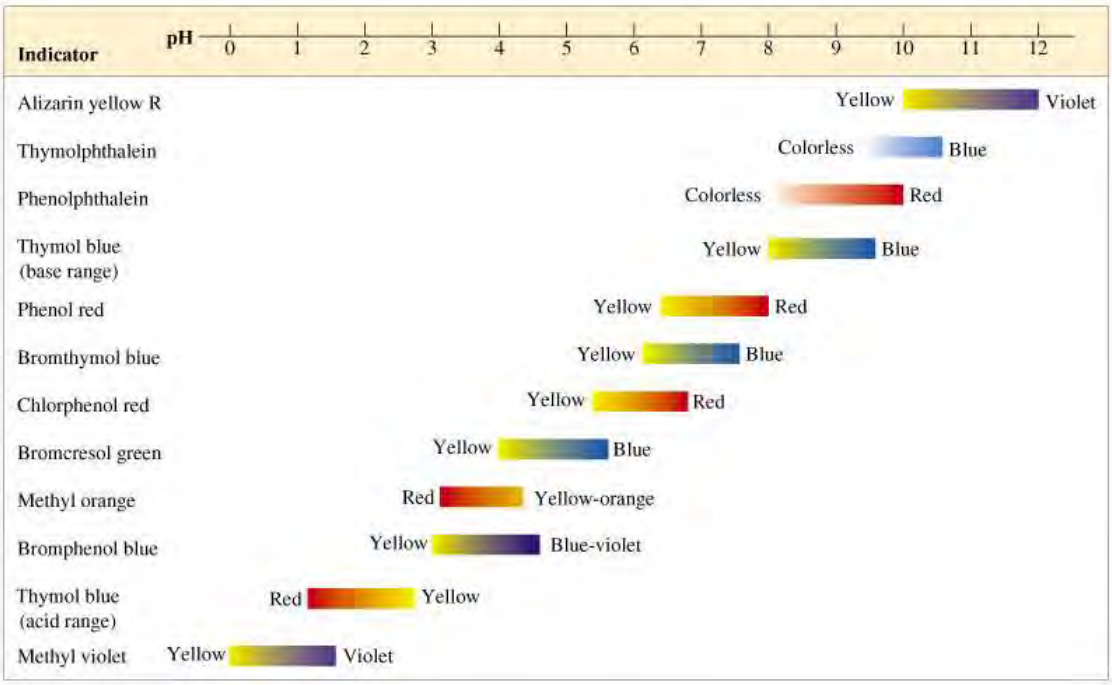

Fig. 6.10: Commonly used indicators, their pH range and color variations. Beware that colors in print do not always resemble actual colors. Figure is from *Cha* [2014].

et al., 2011b]. In Figure 6.10 more examples of commonly used pH indicators are presented.

Titration

Titration is often used to determine the concentration of a dissolved species in a water solution. A titration is carried out by slowly adding a standard solution of known concentration to the sample solution. At a certain point, the equivalence point (see Figure 6.11), the reaction is complete. Thus at the equivalence point the number of OH^- added is exactly equal to the amount of acid originally present (and *vice versa*). Knowing the amount of standard solution added at this point, the concentration in the unknown solution can be determined. The equivalence point is often identified using an indicator, which changes its color exactly at the equivalence point or by determining pH using an electrical probe [*Masterton et al.*, 2011b].

For strong acids and strong bases, many different indicators can be used, because the slope across the equivalence point is large. However for weak acids using a strong base for the titration and weak bases using a strong acid for the titration, the slope is less steep because the liquid ends up with a buffer capacity when $[H^+] = K_a$ and thus more care should be taken when choosing an indicator dye.

Diprotic acids have two equivalence points as they have two ionizable hydrogen ions, each with its own equilibrium constant.

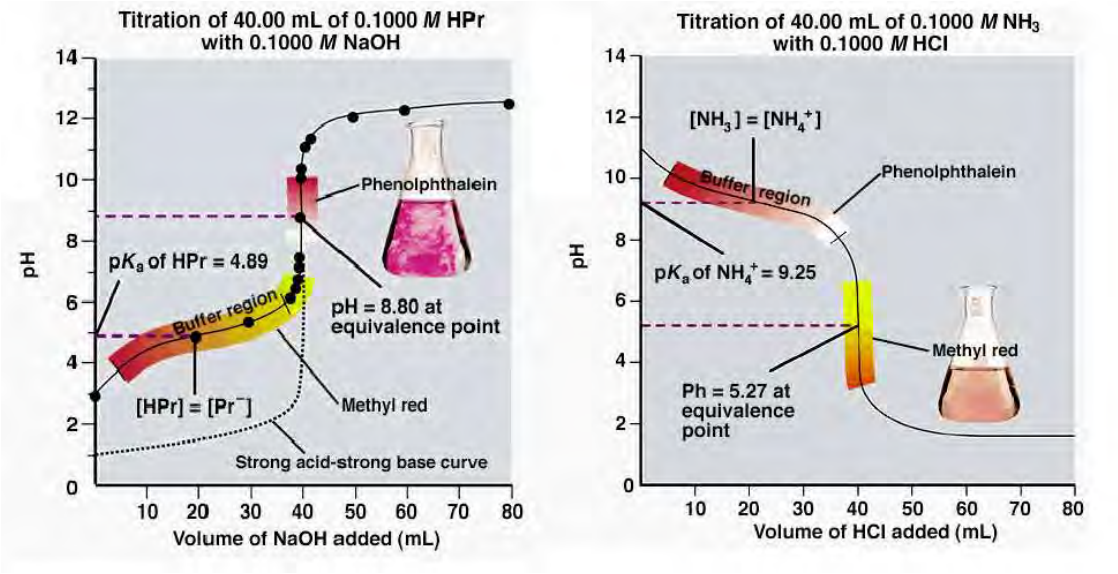

Fig. 6.11: Examples of titration curves for a weak acid (left) and for a weak base (right), note how choosing the right indicator is essential. Figure is from *Brucat* [2014].

6.4.4 pH and acidity detections in snow and ice

For the direct determination of pH in ice cores not many methods are available, however several methods related to the H^+ concentration are regularly employed on ice and melt water from ice.

Methods applied directly on ice

A few non destructive methods exist for determining acidity related properties of ice. These involve Electrical Conductivity Measurements (ECM) and DiElectric Profiling (DEP). For ECM a flat surface of the ice is needed. Such a surface is prepared by honing the surface with a sharp knife (Figure 6.12, top). Both methods determine the electrical properties of the ice and thus are influenced not only by the concentration of H^+ present in the ice, but also by other ions present. Further, both methods require a density correction in the firn[4] as the conductivity is influenced by the air space between ice and snow grains.

Electrical conductivity measurements on ice (ECM)

ECM is performed by dragging a pair of electrodes along an ice core with a typical voltage of 1250 V (see Figure 6.12, bottom). The signal is dominated by the strong acids in the ice and volcanic signals are easily detected [*Hammer et al.*, 1980]. The method was developed by *Hammer et al.* [1980]

A relationship (correlation coefficient 0.9) between the electrical conductivity measurements (ECM) and $[H^+]$ was found to be $[H^+] = 0.054 \cdot I^{1.73}$ [*Hammer et al.*, 1980]. Different relationship are used at different sites, varying from a linear type of relation to a second order function (eg. the often used $[H^+] = 0.045 \cdot I^2$). The

[4] For firn see Figure 9.1

Fig. 6.12: Preparation of an ice core for ECM measurements (top) and the ECM measurements (bottom). Photos from the NEEM ice core drilling project, http://www.neem.ku.dk, by Sepp Kipfstuhl.

relationship between I and $[H^+]$ is also dependent on the ECM instrument, for which the current is affected by the speed of measurements (the operator) as well as the instrument design [*Hammer et al.*, 1980; *Delmas et al.*, 1982; *Kumai*, 1985; *Barrie et al.*, 1985; *Moore et al.*, 1992; *Wolff et al.*, 1995; 1997].

Though most cations have very little effect on the ECM (eg. Na^+ and NH_4^+) some effect of Ca^{2+} has been found. The conductivity is low for alkaline samples and thus the ECM response to alkaline samples are small. Glacial samples from Greenland have high loads of dust and also of Ca^{2+} and thus the concentration of H^+ for those samples are not easily determined using ECM. As an example high loads of calcium cause a correlation coefficient between ECM and $[H^+]$ below 0.7 for ice cores originating from Tiahan area, China [*Dong et al.*, 2009; *Li et al.*, 2007; 2010].

Additional scatter in the ECM signal is believed to derive from the fact that for a given acidity based on HCl the ECM determined was higher than for a similar acidity caused by H_2SO_4 [*Wolff et al.*, 1997].

Furthermore ECM performed on firn cores is influenced by the density as the electrical current is significantly reduced by the large amount of air in between the ice grains. To some degree this effect can be removed if the density is known.

As is evident from above, ECM is not a one to one measurement of $[H^+]$, however it is a non destructive quick method providing instant information about volcanic layers in the ice that can be used for rough field dating of the ice and thus the method is intensively used during ice core drilling campaigns.

Dielectric profiling (DEP)

The DEP method was developed by *Moore and Paren* [1987], with further optimizing reported in *Moore et al.* [1989]; *Moore* [1993]; *Moore et al.* [1994]. The method determines the conductance and capacitance by applying opposing curved electrodes on the ice with alternating current. Based on the high frequency limit (300 kHz) the conductivity (σ_∞) is determined [*Moore*, 1993; *Wolff et al.*, 1997; *Barnes et al.*, 2002].

DEP is influenced mainly by the acidity (H^+), with a 7 times lower effect of sea salts (Cl^- or Na^+), which influence the crystal structure of the ice. As opposed to the ECM technique the DEP is not expected to be influenced by Ca^+ [*Moore*, 1993].

DEP is mainly believed to be a combination of H^+ and a Cl^- concentrations, but during periods of high alkalinity a relationship to NH^+ has also been observed as shown in equation 6.46.

$$\sigma_\infty = 9 + 4[H^+] + 1[NH_4^+] + 0.5[Cl^-] \tag{6.46}$$

where σ_∞ is in $\mu S/m$ and chemical concentrations are in μM [*Barrie et al.*, 1985; *Wolff et al.*, 1997]. The intrinsic conductivity in pure ice ($\sigma_{\infty pure}$) at -15 °C is 9 $\mu S/m$ and is temperature dependent.

Similar to ECM, DEP is influenced by the density. It has been suggested that the DEP can be corrected if the pore volumes as well as the H_2SO_4 concentrations

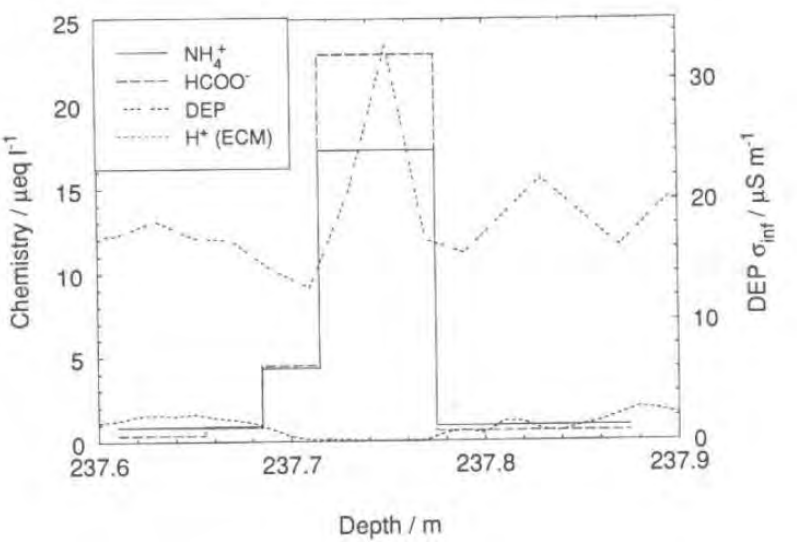

Fig. 6.13: ECM and DEP response to a formate peak. Note that while the response in DEP is significant, the ECM can not resolve the peak. Figure from *Moore et al.* [1994].

are known [*Barnes et al.*, 2002]:

$$\sigma_\infty = \sigma_{\infty\ \mathrm{pure}} + \beta_{H_2SO_4}[\mathrm{H_2SO_4}] + \beta_{HCl}[\mathrm{HCl}] + \beta_{Na}[\mathrm{Na^+}], \tag{6.47}$$

where the β_x refers to the molar conductivity of the species x. *Barnes et al.* [2002] found the best fit ($r^2 = 0.75$) to results from the top 350 meter of the Antarctic Dome C ice core for the density dependence as follows:

$$\sigma_\infty(v) = \sigma_{\infty pure}(1) \cdot v(0.68 + 0.32v)^2 + \beta_{H_2SO_4}(1)1.21(v - 0.075)^{2.5}[\mathrm{H_2SO_4}] \tag{6.48}$$

where v is the ratio of the density in firn to the density in solid ice, *i.e.* $v = 1$ below the close off zone and $v \sim 0.4$ in the top of the firn. Thus $\sigma_{\infty pure}(1)$ and $\beta_{H2SO4}(1)$ refers to the conductivity for pure ice and for H_2SO_4, and is $9\mu S\mathrm{m}^{-1}$ and 4.9 $\mu Sm^{-1}M^{-1}$, respectively.

Methods applied on melt water from ice

Methods for the determination of pH and pH related quantities on melt water samples from snow and ice include both direct detections, such as the methods by *Pasteris et al.* [2012] and *Legrand et al.* [1982] and indirect determinations such as determining the ionic balance to find $[H^+]$, or the determination of the melt water conductivity, which, similarly to ECM and DEP is dependent also, but not exclusively on $[H^+]$. While the dissolution of CO_2 is not an issue in the nondestructive methods of ECM and DEP, when determining the concentration of H^+ in melt water one should be aware of the potential bias from ambient CO_2 or CO_2 dissolved in the ice (see section 6.4-Figure 6.8).

Melt water electrical conductivity measurements (MWEC)

Melt water electrical conductivity measurements are a standard part of a CFA set up[5], which provides a reliable method with high temporal resolution. MWEC is determined by the concentration of soluble ions. Thus it is also influenced by dissolved CO_2. The method works well for identifying volcanic peaks. However as the total amount of ions influences the results, small peaks of H^+ can drown in the background of other ions. This is especially the case in ice cores from the coastal Antarctica where sea salt governs the signal.

Ionic balance equations

The concentration of ions can be determined by Ion Chromatography (IC) or by CFA absorption and fluorescence methods and if all ions but H^+ are known and further a neutral atmosphere is assumed, the H^+ concentration can be evaluated using the ionic balance (equation 6.1).

Figure 6.14 shows the ionic composition for the Greenland ice core Summit and the Antarctic ice core Vostok. In Antarctic ice equation 6.1 is further reduced to equation 6.49, by the assumption that the major ionic components in the Antarctic ice are Ca^{2+},Mg^{2+}, Na^+, Cl^-,NO_3^- and SO_4^{2-} besides H^+, which then can be determined if knowledge on the other ions is provided.

$$[H^+] + 2 \cdot [Ca^{2+}] + 2 \cdot [Mg^{2+}] + [Na^+] = [Cl^-] + [NO_3^-] + 2 \cdot [SO_4^{2-}] \tag{6.49}$$

In Antarctic coastal areas 80% of the ionic budget can be determined from knowing the concentrations of the sea salt related species Ca^{2+}, Mg^{2+}, Na^+, Cl^- as well as a fraction of the SO_4^{3-} related to marine emissions of methanesulfonic acid (MSA). One can determine the sea salt part of species by using the ratio between Na^+ and the sea salt species of interest. The part of the species not arriving from sea salt is called the excess, and dominates the budget further inland. If the sea salt contribution is removed the ionic budget becomes.

$$[H^+] + 2 \cdot [Ca^{2+}_{ex}] + 2 \cdot [Mg^{2+}_{ex}] = [Cl^-_{ex}] + [NO_3^-] + 2 \cdot [SO^{2-}_{4ex}] \tag{6.50}$$

In Antarctic in present times both Ca^{2+}_{ex} and Mg^{2+}_{ex} are limited and can be removed from the budget, and close to Antarctic coastal sites also Cl^-_{ex} is close to zero. In inland Antarctica the Cl^-_{ex} can be both positive and negative as a result of reactions between HNO_3 or H_2SO_4 with Na_2SO_4 or HCl [*Legrand and Mayewski*, 1997].

In Greenland the ionic budget is characterized by a larger content of Ca^{2+}_{ex} due to higher dust inputs and by NH_4^+ and carboxylic acid from the northern biosphere [*Legrand and Mayewski*, 1997].

While it is possible to derive the H^+ concentration by determining concentrations of other ions in the ice and making an ionic budget assuming a neutral atmosphere, the budget is often based on assumptions about governing species. This can cause the H^+ concentrations deduced to actually include the concentrations of other ions.

[5] See also section 1.2.2

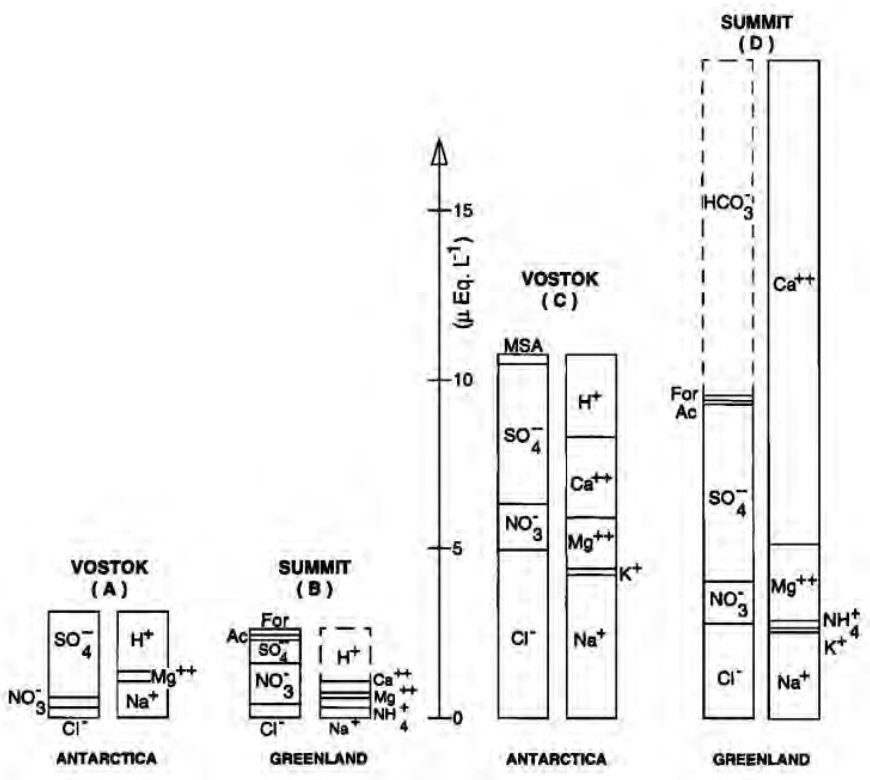

Fig. 6.14: Figure from *Legrand and Mayewski* [1997]. The ionic balance for Antarctica (Vostok) and Greenland (Summit) during current climate (A and B) and during the last glacial maximum (C and D).

Further IC measurements are time consuming as compared to CFA. If however IC measurements of several ions are available in sufficient resolution the method is straight forward.

Titration of discrete samples

Legrand et al. [1982] presented a method for the detection of pH in ice and snow using titration (see section 6.4.3). The method is valid from 0-10 μeq/L acidity and alkalinity ranges with an accuracy of ± 0.2 μequiv/L [6]. The method reduces the sample to a pH of 4.65 by adding a known concentration of acid and an ionic strength adjuster (ISA). Afterwards 10 small increments 20 μL of the acid titrant ($5 \cdot 10^{-5}$ N H_2SO_4) is added and after each addition the pH is determined using an electrode (see section 6.4.3). Finally the original sample acidity can be determined from the intercept difference from zero in a plot of the concentration of H^+ in the sample against the introduced H^+ concentration of the acid titrant.

In the study by *Legrand et al.* [1982] the method was applied only to samples with strong and weak acidities of pK<3.6, but not on alkaline samples. 10 samples an hour were determined and the sample volume was 5 mL. The authors also found that for this method to be capable of determining $[H^+]$ very accurately ($\pm 2\mu$M) several optimizations had to be performed. The ISA consists of 3 M KCl saturated with AgCl and was added to stabilize the ionic strength so that the electrode would provide more stable results. For the same reason a temperature control of $25 \pm 0.5°C$ was introduced. Furthermore it was observed that a porous membrane type electrode would not work due to constant mixing, and that the chosen electrode was affected by a slow drift of the electrode potential (a few millivolts per hour) caused by the liquid leak of the reference electrode. The whole system was isolated by a Faraday cage to reduce electrostatic interference.

The authors also found that the outer part of the ice was contaminated with an alkaline contaminant and not suitable for this kind of detection. Likely this contaminant was the drill liquid used to prevent the drill hole from closing, when extracting the ice core from the ice sheet. Drill liquids have been changed since 1982 and though they might not change the pH as severely as found by *Legrand et al.* [1982] they could potentially still alter the pH of the sample. However recently a continuous flow analysis (CFA) method for the detection of drill liquid has been invented by *Warming et al.* [2013]. Thus if drill liquid does present a problem, by setting up the non-destructive drill liquid detection system prior to a pH detection set up in a CFA system one can know exactly when the drill liquid was influencing the system and discard the data.

The method by Pasteris et al. (2012)-'solving' the problem of CO_2

Clearly CO_2 can alter the pH of a melted ice sample (as shown in Figure 6.7). Obviously the CO_2 can originate from the ambient atmosphere if the sample is not isolated. In laboratory environments the CO_2 concentration can be more than double the normal atmospheric concentration. However air including CO_2 is also

[6] μeq is unit of electrical charge. 1 eq. reacts with or supplies one mole of hydrogen ions (H^+) in an acid base reaction

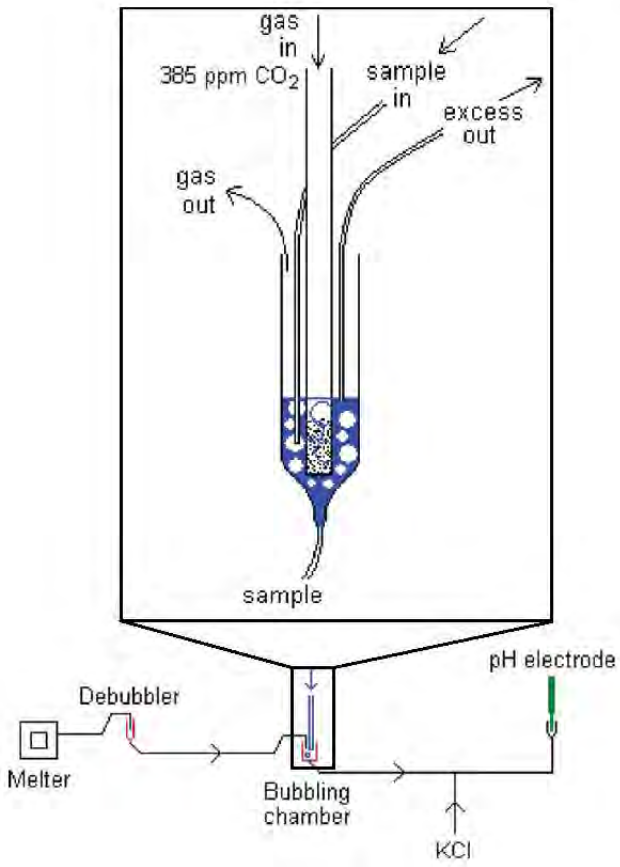

Fig. 6.15: Continuous flow analysis system for the determination of pH at 385 ppm CO_2 as developed by *Pasteris et al.* [2012]. Figure is modified from *Pasteris et al.* [2012].

present in natural ice from polar regions. Thus even if the sample is kept in *vacuo*, CO_2 is released from the ice matrix when the sample is melted and can alter the sample pH by going into solution. This effect is avoided in the titration method by *Legrand et al.* [1982] by removing all CO_2 from the liquid by decreasing the pH. However it is not possible by continuous flow analysis methods to avoid an effect of CO_2 from within the ice. To resolve this problem both *Gfeller* [2011] and *Pasteris et al.* [2012] developed methods were the sample stream was calibrated to a known concentration of CO_2 before the pH was determined using electrical probes. Also in both methods an ionic strength adjuster was added to the sample stream. The method by *Pasteris et al.* [2012] is illustrated in Figure 6.15.

Pasteris et al. [2012] control the concentration of CO_2 in the sample by artificially flushing the sample with a known concentration of CO_2 in a CO_2 bubbler system. They then determine the acidity at this known CO_2 concentration. However such a CO_2 debubbling system significantly decreases the temporal resolution, and in the worst case high peaks in acidity might not be observed due to the low resolution.

Gfeller [2011] tried slightly different approaches where the CO_2 was added to the sample stream in a segmented way or was introduced through a gas permeable membrane. *Gfeller* [2011] obtained different results when segmenting with natural

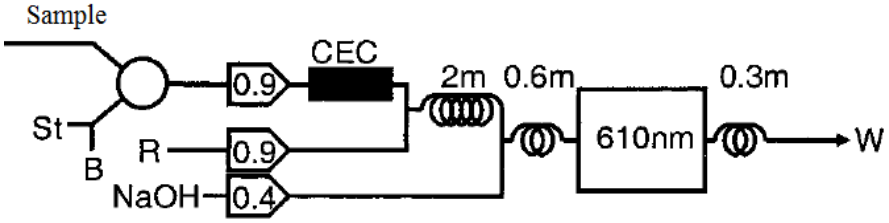

Fig. 6.16: Continuous flow analysis system for the determination of SO_4^{3-} as developed by *Röthlisberger et al.* [2000]. R is reagent, St is standards, B is baseline (milliQ water), CEC is a cation exchange column, and W denotes waste. The method is further explained in the text. Figure is modified from *Röthlisberger et al.* [2000].

air or helium, even after correcting for the known CO_2 in the gases. In the end he concluded that a system without any calibration with air showed the best results, since including a segmented flow of air or a bubble bath decreased the temporal resolution.

Both methods were based on electrical probes, which theoretically are not stable until after approximately 1 minute [*Marinenko et al.*, 1986] and are thus inadequate for the typical flow of 1 mL/min and the wanted temporal resolution of seconds. Also the addition of KCl (0.01 M) to increase the ionic strength of the sample stream as done in the method by [*Pasteris et al.*, 2012] or NaCl (0.002 M) as in [*Gfeller*, 2011] is problematic as it affects not only the mean activity coefficients of the water solution, but may also change the behaviour of the electrodes [*Marinenko et al.*, 1986]. Further in the method by *Pasteris et al.* [2012] the KCl is added after the calibration of CO_2, and could affect the CO_2 in the liquid in a non predictable way.

However to date the method of *Pasteris et al.* [2012] is the fastest way to determine the pH of an ice core sample such that the results be comparable between different laboratories with different CO_2 content.

Continuous sulphate detection systems

Sulphate detection methods are often used to detect volcanic eruptions and their strengths in ice cores and thus is used for some of the same purposes as acidity detection systems. Thus a brief introduction is provided to the two SO_4^{3-} systems applicable for CFA. Additionally (Fast) Ion Chromatography is often used for determining SO_4^{3-} concentrations [*Castellano et al.*, 2004] and inductively coupled plasma mass spectrometry (ICPMS) is used for determining S concentrations [*Sigl et al.*, 2013].

Röthlisberger et al. [2000] developed an indirect method where a reagent of methyl thymol blue (MTB) and $BaCl_2$ is added to a sample stream of continuously melted ice (see Figure 6.16). The reagent consists of methyl thymol blue (MTB) 0.09 mM, 0.09 mM $BaCl_2$, 6 mM HCl mixed with 86% ethanol. The competing reaction between barium and sulphate causes the absorption at 608 nm to decrease with increasing sulphate. To avoid interferences from cations a cation exchange column is inserted prior to the absorption cell. The cation exchange cell needs to be freshly prepared every day. The method is highly sensitive to the precise ratio

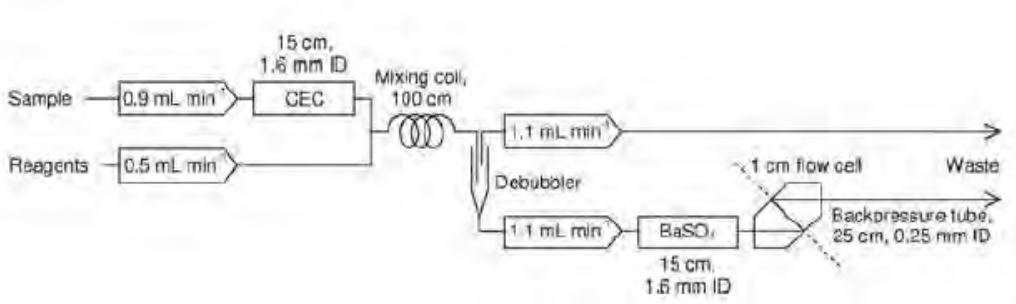

Fig. 6.17: Continuous flow analysis system for the determination of SO_4^{3-} as developed by *Bigler et al.* [2007] and explained in the text. Figure from *Bigler et al.* [2007],

between MTB and barium chloride and while the limit of detection (LOD) is as low as 20 ng/g (3 times standard deviation) when the system is running optimally, in practise during a measurement campaign the LOD is in the order of 100 ng/g. Thus the method requires high purity MTB as well as flow control. Even with optimized set up the method is not capable of resolving the lowest SO_4^{3-} concentrations expected in the ice and the relative errors of the measurements are in the order of 15 %. The method is linear to at least 1000 ng/g. However the content of sulphate in ice cores may be as high as 10000 ng/g. The response time is as short as 20 s, determined as the time it takes to drop 1/e of a step function. The method was successfully applied on the B18, B20 and B21 Greenland firn cores and though the lowest concentrations could not be detected, the method can be used to successfully detect volcanic eruptions as well as the recent anthropogenic increase [*Bigler et al.*, 2002]. Examples of SO_4^{3-} concentrations in the Greenland B20 ice core determined using the method by *Röthlisberger et al.* [2000] are shown in Figure 6.3. Also shown is $[H^+]$ based on the ionic budget as determined using IC measurements.

Bigler et al. [2007] developed another method for the determination of SO_4^{3-} as shown in Figure 6.17. A cation exchanger is placed on the sample stream and used to remove interferences from compounds such as Ca^{2+} and Mg^{2+}. The method by *Bigler et al.* [2007] employs dimethylsulfonazo III(DMS-III) as an indicator and also includes a reactor column containing barium sulphate particles. The absorption is determined at 654-663 nm and the practical limit of detection is decreased to 70 ng/g as compared to the 100 ng/g by *Röthlisberger et al.* [2000]. Furthermore the method is less dependent on the exact concentration of the reagent, making it more stable. However the linear range is smaller than in the method by *Röthlisberger et al.* [2000] and the method of *Bigler et al.* [2007] is linaer only up to 3000 ng/g.

Thus while both methods for the continuous determination of SO_4^{3-} can be used to determine volcanic peaks they are both time consuming and not very robust. Further their LOD is too high to resolve the background variations.

6.4.5 Motivation for a new continuous ice core acidity method

While non destructive methods such as the DEP and ECM methods are – and should be – used intensively to provide rapid determination of the volcanic eruptions recorded in the ice to obtain a reliable dating, potentially while still in the field,

these methods are not uniquely sensitive to the H^+ ion and thus the signal from volcanic eruptions can drown in the background. Further the repeatability of the non destructive ECM and DEP is not very good as especially the ECM is influenced by the person handling the system. Furthermore both methods require a density correction, which calls for time consuming density determinations.

By determining the acidity in the melt water, the density effect is removed. However melted samples are influenced by CO_2 both from the ambient air if the system is not sealed, but also from the ice itself. Though the method by *Legrand et al.* [1982] is accurate in determining the H^+concentration by lowering pH prior to determination, preparing discrete samples and doing titration is time consuming and thus in reality the temporal resolution of such a discrete method is not so much dependent on the amount of ice available (5 mL per sample, 10 samples per hour), as on the patience of the experimenter preparing samples as they need to be cut and cleaned individually.

Continuous flow analysis provides a means for rapid determination of compounds in high resolution. Sulphate detection techniques [*Röthlisberger et al.*, 2000; *Bigler et al.*, 2002; 2007], though suitable for the determination of volcanic peaks, are difficult to work with and require complicated procedures preparing cation exchanger cells and reagents with precise concentrations.

Continuous determination of the melt water conductivity suffers from the same problems as the ECM and DEP and does not provide a unique response to acidity.

Continuous flow analysis (CFA) pH determination techniques based on electrical probes [*Gfeller*, 2011; *Pasteris et al.*, 2012] provide high resolution measurements. Though fairly easy to work with, these techniques are to some degree influenced by the turbidity of the sample stream as well as by fluctuations in the internal liquid volume. The probe determines the pH in a measurement volume. Though this volume can be limited to enhance the response time there is a time constraint in the time it takes for the probe to react. To increase the ionic strength NaCl or KCl is added, however causing a contamination risk and also potentially influencing the response of the electrical probe. Both the methods also include some gas equilibration to a known volume of CO_2. While *Pasteris et al.* [2012] claims that their method is stable with such a CO_2 calibration, *Gfeller* [2011] find no stable way to introduce the CO_2 and also mention the possibility of buffering components in the ice.

To conclude, all of the available methods have deficiencies or limitations and an ideal system for CFA does not exist. This even though pH is crucial for determining the full ionic balance of the ice, could provide knowledge on recent anthropogenic changes resulting in acid rain, and could be used to gain knowledge about volcanic eruptions, which are interesting in themselves, but are also used to cross date ice cores. The following section is a manuscript presenting a method for the continuous determination of acidity using a colorimetric indicator method developed as part of this study. The method is compared to the ionic budget in a section of the Greenland NGRIP ice core. Also shown are results from a firn core from the North East Greenland Ice Stream (NEGIS) as well as results from the Antarctic Roosevelt Island Climate Evolution (RICE) ice core. Further results from the RICE ice core are presented in section 8.

7. AN OPTICAL METHOD FOR CONTINUOUS DETERMINATION OF PH IN ICE CORES

Kjær, H. A., P. Vallelonga, M. E. L. Kristensen, C. Tibuleac and M. Winstrup and S. Kipfstuhl[1]

The pH of polar ice is important for the stability and mobility of impurities in ice cores and can be strongly influenced by volcanic eruptions or anthropogenic emissions. We present a simple optical method for continuous detection of pH in ice cores based on the absorption spectroscopy of two common pH-indicator dyes, bromophenol blue and chlorophenol red. The sealed-system method does not require calibration with CO_2 for Holocene samples and is simpler than existing methods for pH determination in ice cores, offering a 10-90% peak response time of 45 sec and a combined uncertainty of 9%. The method is applied to firn and ice core sections from Greenland and Antarctica and compared to standard techniques such as Electrical Conductivity Measurements (ECM), conducted on the solid ice, and electrolytic conductivity of melted ice samples (electrolytic meltwater conductivity, EMWC). Large resemblance between the H^+ concentration determined using this method and the H^+ concentration found based on the ionic budget observed for a section of the Greenland NGRIP ice core (75.10° N, 42.32° W) covering a volcano in 1259 AD. Conductivity and H^+ are found to be highly correlated in the Greenland NEGIS firn core (75.38° N, 35.56° W), with all signals greater than 3σ variability being related to either volcanic eruptions or forest fire activity. In contrast, the Antarctic Roosevelt Island ice core (79.36 ° S, 161.71 ° W) features an anti-correlation between conductivity and H^+, most likely due to strong influence of marine salts.

7.1 Introduction

Polar ice cores provide continuous archives of past climate and atmospheric conditions [*Zielinski et al.*, 1996; *Fuhrer et al.*, 1996; *McConnell et al.*, 2007b; *Svensson et al.*, 2000; *Ruth et al.*, 2003; *Fischer et al.*, 2007], with the possibility for reconstructions at high temporal resolution. Greenland deep ice cores cover the last glacial-interglacial cycle [*NGRIP members*, 2004; *Dahl-Jensen et al.*, 2013], whereas some Antarctic ice cores archive up to 800.000 years of past climate [*EPICA community members*, 2004].

Ice core impurities occur in solid, liquid and gaseous phases in the ice, with the pronounced seasonality of some impurities [*Legrand and Mayewski*, 1997] allowing

[1] This chapter is intended for publication in Environmental Science & Technology. Co-author S. Kipfstuhl is at the Alfred-Wegener-Institute for Polar and Marine Research (AWI), Bremerhaven, Germany. Remaining co-authors are all from Centre for Ice and Climate, NBI, University of Copenhagen, Denmark.

the potential for establishing ice core chronologies based on the counting of annual layers of deposition [*Dansgaard et al.*, 1993; *Winstrup et al.*, 2012; *Rasmussen et al.*, 2013].

The detection of pH in ice cores provides valuable information on past environmental processes such as volcanic activity [*Clausen and Hammer*, 1988], anthropogenic pollution (particularly NO_x and SO_4) and Arctic haze [*Barrie et al.*, 1985], but the pH in ice cores is also influenced by mineral dust (calcium carbonates), marine biogenic emission products such as methanosulfonic acid (MSA), as well as ammonium and organic acids from terrestrial biogenic emissions and biomass burning[*Legrand et al.*, 1982; *Pasteris et al.*, 2012]. Further pH controls both the solubility of ions and the rate of many chemical reactions. pH has been invoked as the major factor controlling *in situ* production of CO_2 in Greenland ice cores and is thus a critical barrier to reconstructing CO_2 greenhouse gas records for the Northern Hemisphere [*Tschumi and Stauffer*, 2000].

Several methods for the detection of acidity in ice cores have been developed. On solid ice the Electrical Conductivity Measurement(ECM) signal is mainly dominated by strong acids in the ice and provides a fast way to detect volcanic horizons [*Hammer et al.*, 1980; *Hammer*, 1980]. An empirical relationship between ECM and $[H^+]$ has been established. This relationship depends on the ECM instrument, the instrument operator, ambient conditions, and the impurity content of the ice (e.g. dust, major ions, sea salts, organic and/or inorganic acids) [*Hammer et al.*, 1980; *Delmas et al.*, 1982; *Kumai*, 1985; *Barrie et al.*, 1985; *Wolff et al.*, 1995; 1997]. The ECM sensitivity to alkaline ice is low.

Dielectric profiling (DEP) is also applied to solid ice and is mostly associated with the H^+ and Cl^- content of the ice, but during periods of high alkalinity a relationship to NH_4^+ has also been observed [*Moore*, 1993; *Wolff et al.*, 1997; *Barnes et al.*, 2002]. In Greenland Holocene ice DEP is mainly controlled by the ice acidity[*Wolff et al.*, 1997]. The acidity can also be determined using pH probes[*Pasteris et al.*, 2012; *Kuramoto et al.*, 2011].

Previous studies report a pH range of 4.49-6 in ice cores (polar ice); with more acidic values during the second half of the 20th century [*Fischer et al.*, 1998; *Pasteris et al.*, 2012], in ice cores located closer to pollution sources as Europe and North America [*Barrie et al.*, 1985; *Fischer et al.*, 1998] and in ice containing volcanic aerosol deposits [*Clausen and Hammer*, 1988]. More alkaline pH values are observed in ice with high dust concentrations e.g. Greenland glacial ice [*Delmas et al.*, 1982; *Taylor et al.*, 1993]. pH values in the range of 5.05-5.5 were found in snow deposited between 2005-2009 at the NEEM site in Northwest Greenland [*Kuramoto et al.*, 2011]. The seasonality of pH in this snow is not very pronounced, but slightly more acidic values were found in the fall compared to the spring [*Kuramoto et al.*, 2011]. Similar annual variation in pH has been observed in the Greenland Humboldt North record (Figure 7.1) [*Pasteris et al.*, 2012], with the higher acidity occurring when Arctic haze, polar ozone destruction and transport of pollutants from mid-latitudes are peaking [*Law and Stohl*, 2007; *Quinn et al.*, 2007].

Based on those levels it is clear, that methods for continuous detection of pH in ice should preferably be sensitive to resolve pH within the range from 4.49 to 6 as well as being capable of resolving seasonal variations.

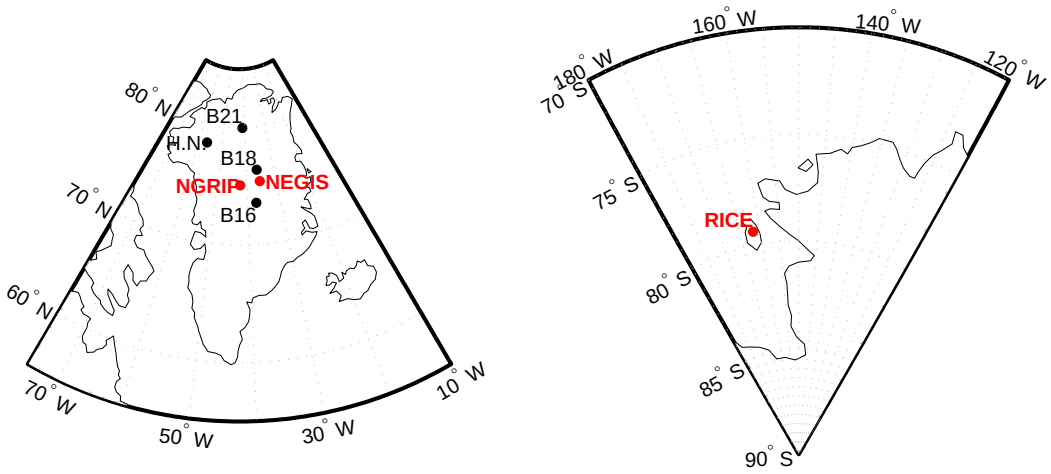

Fig. 7.1: Left: Location of the Greenland NEGIS firn core (red) and the Humboldt North (HN) firn core [*Pasteris et al.*, 2012] as well as the B16, B18 and B21 firn cores [*Fischer et al.*, 1998]. Right: Location of the Antarctic RICE ice core (red).

The polar ice core matrix is relatively pure and unsaturated in CO_2 and ions. Therefore, the ice will readily take up CO_2 from the atmosphere when it is melted. The dissolution of CO_2 in the melt water poses the risk of rapidly altering the sample pH [*Legrand et al.*, 1982].

The use of bench top laboratory techniques to determine pH in melted ice samples require precise monitoring of ambient CO_2 concentrations for corrections (as well as pressure and temperature, more in the supplementary material). Alternatively, the acidity of the sample is artificially lowered to reach a level where the dissociation of carbonic acid is minimized [*Legrand et al.*, 1982].

Continuous Flow Analysis techniques (CFA) are often applied to ice core analysis, allowing rapid throughput and high resolution for a range of analytes [*McConnell et al.*, 2002; *Kaufmann et al.*, 2008; *Bigler et al.*, 2011]. Normally CFA systems are not sealed. However, the Copenhagen CFA system is using a sealed debubbler to remove air dissolved in the ice melt water[*Bigler et al.*, 2011] and thus is sealed from the ambient air. The sealed CFA system offers an advantage for pH determination, allowing the melted ice sample to be handled and analysed soon after melting and without interaction with the ambient laboratory air.

Recent CFA methods using pH electrodes have implemented an equilibration of the sample to a known concentration of CO_2 [*Pasteris et al.*, 2012; *Gfeller*, 2011]. Ensuring the complete calibration of the sample with a precisely known concentration of CO_2 involves complicated CO_2 bubbling and de-bubbling systems introducing sample dispersion and limits the temporal resolution[*Pasteris et al.*, 2012; *Gfeller*, 2011]. The benefit of such a CO_2 calibration is minor on the acid concentrations of H^+ found in ice and segmentation with air or helium may lead to inconsistent results [*Gfeller*, 2011].

Continuous pH measurements using electrodes are further limited by their relatively slow response time at the low ion concentrations of polar ice. Even with the

addition of electrolytes to improve the ionic strength, such as KCl (0.01 M) or NaCl (0.002 M) [*Pasteris et al.*, 2012; *Gfeller*, 2011], electrodes require longer calibration times than the more instant dye methods. In the method by *Pasteris et al.* [2012] as much as 85 seconds to respond to acidic signals or 120 seconds to respond to alkaline signal and even longer times to return to baseline are observed. However, this is mainly due to the CO_2 bath, but also the response of the electrode adds to the long response time..

In this study, we present a simple optical method for continuous determination of pH in polar ice cores that avoids a number of drawbacks associated with electrode-based pH measurement approaches. The method is adapted from the method proposed by *Raghuraman et al.* [2006] by selecting indicator dyes sensitive to the pH range of polar ice and by minimizing the dye concentration to limit sample dilution. The proposed method features similar rapid response times to both acid and alkaline solutions. The response time is about half of the existing method[*Pasteris et al.*, 2012], is sensitive over a broad range of pH values and ionic strengths, can be applied to firn and ice cores equally well and does not require CO_2 equilibrium in case of a sealed CFA system. The technique is advantageous to electrode-based methods and particularly well suited to field-based analytical campaigns.

7.2 Materials and methods

Dye-based pH determination relies on the principle that the spectra of a dye will vary according to the sample pH. Depending on the pH the fraction of the base and acid forms will change. Due to the optical nature of the measurement, dye-based determination can be affected by instabilities resulting from bleaching of the dyes, light source intensity fluctuations and attenuation changes in the optical fiber. These fluctuations can be accounted for by monitoring multiple wavelengths and/or by regular calibration with a set of standards [*Lin*, 2000]. Using a fixed concentration of two dyes, the pH can be determined as a function of the optical density at two wavelengths [*Raghuraman et al.*, 2006]. Such a colorimetric method using dyes has also recently been applied for the detection of pH in sea water [*Rérolle et al.*, 2013].

In this study the dyes used were bromophenol blue (from yellow at pH 3.0 to purple at pH 4.6), and chlorophenol red (from yellow at pH 4.8 to violet at pH 6.7).

7.2.1 Experiment setup

A schematic of the set up is shown in Figure 7.2 with details provided in Table 7.1. A sample flow rate of 0.9 ml/min to which 0.15 ml/min of dye mixture was added, was found to give optimal dye concentrations (Supplementary material Figure 7.7). The dye mixture is made by dissolving 0.025 g of bromophenol blue and 0.025 g of chlorophenol red in 500 mL of milliQ water (Millipore A10 Advantage, 18.2 MΩ.cm and adding 100 μL Brij L23 30%w/v, Sigma-Aldrich). The sample and dye are mixed in a 1 metre long mixing coil kept in a 65°C heat bath, after which the mixture passes through a 6 cm-long Accurel gas permeable membrane to allow the removal of excess air bubbles created during the heating. Finally detection of light intensity takes place in an absorption cell with a 2 cm path length. Brij L23 was

Tab. 7.1: pH CFA detection system parameters

Flow rates:	
Sample	0.9 mL/min
Dye	0.15 mL/min
Reagent mixing length	1.0 m
Reagent mixing temperature	65°C
Absorption path length	2 cm
Absorption wavelength 1	450 nm
Absorption wavelength 2	589 nm
Spectrometer integration time	6000-8000 μs
Light source	white LED
	6000 mcd
	18 °
Response time (5-95%)	45 s
Analytical uncertainty (pH)	8.7% (5.8%)

added to the dye solution to facilitate the removal of air bubbles from the absorption cell, in case they were not removed via the accurel membrane.

A white LED (6000 mcd, 18°dispersion, FIA Lab Inc. USA) was used as a light source and an Ocean Optics USB 2000 spectrometer was used to measure the light intensity. An integration time of 6000-8000 μs was used depending on the age and concentration of the dye-mixture. The optimum response was found at a wavelength of 589 nm, with a second peak at 450 nm (supplementary material Figure 7.8).

The sample was heated to 65°C to ensure a minimized content of CO_2 in the sample stream. CO_2 uptake in water is in theory temperature dependent and thus the effect on the closed system was investigated by changing the temperature in the heat bath between 25 and 75°C. No significant effect of temperature was observed (supplementary material Figure 7.9 and 7.10). This suggests that the pH detection system described here is not affected by ambient CO_2 concentrations to any observable extent, essentially the system is sealed. The temperature effect could also be reduced due to the influence of the Brij L23 surfactant added to the dye mixture. Surfactants have been shown to alter the air-water CO2 exchange rates [*Farajzadeh et al.*, 2007; *Ricaurte et al.*, 2012].

7.2.2 pH standards

For the analysis of rainwater and other low conductivity samples, diluted standard buffers are more suitable than technical buffers, because they are more representative of the low ionic strength of the sample and have minimal memory effects [*Galster*, 2012]. Previous studies have found that diluted HCl or H_2SO_4 are the most suitable standards for calibrating a system as described here [*Koch et al.*, 1986; *Galster*, 2012; *Pasteris et al.*, 2012]. For alkaline standards, however, a strong base such as NaOH does not accurately reflect the properties of polar ice as it rapidly takes up CO_2 from the laboratory air, yet no alternative for alkaline standards has been found[*Koch et al.*, 1986; *Galster*, 2012; *Pasteris et al.*, 2012].

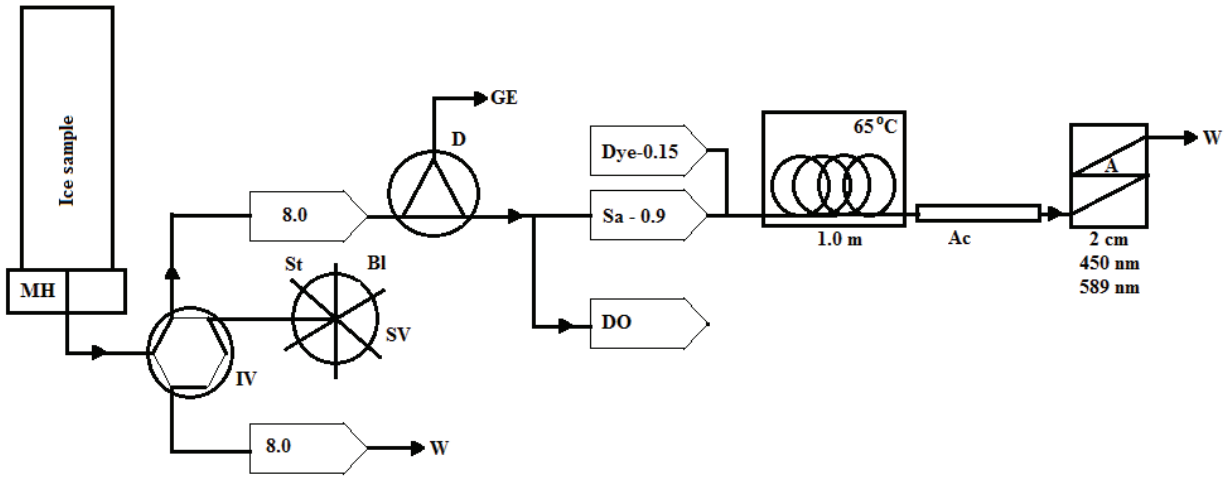

Fig. 7.2: The continuous flow setup for detection of pH. Ice is melted on a melt head (MH) in a freezer kept at -20°C. An injection valve (IV) in combination with a selection valve (SV) for standards (St) and blank (Bl) allows for running either. The sample line is de-bubbled (D) to remove the air bubbles naturally occurring in the ice or firn and the gas (GE) is used for gas extraction measurements. The water line is split into various analytical channels (DO), and the pH line which is the only one shown here. The sample (Sa) is mixed with dye then passed through a 1.0 m heated (65 °C) mixing coil before an air permable membrane, an accurel (Ac), is reached to remove airbubbles formed during heating. Intensity (A) at 450 nm and 589 nm is measured in a 2 cm absorption cell after which the line goes to waste (W). Peristaltic pumps are represented by arrow boxes with flow rates (in mL/min) indicated by the number within the box.

The pH standards used in this study were prepared from standard solutions of HCl (1.001 M, Fluka) and NaOH (1.002 M, Fluka) diluted to concentrations of 19.4 μM, 9.8 μM and 4.9 μM for HCl and 19.5 μM and 9.8 μM for NaOH, with corresponding pH values of the HCl and NaOH concentrations are 4.71, 5.00, 5.26, 6.80 and 6.23 pH respectively. Laboratory milliQ was calculated to have a pH of 5.747 assuming a CO_2 concentration of 385 ppm, the laboratory atmospheric pressure of 1030 hPa and a detection temperature of 65°C. The theoretical calculation of pH of the standards follows the procedure of *Pasteris et al.* [2012] as shown in the supplementary material [*Stumm and Morgan*, 2012].

The stability of the pH standards and their potential response to changes in laboratory CO_2 concentrations have been evaluated. The level of CO_2 in the laboratory during a typical ice core measurement campaign was recorded over a day and was found to be highly variable, with peaks up to 1000 ppm CO_2. Such variations could theoretically have a significant impact on the unbuffered HCl and NaOH standards. For standards with low ($\leq$5μM) HCl or NaOH concentrations it can alter the H^+ concentrations by more than 13% (supplementary material). Such variability is greatly diminished for more concentrated HCl standards, to merely 0.8% for a standard of 20μM H^+ at 65°C.

However as shown in Figure 7.3 and in supplementary Figure 7.11 little variability was observed in a standard over approximately 32 hours (two measurement days). The uncertainty, on a fit based on the standards from the two day campaign, is below 1.5 % for detection at 589 nm. The low variance in the standards over a day can also be seen in the raw data. We found that the response at wavelength 450 nm is not high, while the wavelengths 586 nm and 589 nm, show stronger signals and higher stability (supplementary Figure 7.11). This is mainly due to stronger light intensity at this peak in the spectra. The 450 nm signal was also more prone to drift over time due to ageing of the Bromophenol blue dye (supplementary Figure 7.11), confirming the importance of regular standard calibration if 450 nm is to be used for pH determination, as well as the need for a calibration similar to that done for absorption ($-\log_{10}\frac{I}{I0}$), to correct for baseline drift, though strictly speaking the term absorption does not make sense for I$\geq$I0. The difference between the response (slope in Figure 7.3) to NaOH standards and HCl standards is most likely related to different response strength in the two dyes between more acid and less acid standards.

Furthermore after calibration using HCl standards we do not see an offset in neither the firn core data (NEGIS, Greenland) nor the RICE data between sets of the core calibrated with different sets of standards, suggesting that the effect of lab air on the standards either stayed stable or was insignificant. To further test the variability of standards, similar standard concentrations of H^+ were made, using both HCl and H_2SO_4 (supplementary Figure 7.13). Identical absorption results were found for the two acid standards, leading us to conclude that the standards were made reproducibly, that fluctuations of CO_2 in the laboratory are of minor importance, and finally that the technique reported here is relatively insensitive to ambient CO_2.

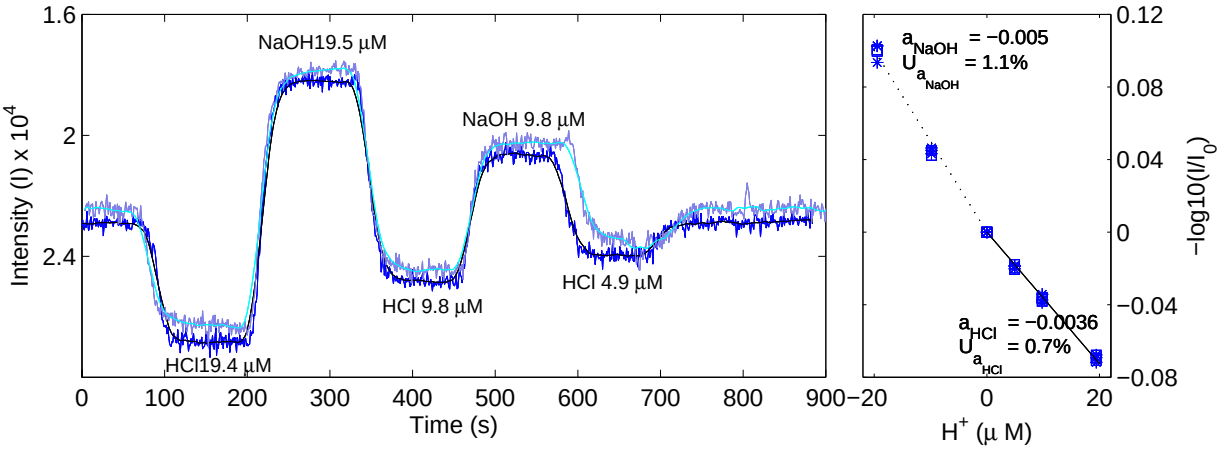

Fig. 7.3: Left: Two examples of standards with concentrations 19.4 μM HCl, 19.5 μM NaOH, 9.8μM HCl, 9.8 μM NaOH and 4.9μM HCl ran with 7 hours interval and measured at 589 nm. The lighter colors are the late run. Right: Example of the $-\log_{10}(I/I_0)$ of HCl and NaOH concentration relative to milliQ, NaOH concentrations are referred to as negative $[H^+]$ on the x-axis. The measurements are performed over two days using the same dye (day 1 squares, day 2 stars). Standards were prepared three times a day. A linear relation is plotted for standards of NaOH (dotted) and for standards of HCl (full) separately. The text a_{NaOH} refers to the slope of the fit found using all NaOH standards (negative H^+) and U_{aNaOH} to the uncertainty of the fit, similar for HCl standards.

7.2.3 Uncertainties

All measurements of firn and ice were calibrated using a linear fit between $-\log_{10}(\frac{I}{I_0})$ and standards of 19, 9.8 and 4.9 μM HCl as these were found to best represent the values found in the ice. The uncertainty on the HCl concentration of the standards is $\pm$5%. An additional uncertainty on the standards relate to the fact that the CO_2 concentration in the lab varies over a day, although this variance is low, in the order of 0.8 % (see supplementary material). The uncertainty on the linear fit is $\sim$ 0.08 $\pm$ 0.08 μM H^+ ($\sim$2.8 %) over the range of concentrations found in the NEGIS firn core.

The largest uncertainty arrives due to drift during detection of ice, a very conservative estimate for the uncertainty caused by the drift is $\sim$ 0.20 $\pm$ 0.24 μM H^+ (6.5%). The drift is determined as the difference between using the baseline before and after detection of a sample for calibration. As the technique is extremely sensitive to the mixing ratio of sample and dye, a steady drift is caused by differential wearing of tubing over time. As mentioned earlier, the ageing of Bromophenol Blue dye also led to drift primarily in the 450 nm signal.

The total combined uncertainty of the described pH technique thus accounts to $\sim$ 8.7% or 5.7% if baseline drift is excluded. This uncertainty does not include the effect of different CO_2 concentrations in the ice itself, which is not accounted for by this new method. The difference between the CO_2 used for calibration (385 ppm) and the CO_2 in glacial samples (180 ppm) could cause the pH found using

this method to be too acid (Figure 7.9).

We found that the 450 nm wavelength was not appropriate for the study of firn/ice cores due to substantial level of noise at this wavelength. However, as the 450 nm and 589 nm wavelengths respond inversely to pH variations, but identically to flow variations, we used the trend of the two wavelengths as a diagnostic tool to identify unexpected flow changes. These could be attributed to the presence of air bubbles in the sample line and/or absorption cell.

7.3 Results

7.3.1 Greenland ice Core (NGRIP)

To validate the optical dye detection method [H^+] a section of the Greenland NGRIP ice core was determined for H^+ and results were compared to the [H^+] concentration calculated based on the ionic budget (Figure 7.4). The section covers a volcanic eruption around 1257 AD, which is commonly observed in ice cores from both hemispheres. The volcanic eruption is large and estimates of its load vary from 2 to 8 times that of Tambora. The eruption is found in the NGRIP ice core at a depth of 161.15 to 161.70 metres. H^+ based on the ionic budget was determined using equation 7.1, and by a simplified version (eq. 7.2) by removing sea salt ions as they (in theory) balance out. Ion concentrations were determined by IC, except for organic acids, which are assumed to have a concentration of 0.3 μeq based on formate (9.4 ng/g) and acetate (7.3 ng/g) determinations in the Greenland GRIP ice core between 1800 and 1980 AD [*Legrand and De Angelis*, 1995].

The [H^+] determined by the optical dye method matches up well with the [H^+] calculated from the ionic budget for large [H^+]. For low concentrations of H^+, however, an offset of about 1.3 μM (about 0.14 pH unit) is observed between the two methods. This offset is most likely due to the amount of carbonic acid in the water having a larger influence at more alkaline waters.

$$\begin{aligned}[H^+] = [F^-] + [MSA^-] + [Cl^-] + [NO_3^-] + 2\cdot[SO_4^{2-}] + [org^-] \\ - [Na^+] - [NH_4^+] - [K^+] - 2\cdot[Mg^{2+}] - 2\cdot[Ca^{2+}]\end{aligned} \quad (7.1)$$

$$[H^+] \simeq 2\cdot[nssSO_4^{2-}] + [NO_3^-] + exc[Cl^-] + [org^-] - [NH_4^+] - 2\cdot[nssCa^{2+}] \quad (7.2)$$

7.3.2 Greenland Firn Core (NEGIS)

pH was determined in the upper part of a firn core from the North East Greenland Ice Stream (NEGIS, 75.38°N, 35.56°W) covering the period 1900 AD-2005 AD. The firn core was analysed on the Copenhagen CFA system[*Bigler et al.*, 2011], optimized for high resolution measurements of impurities in firn or ice samples with a cross-sectional area of 35 mm x 35 mm. Calibrations were made before and after melting 3 samples of firn of 55 cm length. The core chronology was established by counting annual peaks e.g. winter peaks of Na^+ [*Fischer et al.*, 2007; *Rasmussen et al.*,

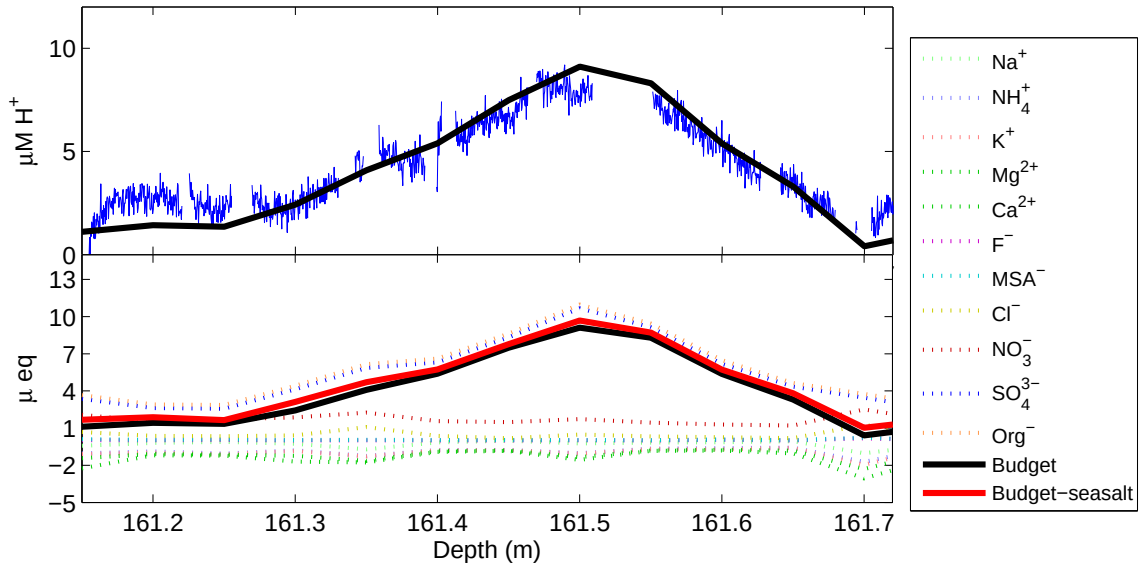

Fig. 7.4: NGRIP data showing the 1257 AD volcano on a depth scale. Top: H^+ determined using the optical dye method (blue) shown together with the ionic budget (black). Bottom: The ionic components in the ice as determined with IC. Notice that cations and anions are added to each other, respectively, following the order shown in equation 7.1. Thus making the line labelled Org^- the sum of all the anions times their charge and Ca^{2+} the sum of all the cations times their respective charge. Also shown is the ionic budget (black) as determined including all species using equation 7.1 and the ionic budget (red) as determined without sea salt species using equation 7.2.

2006; *Legrand and Mayewski*, 1997], between volcanic reference tiepoints identified by DEP and ECM analysis.

Acidity in the NEGIS record shows similar levels to that observed in other Greenland ice core records. The mean acidity level is 2.3 μM H^+ prior to the mid 1940's, after which it strongly increases reaching mean values of 7 μM H^+ in the mid 1970's, and then decreasing to 1.2 μM H^+ by 2004 (Figure 7.5). This trend is similar to that reported by *Pasteris et al.* [2012] for the Greenland Humboldt ice core located in North-western Greenland 615 km from NEGIS. Based on the maximum 1970's concentrations of 200-230 ppb SO_4^{2-} and 100-130 ppb NO_3^- observed in the nearby Greenland firn cores (B16, B18, B21) [*Fischer et al.*, 1998] corresponding increases in H^+ are 4.1-4.8 μM from SO_4^{2-} and 1.6 to 2.1 μM from NO_3^-. Thus the increase in SO_4^{2-} and NO_3^- is enough to explain the 5 year mean increase in the H^+ signal observed in the NEGIS firn core.

The concentration of H^+ in the NEGIS firn core varies throughout the year with the higher levels occurring in winter. As noted by *Pasteris et al.* [2012] higher acidity levels are observed during late winter/early spring when the Arctic haze phenomenon is strongest [*Law and Stohl*, 2007; *Quinn et al.*, 2007]. Similar seasonality is also observed albeit weaker in NEEM snow pit samples as measured by a pH electrode [*Kuramoto et al.*, 2011]. The seasonality of acid deposition (see supplementary material Figure 7.15, bottom) for the period 1950 to 2000 is more pronounced than for the period 1900-1950 and shifts towards the spring months rather than the winter. The pH level and trends reported here for NEGIS closely follow those found in the Greenland Humboldt North firn core, for which a pH-electrode based detection method was used (shown in red in top panel of Figure 7.5).

Most of the acidity peaks in the NEGIS firn core record can be consistently attributed to volcanic activity, though acid peaks in the industrial era can not be excluded from originating from anthropogenic sources. In table 7.2 extreme H^+ concentrations found in the NEGIS record (defined as those exceeding a rolling five-year 3σ (99.8%) probability interval) are compared to contemporaneous volcanic eruptions or extreme wildfire events. Most of the enhanced H^+ events are linked to other volcanic eruption proxies such as ECM, DEP and/or SO_4^{2-}[*Zielinski*, 1995; *Sigl et al.*, 2013; *Arfeuille et al.*, 2013]. Volcanic eruptions that have increased NEGIS H^+ levels above 3σ variability threshold include Redoubt (Alaska, 1989 and 1967), El Chichon (Mexico, 1982), Hekla and Katla (Iceland, 1913, 1918 and 1971), Raikoke (Kuril Islands, 1924) and Katmai (Alaska, 1912) (Figure 7.5). Although Agung (Indonesia, 1963) is commonly observed in Antarctic records it is not prominent in Greenland due to the elevated background level resulting from industrial sulphate emissions in the Northern Hemisphere.

Ice core pH can be influenced by organic acids such as formic acid, produced by enhanced biomass burning events, though in most cases the formic acid will be neutralized by the NH_4^+ arriving simultaneously from the fire event. Only two NEGIS peaks exceeding 3σ variability can be attributed to biomass burning events dated to 1950 and 2002 AD. The Chinchaga fire in 1950 (3,500,000 acres) is likely the largest northern American wild fire in recent history [*Smith*, 1950] and in 2002 the Rodeo-Chediski Fire in Arizona (467,066 acres)[*Kuenzi et al.*, 2008] and/or the Biscuit fire in Oregon state (499,750 acres)[*United States Government Accountability*

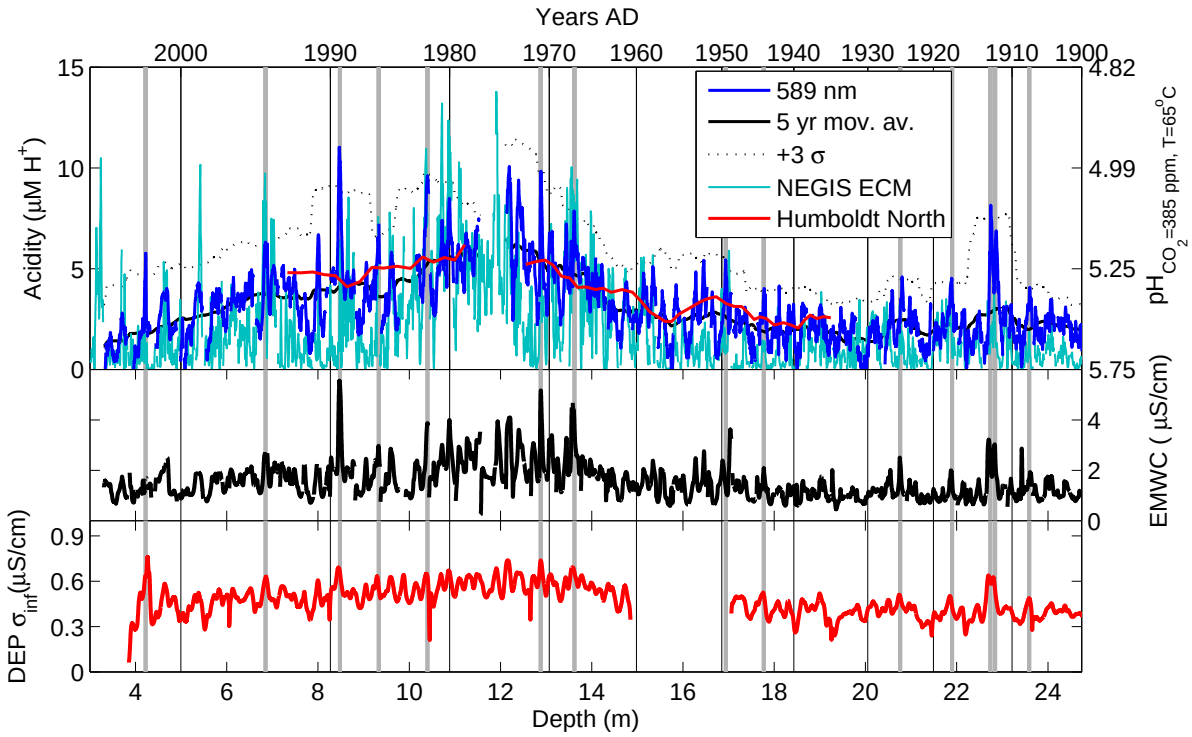

Fig. 7.5: Results from the NEGIS firn core on depth scale. Top; Acidity (589 nm) in high resolution (blue) and as a 5-year moving average (black) and the 5 yr moving average added 3 times the moving standard deviation (dotted black), both y-axes applies. Following only the left y-axis acidity results from the Greenland Humboldt North ice core (red) [*Pasteris et al.*, 2012] and ECM (dotted cyan, left axis) corrected for density. Middle: Conductivity (black). Bottom: DEP (red) corrected for density. Grey vertical bars indicate volcanic eruptions and wildfires [*Sigl et al.*, 2013; *Arfeuille et al.*, 2013; *Pasteris et al.*, 2012]. All graphs fits both time and depth axes, except the Humboldt record which fits only the time axis.

Tab. 7.2: Years of enhanced H^+ level compared to a five year average in the NEGIS firn core for the recent century and suggested cause as well as the enhanced concentration as compared to a five year mean (ΔH^+).

Event, location and date	Years of high H^+ (exceeding 3 STD)	ΔH^+
wildfire (2002)	2002 (sum)	3.6
	1995(spr)	2.5
Redoubt, Alaska (1989)	1989(spr)	6.2
Augustine, Alaska (1986)	1986(spr)	3.4
El Chichon, Mexico (1982)	1982(spr)	4.3
Hekla, Iceland (1970)	1971(spr)	3.8
Redoubt, Alaska (1966 or 1967)	1967(win)	3.0
wildfire(1950)	1949(aut)	2.7
wildfire (1943) or Unknown NH	1944 (spr)	1.8
Raikoke, Kuril Islands (1924)	1925(spr)	0.2
Katla, Iceland (1918)	1918(win)	1.8
Hekla, Iceland (1913)	1913(spr)	4.2
Katmai, Alaska (1912)	1912 (spr)	1.9
Ksudach, Kamchatka (1907)	1907(sum)	1.3

Office, 2004] could have attributed to the peak. *Pasteris et al.* [2012] identified other large biomass burning events, particularly in 1943 and 1951, although those events do not exceed 3σ variability in the NEGIS acidity record. However the events could also be of anthropogenic SO_4^{2-} origin.

7.3.3 Relating pH to ice core conductivity

Electrolytic melt water conductivity (EMWC [*Bigler et al.*, 2011]), electrical conductivity measurements (ECM, [*Hammer et al.*, 1980]) and dielectric profiling (DEP, [*Wolff et al.*, 1997]) are standard ice core measurements that were also obtained for the NEGIS firn core (Figure 7.5). All of those records are related to pH in some manner, although it is important to distinguish that EMWC is measured on the melted sample and hence is influenced by soluble ions and CO_2, whereas ECM and DEP are determined on solid ice. As is often the case[*Hammer*, 1980; *Barrie et al.*, 1985; *Wolff et al.*, 1995] a good correlation (r>0.6) is found between the H^+ concentration and the EMWC, ECM and DEP in the NEGIS firn core (see supplementary material Figure 7.14 and Table 7.3). Furthermore, all four records show similar trends over the 20th century with a peak in the 1970's due to anthropogenic acid deposition.

The NEGIS EMWC can be almost completely reproduced by a linear fit of EMWC= $0.32 \cdot [H^+] + 0.54$. This suggests that the melt water conductivity in the NEGIS firn core is mainly governed by the H^+ content and that other ions such as sea salts are insignificant (mean level of Na^+ is in the order of 25 ppb for NEGIS, peak values 99 ppb).

ECM is often not measured on firn cores as the high porosity in the firn significantly reduces the contact resistance thereby increasing the noise of the signal [*Hammer*, 1980; *Karlöf et al.*, 2006]. We have used the inverse of the ice volume fraction (ρ_{ice}/ρ_{firn}) as a linear correction to the electrical current (i) in combination with the empirical relationship[*Hammer*, 1980] $[H^+] = 0.045 \cdot i^{1.73}$ to determine H^+ concentrations from the ECM measurements (Figure 7.5, cyan). DEP is also affected by densification processes[*Barnes et al.*, 2002], although a complete correction of the DEP requires core volumes and $[H_2SO_4]$ concentration data [*Barnes et al.*, 2002]. Nonetheless DEP was partially corrected by multiplying the original DEP signal with ρ_{ice}/ρ_{firn}. The density-corrected DEP conductivity was consistently substantially lower than the EMWC signal.

The density corrected NEGIS ECM record, is to a first order proportional to the concentration of $[H^+]$ detected using the dye-based optical method. The ECM signal is noisier for shallow firn, but the ECM and dye-based techniques are very comparable in the deeper sections of the NEGIS core. When the firn is melted in the laboratory, to some extent, the percolation of meltwater in loose firn can also smooth out the CFA signal, affecting the resolution of pH (and EMWC) determinations.

Despite these potential amplifying artifacts, the mean difference between the ECM and dye-based pH determination is merely 1.1 $\mu M H^+$ that is well within the uncertainties incurred by the ECM density correction and the calibration of the dye-based pH method.

Further it is interesting that the double spike from the volcanic eruption of Katmai in 1912 AD is not easily visible in the ECM record[*Arfeuille et al.*, 2013; *Sigl et al.*, 2013]. In comparison both for the acidity method described here, the DEP and the melt water conductivity, the eruption of Katmai is clearly distinguishable. A similar search for extreme events was performed on the ECM and the DEP. We found no significant extreme concentrations in the DEP or ECM techniques being related to the minor volcanic events. Thus the new method presented here is more capable of detecting volcanic horizons in the firn.

7.3.4 Antarctic Ice Core (RICE)

The pH method was also applied to the Roosevelt Island Climate Evolution (RICE) Project ice core (79.36 °S, -161.71 °W, see Figure 7.1) drilled in austral summer 2012/2013 and analysed using a modified version of the Copenhagen CFA in Wellington, New Zealand. Results from depth interval 89 to 95 metre for which preliminary dating suggest the ice is from the period ∼1659-1673 AD, are shown in Figure 7.6.

The mean acidity level in the RICE core is 1.6 μM H^+ with spikes of up to 5 μM H^+. The RICE level is thus comparable, but consistently lower than that of the Greenland NEGIS firn core.

The RICE core shows quite a different behaviour to NEGIS with respect to comparisons between acidity and measures of melt water conductivity (EMWC). Contrary to NEGIS, EMWC and H^+ concentrations are anti-correlated (r=-0.35) in RICE, with lowest H^+ concentrations coinciding with EMWC and Ca^{2+} peaks (Figure 7.6). The anti correlation can be explained if the Ca^{2+} signal at the RICE site consists of a seasonal variation forexample related to sea salts peaking in austral winter, with a steady annual background related non-sea salt Ca^{2+}, similar to what

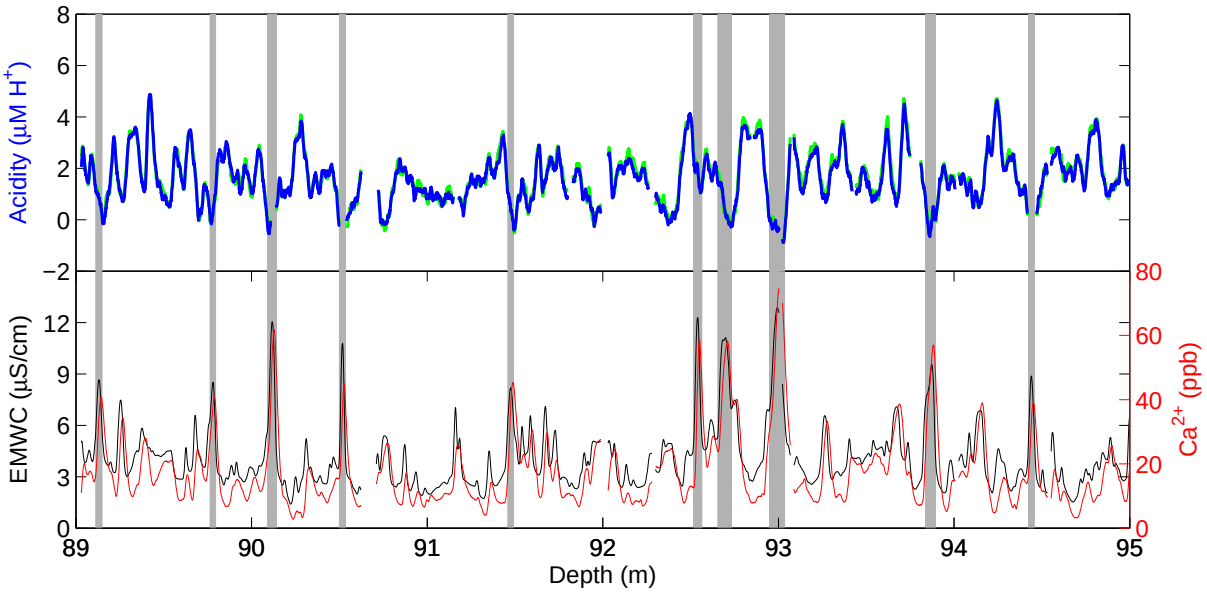

Fig. 7.6: Results from the Antarctic RICE core shown in 1 cm resolution from 89 to 95 meters depth. Top: Acidity (586 nm (green), 589 nm (blue)). Bottom electrolytic melt water conductivity (black) and Ca^{2+} (red). Grey vertical bars indicate melt water conductivity concentrations more than two times the standard deviation.

has been observed at other coastal Antarctic sites [*Hall and Wolff*, 1998; *Curran et al.*, 1998], while the acidity signal is governed by non-sea salt sulphate related to the oxidation of dimethylsulphide (DMS), a volatile compound produced by phytoplankton and peaking in the austral summer[*Curran et al.*, 1998]. An alternative explanation is that there is a relative constant acidity signal, which is decreased when local dust is deposited due to $CaCO_3$.

Although RICE acidity is somewhat lower than that of NEGIS, the EMWC is much greater due to the high loads of sea salt at this low-altitude coastal site. For instance, average 20th century Na^+ concentrations are approximately 300 ppb at RICE (personal correspondence Nancy Bertler) and approximately 20 ppb at NEGIS. The acidity data reported here indicate that the high background levels of EMWC governed by sea salts in RICE ice will mask the presence of volcanic acid peaks in the EMWC.

Acknowledgement

This work is supported by the Center of Ice and Climate at the Niels Bohr Institute. We also thank the Alfred Wegener Institute for polar and marine research (AWI) for supporting the retrieval of the NEGIS firn core. We acknowledge Mathilde Thorn Poulsen and Trine Schmidt Jensen for their preliminary studies of dye-based pH detection. The RICE project is supported by an international collaboration between New Zealand, USA, Denmark, United Kingdom, Germany, Australia, Italy and China. We thank all the people involved in the RICE logistics, fieldwork, sampling and analytical programmes.

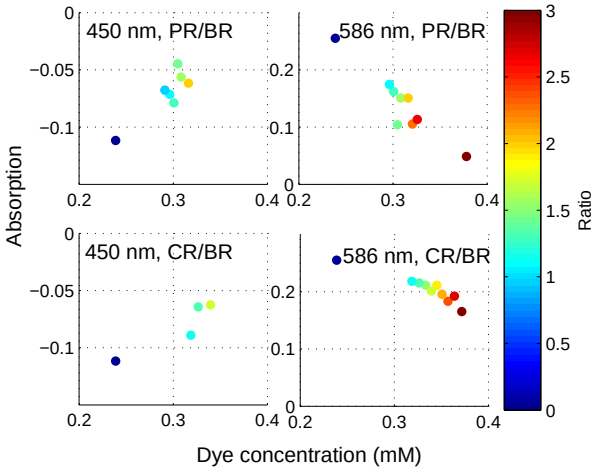

Fig. 7.7: The absorption of a 19.4 μM HCl concentration as a function of the molar concentration of the dye. The colorbar indicates the mixture ratio of either phenol red (PR) over bromophenol blue (BR) (top) or chlorophenol red (CR) over bromophenol blue (BR) (bottom) in the dye. At the left side is shown for a wavelength of 450 nm, while the right hand side represent 586 nm.

7.4 Supplementary material for: An optical method for continuous determination of pH in ice cores

In the supplementary material the following figures are presented: The effect on the absorption ($-\log_{10}(\mathrm{I}/I_0)$) as a function of concentration of the dye (Figure 7.7) and change of temperature (Figure 7.10 and 7.9); Spectra, raw data and linear calibrations for standards (Figure 7.8, 7.11); The variation in linearity over two months (Figure 7.12); The effect of using HCl or H_2SO_4 as standards (Figure 7.13). For the NEGIS firn core ECM, DEP and EMWC as a function of H^+ (Figure 7.14 and Table 7.3) as well as sub-annual resolved data (Figure 7.15); Equations used to determine the pH from the acidity (acidity= $[H^+] - [CO_3^-]$) is also shown.

7.4.1 Dye mixtures

To examine the mixtures of Bromophenol blue (BR) and Chlorophenol red (CR) as well as mixtures of Bromophenol blue (BR) and Phenol red (PR, from yellow at pH 6.8 to red at pH 8.2, Sigma-Aldrich) the response of a 19.4 μM HCl concentration was investigated while varying both the total dye concentration and the ratio of CR over BR and PR over BR. We found an increase in absorption, when diluting the dyes at both $\sim$ 450 nm and $\sim$ 586 nm (Figure 7.7), as a result of enhancing the light penetration. Further we found an increase in the absorption when a larger fraction of the dye was BR.

For large amounts of PR compared to BR the response at $\sim$ 450 nm disappeared, this is due to the PR spectra counteracting the response of the BR at 450 nm. Thus a mixture of CR and BR was used for further experiments.

We found that using a mixture of 0.025g of bromophenol blue added 0.025g of

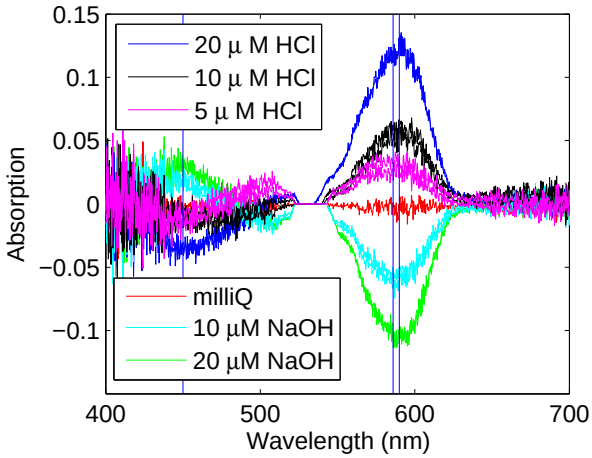

Fig. 7.8: Absorption as a function of wavelength for the different standards of HCl and NaOH using a dye mixture of BR and Cl.

chlorophenol red in 500 mL milliQ added 100 μL Brij worked well at a flow ratio of 0.15 mL/min to a sample flow of 1.1 mL/min. The response in absorption as a function of wavelength to standards made from diluted HCl and NaOH can be seen in Figure 7.8.

7.4.2 pH determination

To determine the pH from the concentration of $[H^+]$. We follow the calculations by *Pasteris et al.* [2012] as also found in *Stumm and Morgan* [2012] to take into account the potential of CO_2 dissolved in the liquid. We calculate the ionization fractions:

$$\alpha_0 = \frac{1}{1 + \frac{k_1}{H^+} + \frac{k_1 * k_2}{H^+}}$$
$$\alpha_1 = \frac{1}{\frac{H^+}{k_1} + 1 + \frac{k_2}{[H^+]}}$$
$$\alpha_2 = \frac{1}{\frac{[H^+]\cdot[H^+]}{k_1 * k_2} + \frac{[H^+]}{k_2} + 1}$$

assuming that the CO_3^{2-} and OH^- terms can be ignored when pH is below pH 8, which is the case in almost all natural ice. The acidity thus yields; acidity=$[H^+]$-$[HCO_3]$, which is what we detect and the concentration of $[H^+]$ is acidity= $10^6 \cdot ([H^+] - (\frac{k_H \cdot P_{CO_2}}{\alpha_0}) \cdot (\alpha_1 + 2 \cdot \alpha_2) - \frac{k_w}{[H^+]})$, where P_{CO_2} is the CO_2 concentration times the local air pressure.

Temperature dependence

The activity coefficients (k) are temperature dependent [*Harned and Davis Jr*, 1943; *Dickson and Riley*, 1979];

$$
\begin{aligned}
pk_H &= -\frac{2622.38}{T} - 0.0178471 * T + 15.5873 \\
pK_1 &= \frac{3404.71}{T} + 0.032786 \cdot T - 14.8435 \\
pK_2 &= \frac{2902.39}{T} + 0.02379 \cdot T - 6.4980 \\
\ln(K_w) &= 148.9802 - \frac{13847.26}{T} - 23.6521 \cdot \log(T)
\end{aligned}
$$

Thus at 65 °C; $K_H = 10^{-1.7972}$, $K_1 = 10^{-6.3117}$, $K_2 = 10^{-10.1297}$ and $k_w = 10^{-12.90185}$.

Due to the activity constant varying with temperature, the theoretical difference in pH when detecting at 20°C and at 60°C is between 0.03 % for a 20 μM HCl standard and up to 1.3% for 20 μM NaOH with more acid pH values for higher temperature.

In Figure 7.9 the difference between acidity and H^+ concentration is shown as a function of H^+ concentration for three different CO_2 concentrations; 180 ppm, 385 ppm, and 700 ppm for both temperatures of 0°C and 65 °C. The uncertainty is high on small concentrations, but improves for low CO_2 and high temperature as expected. The standards used for the results presented in this paper are HCl concentrations of 5, 10 and 20 μM. The difference in acidity vs concentration of H^+ varies from 12.7 %, 3.2% and 0.8%, respectively for the standards up to 23%, 5.7% and 1.43% when increasing the CO_2 content from 385 ppm to 700 ppm CO_2. The local pressure, of 1030 hPa, representative for Copenhagen, and heat bath temperature of 65°C were used to determine the change.

CO_2 uptake in water is temperature dependent and thus the effect on the closed system was investigated by changing the temperature in the heat bath between 25 and 75 °C. Results are shown in Figure 7.10. The errorbars are based on three times standard deviation of a milliQ baseline. No significant effect of temperature was observed.

Response to standards

In Figure 7.11 the response to standards are shown for three wavelengths 450 nm, 586 nm and 589 nm. Figure 7.11 (right) shows that there is limited variation of standards, prepared before each measurement, over two days of measurements (∼32 hours). The uncertainty on a fit based on the standards from the two day campaign, is below 3 %. The low variance in the standards over a day can also be seen in the raw data (Figure 7.11, left). From Figure 7.11 it is also clear that the response at wavelength 450 nm is not high, while the higher wavelengths 586 nm and 589 nm, show stronger signals and higher stability. This is mainly an effect of the spectrometer and the lamp having less signal at 450 nm. Part of the drift over time at 450 nm (Figure 7.11, left), is due to ageing of the dye Bromophenol blue and shows the importance of running standards often if 450 nm is to be used for calibration of the pH.

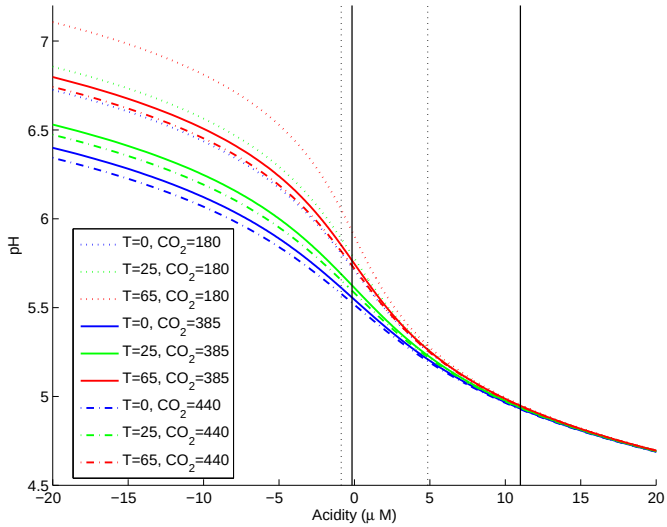

Fig. 7.9: The pH as a function of acidity is shown for various CO_2 concentrations; 180 (dotted line), 385 (full line) and 440 ppm (dashed line) and temperatures of 0°C (blue), 25°C (green) and 65 °C (red) is shown the pH as a function of acidity defined as the amount of $[H^+]$-$[HCO_3]$ relative to that of pure water (0 point). Vertical lines indicate the acidity ranges of the NEGIS firn core (full black) and the RICE core (dotted black).

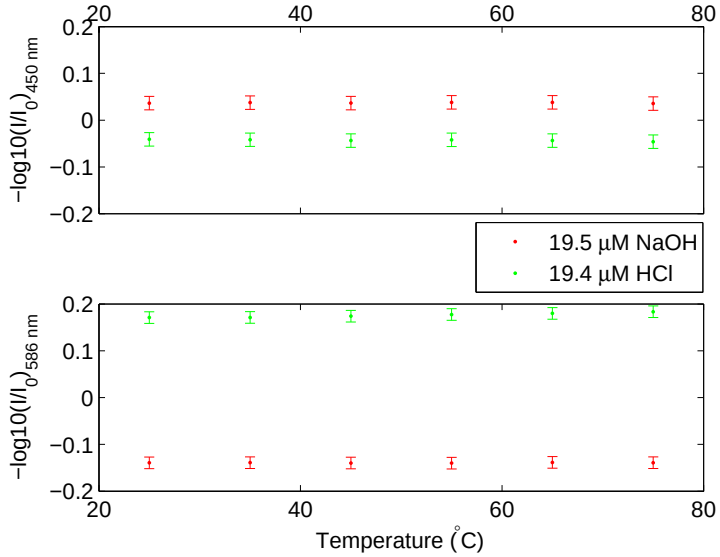

Fig. 7.10: The absorption of a 19.5 μM NaOH concentration (green) and a 19.4 μM HCl concentration standard as a function of temperature for the wavelengths 458 nm (top) and 586 nm (bottom).

Tab. 7.3: NEGIS firn core correlations, for full resolution and in brackets annual resolved.

	H^+	EMWC	ECM	DEP
H^+	1	0.88 (0.95)	0.62(0.70)	0.77(0.82)
EMWC		1	0.61(0.77)	0.73(0.79)
ECM			1	0.59(0.66)
DEP				1

Figure 7.12 shows the low variation for the fit of standards over a two months measurement campaign. For more than 74 fits to HCl standards the variation (1σ) is below $\pm 6\%$ for 589 nm and $\pm 11\%$ for 450 nm and thus more steady than similar fits using NaOH standards ($1\sigma = \pm 9\%$ for 589 nm, $1\sigma = \pm 12\%$ for 450 nm).

Standards based on HCl and H_2SO_4

To investigate the response of the system to different kind of acids used to make standards, similar concentrations of H^+ were prepared from 2.5 M H_2SO_4 (Titripur, Merck) and 0.1001 M HCl. Results show no significant difference (Figure 7.13).

7.4.3 NEGIS

In Figure 7.14 and Table 7.3 the correlation between the H^+ as determined using the optical dye method described in this paper to regularly performed measures also related to pH, such as melt water conductivity (EMWC), DEP and ECM, is shown.

Figure 7.15 show the annual variability of $[H^+]$ for the last 100 yrs as determined in the NEGIS firn core. The subannual variations in the H^+ concentration was investigated by dividing the annual signal into 12 sub-annual periods based on splitting the depth between years in 12 equal sized pieces, thus assuming constant accumulation rate for each month similar to the approach of *Sommer et al.* [2000] and *Bigler et al.* [2002]. The seasons were fixed by assigning the annual Na^+ peak to February-March.

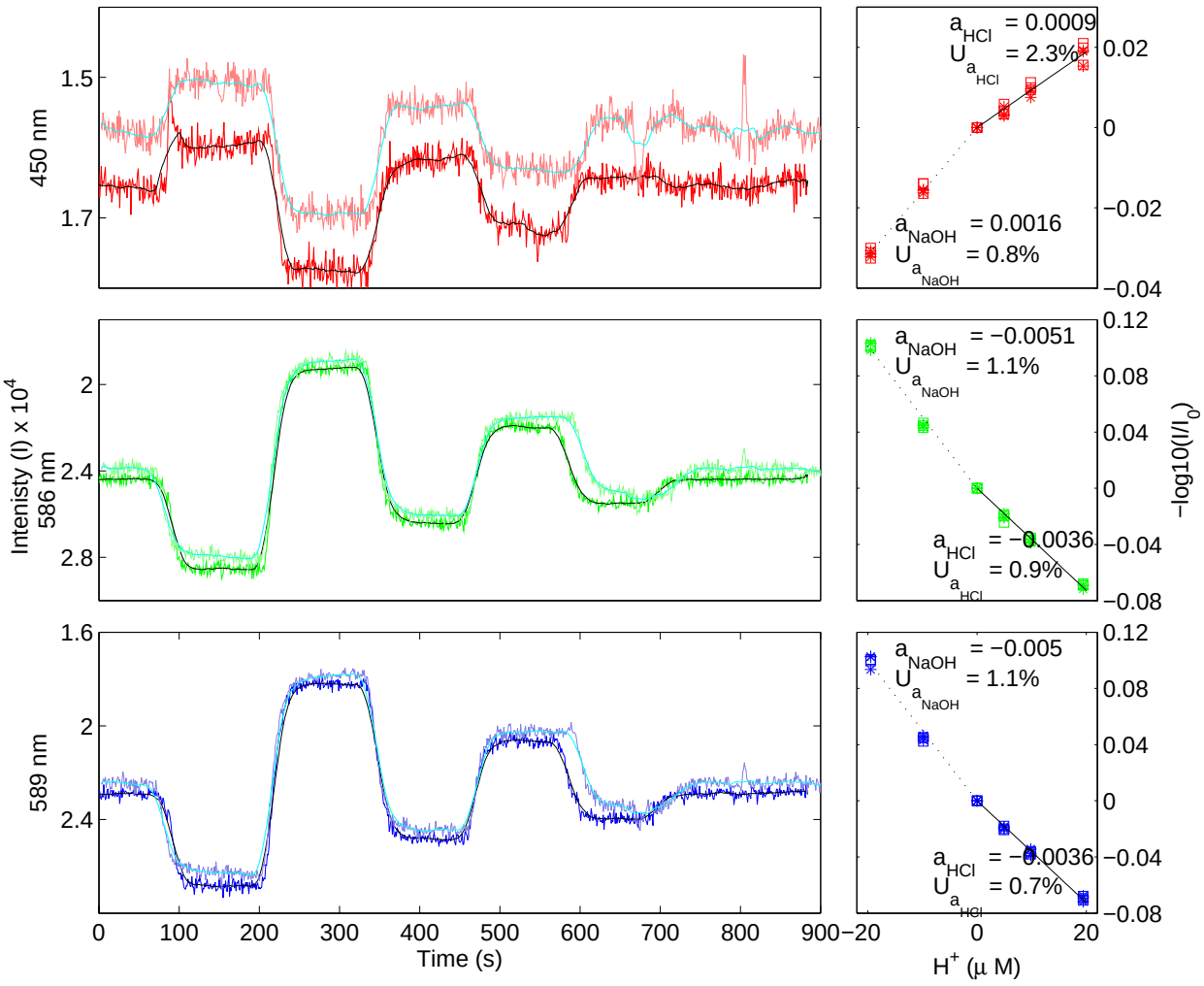

Fig. 7.11: Standard calibration responses are shown for different wavelengths (Top, 450 nm (red), middle 586 nm (green) and bottom 589 nm (blue)). Left: Two examples of standards with concentrations 19μM HCl, 19.5 μM NaOH, 9.8μM HCl, 9.8 μM NaOH and 4.9μM HCl ran with 7 hours interval . The lighter colors correspond to the later run. Notice that the y-axis are different. Right: Examples of the $-\log_{10}(I/I_0)$ of HCl and NaOH concentration relative to milliQ. The measurements we performed over two days using the same dye (day 1 squares, day 2 circles). Standards were prepared three times a day. A linear relation is plotted for standards of NaOH (dotted) and for standards of HCl (full) separately. The text a_{NaOH} refers to the slope of the fit found using all NaOH standards (negative H^+) and U_{aNaOH} to the uncertainty of the fit, similar for HCl standards.

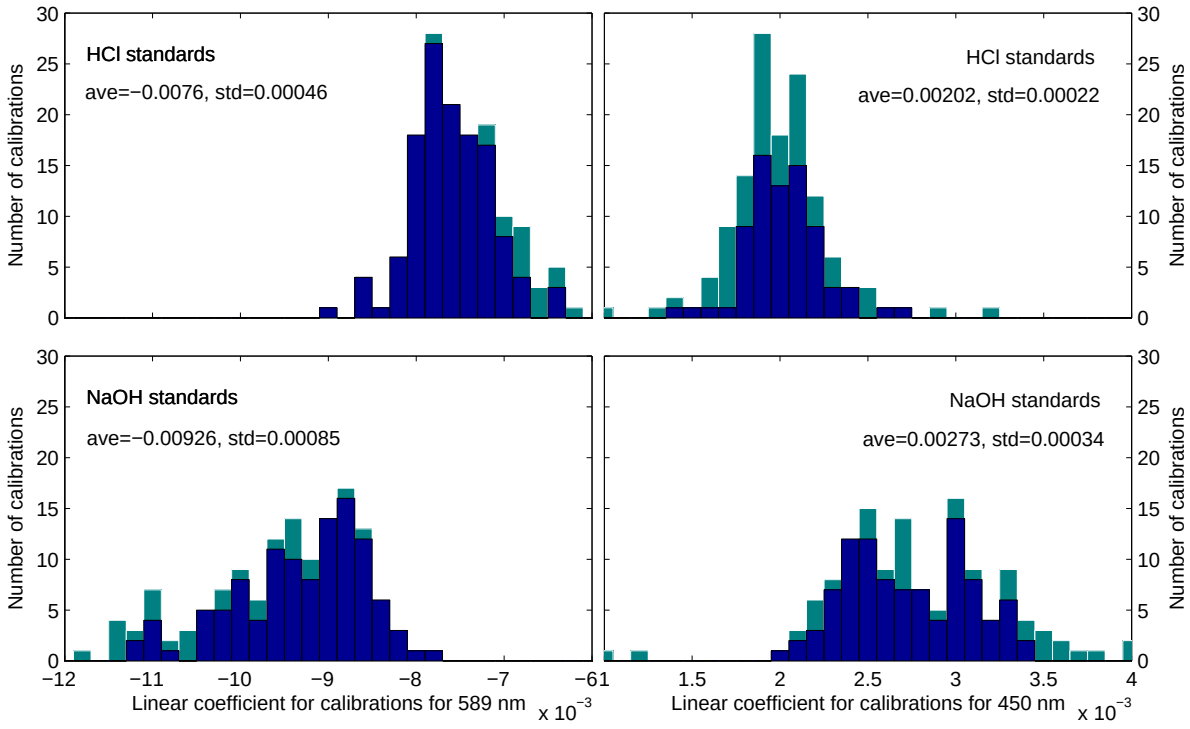

Fig. 7.12: For different wavelengths (left, 589 nm, right 450 nm) are shown 4 histograms of the linear calibration coefficient found when using HCl standards (top) and NaOH standards (bottom). Standards were prepared three times a day and the measurements shown cover 2 months during the RICE campaign. Text show the average calibration and the standard deviation.

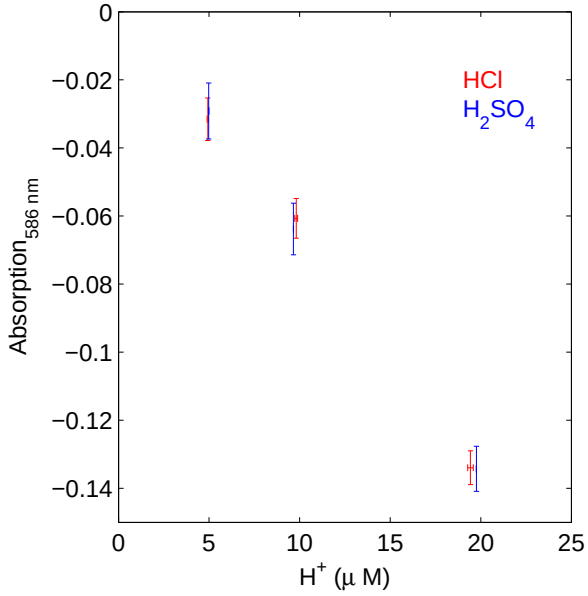

Fig. 7.13: The absorption at 589 nm of HCl(red) and H_2SO_4 (blue) standards of similar concentrations.

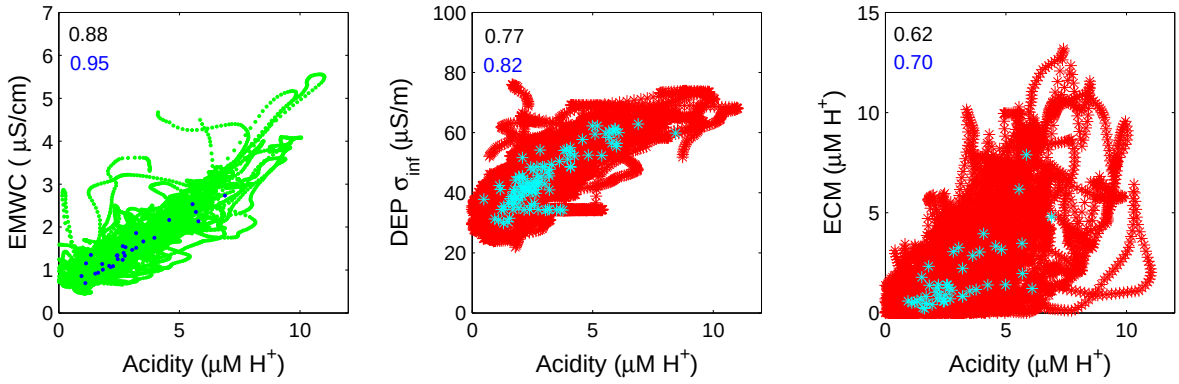

Fig. 7.14: EMWC, DEP, and ECM plotted against acidity as found using the method described in this paper. In green on a 1 cm resolution in blue annual levels. Numbers indicate the correlation coefficient, in black for 1 cm resolution in blue annually resolved. DEP and ECM is both density corrected (red and cyan). EMWC (green and blue) is not corrected.

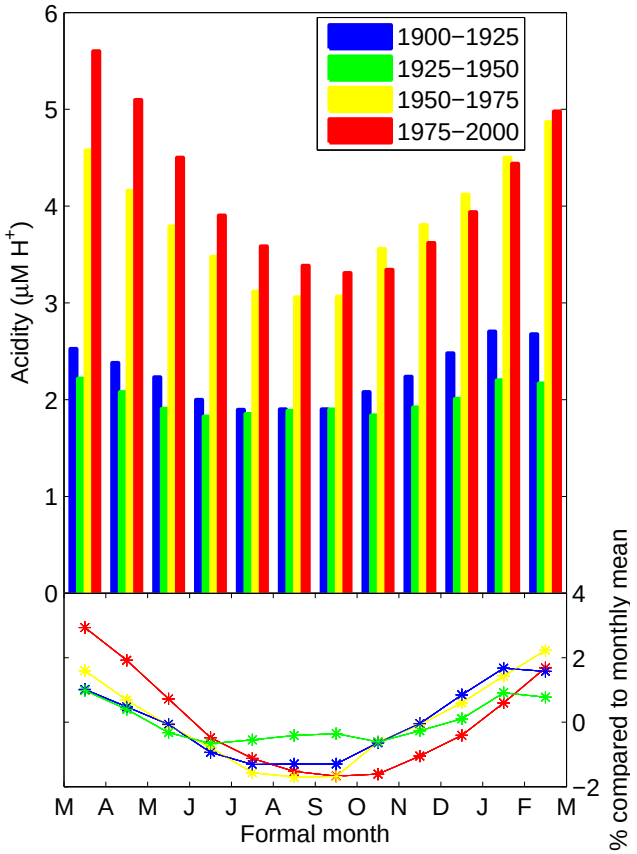

Fig. 7.15: Top: Sub-annual variations for the concentration H^+ for the period 1900 to 1960 yr AD. Bottom: Monthly means compared to annual monthly mean. The sub-annual periods (formal months) are determined based on the winter spike of Na^+ being in February-March.

8. THE ROOSEVELT ISLAND CLIMATE EVOLUTION (RICE) ICE CORE-A SEARCH FOR VOLCANOES

Results from the Antarctic Roosevelt Island Climate Evolution (RICE) ice core record were introduced in section 7. However more information has come out of the RICE record and is presented here; including the CFA record, which includes the dye determined H^+ record, dust, conductivity, and Ca^{2+} as well as ECM down to 500 metres depth. The methods used are valuabl to identify volcanic imprint in the RICE record crucial to constrain the dating of the RICE ice core.

In this section preliminary data from the top 500 metre of the RICE record is presented. Also shown are selected sections and volcanoes that have been identified, such as the 1259 AD volcanic eruption of which the sources are even now speculated. The resolution of the CFA data set is high and annual layers are well preserved allowing for future dating by annual layer counts.

Comparisons of $[Ca^{2+}]$ and $[H^+]$ revealed a strong anti correlation. The cause of this anti correlation is speculated to be a source dependent seasonal effect either with Ca^{2+} from sea salts or a result of calcium carbonates. All are likely influencing the H^+ concentration observed, but calcium carbonates from dust and volcanic sources seem to cause a stronger anti correlation than the sea salt derived Ca^{2+}.

8.1 Background for the RICE ice core project

In West Antarctica, ice shelves have severely disintegrated in recent times and the area is speculated to be particular sensitive to climate change [*Shepherd et al.*, 2004; *Joughin et al.*, 2014]. While there is evidence from marine records that such destabilisation has happened before [*Kirshner et al.*, 2012] it is not known what climatic changes drive this disintegration or if what is happening today is unique to the recent warming.

The Antarctic Roosevelt Island Climate Evolution (RICE) Project ice core (79.36 °S, -161.71 °W, see Figure 8.1) was drilled on the Roosevelt Island in austral summer 2012/2013.

Roosevelt Island is all surrounded by the West Antarctic Ice shelves and thus the RICE ice core provide a unique opportunity to look into the past evolution of the West Antarctic Ice sheet. Further the site has high accumulation; 0.26 m of ice equivalent annually allowing for annual layer determination. The RICE core was drilled to the bottom and has a total length of 763 metres. Preliminary results derived from water isotopes suggest that the oldest ice reach back to the Eemian, with the recent glacial being compressed in the bottom 60 metres (personal correspondence Nancy Bertler).

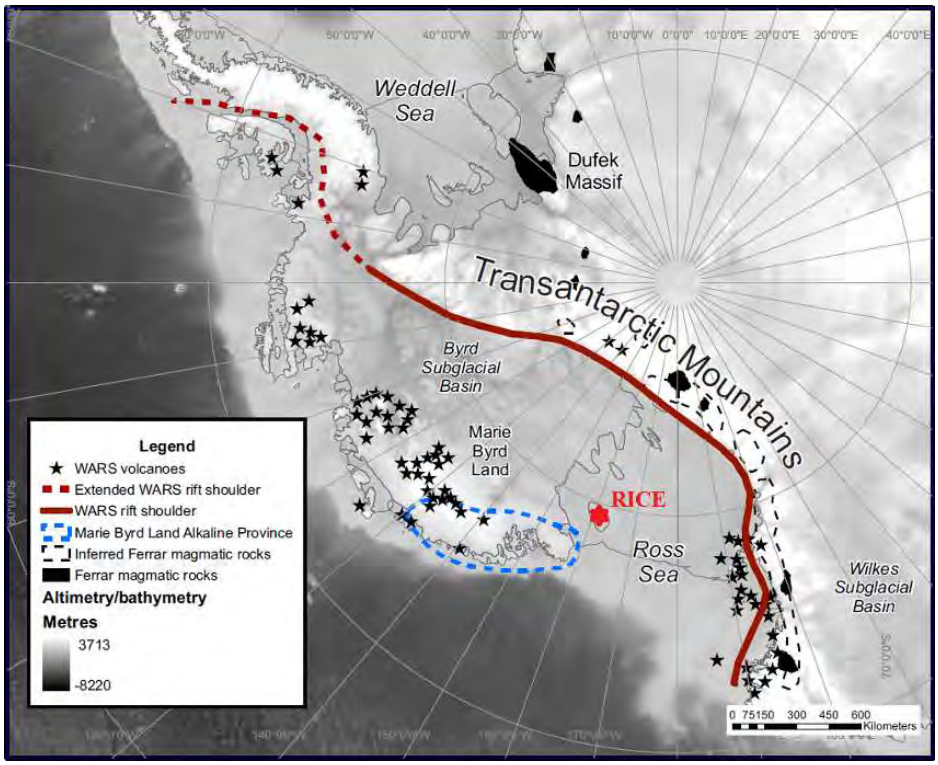

Fig. 8.1: Map showing the position of the Roosevelt Island Climate Evolution ice core (RICE, red) as well as volcanoes in the proximity (black stars). Figure from *Storey et al.* [2013].

8.2 Methods applied to the RICE ice core

The RICE ice core was analysed at the New Zealand National Ice Core Research Facility at GNS Science. The set up used to determine climate proxies in the ice core was a modified version of the Copenhagen CFA system, including continuous measurements of acidity using the method developed in this study (section 7), insoluble dust particles, conductivity, calcium, water isotopes and methane. Further discrete samples were obtained for analysis by Ion Chromatography (IC) and Inductively Coupled Plasma Mass Spectrometry (ICP-MS). Prior to core melting ECM measurements were also performed.

The core was analysed to a depth of 500 metres during a measurement campaign in 2013. The remaining core is to be analysed in July and August 2014. The CFA set up used in 2013 is shown in Figure 8.2 and 8.3. 100 cm length pieces were stacked to ensure high quality methane measurements and 4 times 100 cm ice core were measured between each calibration. The melt rate was 3.2 cm/min and the flow rate was 16.8 mL/min.

8.2.1 ECM

ECM gives the conductivity of the ice before melting and can be used to identify volcanic peaks.

The ECM instrument used for the determination of the electrical conductivity in the RICE ice core was an Icefield instruments ECM unit. This is a small (600 g) hand held ECM recorder and was set up with a wire depth encoder, on a track where the electrodes were dragged along manually. Thus no automation was used causing some issues. The main one being inconsistent electrode pressure affecting the signal. Also as the brittle zone was reached (from 200 m to 500 metres depth) the operator (Peter Neff[1]) found that it was necessary to loosen the pressure of the electrodes against the ice. As a result the conductivity decrease seen over the period is partly an artefact. The method was also effected by fractures and drill liquids over large sections of the ice core.

The direct ECM measurements were influenced by artefacts as mentioned above. However the signal was anyhow changed into $[H^+]$ by converting the raw conductivity signal (i) using the relationship $[H^+_{ECM}] = 0.045 \cdot i^2$. Despite this relationship being inaccurate for the RICE ice core it provides the exponentiated relationship between i and $[H^+_{ECM}]$ making comparison to $[H^+_{dye}]$ as determined using the optical dye method easier.

8.2.2 Electrolytic melt water (MWEC) conductivity, dust and "pH"

Similar to ECM the acidity method developed through this study (section 7) can be used to identify volcanic eruptions. This is particular valuable at the RICE site where Ca^{2+} and melt water conductivity (MWEC) show a very similar signal.

The electrolytic melt water (MWEC) conductivity and dust were determined on the CFA melt water stream. MWEC is further described in section 1.2.2. The

[1] Peter Neff is a graduate student at University of Wellington, New Zealand and measured ECM during the lab campaign in 2013.

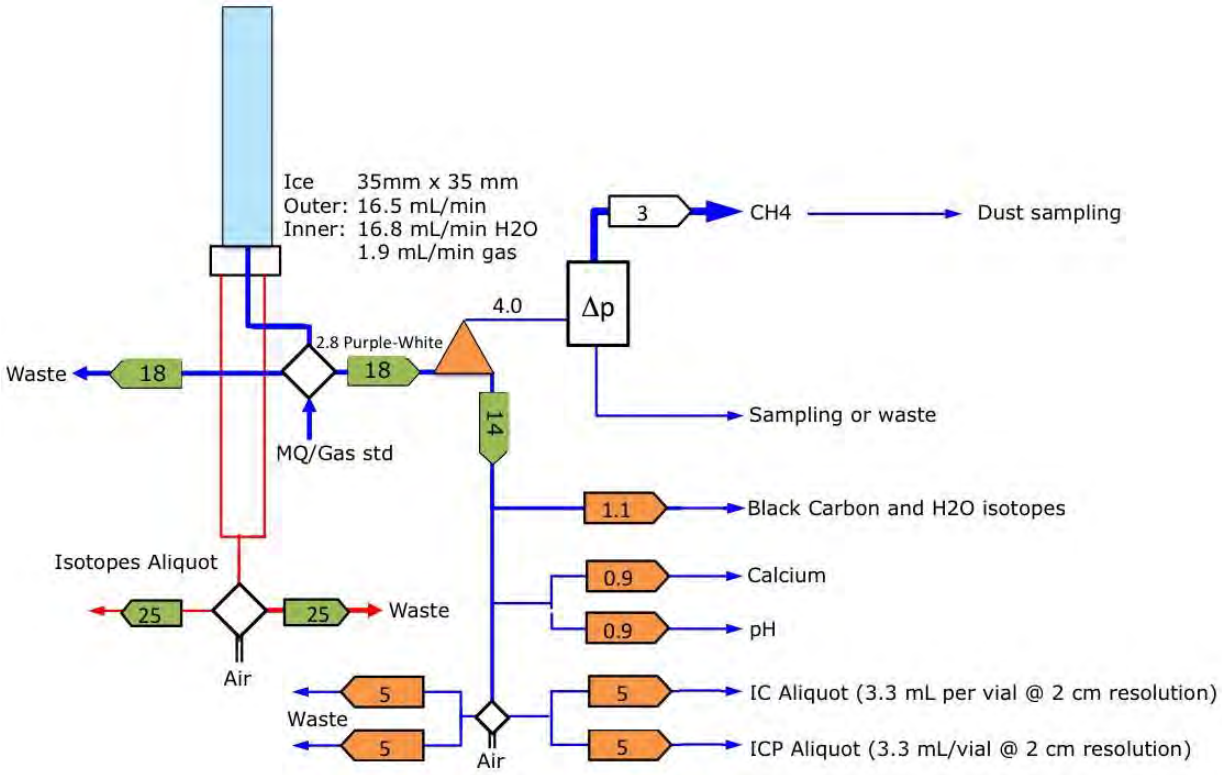

Fig. 8.2: Sketch of the CFA set up used for analysis of the RICE ice core in New Zealand 2013. The melt stream is split in an inner (blue) and an outer (red) stream. The outer stream is used for the determination of water isotopes. The inner sample is debubbled (orange triangle) and slit into gas for determination of methane and water CFA streams. The water CFA stream is further split for the determination of black carbon and water isotopes, calcium, pH and semi-discrete aliquots intended for IC and ICP-MS measurements. Open squares denote valves used to introduce standards or air, when the system is not used for ice determinations. Pentagons are pumps and numbers inside indicate the flow rate in ml/min. Colour of the pentagons refer to different pump systems; green a 24 channel IPC pump, orange a 8 channel IPC pump, white a 4 channel MP2 pump. Figure by Paul Vallelonga.

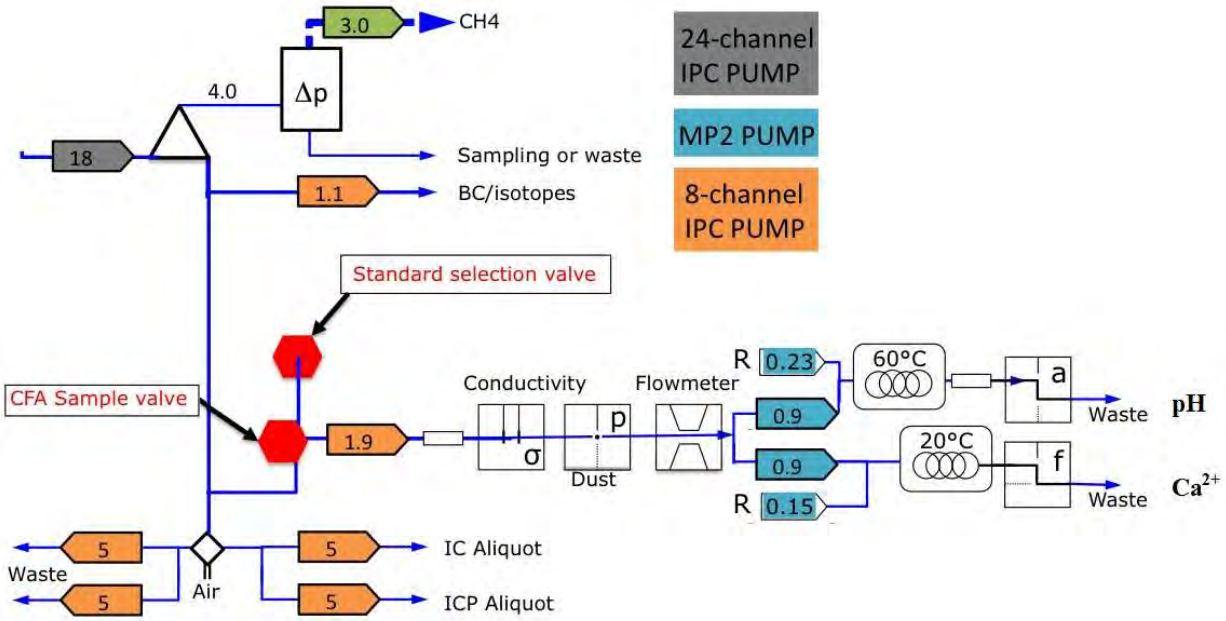

Fig. 8.3: Similar to Figure 8.2, but showing only the inner sample line and with more detail on individual detection systems. R indicate reagent. Pentagons are pumps and numbers inside indicate the flow rate in ml/min. Colour of the pentagons refer to different pump systems; grey a 24 channel IPC pump, orange a 8 channel IPC pump, green a 4 channel MP2 pump and blue a 4 channel MP2 pump. Figure by Paul Vallelonga.

determination of dust took place using a Klotz Abakus laser particle counter as described in section 1.2.2. Optical measurements of the acidity were performed following the method described in section 7.

Calcium was determined using a fluorescence technique similar to the one used by *Traversi et al.* [2007]. To the water sample (1 mL/min) a reagent (0.23 mL/min) is added. The system is introduced into a dark temperature controlled mixing column (0.85 m) and determination also takes place in the dark box to avoid photolytic reactions [*Traversi et al.*, 2007]. Excitation took place at 334 nm and detection of the emission at 489 nm.

The reagent was mad by 750 mL milliQ water added 10 mg QUIN-2 Potassium hydrate, which was kept in the fridge when not used. Further 2.91 g PIPES was added and the liquid was buffered to approximately 7 pH using 1500 μL NaOH.

15 ppb and 30 ppb Ca^{2+} standards were used to linearly calibrate the data. The method has a limit of detection (LOD) of 15 ppt Ca^{2+} and is linear up to 330 ppb Ca^{2+}[*Traversi et al.*, 2007] far above the concentrations found in the RICE ice core.

8.2.3 Continuous methane

Methane, besides being an interest in itself, is used to transfer the time scale from the nearby West Antarctic Ice Sheet Divide (WAIS) ice core to the RICE ice core by matching up rapid events recorded in the methane at both sites. The methane was determined continuously by a Picarro cavity ring down spectrometer (see section 1.2.2) following the method by *Stowasser et al.* [2012]. The method requires 1.6 mL/min gas flow and has a precision of 0.8 ppbv (1σ). The accuracy ($\pm$8 ppmv) of the continuous system is dependent on the gas extraction unit. However results from the NEEM ice core indicated that the method was shifted about 25 ppmv as compared to discrete measurements. Similar shift could be expected in the methane record from the RICE ice core.

8.3 Preliminary results from the RICE record

The RICE CFA record at a depth of 50 to a depth of 500 metres is shown for ECM (on courtesy of Peter Neff), dust, MWEC, and dye determined H^+ in Figure 8.4. Please note that due to the time limit of this PhD, this data is not cleaned for air bubbles and thus contain artefacts also the calibration has not yet been thoroughly checked. Thus all results should be viewed as preliminary.

The resolution of the CFA data set is high for all components determined and annual layers are well preserved allowing for future dating by annual layer counting.

The MWEC show higher peaks in the top part of the record and slowly decreases towards the bottom, the mean level stays roughly the same throughout. This is most likely a result of the temporal resolution which changes with depth as annual layers gets thinner. This trend is also observed in the calcium signal where greater concentration levels are reached in the top of the core and peak height decreases towards the bottom. Similar trend is furthermore observed in ECM, but as mentioned above this could be an artefact of the operator of the instrument using different pressure

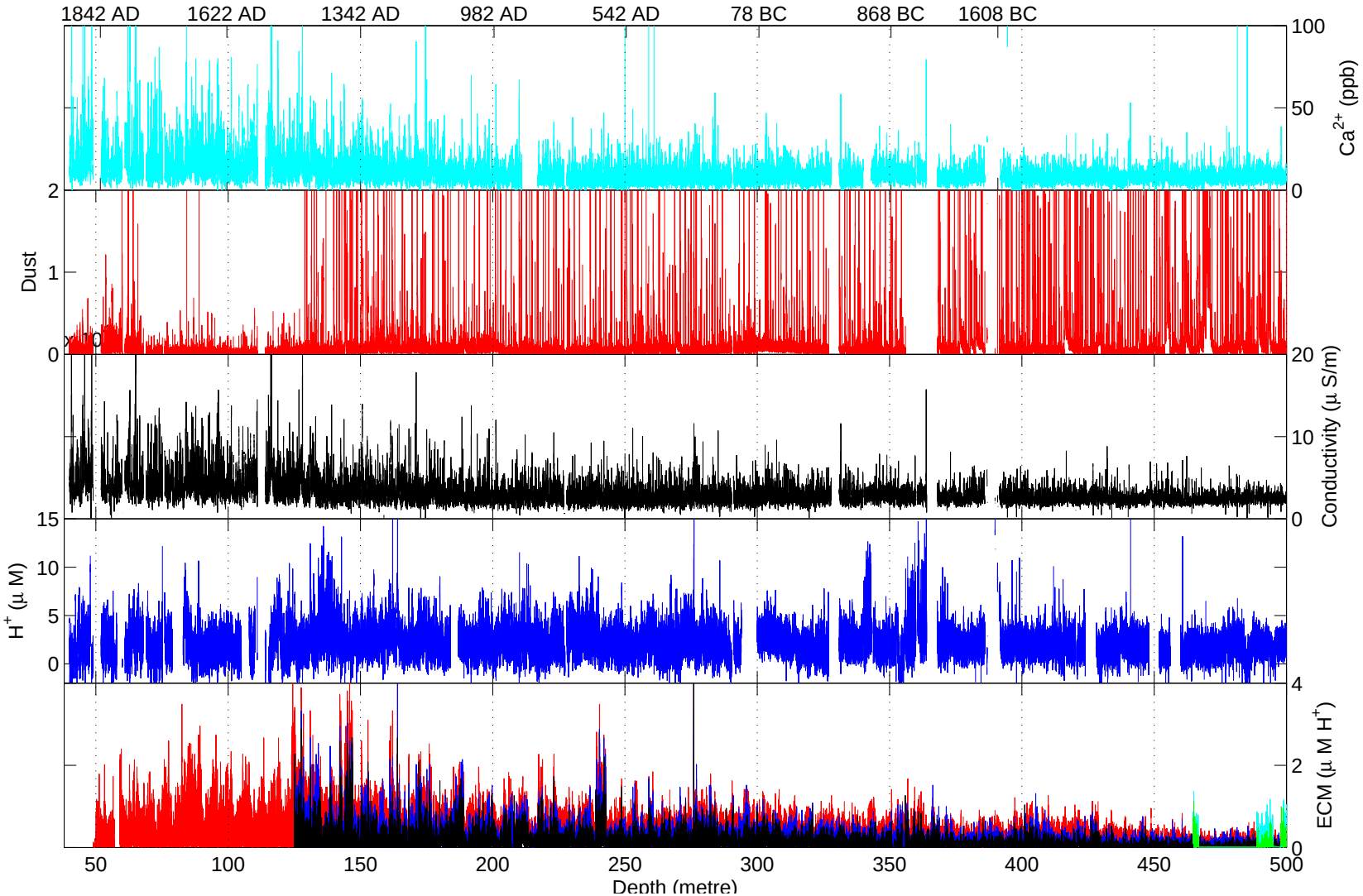

Fig. 8.4: The RICE CFA record. From the top is shown Calcium (blue), Dust (red), Conductivity (black), Dye determined H^+ (blue) and ECM determined 'H^+'. In the bottom panel the different colors show the variability in ECM for different runs on the same section of ice.

with depth. Note also how multiple runs with the ECM instrument gives a slightly different base signal.

The optical dye method has some areas where the concentration is high as compared to the mean, such as around 140, 340 and 370 metres depth. These are most likely the result of poor calibration or air bubbles interfering. These sections are not removed as, even if the calibration is dubious, they are useful to identify volcanic eruptions. The section at around 370 m were removed for dust as it was highly effected by air, likely this air is what causes the dye optical method to record enhanced H^+ in the area. Some sections are also not shown for the H^+_{dye} record whether as a result of corrupted data files or missing baselines. The mean H^+ signal is 2.5 μM H^+ with the highest peak reaching 24 μM H^+. The mean concentration of H^+ found using this dye method is thus similar to the mean concentration of 2.03 μeq found by the method of *Pasteris et al.* [2012] observed in an ice core from Dronning Maud Land, East Antarctica covering the past 2000 yrs [*Pasteris et al.*, 2014]. *Pasteris et al.* [2014] also found evidence of decreased acidity during the little ice age (1300-1900 AD). The RICE ice core H^+ dataset needs to be thoroughly checked for artefacts such as from air bubbles before any investigation of such long term decreases can be addressed.

The mean Ca^{2+} signal is 17 ppb Ca^{2+} in the top 130 metres, with single peaks reaching more than 100 ppb Ca^{2+}.

The conductivity, calcium and the optical dye method all worked well. Contrarily, the continuous dust record is subject to high peaks starting from 130 metres depth and downwards. The dust record peak to unreasonable numbers whenever a break between coherent ice samples (100 cm) was introduced (Figure 8.5). This suggest that the method is influenced by the presence of drill liquid, which was added exactly from 130 metres depth. Drill liquid (estisol and coasol oil) is sticky and hangs in the line of the CFA system. The effect during the RICE melt camapaign in 2013 grew over time and at the end of the campaign the sticky drill liquid affects the measurements during longer periods of time than in the beginning of the campaign. Further the brittle zone was entered with depth making the drill liquid a larger problem. The brittle zone is a fragile zone, with multiple breaks and intrusions of drill liquid were observed in visual investigations. While the dust record could possibly be cleaned the dust record was for this study not used below 130 metres. Luckily the effect of drill liquid was not observed in any of the other CFA systems, but unfortunately it may very well effect the discrete samples obtained for analysis of IC (e.g. acetate and formate) and ICP-MS.

8.3.1 Covariation of Calcium and H^+

The relationship between the dye determined H^+ and the melt water conductivity in the RICE ice core is very different from the relationship found in the Greenland NEEM record. This difference is caused by high loads of sea salt in the coastal influenced RICE record.

As also mentioned in section 7 a strong covariation of MWEC and calcium to H^+ concentration as determined by the dye method was observed (see e.g. Figure 8.6). This anti-correlation could be explained by multiple processes:

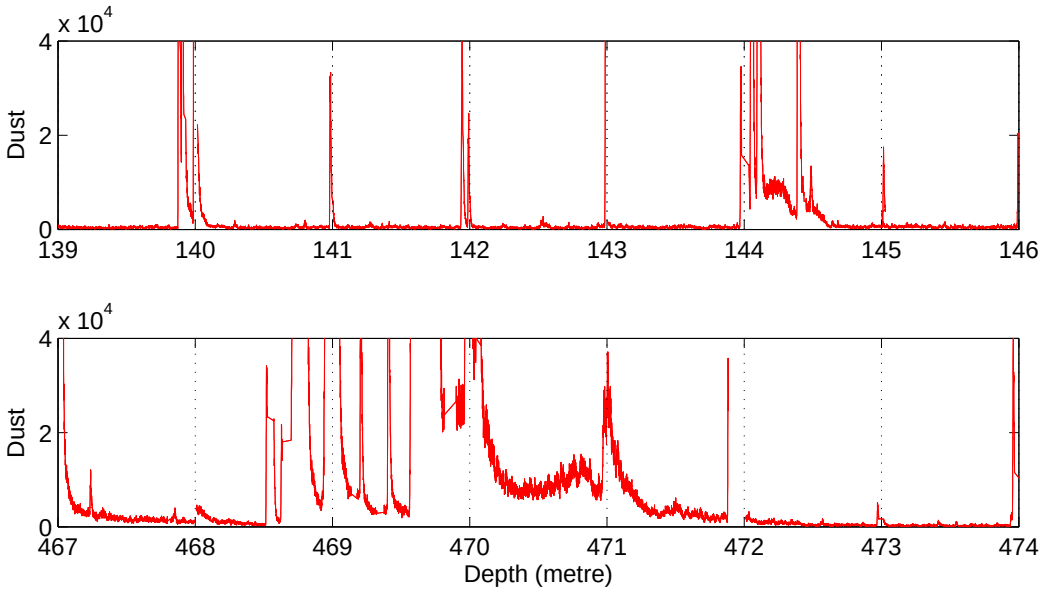

Fig. 8.5: Dust as determined in the RICE ice core. Clearly at breaks (whole metres) some contamination is introduced which hangs in the system and is only slowly removed.

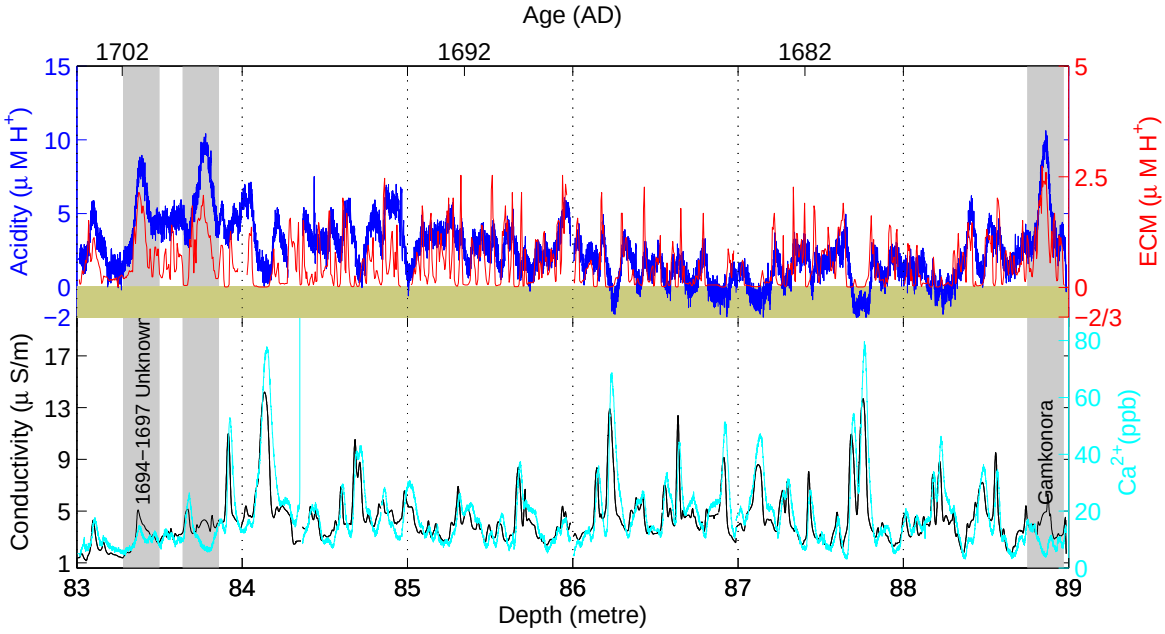

Fig. 8.6: RICE data covering the depth 83-89 m. Top) Acidity determined using the optical dye method (blue) and acidity determined by ECM (red). Bottom) Calcium (cyan) and melt water conductivity (black). Vertical grey bars indicate eruptions determined by the H^+_{dye} exceeding 3 standard deviations. Dating shown for the x-axis is as determined from methane comparisons to the WAIS record.

1) In January (austral summer) primary production peak and DMS is formed over the ocean. During transport the DMS is transformed to MSA and SO_4^{2-} causing an acidity peak in the RICE record. Contrary the Ca^{2+} signal in Antarctica is a mixture of both a summer peak of crustal origin and a marine peak in winter time from sea salts. In inland Antarctica Ca^{2+} from sea salt is only a small fraction of the total Ca^{2+} arriving at site, however at the RICE site the ocean is nearby. While sodium was not determined in the RICE ice core yet, two shallow cores were obtained nearby the RICE site and yield Na^+ up to a concentration of 300 ppb (personal correspondence Nancy Bertler). Thus making the sea salt derived calcium in the order of 11 ppb. This is enough to explain a large part of the Ca^{2+} signal found in the RICE ice core (17 ppb Ca^{2+} in the top 130 metres). Thus I find it likely that the winter sea salt peak drives the most of the signal and that the difference in seasonality to SO_4^{2-} and MSA causes the antiphase between Ca^{2+} (and MWEC) and H^+ observed in the RICE record.

2) Dust and volcanic source areas in the proximity of the RICE ice core site consist of calc-alkaline rocks rich on CaO and Mg^{2+}[*Storey et al.*, 2013]. Thus the acidity of the ice in relation to dust from such local regions is towards more alkaline ice:

$$CaO + H_2O \rightarrow Ca(OH_2) \rightarrow Ca^{2+} + 2OH^- \tag{8.1}$$

The volcanic magma from the area is alkaline rich (phonolite, trachyte and rhyolite) too and during an eruption $CaSiO_3$ is capable of neutralising the acidity:

$$CaSiO_3 + CO_2 \rightarrow CaCO_3 + SiO \tag{8.2}$$
$$CaCO_3 + HCl \rightarrow CaCl + CO_2 + H_2O \tag{8.3}$$
$$\tag{8.4}$$

To investigate how the different calcium sources effect H^+_{dye}, calcium was split into a volcanic, sea salt and dust groups based on the relationship to conductivity and insoluble dust: A 'volcanic' imprint was defined as Ca^{2+} being smaller than MWEC ($Ca^{2+} < \text{MWEC}\cdot\frac{100}{22} - 10$), a dust source was chosen when insoluble dust exceeded 3000 # /mL and a 'seasalt' mode was defined for the Ca^{2+} which was not dust and exceeded MWEC ($Ca^{2+} > \text{MWEC}\cdot\frac{100}{22} + 10$). The relationships between H^+ and calcium with these different imprints are shown in Figure 8.7. In appendix E additional plots of Ca^{2+}, MWEC, insoluble dust and H^+ illustrate the boundaries used to define volcanic, sea salts and dust derived fractions.

The Ca^{2+} from sea salt as defined above had a small impact on H^+ concentrations measured ($-0.032\cdot Ca^{2+}+2 = H^+$, $R = -0.35$). The dust-Ca^{2+} had a slightly larger impact ($-0.088\cdot Ca^{2+}+4 = H^+$,$R = -0.46$), while the Ca^{2+}, which was recorded simultaneously with volcanic eruptions had a significant impact ($-0.11\cdot Ca^{2+}+5 = H^+$,$R = -0.46$). The more significant impact from dust and volcanic sources relative to calcium from the ocean is not surprising as $CaCO_3$ and CaO would directly influence the acidity, while if the source of Ca^{2+} is sea salts Ca^{2+} and H^+ could be deposited simultaneously as result of annual variability in the two.

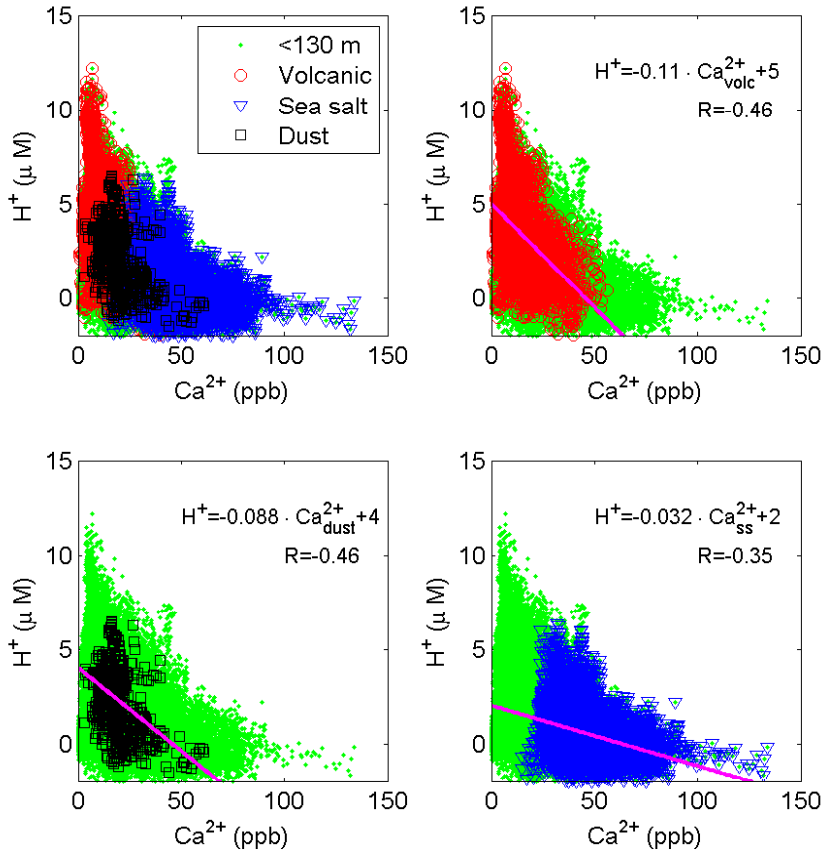

Fig. 8.7: RICE H^+ and Ca^{2+} in the RICE record plotted against each other. Colors indicate sources; all sources (green), volcanic origin (red, shown top right), dust sources (black, shown bottom left) and sea salt derived (blue, bottom right). Also shown is linear correlations and correlation coefficients.

8.3.2 Volcanic layers in the RICE record

Multiple peaks related to volcanic eruptions are observed in the RICE H^+_{dye} record (see e.g. Figure 8.13). Some of the stronger volcanic peaks are identified by the dye optical method only by assigning peaks larger than 3 times the standard deviation as volcanic eruptions (grey bars in Figures 8.6, 8.8 to 8.10, and Figure 8.12 and 8.13). Other smaller peaks, possibly also related to volcanic layers, are identified by comparing ECM and the optical dye method, as well as comparing with excess peaks observed in MWEC as compared to calcium.

A preliminary time scale was provided by T.J. Fudge[2]. He used a flow model to create an age model for the RICE ice core, constrained by a transfer of the WAIS ice core timescale (WDC06A-7). The transfer was performed by matching up the methane signal determined in the RICE and WAIS ice cores. The transfer of the time scale using methane as a constraint was done by Thomas Blunier[3] and James Lee [4]. Further the transfer of the gas age time scale to the ice age timescale requires knowledge of the lock in depth and Δage[5]. James Lee found, while assuming a constant climate over time, that the Δage was 130.8 years. While the WAIS time scale transferred to RICE is based on assumptions, it is accurate to about $\pm$ 20 years. This is the time scale provided for Figures 8.6 to 8.13.

Next step to get an accurate time scale is to determine and count annual layers in the ice. Identifying individual volcanic peaks are crucial to constrain the annual layer counting. By mainly using the list of volcanic eruptions in the nearby WAIS ice core *Sigl et al.* [2013], but also adding information from other Antarctic ice core records, the exact age, and for some peaks also the origin, of the volcanic eruptions was identified (Table 8.1) and is discussed below. A full list of the volcanoes seen in the RICE ice core on a depth scale with some age constraints as found using the method described above is available in appendix E.

Unknown 1694-97 AD and Gamkonora, Indonesia 1673-76

A section of the RICE ice core from 83 to 89 metres depth is shown in Figure 8.6. Two volcanoes are identified in this section. The 1694-1697 yr AD unknown volcano occur over two years (8.4 μM H^+ and 9.1 μM H^+), while the Gamkonora (VEI 5, 9.3 μM H^+), Indonesian eruption identified at the ages 1673-1676 yr AD in the WAIS record show up as a single year event in the RICE record. The magnitude of the two volcanoes follow the peaks identified by *Sigl et al.* [2013] (WAIS) and *Plummer et al.* [2012] (Law Dome) well, where the Gamkonora event is smaller than the unknown 1694-97 volcanic event. The annual layer thickness in the area would be in the order of 0.25 m if these volcanoes are correctly identified.

[2] PhD student at University of Washington, USA

[3] Professor at Centre for Ice and Climate, Niels Bohr Institute, University of Copenhagen, Denmark

[4] PhD student at College of Earth, Ocean, and Atmosheric Sciences, Oregon State University, Corvallis, OR, USA

[5] see Figure 9.1 for an illustration of lock in depth and Δage definitions

Tab. 8.1: Selected volcanic eruptions with their age and magnitude in the West Antarctic ice cores RICE and WAIS ice cores. Positive ages indicate years AD and negative ages indicate years BC.

Age of eruption WAIS timescale	RICE this study H^+_{dye} (μM)	WAIS *Sigl et al.* [2013] SO_4^{3-} (kg km^{-2})
1694 Unknown	10	39
1673 Gamkonora, Indonesia	10	12
1504 Unknown	6	8
1458 Kuwae	12	104
1452/53 Unknown	9	8
1447 Unknown	10	8
1277	8	32
1271	20	20
1259 Samalas, Indonesia	20	80
262	24	17
233 Taupo, New Zealand	8	13
-107	6	25
-159	7	8
-182	4	16

Unknown 1504 AD and a new unknown ∼1490 AD

In the section covering 121 to 126 metres depth (Figure 8.8) two volcanic eruptions are identified at depths 122.7 and 125.2 metres depth respectively. The volcano at 122.7 metres depth is the small unknown volcano observed in 1505-1508 AD in the WAIS ice core. If applying an annual layer thickness of 0.18 m the other peak at 125.2 metres depth is deposited around year 1490 AD. Such an event was not identified in any other records from Antarctica [*Castellano et al.*, 2004; *Ferris et al.*, 2011; *Plummer et al.*, 2012; *Sigl et al.*, 2013]. However the height of the ECM combined with the offset of the conductivity from the calcium indicate that the event is real.

Kuwae 1458/1459 AD

In Figure 8.9 a section from 130 to 135 metres depth is shown. The section cover the Kuwae eruption (131.05 and 131.2 m depth). In Figure 8.9 the purple area indicate an area, where the H^+_{dye} is enhanced. However the calcium present diminishes the H^+_{dye} signal in between, causing it to be highly variable rather than one big eruption.

The Kuwae eruption is the 7th biggest caldera eruption in the last 10000 yrs and is assigned a VEI 7 [*Monzier et al.*, 1994]. The eruption is found in multiple other Antarctic ice cores as a large eruption at an age between 1458-1461 AD [*Ferris et al.*, 2011; *Plummer et al.*, 2012; *Sigl et al.*, 2013], and can even be observed in Greenland records, though as a minor eruption [*Plummer et al.*, 2012; *Sigl et al.*, 2013]. The section also holds other eruptions eg. the unknown volcano of 1447 which is identified in also in the WAIS record [*Sigl et al.*, 2013]. In the WAIS record

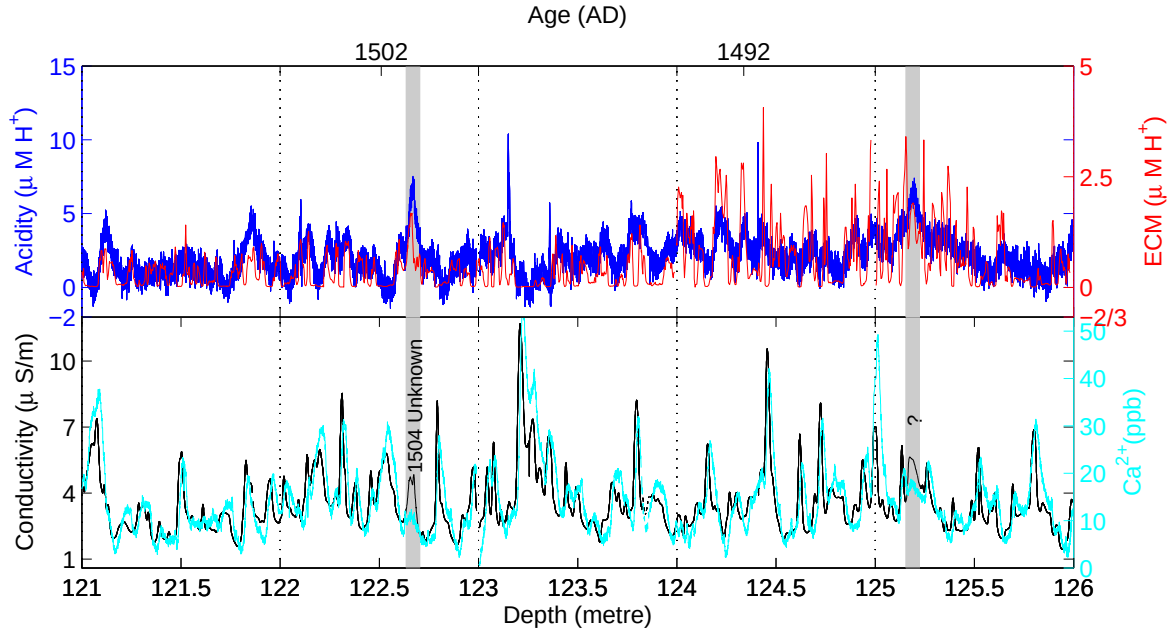

Fig. 8.8: RICE data covering the depths 121-126 m. Top) Acidity determined using the optical dye method (blue) and acidity determined by ECM (red). Bottom) Calcium (cyan) and melt water conductivity (black). Vertical grey bars indicate eruptions determined by the H^+_{dye} exceeding 3 standard deviations. Dating shown for the x-axis is as determined from methane comparisons to the WAIS record.

a peak at 1452/1453 AD [*Sigl et al.*, 2013] was also observed, that peak was not identified in the RICE record. The unknown volcano in 1447 yr AD is likely a local one as it does not show up in the eastern Antarctic records.

1257/59 AD Unknown and 1271 AD Unknown

Figure 8.10 show an interesting section with two very large volcanic eruptions both reaching 20 μM H^+_{dye}. Multiple smaller volcanoes are also identified. The two large volcanoes were identified as the 1257-59 AD and 1271 AD volcanoes making the annual layer thickness approximately 0.16 m. Further, also a smaller volcano, potentially identical to the 1276.5-1278.7 AD volcano as identified in the WAIS record, was observed. Thus all three peaks are found both in WAIS [*Sigl et al.*, 2013] and RICE ice cores as well as in the SP04 (south pole) ice core record[*Ferris et al.*, 2011]. In the Law Dome ice core record from East Antarctica only the eruptions at 1258 yr AD and and 1271 yr AD are identified. This could indicate that the smaller 1277 AD peak is from a local West Antarctic source, while the other two peaks (1271 AD and 1258 AD) are from other regions of Antarctica or from outside Antarctica.

The eruption at 1257 AD is a significant eruption observed in both hemispheres and estimate of its load vary from 2 to 8 times that of Tambora. The 1257 volcano is assigned a VEI 7. However its origin has been disputed and suggestions of two separate volcanoes one in each hemisphere has been proposed. Based on evidence from multiple methods, such as tephra geochemistry and chronicles *Lavigne et al.* [2013] identified the 1257 AD volcano as an eruption of the Samalas volcano in

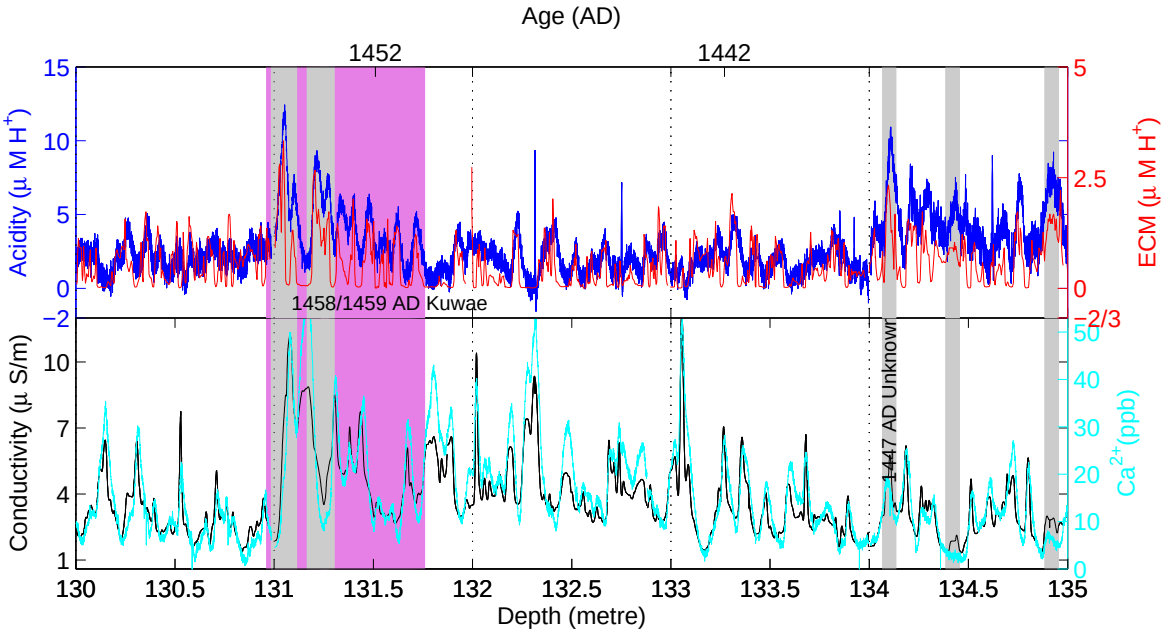

Fig. 8.9: RICE data covering the depth 129.8-132.0 m. Top) Acidity determined using the optical dye method (blue) and acidity determined by ECM (red). Bottom) Calcium (cyan) and melt water conductivity (black). Vertical grey and blue bars indicate eruptions determined by the H^+_{dye} exceeding 3 standard deviations. Blue bars indicate that the eruptions could not be identified in ECM, grey are clearly identified also in ECM. Vertical purple bars are volcanoes identified by eye, based on ECM, acidity (dye method) and conductivity. Dating shown for the x-axis is as determined from methane comparisons to the WAIS record.

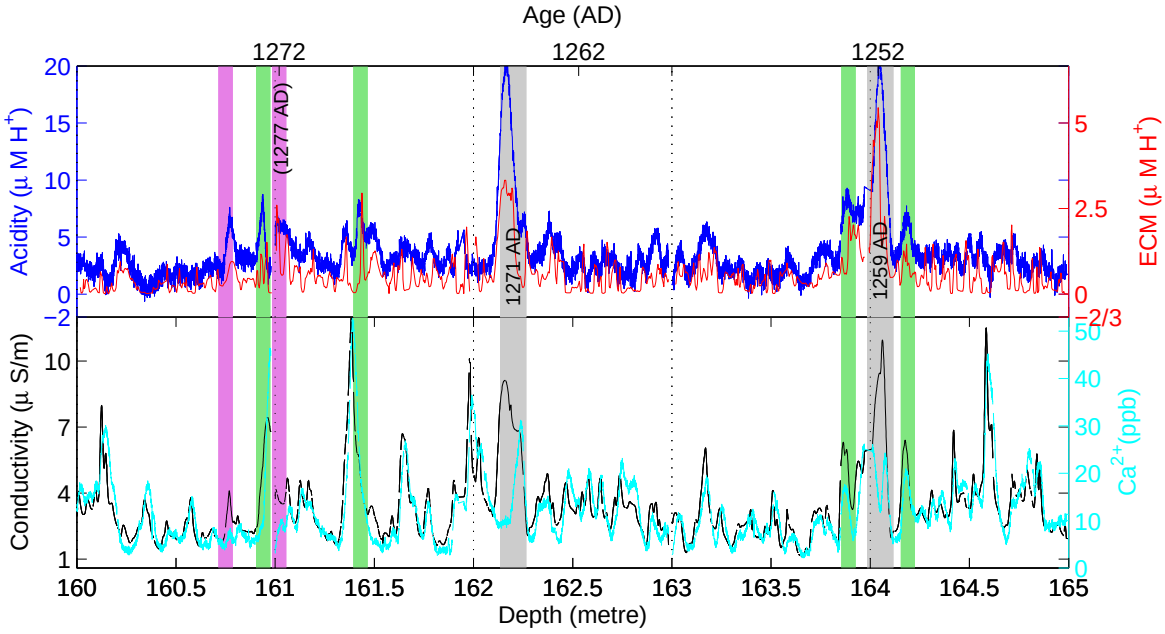

Fig. 8.10: RICE data covering the depths 160-165 m. Top) Acidity determined using the optical dye method (blue) and acidity determined by ECM (red). Bottom) Calcium (cyan) and melt water conductivity (black). Vertical grey and blue bars indicate eruptions determined by the H^+_{dye} exceeding 3 standard deviations. Blue bars indicate that the eruptions could not be identified in ECM, grey are clearly identified also in ECM. Vertical purple bars are volcanoes identified by eye, based on ECM, acidity (dye method) and conductivity. Dating shown for the x-axis is as determined from methane comparisons to the WAIS record.

Indonesia. They found evidence for at least 43 km^3 of tephra deposited as a result of the eruption and argue that the eruption column made it to 43 km height and thus high into the stratosphere.

Lavigne et al. [2013] also mention potential impacts from the volcanic eruption in London, where mass burial of thousands of skeletons is dated to 1258 AD believed to be a result of poor crops that year. But also mention that the local impact was severe in form of a potential "Pompei of the far east" at the capital Pamatan of the Lombok empire in Indonesia.

Narcisi et al. [2012], who identified tephra layers in the Talos Dome ice core, found a tephra layer at 86 metres depth and dated it to 1256 AD (±7 yr). We found an ash layer in the RICE ice core at 1250 AD. *Narcisi et al.* [2012] found that the tephra in Talos Dome is similar to what is expected from the Antarctic Melbourne and Mt. Berlin volcanoes by the use of wavelength-dispersive X-ray spectrometry. They also identified a layer of age 1280 AD prescribed Melbourne. The discussion of the source of the 1257-59 AD volcano(es) is not yet settled.

262 AD

The largest eruption in the record was observed in the depth of 276.06 metre reaching 24 μM H^+_{dye}. Choosing the origin for this eruption is however no easy task. In the WAIS divide ice core some eruptions around that period are; 262 AD Unknown (17.4

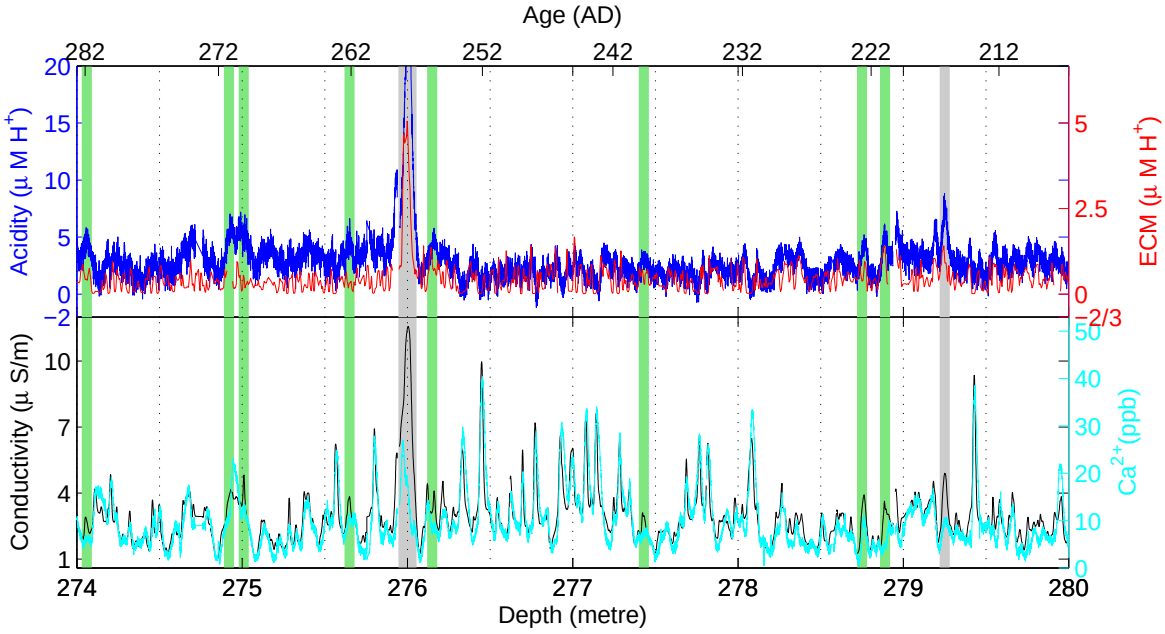

Fig. 8.11: RICE data covering the depth 274-280 m. Top) Acidity determined using the optical dye method (blue) and acidity determined by ECM (red). Bottom) Calcium (cyan) and melt water conductivity (black). Vertical grey bars indicate eruptions determined by the H^+_{dye} exceeding 3 standard deviations, green bars are peaks identified by eye, based on ECM, acidity (dye method) and conductivity.

kg/km SO_4^{3-}), 233 AD Taupo, New Zealand (13.2 kg/km SO_4^{3-}), 213 AD Unknown (8.6 kg/km SO_4^{3-}). If assigning the large peak of 24 μM H^+_{dye} to the 262 AD Unknown volcano found at WAIS, several choices are available for assigning the other peaks. If the peak observed in the RICE record at 279.3 m depth is assigned the Taupo eruption the annual layer thickness will be about 0.11 m. However in other records the VEI 6 Taupo eruption is dated quite different *eg.* 229 AD by *Plummer et al.* [2012], while earlier estimates were 181 AD. Tree ring evidence of carbon, dates the Taupo eruption to 233±13 AD [*Sparks et al.*, 1995]. *Ferris et al.* [2011] working with an East Antarctic core found volcanic peaks at 261, 244 and 241 AD, but no peak at 233 AD.

As the dating is constrained by the methane comparison to the WAIS ice core and is estimated to be below 15 yrs off at this particular depth there is not too much wiggle matching that can be done. My best estimate is that the large volcano is the 262 AD unknown and I suggest that it is a local West Antarctic volcano as it is not observed strongly in any of the other ice cores. The 231 AD Taupo could be the other peak identified using 3 standard deviations above the mean for the $[H^+]$ determined by the optical dye method. This would make the other peaks date 233 AD, 234 AD, 247 AD, 260 AD, 262 AD, 271 AD and 281 AD when assuming a constant annual layer thickness of 0.11 m. Neither of those additional identified volcanoes in the RICE record are observed in the WAIS record. Whether these additional peaks are truly volcanic peaks can be further investigated when sulphate is available from the discrete IC samples.

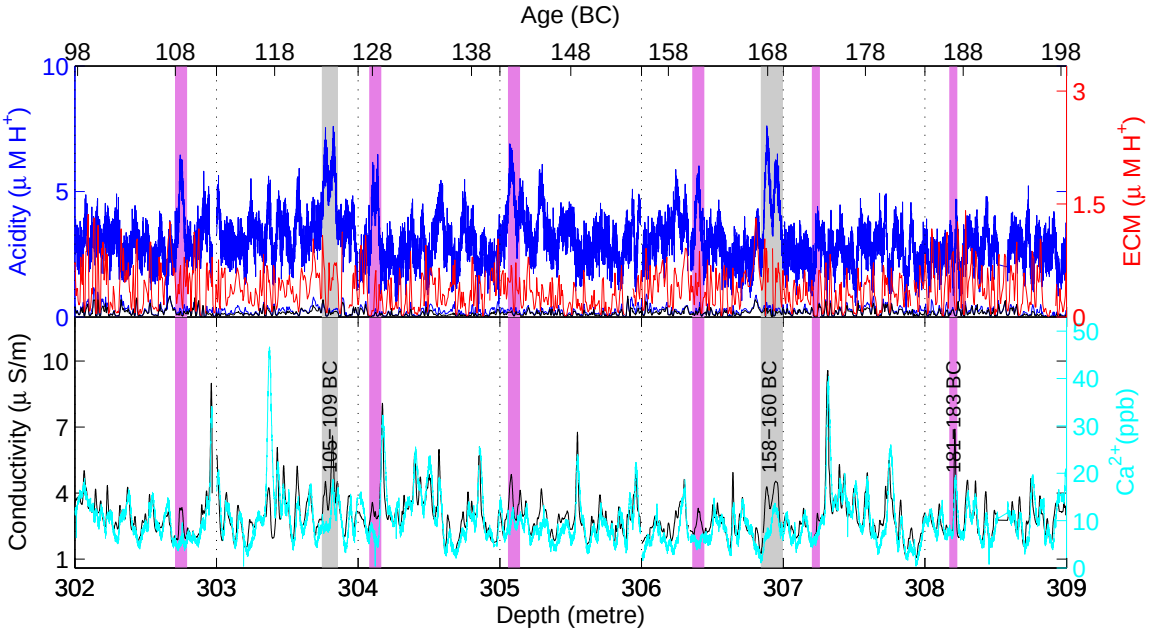

Fig. 8.12: RICE data covering the depth 302 to 309 m. Top) Acidity determined using the optical dye method (blue) and acidity determined by ECM (red). Bottom) Calcium (cyan) and melt water conductivity (black). Vertical grey bars indicate eruptions determined by the H^+_{dye} exceeding 3 standard deviations. Vertical purple bars are volcanoes identified by eye, based on ECM, acidity (dye method) and conductivity.

~100 BC

As evident already from the previous section the volcanic match making gets more complicated with depth. This is partly due to lack of precise dating of volcanoes, partly due to lack of temporal resolution with depth and partly as a result of the preliminary time scale produced by match making to other records becoming more uncertain with depth. In Figure 8.12 a section at the depth 302 to 309 metre is shown. According to the preliminary dating the section covers from 180 to 98 yrs BC. In the WAIS record a set of unknown eruptions are identified at this age; 107 BC, 146 BC, 159 BC and 182 BC. The best matching is 107 BC, 159 BC and 182 BC with the depths 303.77, 306.89 and 308.20 m. If this is the right matching the annual layer thickness between the sections are 0.09 m and 0.06 m respectively, which is not unreasonable given the depth. However the certainty of this assignment is low.

Age unknown >2050 BC

The peak shown in Figure 8.13 is the largest eruption recorded between 300 and 500 metres depth in the RICE ice core. According to the preliminary dating the peak is more than 4000 yrs old. The peak height is 13 μM H^+_{dye}. However at this depth dispersion of the individual signals occurring due to the CFA system could cause significant smoothing. Thus after a deconvolution of the signal[6] the eruption

[6] see section 1.2.3

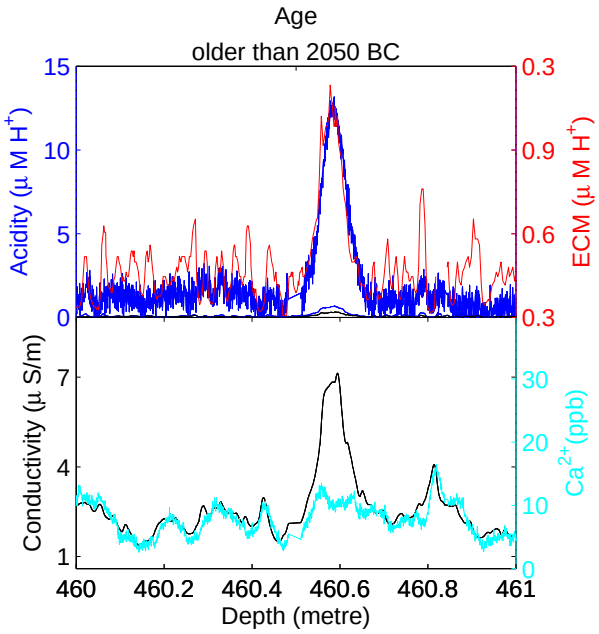

Fig. 8.13: RICE data covering the depth 460-461 m. Top) Acidity determined using the optical dye method (blue) and acidity determined by ECM (red). Bottom) Calcium (cyan) and melt water conductivity (black).

likely would be of even greater magnitude. The *Sigl et al.* [2013] record of Volcanic eruptions as determined in the WAIS ice core only reach back to 405 BC, and the *Ferris et al.* [2011] only to year 0. The record by *Cole-Dai et al.* [2000] from East Antarctica reach back to 2000 BC. The record from Dome C however reach back to 8000 BC [*Castellano et al.*, 2004]. In Dome C peaks are identified at 2288, 2389 and 2509 yr BC, however neither of these peaks are exceptionally big compared to younger volcanoes. In the Talos Dome ice core evidence of tephra layers at ages 2470 ($\pm$ 88) yr BC with a source region outside of Antarctica is found [*Narcisi et al.*, 2012].

8.3.3 Outlook on the RICE dataset

The RICE dataset presented here is a preliminary version of the dataset we hope to publish. The dataset is not yet checked for artefacts such as introduced by air bubbles which could cause 'false' volcanoes and some sections are still not processed due to corrupt files or poor baseline. Some of these poor sections include the Tambora eruption in 1815, expected somewhere at RICE depths 57-61 metres and an unknown volcano in 1809 AD, which would be very helpful in accurately dating the top section. Further there is evidence that at deeper depths the CFA depth scale is off as compared to the ECM; This was e.g. the case in Figure 8.11 at depth 270 metres where the CFA records were shifted by 0.05 metre to match the ECM for the section, while at depth 460 metre (Figure 8.13) the shift had increased to 0.16 m suggesting that the offset is slowly increasing over time. Why this is occurring I have not been able to identify; Each bag ($\sim$100 cm) melted, when cut from the original 3 metres drilled in a run, is not always exactly 100 cm, sometimes they are

99.9 cm sometimes 100.2 cm. These variations from the intended 100 cm are always carefully logged. If either the CFA depth recording or the ECM depth recording is not using the true length of the cores it could explain the discrepancy. Due to the additive effect of the bag lengths, but also due to the thinning of layers with depth the discrepancy is enough to offset age models and also complicates talking about data with colleagues about volcanoes at large depth. It is crucial that the cause of the offset is identified and corrected before an age model can be established for the deeper part of the record.

The RICE dataset is not yet complete. The bottom 200 metres are being analysed as this is written (summer 2014). We hope that the remainder of the record will help constrain the ages by comparisons to other ice core records of the transition from glacial to interglacial. We also expect to find the well known volcanic event "old faithful" at about 17.5 kyr BP, which appear through Antarctic ice cores [*Jacobel and Welch*, 2005]. Further the bottom 50 metres of the record is expected to hold the glacial and it will be interesting to observe what the new high resolution acidity proxy method using optical dye will look like in such a different climate state.

8.4 Outlook on the pH method

A method for the continuous determination of pH in ice cores was developed as part of this study. The $[H^+]$ found using the method follows the amount of $[H^+]$ found based on the ionic budget in the acid layer of the 1259 AD volcano in the Greenland NGRIP ice core and also show similar history over the past 100 yrs as to that observed using the method by *Pasteris et al.* [2012]. However the two methods were used on different firn cores. The method is applicable as is for the determination of acid layers and was used on the Antarctic RICE ice core as a means of determining volcanic reference layers as well as for annual layer counting.

The method is not absolutely calibrated, however, and remain to be tested, against other methods available, on more alkaline ice samples. This is to evaluate the potential more-severe effect of CO_2 on such ice samples. The NGRIP ion data set is in 5 cm resolution down to 1371.15 metres depth. Thus to make a high resolution comparison to the ion budget derived H^+, while evaluating the method on more alkaline ice we wish to investigate a section of about 5 metres covering some alkaline peaks during the Holocene, e.g. in relation to large depositions of NH_4^+. Such a section could be the section from 180 to 187 metres depth (about 50 yrs within the 12th century), which holds several alkaline peaks; 2 in relation to NH_4^+ and 3 in relation to Na^+.

To evaluate the effect of carbonates, pH using the dye method should be determined in a glacial section of a Greenland ice core. Below a depth of 1371.15 metres the IC measurements are made in 55 cm resolution. Thus a comparison to the ion budget in the more alkaline glacial part of the NGRIP ice would require several metres of ice to be melted, to ensure enough data points. For the NEEM ice core IC resolution is 110 cm in the deep part, however, most of the ions are also determined using high resolution CFA making a high resolution comparison possible.

Further using a set up where first the $[H^+]$ is determined by the method presented here, then on the same line a CO_2 bubbling unit is added and after the unit another

heat bath and accurel to remove the CO_2 is added before the H^+ concentration of the sample is re-measured by a optical means. In such a set up the difference between the two measurements would be related to the CO_2 uptake and could be used to quantify the CO_2 effect on the method.

If an effect of the CO_2 was observed. A similar set up could be used to determine if the surfactant Brij L23 does influence the uptake of CO_2 by varying the amount of the surfactant in the reagent.

The ice itself could also hold buffering substances and thus ideally the experiment should be performed on real ice samples.

REFERENCES 'PH' DETERMINED IN ICE

Anthoni, J. F. (2005), pH meter principles, http://www.seafriends.org.nz/dda/ph.htm.

Arfeuille, F., D. Weisenstein, H. Mack, E. Rozanov, T. Peter, and S. Brönnimann (2013), Volcanic forcing for climate modeling: A new microphysics-based dataset covering years 1600-present, *Clim. Past. Discuss.*, *9*(1), 967–1012, doi:10.5194/cpd-9-967-2013.

Barnes, P., E. W. Wolff, R. Mulvaney, R. Udisti, E. Castellano, R. Röthlisberger, and J.-P. Steffensen (2002), Effect of density on electrical conductivity of chemically laden polar ice, *J. Geophys. Res.*, *107*(B2), 2029.

Barrie, L., D. Fisher, and R. Koerner (1985), Twentieth century trends in Arctic air pollution revealed by conductivity and acidity observations in snow and ice in the Canadian High Arctic, *Atmospheric Environment (1967)*, *19*(12), 2055 – 2063, doi:10.1016/0004-6981(85)90114-3.

Bhargava, S., and S. Bhargava (2013), Ecological consequences of the acid rain, *IOSR Journal of applied chemistry*, *5*(4), 19–24.

Bigler, M., D. Wagenbach, H. Fischer, J. Kipfstuhl, H. Miller, S. Sommer, and B. Stauffer (2002), Sulphate record from a northeast Greenland ice core over the last 1200 years based on continuous flow analysis, *Ann. Glaciol.*, *35*(1), 250–256.

Bigler, M., A. Svensson, J. P. Steffensen, and P. Kaufmann (2007), A new continuous high-resolution detection system for sulphate in ice cores, *Annals of Glaciology*, *45*(1), 178–182.

Bigler, M., A. Svensson, E. Kettner, P. Vallelonga, M. E. Nielsen, and J. P. Steffensen (2011), Optimization of high-resolution continuous flow analysis for transient climate signals in ice cores, *Environ. Sci. Technol.*, *45*(10), doi:10.1021/es200118j.

Brucat, P. J. (2014), http://www.chem.ufl.edu/ itl/4411/lectures/lec_z2.html.

Castellano, E., S. Becagli, J. Jouzel, A. Migliori, M. Severi, J. Steffensen, R. Traversi, and R. Udisti (2004), Volcanic eruption frequency over the last 45 ky as recorded in Epica-Dome C ice core (East Antarctica) and its relationship with climatic changes, *Global and Planetary Change*, *42*(1), 195–205.

Cha, W. (2014), pH review, http://isbchem1.pbworks.com/w/page/9206118/pH%20Review.

Clausen, H., and C. Hammer (1988), The Laki and Tambora eruptions as revealed in Greenland ice cores from 11 locations, *Ann. Glaciol.*, *10*, 16–22.

Cole-Dai, J., E. Mosley-Thompson, S. P. Wight, and L. G. Thompson (2000), A 4100-year record of explosive volcanism from an East Antarctica ice core, *Journal of Geophysical Research: Atmospheres (1984–2012)*, *105*(D19), 24,431–24,441.

Curran, M. A., T. D. Van Ommen, and V. Morgan (1998), Seasonal characteristics of the major ions in the high-accumulation Dome Summit South ice core, Law Dome, Antarctica, *Ann. Glaciol.*, *27*, 385–390.

Dansgaard, W., S. J. Johnsen, H. B. Clausen, D. Dahl-Jensen, N. S. Gundestrup, C. U. Hammer, C. S. Hvidberg, J. P. Steffensen, A. E. Sveinbjörnsdottir, J. Jouzel, and other GRIP members (1993), Evidence for general instability of past climate from a 250-kyr ice-core record, *Nature*, *364*(6434), 218–220.

Davies, S. M., S. Wastegård, T. L. Rasmussen, A. Svensson, S. J. Johnsen, J. P. Steffensen, and K. K. Andersen (2008), Identification of the Fugloyarbanki tephra in the NGRIP ice core: a key tie-point for marine and ice-core sequences during the last glacial period, *Journal of Quaternary Science*, *23*(5), 409–414.

Delmas, R., M. Briat, and M. Legrand (1982), Chemistry of south polar snow, *J. Geophys. Res.*, *87*(C6), 4314 – 4318.

Dickson, A., and J. Riley (1979), The estimation of acid dissociation constants in seawater media from potentionmetric titrations with strong base. I. The ionic product of water–Kw, *Marine Chemistry*, *7*(2), 89–99.

Dong, Z., M. Zhang, Z. Li, F. Wang, and W. Wang (2009), The pH value and electrical conductivity of atmospheric environment from ice cores in the Tianshan Mountains, *Journal of Geographical Sciences*, *19*, 416–426, 10.1007/s11442-009-0416-2.

EPICA community members (2004), Eight glacial cycles from an Antarctic ice core, *Nature*, (431), 623–628.

Farajzadeh, R., A. Barati, H. A. Delil, J. Bruining, and P. L. Zitha (2007), Mass transfer of CO_2 into water and surfactant solutions, *Petroleum Science and Technology*, *25*(12), 1493–1511.

Ferris, D. G., J. Cole-Dai, A. R. Reyes, and D. M. Budner (2011), South Pole ice core record of explosive volcanic eruptions in the first and second millennia AD and evidence of a large eruption in the tropics around 535 AD, *Journal of Geophysical Research: Atmospheres (1984–2012)*, *116*(D17).

Fischer, E. (2006), Volcanic response to tropical eruptions, http://www.cgd.ucar.edu/ccr/efischer/volcanoes.html.

Fischer, H., D. Wagenbach, and J. Kipfstuhl (1998), Sulfate and nitrate firn concentrations on the Greenland ice sheet: 2. Temporal anthropogenic deposition changes, *J. Geophys. Res.: Atm.*, *103*(D17), 21,935–21,942, doi:10.1029/98JD01886.

Fischer, H., M.-L. Siggard-Andersen, U. Ruth, and R. W. E. Röthlisberger (2007), Glacial-interglacial changes in mineral dust and sea-salt records in polar ice cores Sources transport and deposition, *Rev. Geophys.*, *45*(1002).

Fuhrer, K., A. Neftel, M. Anklin, T. Staffelbach, and M. Legrand (1996), High-resolution ammonium ice core record covering a complete glacial inter-glacial cycle, *J. Geophys. Res.*, *101*(D2), 4147–4164.

Galster, H. (2012), pH measurement and control, Ullmann's encyclopedia of industrial chemistry, *Wiley-VCH Verlag GmbH & Co. KgaA, Weinheim*, doi:10.1002/14356007.e19_e01.

Gao, C., A. Robock, and C. Ammann (2008), Volcanic forcing of climate over the past 1500 years: An improved ice core-based index for climate models, *Journal of Geophysical Research: Atmospheres (1984–2012)*, *113*(D23).

Gfeller, G. (2011), Continuous acidity measurements on polar ice cores, Ph.D. thesis, Division for Climate and Environmental Physics.

Hall, J., and E. Wolff (1998), Causes of seasonal and daily variations in aerosol sea-salt concentrations at a coastal Antarctic station, *Atmospheric Environment*, *32*(21), 3669–3677.

Hammer, C. U. (1980), Acidity of polar ice cores in relation to absolute dating, past volcanism, and radioechoes, *Journal of Glac.*, *25*(93), 359–372.

Hammer, C. U., H. B. Clausen, and W. Dansgaard (1980), Greenland ice sheet evidence of post-glacial volcanism and its climatic impact, *Nature*, *288*, 230–235.

Harned, H. S., and R. Davis Jr (1943), The ionization constant of carbonic acid in water and the solubility of carbon dioxide in water and aqueous salt solutions from 0 to 50, *Journal of the American Chemical Society*, *65*(10), 2030–2037.

Harned, H. S., and S. R. Scholes Jr (1941), The ionization constant of HCO^{3-} from 0 to 50, *Journal of the American Chemical Society*, *63*(6), 1706–1709.

Hites, R. A., and J. D. Raff (2012), *Elements of environmental chemistry*, 153-187 pp., John Wiley & Sons.

Iizuka, Y., S. Horikawa, T. Sakurai, S. Johnson, D. Dahl-Jensen, J. P. Steffensen, and T. Hondoh (2008), A relationship between ion balance and the chemical compounds of salt inclusions found in the Greenland Ice Core Project and Dome Fuji ice cores, *Journal of Geophysical Research: Atmospheres (1984–2012)*, *113*(D7).

Iizuka, Y., R. Uemura, H. Motoyama, T. Suzuki, T. Miyake, M. Hirabayashi, and T. Hondoh (2012), Sulphate-climate coupling over the past 300,000 years in inland Antarctica, *Nature*, *490*(7418), 81–84.

Jacobel, R. W., and B. C. Welch (2005), A time marker at 17.5 kyr bp detected throughout west antarctica, *Annals of Glaciology*, *41*(1), 47–51.

Joughin, I., B. E. Smith, and B. Medley (2014), Marine ice sheet collapse potentially under way for the Thwaites Glacier Basin, west Antarctica, *Science*, *344*(6185), 735–738.

Karlöf, L., D. P. Winebrenner, and D. B. Percival (2006), How representative is a time series derived from a firn core? a study at a low-accumulation site on the Antarctic plateau, *J. Geophys. Res.: Earth Surface (2003–2012)*, *111*(F4).

Kaufmann, P. R., U. Federer, M. A. Hutterli, M. Bigler, S. Schüpbach, U. Ruth, J. Schmitt, and T. F. Stocker (2008), An improved continuous flow analysis system for high-resolution field measurements on ice cores, *Environ. Sci. Technol.*, *42*(21), 8044–8050.

Kirshner, A. E., J. B. Anderson, M. Jakobsson, M. O Regan, W. Majewski, and F. O. Nitsche (2012), Post-LGM deglaciation in Pine Island bay, west Antarctica, *Quaternary Science Reviews*, *38*, 11–26.

Koch, W., G. Marinenko, and R. C. Paule (1986), An interlaboratory test of pH measurements in rainwater, *Journal of Research of the National Bureau of Standards*, *91*, 23–32.

Krug, E. C., C. R. Frink, et al. (1983), Acid rain on acid soil: A new perspective., *Science(Washington)*, *217*(4610), 520–525.

Kuenzi, A. M., P. Z. Fulé, and C. H. Sieg (2008), Effects of fire severity and pre-fire stand treatment on plant community recovery after a large wildfire, *Forest Ecology and Management*, *255*(3), 855 – 865, doi:http://dx.doi.org/10.1016/j.foreco.2007.10.001.

Kumai, M. (1985), Acidity of snow and its reduction by alkaline aerosols, *Ann. Glac.*, *6*, 92–94.

Kuramoto, T., K. Goto-Azuma, M. Hirabayashi, T. Miyake, H. Motoyama, D. Dahl-Jensen, and J. P. Steffensen (2011), Seasonal variations of snow chemistry at NEEM, Greenland, *Ann. Glac.*, *52*(58), 193–200, doi:doi:10.3189/172756411797252365.

Lamb, H. H. (1970), Volcanic dust in the atmosphere; with a chronology and assessment of its meteorological significance, *Philosophical Transactions of the Royal Society of London. Series A, Mathematical and Physical Sciences*, *266*(1178), 425–533.

Lavigne, F., J.-P. Degeai, J.-C. Komorowski, S. Guillet, V. Robert, P. Lahitte, C. Oppenheimer, M. Stoffel, C. M. Vidal, I. Pratomo, et al. (2013), Source of the great AD 1257 mystery eruption unveiled, Samalas volcano, Rinjani Volcanic Complex, Indonesia, *Proceedings of the National Academy of Sciences*, *110*(42), 16,742–16,747.

Law, K. S., and A. Stohl (2007), Arctic air pollution: Origins and impacts, *Science*, *315*(5818), 1537–1540.

Legrand, M., and M. De Angelis (1995), Origins and variations of light carboxylic acids in polar precipitation, *Journal of Geophysical Research: Atmospheres (1984–2012)*, *100*(D1), 1445–1462.

Legrand, M., and P. A. Mayewski (1997), Glaciochemistry of polar ice cores: A review, *Reviews of Geophysics*, *35*.

Legrand, M. R., A. J. Aristarain, and R. J. Delmas (1982), Acid titration of polar snow, *Anal. Chem.*, *54*, 1336 – 1339.

Li, X., Z. Li, Y. Ding, S. Liu, Z. Zhao, L. Luo, H. Pang, C. Li, H. Li, X. You, and F. Wang (2007), Seasonal variations of pH and electrical conductivity in a snow-firn pack on Glacier No. 1, eastern Tianshan, China, *Cold Regions Science and Technology*, *48*(1), 55 – 63, doi:10.1016/j.coldregions.2006.09.006.

Li, Z., Y. He, W. Theakstone, W. Jia, H. Xin, W. Zhang, J. Liu, and S. Wang (2010), Characteristics and environmental significance of pH and EC in summer rainfall and shallow firn profile at Yulong Snow Mountain, Lijiang City, China, *Journal of Earth Science*, *21*, 157–165, 10.1007/s12583-010-0014-3.

Likens, G. E., and F. H. Bormann (1974), Acid rain: a serious regional environmental problem, *Science*, *184*(4142), 1176–1179.

Lin, J. (2000), Recent development and applications of optical and fiber-optic pH sensors, *TrAC Trends in Analytical Chemistry*, *19*(9), 541 – 552, doi:10.1016/S0165-9936(00)00034-0.

Marinenko, G., R. C. Paule, W. F. Koch, and M. Knoerdel (1986), Effect of variables on pH measurement in acid-rain-like solutions as determined by ruggedness tests, *Journal Research of the National Bureau of Standards*, *91*, 17–22.

Masterton, W. L., C. N. Hurley, and E. J. Neth (2011a), *Chemistry: Principles and Reactions: 13. Acids and bases*, Cengage Learning.

Masterton, W. L., C. N. Hurley, and E. J. Neth (2011b), *Chemistry: Principles and Reactions: 14. acid-base indicators*, Cengage Learning.

Masterton, W. L., C. N. Hurley, and E. J. Neth (2011c), *Chemistry: Principles and Reactions: 17. Electrochemistry*, Cengage Learning.

McConnell, J. R., G. W. Lamorey, S. W. Lambert, and K. C. Taylor (2002), Continuous ice-core chemical analyses using inductively coupled plasma mass spectrometry, *Environmental science & technology*, *36*(1), 7–11.

McConnell, J. R., R. Edwards, G. L. Kok, M. G. Flanner, C. S. Zender, E. S. Saltzman, J. R. Banta, D. R. Pasteris, M. M. Carter, and J. D. W. Kahl (2007), Microparticle and trace element studies, *Elsevier*, pp. 1207–1211.

Milieu Ltd, t., and the Center for Clean Air Policy (2004), Assesment of the effectiveness of european air quality policies and measures, http://ec.europa.eu/environment/archives/cafe/activities/pdf/case_study1.pdf.

Millero, F. J., T. B. Graham, F. Huang, H. Bustos-Serrano, and D. Pierrot (2006), Dissociation constants of carbonic acid in seawater as a function of salinity and temperature, *Marine Chemistry*, *100*(1), 80–94.

Monzier, M., C. Robin, and J.-P. Eissen (1994), Kuwae (≈ 1425 AD): The forgotten caldera, *Journal of Volcanology and Geothermal Research*, *59*(3), 207–218.

Moore, J. (1993), High-resolution dielectric profiling of ice cores, *Journal of Glac.*, *39*(132), 245–248.

Moore, J., and J. Paren (1987), A new technique for dielectric logging of Antarctic ice cores, *Le Journal de Physique Colloques*, *48*(C1), C1–155.

Moore, J., R. Mulvaney, and J. Paren (1989), Dielectric stratigraphy of ice: A new technique for determining total ionic concentrations in polar ice cores, *Geophysical Research Letters*, *16*(10), 1177–1180.

Moore, J. C., E. W. Wolff, H. B. Clausen, and C. U. Hammer (1992), The chemical basis for the electrical stratigraphy of ice, *Journal of Geophysical Research: Solid Earth (1978–2012)*, *97*(B2), 1887–1896.

Moore, J. C., E. W. Wolff, H. B. Clausen, C. U. Hammer, M. R. Legrand, and K. Fuhrer (1994), Electrical response of the summit-Greenland ice core to ammonium, sulphuric acid, and hydrochloric acid, *Geophys. res. letters*, *21*(7), 565–568.

Myhre, D. S. F.-M. B. W. C. J. F. J. H. D. K. J.-F. L. D. L. B. M. T. N. A. R. G. S. T. T., G., and H. Zhang (2013), *Climate Change 2013: The Physical Science Basis. Contribution of Working Group I to the Fifth Assessment Report of the Intergovernmental Panel on Climate Change*, Cambridge university press.

Narcisi, B., J. R. Petit, B. Delmonte, C. Scarchilli, and B. Stenni (2012), A 16,000-yr tephra framework for the Antarctic ice sheet: a contribution from the new Talos Dome core, *Quaternary science reviews*, *49*, 52–63.

NEEM members (2013), Eemian interglacial reconstructed from a Greenland folded ice core, *Nature*, *493*, 489–494.

NGRIP members (2004), High-resolution record of northern hemisphere climate extending into the last interglacial period, *Nature*, *431*, 147–151.

Pasteris, D., J. R. McConnell, R. Edwards, E. Isaksson, and M. R. Albert (2014), Acidity decline in antarctic ice cores during the little ice age linked to changes in atmospheric nitrate and sea salt concentrations, *Journal of Geophysical Research: Atmospheres*, *119*(9), 5640–5652.

Pasteris, D. R., J. R. McConnell, and R. Edwards (2012), High-resolution, continuous method for measurement of acidity in ice cores, *Environ. Sci. Technol.*, *46*(3), 1659–1666, doi:10.1021/es202668n.

Plummer, C., M. Curran, T. D. van Ommen, S. O. Rasmussen, A. Moy, T. Vance, H. B. Clausen, B. M. Vinther, and P. Mayewski (2012), An independently dated 2000-yr volcanic record from Law Dome, East Antarctica, including a new perspective on the dating of the 1450s CE eruption of Kuwae, Vanuatu., *Climate of the Past*, *8*(6).

Quinn, P. K., G. shaw, E. Andrews, E. G. Dutton, T. Ruoho-Airola, and S. L. Gong (2007), Arctic haze: Current trends and knowledge gaps, *Tellus B*, *59*(1), 99–114, doi:10.1111/j.1600-0889.2006.00238.x.

Raghuraman, B., G. Gustavson, R. E. G. Van Hal, E. Dressaires, and O. Zhdaneev (2006), Extended-range spectroscopic pH measurement using optimized mixtures of dyes, *Applied Spectroscopy*, *60*(12), 1461–1468.

Rasmussen, S., K. Andersen, A. M. Svensson, J. P. Steffensen, B. M. Vinther, H. B. Clausen, M.-L. Siggaard-Andersen, S. J. Johnsen, L. B. Larsen, D. Dahl-Jensen, M. Bigler, R. Röthlisberger, H. Fischer, K. Goto-Azuma, M. E. Hansson, and U. Ruth (2006), A new Greenland ice core chronology for the last glacial termination, *J. Geophys. Res.*, *111*, D06,102.

Rasmussen, S., P. Abbott, T. Blunier, A. Bourne, E. Brook, S. Buchardt, C. Buizert, J. Chappellaz, H. Clausen, E. Cook, et al. (2013), A first chronology for the NEEM ice core, *Climate of the Past Discussions*, *9*(3), 2967–3013.

Rérolle, V., C. F. Floquet, A. J. Harris, M. C. Mowlem, R. R. Bellerby, and E. P. Achterberg (2013), Development of a colorimetric microfluidic pH sensor for autonomous seawater measurements, *Analytica Chimica Acta*.

Ricaurte, M., J.-P. Torré, A. Asbai, D. Broseta, and C. Dicharry (2012), Experimental data, modeling, and correlation of carbon dioxide solubility in aqueous solutions containing low concentrations of clathrate hydrate promoters: Application to CO_2–CH_4 gas mixtures, *Industrial & Engineering Chemistry Research*, *51*(7), 3157–3169.

Robock, A. (2000), Volcanic eruptions and climate, *Reviews of Geophysics*, *38*(2), 191–219.

Röthlisberger, R., M. Bigler, M. Hutterli, S. Sommer, B. Stauffer, H. G. Junghans, and D. Wagenbach (2000), Technique for continuous high-resolution analysis of trace substances in firn and ice cores, *Environmental Science & Technology*, *34*(2), 338–342.

Ruth, U., D. Wagenbach, J. P. Steffensen, and M. Bigler (2003), Continuous record of microparticle concentration and size distribution in the central Greenland NGRIP ice core during the last glacial period, *J. Geophys. Res.: Atm.*, *108*(D3), doi:10.1029/2002JD002376.

Seierstad, I. K., P. M. Abbott, M. Bigler, T. B. A. J. Bourne, E. Brook, S. L. Buchardt, C. Buizert, H. B. Clausen, E. Cook, D. Dahl-Jensen, S. M. Davies, M. Guillevic, S. J. Johnsen, D. S. Pedersen, T. J. Popp, S. O. Rasmussen, J. Severinghaus, A. Svensson, and B. M. Vinther (2014), Consistently dated records from the Greenland GRIP, GISP2 and NGRIP ice cores for the past 104 ka reveal regional millennial-scale isotope gradients with possible Heinrich Event imprint, *Quaternary Science Reviews*, (unpublished).

Shepherd, A., D. Wingham, and E. Rignot (2004), Warm ocean is eroding West Antarctic ice sheet, *Geophysical Research Letters*, *31*(23).

Sigl, M., J. R. McConnell, L. Layman, O. Maselli, K. McGwire, D. Pasteris, D. Dahl-Jensen, J. P. Steffensen, B. Vinther, R. Edwards, R. Mulvaney, and S. Kipfstuhl (2013), A new bipolar ice core record of volcanism from WAIS Divide and NEEM and implications for climate forcing of the last 2000 years, *J. Geophys. Res.: Atm.*, *118*(3), 1151–1169, doi:10.1029/2012JD018603.

Singh, A., and M. Agrawal (2008), Acid rain and its ecological consequences., *Journal of Environmental Biology*, *29*(1).

Smith, C. D. (1950), The widespread smoke layer from Canadian forest fires during late september 1950, *Mon. Wea. Rev.*, (78), 180–184, doi:http://dx.doi.org/10.1175/1520-0493(1950)078⟨0180:TWSLFC⟩2.0.CO;2.

Smith, S. J., J. v. Aardenne, Z. Klimont, R. J. Andres, A. Volke, and S. Delgado Arias (2011), Anthropogenic sulfur dioxide emissions: 1850–2005, *Atmospheric Chemistry and Physics*, *11*(3), 1101–1116.

Sommer, S., D. Wagenbach, R. Mulvaney, and H. Fischer (2000), Glacio-chemical study spanning the past 2 kyr on three ice cores from Dronning Maud Land, Antarctica 2. Seasonally resolved chemical records, *J. Geophys. Res.*, *105*(D24), 29,423–29.

Sparks, R. J., W. Melhuish, J. W. McKee, J. Ogden, J. Palmer, and B. Molloy (1995), 14C calibration in the Southern Hemisphere and the date of the last Taupo eruption: evidence from tree-ring sequences, *Radiocarbon*, *37*(2), 155–163.

Storey, B. C., A. P. Vaughan, and T. R. Riley (2013), The links between large igneous provinces, continental break-up and environmental change: Evidence reviewed from Antarctica, *Earth and Environmental Science Transactions of the Royal Society of Edinburgh*, *104*(01), 17–30.

Stowasser, C., C. Buizert, V. Gkinis, J. Chappellaz, S. Schuepbach, M. Bigler, X. Fain, P. Sperlich, M. Baumgartner, A. Schilt, et al. (2012), Continuous measurements of methane mixing ratios from ice cores, *Atmospheric Measurement Techniques*, *5*(5), 999–1013.

Stumm, W., and J. J. Morgan (2012), *Aquatic chemistry: chemical equilibria and rates in natural waters*, vol. 126, John Wiley & Sons.

Svensson, A., P. E. Biscaye, and F. E. Grousset (2000), Characterization of late glacial continental dust in the Greenland Ice Core Project ice core, *J. Geophys. Res.*, *105*(D4), 4673–4556.

Svensson, A., K. Andersen, H. Clavsen, S. Johnsen, S. Rasmussen, J. Steffensen, and B. Vinther (2006), Extending the Greenland Ice Core Chronology 2005 (gicc05) back to 60 Kyr 2bK, in *Geophysical Research Abstracts*, vol. 8, p. 05601.

Svensson, A., M. Bigler, T. Blunier, H. B. Clausen, D. Dahl-Jensen, H. Fischer, S. Fujita, K. Goto-Azuma, S. Johnsen, K. Kawamura, et al. (2013), Direct linking of Greenland and Antarctic ice cores at the Toba eruption (74 ka BP)., *Climate of the Past*, *9*(2).

Taylor, K., C. Hammer, R. Alley, H. Clausen, D. Dahl-Jensen, A. Gow, N. Gundestrup, J. Kipfstuhl, J. Moore, and E. Waddington (1993), Electrical conductivity measurements from the GISP 2 and GRIP Greenland ice cores, *Nature*, *366*(6455), 549–552.

Traversi, R., S. Becagli, E. Castellano, V. Maggi, A. Morganti, M. Severi, and R. Udisti (2007), Ultra-sensitive Flow Injection Analysis (FIA) determination of calcium in ice cores at ppt level, *Analytica chimica acta*, *594*(2), 219–225.

Tschumi, J., and B. Stauffer (2000), Reconstructing past atmospheric CO_2 concentration based on ice-core analyses: open questions due to in situ production of CO_2 in the ice, *Jour. of Glac.*, *46*(152), 45–53, doi:doi:10.3189/172756500781833359.

United States Government Accountability Office (2004), Biscuit Fire - analysis of fire response, resource availability, and personnel certification standards, *Tech. Rep. GAO-04-426*, http://www.gao.gov/assets/250/242009.pdf.

Vinther, B. M., S. L. Buchardt, H. B. Clausen, D. Dahl-Jensen, S. J. Johnsen, D. Fisher, R. Koerner, D. Raynaud, V. Lipenkov, K. Andersen, et al. (2009), Holocene thinning of the Greenland ice sheet, *Nature*, *461*(7262), 385–388.

Warming, E., A. Svensson, P. Vallelonga, and M. Bigler (2013), A technique for continuous detection of drill liquid in ice cores, *Journal of Glaciology*, *59*(215), 503–506.

Winstrup, M., A. Svensson, S. O. Rasmussen, O. Winther, E. Steig, and A. Axelrod (2012), An automated approach for annual layer counting in ice cores, *Clim. Past.*, *8*(6), 1881–1895.

Wolff, E. W., J. C. Moore, H. B. Clausen, C. U. Hammer, J. Kipfstuhl, and K. Fuhrer (1995), Long-term changes in the acid and salt concentrations of the Greenland Ice Core Project ice core from electrical stratigraphy, *J. Geophys. Res.*, *100*(D8), 16,249–16.

Wolff, E. W., D. William, J. C. Moore, and J. G. Paren (1997), Factors controlling the electrical conductivity of ice from the polar regions a summary, *The Journal of Phys. Chem. B*, *101*(32), 6090–6094.

Zielinski, G. A. (1995), Stratospheric loading and optical depth estimates of explosive volcanism over the last 2100 years derived from the Greenland Ice Sheet Project 2 ice core, *J. Geophys. Res.*, *100*(D10), 20,937–20.

Zielinski, G. A., P. A. Mayeski, L. D. Meeker, S. Whitlow, and M. S. Twickler (1996), A 110.000-yr record of explosive volcanism from the GISP2 (Greenland) ice core, *Quat. Res.*, *45*, 109–118.

Part III

IN SITU PRODUCTION OF CO_2

Glacial records are the only paleo-records to directly record greenhouse gas concentrations of the past [*Le Treut et al.*, 2007]. Ice cores from Antarctica record CO_2 variations of the last eight glacial cycles (800 ka BP)[*EPICA community members*, 2004]. The Greenland ice core records, while only covering one glacial cycle, have a much higher resolution due to higher annual snow fall making the lock in depth age less. The concentration of CO_2 recorded in the ice at the two hemispheres should be similar except for changes in temporal resolution. However, in some cases, the records of CO_2 from the two hemispheres differ by as much as 20 ppmv, greatly exceeding the hemispheric gradient. Furthermore in Greenland ice cores rapid increases in CO_2 of up to 50 ppm are observed [*Anklin et al.*, 1995]. It is suspected to be a result of in situ production of CO_2 within the Greenland glacier.

The source(s) of the in situ production are debated and several hypotheses have been proposed including oxidation of organic carbonates and protonation of carbonates[*Anklin et al.*, 1995; *Tschumi and Stauffer*, 2000]. The mechanisms have been tested by correlation analyses between the oxidant hydrogen peroxide, the organic compound formaldehyde, carbonates (represented by the Ca^{2+} ion) and pH with CO_2. The tests are somewhat inconclusive and both processes could be equally important [*Tschumi and Stauffer*, 2000]. Recently a third mechanism was suggested, the photolysis of pyruvic acid [*Guzmán et al.*, 2007]. A more thorough introduction to the CO_2 records from ice and the suggested causes for in situ production are presented in chapter 9.

It is evident from above that several theories exist on the causes of in situ production of CO_2 in the Greenland ice. Motivated by this uncertainty and to further investigate if photolysis of pyruvic acid (and other humic like substances (HULIS)) is a likely source of CO_2 production in situ a review on the concentration of organics in snow and ice as well as their sources is presented in chapter 10. Also the light penetration in ice and snow has been reviewed (chapter 11) and a small study of light penetration in surface snow at the NEEM site which was performed as part of this PhD is presented in section 11.2. Please also note that the method for the determination of acidity in ice presented in part II could be used to evaluate the hypothesis of acidification of carbonates as a cause of the in situ CO_2 production.

Furthermore as pyruvic acid is not easy to determine in snow and ice a computational study using density function theory (DFT) of pyruvic acid and its 4 most likely conformers has been performed in Self-Consistent Reaction Field (SCRF) representing both gas, water and solid water (ice) and is presented in chapter 12. Finally the conclusions on whether the photolysis of pyruvic acid is a likely cause of CO_2 in situ production in Greenland ice is presented in chapter 13.

9. CO_2 RECORDS FROM ICE CORES AND IN SITU PRODUCTION

Glacial records of CO_2 are of great interest in studies of past climate[Le Treut et al., 2007] and reliable records of CO_2 are available from Antarctic ice cores. They confirm a lower concentration of CO_2 during the glacial with lowest concentrations observed in glacial maxima (180 ppm), while the Holocene concentrations are in the order of 260 ppm to 280 ppm CO_2. The Greenland ice core would provide a higher temporal resolution as the age of the lock in depth is less than that of Antarctica. Unexpected differences between the two hemispheres, however, are observed with longer sections differing by 20 ppmv, greatly exceeding the hemispheric gradient. Further rapid increases of up to 50 ppm within 1 or 2 years is found in the Greenland records [Anklin et al., 1995]. Clearly something is happening within the Greenland ice, which produces the CO_2 excess.

Several mechanisms are suggested, however three are currently the main ones being hypothesised: 1) The acidification of carbonates, 2) the oxidation of organics and 3) the photolysis of organics such as pyruvic acid. There is evidence that the in situ production cause higher excess CO_2 peaks in the older ice than in the younger ice, suggesting that concentrations of the reactive compound should be higher in the older ice or that the reaction should be slow enough to keep going or that it is a light dependent reaction so that the reacting substance is photolysed slowly over time. Further recent evidence by CO and $\delta^{13}C$ measured within the ice points toward organics playing a major role.

In this chapter CO_2 in ice and its variability is presented as well as the suggested mechanisms and evidence of CO_2 production in situ.

9.1 Past CO_2 from Antarctic ice core records

Ice produced from snow accumulation contains about 10 % air that is released upon melting or crushing. The detection of this air caught within the ice provide a record of past CO_2 reaching up to 800.000 years back.

As snow crystals fall and settle on the surface of the ice sheets their surface is big and plenty of air is present in between individual snowflakes. As more snow falls, the snow undergoes transformations and the density increases. However air remains in between the individual snow grains and it is possible for the air to be exchanged with air from the atmosphere above. At a certain depth (pore close off (PCO) or lock in depth (LID), see Figure 9.1) the air can no longer escape to the ambient atmosphere and at this depth, typically between 60-110 meters depth [*Paterson and Cuffey*, 1994; *Veres et al.*, 2012], the air is enclosed in air bubbles of about 1 mm diameter[*Anklin et al.*, 1995]. As the pressure on the ice increases with depth the

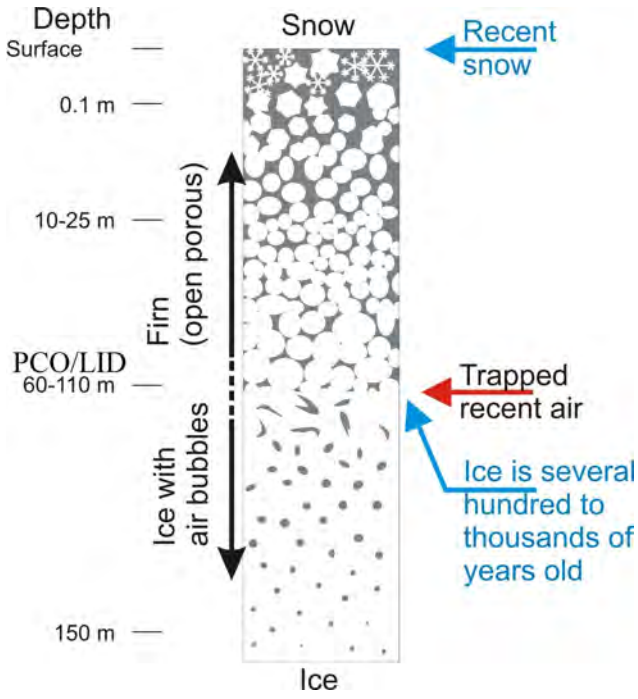

Fig. 9.1: The firnification of snow, resulting in an age difference between snow and gas trapped in ice.

bubbles get more compressed, and finally at a depth below several hundred metres they form clathrates making the air invisible in the ice.

By analysis of the air trapped inside the ice a record of the past atmosphere is determined including CO_2 concentrations among many others. Due to the exchange between the atmosphere and the gas in the firn down to the LID, the ages of the gas in the ice and the surrounding snow are different. Depending on the precipitation and temperature of the site, which likely have varied over time, a difference between the ice age and gas age, Δage [*Vallelonga et al.*, 2012], is determined and the gas records are corrected to a true time scale. The Δage can be from several thousand of years, for e.g. low precipitation Antarctic records during the glacial, down to a couple of hundred years if the ice core originate from areas with high annual accumulation (eg. Greenland in recent times) [*Vallelonga et al.*, 2012; *Goujon et al.*, 2003].

Further the exchange of gases above the LID in the firn ensures that the annual variation, found for some gases in the atmosphere, is smoothed out.

In Figure 9.2 the concentrations of CO_2 from various Arctic and Antarctic ice cores are shown together with the temperature proxy $\delta^{18}O$, while Figure 9.3 shows the recent trend. The location of the ice cores are shown in Figure 1.2. CO_2 as determined in ice cores is found to co-vary with the temperature determined in Antarctic ice cores on a millennial time scale [*Petit et al.*, 1999]. The minimum CO_2 concentrations are found during the glacial and show concentrations in the order of 180-200 ppmv. During the interglacial periods (warm periods) concentrations of CO_2 are higher and reaches 270 to 300 ppmv [*Petit et al.*, 1999; *Fischer et al.*, 1999; *Kawamura et al.*, 2003]. Thus the CO_2 concentrations to a first degree strongly

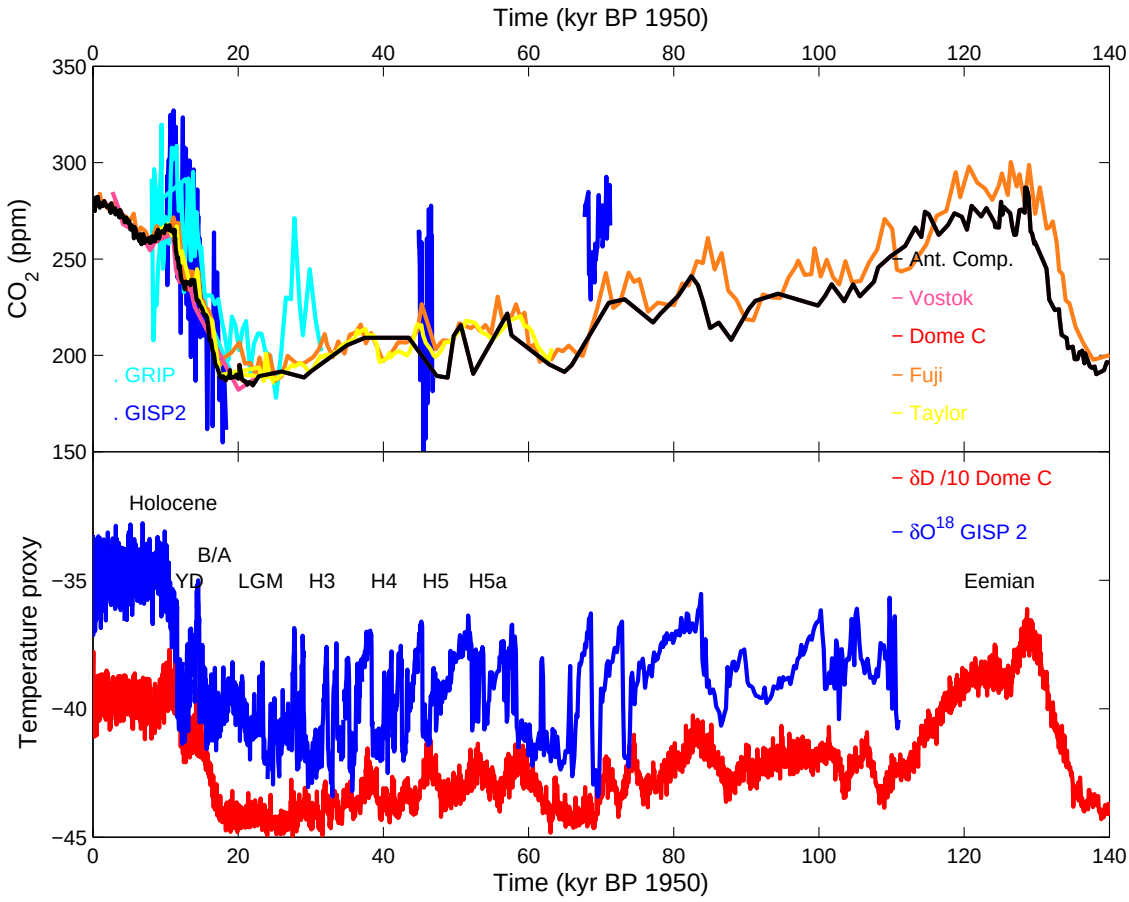

Fig. 9.2: CO_2 concentrations as determined in the Greenland ice cores GRIP [*Anklin et al.*, 1995; *Barnola et al.*, 1995; *Anklin et al.*, 1997] and GISP 2 [*Wahlen et al.*, 1991; *Smith et al.*, 1997] (blue colors) and Antarctic ice cores (red colors); Antarctic composite (black) [*Lüthi et al.*, 2008], Dome C [*Monnin et al.*, 2001], Vostok [*Petit et al.*, 1999; *Pépin et al.*, 2001; *Raynaud et al.*, 2005], Taylor dome [*Indermühle et al.*, 1999] and dome Fuji [*Kawamura et al.*, 2003] on an EDC gas age timescale. In the bottom is shown temperature proxies (low values cold, high values warm) for Greenland (blue) and Antarctic (red). The graphs span from our warm period (the Holocene) to the previous warm period (the Eemian). Also indicated are the last glacial maximum (LGM), Younger Dryas (YD), Bølling-Allerød (B/A), and some Heinrich events (H).

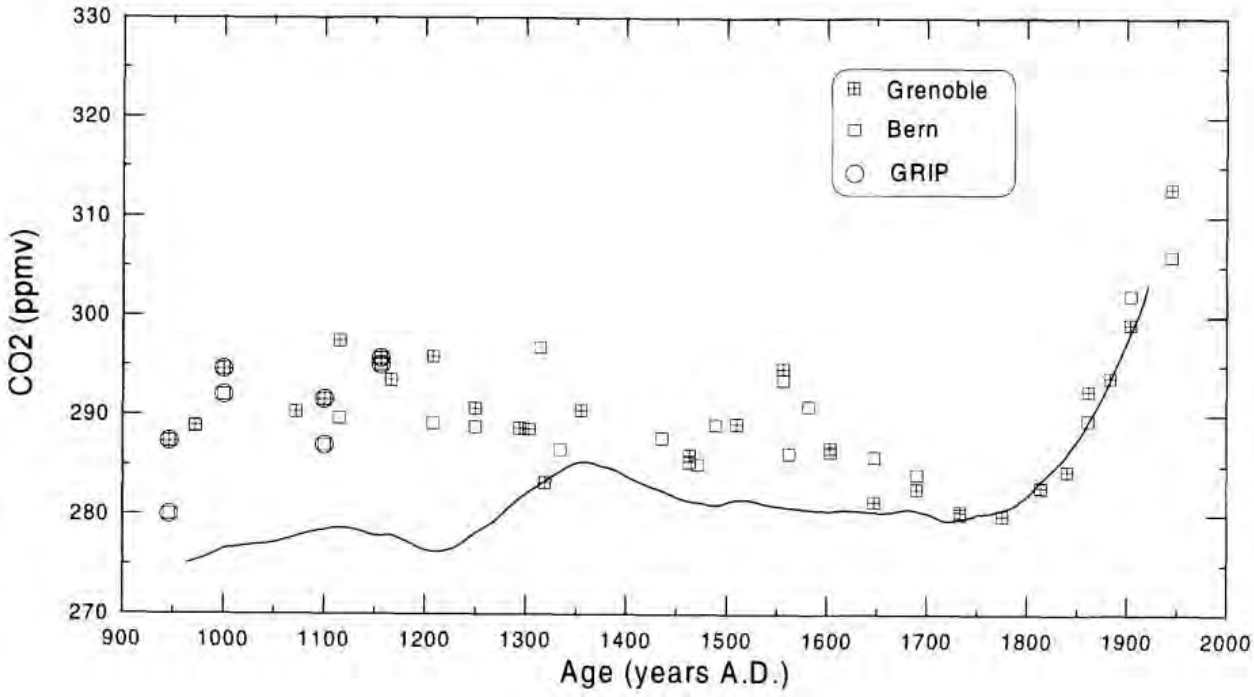

Fig. 9.3: CO_2 as determined in Antarctica (full line) shown together with results from Greenland Summit (Eurocore) and GRIP ice cores circles as determined in two different laboratories; Bern and Grenoble. Figure from *Barnola et al.* [1995].

correlates with Antarctic temperatures, though the time lag to the temperature is neither constant in time or between sites or generally agreed upon [*Monnin et al.*, 2001; *Caillon et al.*, 2003; *Pedro et al.*, 2012]. The changes in CO_2 concentrations over time are believed to be controlled by the Southern Ocean, however the exact mechanism is still debated and mechanisms suggested to be involved are sea ice, out-gassing, changes of wind circulation (overturning of deep water), changes in stratification, changes in sea surface and/or deep water temperatures [*Ahn and Brook*, 2007].

Greenland ice cores should provide higher resolution CO_2 records than their Antarctic counterparts covering the late Holocene as well as the recent glacial period. However significant differences between Greenland records of CO_2 and Antarctic records are found exceeding what can be explained by the hemispheric gradient [*Anklin et al.*, 1997; *Tschumi and Stauffer*, 2000].

9.1.1 Variation of CO_2 records between hemispheres and between ice cores

The CO_2 records obtained from Greenland ice cores are generally 10 ppmv above the Antarctic counterparts in the period 1300-1920 AD and about 20 ppmv in the period 100-1300 AD and in the early Holocene [*Anklin et al.*, 1995; 1997; *Tschumi and Stauffer*, 2000].

During the Yonger Dryas (YD) cold period the Greenland records of CO_2 decrease, while the Antarctic CO_2 records increase and during Bølling-Allerød the GRIP record show high CO_2 concentrations compared to Antarctic counterparts

[*Anklin et al.*, 1997].

Besides these long trends in differences between the CO_2 records from the two hemispheres short term peaks of up to 60 ppmv CO_2 are also found in Greenland ice core records spanning just two annual layers. These rapid excess peaks of CO_2 are especially common during the last glacial, but not limited to this period [*Tschumi and Stauffer*, 2000]. If such a two year increase in the atmospheric CO_2 would indeed happen it could not be recorded in the ice, due to the smoothing process in the firn above the LID and furthermore a variation of 60 ppmv is unlikely to occur naturally in earths atmosphere over such a short period. Thus these peaks are proof of in situ production of CO_2 in the Greenland ice cores [*Anklin et al.*, 1995; 1997; *Tschumi and Stauffer*, 2000]. Furthermore the amount of excess CO_2 in Greenland ice cores is a function of the ice age [*Jenk et al.*, 2013; *Tschumi and Stauffer*, 2000].

Though different Antarctic ice core records show very similar CO_2 concentrations, small differences between Antarctic CO_2 records also exists [*Kawamura et al.*, 2003]. These differences are often explained by differences in measurement techniques and/or sample preparation [*Anklin et al.*, 1997; *Kawamura et al.*, 2003]. However recent evidence from Antarctic high resolution records of CO_2 from Taylor Dome and WAIS divide also show small differences to the law Dome record of a few ppbv CO_2 in the Holocene, which cannot be explained by laboratory measurement differences [*Brook*, 2013].

9.1.2 Method differences in the determination of past CO_2

To extract the gas from the ice two different methods are used. Either it is done with a crusher (dry extraction, e.g. [*Barnola et al.*, 1995]) or the ice is melted (wet extraction, e.g. [*Kawamura et al.*, 2003]) in a vacuum or in a gas of known concentration.

Dry extraction is considered the most accurate since there is no risk of any acid carbonate reaction, which could occur in relation to melt water[1]. Antarctic ice is acidic throughout, but the impurity content in Antarctic ice cores is very low (low concentration of carbonates) and thus the difference between results from dry and wet extraction in Antarctic cores is mostly small [*Anklin et al.*, 1997].

However dry extraction can also be problematic as it is hard to ensure all ice is sufficiently crushed. If gas within part of the ice is not released it could cause low readings of the CO_2 concentrations. Especially a scatter effect in the transition zone between gas in the ice being stored as bubbles or as clathrates (the brittle zone) has been observed when using dry extraction techniques. Increased storage time partly solves this issue [*Anklin et al.*, 1997], because the clathrates become unstable when the ice relaxes to the ambient pressure[2]. The different dry extraction techniques involve a needle crusher, a ball crusher and a grinder and depending on type, they can be more or less efficient in getting all air out of the ice [*Anklin et al.*, 1997]. Wet extraction technique does not have specific problems in the determination of CO_2 concentrations in relation to clathrates [*Kawamura et al.*, 2003].

[1] More on the acid carbonate reaction in section 9.2.1

[2] Inside the ice sheet the pressure is very large, after retrieval of the ice core the core experiences a large pressure gradient. This pressure gradient affects the clathrates.

After extraction the determination of the CO_2 concentration is generally performed using by mass spectrometry after a purification by gas chromatography[*Anklin et al.*, 1997].

The difference between extraction methods and detection methods amount up to ± 5 ppmv CO_2 [*Anklin et al.*, 1997; *Kawamura et al.*, 2003], and is thus insufficient to explain the differences in CO_2 records from Antarctic and Greenland ice cores.

9.2 Suggested causes of in situ production of CO_2 in ice cores

To explain the excess CO_2 (ΔCO_2) several mechanisms have been suggested. These involve melt layers, microbubbles in snow flakes, gravitational seperation, acid-carbonate reactions [*Delmas*, 1993; *Anklin et al.*, 1995; *Tschumi and Stauffer*, 2000], oxidation of organic species [*Tschumi and Stauffer*, 2000] as well as photolysis of pyruvic acid and/or other organic acids [*Guzmán et al.*, 2007]. Further in theory methane could transform to excess CO_2, but the capacity is below 1 ppmv CO_2 [*Anklin et al.*, 1995] and black carbon, which also theoretically could produce CO_2 is believed chemically inert [*Anklin et al.*, 1995].

In Dye 3, a southern Greenland ice core, elevated concentrations of CO_2 have been observed in occluded air bubbles in relation to melt layers in the Holocene [*Tschumi and Stauffer*, 2000]. However only very few melt layers occur in Northern Greenland ice cores. Micro-bubbles in snow flakes are observed with highly elevated concentrations of CO_2. During the firnification process the properties of the snow changes and the snow flake micro bubble effect disappears. The snow grain effect explain an excess of 0.3 ppmv ΔCO_2 [*Anklin et al.*, 1997]. The gravitational separation can cause an overestimation of 2 ppmv ΔCO_2 [*Anklin et al.*, 1997]. Thus even if both snowflakes, gravitational settling an methane caused part of the excess it would only add up to less than 3.3 ppmv CO_2 and they cannot be the main cause of the high excess spikes of CO_2 observed in the Greenland ice core records.

9.2.1 Carbonates and acidity

It is well known that carbonates in an environment with excess H^+ can react to form CO_2.

$$2H^+ + CO_3^{2-} \Leftrightarrow CO_2 + H_2O \tag{9.1}$$

For the acid-carbonate reaction to be a likely candidate for in situ production a requirement is that the acidification is not complete prior to deposition on the ice [*Delmas*, 1993; *Anklin et al.*, 1995]. In the atmosphere carbonates such as $CaCO_3$, $NaCO_3$ and/or $MgCO_3$ is neutralized to forms such as $CaSO_4$ and $Ca(NO_3)_2$ before deposition on the ice [*Delmas*, 1993; *Anklin et al.*, 1995; *Smith et al.*, 1997]. However a full neutralization does not always occur.

To investigate if acidification of carbonates reactions are likely to occur in the ice correlation between the involved species are often investigated. One should, however, be aware that even if part of the compound necessary to perform the reaction is used, the resulting ice core record of that compound could still show up as a peak rather than a depletion given that not all of the compound has reacted.

Further the fact that some of the reactants are detected in the ice, shows that the reaction does not necessary take place even if concentrations are high [*Tschumi and Stauffer*, 2000]. To perform such correlation studies it is also of great importance to keep depth resolution high [*Tschumi and Stauffer*, 2000], to ensure that potentially large variations occurring over short distances are resolved.

If the carbonate-acid reaction is the cause of CO_2 production in situ a decrease in the carbonates and H^+ concentrations should be observed in relation to excess CO_2. The reaction should occur post deposition and post burial, most likely in layers containing a change in acidity (eg. volcanic layers) and/or a change in carbonate content [*Anklin et al.*, 1995]. Rapid changes in the concentration of carbonates or the acidity within the ice could happen as a result of decreasing annual layer thickness with depth. *Delmas* [1993] speculates that the acid carbonate reaction would be favoured in older ice, where layers are thinner bringing closer together alkaline (carbonate/dust rich) and acid ice layers [*Anklin et al.*, 1995].

The carbonate content in Greenland ice was determined by *Anklin et al.* [1995] using the difference between CO_2 as detected using dry and wet extraction systems. The results indicate a concentration of 0.4 ± 0.2 μM carbonate in Greenland ice. *Tschumi and Stauffer* [2000] assumed that half the Ca^{2+} was $CaCO_3$ and found 0.05 to 0.4 μM $CaCO_3$. However others assume all Ca^{2+} originate from carbonates [*Smith et al.*, 1997].

Acidity can be determined using Electrical conductivity measurements (ECM), titration, electrical pH probes and dye techniques (see section 6.4.4). In the study by *Anklin et al.* [1995] an acidity concentration of 0.5 to 1.5 μeq was observed, which if unlimited carbonates were available could create 20 to 120 ppmv CO_2. The carbonate acidity reaction is quite slow in ice and *Anklin et al.* [1995] suggest that the reaction is limited by the carbonate access and speculate that the reaction might take place in grain boundaries where a liquid phase can exist. The thickness of this liquid phase in between grain boundaries is temperature dependent [*Anklin et al.*, 1995] making the acidification of carbonate reaction more likely in warmer ice. However, contrarily the limiting chemicals could exist in higher concentrations in the liquid phase in colder ice, as they are frozen out of the ice matrix. For Antarctic ice, the carbonate-acid reaction is thought not to occur, because the carbonate content in Antarctic ice cores is low [*Legrand et al.*, 1982].

Smith et al. [1997] suggest that production of CO_2 only occurs when the content of carbonates is intermediate (Ca^{2+} between 5 and 70 ppb), as low loads are speculated to be acidified already in the atmosphere, while higher loads of carbonate would neutralize the available H^+, without the formation of CO_2. Very alkaline conditions is thus speculated to result in an in situ decrease of CO_2 as a result of a transformation of CO_2 into $2\,HCO_3^-$ (bicarbonates) [*Smith et al.*, 1997].

Anklin et al. [1995] investigated the cause of three (ΔCO_2) peaks in the Greenland GRIP ice core during the Holocene and find that the acidification of carbonates is the most likely cause of excess CO_2 for two of the peaks. Newer studies, based on evidence of excess CO_2 increasing over time in Greenland ice cores, suggest that acidification of carbonates can not be the only source of in situ production [*Jenk et al.*, 2013]. Theo Jenk (personal correspondence) suggest that about 21% to 65% of the three CO_2 peaks investigated by *Anklin et al.* [1995] could be explained by the

acid-carbon reaction if including a time factor accounting for the slow process of acid carbon reaction, with the remainder explained by oxidation of organic compounds. In another study *Tschumi and Stauffer* [2000] does not exclude the acidification of carbonates, but find that the oxidation of organic compounds at least as important. Please note that the studies mentioned above is based on just a few low resolution measurements and thus if records were presented in high resolution conclusions could perhaps be different.

In the Antarctic Dome Fuji ice core *Kawamura et al.* [2003] found no correlation between excess CO_2 and Ca^{2+}, suggesting that the acidification of carbonates is not a main driver of the excess observed there.

9.2.2 Oxidizing organic compounds

Oxidation of organic matter is another process suggested to be the source of in situ production of CO_2 in ice cores [*Tschumi and Stauffer*, 2000]. The oxidant could be hydrogen peroxide (H_2O_2) for example causing a reaction with formaldehyde as shown below [*Tschumi and Stauffer*, 2000].

$$2H_2O_2 + HCOH \Rightarrow CO_2 + 3H_2O \tag{9.2}$$

Tschumi and Stauffer [2000] finds that a 6 ppmv CO_2 depletion could result from a depletion in HCHO and H_2O_2 in a section of the Greenland ice. However HCHO is not the only organic in the ice and the study suggest that other organics not determined as part of the study could cause a similar depletion, while *Anklin et al.* [1995] find that formaldehyde during the Holocene is stable and conclude that formaldehyde is not a likely candidate for Holocene excess CO_2. However in the study the resolution of formaldehyde might not be sufficient to make any firm conclusions. *Guzmán et al.* [2007] claim that the oxidation of aldehydes by H_2O_2 is unlikely due to the reaction being slow and that in aqueous solutions instead of carbon oxides stable carboxylic acids would form.

The drop in H_2O_2 in the study by *Tschumi and Stauffer* [2000] is large enough to explain a 130 ppmv ΔCO_2 and H_2O_2 is not the only available oxidant within the ice. Theo Jenk (personal correspondence), however, points out that the oxidation reagent could be used by other competing reactions such as an oxidation of volcanic SO_2.

Theo Jenk (personal correspondence) finds that the ΔCO_2 explained by oxidation of organics is between 35 % and 79% and further find that only part of the HCOH is used up in order to produce ΔCO_2 thus differing from the conclusion of *Tschumi and Stauffer* [2000].

More recent investigations also involve determination of CO and $\delta^{13}C$. The isotope, δ^{13}C, for organic compounds is in the order of -25 ‰ δ^{13}C, while carbonates have a δ^{13}C value close to 0 ‰. In the Greenland GRIP ice core a δ^{13}C -4 ‰ was measured indicating a carbonate reaction, while δ^{13}C of -22 ‰ was found for South Yamato (Antarctica) suggesting organics causing the in situ production of CO_2 found there [*Francey et al.*, 1997; *Tschumi and Stauffer*, 2000].

From a combined study of CO_2, $\delta^{13}C$ and other impurities *Jenk et al.* [2013] finds that about 30% of removed formaldehyde reacts to form CO_2, but that a 3-

4 times higher production is found in the Greenland core thus emphasizing that formaldehyde is not the only organic and that the path way, though it based on the $\delta^{13}C - CO_2$ values stems from organics, could be a different organic related one.

Francey et al. [1997] investigated the same species and conclude that a slow oxidation is the most likely explanation of in situ production in Greenland ice cores in the recent Holocene (1000-2000 AD). They find increased CO and suggest this could be further evidence of organics being the cause of in situ CO_2 formation [*Tschumi and Stauffer*, 2000; *Francey et al.*, 1997; *Guzmán et al.*, 2007]. *Faïn et al.* [2014] investigated CO in the Greenland NEEM S1 shallow core and found 96 elevated peaks of CO in the period 200-2000 AD. They find an increase of CO peaks both in number and elevation with depth. *Faïn et al.* [2014] suggest the source of these in situ CO peaks is related to chemical or microbiological content of the ice. They find some relation to forest fires as determined by excess ammonium (68% of the CO excess events) and suggest that the excess CO within the ice is age dependent and caused by oxidation of organics and possibly photo-induced. They do not find HCHO involved in the process of excess CO.

9.2.3 Photolysis of pyruvic acid

A third mechanism, for the in situ production of CO_2, also related to organic matters is the photolysis of pyruvic acid (PA)–an oxocarboxylic acid [3]. The reaction includes an electron transfer from an excited carbonyl chromophore to the neighbouring carbonyl acceptor [*Guzmán et al.*, 2006b;a; 2007]. The net reaction is shown below:

$$CH_3C(O)C(O)OH + h\nu \rightarrow CO_2 + \text{other products} \tag{9.3}$$

Humic and humic like substances, such as oxocarboxylic acids as e.g. pyruvic acid, photodegrade by sunlight to CO and CO_2 in ratio $\sim 1:50$ and thus *Guzmán et al.* [2007] suggest that excess CO is a significant clue that organics and not carbonates is the more likely cause, further adding that the carbonate reaction is unlikely because it is slow.

For pyruvic acid (and other organics) to photolyse and form CO_2 in situ the necessary wavelengths to initiate the reaction should reach deep into the ice. The absorption peak for pyruvic acid is 300-380 nm in gas phase and peak at 350.12 nm [*Horowitz et al.*, 2001]. Whether indeed light is available at these wavelengths are further discussed in section 11.

The pyruvic acid hypothesis assume much higher concentration of pyruvic acid in the grain boundaries than the 0.2-82 pmol/g determined as bulk concentrations in ice and snow samples [*Guzmán et al.*, 2006a; 2007]. Laboratory experiments have been performed to investigate the photolysis of pyruvic acid, however using concentrations several magnitudes larger than what is found in snow and ice [*Guzmán et al.*, 2006a; 2007].

Using an initial concentration of pyruvic acid of 0.1 M and investigating the equilibrium constant (K_H, see equation 9.4, where a_w represents the water acitivity) between pyruvic acid and its gem-diol (2,2-dihydroxypropoanoic acid, PAH) *Guzmán et al.* [2006c] finds evidence that PA freezes into ice and an up-concentrated

[3] pyruvic acid is also called 2-oxopropanoic acid

fluid solution, they find that the system remains dynamic (water is available to run reaction to PAH) down to a temperature of 250 K when all mobile water is gone.

$$K_H = \frac{[CH_3C(OH)_2COOH(H_2O)_{n-1}]}{[CH_3COCOOH]a_w^n} \tag{9.4}$$

The photolysis of pyruvic acid is suggested to occur in ice following the scheme presented in Figure 9.4. Pyruvic acid (PA) is photolysed and the excited state occurs. The excited state (3PA*) then reacts with a nearby PA to form ketyl (K.)- and carbonyloxyl (X.) radicals. The carbonyloxyl radical (X.) is unstable and transforms to the acetyl radical, $CH_3C(O)\cdot$ (Y.), which produces CO_2 instantly. The ketyl radical is stable and can react with other ketyl radicals (K.+K.) and thus oligomerize[4] and form 2,3-dimethyl tartaric acid (A (C_6)) or alternatively the ketyl radical (K.) can react with pyruvic acid (PA) to form another radical (D), which after recombination with the acetyl radical form the molecule C_8 β-oxocarboxylic acid (D), which slowly decomposes producing CO_2 (Figure 9.4)[*Guzmán et al.*, 2006b;a; 2007]. Thus CO_2 is released both fast and slow as also shown during experiments [*Guzmán et al.*, 2006b; 2007]. The last mentioned oligomerization (D to CO_2 and a C_7 compound) is suggested inhibited by the ice matrix as it involves multiple rotations[*Guzmán et al.*, 2007; *McNeill et al.*, 2012].

Evidence from *Guzmán et al.* [2006a; 2007], show that about 1% of 400 μM PA was photolysed at 313±20 nm (UV), releasing about 1.54 μM CO_2. The study also confirms the suggested pathways by the finding that only about half the CO_2 is promptly released while the other half is released through intermediate pathways (see Figure 9.5) [*Guzmán et al.*, 2006b]. The quantum yield[5] for the UV excitation of pyruvic acid is 0.78 in water *Guzmán et al.* [2007], however also 0.39 have been reported [*Guzmán et al.*, 2006b]. However the quantum yield of CO_2 formation in frozen pyruvic acid solutions is temperature dependent and given by $\phi_{CO_2}(\lambda, T) = (0.81 \pm 0.33) - \frac{338\pm81}{T}$, where T is given in °K. Thus if extrapolating up to 293 K ice is $\phi_{CO_2} = 0.45$ [*Guzmán et al.*, 2007] and thus 40% smaller than observed for water [*Guzmán et al.*, 2006b].

Other processes involving organics to produce CO_2 are a near infra red excitation of pyruvic acid (and other similar organics) and a redox conversion of Cr^{VI} to Cr^{III}.

A study by *Larsen and Vaida* [2012] finds that pyruvic acid (in water) also produces CO_2 at near infra red light (850 nm to $\geq$ 1150) through an excitation of the acidic OH vibrational stretching second overtone (1003 nm). They estimate the quantum yield for OH vibrational overtone excited pyruvic acid in aqueous solutions to be $\phi(\lambda) = 3.5(\pm1) \cdot 10^{-4}$. Thus much smaller than the quantum yield for UV excitation of pyruvic acid observed by *Guzmán et al.* [2006b] of 0.39. The reason for the low quantum yield for the OH vibrational overtone excited pyruvic acid is suggested caused by either the isomers[6] responsible of overtone reaction occurring in low abundance or that other processes such as vibrational relaxation

[4] forms oligomers, which is a molecular complex that consists of a few monomer units, in contrast to a polymer that consists of a nearly unlimited number of monomers

[5] The quantum yield is the number of times a specific event, in this case the photolysis of pyruvic acid, occurs per photon

[6] Molecules with similar molecular structure can have different chemical structures. The different chemical structures are called isomers.

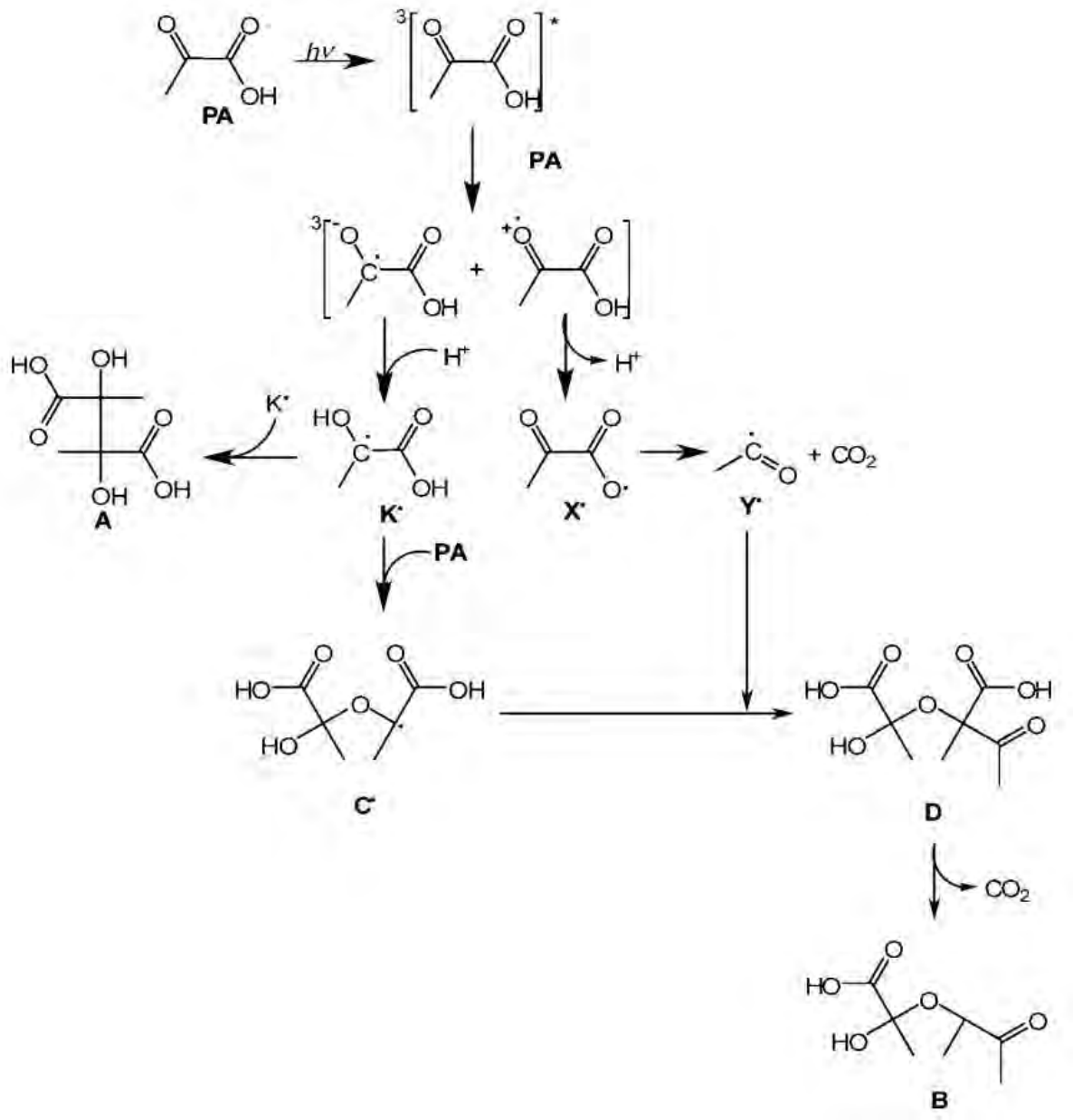

Fig. 9.4: Mechanism of pyruvic acid photolysis in ice. Path ways are described in the main text. Figure by *Guzmán et al.* [2007].

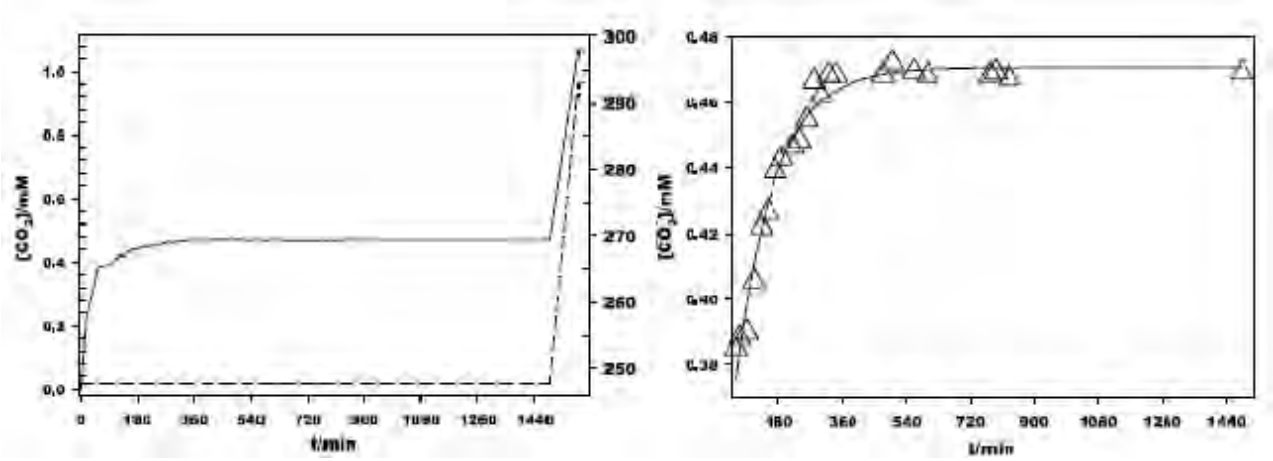

Fig. 9.5: Figures from *Guzmán et al.* [2007]. Left; CO_2 (full line) and temperature(dotted line) as a function of time. CO_2 is released during the initial 60 minutes photolysis at 313 nm (full line). However CO_2 is also released after the irradiation period (after 60 min). Furthermore CO_2 is released after melting of the ice. On the right a zoom in of the post irradiation release of CO_2.

and/or recombination compete with the excitation of the OH vibrational overtone [*Larsen and Vaida*, 2012]. In conclusion this process can not possibly compete with UV excitation of pyruvic acid, however other organics and alcohols, which does not excite in the UV, could have a similar overtone excitation and thus produce CO_2 [*Larsen and Vaida*, 2012].

Another different path way investigated in the laboratory and involving organics are a redox conversion from Cr^{VI} to Cr^{III} in ice. The reaction is believed to occur in the grain boundaries and proved to occur much faster in the presence of oxalic acid resulting in a CO_2 production[7][*Kim and Choi*, 2011]. However as with other laboratory experiments concentrations used were higher than what is observed in natural polar ice and the acidity was also kept lower than what is observed within the ice.

From the discussion above it is evident that multiple possible causes for the in situ production of CO_2 in the Greenland ice exist. Many of the processes are investigated in laboratory conditions that are not representative for polar ice and the experiments are often performed on water or gas and not ice. For those analysis using polar ice often the resolution of the measurement techniques are low as the concentration in the ice is low. Because of the low resolution assumptions about the effect of grain boundary concentrations severely influence on the analysis.

It is clear, however, that the in situ production increases over time and that the $\delta^{13}C$ and CO concentrations suggest organics are playing a significant role in some ice cores, though whether CO_2 is produced as a result of photolysis or oxidation is not clear. In the next section the concentration of organics within the ice is investigated.

[7] Net reaction: $2\,HCr^{VI}O_4^- + 3\,C_2O_4H_2 + 8\,H^+ \rightarrow 2Cr^{3+} + 6\,CO_2 + 8\,H_2O$

10. CONCENTRATION AND VARIABILITY OF ORGANICS IN SNOW AND ICE

Humic like substances (HULIS) is the organic residue of decaying organic substances, they consist of complex macromolecular networks including carbons and other elements and radicals. Humic like substances also includes pyruvic acid. HULIS are present in the Greenland ice cap and in Arctic snow [Kawamura et al., 2001; Voisin et al., 2012]. For the purpose of investigating the likelihood of organics as a cause of in situ production of CO_2 this section presents the concentration levels of carboxylic acids (e.g. pyruvic acid) and other HULIS together with their sources in snow and ice. Unfortunately most methods for the determination of organics in snow and ice require up-concentration techniques, which increases the risk of contamination limiting the trust that can be put into the results. The low concentration observed also makes it impossible to do continuous analysis of organics in polar ice. As a result of the low concentrations the number of studies of organics in snow and ice are limited.

10.1 Definitions of organic substances

Organic substances are complex substances that as a minimum include carbon, oxygen and hydrogen. Compounds identified in ambient aerosols include large variety of organic compounds. They are subdivided using a range of different methods.

One way of subdividing organics are to talk about **humic like substances (HULIS)**. HULIS are polyacidic and relatively large compounds, and typically contain mass from 50% carbon and a mole ratio of O/C of 50%. Typically sulphur is also present. However, there is no exact definition of HULIS [*Kristensen et al.*, 2012]. The humic like subtances originate from decayed matter (humus) broken down by microorganisms to a degree so that it is difficult to recognize the original substance [*Harnung and Johnson*, 2012].

The humic like substances are subdivided into three categories; fulvic, humic and humin acids. The division is based on an extraction method from 1839 [*Berzelius*, 1839a;b; *Manlay et al.*, 2007]: First NaOH is added to the humus, resulting in an insoluble part (the humin) and a solution. The remaining solution is treated with HCl causing humic acids (average structure $C_{187}H_{186}O_{89}N_9S$) to precipitate out, while fulvic acids (average $C_{135}H_{182}O_{95}N_5S$) remain in the solution and thus is soluble in both acid and basic conditions [*Harnung and Johnson*, 2012]. Some general properties result from this subdivison of HULIS as shown in Figure 10.1. Though the subdivison into humic, humin and fulvic acids is not strict and different extraction methods will provide different ratios between the HULIS compounds, HULIS, humic, humin and fulvic acids are often used in the literature, especially since a complete knowledge of composition between the several hundred different

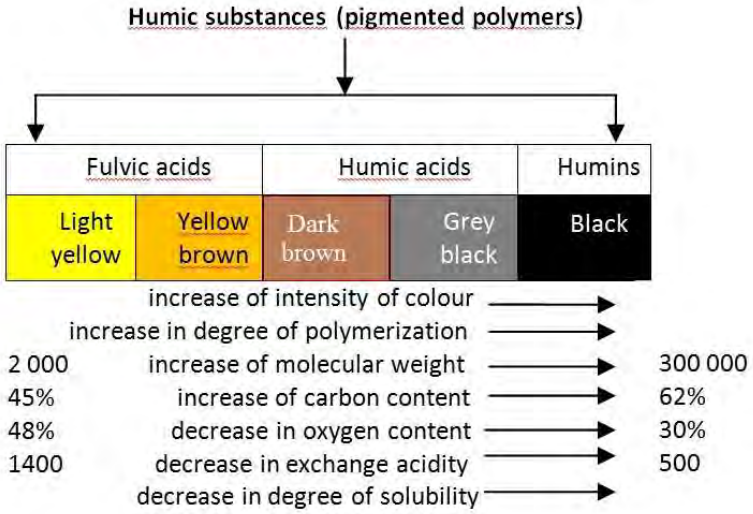

Fig. 10.1: Figure from *Rutkowska and Pikuła* [2013] adapted from [*Stevenson*, 1982]. HULIS and the subdivisions; fulvic acid, humic acid and humin shown together with physiochemical aspects.

compounds is difficult and time consuming to extract [*Kristensen et al.*, 2012].

Another way to look at carbonaceous aerosols is through a **subdivison of the total carbon (TC)**. TC can be subdivided into elemental carbon (EC/black carbon (BC)) and organic carbon (OC) as shown in Figure 10.2 [*Andreae and Gelencsér*, 2006]. The OC can further be subdivided between water soluble organic carbons (WSOC) and water insoluble organic carbons (WinSOC). Furthermore Brown carbon (BrC) or light absorbing carbons (LAC) that are not black are also definitions found in newer literature and refers to organics, which are strongly absorptive in the UV [*Andreae and Gelencsér*, 2006]. BrC/LAC thus also cover humic like substances, eg. pyruvic acid [*Andreae and Gelencsér*, 2006]. The ratio of HULIS carbon to WSOC is found to vary between 9% and 72% depending on both the extraction method and the environmental origin [*Kristensen et al.*, 2012].

Organic acids can also be **defined by their chemical structure**. Carboxylic acids (...-COOH) is the most common organic acid, other organic acids include e.g. alcohols (...-OH) and sulfonic acids (...-SO_2OH). Carboxylic acids can be further subdivided into e.g. monocarboxylic acids (R-COOH), keto acids (also called oxoacids) containing a carboxylic acid group and a ketone group (e.g. H_3C-C=O-R-COOH) and di-carboxylic acids that contain two carboxylic acid functional groups (HOOC-R-COOH), as well as the ω-acids (HC=O−R−COOH) and several more subdivisons. In Figure 10.3 some different carboxylic compounds are shown. Figure 10.4 specify the naming of some chemical substructures. As an example maleic acid ($HO_2CCHCHCO_2H$) would be specified as both a dicarboxyl and an unsaturated carbonyl.

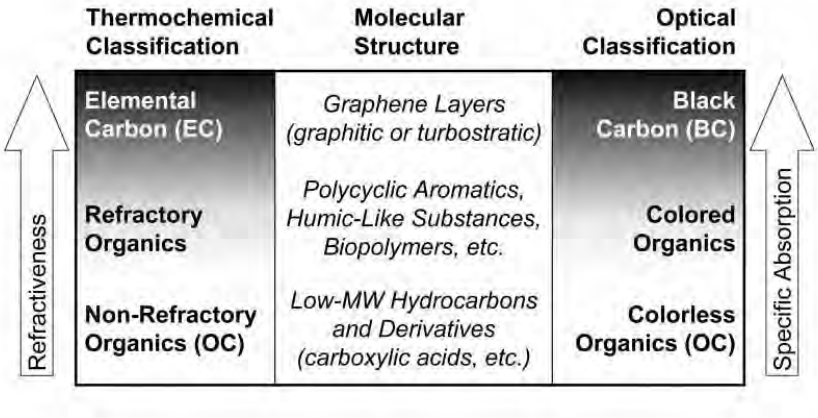

Fig. 10.2: Figure from *Andreae and Gelencsér* [2006]. Classification and molecular structure of carbonaceous aerosols.

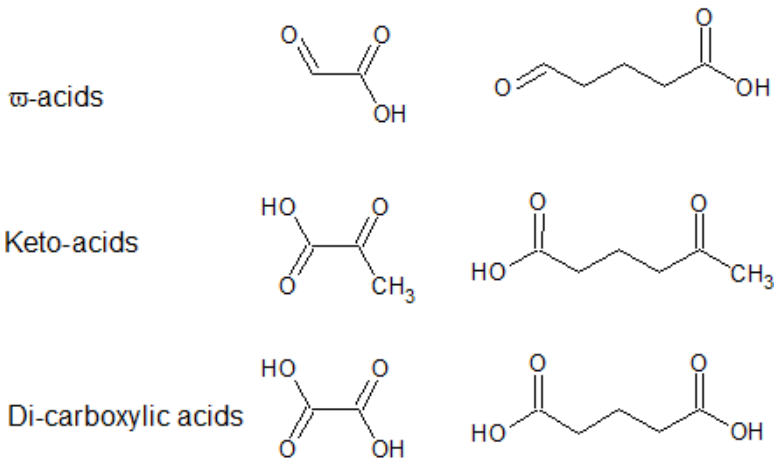

Fig. 10.3: The molecular structure of some different carboxylic acids.

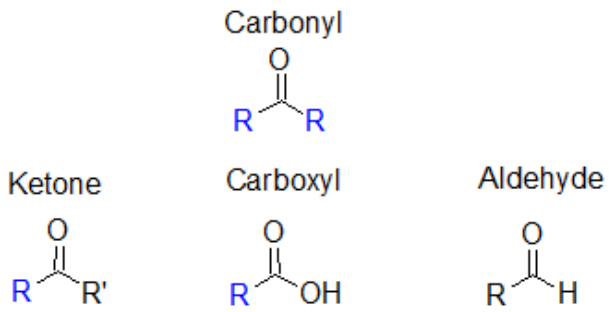

Fig. 10.4: The molecular structures of carbonyls (R−C=O): Ketone is bound to carbon structures, carboxyl is bound to an OH and aldehyde is bound to H on one side.

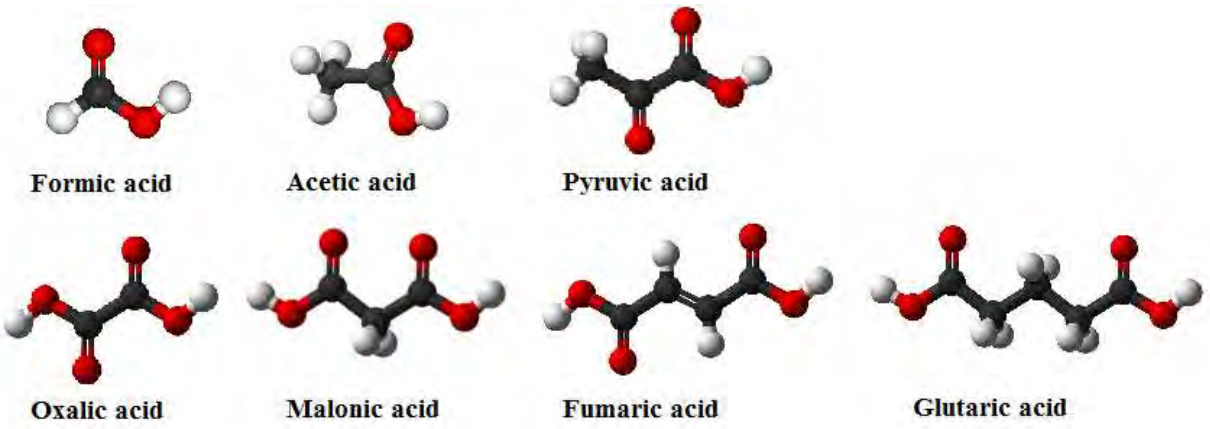

Fig. 10.5: The 3D molecular structures of some organic acids.

10.2 Sources of organic acids

Organic carbon containing aerosols are either primary or secondary and some of the organics exist both in gas phase and as particulates and are referred to as semi volatile compounds [*Seinfeld and Pandis*, 2012].

10.2.1 Primary organic carbon sources

Primary organic sources are natural as well as combustion and combustion related sources (pyrogenic, commercial products, fossil fuels)[*Seinfeld and Pandis*, 2012]. Each of the sources emit a variety of chemical compounds. Global primary organic carbon emissions are estimated to be between 17-77 Tg/yr with open biomass burning contributing about 75% and 7% originating from fossil fuel burning[*Seinfeld and Pandis*, 2012]. Alkanes (53.3 ng/m^3), alkanoic acids (294.3 ng/m^3), dicarboxylic acids (213.8 ng/m^3), aromatic polycarboxylic acids (107.7 ng/m^3) identify 10-40% of the known primary organic compounds. Some tracer compounds have been suggested to identify specific sources, such as cholesterol for meat cooking, benzothiazole for tire wear, steranes for automobiles, C27-,C29-, C31- and C33-n-alkanes for biogenics and iso-alkanes from cigarette smoke.

10.2.2 Secondary organic carbon sources

Secondary organic aerosols (SOA) normally start off as a volatile organic carbon (VOC) and is transformed, e.g. from oxidation by a hydroxyl radicale (OH) or ozone (O_3), into a less volatile compound that will transform to a particulate through either condensation or nucleation [*Seinfeld and Pandis*, 2012]. Thus secondary organic aerosols are defined as organic compounds that have experienced both a phase change and a chemical reaction. Making e.g. condensed matter from initial warm gaseous exhaust a primary aerosol [*Seinfeld and Pandis*, 2012].

The reaction of one primary exhaust organic molecule to secondary organic aerosols can involve multiple reactions and result in a variety of compounds. The oxidation of cyclohexene by O_3 result in a number of different compounds amongst

these oxalic-, malonic- and glutaric-acids as well as 4-oxobutanoic-, 5-oxopentanoic-, and 6-oxohexanoic acids and several more compounds[*Seinfeld and Pandis*, 2012]. Thus the oxidation of VOC produce HULIS.

10.3 Sources of organic acids in the Arctic

As described above organic aerosols form a complex system of primary and secondary aerosols and thus estimating the exact sources for each compound is not an easy task. Further only limited studies for the Arctic exist and as the concentrations are low distinguishing sources are further complicated.

Soluble HULIS in snow at Barrow Alaska is explained by long range transport of biomass burning plumes. Due to the low aromatic concentration of compounds a source region far from the Arctic is speculated, however the content of aromatic substances in the water soluble HULIS was still higher than what would be expected for secondary aerosol soluble HULIS. The HULIS was also speculated to be of marine origin, such as biogels from open sea ice leads [*Voisin et al.*, 2012].

Kawamura et al. [2010] found an annual cycle of TC with high loads in spring and early summer and a decrease towards winter, as a result of frequent snow fall and less transport from polluted areas. They found the spring peaks of TC related to the polar sunrise, which causes photochemical oxidation of VOC and that the in situ production in snow of particulate organic compounds increases as an effect of the polar sunrise. Similarly an increase of WSOC was found with polar sunrise, as the photochemistry break down long organics, making them more soluble. In the study it is also suggested that some increase of WSOC is related to an increase in anthropogenic aerosols in the spring, where transport from lower latitudes is increased [*Kawamura et al.*, 2010]. Further the study found an increase in TC, which through studies of redfield ratio and MSA[1] was related to marine organic matter.

About 7% of WSOC is simple carboxylic acids. The remainder is believed to be originating from plant waxes, microbial/marine sources, biomass burning, fossil fuels combustion, soil re-suspension, plastics and secondary oxidation products, while carbohydrate-like materials is suggested from wave breaking and to be a major fraction of WSOC in the Arctic [*Kawamura et al.*, 2010].

10.3.1 Simple organics

Simple carboxylic acids like formic acid (HCOOH) and acetic acid (CH_3COOH), are believed to be directly emitted by vegetation and biomass burning [*Legrand and De Angelis*, 1995]. Acetic acid is also a result of oxidation of isoprene (CH_2=CCH=CH_2) by ozone and OH, and thus also increased during polar sunrise [*Legrand and De Angelis*, 1995]. Formic acid in the Greenland ice core GRIP was found to increase during the onset of the Holocene as the Laurentide icesheet[2] decreased [*Legrand and De Angelis*, 1995].

[1] Methanesulfonate, for more on MSA see section 1.1.1.

[2] The Laurentide ice sheet was a large ice sheet covering most of North America during the last glacial period.

Glyoxal (OCHCHO) and diacetyl ($(CH_3CO)_2$, C4 diacid) are found to be a product of NO_x-air photo-oxidation of aromatic hydrocarbons [*Horowitz et al.*, 2001].

Aldehydes, including formaldehyde, are produced by the oxidation of hydrocarbons, which also produces other ketones. The source of hydrocarbons are mainly anthropogenic [*Legrand and De Angelis*, 1995].

10.3.2 Keto-acids

The marine atmosphere of the pacific was found to be the origin of homologous[3] 4-ketocarboxylic acids (C7-C13) observed for Arctic aerosols [*Kawamura et al.*, 2010].

Pyruvic acid is believed to arrive to the Arctic from biomass burning, domestic animals, plants, automotive exhaust, while also being produced by the atmospheric oxidation of isoprene, which originate from forest fires and thus pyruvic acids will be enriched in ice core records in relation to forest fire events [*Talbot et al.*, 1990; *Legrand and De Angelis*, 1995].

Further experimental evidence show that pyruvic acid and hydrogen peroxide photolyse in clouds and form SOA, such as oxalic, glyxolic, acetic and formic acids *Carlton et al.* [2006]. While *Kawamura et al.* [2010] found evidence of photochemically induced pyruvic acid; the source of the original compound photochemically changed to pyruvic acid was not suggested.

10.3.3 Di-carboxylic acids

Similar to formic acid major diacids was found related to temperatures in the Northern hemisphere in an ice core study by *Kawamura et al.* [2001]. The oxidation capacity of the atmosphere can be derived from the variation between concentrations of diacids [*Kawamura et al.*, 2001] and MSA (from plankton and photochemistry) changes simultaneously to dicarboxylic acids [*Kawamura et al.*, 2001]. Dicarboxylic acids were found to be present in snow and ice as particles (low vapour pressure) also in the study by *Kawamura et al.* [2001], while smaller organics as formic and acetic were in gas phase.

Water soluble dicarboxylic acids (short chained) are enriched in Arctic aerosols as compared to near source aerosols. This enrichment is an effect of photochemical ageing during long range transport (of e.g. VOC) as well as strong radiation during solar sunrise[*Kawamura et al.*, 2010]. One of the simplest dicarboxylic acids, oxalic acid (C2[4]), however, decreases relative to TC after polar sunrise, caused perhaps by a preferred degradation of C2. Such a degradation of C2 could be caused by a complex with Fe(III) being photolysed into CO_2 and Fe(II). The relative low concentrations of C2 compounds relative to TC after polar sunrise could also be explained by an enhanced production of malonic (C3) and fumaric acid (C4) by the break down of longer chained dicarboxylic acids [*Kawamura et al.*, 2010].

A source of oxalic acid (C2) is combustion of fossil fuels, but a trend related to fossil fuel combustion was not found in ice cores [*Kawamura et al.*, 2001]. *Kawamura et al.* [2001] suggest the lack of relation being caused by post depositional change, and note that biomass burning does relate to the content of oxalic acid in ice cores

[3] A homologue series of compounds differ from each other by a repeating unit, such as e.g. -CH_2-

[4] In the following Cx, refers to the number (x) of carbon atoms in the compound

[*Kawamura et al.*, 2001]. Oxalic acid can also be produced by photochemical oxidation of organic compounds (SOA) such as natural fatty acids and the ratio of oxalic acid carbon over total carbon in a Greenland ice core record was found related to solar irradiance (from yr 1600 AD-today) [*Kawamura et al.*, 2001]. Further a decrease in malonic acid (C3) was found in mid april, and it was suggested that malonic acid is decomposed to oxalic acid, when the sun is above the horizon all day [*Kawamura et al.*, 2010].

Similarly sources such as gasoline, can cause the formation of SOA such as glutaric acid (C_5) by oxidation of cyclobenzene and SOA in the form of adipic acid (C_6), which can originate from the oxidation of cyclohexene, methylene-cyclohexane and 1-methyl-cyclohexene [*Winterhalter et al.*, 2009].

Phthalic acid, an aromatic dicarboxylic acid, is also a SOA again from the oxidation of other more complicated organic compounds [*Winterhalter et al.*, 2009], and similarly azelaic acid (C_9) result from oxidation of unsaturated fatty acids by OH or O_3, which contain a double bond at 9th C, such as oleic and linoleic acids. Some fatty acids, however, contain a double bond at a higher position of the molecule and thus the oxidation results in longer carboxylic acids [*Winterhalter et al.*, 2009].

Adipic and phthalic acids are thus mainly SOA from anthropogenic sources, while azelaic arrives from biogenic longer chained organic compounds. Thus the biogenic ratios between C_6 and C_9 can be used to differ between an anthropogenic and biogenic origin [*Winterhalter et al.*, 2009]. Oleic and linoleic acids, forming the azealic acid, is suggested to originate from the Arctic ocean and an increase is found when sea ice retreats (May and June). Fumaric acid (C4) also increases in late spring and to early summer, though it originates from the *cis* to *trans* isomerisation[5] of maleic acid (unsaturated carbonyl both C4, dicarboxylic acid) during strong solar radiation. Similarly also in late spring and early summer an increase in 4-oxopimelic acid (a C7 dicarboxylic acid containing an additional ketone group) from oxidation of pimelic (C7) acid was observed. [*Kawamura et al.*, 2010]

In the Arctic atmosphere today diacids decrease in May and June due to limited anthropogenic transport [*Kawamura et al.*, 2010].

10.3.4 Omega acids

Glyoxylic acid (ωC2) is one of the most abundant ω-acids. It is a SOA and the intermediate of the oxidative reactions of anthropogenic VOC's forming oxalic acid (C2, dicarboxyl) [*Kawamura et al.*, 2010]. Similarly ωC3-ωC9 show maxima in early april as they are photochemically induced [*Kawamura et al.*, 2010]. 4-oxobutanoic acid (ωC4) is found in realtion to sea ice and is more abundant than glyoxylic acid (ωC2) in spring and early summer [*Kawamura et al.*, 2010].

[5] *cis trans* isomerism, geometric isomerism, occur when there is a restricted rotation somewhere in a molecule. A *trans* (latin:across) isomer have different structure on the same side of the molecule, while the *cis* (latin:"on this side") have similar.

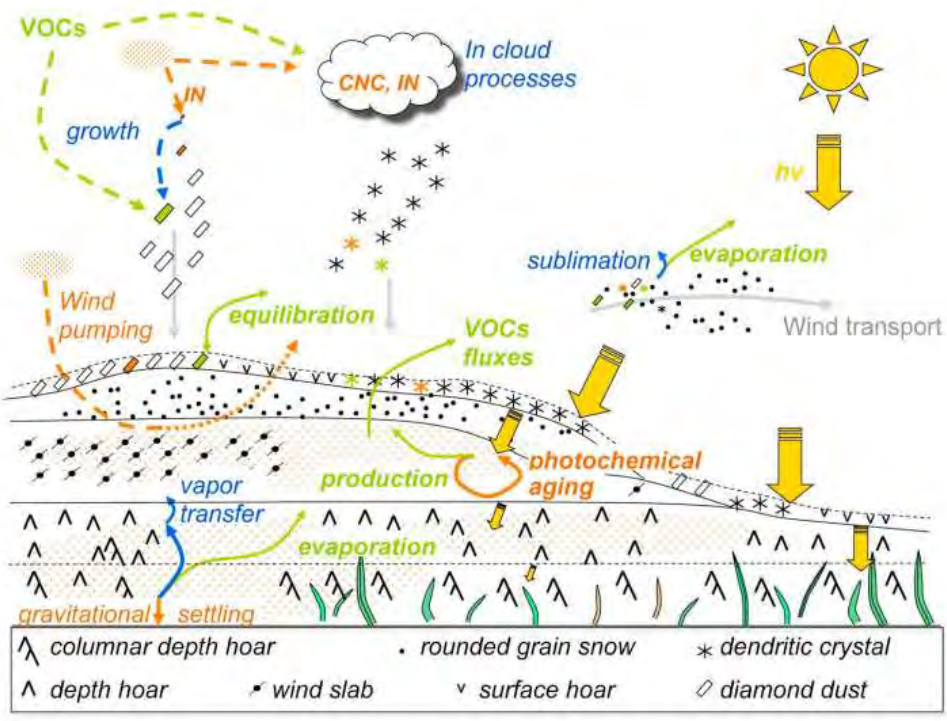

Fig. 10.6: Illustration of physical and chemical processes involved in changes of the chemical composition of various snow types at Barrow, Alaska. Figure by *Voisin et al.* [2012].

10.4 Post depositional changes of organics in snow and ice

As many organic molecules are excited in the range of UV light, which can penetrate into snow (and form in ice) some changes of the organic molecules does occur post deposition. Furthermore bulk concentrations do not necessarily represent the actual concentration in ice, as grain boundaries are speculated to contain enhanced concentrations of organics and volcanic horizons have enhanced acidity, also affecting the fractionation between the different organics. If such thin layers are not sufficiently resolved in a set of measurements the true local concentrations cannot be determined.

10.4.1 Changes of HULIS and carbon species in snow

Several chemical and physical processes can change the content and distribution of carbonaceous species in snow. In Figure 10.6, the processes are illustrated. The Figure is by *Voisin et al.* [2012] and is based on chemical measurements of TOC, DOC, EC, HULIS, carbonates and aldehydes from snow in Barrow, Alaska. Further the study investigated changes in species composition in relation to snow types.

Five processes are believed to be the main drivers of changes in distribution of carbonaceous species:

1 **Physical equilibration with the surrounding atmosphere** The physical equilibration is mainly governed by thermodynamics, it involves absorption

and desorption, as well as liberation and trapping by sublimation and condensation processes. The physical equilibration can be significantly enhanced by wind pumping, metamorphism and lifting of individual grains at the surface [*Voisin et al.*, 2012].

2 **Photochemical fragmentation** Radicals such as OH is known to form in the surface layers from the photolysis of NO_x and formaldehyde [*Jones et al.*, 2001; *Chu and Anastasio*, 2005]. These radicals can interact with carbonates and produce shorter chained compounds. The short chained compounds are often volatile and can be released to the ambient atmosphere and be lost from the snow pack [*Voisin et al.*, 2012].

3 **Photochemical functionalization** Photochemistry can also oxidize carbonate species without bond breaking, this can make the species more water soluble, thus less volatile, and less likely to leave the snow pack [*Voisin et al.*, 2012]. Long chained fatty acids and long chained alkalenes (C18-C22) are usually insoluble and is primarily altered in the snow pack by photochemical fragmentation and transformation into dissolved organic carbon (DOC) by photochemical functionalization [*Voisin et al.*, 2012].

4 **Dry deposition through wind pumping** Aerosols can be trapped by the snow and thus dry deposition during wind events can increase the carbon load especially in the surface snow. It is suggested that the effect of dry deposition for organic aerosols is size dependent [*Voisin et al.*, 2012].

5 **Gravitational deposition at the base of depth hoar layers** When the temperature gradient is large ($\geq$10 °C/s) depth hoar forms. The formation of depth hoar is fast and up to 60% of the ice lattice is redistributed. It has been suggested that aerosols at the surface of the snow grain in such circumstances fall toward the bottom of the depth hoar layer [*Voisin et al.*, 2012]. Depth hoar is observed on the Greenland ice in layers representing the late summer and early autumn where the density is low, due to high snow falls, and in case of intensive temperature fluctuations [*Alley et al.*, 1990].

10.4.2 Grain boundary concentrations

It is well known that if an aqueous solution of an organic compound (or another chemical) is frozen down it can results in a lower concentration in the water ice, while the concentration of the organic is high in the remaining liquid water. The highly concentrated mixture also solidify below the eutectic point (the point of lowest possible temperature of solidification for any mixture of specified constituents). Many experiments investigating such up-concentrations have been performed in the laboratory [*McNeill et al.*, 2012; *Kim and Choi*, 2011]. Enhancements between 4 and 40 times has been observed depending on the solution in question [*McNeill et al.*, 2012]. However it is also possible that compounds are included in ice as hydrates, though intuitively only small molecules can be accommodated in the ice crystal lattice [*McNeill et al.*, 2012]. The question is if an up concentration in between the ice grains in natural glacier ice formed by precipitation of individual snow grains, thus already

frozen prior to the compression to the formation of glacier ice, takes place. Some evidence from early SEM analysis suggested that between 40% and 100% of the bulk sulphuric acid remains in the triple junction between grains [*Mulvaney et al.*, 1988], while other recent studies suggest that the picture is much more complicated and that the amount of impurities in e.g. Antarctic ice is sufficient to cover only a very small part of the grain boundaries in a monolayer [*Cullen and Baker*, 2001; *Barnes et al.*, 2002; *Barnes and Wolff*, 2004], *Barnes et al.* [2002] suggest that first when all grain boundaries are covered with monolayers the triple junctions start to fill.

10.4.3 Acidity

In ice cores layers of enhanced acidity is found in relation to volcanic horizons [*Clausen et al.*, 1997] (see section 6.1.1 and 8). The acidity can change the fractionation between different organics. For example the concentrations of formic and acetic acid in the Greenland ice core GRIP found to be strongly pH dependent increasing and decreasing with H^+ respectively [*Legrand and De Angelis*, 1995]. Similar to the organics it is not well addressed how different the concentration of acidity in between individual ice grains might be compared to the bulk concentration.

10.5 Concentrations of organic compounds in snow and ice

The absolute concentrations of organic species and the variability between them is not easy to determine in polar snow and ice as the concentrations are low. Though total carbon and water soluble organic carbons can be determined without a pre-concentration step for the detection of carboxylic acids a pre-concentration step is often necessary. Pre-concentration can be either done using a liquid-liquid extraction (LLE) or a solid liquid (SLE). SLE, use solid phase resins on which the molecules of interest are adsorbed, then the solids are eluted in a suitable solvent. The LLE uses a non-water organic solvent, the organic phase is separated from the water phase, after which the organic solution is concentrated through an evaporation step. Clearly both solid phase resins and organic solvents can be chosen to suit extraction of the molecule(s) of interest [*Winterhalter et al.*, 2009]. After the pre-concentration step detection of the now enhanced concentrations can be performed using various detection methods.

Just to exemplify the Liquid-chromatography-mass spectrometry-time of flight detector set-up (LC-MS-TOF) presented by *Winterhalter et al.* [2009] requires initial sample volume between 200 and 500 mL and thus very large samples compared to the low resolution wanted if the aim is to estimate causes of in situ production in ice cores. Further the extraction efficiency for different compounds vary, in the case of LC-MS-TOF between 41% and 102%, depending on the molecule in question.

Thus absolute concentrations of organics molecules in ice and snow are scarce and for some molecules very uncertain.

10.5.1 Concentration of organic compounds in snow

Despite this large uncertainty on the determined concentrations of organics in snow and ice related to both detection methods and uncertainty in the distribution in the

ice of the compound in question, below are given some concentrations of organics in snow and ice. Further the study is complicated by the difference in how the molecules are grouped in the different studies.

Soluble HULIS in snow around Barrow, Alaska was determined to be between 1 and 16 μg/L (2-15 % of DOC), while 5-20% of DOC was found to be aldehydes, carboxylic acids and HULIS [*Voisin et al.*, 2012].

40% of DOC in snow was found to be formaldehyde, and short chain mono and diacids (Arctic alaska) and only 20% was HULIS and short chain aldehydes and diacids in Alaskan snow [*McNeill et al.*, 2012].

In Arctic aerosols the WSOC was 39-69% (average 56%) of TC (total carbon) [*Kawamura et al.*, 2010], while the WSOC in average was 5% of the aerosol mass [*Kawamura et al.*, 2010]. The diacids comprised 1.5-9.0% of the TC in aerosols (Alaska) and 3-13% of WSOC [*Kawamura et al.*, 2010]. The variation of diacids was towards short chained species; 75% was oxalic (C2), succinic (C4) or malonic (C3). The amount of total diacids (saturated, unsaturated, branched chain and keto and hydroxy diacids) was 7.4-84.5 ng/m^3, with ketoacids (e.g. pyruvic acid) being 0.76-8.9 ng/m^3 and α-dicarbonyls (glyoxal, methylglyoxal) comprising 0.05-2.8 ng/m^3 [*Kawamura et al.*, 2010]. The same study found total ketoacids comprised 0.2-0.6% of TC by weight and 0.4-1.5 % of WSOC, while α-dicarbonyls only comprised 0.02-0.35 % of WSOC [*Kawamura et al.*, 2010]. The low ratios of WSOC explained by ketoacids and α-dicarbonyls means that quite some organics are not detected in the study, those could be monocarboxylic acids, carbohydrates, amino acids, humic-like polymers with more; carbohydrates is believed the major part [*Kawamura et al.*, 2010].

TC was found to vary between 100 and 400 μg C/L in Barrow, Alaskan snow [*Voisin et al.*, 2012]. EC was about 5 % (by mass) and water insoluble organic carbon (WinOC) 28-42% of TC. WSOC was found to decrease from fresh to older snow [*Voisin et al.*, 2012], however enhanced in early season from high winds dry deposition (especially di-acids), because of deposition from excavated surfaces during wind events [*Voisin et al.*, 2012]. As the ground surface is far away for polar ice cores the enhancement in early season is not an effect expected in ice cores or snow on polar ice caps. *Voisin et al.* [2012] estimate that 31-76% of the TC is released back to the atmosphere, by photochemistry and or in relation to the formation of depth hoar.

10.5.2 Concentrations of organic compounds in ice

Few studies have investigated organics substances in polar ice, neither in terms of total organic carbon (TOC) nor the fraction of different organics. Humic like substances (HULIS) is believed to be a major contributor to the organic molecules. Fatty acids in polar ice was found to be 0.14-9.9 % of TOC [*Kawamura et al.*, 2001].

Kawamura et al. [2001] finds di-carboxylic acids, ω-oxoacids and α-dicarbonyls in a Greenland ice core (66°51.9'N, 46°15.9'W, site-J) representing the past 450 years in concentrations of 3.1-32.5 ng/g, 0.13-2.8 ng/g and 0.09 to 1.7 ng/g respectively. The oxalic acid (C2 dicarboxylic acid) accounted 8.4-47% of TC (0.36-20 ng/g) in the ice samples, while (C4 dicarboxylic acid) was 17-67% [*Kawamura et al.*, 2001]. Pyruvic

acid was merely 0.02-7.23 ng/g, but generally showed less than 1 ng/g concentration [*Kawamura et al.*, 2001].

An older study by *Legrand and De Angelis* [1995] investigated the GRIP ice core and Antarctic snow pits and claim that carboxylic acids are a magnitude more abundant in Greenland than Antarctica and further finds, using ion chromatography (IC), formic and acetic acid of 10 ng/g, glycolic and oxalic acid of 1 ng/g [*Legrand and De Angelis*, 1995]. They also detected a 10 to 100 fold enhance during forest fires and that formate and acetate are 2 to 5 times lower during LGM vs holocene in the Greenland GRIP ice core.

The sources of organic molecules are manifold, marine biofilms, terrestrial biosphere and forest fires are some. The organics, however, are modified on their way to Greenland and longer organic chains can oxidize or photolyse to produce shorter chained species. Thus the atmospheric composition at the time of transport is crucial to evaluate from where the species have originated. Further because of the complication of SOA it is very hard to guess how the species might have changed in glacial times as compared to today. Obviously with the Laurentide ice sheet the concentrations in general should be lower, and Legrand and De Angelis [1995] found 10 to 100 times lower concentrations of formate and acetate. However also the exact composition of species will also rely on the type of biosphere and the change found for acetate and formate might not be similar to that for pyruvic acid.

To further complicate matters post depositional changes are many and involve higher concentration due to wind pumping, photochemical fragmentation creating shorter chained species from longer chained ones and increasing the risk that concentrations are lowered as VOC escapes the snow pack.

Concentrations in the ice is low and up-concentration is required to distinguish between the different organic species. This increases the risk of contamination. However, measurements by Legrand and De Angelis [1995] and Kawamura et al. [2001] suggest dicarboxylic acids, which could photolyse and produce CO_2, are found in concentrations of 3.1 to 32.5 ng/g, while α-dicarbonyls concentrations are about 15 times lower. 0.02-7.23 ng/g pyruvic acid was observed.

In the next chapter I review the literature about light penetration in snow and ice to evaluate if photolysis could occur in the deep ice.

11. LIGHT PENETRATION IN SNOW AND ICE

For pyruvic acid (and other HULIS) to photolyse and create CO_2, light is needed at the right wavelengths (300-380 nm) and with sufficient intensity. In this chapter a compilation of light penetration in snow and ice is presented. The chapter also includes an experimental study of the light penetration in surface snow performed during a field campaign at the NEEM site in north-west Greenland in 2012.

11.1 Background on light penetration in snow and ice

Ultraviolet radiation can break chemical bonds and is critical for photochemistry. For the Arctic, due to the high albedo, at the surface of a snow pack photolysis rates in the UV-A region (320-400nm) can reach intensities similar to mid-latitude intensities [*Grannas et al.*, 2007]. The UV-B region (290-320 nm) is subject to a similar albedo effect, but the radiation reaching the snow is low in the UV-B region due to Arctic ozone decreasing the photolysis rates by as much as an order of magnitude below those found at mid latitude.

$$J = \int \sigma(\lambda, T)\phi(\lambda, T)F(\lambda)d\lambda \tag{11.1}$$

The photolysis rate J(reactions/s) depends on the absorption cross section σ (cm^2/molecule), the quantum yield[1] for the production of the compound ϕ, as well as on the actinic flux F (photons $cm^{2-}nm^{-1}s^{-1}$) as shown in equation 11.1. It is difficult to directly determine the actinic flux in snow and ice, thus irradiance is typically detected and used to constrain radiation transfer models and then inverted to obtain actinic fluxes. The simplest models take only scattering and absorption into account[*Grannas et al.*, 2007].

Whether photolysis occurs in the snow is dependent on the precipitation rate too [*France et al.*, 2011a]. Because higher precipitation rate will tend to bury the active compound faster and because light is diffuse in snow depths greater than a few cm [*Warren et al.*, 2006]. Assuming that snow is a uniform medium the intensity decays exponentially with depth. For snow the absorption depth depth[2] is mere 5-25 cm at 400 nm [*Grannas et al.*, 2007]. Thus photolysis occurs mainly in the surface layers and very little light penetrates deeper.

Ice (and snow) has a strong absorption at less than 170 nm, minimum absorption between 179 and 400 nm, moderate absorption is found in the infrared (1-3 μm), while strong absorption is observed at 3-150 μm and in the microwave region only

[1] The quantum yield is the number of molecules decomposed per photon absorbed

[2] The absorption depth is the depth to which only 1/e of the light intensity penetrates and is denoted 1/k in the following.

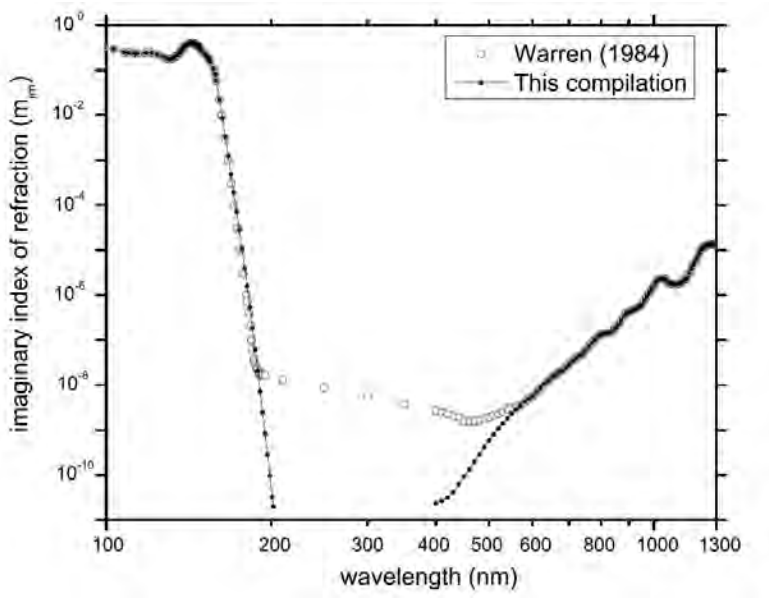

Fig. 11.1: Figure from *Warren and Brandt* [2008]. The imaginary index of refraction in ice shown as a function of wavelength.

a weak absorption takes place. Between 200 and 390 nm absorption is very low and an absorption depth of ∼1.5 km is found [*Warren and Brandt*, 2008].

Figures 11.1 and 11.2 are from *Warren and Brandt* [2008] and *Askebjer et al.* [1997], respectively, and show compilations of light penetration in ice. Notice the large variation between different experiments (Figure 11.2). m_{im} relates linearly to the absorption constant $k_{ice} = 4\pi m_{im}/\lambda$, where λ is the wavelength. The values shown in the figures are appropriate for ice close to the melting point (T=266 K) and the temperature dependence of the absorption in ice k_{ice} is in the order of 1% per °C for wavelengths of λ =175 nm-1 cm with higher absorption at warmer temperature [*Woschnagg and Price*, 2001].

Previous experiments in laboratories have shown that ice blocks of 15-50 cm do not have enough attenuation for the absorption at 400 nm to be determined [*Warren et al.*, 2006]. However using artificially grown ice of 2.8 meter a minimum of $k_{ice} = 0.04m^{-1}$ has been detected at 470 nm. Other experiments using 3 meter blocks of ice determined the absorption in ice to be $k_{ice} = 0.7m^{-1}$ at 250 nm and down to $k_{ice} = 0.08m^{-1}$ at 400 nm, thus giving a absorption length of mere ∼13 m [*Warren et al.*, 2006].

The Antarctic Muon And Neutrino Detector Array (AMANDA) experiment, which is a large scale experiment on the Antarctica, intended for the determination of muon showers, has photon counters in depths of 800 to 1800 m in the actual polar ice. In order for the set up to be able to determine the showers of particles from the universe, exact knowledge of the attenuation in the polar ice is needed. Thus the background absorption and scattering in the ice is measured by determining pulses of light with photomultiplier tubes [*Abbasi et al.*, 2011]. In the AMANDA experiment *Askebjer et al.* [1997] found the minimum absorption between 350 and 400 nm and

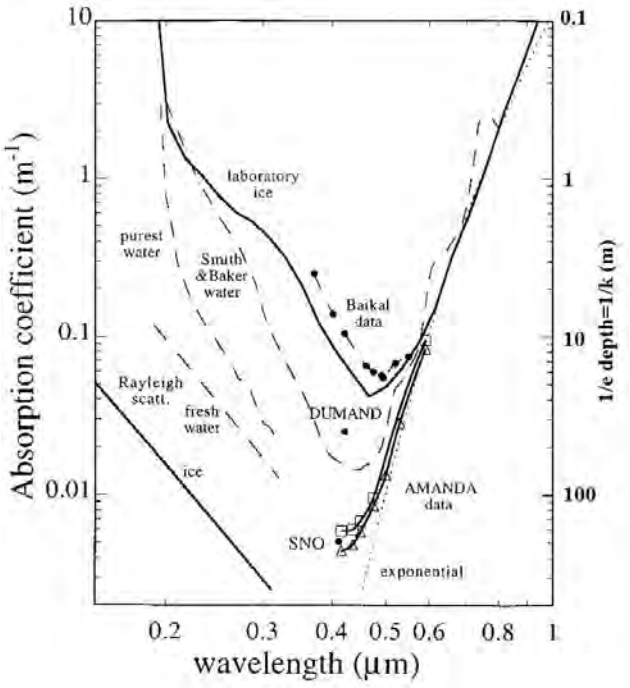

Fig. 11.2: Figure from *Askebjer et al.* [1997]. The absorption coefficient between 100 and 1000 nm in ice.

that the absorption depth in that range is about 240 m. Due to the length of the photo cables the absorption at lower wavelengths could not be determined in the AMANDA experiment. The IceCube experiment builds upon the experience from the AMANDA experiment and similar tubes were inserted at greater depths (1.45 km to 2.45 km)[*Abbasi et al.*, 2011].

Warren et al. [2006] did 25 experiments in snow at Dome C, Antarctica in the period Dec 2004 to Jan 2005 using a spectrometer. The absorption coefficient was found to be less than 0.1 m^{-1} for 300-600 nm with the absorption minimum at 390 nm giving an absorption length of 700 m [*Warren et al.*, 2006].

As is evident from the discussion above, the values for penetration of light in snow and ice vary significantly between studies. One explanation of such variation is that some experiments are conducted using artificial "pure" ice, while others are experiments conducted on real snow and ice. In snow and ice containing air bubbles a lot of scattering occurs and in natural ice impurities influence the attenuation. High loads of impurities are found in glacial cold periods, where the dust loads are 10-100 times higher than from the current atmosphere [*Rothlisberger et al.*, 2002; *Fischer et al.*, 2007].

11.1.1 Scattering

In snow the scattering is mainly related to snow grain size, with a weak dependence on wavelength [*Grannas et al.*, 2007]. The scattering and absorption cross sections per mass in various Arctic snow packs is known to vary from 0.8 to 30 m^2/kg^{-1} and

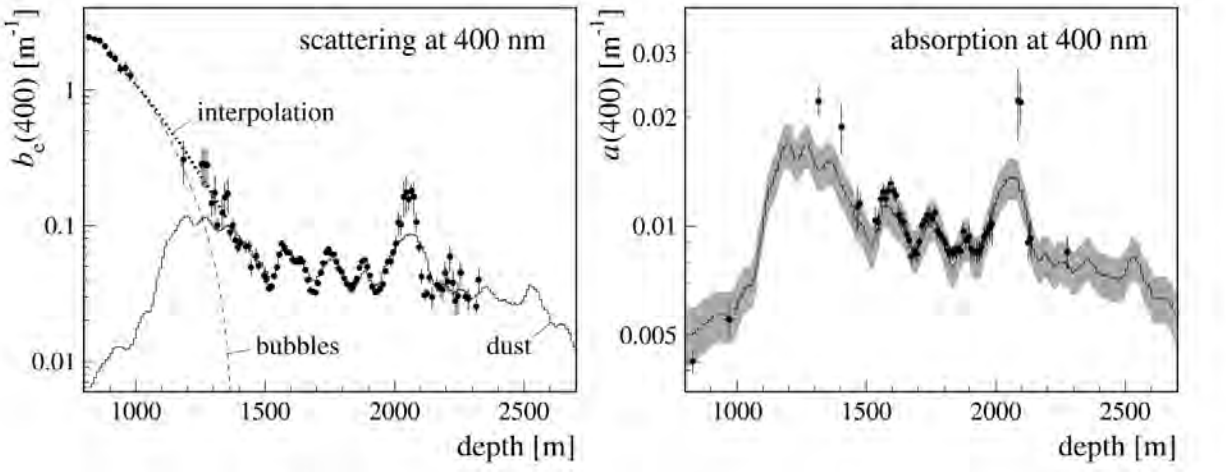

Fig. 11.3: From *Ackermann and Others* [2006]. Scattering and absorption for 400 nm shown with theoretical contributions by dust and bubbles. The y-axis for the absorption a is similar to the definition of k_{abs} and similarly the y-axis for the scattering b is equal to $k_{scatter}$.

from 1 to 25 cm/kg^{-1} respectively [*France et al.*, 2012].

In the AMANDA ice experiment factors influencing the scattering were found to include air bubbles, air hydrates, crystal defects e.g. from impurities (acids, salts, dust), as well as direct impurity scattering. The scatter coefficient $\tau = 1/k_s$ was found to vary between 10^{-27} and 10^{-5} in a model study [*Price and Bergström*, 1997], while the observed variation in τ during the AMANDA experiment was between 10^{-12} and 10^{-3}. Estimates of the wavelength dependencies of these different factors vary between no wavelength dependence to proportional to λ^{-1}. In the AMANDA experiment, for the depth range of 1300 m to 2300 m, the scatter coefficient was found to vary by a factor 7. Air bubbles, causing scattering when present, were found below 1350 m to have been converted to air hydrates that cause close to no scattering [*Ackermann and Others*, 2006]. How the air bubbles and dust affect the scattering and absorption in the Antarctic ice at 400 nm is shown in Figure 11.3.

Clearly it is not sufficient to just know the light absorption in pure ice, the content of impurities, crystal size and shape, as well as air content and distribution is critical to estimate the light penetration in real ice.

11.1.2 Means of detecting light in snow and ice

Large scale experiments like AMANDA and IceCube[*Askebjer et al.*, 1997; *Abbasi et al.*, 2011] are costly and thus to advantage we might increase our knowledge also from laboratory experiments on smaller sections of ice or by means of smaller scale experiments in natural snow. A straight forward method is insert spectrometers and in ice and snow at different depths to investigate the direct absorption [*France et al.*, 2011a;b; 2012], another frequently used method determines the light penetration indirectly by means of chemical actinometry [*Galbavy et al.*, 2007b; 2010].

Determination of light penetration using spectrometers

Spectrometers can be used in series to determine the light attenuation in the near-surface snow [*France et al.*, 2011a;b; 2012]. *France et al.* [2011a] used 6 spectrometers (Ocean Optics) simultaneously detecting at 6 different depths to obtain the spectra for the light penetration between 320 and 700 nm. In that study a multimode silica fiber optic was glued into a 50 cm long by 6.35 mm diameter stainless steel tubing, with a PTFE cosine corrector as a robust entrance optic. Using such a set up the full spectra (limited by the type of spectrometer used) can be obtained using a series of integration times, thus also the UV can be detected if sufficiently high integration times are used [*France et al.*, 2012]. The repeatability of such measurements are $\pm 20\%$ and are related to local snow variability as well as to measurement uncertainty [*France et al.*, 2012].

In the studies by *France et al.* [2012] Nadir reflectance was also determined. The Nadir reflectance is the reflectivity at vertical incidence and can be determined using a Dual Field of View (DFoV) method; two spectrum radiometers placed on tripods see vertically downwards, one detects the snow, the other a reference white plate of known reflectance. Thus the precise solar reflectance in the surface snow can be determined.

Further, snow pack measurements such as stratigraphy, temperature and density are determined in high resolution for such experiments and if all the information is available a radiation transfer model, such as the Tropospheric Ultraviolet and Visible (TUV) Radiation Model[3] can determine a unique scattering and absorption coefficient for each layer [*Lee-Taylor and Madronich*, 2002]. The TUV model has 106 snow layers. The layers have 1 mm spacing in the top 0.5 cm and 1 cm spacing in the remaining 1 m snow pack. A snow asymmetry factor can be inserted in this model and also the size of snow grains can be adjusted. However the TUV model is thought to overestimate photon fluxes below 330 nm [*Galbavy et al.*, 2007b] and a factor 10 discrepancy to observations of black carbon (BC) compared to estimated BC from the TUV model has also been reported [*McNeill et al.*, 2012].

Determination of light penetration by chemical actinometry

Another method for the determination of light penetration in snow (or ice) is by chemical actinometry. By burying or inserting, in known depths in the snow or ice, a series of light transmittive tubes (e.g. made from GE 021 quartz tubing) containing a light-sensitive chemical and leaving them for a known period of time, the absorption can be determined. The sunlight drives a chemical reaction inside the tube to a stable product and the amount of stable product formation (or loss) can be converted to rate constants of photolysis [*Galbavy et al.*, 2007b; 2010].

Dependent on the wavelength of interest different light sensitive compounds can be used. Experiments using actinometric solutions involve the use of nitrite and HOOH as chromophores in solutions of acetonitrile and water. Determination of PhOH by high-performance liquid chromatography (HPLC) allows for the determination of 1/e depths for wavelengths relevant for photolysis of NO_3^{-2} [*Galbavy et al.*, 2007a]. In a similar fashion 10 μM 2-nitrobenzaldehyde in water has also been used

[3] The model is available at http://cprm.acd.ucar.edu/Models/TUV/ free of charge

as a actinometric solution to determine 1/e depths relevant for NO_3^{-2} photolysis [*Galbavy et al.*, 2010].

The actinometer method is time consuming and difficult as compared to the method using spectrometers. Transport to a laboratory, where samples can be determined, can take time and if samples are not kept dark during transportation erroneous results can be obtained. Also the analysis of each tube can be time consuming. Transport and storage effects are mostly unknown. However the method has the advantage that it is possible to select an actinometric compound with a light absorbing spectrum similar to the molecule of interest (say pyruvic acid). Thus the entire light spectrum is covered in one measurement. Further burial times (that in principle could be years) and depths (light intensity) can be varied according to the combination of actinometric solution and thus measurements in deep ice are possible. However depositing the actinometric tube at sufficient depth and retrieving it could prove very challenging.

11.2 A light penetration study at the NEEM site

In 2012 during the field season at the NEEM site, Greenland (77.49°N; 51.2°W, 2480 masl, see Figure 1.2) studies were performed in snow pits in order to investigate the light intensity with depth at different wavelengths.

On June 30th a 2 m deep snow pit was dug and samples for density as well as a description of stratigraphy features were taken. Local density was determined every 3 cm with a density sampler (volume 100.5 cm^3) and samples were collected in powder free plastic bags. Further in two shallow pits (∼60 cm) light absorption was obtained *vs.* depth within 5 meters from the deep pit also June 30th. The 1st of July the deep pit was further excavated one meter in the horizontal direction and on July 2nd light penetration was determined. For the deep pit one meter in the vertical was once again removed and measurements were repeated on the 14th of July. These last measurements (14th) took place after the largest melt event in the satellite era (12th of July, 2012) that caused the entire surface of Greenland to compact and ice layers to form within the snow pack [*Nghiem et al.*, 2012; *Hanna et al.*, 2013]. Unfortunately no density profile was obtained on the 14th of July 2012, only stratigraphic features were noted.

11.2.1 Instrumentation for the determination of light in snow pits

To determine the light penetration an Ocean Optics 2000S spectrometer with a UV-VIS (200 nm-700 nm) optical cable and a diffusive cosine correction head (CC-3-UV-S, 180°, 200-2500 nm, 6.35 mm OD) was used. A round hollow metal stick was used to displace the snow about 60 cm into the vertical snow face. After removal of the stick the optical cable with the diffusive head was inserted and a glove was used to cover for the hole in the snow wall, while light spectra were recorded.

Measurements were conducted from the bottom of the pit moving upwards with 2.5 or 5 cm spacing. Dark spectra were recorded at the beginning and end of each pit. Furthermore spectra representing the light arriving at the the snow were recorded by pointing the optical cable directly to the sun. The sun spectrum was recorded after

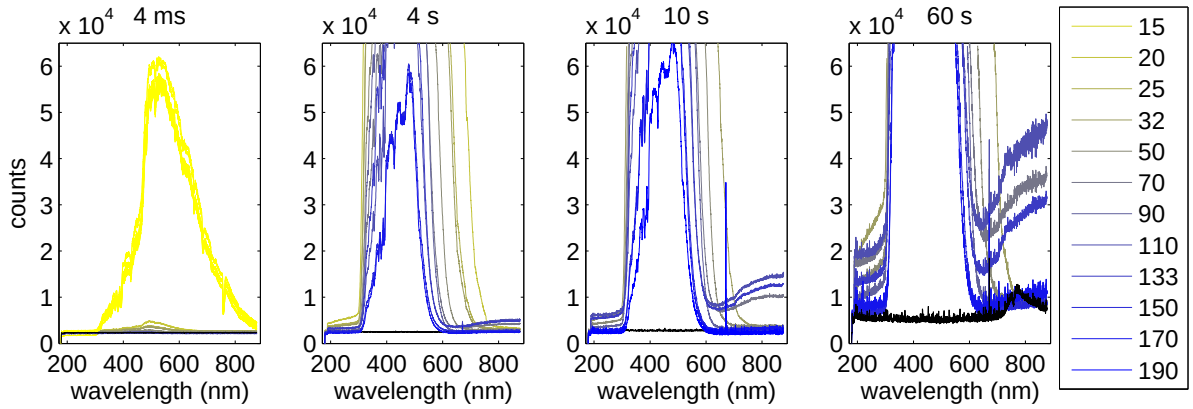

Fig. 11.4: Raw measurements from the large snow pit (2nd July), showing solar intensity (yellow), dark signal (black) as well as the intensity recorded at different snow depths (see legend for relation between colors and depth in cm).

each depth to ensure that the sky had not dramatically changed during detection. Integration times between 4 ms and 45 s were used. The investigation took place around noon only on days with a clear blue sky.

Also measurements deeper than two metres were attempted, as the real interest is the penetration of light in deeper Greenland ice. These measurements were performed in the NEEM science trench (firn wall). The science trench is a 5 meter deep trench excavated for the study of ice cores. Here the optical cable was inserted into the firn ceiling and wall, and lights were turned off. However even after maximising the integration time (1 minute), we were not able to detect any light at any wavelength using the ocean optics set up (200-700 nm).

11.2.2 Results of light penetration in NEEM snow pits

The raw data obtained at different depths for the pit dug on July 1st (data obtained July 2nd 2013) are shown in Figure 11.4 for four different integration times (4ms, 4s, 10s and 60s) also shown is the solar light intensity (at 4 ms) and the dark spectrum for each integration time. Similar measurements were performed in the shallow pits 30th of June and in the pit after the melting event, however the lack of a detailed density profile makes the correction to ice equivalent depths impossible. Therefore these data sets are not used further.

The signal obtained 2nd of July was put on an ice equivalent depth scale using the density obtained on 30th of July, thus assuming no density change between the three subsequent days and further assuming that the snow pack had similar features over 2 m^2. Figure 11.5 shows the density profile as well as the determined ice equivalent depth as a function of snow depth for the pit of 2nd july 2013. The ice equivalent depth (d_{ice}) is determined using the local density (ρ_{d_x}) at depth d_x:

$$d_{ice} = \frac{\left(\sum_{x=surface}^{x=bottom} \rho_{d_x}(d_x - d_{x-1}) \right)}{\rho_{ice}} \tag{11.2}$$

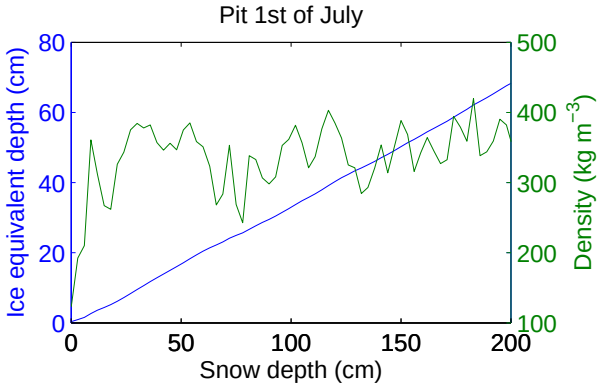

Fig. 11.5: Ice equivalent depth (blue) and density (green) as a function of snow depth.

The absorption was determined using the solar spectra determined at 4 ms relative to the spectra with depth also obtained at 4 ms. To investigate the absorption deeper in the snow, higher integration times proved necessary. However, these high integration times maxed out the spectrum of the sun. Thus for higher integrations time the the solar spectra is determined by linearly scaling the spectra obtained at 4 ms to eg. 4 s after both signals were corrected for the dark signal. Figure 11.6 shows the absorption for wavelengths between 250 nm and 490 nm from the large pit (2nd July) after transferring to ice equivalent depth.

Finally the 1/e depths were determined using a linear fit between ice depth and absorption. As is evident in Figure 11.6 a linear relation is a very rough approximation for some wavelengths. Results are shown in Figure 11.7. For wavelengths significant for the reaction of pyruvic acid (300-380 nm), we find that the absorption coefficient k_{ice} varies between 1.46 and 1.03 m^{-1}.

Uncertainties related to determination of light penetration in NEEM surface snow

Several uncertainties relate to the determination of 1/e depths in Greenland surface snow as performed during the NEEM 2012 field campaign.

The density determination and the following determination of ice equivalent depth is partly estimated based on correct depth determination. However it is not unlikely that the local pit depth is off by up to 0.5 cm. Further the density is dependent on the measured mass, and is accurate to approximate 1 kg/m^3. All this amounts to an uncertainty on the ice equivalent depth from 20 to 85 % with higher uncertainty deeper down with accumulated error.

Furthermore the determination of light and the density was performed about 1 meter apart and on two different days. Local variation in the level of wind crust layers can be quite significant, causing the density determined in one snow pit to not exactly match the density in a snow pit further away. However, we assume that this difference is of minor importance compared to the high uncertainty resulting from the calculation of the ice equivalent depth.

Also the spectra have some uncertainty. The sun spectrum changes over time and as the sun spectrum is only taken once for each depth, whereas obtaining the spectra

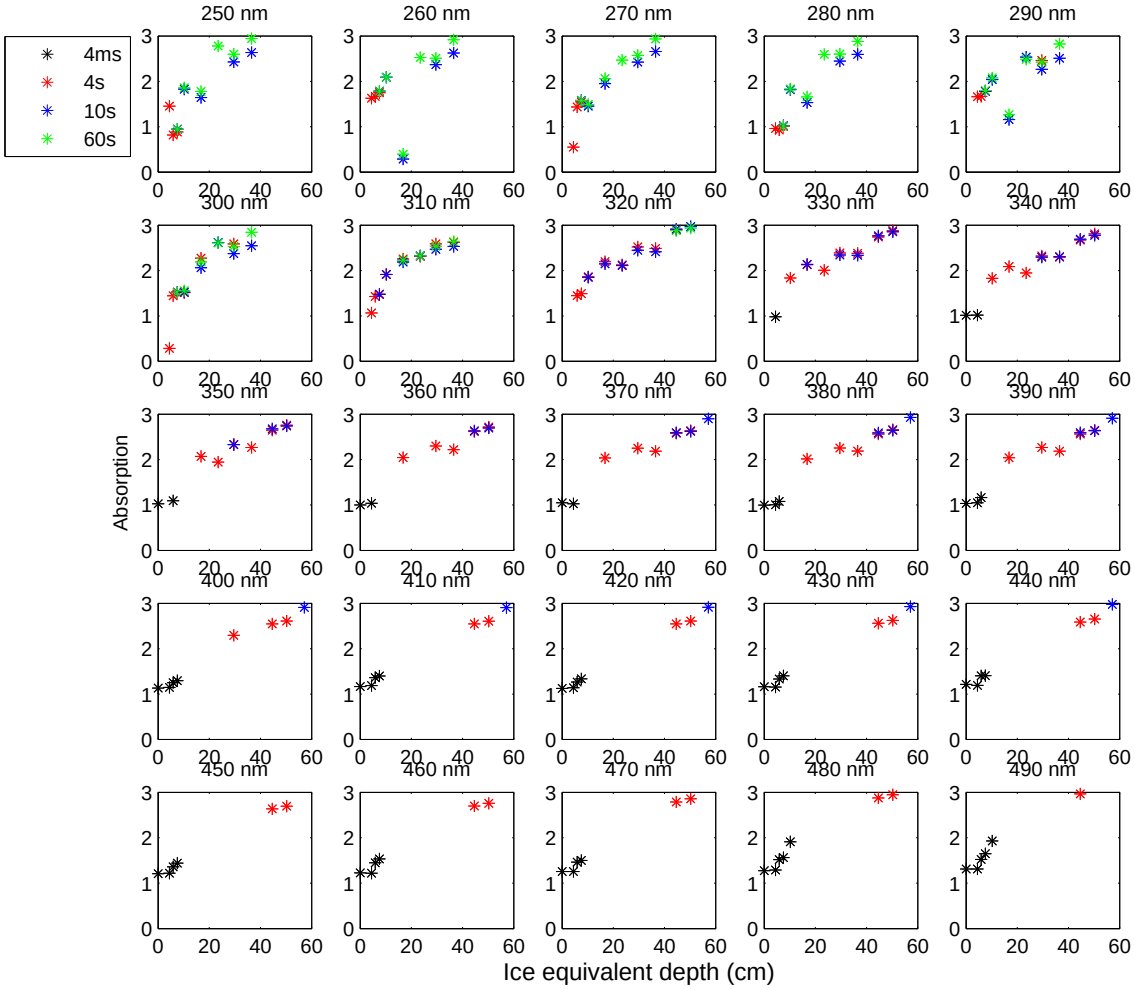

Fig. 11.6: The absorption for different wave lengths on an ice equivalent depth scale as observed for the large snow pit (2nd July). Colours relate to the integration time used.

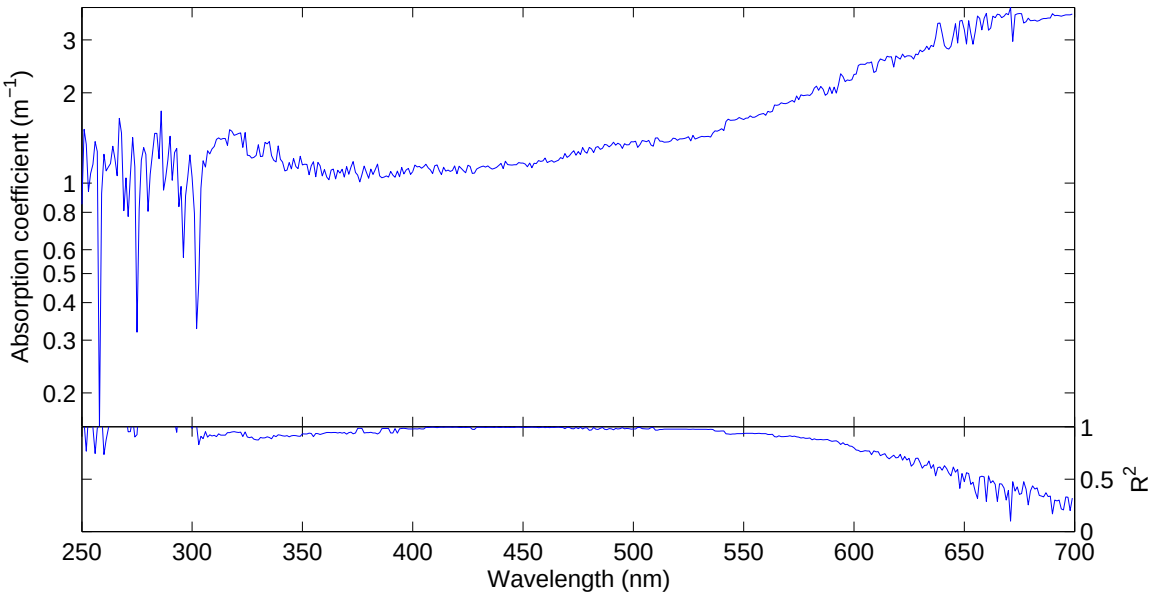

Fig. 11.7: Top: The absorption coefficient (e-folding depth) for different wave lengths on an ice equivalent depth scale as calculated for the large snow pit (2nd July). Bottom: The R^2 of the linear fit used to determine the absorption coefficient.

for one depth took up to 2 minutes, the actual light reaching the surface during the detection at a specific depth could have changed. The standard deviation of the sun spectrum obtained July 1st is shown in Figure 11.8 (dotted line), the uncertainty on the spectrum relevant for pyruvic acid (300-380 nm) varies from 15% at 380 nm up to 21% at 320 nm. Further the spectrometer was somewhat temperature sensitive, making the dark spectra larger with colder temperatures.

Finally the linear fit to the data shown in Figure 11.6 is not very convincing, even when R^2 is high (0.94 for wavelengths between 320 to 380 nm, Figure 11.7).

Thus the combined uncertainty on the estimated 1/e depth is high and any interpretation of the data should be done with great care.

11.2.3 Discussion of light penetration in NEEM snow pits

The resulting absorption depths, k_{ice}, from the NEEM snow pit study (Figure 11.7) are high compared to the results from *Warren et al.* [2006]. However as anticipated the maximum 1/e depth of the light occurs around 400 to 420 nm, k_{ice} ~1.04 cm^{-1}, with a steep increase towards higher wavelengths. We can not provide an estimate for wavelengths lower than 300 nm due to the noise in the spectrometer as uncertainties in the solar spectra are significant below 320 nm.

It is not surprising that the light penetrates deeper in ice (e.g. the AMANDA/IceCube experiments) than in the snow pit, as the scattering in snow is larger than in ice. Further, Greenland ice (ans snow) has an impurity content, from dust and black carbon, about 10 times higher than what is observed for Antarc-

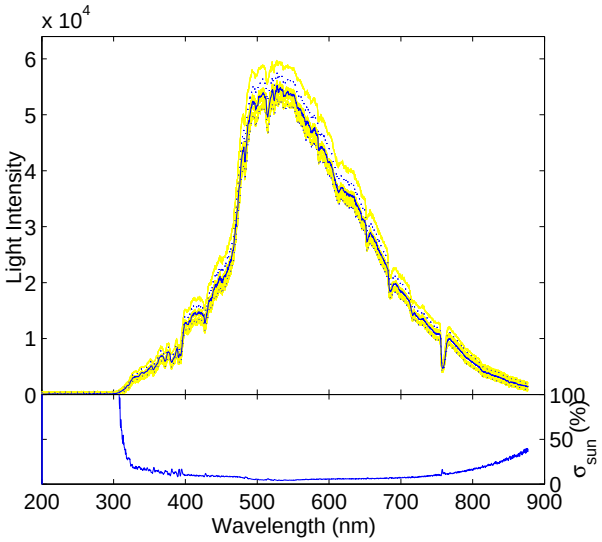

Fig. 11.8: Top: The intensity as detected for the sun using an integration time of 4 ms during campaign at NEEM site 2nd of July as a function of wave lengths, in yellow raw data, in blue full line the mean of the spectra and in dotted blue is mean +-σ. Bottom: One standard deviation in % of the sun spectra obtained.

tica. However the results should be comparable to other snow studies from the Arctic. The k observed in Alaskan snow using a similar method was between 8 and 12 cm^{-1} (snow, [*France et al.*, 2012]), in Svalbard snow 1.7 to 2.8 cm^{-1} (water equivalent,[*France et al.*, 2011b]), and 10 to 12 cm^{-1} at Dome C, Antarctica (snow [*France et al.*, 2011a]) at 400 nm. It is very hard to compare these results to the ice equivalent k_{ice} we have obtained in this study. However, the Dome C and Alaska snow results can be converted to ice equivalent k by assuming the snow density was 250 kg/m^3, while the results from Svalbard can be converted using the density ratio between water and ice. Thus making the e-folding depths approximately 2.5-3.0 cm^{-1}, 1.7-2.8 cm^{-1} and 2.5-3.0 cm^{-1} in ice equivalent depths for the three sites respectively.

Our findings suggest that the light at NEEM penetrates deeper than at all the other sites, however the conversion from snow to ice equivalent e-folding depths is highly speculative and one would expect the light to penetrate to greater depths at Dome C, while Svalbard and Alaska snow contains higher loads of impurities and thus light penetration in these areas should be less than what was observed for the NEEM site.

Had the Nadir reflectance been determined it would have been possible to determine also the absorption and scatter coefficients. However the Nadir reflectance at the surface was not detected at the NEEM site and as uncertainty is significant on the 1/e depths I have not pursued this track of investigations.

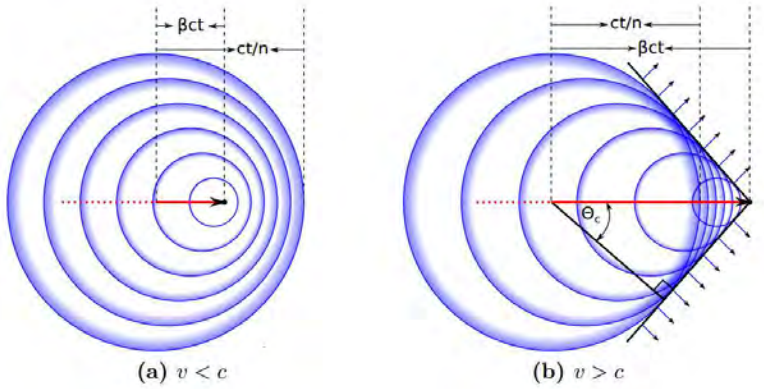

Fig. 11.9: Principle of Cherenkov radiation. a) particle velocity v is below the threshold ($v < c/n$), b) the particle velocity is above the threshold ($v > c/n$) and a wave front is generated. Figure by *Rädel* [2012].

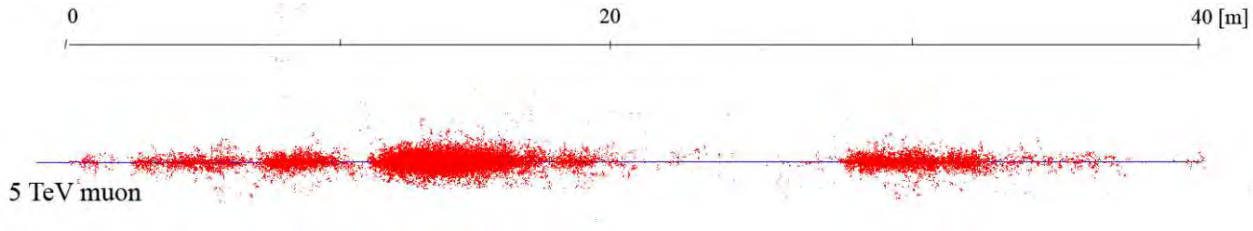

Fig. 11.10: Simulated track of a 5 TeV muon's track over 40 meters in water. Charged particles with a mean range larger than 100 μm generated due to the muon are shown. Figure by *Rädel* [2012].

11.3 Cherenkov radiation

Evidently the scattering in the surface of the snow and in ice containing air bubbles is large. Thus the light to drive the photolysis of pyruvic acid cannot originate at the surface, but must be produced within the ice.

Cherenkov radiation from cosmic rays is one way that photons could be produced *in situ*. Cherenkov radiation is produced when a charged particle travels through a dielectric medium with a speed faster than the phase velocity of light in the media [*Jelley*, 1955]. The charged particle will disrupt the local electrical field and if the particle travels with sufficient speed $\beta = v/c > 1/n$, where n is the refractive index of the medium, the electric field does not relax in time and a shock wave is generated in a half cone around the particle track (see Figures 11.9 and 11.10). The angle of emission, θ is given by the Cherenkov relation:

$$cos(\theta) = 1/(\beta n) \tag{11.3}$$

If the medium is a continuum and is a perfect isotropic dielectric, if the electrically charged particle travels at constant velocity, if dispersion is ignored, and if the radiation reaction is neglected, the amount of energy radiated (W) is given by

the Frank-Tamm relationship (equation 11.4), where c is the speed of light, e is the charge of the particle, ω is the frequency time 2π and l is the path length:

$$\frac{dW}{dl} = \frac{e^2}{c^2} \int_{\beta n>1} \left(1 - \frac{1}{\beta^2 n^2}\right) \cdot \omega d\omega \tag{11.4}$$

By reducing and further defining the fine structure constant $\alpha = \frac{e^2}{\hbar c} \simeq 1/137$, one can obtain the amount of photons (N) emitted between wavelengths λ_1 and λ_2:

$$N = 2\pi\alpha l \left(\frac{1}{\lambda_2} - \frac{1}{\lambda_1}\right)\left(1 - \frac{1}{\beta^2 n^2}\right) \tag{11.5}$$

$$N = 2\pi\alpha l \left(\frac{1}{\lambda_2} - \frac{1}{\lambda_1}\right)\sin^2(\theta) \tag{11.6}$$

Setting $\beta \sim 1$ for ultra relativistic cosmic rays, we find $\sin^2(\theta) = 0.44$. The AMANDA and IceCube experiments seek to determine the amount of particles from outer space. According to *Abbasi et al.* [2011] 36900 events of muon hits were recorded in the IceCube set up during a period of 375.5 days. The typical energies of the muons were 10^3 to 10^6 GeV, with the lower energies being the more likely. The IceCube set up at the time included 40 strings in a depth of 1.45 km to 2.45 km with a photo tube sensor (25 cm diameter) for each 17 meters. The strings were deployed with a distance of 125 meters. The approximate area covered by the set up is 1200 m times 600 m. Thus each photo tube (490 cm^2) is hit by a mean of 15.7 muons per 375.5 days. Making the rate of muon hits $2.5 \cdot 10^{-10} cm^{-2}\ s^{-1}$.

The Cherenkov radiation not only generates the direct wave, but secondary cascades may also be generated. According to *Zornoza and Chirkin* [2008] the photons generated by Cherenkov radiation per metres of muon track in ice is as given in equation 11.7, when the critical energy exceeds (∼1 TeV). Here N_c is the number of photons generated by Cherenkov radiation and E_m is the muon energy. The formula includes both the direct Cherenkov production of photons, but also secondary components related to secondary waves (*e.g.* by pair production and bremsstrahlung). Further it assumes that the light due to scattering is isotropic [*Zornoza and Chirkin*, 2008].

$$N_c = 3 \cdot 10^4 [m^{-1}] \left(1.22 + 1.36 \cdot 10^{-3} \cdot E_m [\frac{1}{GeV}]\right) \tag{11.7}$$

According to *Ahrens et al.* [2004] mean track lengths of muons are 33 metres in ice. In equation 11.7 no wavelength dependence is accounted for, however, we note that the Cherenkov radiation spectra is dominated by higher frequencies and thus most of the energy is emitted in the UV, where pyruvic and other organic molecules photolyse [*Jelley*, 1955]. Further the minimum absorption in those wavelength by the ice make the UV dominate the light generated by Cherenkov radiation within the ice.

In this section light penetration in snow and ice were evaluated. While in the surface snow most of the light is scattered and does not penetrate to large depths,

in pure ice the absorption length is larger than 1 km for wavelengths relevant for the photolysis of organic compounds. The amount of light in both snow and ice is affected by impurity content and scatter by air bubbles above and in the brittle zone.

A small snow pit study of the light penetration at NEEM was performed using a simple set up with a spectrometer and a light transmissive optical cable with a diffusive head. Though the uncertainty on the data is large we find similar 1/e depths at 400 nm as found for Antarctica (Dome C), Svalbard and Alaska snow. If such an investigation is to be performed again it is crucial that a fine scale density profile is obtained. Further determination of the light penetration at several depth simultaneously as done by Francis and co-workers would decrease the uncertainty related to changes in the surface light. Finally the reflectance at the surface should be determined to make the data applicable for determination of absorption and scatter coefficients.

If one wants to investigate the amount of light generated deep in the Greenland or Antarctic ice cap, there is no easy way to do so at the moment. Big scale expensive[4] *experiments like AMANDA or IceCube provide the best knowledge available on how impurities, crystal sizes, air bubbles etc. affect the light penetration in natural ice, as well as on how much light is produced in situ due to muons and other charged particles.*

[4] The IceCube experiment cost 271 million US$

12. AB INITIO EFFECTS OF PYRUVIC ACID CONFORMERS IN VACUO, AND IN LIQUID AND SOLID WATER

Ultraviolet radiation has the power to break chemical bonds and is critical for photochemistry. To evaluate the likelihood of photolysis not only knowledge about the concentration of organics in the ice required and the light available to estimate whether production of CO_2 by UV excitation takes place are required. Needed is also detailed knowledge of the excitation wavelengths for the different compounds. The excitation wavelength is dependent on the exact structure of the molecule, which is influenced by the proximity to other molecules as well as by the general electrical field of the media it is in. Thus a computational study was performed to evaluate the structure of pyruvic acid in vacuum, water and water ice. However, first a brief introduction to excitation of carbonyls.

12.1 Excitations of carbonyls

Organic materials are mostly light absorbing species and "brown carbon" contributes to about 40 % of the absorbed light in snow in the wavelengths between 300 and 750 nm [*McNeill et al.*, 2012]. In Summit Greenland, and Dome C, Antarctica about half of the absorption in the surface snow is estimated to be due to organic chromophores [*McNeill et al.*, 2012].

As a molecule absorbs energy, an electron jumps from an occupied orbital to a higher unoccupied orbital (see Figure 12.1). Several different transitions are theoretically possible, but electronic excitations typically happen from the lowest energy state (ground state) to the nearest state of higher energy (the excited state).

Some transformations that are possible in the cis structured version of a molecule might not be possible in a trans version of a molecule and thus the evaluation of the change in structure as obtained from the computational study is valuable (chapter 12).

A typical carbonyl compound undergo transition from $n \rightarrow \pi^*$ at about 280-290 nm, with a molar absorptivity of about 15. However the carbonyl also have a transition from $\pi \rightarrow \pi^*$ at about 188 nm with a much stronger molar absorptivity (ϵ =900) [*Pavia et al.*, 1996].

Conjugation[1] will typically red shift the spectra (bathochromic shift) as well as lead to an increase the intensity of the absorption (see Figure 12.2). Another way to increase intensity of absorption is by addition of auxochromes, such as methyls (-CH_3) and hydroxyls (-OH) [*Pavia et al.*, 1996]. The carbonyl $\pi \rightarrow \pi^*$ excitation will, in the addition of an auxochrome with a lone pair of electrons (-OH, -OR), be red

[1] Conjugation is the overlap of one p-orbital with another across an intervening sigma bond

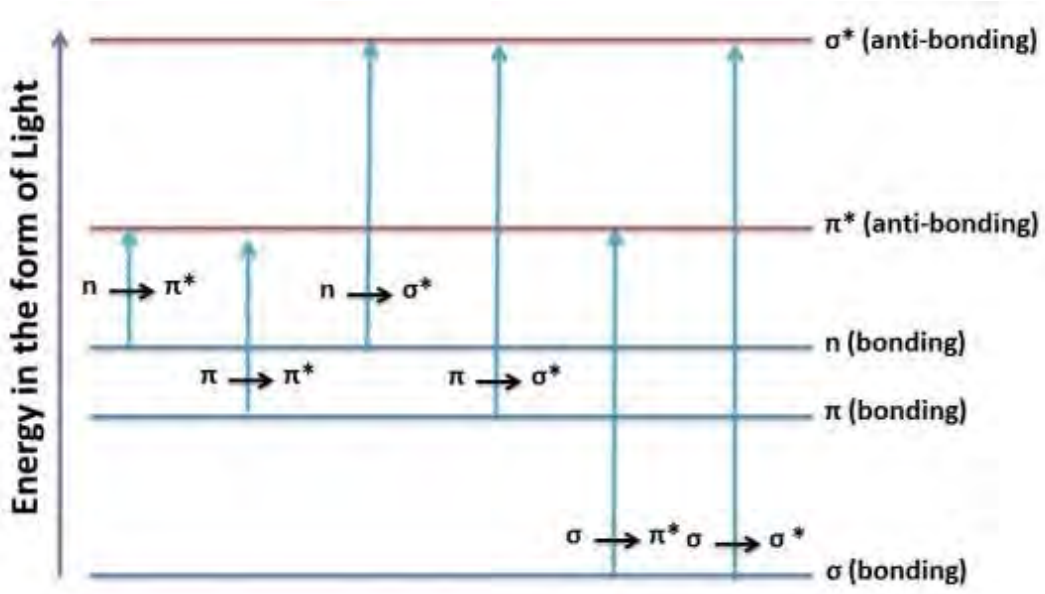

Fig. 12.1: Figure from *Mehta* [2011]. Transitions between bonding and anti-bonding states when light energy is absorbed in the UV-VIS spectra.

shifted, while the n $\rightarrow \pi^*$ is blue shifted (hypsochromic effect). The hypsochromic effect is caused by the added auxochrome withdrawing electrons from the carbonyl carbon, thus causing the lone pair electrons on oxygen to be held more firmly. Thus larger organic conjugated compounds will typically have n $\rightarrow \pi^*$ transitions higher than 280-290 nm [*Pavia et al.*, 1996].

In the case where the carbonyl group is part of a conjugated system of double bonds both excitations are shifted towards longer wavelengths. However the intensity shift occurs with different rates for the two excitations causing the n $\rightarrow \pi^*$ for long chained carbonyls to be buried from the spectra of the $\pi \rightarrow \pi^*$ [*Pavia et al.*, 1996].

However ice is a dielectric media and as such also influences on the exact molecule structure and thereby on the excitation spectra. Thus to evaluate pyruvic acid and its structures in water ice a computational study was performed and is presented on the next page.

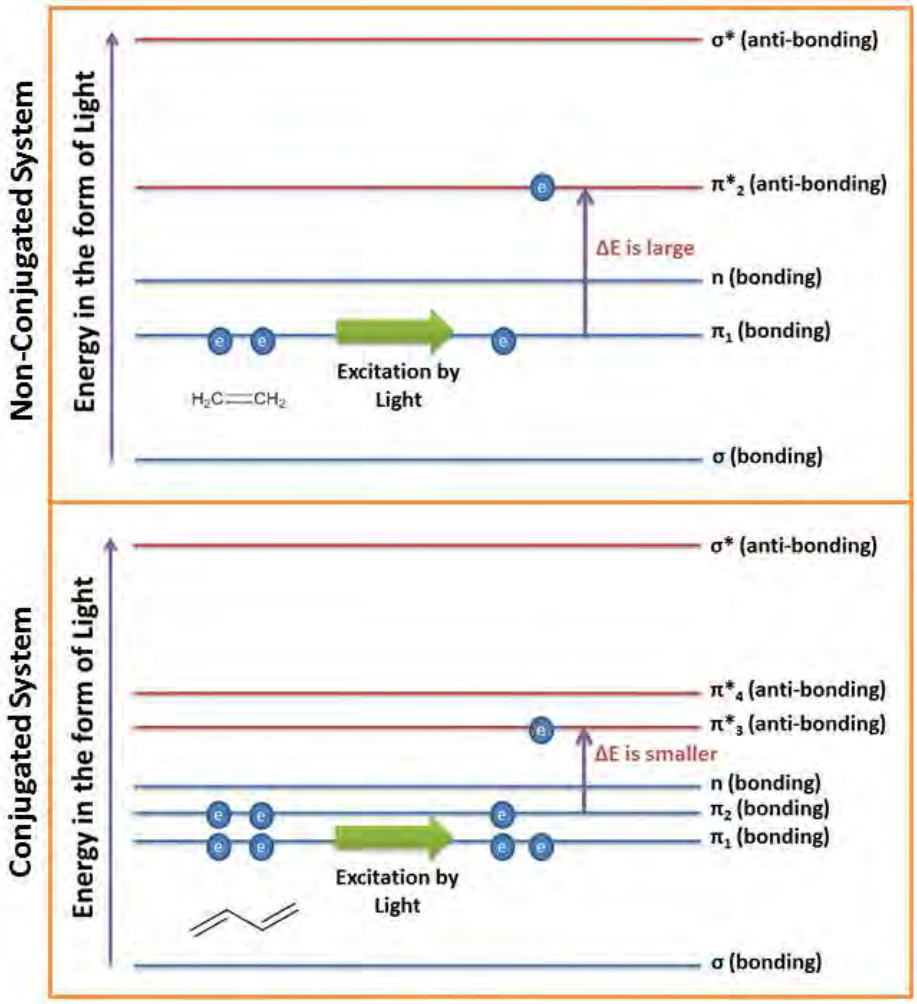

Fig. 12.2: Figure from *Mehta* [2011] showing how conjugation minimizes the energy necessary to shift electronic state.

12.2 Ab Initio effects of pyruvic acid conformers in vacuo, and in liquid and solid water

Kjær, H. A., K. V. Mikkelsen and M. S. Johnson[2]

Ice cores can contain anomalous excess CO_2 in association with organic material. Pyruvic acid (and other alpha-carboxyl organic acids) has been identified as a possible source of CO_2. Pyruvic acid has several low-lying conformers and the partitioning of population between them changes due to interactions with liquid water and ice. In this work we use high level computational methods to provide clarity regarding the pyruvic acid conformers that will be present in different environment; in particular this is the first study to address the structure and vibrational frequencies of pyruvic acid in ice. This project has investigated the most important pyruvic acid conformers using density functional theory (DFT/CAM-B3LYP) with dielectric medium methods to model liquid water and ice, to obtain clarity regarding the pyruvic acid conformers that will be present in different environments, a necessary first step in quantifying photolytic and chemical production of CO_2 in glacial ice. The study shows that the Tt and Ct structures both become more likely in a condensed environment. Further when the dielectric constant increases the differences between the four conformers decrease, suggesting that the inhomogeneous nature of glacial ice will affect partitioning between the various structures.

12.3 Introduction

Glacial records of CO_2 are of great interest in studies of past climate[*Le Treut et al.*, 2007]. Ice cores from Antarctica record CO_2 covering the eight most recent glacial cycles (800 ka BP)[*EPICA community members*, 2004]. The Greenland ice core records, while only covering one glacial cycle, have a much higher resolution due to higher annual snow fall. In some cases, the records of CO_2 from the two hemispheres differ by as much as 20 ppmv, greatly exceeding the hemispheric gradient. In addition, the Greenland records contain rapid CO_2 changes of up to 50 ppm within a single year [*Anklin et al.*, 1995]. On the basis of this and other evidence it has been suggested that in situ production of CO_2 occurs in the Greenland glacier. Recently, the Dome Fuji CO_2 record from Antarctica was also shown to have layers and longer series that differ from the Antarctic Vostok record seeming to indicate in situ production of CO_2[*Kawamura et al.*, 2003].

The source(s) of the hypothesized in situ production is debated and several mechanisms have been proposed including oxidation of organic carbonates and protonation of carbonates[*Anklin et al.*, 1995; *Tschumi and Stauffer*, 2000] These mechanisms were tested by analysing correlations between the oxidant hydrogen peroxide, the organic compound formaldehyde, carbonates (represented by the Ca^{2+} ion) and pH with CO_2. The tests were not conclusive but it was suggested that both processes could be equally important [*Tschumi and Stauffer*, 2000].

[2] This Chapter is intended for publication. Both co-authors are from Department of Chemistry, University of Copenhagen, Copenhagen, Denmark

Recently a third mechanism was suggested, the photolysis of pyruvic acid [*Guzmán et al.*, 2007]: $CH_3C(O)C(O)OH + h\nu \rightarrow CO_2$ + other products. Humic like substances (HULIS), including pyruvic acid, are present in the Greenland ice cap and in Arctic snow [*Kawamura et al.*, 2001; *Voisin et al.*, 2012]. Further, light penetrates deeply into the ice at sufficiently short wavelengths to photolyse HULIS [*Grannas et al.*, 2007].

A recent study by *Larsen and Vaida* [2012] found that pyruvic acid in water produces CO_2 at near infra red wavelengths (850 nm to $\geq$ 1150) through an excitation of the acidic OH vibrational stretching second overtone (1003 nm). The quantum yield for this reaction is however much lower than that for the UV excitation of pyruvic acid observed by *Guzmán et al.* [2006b] of 0.39 and the light is not expected to penetrate deep into natural ice at NIR [*Grannas et al.*, 2007].

The photochemistry of pyruvic acid in ice compared to vacuum and liquid water is relatively unexplored. This is the first computational study to address the structure and vibrational frequencies of pyruvic acid in ice. Further, pyruvic acid plays a significant role in biological systems as part of the Krebs cycle [*Busch et al.*, 1954] and is found in the atmosphere[*Andrae et al.*, 1987], where it will be present in ices.

This project has investigated the most important pyruvic acid conformers using density functional theory (DFT/CAM-B3LYP) with dielectric medium methods to model liquid water and ice, to obtain clarity regarding the pyruvic acid conformers that will be present in different environments, a necessary first step in quantifying photolytic and chemical production of CO_2 in glacial ice. The study shows that the Tt and Ct structures both become more likely in a condensed environment.

The dielectric constant of glacial ice is known to vary [*Moore*, 1993; *Kovacs et al.*, 1995] and the effect of this variation on the pyruvic acid chromophore has not previously been described. We find that when the dielectric constant increases the differences between the four conformers decrease, suggesting that the inhomogeneous nature of glacial ice will affect partitioning between the various structures.

12.4 Computational methods

Hybrid density functional methods (DFT) were used for this study. Previous work suggests that bond lengths, energies, dipole moments and frequencies are slightly better represented using the B3LYP [*Becke*, 1988; *Lee et al.*, 1988] than the PW1 methods [*Adamo and Barone*, 1998]. Although B3LYP has proven successful in many applications its success is not universal, with exceptions including the polarizability of long chains, excitations using time dependent theory for Rydberg states, and charge transfer excitations. This is because the exchange potential behaves as $-0.2r^{-1}$ at long distances rather than the desired $-r^{-1}$ [*Yanai et al.*, 2004]. CAM-B3LYP was developed by *Yanai et al.* [2004] to solve some of these problems using a Coulomb attenuation method. In this study CAM-B3LYP [*Yanai et al.*, 2004; *Peach et al.*, 2006; *Toffoli et al.*, 2006; *Biczysko et al.*, 2010] was used to determine the structure, energies and vibrational frequencies of pyruvic acid conformers in vacuum, liquid water and ice. In addition comparisons to other (hybrid) DFT methods were made for the unperturbed molecule: PBEPBE (pure GGA [*Perdew et al.*, 1996]), B3PW1 (hybrid [*Perdew and Wang*, 1992; *Becke*, 1988]), mPW1PW91 (pure GGA

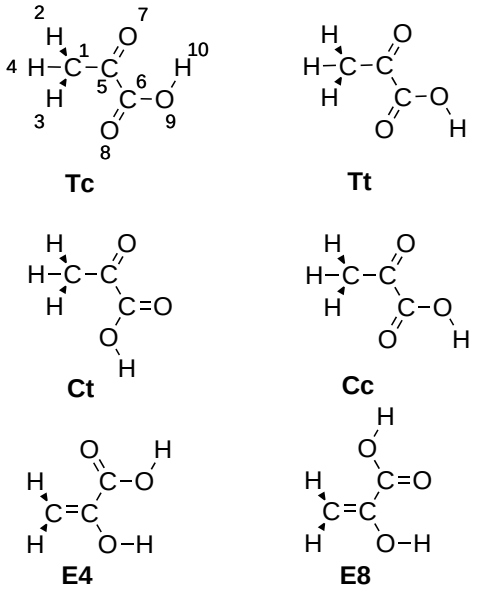

Fig. 12.3: Geometries of the Tc, Tt, Ct and Cc conformers and the labels as used in this study.

[*Adamo and Barone*, 1998]), and B3LYP (hybrid [*Lee et al.*, 1988; *Becke*, 1988]). The basis sets were varied using Dunning and co-worker's correlation consistent basis sets up to the augmented quadruple level [*Dunning*, 1989; *Kendall et al.*, 1992]. As the amount of liquid water present in natural ice is debated, the effects of both liquid water and ice on the structure of pyruvic acid were calculated using dielectric medium methods. For liquid water the dielectric constant ϵ =78.3553 was used and for ice the relative permittivity was taken as ϵ =3.2. Furthermore we conducted a test varying the relative permittivity using the values ϵ =[3.0,3.2,3.6,4.0,4.5] with the basis set aug-cc-pVTZ to explore the freezing coordinate. This study is the necessary first step for further investigations of spectrum of pyruvic acid as it has previously been found that even small perturbations in bond lengths can significantly alter the computed excitation energy [*Aidas et al.*, 2008].

12.4.1 Previous computational work on pyruvic acid

Previous investigations examined the structure of pyruvic acid in vacuum using the semi-empirical PM3 method [*Kakkar et al.*, 2003], the MP2/aug-cc-pVDZ and DFT/B3LYP/aug-cc-pVDZ [*Reva et al.*, 2001] methods, the MP2/aug-cc-pVTZ and DFT/B3LYP/6-31+G(d,p) [*Plath et al.*, 2009] and using MP2/6-311++G(2df,p) and B3LYP/6-311++G(2df,p) methods [*Valadbeigi and Farrokhpour*, 2013]. *Reva et al.* [2001] and *Plath et al.* [2009] also investigated the vibrational frequencies. The investigations found that the conformers Tc, Tt, Ct and Cc were the most stable in vacuum. The structures are named according to the orientation of the CCC-O bond using lower case letters (c, *cis* and t, *trans*), and the CCOH bond (C, *cis* and T, *trans*) as was done in *Reva et al.* [2001] and shown in Figure 12.3.

Tc was found to be the most stable conformer as has also been identified experi-

mentally using spectroscopic methods, where observations of the low-frequency OH and C=O stretching bands were used for identification. A second conformer has also been seen experimentally and computational studies found Tt to have the second lowest energy; the Ct conformation is, however, found to have a similar energy. The conformer Cc was found to be stable in some studies at much higher energies, while other studies did not find a minimum [*Kakkar et al.*, 2003; *Reva et al.*, 2001; *Plath et al.*, 2009; *Kakkar et al.*, 2006]. The study by *Valadbeigi and Farrokhpour* [2013] finds that each of the 8 enol structures and 4 keto structures have equal abundances in vacuum as the energy differences between the isomers are very small, further they find that the interconversion between keto and enol structures proceed through the rotation of C-C and O-H bonds as well as through proton transfer.

Few studies address pyruvic acid in soluble media. It has been investigated in aqueous solutions using DFT/B3LYP/ 6-311++G(3df,3pd)// B3LYP/6-31G(d) and a continuum solution model, in combination with a few explicit water molecules, and the keto and enol forms were found to coexist in aqueous solution although the energy favours the keto form [*Kakkar et al.*, 2008; *Valadbeigi and Farrokhpour*, 2013]. It was discovered that only two water molecules directly influence the structure of pyruvic acid [*Kakkar et al.*, 2008]. The vibrational frequencies have been investigated using a Self-Consistent Reaction Field (SCRF) Polarizable Continuum Model (PCM) approach, in addition taking two or four water molecules into account. It was found that the most important changes when going from gas to liquid water were the lengthening of the OH bonds and widening of the C_5-C_6-O_9 and C_5-O_9-H_{10} angles leading to the disappearance of the hydrogen bond in the O_8...H_{10}-O_9 angle. The frequencies of the carbonyl groups were less affected than those of the OH-group [*Buemi*, 2009]. Further it has been found that the activation energy needed for isomerization and tautomerism reactions of pyruvic acid decreases in presence of water, because the water molecule acts as an intermediate for the proton transfer reactions [*Valadbeigi and Farrokhpour*, 2013].

12.5 The conformations of pyruvic acid in vacuum

To test the CAM-B3LYP approach against previous results pyruvic acid was investigated in vacuum. Energies for the conformers (Tc, Tt, Ct and Cc) are shown in Table 12.1. The Tc conformation was found to have the lowest energy. With increasing basis set size the energy of the Tc conformation decreases. The system appears to converge at the cc-pVQZ level.

The results agree with previously determined energies where Tc was found to vary from -340.53 (HF/g-31G* correcting zero point energy by scaling vibrations with 0.9) to -342.45 (DFT/B3LYP/aug-cc-pVDZ, correcting zero point energy by scaling with 0.96 for C-H and O-H stretching vibrations and 0.9 for other vibrations) equivalent to a difference of 5 MJ mol^{-1} [*Reva et al.*, 2001]. No vibrational scaling was used for the energy determinations in the present work.

Similarly the energy differences in vacuo between Tc and Tt (12.24), Ct (19.39) and Cc (47.02) of 12.24, 19.39 and 47.02 kJ mol^{-1} respectively were of similar magnitude as suggested in previous studies [*Reva et al.*, 2001; *Kakkar et al.*, 2006]. In this study conformer Cc was found to be a stable minimum and the difference

Tab. 12.1: Relative energy instabilities for enol (E1-E8) and keto (Tc, Tt, Ct, Cc) structures given in kJ mol^{-1} as compared to the structure Tc given in au. Determined using DFT/CAM-B3LYP with a aug-cc-pVQZ basis set in vacuum, liquid and solid water and corrected for ZPE.

	Tc	Tt	Ct	Cc
VACUUM	-342.4364	12.2401	19.3893	47.0174
AQUEOUS PHASE	-342.4457	8.9346	10.8564	25.5750
WATER ICE	-342.4475	10.6923	15.2594	34.6671
	E1	E2	E3	E4
VACUUM	46.2996	46.2991	46.7499	35.4309
AQUEOUS PHASE	70.6275	70.6270	71.0778	59.7587
WATER ICE	75.5057	75.5052	75.9560	64.6369
	E5	E6	E7	E8
VACUUM	70.8236	42.5158	48.1149	23.8695
AQUEOUS PHASE	95.1515	66.8436	72.4428	48.1973
WATER ICE	100.0297	71.7218	77.3210	53.0755

Tab. 12.2: Energies (atomic units) corrected for zero-point vibrational energy for the lowest energy conformer Tc and the relative instabilities in kJ mol^{-1} for Tt, Ct and Cc. Determined using DFT methods and aug-cc-pVQZ basis sets and corrected for ZPE

VACUUM	PBEPBE	B3LYP	B3PW91	MPW1PW91	CAM-B3LYP
Tc / au	-342.194455	-342.571078	-342.432271	-342.476571	-342.4364140
Tt / kJ mol^{-1}	14.2013	11.5811	13.0697	13.1144	12.2401
Ct / kJ mol^{-1}	20.3765	18.3339	20.1822	20.4196	19.3893

between the most stable conformer Tc and Cc diminished as the basis set increased from cc-pVDZ (51.24 kJ mol^{-1}) to aug-cc-pVQZ (47.02 kJ mol^{-1}), suggesting that the larger the basis set the more likely the Cc geometry becomes. Despite this effect, Cc has a relatively high energy and is of less experimental interest since it is not likely to be found for the ground electronic state of pyruvic acid. Most enol structures had energies similar to Cc (Table 12.1). The exceptions to this are E4 and E8 (Figure 12.3), having an energy difference relative to Tc of 35 and 24 kJ mol^{-1}.

To further validate the method, the CAM-B3LYP results were compared to other DFT methods; PBEPBE (Pure GGA), B3LYP (hybrid), B3PW91 (hybrid), MPW1PW91 (pure GGA) in combination with the aug-cc-pVQZ basis set. Results are shown in Table 12.2. The order of the structures are the same as found using the CAM-B3LYP method. However, the energy difference between Tc and Tt, as well as the difference between Tc and Ct, vary from low for hybrid DFTs (B3LYP, CAM-B3LYP, B3PW91) to higher for the pure GGA (MPW1PW91, PBEPBE). The energy differences between the conformers obtained in this study using CAM-B3LYP are only a little larger than those found in high level CCSD(T)/aug-cc-pVDZ calculations, which determined the difference between conformer Tc and Tt to be 9.6 kJ mol^{-1}, and between Tc and Ct to be 17.4 kJ mol^{-1} [*Reva et al.*, 2001].

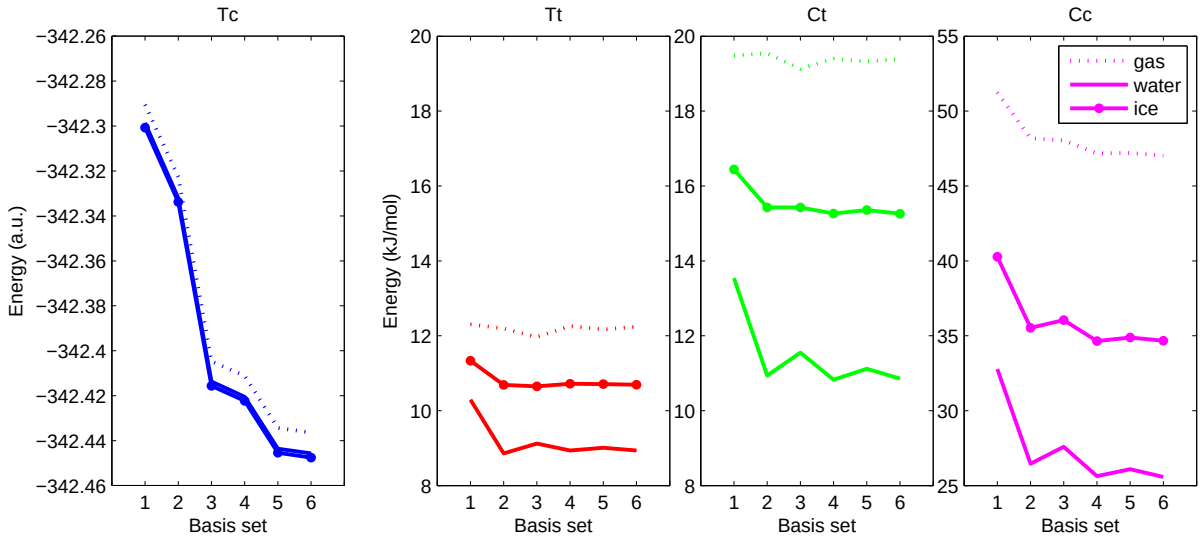

Fig. 12.4: Pyruvic acid conformers in liquid water and ice using CAM-B3LYP and a dielectric medium method. Numbers 1 to 6 correspond to basis sets cc-pVDZ to aug-cc-pVQZ. Note changes in the y-axis.

12.5.1 The conformations of pyruvic acid in solution

The energies for four pyruvic acid conformers in liquid water and ice are shown in Table 12.1 as well as in Figure 12.4. For the solutions, the equilibrium structure of the Tc conformer converges with cc-pVQZ. However, the relative energy between conformers converges already at the aug-cc-pVTZ level. Conformer Tc has the lowest energy in both condensed phases, and both the condensed phases stabilize energy for Tc relative to vacuum. In the condensed phases the relative differences between the four conformers is smaller, however, the ordering is preserved. The difference between Tc and Tt is diminished by 3 kJ mol^{-1} ($\sim$ 30%) for liquid water compared to gas, while the difference between Tc and Ct is decreased by $\sim$8 kJ mol^{-1} ($\sim$ 44%) reducing the difference between Ct and Tt to just 2 kJ mol^{-1} as also found by *Kakkar et al.* [2008]. These authors also found that when adding water molecules into the calculations, two of the H_2O molecules would bond causing Ct to rotate to Tt making Tt the most stable. According to that study the hydrogen bonds also stabilize Tt more than Tc by $\sim$4 kJ mol^{-1}. The energy difference between Tc and Tt found in the present study is very similar to the 8.80 kJ mol^{-1} found using a dielectric medium method but with B3LYP/6-311++G(d,p) [*Buemi*, 2009]. For Cc the difference to Tc was lowered by $\sim$ 46% in liquid water.

For ice the energy differences are larger than for liquid water. The differences for Tt, Ct and Cc are 11, 15 and 35 kJ mol^{-1} relative to Tc respectively. The dielectric constant was varied in the dielectric medium model for ice using CAM-B3LYP/aug-cc-pVTZ, to more closely resemble natural ice (see Figure 12.5). Glacial ice contains impurities, in particular the dust concentration can be significant during cold glacial periods, and therefore the dielectric constant is higher than the 3.2 reported for pure ice [*West et al.*, 2007]. The difference between Cc and Tc was influenced the most

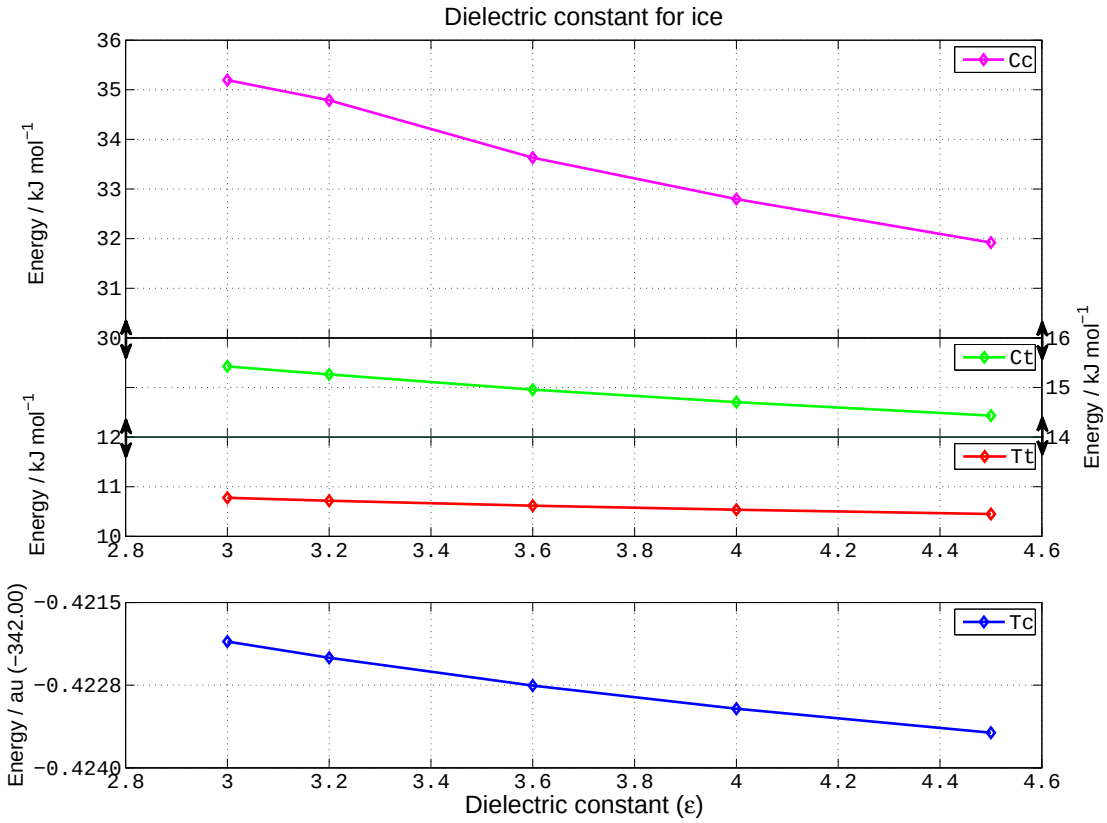

Fig. 12.5: Pyruvic acid conformers in water ice using CAM-B3LYP/aug-cc-pVTZ, while varying the dielectric constant (ϵ). Blue is Tc in au, while Tt (red), Ct (green) and Cc (purple) are presented in kJ mol^{-1}. Note changes in the y-axis.

($\sim$ -3 kJ mol^{-1}) when varying ϵ from 3 to 4.5. For Ct the difference is about $\sim$ -1 kJ mol^{-1} while Tt changed even less. The decrease follows the dipole moments of the isomers.

The energies of the enol structures all became significantly higher in solution. The energy levels for the enol structures in liquid water varied from 48 kJ mol^{-1} (E8) and up to 95 kJ mol^{-1} as compared to Tc. Frozen water had slightly higher energies (53 to 100 kJ mol^{-1}). Thus we find that enol structures are unlikely in natural ice, while the *cis* CCOH structures become more likely in solution compared to vacuo.

12.6 Molecular structures of pyruvic acid in vacuum

The experimental values for bond lengths, determined using microwave spectroscopy by *Reva et al.* [2001], are compared to DFT models. Information on bond lengths and angles in vacuum is presented in supplementary material (Figure F.1 and F.2 and Table F.3). We find that the structures converged at the aug-cc-pVTZ level, and that deviation from the experimental determined bond lengths was below 2.2 %, with double bonds least well represented.

The keto bonds in the Tc and Tt conformations are long relative to experiment. This is especially true for the $C_{(5)}O_{(7)}$ bond, followed by a shortening in $C_{(1)}C_{(5)}$ for the Tc structure. The $C_{(6)}O_{(8)}$ bond length increases from Cc⇒ Ct⇒ Tc⇒ Tt. This can be explained by considering the parallel double bonds in the *cis* structures versus the opposite C=O bonds in the *trans* structures. For Tc the $C_{(1)}C_{(5)}$ bond is too short. For the Tc the planar $H_{(4)}$ is bent farther away from the C-C than for the other conformers. Bond lengths and angles for structures in vacuo can be found in supplementary material Figures S3 and S4.

All DFT methods show similar bond lengths, except for PBEPBE. Whereas the other DFT methods are all short compared to experiment, PBEPBE fits the O-H bond and the double bonds better. In the methyl group the out of plane H's are most well represented by PBEPBE, while for the in plane H the others do a better job. The C-C and the C-O bond lengths are equally well represented by CAM-B3LYP, B3PW1 and MPW1PW91. For the angles all DFT models are similar, thus we can trust the structures found by the CAM-B3LYP model. The order of how the C-C-O angles in the carboxyl are presented follow the order found for the energy difference between compounds closest to the high level CCSD(T) method (see section on energy). The results for the Tc geometry were compared to the PM3, MP2 and DFT/B3LYP data [*Kakkar et al.*, 2003]. The sum of absolute errors for the DFT/CAM-B3LYP compared to experimentally determined values for bond lengths is 16%. In comparison MP2 has the closest match to experiment (12%) followed by DFT/B3lYP/6-311++G(3df,3pd) (19%) and PM3 (33%). Thus using the CAM-B3LYP method is reasonable.

12.6.1 Molecular structures of pyruvic acid in liquid and solid water

Selected parts of the structures of pyruvic acid in the condensed phases determined using CAM-B3LYP/aug-cc-pVQZ are shown in Table 12.3, further information on structures can be found in the supplementary material.

For all conformers in liquid water and ice the main changes in bond lengths are in the carboxyl group. $C_{(1)}$-$C_{(5)}$ is shorter in ice than in vacuum and even more so in liquid water. The bond length $C_{(6)}$ =$O_{(8)}$ is longer for all conformers, most significantly for liquid water; in Ct and Tt the other double bond is lengthened too. For all conformers C-O is shortened, and the change is larger in liquid water than in ice. Especially for Ct and Cc, a very significant shortening of $C_{(6)}$-$O_{(9)}$ is observed for liquid water compared to vacuum (0.016 Å). This change is probably the main cause of the stabilization of the *cis* conformers in solution, and is a consequence of the dielectric medium. The effect is larger for liquid water than for solid. The O-H bond is generally a little longer, more for ice than water, as also found by *Buemi* [2009]. In aqueous phase the methyl group does not undergo much change compared to vacuum. In ice the C-H bonds are slightly lengthened.

Considering the angles, as with the bond lengths, the largest changes are found in the carboxyl group, when comparing vacuum and solution. For all compounds the C-C=$O_{(7)}$ angle is more acute than in vacuum as is the C-C=$O_{(8)}$ angle for Ct and Cc, while for Tc it is wider. Correspondingly, the $O_{(8)}$-$C_{(6)}$-$O_{(9)}$ angle shows the opposite tendency. The C-O-H angle is broadened most for Ct and Tt. This follows the results obtained by *Buemi* [2009]. The changes in the angles in the methyl

Tab. 12.3: The geometry for the Tc, Tt and Ct conformers in water solution using CAM-B3LYP/cc-pVQZ when using the polarizable continuum model (PCM) with self consistent reaction field (SCRF) keywords for water. The Tc and Ct structures are shown for ice using SCRF with specified keywords

	$\mathbf{Tc_{vacuum}}$	$\mathbf{Tc_{water}}$	$\mathbf{Tc_{ice}}$	$\mathbf{Tt_{vacuum}}$	$\mathbf{Tt_{water}}$	$\mathbf{Tt_{ice}}$	$\mathbf{Ct_{vacuum}}$	$\mathbf{Ct_{water}}$	$\mathbf{Ct_{ice}}$	$\mathbf{Cc_{vacuum}}$	$\mathbf{Cc_{water}}$	$\mathbf{Cc_{ice}}$
Distances (Å)												
$C_{(1)}C_{(5)}$	1.486	1.482	1.482	1.495	1.489	1.490	1.497	1.490	1.492	1.506	1.494	1.498
$C_{(5)}O_{(7)}$	1.204	1.205	1.205	1.196	1.200	1.198	1.194	1.199	1.197	1.192	1.197	1.195
$C_{(6)}O_{(8)}$	1.193	1.197	1.195	1.198	1.199	1.199	1.189	1.196	1.192	1.184	1.193	1.189
$C_{(6)}O_{(9)}$	1.325	1.321	1.323	1.328	1.323	1.326	1.343	1.327	1.335	1.347	1.331	1.338
$O_{(9)}H_{(10)}$	0.973	0.974	0.974	0.967	0.968	0.969	0.967	0.968	0.969	0.961	0.964	0.964
Angles (°)												
$H_{(2)}C_{(1)}H_{(3)}$	106.1	106.6	106.4	106.3	106.7	106.6	106.5	106.7	106.7	108.2	108.0	108.3
$H_{(3)}C_{(1)}H_{(4)}$	110.8	110.5	110.5	110.6	110.4	110.3	110.3	110.3	110.1	108.9	109.1	108.8
$H_{(4)}C_{(1)}C_{(5)}$	110.1	110.2	110.3	109.4	109.8	109.7	109.3	109.7	109.6	109.0	109.6	109.4
$C_{(6)}C_{(5)}O_{(7)}$	117.5	116.8	116.9	120.2	119.6	119.8	117.7	117.1	117.3	118.1	117.0	117.3
$C_{(5)}C_{(6)}O_{(8)}$	122.9	123.5	123.5	122.7	122.5	122.8	124.1	122.9	123.5	122.1	121.5	121.8
$O_{(8)}C_{(6)}O_{(9)}$	124.5	123.5	123.9	124.6	125.0	124.6	124.1	124.9	124.4	121.6	121.2	121.2
$C_{(6)}O_{(9)}H_{(10)}$	107.2	107.8	107.5	107.8	109.0	108.4	107.7	109.4	108.6	112.2	113.0	112.4
Dihedral Angles (°)												
$H_{(2)}C_{(1)}C_{(5)}C_{(6)}$	-58.0	-58.2	-59.2	-58.4	-58.5	-58.5	-58.6	-58.5	-58.7	-60.1	-59.8	-60.1
$H_{(2)}C_{(1)}C_{(5)}O_{(7)}$	122.0	121.8	120.8	121.6	121.5	121.5	121.4	121.4	121.3	119.9	120.2	119.9
$H_{(3)}C_{(1)}C_{(5)}O_{(7)}$	57.9	58.4	57.3	58.4	58.5	58.5	58.6	58.6	58.7	60.1	59.8	60.1

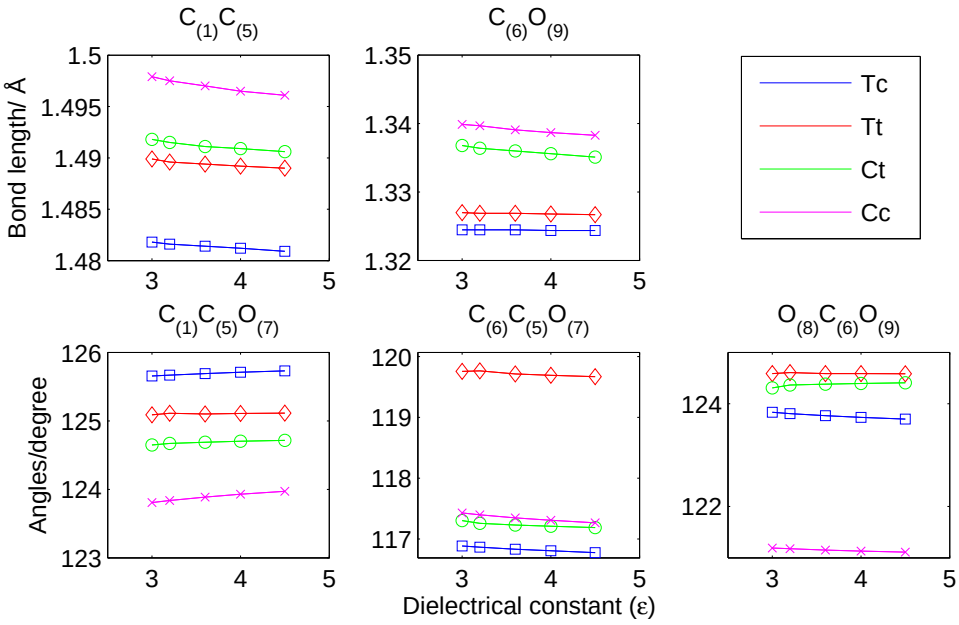

Fig. 12.6: Selected geometrical changes for pyruvic acid structures as a function of dielectric constant. Computed using CAM-B3LYP/aug-cc-pVTZ with SCRF keywords varying from ϵ 3.0 to 4.5.

group are much smaller and all conformers except Cc show a widening of the angle between the out of plane H's. The angle in Cc is slightly wider for $H_{(2)}$-$C_{(1)}$-$H_{(3)}$ and more narrow for $H_{(3)}$-$C_{(1)}$-$H_{(4)}$ in ice as compared to vacuum while the opposite is the case for liquid water. The $H_{(3)}$-$C_{(1)}$-$C_{(5)}$ angle is wider for Tc in ice compared to vacuum, while for Ct and Cc it is narrower.

The effect on the structure of changing the ϵ of ice from 3.0 to 4.5 is shown in figure 12.6. For bond lengths the changes are less than one percent. The most significant length change is for the $C_{(1)}$-$C_{(5)}$ bond in all compounds which gets shorter as ϵ is increased. The *cis* structures have the most pronounced shortening of this bond and the C-O bond with increasing ϵ.

Changes in the angles are not greater than 0.2°. The changes in the structures as a function of basis set are in general similar to the changes found from the study of pyruvic acid in vacuum (Figure 12.7) with convergence at cc-pVTZ.

The generally more compressed structures for Cc and Ct pyruvic acid in solutions show that they are more likely in natural ice than in vacuum and especially wet ice.

In conclusion, for all structures the largest changes relative to vacuum take place in the carboxyl region of the molecule. The conformations Tc and Ct show a greater geometric change for liquid water than for ice, determined by looking at the sum of absolute percentage changes relative to the vacuum structure. The most stable conformer in solution is, as in vacuum, Tc; the other conformers are more likely in solutions and the change relative to vacuum is most closely associated with changes in the geometry of the carboxyl group.

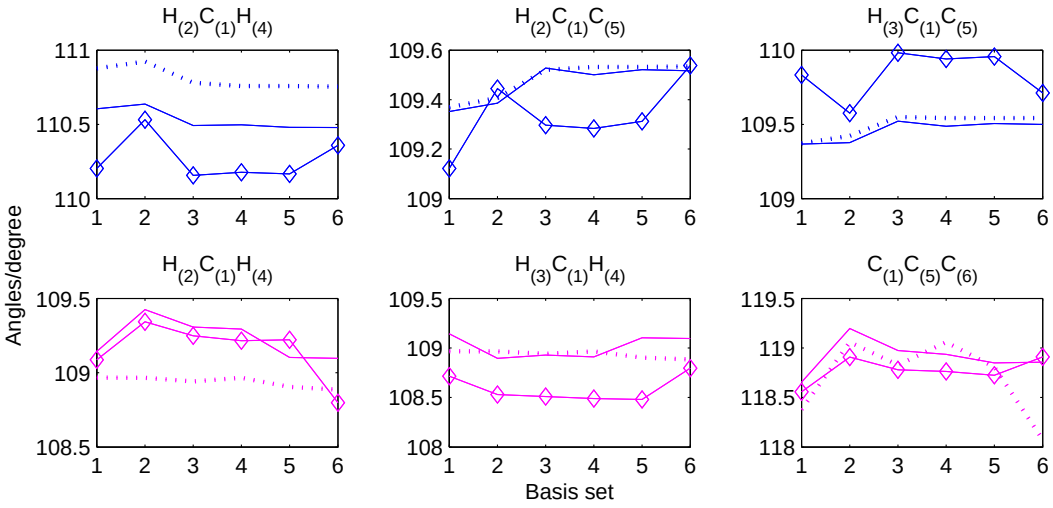

Fig. 12.7: Variations in selected angles as a function of basis set: 1 is cc-pVDZ, 2 is aug-cc-pVDZ, 3 is cc-pVTZ, 4 is aug-cc-pVTZ, 5 is cc-pVQZ and 6 is aug-cc-pVQZ. Top for Tc (blue) and bottom Cc (purple) for vacuum (dotted line), aqueous phase (full line) and ice (full line with diamonds).

12.7 Vibrational frequencies

Analysis of the relative stabilities of the conformers in the three phases is guided by the theoretical analysis, which we use to interpret and extend the experimental studies of vibrational spectra. Vibrational frequency calculations were performed using CAM-B3LYP and varying basis sets in vacuum, liquid water and ice, as well as for various DFT methods using the aug-CC-pVQZ basis set in vacuum. The frequencies were scaled by 0.96 for the OH and CH stretches and by 0.99 for all other vibrations, as was done by *Reva et al.* [2001]. *Reva et al.* [2001] also determined the experimental spectra using a Mattson FTIR spectrometer (Infinity 60AR series) in the range 4000-400 cm^{-1} with a resolution of 0.5 cm^{-1}. Computational calculations using MP2 and DFT/B3LYP with the aug-cc-pVDZ basis sets showed that Tt is the second most likely conformation in vacuum. The vibrational frequencies and intensities determined using CAM-B3LYP/aug-cc-pVQZ in gas, liquid water and solid water, as well as the experimental spectra obtained by *Reva et al.* [2001] are shown in Figures 12.8 to 12.11.

In the following discussion the nomenclature used is ν for stretching, δ for bending, γ for rocking and τ for torsion. It is clear from CAM-B3LYP frequencies (Figures 12.8-12.11) that Tc best fits the observed data in vacuo. In the supplementary material, Tables S4 and S5, the results from *Reva et al.* [2001] are shown together with selected scaled vibrational frequencies obtained in this study. We find that in general the frequencies obtained using CAM-B3LYP are larger than the ones obtained by *Reva et al.* [2001] using MP2, by 1% to 6%, except for the torsions which are generally lower. It is also evident that the experimentally determined frequencies are better replicated by MP2 than by CAM-B3LYP. Further comparisons between

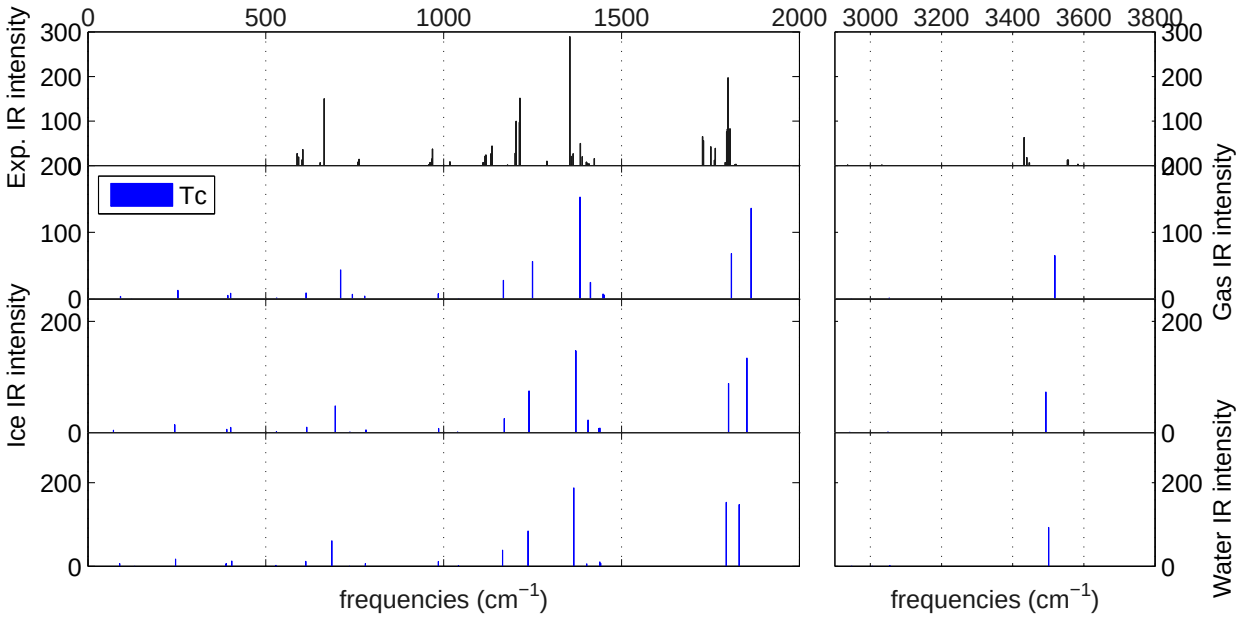

Fig. 12.8: Vibrational frequencies and intensities for pyruvic acid Tc conformer. From top as observed by *Reva et al.* [2001] in experiment. Remaining graphs show Tc (blue computed using CAM-B3LYP/aug-cc-pVQZ). Second frame is for gas, third for ice and bottom graph for ice. The experimentally determined intensities were scaled using the maximum IR intensity found with the CAM-B3LYP method. The computed frequencies are scaled by 0.96 for the OH and CH stretching vibrations and 0.99 for all other vibrations

the experimental frequencies and intensities and the CAM-B3LYP/aug-cc-pVQZ calculation were performed by comparing the highest intensities, and by comparing frequencies directly and using the difference to neighbouring frequencies.

Peak positions determined using the CAM-B3LYP model are generally off by 50 cm^{-1}. Despite this deviation, the model generates similar conclusions as found in previous studies: The most stable conformer is Tc as found using the calculated energies. But whether Tt or Ct is the second most dominant form can't be determined through spectral analysis using CAM-B3LYP and comparison to experimental data. The ν(C=O) double bonds do not, as in *Reva et al.* [2001], identify Tt to be the second most likely conformer, since both Ct and Tt exhibit them in the CAM-B3LYP calculations. In addition, some weak previously unassigned vibrational frequencies were found in the Ct model including 967.1, 1179.6, 1290.3 and 1364.1 cm^{-1} and the peak previously assigned to Tt at 1116.6 cm^{-1}.

One of the stronger arguments in *Reva et al.* [2001] for assigning Tt as the second most likely conformation is that the split band arising from C=O stretching is found experimentally to be 1763.7/1761.4 cm^{-1} and 1750.8/1749.4 cm^{-1}, and thus has a difference of 13 cm^{-1}, which was replicated by the computed frequencies for Tt (MP2: 11 cm^{-1}, B3LYP: 26 cm^{-1}) in the study by *Reva et al.* [2001]. This is also the case for the CAM-B3LYP model for which the difference for Tt is 16 cm^{-1}. However the Ct difference does not stand out in the CAM-B3LYP model (16 cm^{-1})

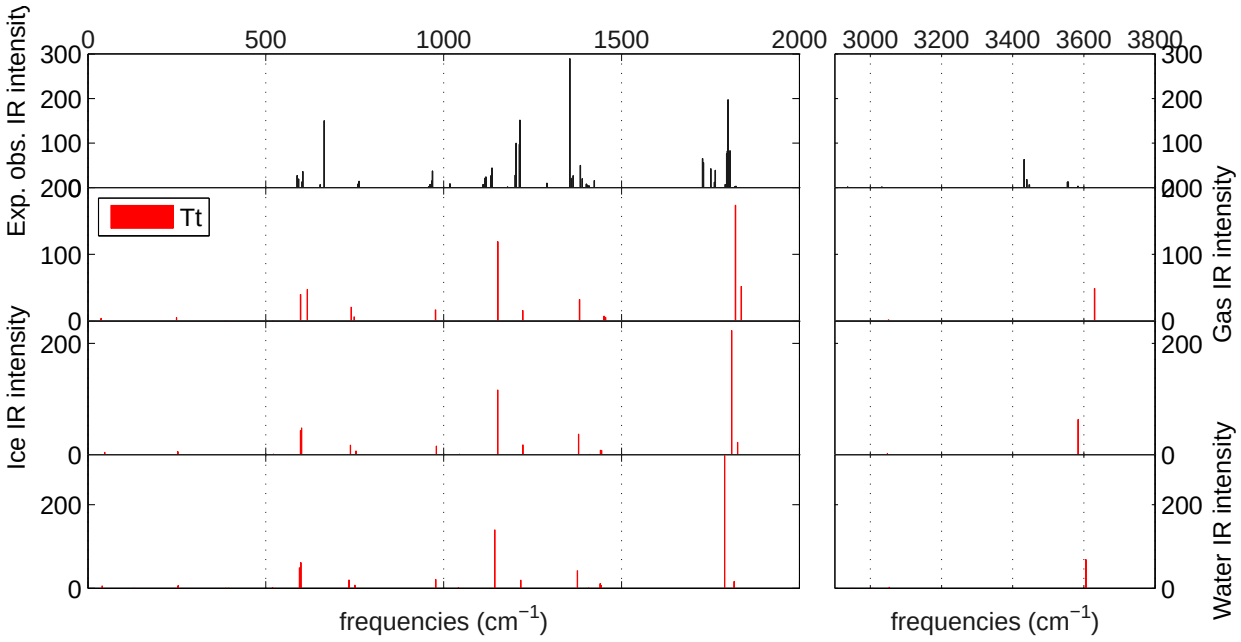

Fig. 12.9: Vibrational frequencies and intensities for the Tt conformer. From top as observed by *Reva et al.* [2001] in experiment. Remaining graphs show Tt (red) computed using CAM-B3LYP/aug-cc-pVQZ. Second frame is for gas, third for ice and bottom graph for ice. The experimentally determined intensities were scaled using the maximum IR intensity found with the CAM-B3LYP method. The computed frequencies are scaled by 0.96 for the OH and CH stretching vibrations and 0.99 for all other vibrations.

as it did for the MP2 (72 cm^{-1}) and B3LYP (57 cm^{-1}) models in the study by *Reva et al.* [2001], and thus the double bonds assigned to Tt are just as likely to arise from Ct according to this study. It is worth noting that all the DFT methods show a split band for the C=O stretch below that for Ct relative to the *Reva et al.* [2001] study. The range of the split was 16 to 12 cm^{-1} for Tt (CAM-B3LYP to B3PW91) and 25 to 16 cm^{-1} for Ct (PBEPBE to CAM-B3LYP). We tested whether the splitting determined by *Reva et al.* [2001] using B3LYP/aug-cc-pVDZ could be replicated, but in this study the C=O stretching split was found to be 20 and 23 cm^{-1} for Tt and Ct respectively. The ν(OH) strech, is experimentally found as a relatively broad peak. The difference in ν(OH) between the various conformers using CAM-B3LYP was found to be 112 cm^{-1} for the Tt to Tc conformers and 105 cm^{-1} for Ct and Tc, which fit well when assigning the experimental peak at 3432.3 cm^{-1} to Tc, 3556.1 cm^{-1} to Tt and 3554.1 cm^{-1} to Ct, giving relative differences of 124 cm^{-1} and 110 cm^{-1}. Intensities from the computational study suggest that Tc is the most dominant form (obs: 0.0206, CAM: 130.71), followed equally by Tt (obs: 0.040, CAM:97.54) and Ct (obs: 0.041, CAM:90.08).

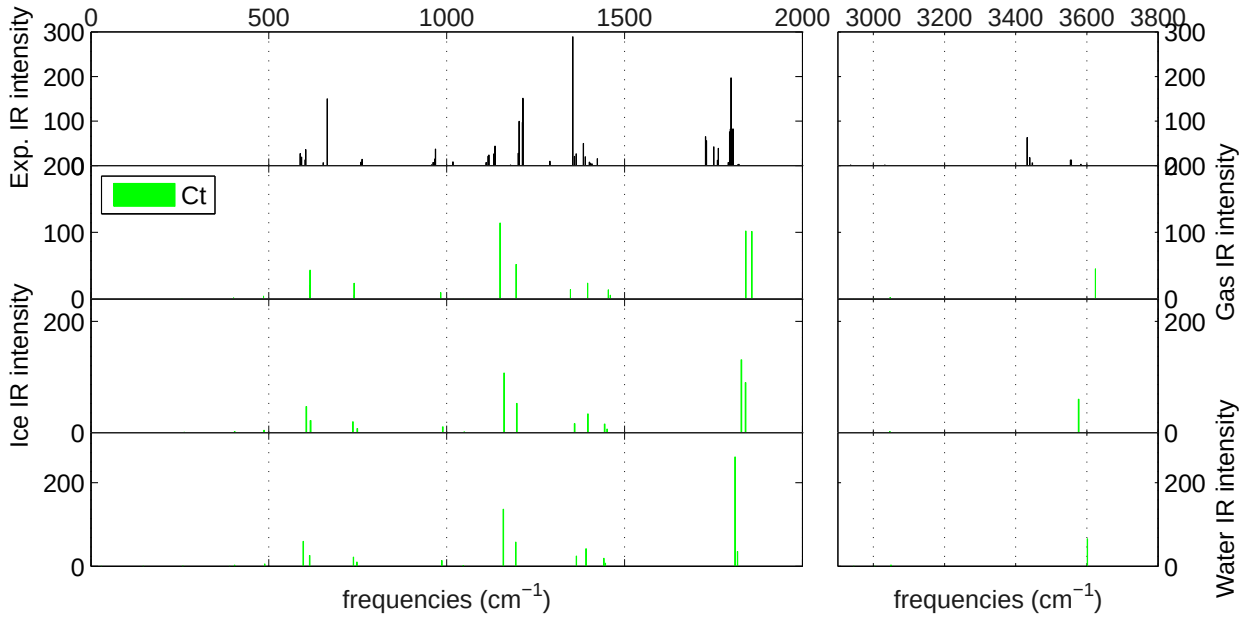

Fig. 12.10: Vibrational frequencies and intensities for the Ct conformer. From top as observed by *Reva et al.* [2001] in experiment. Remaining graphs show Ct (green) computed using CAM-B3LYP/aug-cc-pVQZ. Second frame is for gas, third for ice and bottom graph for ice. The experimentally determined intensities were scaled using the maximum IR intensity found with the CAM-B3LYP method. The computed frequencies are scaled by 0.96 for the OH and CH stretching vibrations and 0.99 for all other vibrations.

12.7.1 Vibrational Frequencies of pyruvic acid in solutions

Only a few general observations are possible for liquid water and ice (Figures 12.8 to 12.11). Vibrational frequencies are generally lower than found for vacuum. The largest changes are found for Cc $\nu(C_5{=}O)$, which has a higher frequency in both ice and liquid water by 5%, while the remaining compounds have lower vibrational frequencies as compared to the gas phase. Related to this change, the Tt intensity for both liquid water and ice is lower than found in vacuum, similar to the behaviour of Ct in the aqueous phase (-114), while the remaining compounds in liquid water and ice have intensities increased by up to 108 for Cc in liquid water. This differs from the study by *Buemi* [2009] which found the largest changes in the methyl frequencies. Although we did not find significant changes in the position of the methyl frequencies, δCH_3 showed an increase in the intensity of Tc and Cc in both water (+164 and +224) and ice (+62 and +91).

All compounds but Tt experience changes in the frequencies related to carbon frame bending; Tc has a lower frequency while Cc has a higher frequency for both aqueous phase and solid ice. Ct shows the opposite effect for liquid water (widening) and ice (narrowing). As was the case for the structural changes, the Cc conformer also experiences the greatest changes in the vibrational frequencies, involving bending of the double bonds as well as higher frequencies related to rocking of $C_{(6)}{=}O$.

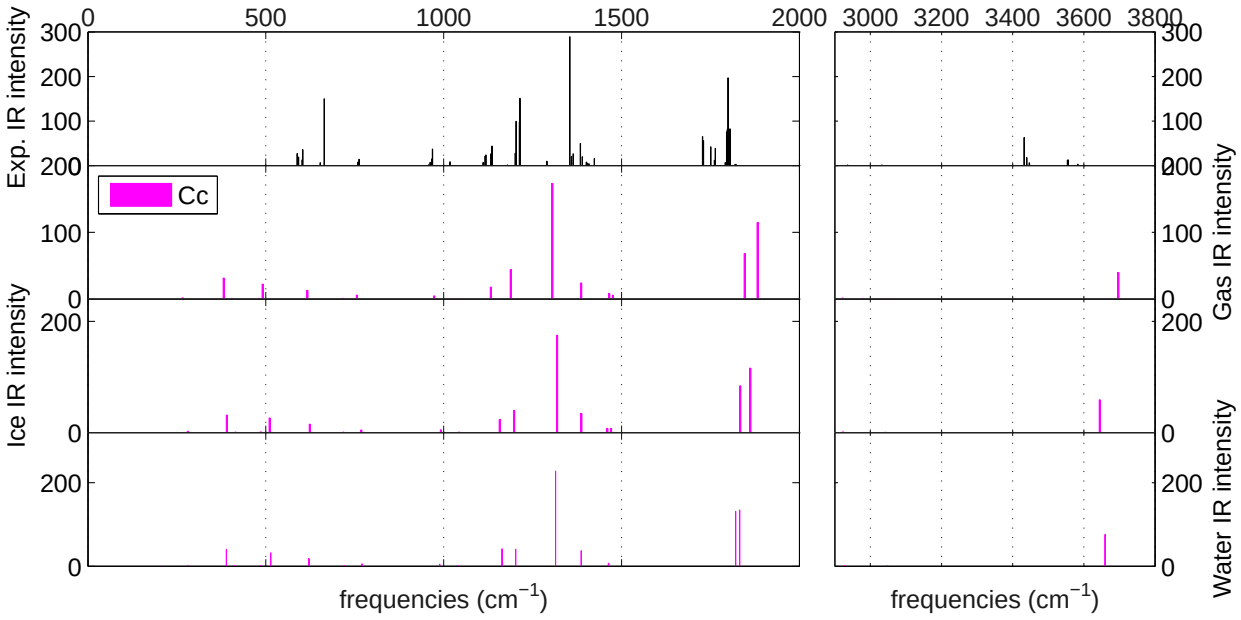

Fig. 12.11: Vibrational frequencies and intensities for the Cc conformer. From top as observed by *Reva et al.* [2001] in experiment. Remaining graphs show Cc (purple) computed using CAM-B3LYP/aug-cc-pVQZ. Second frame is for gas, third for ice and bottom graph for ice. The experimentally determined intensities were scaled using the maximum IR intensity found with the CAM-B3LYP method. The computed frequencies are scaled by 0.96 for the OH and CH stretching vibrations and 0.99 for all other vibrations.

Tc and Tt show lower frequencies, related to rocking of the other ketone. These changes are more pronounced for liquid water than ice, and the difference between ice and liquid water is more significant for Tt. Further, Tt also shows a lowering of the $\delta(C_{(6)}{=}O)$ frequency for liquid water. For $C_{(5)}{=}O$ stretching, significant changes in intensity were observed for $\nu(C_{(6)}{=}O)$; for liquid water an increase of the calculated intensities of 450 compared to vacuum was found for Tt and Ct, while for ice the increase in the calculated intensity was 210 and 124 respectively. Changes for Cc and Tc were about half as large. Both Cc and Tc show a lower frequency for methyl torsion. The largest difference between liquid water and ice is seen for the double bond stretching for all compounds, as well as for Tt $\delta(C_{(6)}{=}O)$ as mentioned above; the frequency is generally lower than in the gas phase, more so for liquid water than for ice. The vibrational frequency of the OH stretching is lowered more for ice than liquid water and intensity is increasing by 60 to 100. Thus the overtones of the OH stretching will be closer to the near infra red where water/ice absorbs light making the overtone excitation path way for the production of CO_2 as suggested by *Larsen and Vaida* [2012] less likely in solid water than in ice.

12.8 Conclusions

This study has investigated the stability and infra red spectra of four conformers of pyruvic acid in vacuum, and in liquid water and solid water using CAM-B3LYP. These are the first calculations of the structure and vibrational frequencies of pyruvic acid conformers determined in a dielectric media resembling ice, and provide important first results for the further study and understanding of pyruvic acid in ice.

In vacuum conformer Tc was found to be the most stable followed by Tt, Ct and Cc as was found in earlier [*Reva et al.*, 2001; *Kakkar et al.*, 2003; 2006; *Plath et al.*, 2009]. Comparisons of the structures found in vacuum to other DFT methods, as well as to results obtained by others, show that the CAM-B3LYP model does reasonably well at estimating the energies. The energy and frequency calculations converged using the basis set cc-pVQZ. For structures the convergence was obtained at the aug-cc-pVTZ level. The carboxyl angles in the DFT models show that the $O_{(7)}...H_{(10)}$ bond is strengthened in the most developed models. Though CAM-B3LYP vibrational frequencies generally are red shifted compared to experimental data we found that for all DFT models the difference between the C=O vibrational frequencies were equal for Ct and Tt; the difference was closest to experiment for CAM-B3LYP. This contradicts the study by *Reva et al.* [2001], who, mainly based on differences between these frequencies, concluded that the Tt compound is the second most likely structure.

The energy differences between Tt and Ct were minimized for pyruvic acid conformers in a liquid water environment using a dielectric medium method. The differences for both Tt and Ct relative to Tc, as compared to vacuum, were minimized by $\sim$3 kJ mol^{-1} and $\sim$8 kJ mol^{-1} respectively. The structure and energetics of Cc are significantly altered compared to vacuum, the energy is $\sim$22 kJ mol^{-1} lower. The largest geometrical changes occurred in *cis* CCOH, which showed a significant shortening of the C-O bond. For all conformers the largest change was a carboxyl group enlargement following the result by *Buemi* [2009]. The vibrational frequencies in liquid water showed changes of less than 5% relative to vacuum. Large changes were observed in the transition intensities.

In ice Tc again had the lowest minimum energy, with Tt, Ct and Cc being higher by 11, 15 and 35 kJ mol^{-1} respectively (CAM-B3LYP/aug-cc-pVQZ). Thus for ice the relative differences were larger than observed for water. The influence of ϵ_r was most significant on the *cis* (CCOH) structures. As the relative permittivity increases the differences between the four conformers decrease, suggesting that the inhomogeneous nature of glacial ice will affect partitioning between the various structures. As for liquid water the structural changes for ice were most significant for Cc and Ct. And, as for liquid water, the largest changes were seen in the carboxyl moiety. The largest shift in the vibrational frequencies were seen for the vibration related to the angle of the double bond ($\delta C_{(6)}$=O). In addition the frequency of the OH stretching vibration was lower for ice than for liquid water and the intensity is larger suggesting that the CO_2 production due to overtone initiated photochemical reaction of pyruvic acid as suggested by *Larsen and Vaida* [2012] is even less likely in solid ice than in liquid water.

This study has shown that the Tt and Ct structures both become more likely in a condensed environment, and in the aqueous phase the difference between the two is only 2 kJ mol^{-1}. Further the Cc structure becomes far more likely in solution. For enol structures the energy destabilization to Tc increased, thus they are unlikely to exist in natural ice. This work will serve as the basis of future studies of the photolytic production of CO_2 from pyruvic acid and other β-carbonyl humic-like substances found in glacial ice.

Supplementary material

Supplementary material is available in section F.

13. PYRUVIC ACID AND COSMIC RAYS AS THE SOURCE OF IN SITU PRODUCTION OF CO_2 IN GREENLAND

Chapters 10 to 12 presented the information needed for discussing if pyruvic acid is a major source of in situ production of CO_2 within the Greenland ice. In this section the information is summarised and the CO_2 contribution is determined.

13.1 Pyruvic acid as a source of in situ CO_2 production in Greenland ice

A compound A (e.g. pyruvic acid) is photolysed to produce B (e.g. CO_2 and additional compounds) at a rate J_A:

$$\mathrm{A} + h\vartheta \longrightarrow \mathrm{B} \tag{13.1}$$

$$\frac{d[\mathrm{A}]}{dt} = -J_A[\mathrm{A}] \tag{13.2}$$

The photolysis rate (J) of pyruvic acid can be determined by using equation 13.3, which was introduced in chapter 11 (eq. 11.1).

$$J = \int \sigma(\lambda, T)\phi(\lambda, T)F(\lambda, l)d\lambda \tag{13.3}$$

The molar absorptivity and the absorption cross section ($\sigma(\lambda)$) are related by Avogardos number (N_A=6.02214129·10^{23} mol^{-1}):

$$\sigma(\lambda) = 1000 \cdot ln(10)\frac{\epsilon(\lambda)}{N_A} = 3.82 \cdot 10^{-21}\epsilon(\lambda) \tag{13.4}$$

The absorption cross section ($\sigma(\lambda)$) for pyruvic acid at the absorbance peak is observed to be between $2 \cdot 10^{-21}$ to $4.62 \cdot 10^{-20}$ cm^2 per molecule (given for base ten $\epsilon(\lambda)$ =0.52-12.1 M^{-1} cm^{-1}) [*Horowitz et al.*, 2001].

We also know from *Guzmán et al.* [2007] that the quantum yield $\phi_{CO_2}(\lambda, T)$ in ice at the absorption peak is dependent of temperature such that $\phi_{CO_2}(\lambda, T) = (0.81 \pm 0.33) - \frac{338 \pm 81}{T}$, where T is given in K. Thus assuming a temperature of -25 °C during the Holocene gives a quantum yield 0.28, while Glacial values (-45 °C) gives a quantum yield of 0.23.

The actinic flux (F) is dependent on the amount of light penetrating into the Greenland ice as well as on the internal production from cosmic ray production of Cherenkov radiation. Further, the light within the ice depends on the changing absorption and reflection down through the ice. These properties depend on the

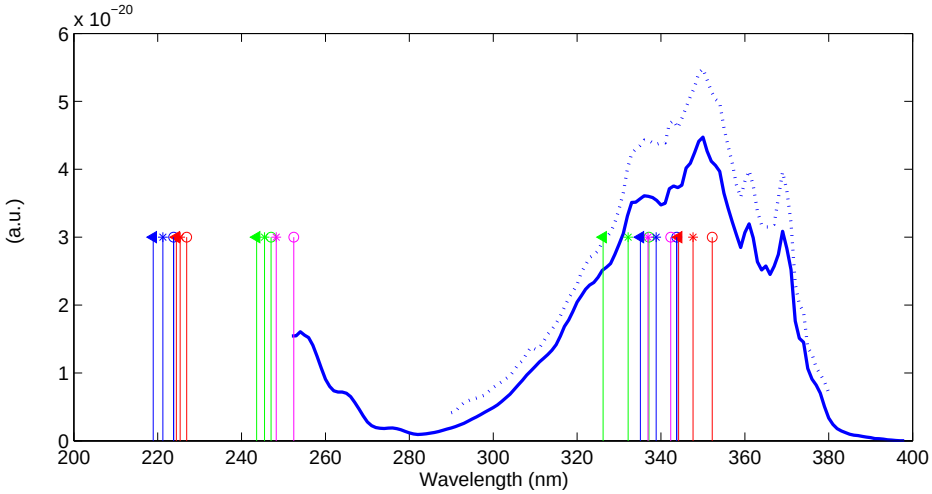

Fig. 13.1: Absorption peak of pyruvic acid. In full blue and dotted blue are shown experimentally determined values in gas phase as determined by *Horowitz et al.* [2001]. Vertical lines indicate computationally derived results. The colors relate to the conformers Tc (blue), Tt (red), Ct (green) and Cc (purple). The symbols relate to calculations performed for gas phase (open circles), water (triangles) and ice (stars).

type of bulk ice (impurities, air bubbles etc.). Finally the amount of CO_2 produced will also depend on the concentration of pyruvic acid (and other carboxylic acids) initially present in the ice.

Below are provided a discussion of parameters influencing F as well as other quantities, *e.g.* assumptions on pyruvic acid concentrations, wavelength dependencies etc. necessary to determine if CO_2 produced *in situ* is an important part of the excess CO_2 observed in Greenland ice cores.

13.1.1 Light available within the Greenland ice

The light available to run the photolysis within the Greenland ice is dependent on the light at the surface as well as on both the absorption and the scatter within both the snow covering the surface and within the ice. However the main source of light is produced *in situ* by Cherenkov radiation.

The light required to excite Pyruvic acid is observed in gas phase to be between 300-380 nm, with the peak at 350 nm (see Figure 13.1) [*Horowitz et al.*, 2001]. Further, using methods similar to those presented in chapter 12, we have preliminary findings that suggest that all the conformers experience a blue shift of about 10 nm in liquid water and about 5 nm for solid water (ice) as compared to the gas spectra (Figure 13.1). Furthermore from the computational study presented in chapter 12, we know that the conformers Tt and Ct become more likely in solution and while Tt remains the most likely of the two, Ct changes the most suggesting that the spectra would be even a little further blue shifted.

Today the solar light reaching the surface (E) at the NEEM site is approximately 140-160 W/m^2. From this energy the equivalent number of photons in the relevant wavelengths could be determined.

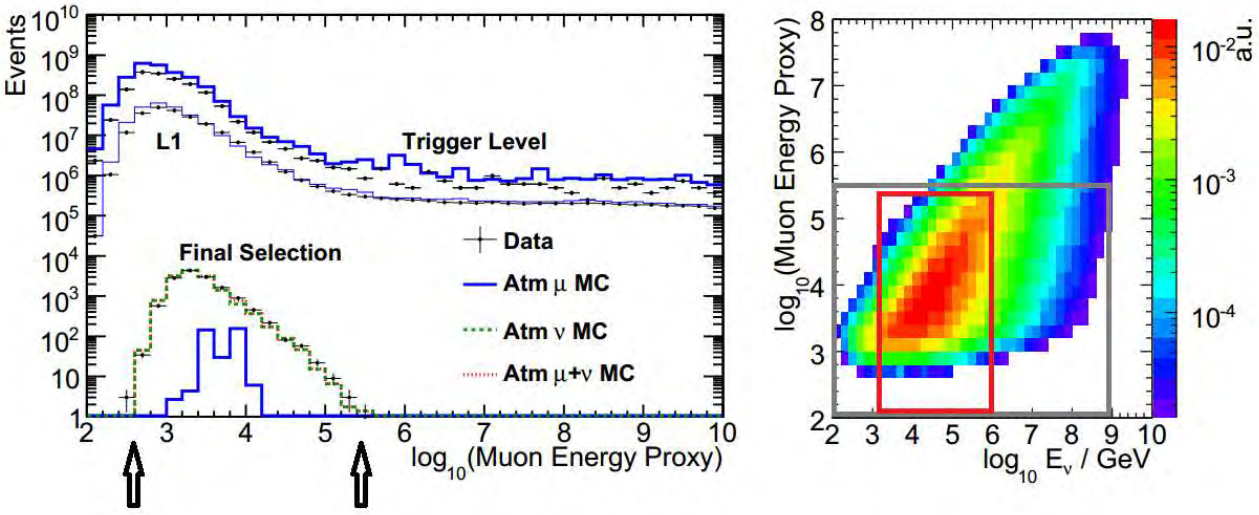

Fig. 13.2: Left; the probability function of getting a muon with a certain "muon energy proxy" level (green dotted line) within the IceCube experiment. Arrows indicate minimum and maximum distribution. Right; Transfer between "muon energy proxy" and true muon energy. Colours indicate likely energies. The blue box indicate the full range of muon energies to which the proxy muon energy found within the IceCube experiments can be transferred, red box the likely range of muon energies. Figure modified from *Abbasi et al.* [2011].

However, we also know that the photons are absorbed and scattered within the ice, making the actinic flux F from sunlight a function not only of time (insolation variations) but also a function of depth.

From the AMANDA study we know that the absorption coefficient in the ice at Antarctica varies between a mere 0.005 m^{-1} in the top 1000 meters (the Holocene), increases at about 1200 metres depth to a maximum of 0.02 m^{-1} (the LGM) and decreases again down to 2500 meters with large variations as a function of the impurity content. At 2500 meters depth the absorption is roughly 0.007 m^{-1} (see Figure 11.3). However these values are for Antarctic ice and reasonable values for Greenland ice are likely 10 times larger due to the impurity content. Similarly scatter coefficients between 0.1 and 0.01 m^{-1} were observed in the AMANDA experiment at 1200 to 2500 meters depth, where air is present as clathrates. In the top of the ice the scattering is driven by air bubbles yielding a scatter coefficient of 2.5 m^{-1} at the surface. We also found that in surface snow the light is scattered and thus it is not likely that light penetrates from the surface to within the ice. Thus the photolysis of pyruvic acid by means of solar light as a cause of *in situ* production of CO_2 seems very unlikely.

We know from the IceCube experiment that the amount of muons reaching the ice is $2.5 \cdot 10^{-10} cm^{-2}\ s^{-1}$. Further we know that the mean track length of a muon is 33.3 metres and that the energy for muons (E_m) varies significantly from about 10^3 GeV to 10^6 GeV (see Figure 13.2). From this using equation 13.6 we can determine the amount of photons generated from a muon hit and the additional cascades generated and we obtain:

$$N_c = 33.3m \cdot 3 \cdot 10^4[m^{-1}] \left(1.22 + 1.36 \cdot 10^{-3} \cdot E_m[\frac{1}{GeV}]\right) \tag{13.5}$$

$$= 1.6 \cdot 10^6 \text{ to } 1.6 \cdot 10^9 \text{photons} \tag{13.6}$$

However we also know that the pyruvic acid excitation to form CO_2 only occurs with wavelengths between approximate 300 and 380 nm. Thus we can use the Frank-Tamm approximation (equation 13.10) to find the number of photons generated. The Frank-Tamm equation does however not include secondary products from the muon track and thus likely underestimates the amount of photons generated. Further prior to applying Frank-Tamms equation we need to determine the speed of the muons based on the muon energy. For this we need to also know the muon mass (105.7 Mev/c^2).

$$E = \gamma mc^2 \tag{13.7}$$

$$= \frac{mc^2}{\sqrt{1 - \frac{v^2}{c^2}}} \tag{13.8}$$

$$\Leftrightarrow \frac{\beta}{c} = \sqrt{1 - (\frac{mc^2}{E})^2} \sim 1 \tag{13.9}$$

Now we can apply Frank-Tamms equation for wavelengths between 300 and 380 nm. The muon track length, l, is on average about 33 metres, the fine structure constant is 1/137 and the refractive index for ice is ∼1.34. We notice that in ice $\sin^2(\theta) \sim 0.44$. Thus we obtain:

$$N_{300\text{nm to }380\text{nm}} = 2\pi\alpha l \left(\frac{1}{\lambda_2} - \frac{1}{\lambda_1}\right) \sin^2(\theta) \sim 5 \cdot 10^5 \text{photons} \tag{13.10}$$

If we now recall that the spectra needed to photolyse pyruvic acid in water and ice is blue shifted by about 10 nm, the number of photons available found using Frank-Tamms equation are $N_{290\text{nm to }370\text{nm}} = 5.01 \cdot 10^5$ photons.

However we are interested in the number of photons generated. Thus numbers should be divided with the muon track. This also assumes that the density of the photons created by the muons are equal all over, which as shown in Figure 11.10 is not the case.

Finally we can determine the photolysis rate J and determine how much CO_2 is produced as a result of photolysis of pyruvic acid.

13.2 CO_2 produced in situ as a result of photolysis

The CO_2 produced within the ice as a result of pyruvic acid being photolysed by Cherenkov radiation, with an assumption of the radiation being distributed equally throughout the ice, is small. The production of CO_2 was determined while varying

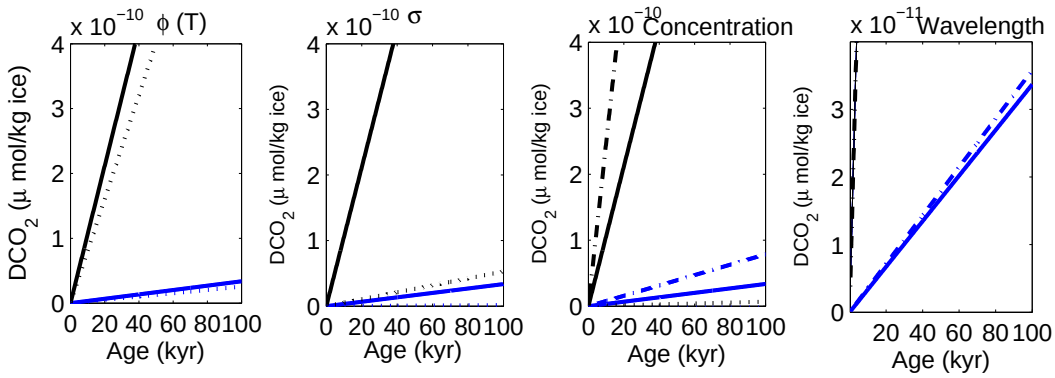

Fig. 13.3: The amount of pyruvic acid produced over time within the ice. Results show the variability using equation 13.10 (blue) or equation13.6 (black) to determine the amount of photons generated all for muon energies of 10^4 GeV with the following constraints; wavelengths assumed are 300 to 380 nm; temperature of -25 °C; $\sigma = 4 \cdot 10^{-20}$; and a pyruvic acid concentration of 3.1 ng/g unless anything else is noted. Left most plot) Variation of $\phi(T)$– full lines at a temperature of -25 °C, dotted lines for a temperature of -45°C. Second plot) Variation of σ–full lines show results for $\sigma = 4 \cdot 10^{-20}$, dotted for $\sigma = 4 \cdot 10^{-21}$. Third plot) Variation with pyruvic acid concentration–full lines show results for a pyruvic acid concentration of 3.1 ng/g, dotted for 7.23 ng/g. Fourth plot) Variability with wavelength–full lines between 290 and 300 nm, dotted line between 290 and 370 nm.

the pyruvic acid concentration, the temperature of the ice influencing the quantum yield, the absorption cross section, as well as the excitation wavelengths. Results are shown in Figure 13.3.

After 100000 years the amount of pyruvic acid produced is at most in the order of 10^{-3} μmol/kg, while the lower concentrations yield 10^{-9} μmol/kg ice. Thus while the largest results are close, but still in the low end of the observed variations of excess CO_2 in the Greenland ice (20 ppmv CO_2~0.04 μmol/kg ice), the low and more likely muon energies generate much too low CO_2 concentrations.

Evidently there are significant uncertainties in the calculations performed here. The main uncertainty results from trying to estimate the actinic flux (F). Firstly the results are based on only one year of data from the IceCube experiments and variations regarding the amount of muons a year could be expected. Further the energy of the muons is largely variable and while energy rich photons according to equation 13.6 [*Zornoza and Chirkin*, 2008] generate linearly more photons the Frank-Tamm relationship does not reproduce such a dependence. Contrary to the amount of photons generated by the Frank-Tamm equation, the equation 13.6 has no wavelength dependence, but does include secondary cascades, something not included in the Frank-Tamm approximation. Thus while the Frank-Tamm equation is rather robust and generate similar amount of photons for all muon energies, equation 13.6 generate a more likely picture with an energy dependency. The Frank-Tamm approximation on the other hand does not vary with energy of the muon, but does vary with the wavelengths over which the integration is performed. However this variation is minor (figure 13.3, 4th plot).

The amount of produced CO_2 vary with about 25% when determining the quantum yield using a temperature of -25 °C or -45 °C (Figure 13.3, 1st plot). The lower is a likely mean annual temperature for Greenland during the glacial, while the higher temperature is similar to mean annual temperatures found on the Greenland ice sheet today. The relationship between quantum yield and temperature is based on only one study [*Guzmán et al.*, 2007] and the uncertainty on the quantum yield of pyruvic acid is much larger as other studies have reported the quantum yield of pyruvic acid in waters about double.

The uncertainty related to the absorption cross section is also significant and is of an order of magnitude (Figure 13.3, 2nd plot). Further the absorption cross section could be different when in water or ice, as the media changes the angles and bond lengths of the pyruvic acid molecule.

The concentration of pyruvic acid in recent Greenland ice is 0.02-7.23 ng/g, with the high concentrations related to only a few peaks [*Kawamura et al.*, 2001]. The molar weight of pyruvic acid is 88.06 g/mol yielding in ice pyruvic acid concentrations between 0.2 and 82 pmol/g. The amount of CO_2 produced as a result of photolysis of pyruvic acid within the ice was generated while assuming constant pyruvic acid concentrations deposited in Greenland over time. However the true concentrations in Greenland ice expected during the glacial are likely lower than the concentrations reported for the Holocene. Further, organic acids other than pyruvic acid could also photolyse and produce CO_2. To account for this larger amount of carboxylic acids the excess CO_2 was also determined using the concentration of carboxyls obtained in the study by *Kawamura et al.* [2001] (3.1 ng/g) and assuming similar molecular weight to that of pyruvic acid. When doubling the concentrations of pyruvic acid the amount of CO_2 produced is about 30% higher (Figure 13.3, 3rd plot). As pyruvic acid partly is deposited on the Greenland ice during forest fires, peaks with large pyruvic acid concentration can be expected. These peaks could have a much larger concentration than even the 7.23 ng/g reported by *Kawamura et al.* [2001], because the sample size used in that study was large (500 mL).

In conclusions a high number of unknowns and poorly constrained parameters need to be re-evaluated before a final conclusion can be reached on whether the photolysis of pyruvic acid is a likely source of *in situ* CO_2 production within the Greenland ice. However the low and more likely numbers used here suggest it is only a minor contributor.

REFERENCES PYRUVIC ACID

Abbasi, R., Y. Abdou, T. Abu-Zayyad, J. Adams, J. Aguilar, M. Ahlers, K. Andeen, J. Auffenberg, X. Bai, M. Baker, et al. (2011), Time-integrated searches for point-like sources of neutrinos with the 40-string IceCube detector, *The Astrophysical Journal*, *732*(1), 18.

Ackermann, and Others (2006), Optical properties of deep glacial ice at the south pole, *Journal of Geophysical Research*, *111*(D13), D13,203, doi:doi:10.1029/2005JD006687.

Adamo, C., and V. Barone (1998), Exchange functionals with improved long-range behavior and adiabatic connection methods without adjustable parameters: The mPW and mPW1PW models, *J. Chem. Phys.*, *108*(2), 664–676, doi:doi:10.1063/1.475428.

Ahn, J., and E. J. Brook (2007), Atmospheric CO_2 and climate from 65 to 30 ka BP, *Geophysical Research Letters*, *34*(10).

Ahrens, J., X. Bai, R. Bay, S. Barwick, T. Becka, J. Becker, K.-H. Becker, E. Bernardini, D. Bertrand, A. Biron, et al. (2004), Muon track reconstruction and data selection techniques in AMANDA, *Nuclear Instruments and Methods in Physics Research Section A: Accelerators, Spectrometers, Detectors and Associated Equipment*, *524*(1), 169–194.

Aidas, K., A. Møgelhøj, E. J. Nilsson, M. S. Johnson, K. V. Mikkelsen, O. Christiansen, P. Söderhjelm, and J. Kongsted (2008), On the performance of quantum chemical methods to predict solvatochromic effects: The case of acrolein in aqueous solution, *The Journal of chemical physics*, *128*, 194,503.

Alley, R., E. Saltzman, K. Cuffey, and J. Fitzpatrick (1990), Summertime formation of depth hoar in central Greenland, *Geophysical research letters*, *17*(13), 2393–2396.

Andrae, M. O., R. W. Talbot, and S.-M. Li (1987), Atmospheric measurements of pyruvic and formic acid, *J. Geophys. Ress.*, *92*(D6), 6635, doi:doi:10.1029/JD092iD06p06635.

Andreae, M., and A. Gelencsér (2006), Black carbon or brown carbon? The nature of light-absorbing carbonaceous aerosols, *Atmospheric Chemistry and Physics*, *6*(10), 3131–3148.

Anklin, M., J.-M. Barnola, J. Schwander, B. Stauffer, and D. Raynaud (1995), Processes affecting the CO_2 concentrations measured in Greenland ice, *Tellus B*, *47*(4), 461–470, doi:10.1034/j.1600-0889.47.issue4.6.x.

Anklin, M., J. Schwander, B. Stauffer, J. Tschumi, A. Fuchs, J. Barnola, and D. Raynaud (1997), Co2 record between 40 and 8 kyr BP from the Greenland Ice Core Project ice core, *Journal of Geophysical Research: Oceans (1978–2012)*, *102*(C12), 26,539–26,545.

Askebjer, P., S. W. Barwick, L. Bergström, A. Bouchta, S. Carius, E. Dalberg, K. Engel, B. Erlandsson, A. Goobar, L. Gray, A. Hallgren, F. Halzen, H. Heukenkamp, P. O. Hulth, S. Hundertmark, J. Jacobsen, A. Karle, V. Kandhadai, I. Liubarsky, D. Lowder, T. Miller, P. Mock, R. M. Morse, R. Porrata, P. B. Price, A. Richards, H. Rubinstein, E. Schneider, C. Spiering, O. Streicher, Q. Sun, T. Thon, S. Tilav, R. Wischnewski, C. Walck, and G. B. Yodh (1997), Optical properties of deep ice at the South Pole – absorption, *Appl. Opt.*, *36*(18), 4168–4180.

Barnes, P. R., and E. W. Wolff (2004), Distribution of soluble impurities in cold glacial ice, *Journal of Glaciology*, *50*(170), 311–324.

Barnes, P. R., R. Mulvaney, K. Robinson, and E. W. Wolff (2002), Observations of polar ice from the Holocene and the Glacial period using the scanning electron microscope, *Annals of Glaciology*, *35*(1), 559–566.

Barnola, J., M. Anklin, J. Porcheron, D. Raynaud, J. Schwander, and B. Stauffer (1995), CO_2 evolution during the last millennium as recorded by Antarctic and Greenland ice, *Tellus B*, *47*(1-2), 264–272.

Becke, A. D. (1988), Density-functional exchange-energy approximation with correct asymptotic behavior, *Phys. Rev. A*, *38*, 3098–3100, doi:10.1103/PhysRevA.38.3098.

Berzelius, J. J. (1839a), Lehrbuch der chemie, *8*, 11–16.

Berzelius, J. J. (1839b), Lehrbuch der chemie, *8*, 384–341.

Biczysko, M., P. Panek, G. Scalmani, J. Bloino, and V. Barone (2010), Harmonic and anharmonic vibrational frequency calculations with the double-hybrid B2PLYP method: Analytic second derivatives and benchmark studies, *Journal of Chemical Theory and Computation*, *6*(7), 2115–2125, doi:10.1021/ct100212p.

Brook, E. (2013), Personal correspondence.

Buemi, G. (2009), DFT study of the hydrogen bond strength and IR spectra of formic, oxalic, glyoxylic and pyruvic acids in vacuum, acetone and water solution, *Journal of Physical Organic Chemistry*, *22*(10), 933–947, doi:10.1002/poc.1543.

Busch, H., R. B. Hurlbert, and V. R. Potter (1954), Anion exchange chromatography of acids of the citric acid cycle, *Journal of Biological Chemistry*, *196*, 717–7127.

Caillon, N., J. P. Severinghaus, J. Jouzel, J.-M. Barnola, J. Kang, and V. Y. Lipenkov (2003), Timing of atmospheric CO_2 and Antarctic temperature changes across termination III, *Science*, *299*(5613), 1728–1731.

Carlton, A. G., B. J. Turpin, H.-J. Lim, K. E. Altieri, and S. Seitzinger (2006), Link between isoprene and secondary organic aerosol (soa): Pyruvic acid oxidation yields low volatility organic acids in clouds, *Geophysical Research Letters*, *33*(6).

Chu, L., and C. Anastasio (2005), Formation of hydroxyl radical from the photolysis of frozen hydrogen peroxide, *The Journal of Physical Chemistry A*, *109*(28), 6264–6271.

Clausen, H. B., C. U. Hammer, C. S. Hvidberg, D. Dahl-Jensen, J. P. Steffensen, J. Kipfstuhl, and M. Legrand (1997), A comparison of the volcanic records over the past 4000 years from the Greenland Ice Core Project and Dye 3 Greenland ice cores, *Journal of Geophysical Research: Oceans (1978–2012)*, *102*(C12), 26,707–26,723.

Cullen, D., and I. Baker (2001), Observation of impurities in ice, *Microscopy research and technique*, *55*(3), 198–207.

Delmas, R. J. (1993), A natural artefact in Greenland ice-core CO_2 measurements, *Tellus B*, *45*(4), 391–396.

Dunning, T. H. (1989), Gaussian basis sets for use in correlated molecular calculations. I. the atoms boron through neon and hydrogen, *J. Chem. Phys.*, *90*, 1007–1023.

EPICA community members (2004), Eight glacial cycles from an Antarctic ice core, *Nature*, (431), 623–628.

Faïn, X., J. Chappellaz, R. Rhodes, C. Stowasser, T. Blunier, J. McConnell, E. Brook, S. Preunkert, M. Legrand, T. Debois, et al. (2014), High resolution measurements of carbon monoxide along a late holocene greenland ice core: Evidence for in situ production, *Climate of the Past*, *10*(3), 987–1000.

Fischer, H., M. Wahlen, J. Smith, D. Mastroianni, and B. Deck (1999), Ice core records of atmospheric CO_2 around the last three glacial terminations, *Science*, *283*(5408), 1712–1714.

France, J. L., M. D. King, M. M. Frey, J. Erbland, G. Picard, A. MacArthur, and J. Savarino (2011a), Snow optical properties at Dome C, Antarctica implications for snow emissions and snow chemistry of reactive nitrogen, *Atmospheric Chemistry and Physics Discussions*, *11*(4), 11,959–11,993, doi:10.5194/acpd-11-11959-2011.

France, J. L., M. D. King, J. Lee-Taylor, M. J. Beine, a. Ianniello, F. Domine, and A. MacArthur (2011b), Calculations of in-snow NO_2 and OH radical photochemical production and photolysis rates: A field and radiative-transfer study of the optical properties of Arctic (Ny-Ålesund, Svalbard) snow, *Jour. Geophys. Ress.*, *116*, F04,013, doi:doi:10.1029/2011JF002019.

France, J. L., H. J. Reay, M. D. King, D. Voisin, H. W. Jacobi, F. Domine, M. J. Beine, C. Anastasio, A. MacArthur, and J. Lee-Taylor (2012), Hydroxyl radical and NO_x production rates, black carbon concentrations and light-absorbing impurities in snow from field measurements of light penetration and nadir reflectivity of onshore and offshore coastal Alaskan snow, *J. Geophys. Res.*, *117*, D00R12, doi:doi:10.1029/2011JD016639.

Francey, R. J., E. Michel, D. M. Etheridge, C. E. Allison, M. L. Leuenberger, and D. Raynaud (1997), The pre-industrial differnce in CO_2 from Antarctic and Greenland ice (AB0170), *Fifth international carbon dioxide conference*.

Galbavy, E., C. Anastasio, B. Lefer, and S. Hall (2007a), Light penetration in the snowpack at Summit, Greenland: Part 1: Nitrite and hydrogen peroxide photolysis, *Atmospheric Environment*, *41*(24), 5077–5090, doi:10.1016/j.atmosenv.2006.04.072.

Galbavy, E. S., C. Anastasio, B. Lefer, and S. Hall (2007b), Light penetration in the snowpack at Summit, Greenland: Part 2 Nitrate photolysis, *Atmospheric Environment*, *41*(24), 5091 – 5100, doi:10.1016/j.atmosenv.2006.01.066.

Galbavy, E. S., K. Ram, and C. Anastasio (2010), 2–nitrobenzaldehyde as a chemical actinometer for solution and ice photochemistry, *Journal of Photochemistry and Photobiology A: Chemistry*, *209*(2), 186 – 192, doi:10.1016/j.jphotochem.2009.11.013.

Goujon, C., J.-M. Barnola, and C. Ritz (2003), Modeling the densification of polar firn including heat diffusion: Application to close-off characteristics and gas isotopic fractionation for Antarctica and Greenland sites, *Journal of Geophysical Research: Atmospheres (1984–2012)*, *108*(D24).

Grannas, A. M., A. E. Jones, J. Dibb, M. Ammann, C. Anastasio, H. J. Beine, M. Bergin, J. Bottenheim, C. S. Boxe, G. Carver, G. Chen, J. H. Crawford, F. Dominé, M. M. Frey, M. I. Guzmán, D. E. Heard, D. Helmig, M. R. Hoffmann, R. E. Honrath, L. G. Huey, M. Hutterli, H. W. Jacobi, P. Klán, B. Lefer, J. McConnell, J. Plane, R. Sander, J. Savarino, P. B. Shepson, W. R. Simpson, J. R. Sodeau, R. von Glasow, R. Weller, E. W. Wolff, and T. Zhu (2007), An overview of snow photochemistry: Evidence, mechanisms and impacts, *Atmospheric Chemistry and Physics*, *7*(16), 4329–4373, doi:10.5194/acp-7-4329-2007.

Guzmán, M. I., A. Colussi, and M. R. Hoffmann (2006a), Photogeneration of distant radical pairs in aqueous pyruvic acid glasses, *The Journal of Physical Chemistry A*, *110*(3), 931–935.

Guzmán, M. I., A. J. Colussi, and M. R. Hoffmann (2006b), Photoinduced oligomerization of aqueous pyruvic acid, *The Journal of Physical Chemistry A*, *110*(10), 3619–3626, doi:10.1021/jp056097z, pMID: 16526643.

Guzmán, M. I., L. Hildebrandt, A. J. Colussi, and M. R. Hoffmann (2006c), Cooperative hydration of pyruvic acid in ice, *J. Am. Chem. Soc.*, *128*(32), 10,621–4.

Guzmán, M. I., M. R. Hoffmann, and A. J. Colussi (2007), Photolysis of pyruvic acid in ice- possible relevance to CO and CO_2 ice core record anomalies, *Journal of Geophysical Research*, *112*(D10123), doi:10.1029/2006JD007886.

Hanna, E., X. Fettweis, S. H. Mernild, J. Cappelen, M. H. Ribergaard, C. A. Shuman, K. Steffen, L. Wood, and T. L. Mote (2013), Atmospheric and oceanic climate forcing of the exceptional greenland ice sheet surface melt in summer 2012, *International Journal of Climatology*.

Harnung, S. E., and M. S. Johnson (2012), *Chemistry and the Environment*, Cambridge University Press.

Horowitz, A., R. Meller, and G. K. Moortgat (2001), The UV-VIS absorption cross sections of the α-dicarbonyl compounds: Pyruvic acid, biacetyl and glyoxal, *Journal of Photochemistry and Photobiology A Chemistry*, *146*(1), 19–27.

Indermühle, A., T. Stocker, F. Joos, H. Fischer, H. Smith, M. Wahlen, B. Deck, D. Mastroianni, J. Tschumi, T. Blunier, et al. (1999), Holocene carbon-cycle dynamics based on CO_2 trapped in ice at Taylor Dome, Antarctica, *Nature*, *398*(6723), 121–126.

Jelley, J. V. (1955), Cerenkov radiation and its applications, *British Journal of Applied Physics*, *6*(7), 227.

Jenk, T., M. Rubino, D. Etheridge, M. Bigler, and T. Blunier (2013), Sources of excess CO_2 in Greenland ice cores.

Jones, A., R. Weller, P. Anderson, H.-W. Jacobi, E. Wolff, O. Schrems, and H. Miller (2001), Measurements of NO_x emissions from the antarctic snowpack, *Geophysical Research Letters*, *28*(8), 1499–1502.

Kakkar, R., P. Chada, and D. Verma (2003), Structure and unimolecular decomposition pathways of pyruvic acid, *Internet Electronic Conference of Molecular Design*.

Kakkar, R., M. Pathak, and N. P. Radhika (2006), A DFT study of the structures of pyruvic acid isomers and their decarboxylation, *Org. Biomol. Chem.*, *4*, 886–895, doi:10.1039/B516355B.

Kakkar, R., M. Pathak, and P. Gahlot (2008), Effect of aqueous solvation on the structures of pyruvic acid isomers and their reactions in solution: a computational study, *Journal of Physical Organic Chemistry*, *21*(1), 23–29, doi:10.1002/poc.1270.

Kawamura, K., K. Yokoyama, Y. Fujii, and O. Watanabe (2001), A Greenland ice core record of low molecular weight dicarboxylic acids, ketocarboxylic acids, and α-dicarbonyls: A trend from Little Ice Age to the present (1540 to 1989 A.D.), *J. Geophys. Res.*, *106*(D1), 1331–1345, doi:10.1029/2000JD900465.

Kawamura, K., T. Nakazawa, S. Aoki, S. Sugawara, Y. Fujii, and O. Watanabe (2003), Atmospheric CO_2 variations over the last three glacial - interglacial climatic cycles deduced from the Dome Fuji deep ice core Antarctica using a wet extraction technique, *Tellus B*, *55*(2), 126–137, doi:10.1034/j.1600-0889.2003.00050.x.

Kawamura, K., H. Kasukabe, and L. A. Barrie (2010), Secondary formation of water-soluble organic acids and α-dicarbonyls and their contributions to total carbon and water-soluble organic carbon: Photochemical aging of organic aerosols in the arctic spring, *Journal of Geophysical Research: Atmospheres (1984–2012)*, *115*(D21).

Kendall, R. A., T. H. Dunning, and R. J. Harrison (1992), Electron affinities of the first-row atoms revisited. Systematic basis sets and wave functions, *J. Chem. Phys*, *96*, 6796–6806.

Kim, K., and W. Choi (2011), Enhanced redox conversion of chromate and arsenite in ice, *Environmental science & technology*, *45*(6), 2202–2208.

Kovacs, A., A. J. Gow, and R. M. Morey (1995), The in−situ dielectric constant of polar firn revisited, *Cold Regions Science and Technology*, *23*(3), 245–256.

Kristensen, T. B., H. Wex, B. Nekat, J. K. Nøjgaard, D. Pinxteren, D. H. Lowenthal, L. R. Mazzoleni, K. Dieckmann, C. Bender Koch, T. F. Mentel, et al. (2012), Hygroscopic growth and CCN activity of HULIS from different environments, *Journal of Geophysical Research: Atmospheres (1984–2012)*, *117*(D22).

Larsen, M. C., and V. Vaida (2012), Near infrared photochemistry of pyruvic acid in aqueous solution, *The Journal of Physical Chemistry A*, *116*(24), 5840–5846.

Le Treut, H., R. Somerville, U. Cubasch, Y. Ding, C. Mauritzen, A. Mokssit, T. Peterson, and M. Prather (2007), Historical overview of climate change, in *Climate Change 2007: The Physical Science Basis. Contribution of Working Group I to the Fourth Assessment Report of the Intergovernmental Panel on Climate Change*, chap. 1, Cambridge University Press, Cambridge, United Kingdom and New York, NY, USA.

Lee, C., W. Yang, and R. G. Parr (1988), Development of the colle-salvetti correlation-energy formula into a functional of the electron density, *Phys. Rev. B*, *37*, 785–789, doi:10.1103/PhysRevB.37.785.

Lee-Taylor, J., and S. Madronich (2002), Calculation of actinic fluxes with a coupled atmosphere–snow radiative transfer model, *Journal of geophysical research*, *107*(D24), 4796.

Legrand, M., and M. De Angelis (1995), Origins and variations of light carboxylic acids in polar precipitation, *Journal of geophysical research*, *100*(D1), 1445–1462.

Lüthi, D., M. Le Floch, B. Bereiter, T. Blunier, J.-M. Barnola, U. Siegenthaler, D. Raynaud, J. Jouzel, H. Fischer, K. Kawamura, et al. (2008), High-resolution carbon dioxide concentration record 650,000–800,000 years before present, *Nature*, *453*(7193), 379–382.

Manlay, R. J., C. Feller, and M. Swift (2007), Historical evolution of soil organic matter concepts and their relationships with the fertility and sustainability of cropping systems, *Agriculture, ecosystems & environment*, *119*(3), 217–233.

McNeill, V. F., A. M. Grannas, J. P. Abbatt, M. Ammann, P. Ariya, T. Bartels-Rausch, F. Domine, D. J. Donaldson, M. I. Guzmán, D. Heger, et al. (2012), Organics in environmental ices: sources, chemistry, and impacts, *Atmospheric Chemistry and Physics*, *12*(20), 9653–9678.

Mehta, A. (2011), Ultraviolet-visible (UV-Vis) spectroscopy - principle.

Monnin, E., A. Indermühle, A. Dällenbach, J. Flückiger, B. Stauffer, T. F. Stocker, D. Raynaud, and J.-M. Barnola (2001), Atmospheric co2 concentrations over the last glacial termination, *Science*, *291*(5501), 112–114.

Mulvaney, R., E. Wolff, and K. Oates (1988), Sulphuric acid at grain boundaries in antarctic ice, *Nature*, *331*(6153), 247–249.

Nghiem, S., D. Hall, T. Mote, M. Tedesco, M. Albert, K. Keegan, C. Shuman, N. DiGirolamo, and G. Neumann (2012), The extreme melt across the greenland ice sheet in 2012, *Geophysical Research Letters*, *39*(20).

Paterson, W. S. B., and K. M. Cuffey (1994), *The physics of glaciers*, vol. 3, Pergamon Oxford.

Pavia, D., G. Lampman, and G. Kriz (1996), Introduction to spectroscopy.

Peach, M. J. G., T. Helgaker, P. Salek, T. W. Keal, O. B. Lutnaes, D. J. Tozer, and N. C. Handy (2006), Assessment of a Coulomb-attenuated exchange-correlation energy functional, *Phys. Chem. Chem. Phys.*, *8*, 558–562, doi:10.1039/B511865D.

Pedro, J. B., S. O. Rasmussen, and T. D. van Ommen (2012), Tightened constraints on the time-lag between Antarctic temperature and CO_2 during the last deglaciation, *Climate of the Past*, *8*(4), 1213–1221.

Pépin, L., D. Raynaud, J.-M. Barnola, and M. Loutre (2001), Hemispheric roles of climate forcings during glacial-interglacial transitions as deduced from the Vostok record and LLN-2D model experiments, *Journal of Geophysical Research: Atmospheres (1984–2012)*, *106*(D23), 31,885–31,892.

Perdew, J. P., and Y. Wang (1992), Accurate and simple analytic representation of the electron-gas correlation energy, *Phys. Rev. B*, *45*, 13,244–13,249, doi:10.1103/PhysRevB.45.13244.

Perdew, J. P., K. Burke, and M. Ernzerhof (1996), Generalized gradient approximation made simple, *Phys. Rev. Lett.*, *77*, 3865–3868, doi:10.1103/PhysRevLett.77.3865.

Petit, J.-R., J. Jouzel, D. Raynaud, N. Barkov, J.-M. Barnola, I. Basile, M. Bender, J. Chappellaz, M. Davis, G. Delaygue, et al. (1999), Climate and atmospheric history of the past 420,000 years from the Vostok ice core, Antarctica, *Nature*, *399*(6735), 429–436.

Plath, K. L., K. Takahashi, R. T. Skodje, and V. Vaida (2009), Fundamental and overtone vibrational spectra of gas-phase pyruvic acid, *Journal of Physical Chemistry A*, *113*(26), 7294–7303, doi:10.1021/jp810687t.

Price, P. B., and L. Bergström (1997), Optical properties of deep ice at the South Pole: Scattering, *Appl. Opt.*, *36*, 4181–4194.

Rädel, L. (2012), Simulation studies of the Cherenkov light yield from relativistic particles in high-energy neutrino telescopes with GEANT4, *Master's thesis, RWTH Aachen*.

Raynaud, D., J.-M. Barnola, R. Souchez, R. Lorrain, J.-R. Petit, P. Duval, and V. Y. Lipenkov (2005), Palaeoclimatology: The record for marine isotopic stage 11, *Nature*, *436*(7047), 39–40.

Reva, I. D., S. G. Stepanian, L. Adamowicz, and R. Fausto (2001), Combined FTIR matrix isolation and ab initio studies of pyruvic acid: Proof for existence of the second conformer, *The Journal of Physical Chemistry A*, *105*(19), 4773–4780, doi:10.1021/jp0101458.

Rutkowska, A., and D. Pikuła (2013), Effect of crop rotation and nitrogen fertilization on the quality and quantity of soil organic matter, in *Soil Processes and Current Trends in Quality Assessment*, edited by M. C. Hernandez-Soriano, chap. 9, InTech.

Seinfeld, J. H., and S. N. Pandis (2012), Organic atmospheric aerosols, in *Atmospheric chemistry and physics: From air pollution to climate change*, chap. 14, John Wiley & Sons.

Smith, H., M. Wahlen, D. Mastroianni, and K. Taylor (1997), The CO_2 concentration of air trapped in GISP2 ice from the Last Glacial Maximum-Holocene transition, *Geophysical Research Letters*, *24*(1), 1–4.

Stevenson, F. (1982), Reactive functional groups of humic substances, in *Humus Chemistry. Genesis, Composition, Reactions*, Wiley.

Talbot, R., M. Andreae, H. Berresheim, D. Jacob, and K. Beecher (1990), Sources and sinks of formic, acetic, and pyruvic acids over central Amazonia 2 Wet season, *Journal of Geophysical Research*, *95*(D10), 16,799–16.

Toffoli, D., J. Kongsted, and O. Christiansen (2006), Automatic generation of potential energy and property surfaces of polyatomic molecules in normal coordinates, *J. Chem. Phys*, *127*, 204,106, doi:10.1063/1.2805085.

Tschumi, J., and B. Stauffer (2000), Reconstructing past atmospheric CO_2 concentration based on ice-core analyses: Open questions due to in situ production of CO_2 in the ice, *Journal of Glaciology*, *46*(152), 45–53.

Valadbeigi, Y., and H. Farrokhpour (2013), Theoretical study on keto enol tautomerism and isomerization in pyruvic acid, *International Journal of Quantum Chemistry*.

Vallelonga, P., G. Bertagna, T. Blunier, H. A. Kjær, T. J. Popp, S. O. Rasmussen, J. P. Steffensen, C. Stowasser, A. Svensson, E. Warming, et al. (2012), Duration of Greenland stadial 22 and ice-gas Δage from counting of annual layers in Greenland NGRIP ice core, *Climate of the Past Discussions*, *8*(4), 2583–2605.

Veres, D., L. Bazin, A. Landais, H. Toyé Mahamadou Kele, B. Lemieux-Dudon, F. Parrenin, P. Martinerie, E. Blayo, T. Blunier, E. Capron, et al. (2012), The antarctic ice core chronology (aicc2012): an optimized multi-parameter and multi-site dating approach for the last 120 thousand years, *Climate of the Past Discussions*, *8*(6), 6011–6049.

Voisin, D., J.-L. Jaffrezo, S. Houdier, M. Barret, J. Cozic, M. D. King, J. L. France, H. J. Reay, A. Grannas, G. Kos, P. A. Ariya, H. J. Beine, and F. Domine (2012), Carbonaceous species and humic like substances (HULIS) in Arctic snowpack during OASIS field campaign in Barrow, *J. Geophys. Res.*, *117*(D00R19), doi:10.1029/2011JD016612.

Wahlen, M., D. Allen, B. Deck, and A. Herchenroder (1991), Initial measurements of CO_2 concentrations (1530 to 1940 AD) in air occluded in the GISP 2 ice core from central Greenland, *Geophysical Research Letters*, *18*(8), 1457–1460.

Warren, S. G., and R. E. Brandt (2008), Optical constants of ice from the ultraviolet to the microwave: A revised compilation, *J. Geophys. Res.*, *113*(D14220), doi:doi:10.1029/2007JD009744.

Warren, S. G., R. E. Brandt, and T. C. Grenfell (2006), Visible and near-ultraviolet absorption spectrum of ice from transmission of solar radiation into snow, *Applied Optics*, *45*(21), 5320–5334, doi:doi:10.1364/AO.45.005320.

West, L. J., D. M. Rippin, T. Murray, H. M. Mader, and B. Hubbard (2007), Dielectric permittivity measurements on ice cores: Implications for interpretation of radar to yield glacial unfrozen water content, *J. Environ. Eng. Geophys.*, *12*, 27–45.

Winterhalter, R., M. Kippenberger, J. Williams, E. Fries, K. Sieg, and G. K. Moortgat (2009), Concentrations of higher dicarboxylic acids C-5–C-13 in fresh snow samples collected at the High Alpine Research Station Jungfraujoch during CLACE 5 and 6, *Atmospheric Chemistry and Physics*, *9*(6), 2097–2112.

Woschnagg, K., and P. B. Price (2001), Temperature dependence of absorption in ice at 532 nm, *Applied Optics*, *40*(15), 2496–2500.

Yanai, T., D. P. Tew, and N. C. Handy (2004), A new hybrid exchange-correlation functional using the coulomb – attenuating method (CAM-B3LYP), *Chemical Physics Letters*, *393*(1-3), 51 – 57, doi:10.1016/j.cplett.2004.06.011.

Zornoza, J.-D.-D., and D. Chirkin (2008), Muon energy reconstruction and atmospheric neutrino spectrum unfolding with the IceCube detector, in *International Cosmic Ray Conference*, vol. 5, pp. 1275–1278.

APPENDIX

A. ABBREVIATIONS

AMANDA Antarctic Muon And Neutrino Detector Array
AWI Alfred Wegener Institute
BC Black Carbon
BrC Brown Carbon
CFA Continuous flow analysis
CPH Copenhagen
CLRTAP Convention on Long-range Transboundary Air Pollution
Cx , where x is a number denotes the number of carbon atoms in an organic compund, eg. pyruvic acid is a C3, and succinic acid is C4
DEP di-electric profiling
DIP Dissolved inorganic phosphorus
DRI Desert Research Institute
DOC Dissolved organic carbon
DOP Dissolved organic phosphorus
DFoV Dual Field of View
DVI dust veil index
EC elemental carbon
ECM electric conductivity measurement
GGCI Name of samples obtained from the Gregoriev glacier
HPLC High-performance liquid chromatography
HULIS Humic like substances
IC Ion Chromatography
ICP-MS Inductively coupled plasma mass spectroscopy
ICP-SFMS Inductively coupled plasma sector field mass spectroscopy
ISA Ionic strength adjuster
LAC Light absorbing carbons
LC-MS-TOF Liquid-chromatography-mass spectrometry-time of flight detector
LLE Liquid liquid extraction
LWCC Liquid waveguide capillary cell
MB Molybdenumblue
MSA methansulfonic acid
MTB methyl thymol blue
MWEC melt water electrolytic conductivity
NEEM
NEGIS North East Greenland Ice Stream
NZ New Zealand
NIR Near infra red
NIPR National Institute for polar research

OC organic carbon
PA pyruvic acid
RICE Roosevelt Island Climate evolution
SLE Solid liquid extraction
SOA Secondary organic aerosols
SP2 single particle soot photometer
TC Total carbon
TOC total organic carbon
TUV tropospheric ultraviolet and visible model
VEI volcanic explosivity index
VOC volatile organic compounds
WAIS West Antarctic Ice Sheet
WinSOC Water insoluble organic carbon
WSOC water soluble organic carbon

B. LIST OF ICE CORES

In table B.1 some key information about some of the ice cores mentioned in this study is presented and in Figure B.1 the position of some of the ice cores are shown. Please note that the list is not a full list of all ice cores drilled.

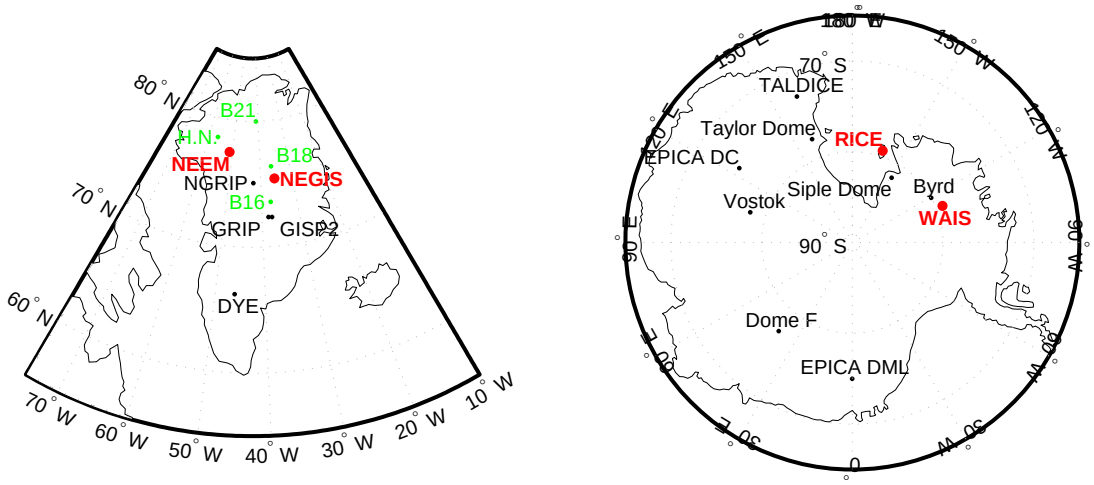

Fig. B.1: Positions of deep ice cores (black) together with ice cores measured for dissolved reactive phosphorus and/or colorimetric acidity (red). Also shown are a few shallow cores (green) mentioned within this thesis.

Tab. B.1: Information about selected ice cores

Ice core	Position			Depth	Age	Drill year
Antarctic ice cores	°S	°E	m.a.s.l	(m)		
EPICA/Dome C	75	123	3233	3190	800 kyr	1996-2004
VOSTOK	78.27	106.50	3488	2623	420 kyr	1993-1996
Dome Fuji	77.19	39.42	3810	3035	720 kyr	2003-2007
RICE	79.36	161.71	1230	763	∼110 kyr	2012-2013
TALDICE	72.49	159.11		1620	250 kyr	
WAIS	79.28	112.05	1766	3400	68 kyr	2005-2010
Greenland ice cores	°N	°W	m.a.s.l	(m)		
Dye 3	66.23	46.11	2338	2040		1979-1981
GRIP	72.35	37.38		3027	∼100 kyr	1989-1992
GISP	72.36	38.30	3200	3053	∼100 kyr	1988-1993
NGRIP	75.10	42.32	2917	3085	105 kyr	1999-2003
NEEM	77.27	51.30		2540	128 kyr	2009-2011
NEGIS	75.6	36.0	2684	68	1607 AD	2012
B20	78.50	36.30	2150	150	830 AD	1993-1995
Humboldt North	78.45	56.50	1905	21	1932 AD	1995

C. DANISH OUTREACH ARTICLE ABOUT CFA

This article written together with David Baslev-Clausen intended for Danish high school students was published by the Danish chemistry publisher ("Kemiforlaget") as a chapter in the book "Aspekter af dansk kemi i det 20. og 21. århundrede" published in relation to the international chemistry year; 2011.

Iskerner

– et indblik i fortidens klimaforandringer

Iskerner gemmer tidligere tiders klima, og når vi analyserer på de grønlandske iskerner, frembringes et klimaarkiv, der går mere end 110.000 år tilbage.

AF
HELLE ASTRID KJÆR OG DAVID BALSLEV-CLAUSEN

Willi Dansgaard, der i 1950 var ung forsker ved Københavns Universitet, havde fået ansvar for et massespektrometer. Der var ikke den store brug for massespektrometriske målinger, og derfor gav Willy sig til at måle på regnvand. I 1952 opdagede han, ved hjælp af massespektrometret, at der var en sammenhæng mellem temperatur og det, man kalder $\delta^{18}O$, se Boks 1. I 1954 fandt Willi Dansgaard på, at man

Boks 1. $\delta^{18}O$

$\delta^{18}O$ (siges "delta-18-O") er et mål for det relative blandingsforhold mellem den lette ^{16}O-isotop og den tungere ^{18}O i H_2O, målt i forhold til en standardvæske af velbestemt blandingsforhold (f.eks. SMOW – *Standard Mean Ocean Water*). $\delta^{18}O$ opgives i promille:

$$\delta^{18}O = \frac{R - R_{SMOW}}{R_{SMOW}} \cdot 10^3 \text{ ‰} \quad , \qquad R = \frac{[^{18}O]}{[^{16}O]}$$

De vandmolekyler, der indeholder ^{18}O har på grund af deres lidt højere masse sværere ved at fordampe end dem der indeholder ^{16}O. Tilsvarende kondenserer vandmolekyler med ^{18}O hurtigere, f.eks. når der dannes skyer. Blandingsforholdet for den tunge isotop er afhængig af temperaturen på nedbørstidpunktet, med færre ^{18}O-vandmolekyler ved koldere temperaturer. Lave $\delta^{18}O$-værdier svarer altså til lave temperaturer.

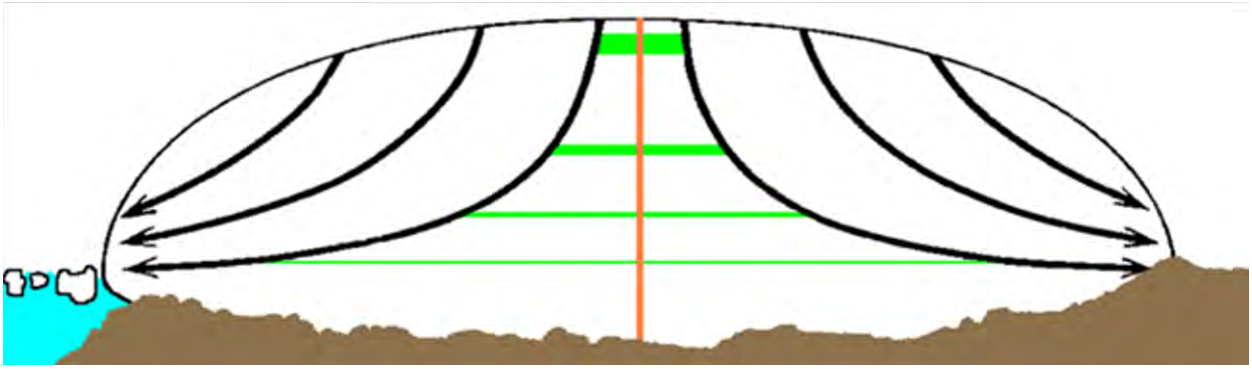

Figur 1. Iskappen
Et årlag (grøn streg) deponeret på toppen af iskappen bliver tyndere og tyndere pga. isens flydning. Den orange vertikale angiver et typisk borested for en iskerne der rækker langt tilbage i tiden.

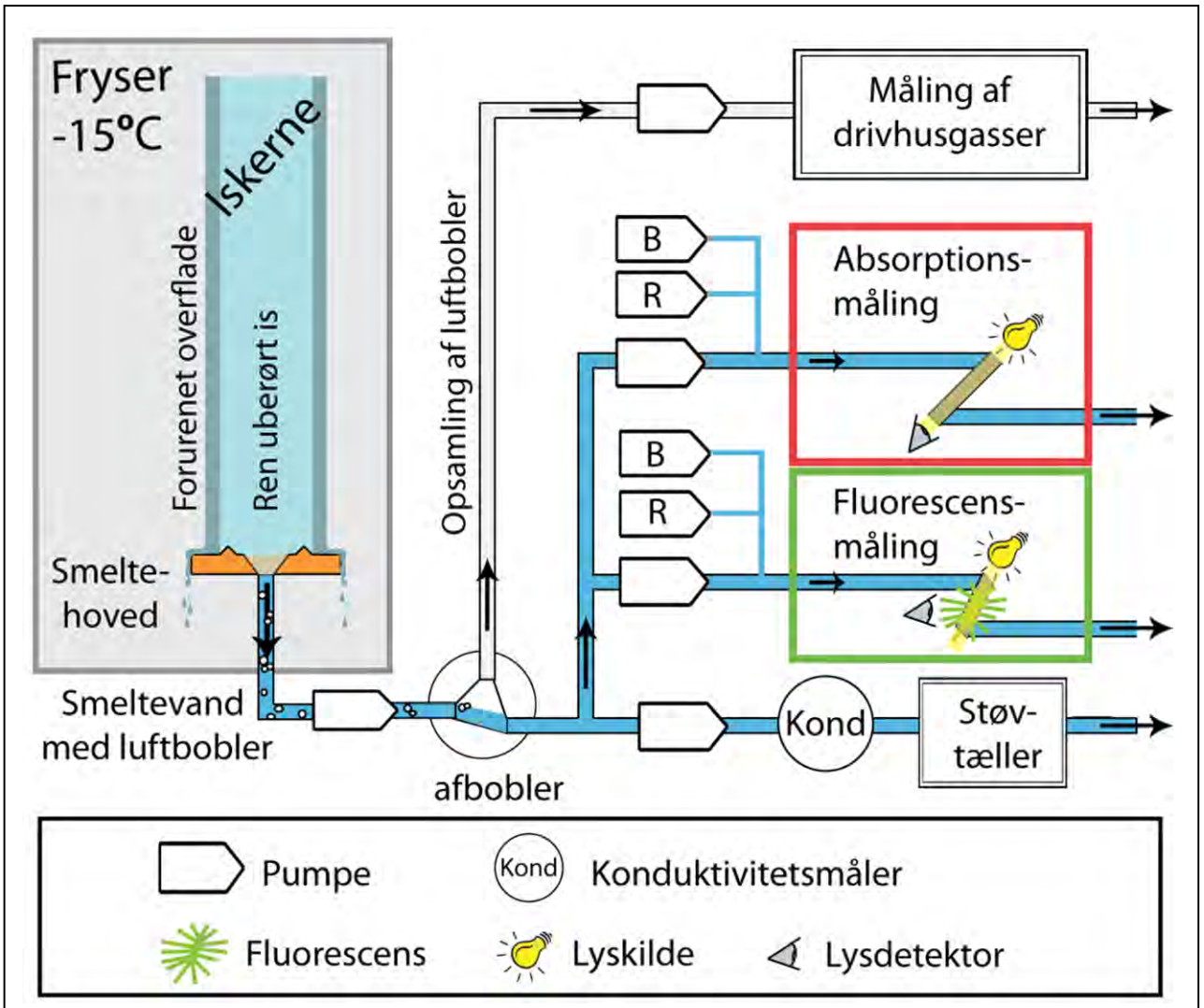

Figur 2. Eksempel på CFA set-up.
Isen smeltes, og det smeltevand, der ikke er kontamineret, ledes videre i systemet. Luftboblerne opsamles til gasmålinger, mens væsken splittes og ledes videre til målinger. I en linje måles konduktivitet (Kond) og støvindhold. I andre linjer iblandes reagens (R) og puffer (B), og absorption eller fluorescens detekteres. I et CFA system er der ofte mange fluorescens- og absorptionsmålinger samtidig.

også kunne måle temperaturudsving i iskerner ved blandt andet at måle $\delta^{18}O$ værdier, altså en parameter for temperaturen i historisk nedbør. Dette var starten på et helt nyt vidensområde, som siden gjorde Willi Dansgaard til professor i palæoklima ved Københavns Universitet.

Willy Dansgaard var forud for sin tid. I dag er klima på alles læber, og man er særligt interesseret i, hvordan klimaforandringer kommer til at påvirke os de næste 100 år. Men hvad er klimaforandringer? Det kan være svært at bedømme, om der virkelig er forandringer, hvis man ikke ved, hvordan klimaet normalt er. Ligesom det kan være svært at tro på modeller, der forudsiger klimaforandringer, hvis de ikke kan genskabe tidligere tiders klima. For at forstå de klimaforandringer, vi ser i dag, og beregne de forandringer, vi kommer til at se i fremtiden, er vi altså nødt til at have et arkiv over tidligere tiders forandringer. Iskernerne er et sådant arkiv.

ISKERNER

Iskerner har den fordel, at de indeholder informationer om klimaet lang tilbage i tiden. Iskerner fra Grønland dækker de seneste ca. 123.000 år, mens

iskerner fra Antarktis går 800.000 år tilbage.

En anden fordel ved at bruge iskernerne som klimaarkiv er, at de har høj opløsning. På Grønland falder der 19–50 cm is om året. Det betyder, at man kan se de enkelte årlag helt tilbage til 80.000 år f.Kr. Den øverste halvdel af de Grønlandske kerner dækker hele vores mellemistid, altså de sidste ca. 11.700 år, mens den nederste halvdel af de Grønlandske kerner dækker ca. 120.000 år tilbage i tiden. Det er fordi isen er plastisk og flyder. Dermed bliver årlagene udglattede over tid. De bliver altså tyndere og tyndere, jo ældre de er, som det ses i Figur 1.

Hvor er det bedste sted at bore en iskerne? Hvis man gerne vil nå langt tilbage i tiden, er det bedste sted at bore en iskerne ved iskappens højderyg (se Figur 1). Her har isen nemlig ingen horisontal transport og udtyndes blot, derfor er isens lag uforstyrrede og lagene i bunden er meget gamle. Hvis man gerne vil have meget høj opløsning af f.eks. menneskeskabte forandringer, er det bedre at bore en iskerne et sted med meget nedbør. Der er årlagene nemlig tykkere, og man har bedre mulighed for at bedømme, hvornår på året sneen med de mange urenheder er faldet.

MÅLINGER PÅ ISKERNER

Iskerner fortæller om fortidens temperaturer målt ved isens $\delta^{18}O$-sammensætning, mens støvparametre som Mg^{2+}- og Ca^{2+}-indhold fortæller om atmosfærens cirkulationsmønstre. Tidligere tiders atmosfærisk luft er indesluttet i isen i små luftbobler, fra hvilke tidligere tiders drivhusgas koncentrationer af f.eks. CO_2 og CH_4 kan måles. Vulkanudbrud kan findes i isen ved høje koncentrationer af SO_4^{2-}, og et billede af biomassen på land kan man få ved at kigge på NH_4^+.

Traditionelt har man målt isen ved at skære den i stykker og måle hvert stykke for sig. Men jo mere isen berøres og skæres i stykker, jo større er sandsynligheden for forurening. Derfor måler man nu helst is kontinuert, og man bruger den såkaldte "Continuous Flow Analysis" (CFA) metode (Figur 2).

KONTINUERTE MÅLINGER (CFA)

CFA målinger bruges primært til måling af ioner som Cl^-, Na^+, SO_4^{2-}, NH_4^+, Mg^{2+}, Ca^{2+} og andre, men systemet måler også elektrisk ledningsevne og kontinentalt støv. Ved CFA målinger skæres isen først ud i et stykke som er ca. 3 x 3 cm og mellem 55 og 110 cm langt. Stykket placeres oprejst ovenpå et smeltehoved i en fryser. Smeltehovedet er typisk lavet af guld, som ikke binder ionerne fra isen. Under smeltningen er der hele tiden en smule mere, der smelter i den inderste del af smeltehovedet, end der bliver trukket videre i systemet, altså et overflow fra den indre del af smeltehovedet til den ydre. Dette gør man for at undgå, at den ydre is, som kan være forurenet, bliver målt. Smel-

Boks 2. Absorption

Absorption er dæpningen af lys igennem et medium. For at måle koncentrationen af ioner tilsættes et reagens og evt. en puffer til iskernevandet. Reagenset danner et farvestof, når det går i forbindelse med ionen, som vi ønsker at bestemme koncentrationen af. Vandet strømmer igennem en absorptionscelle, hvor man lader en lampe lyse igennem vandet. Jo højere koncentration af ioner, des mindre lys vil komme ud på den anden side. Man kan altså måle lysintensiteten før (I_0) og efter (I) absorptionen og herved bestemme absorbansen, som er afhængig af koncentrationen af det absorberende stof. Na^+ og SO_4^{2-} er eksempler på ioner, hvis koncentration kan bestemmes med absorptionsmålinger. Gaskoncentrationer kan også bestemmes ved absorptionsmålinger.

Boks 3. Fluorescens.

Fluorescensmålinger er også lysafhængige. Med en lampe exciteres ionerne ved en given bølgelængde, og når de igen henfalder til grundtilstanden, bliver fotoner udsendt. Antallet af ioner bestemmes ved at måle lysintensiteten. Mængden af lys afhænger altså af koncentrationen af ionen. Na^+, Ca^{2+} og NH_4^+ er eksempler på ioner, hvis koncentration måles ved fluorescens.

tevandet skilles i forskellige vandlinjer og tilføres reagenser og puffer. Reagenserne reagerer med forskellige ioner i vandet og via absorptionsmålinger (Boks 2) eller en fluorescensmetode (Boks 3) måles koncentrationerne af de forskellige ioner, der er i vandet fra isen.

ISKERNERNES HISTORIE

Målingerne fra CFA systemet bruges til mange ting. Generelt har de ioner, man finder i isen, en top om foråret. Det er fordi kraftigere vind på dette tidspunkt af året transporterer flere ioner til iskappen fra kildeområderne. De årlige udsving kan bruges til at tælle år for år 80.000 år tilbage i tiden. På den måde kan man datere isen med meget høj præcision. Denne nøjagtige datering fra iskerner har bl.a. hjulpet historikere med at finde den helt rigtige datering af vulkanudbruddet ved Vesuv (79 e.Kr.). Det er også via iskernedateringerne, at slutningen på sidste istid er blevet fastsat til 11.703 år før år 2000.

VULKANER

Vulkanske udbrud er kendetegnet ved samtidige høje koncen-

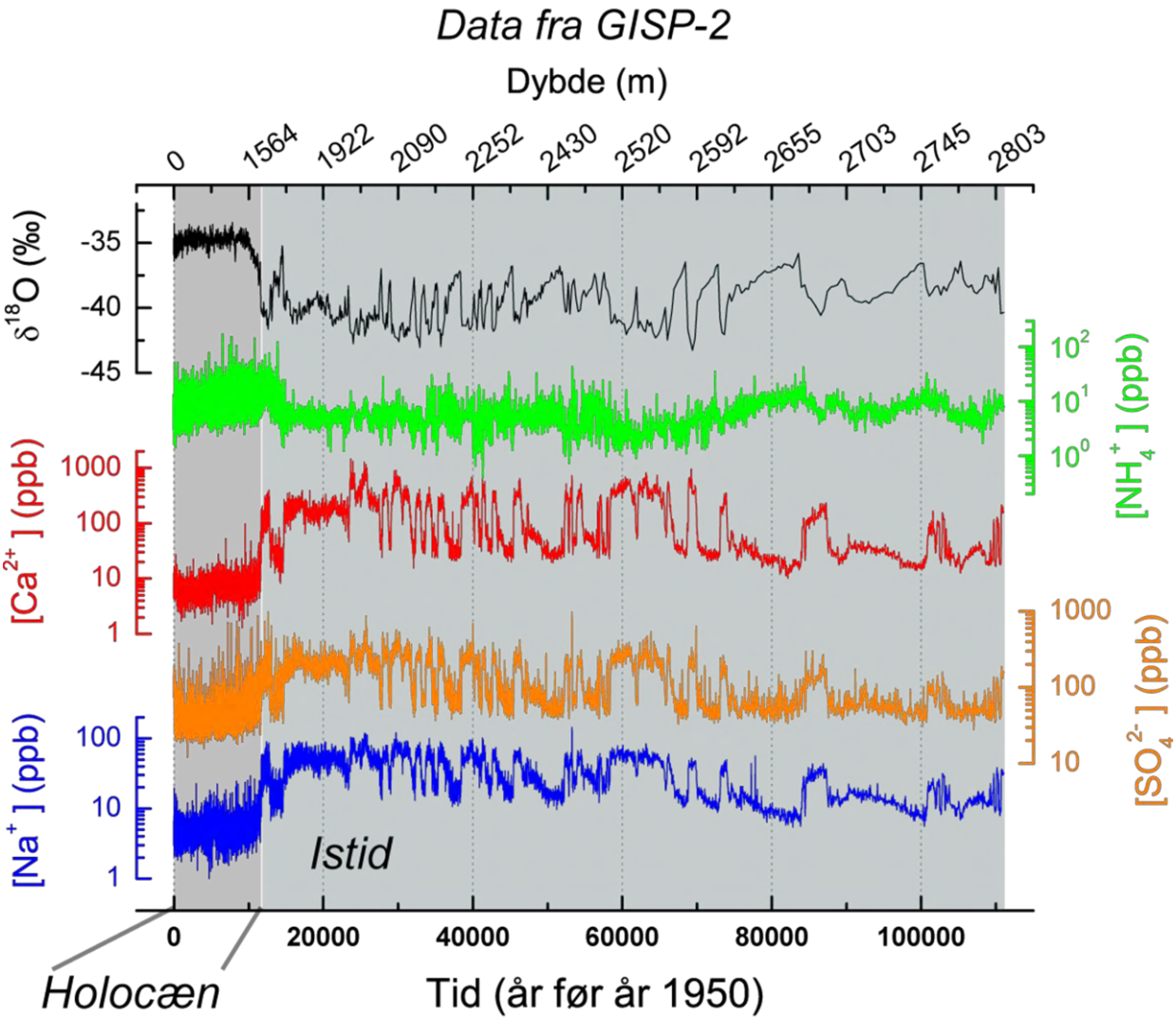

Figur 3. Eksempler på målinger fra den grønlandske iskerne GISP-2.
Øverst (sort) er $\delta^{18}O$, et mål for temperaturen, jo mere negativ, des koldere. Ammonium (grøn) er et mål for biologisk aktivitet. Calcium (rød) er en støvparameter. Sulfat (orange) indikerer vulkanudbrud, men har også en biologisk oprindelse. Natrium (blå) relaterer til oceanet.

trationer af SO_4^{2-} og NO_3^-. Vulkanske lag er meget vigtige i dateringen af isen. F.eks. kan man bruge dem til at krydsdatere kerner. Er det en vulkan, der har haft et stort udbrud som f.eks. Tambora i år 1815, kan man se det både i de Grønlandske og i de Antarktiske iskerner. Vi ved også fra iskernerne, at der var en meget større vulkansk aktivitet i starten af vores mellemistid. Under istiden lå der store masser af is henover Nordamerika, faktisk så langt sydpå som New York, men også store dele af Europa var dækket af is. Da isen smeltede væk under overgangen til vores mellemistid, Holocæn, blev trykket på jorden flyttet, og det udløste jordskælv og vulkanudbrud.

STØV

Mængden af støvpartikler måles direkte ved CFA, men også ioner som Ca^{2+} og Mg^{2+} kommer primært fra støv. Støvet kan fortælle os om vindhastigheder, men også om kildeområder. Under sidste istids maksimum (ca. 20.000−25.000 f.Kr.) ses et op til 1000 gange større indhold af støv i iskernerne end der er i dag. Det tolker man som en følge af den ca. 120 m lavere vandstand, og det dermed større landareal. Derudover ser man større støvkorn, og de kan kun komme op på iskappen, hvis der er kraftigere vind. Vinden er kraftigere under istiden, fordi der er en større temperaturforskel mellem ækvator og polerne.

DANSGAARD-OESCHGER BEGIVENHEDER

I støvet og ionerne ser man store udsving under istiden. Disse klimaskift har fået betegnelsen *Dansgaard-Oeschger begivenheder* efter danske Willi Dansgaard og hans schweiziske kollega Hans Oeschger. D/O-begivenheder er perioder med en kraftig stigning i temperaturen på op til 20 graders opvarmning på bare 50 år, efterfulgt af en gradvis afkøling til istidens normale kolde klima. Når temperaturen stiger under en D/O begivenhed, falder mængden af urenheder i isen. Under den sidste istid var der 25 D/O begivenheder. Man ser ikke D/O-begivenheder i de varme mellemistider (f.eks. Holocæn). Mellemistiderne har et langt mere stabilt klima end istiden. I vores mellemistid (Holocæn) ses i iskernerne en jævn afkøling på ca. 3 grader i løbet af de sidste ca. 10.000 år.

MENNESKESKABTE FORANDRINGER

Menneskabte forandringer kan også ses i iskernerne. Udover en stigning i CO_2 ses også forandringer i NH_4^+-sommertoppen. Den er fordoblet i løbet af de sidste ca. 100 år som følge af menneskets brug af kunstgødning. Der er også tydelige tegn på menneskabte forandringer i mængden af NO_3^- og SO_4^{2-} i de grønlandske iskerner (se Figur 3). Disse forandringer menes at stamme fra fabrikkers udledning. For nogle udledninger ser man i isen, at koncentrationen falder igen. Det skyldes, at man har indført reguleringer (f.eks. Kyoto protokollen) på hvor meget forurening, der må udledes.

Iskernearkivet har medført en revurdering af opfattelsen af klimaet på vores jord. Tidligere tænkte man på klimaet som noget statisk og uforanderligt. Men iskernerne har vist, at klimaet kan variere kraftigt over meget kort tid, som f.eks. D/O-begivenhederne. Iskernerne giver vigtig viden om klimaet og har noget af den bedste opløsning, der findes tilbage i tiden. Derfor er iskernerne også et af de bedre palæoarkiver til at bedømme, hvor hurtigt forandringerne sker i jordens klima og ikke mindst i hvilken rækkefølge. Det er præcis den viden, der er nødvendig for at lave gode klimamodeller, der kan forudsige fremtidens klima.

Om forfatterne

Helle Astrid Kjær *er Ph.D-studerende ved Center for Is og Klima, Niels Bohr Instituttet, Københavns Universitet.*

David Balslev-Clausen, *Ph.D., er post.doc. ved Center for Is og Klima, Niels Bohr Instituttet, Københavns Universitet.*

Referencer

Besøg www.isarkiv.dk og www.isogklima.dk for mere information om isens hemmeligheder.

D. MANUSCRIPT ABOUT THE JAPANESE CFA SYSTEM

High Resolution Continuous Flow Analysis System for Polar Ice Cores

REMI DALLMAYR[1], KUMIKO GOTO-AZUMA[1], HELLE ASTRID KJÆR[2], PAUL VALLELONGA[2], HIRONOBU YAMADA[1], NOBUHIKO AZUMA[3], MORISAMA TAKATA[3], SIMON SCHUPBACH[4], TAKAHIRO SEGAWA[1]

[1]*National Institute of Polar Research, Tachikawa, Tokyo 190-8518, Japan*
[2]*Centre for Ice and Climate, Niels Bohr Institute, Copenhagen , 2100, Denmark*
[33] *Nagaoka University of Technology, 940-2188, Japan*
[4]*Climate and Environmental Physics, Physics Institute, University of Bern, Bern, Switzerland,*

- Abstract

In the last decades, Continuous Flow Analysis (CFA) technology for ice core analyses has been developed to reconstruct the past changes of the climate system with fast and high depth resolution analyses. We present here such a CFA system for fast and rapid analysis of ice cores that is currently able to continuously measure stable water isotopes and electrolytic conductivity, as well as to collect discrete samples from both inner and outer areas of the core with variable depth resolutions, thus ensuring that no ice is wasted while simultaneous keeping clean samples for discrete high purity measurements. This system presents an optimized resolution in the determination of quick signals in deep polar ice cores. Measurements of different climate intervals in glacial Greenlandic ice from NEEM and comparison with earlier studies show the high resolution of this system as compared to other CFA systems.

- Introduction

The last few decades increased importantly our understanding of the global climatic changes especially driven by results from ice cores (1-5). Deep polar drilling projects in Greenland and Antarctica provide valuable information about past climates covering a time scale up to 800 kyr before present with a high temporal resolution (3,4). During the last decades, Continuous Flow Analysis techniques (CFA) have improved the temporal resolution of ice core chemical measurements as well as the time of the measurements (5-7,10,11). With such CFA systems a longitudinal subsection of an ice core kept in freezing conditions is melted continuously on a chemically inert melt head adapted to provide 2 or more (11) separated streams, inner and outer parts of the sample core. Thus generating an uncontaminated sample stream by splitting the outer possible contaminated sample from the analyze of the inner part of the ice core (5-7,10,11). All the different analytical systems connected to this melting unit are located in a +20°C laboratory. Controlling the speed of the melt, thus the resolution, the CFA allow a fast, accurate and reliable analyze of the full length of a deep ice core (5,6,7).

The system we present in this work has been developed at the National Institute of Polar Research, Japan. It is currently able to continuously detect stable water isotopes (8,9) and electrolytic conductivity (hereafter σ), as well as to collect discrete samples (10) for the both inner and outer areas with variable depth resolutions. Implementations of the current system are planned (chemical analyses by ICPMS (11), dust particle distribution (5), methane-gas analysis (12,13), but will not be developed in this work. A new, specific high quality sample positioning in the core is achieved by the use of a high accuracy laser positioning sensor. As the continuous sample stream can be smoothed because of mixing, we spend time optimizing all volumes to ensure a minimum of smoothing. The degassing unit represents the main mixing volume of a CFA system. A minimum volume in the debubbler is needed to

keep a safe buffer and avoid air in the system at all times. Therefore, a novel approach to the regulation of this module has been achieved to minimize it.

- Material and methods:

In Figure 1 is shown the NIPR CFA set up. It consists of a melting unit located at -20°C in a freezer and provides online analytical systems (δ18O, δD, σ) and samples collector modules (Fraction Collectors, Gilson FC204) after a gas-water separation step in the degassing unit. Add to these systems, one line was used for the newly developed dissolved reactive phosphorus detection technique (Kjær, 2013), but is not further discussed as it is beyond the scope of this paper."

Melting Unit

A sample core holder made of Plexiglas, 600mm long and 34mm x 34mm cross section is positioned above and central over the melt head to guide the ice sample during the melting experiment. An 850 g weight made of an alloy of copper and zinc, surrounded by two polypropylene end pieces to avoid contamination of metals is positioned on top of the ice and applies a constant force to stabilize the melt speed. The Melt speed is calculated by the acquisition of the weight's top position. In this study, instead of using a wire position encoder, which is common in CFA detection systems (5,7, 16), we use a high-accuracy Charge Coupled Device Laser displacement sensor, which uses triangulation to determine the distance to the top of the weight (LKG-G505, Keyence). The accuracy of this novel employed sensor is very high (0,05mm precision with a 2μm repeatability), and thus a high quality determination of the sample depth is possible during the further data processing step. The melt head we use is similar to the one used at University of Maine (10,15,16). It has been made by the engineering team of Nagaoka University. The melt head temperature is controlled by a PID (proportional-integral-derivative) temperature controller MTCD, Misumi Corp) using two 250W heating cartridges and a Platinum resistance thermometer (Pt100). Similarly to other CFA systems, the melt temperature, thus the melt speed, and thus the resolution is controlled to high degree.

To avoid mixing of the center part of the ice sample by the potentially contaminated outer part, the melt head separates the sample in two drainage channels via two different collection areas. The inner channel has a square size of 20 mm and the outer channel 34 mm. The two melt streams separation is guaranteed by a 1 mm high ridge to physically separate the areas. We also apply a > 10% overflow pumping rate from the inner to the outer melt head area.

With minimal sample volumes requirements, a low melting rate of typically 1.6 cm/min is set to optimize our CFA system resolution. At this speed, and regarding the use of the pump tubes, we apply 6.5 and 15.5 ml/min pumping rates to respectively the inner and outer channels.

Streams paths to the different analytical systems

An automated 6 port injection valve (Upchurch scientific, V2500) switches between ice samples and a selection between our ultrapure blank water (Milli-Q ≥ 18.2 MΩ/cm, Millipore Advantage), the conductivity standard (Amber Sciences conductivity calibration solution, 74.7 μS/cm),and our internal laboratory isotopic standards. The isotopic concentrations of these standards have been confirmed

regarding to the international VSMOW/SLAP2 isotopic scale through an interlaboratory comparison (collaboration with the LSCE Laboratoire des Sciences du Climat de l'environnement, Saclay).
The non contaminated melt water from the inner channel to the melt head is carried through a 1/16"OD, 0.2 mm ID PFA tube, via a Gilson Minipuls3 peristaltic pump. At the melting unit outlet, a first conductivity cell (C1, amber sciences, conductivity meter model 1056) is placed. It measures the conductivity of the air water mixture arriving from the ice and gives an essential high resolution reference conductivity signal. Each of our analytical systems presents a conductivity cell (Ci) as close as possible of the inlet of that particular system to obtain an instrument conductivity signal. These signals allow an easy and efficient synchronization of the different analytical systems during the data analyze, as done by (17) at the Desert Research Institute in Reno.
The outer channel of the melthead is drained by a second Gilson Minipuls3 pump through a 1/8" OD (ID: 1.57 mm) PFA tube. This channel is not analyzed online but connected to a fraction collector, and therefore we placed conductivity detection unit before the collection in 30ml PolyPropylene vials for further analyzes of species less prone to contamination.

Degassing unit

10 % of natural ice is air, so when melted the melt stream contains both gas and water. Most detections systems can be severely affected by air and thus a debubbler is necessary on the sample inlet line. In Figure 2 the setup of the degassing unit used in this study is shown. The debubbler is a simple polypropylene open split. Water drips into the vial, while gas is released in the air. The exact distribution of air in the water can however vary, thus the volume that occurs at the bottom of the debubbler is not stable. To keep the mixing in the debubbler stable we vary the amount of water that is removed from the bottom of the debubbler by inserting a variable overflow. The overflow is set in such a way that the mixing volume is minimized, but also set to a minimum safety volume to avoid air bubbles, which can significantly alter or destroy detections downstream. The overflow line is regulated by a pump. This pump is controlled by the weight of the debubbler, which stands fixed on a mass balance (Mettler Toledo, NewClassic MF MS603S) connected to a computer. The Figure 2 provides a picture of the real set up. The computer controls the rate of our overflow peristaltic pump (Gilson, Minipuls3). A handmade software algorithm has been developed using LabView (National Instrument) for the purpose. Not to disturb the analyzed sample stream, the 3 parameters (proportional P, integrate I, and derivative D) have been optimized to ensure a smooth but effective reactivity of the overflow pumping rate. The typical mixing volume of the debubbler is set and kept around 400 µL(mg) and the PID control gives a typical variation of less than 10 µL (mg) around the set point.
After the debubbler the degassed water stream is split in a PEEK manifold (Upchurch scientific P-150) to the different detection units.

- Analytical systems:

Water Isotopes

The water isotopes stream is carried by a Reglo Digital Ismatec peristaltic pump through a 10 µm stainless steel filter and a data synchronization conductivity cell (C3) at a rate of 0.2 ml/min after which it enters a spectrometer for detection of water isotopes. We continuously determine δD and δ18O in a Wavelength Scanned Cavity Ring Down Spectrometer (WS-CRDS, L2130-i, Picarro, Inc.). The WS-CRDS optimum performances are obtained with a continuous injection of sub µl/min water vapor flow in the optical cavity.

To obtain such a low continuous and stabile vapor flow rate for the Picarro instrument a stream vaporization module was developed, based on the method of Gkinis and colleagues (8) and further implementing the upgrades applied by (17). A bloc diagram of the technique is presented in Figure 3. We split a micro flow from the main flow in a stainless micro-volume tee (T1 in fig.3, U-428 Upchurch Scientific). To obtain the micro flow, we use a fused silica capillary with 40 µm ID. The flow through the capillary is kept stable by control of the back pressure, imposed by a restriction on the waste line downstream of T1. To have a better control of the back pressure, we divided the waste line using a PEEK tee (T3) and added in one of the two sub waste lines, the use a 10 turns needle valve (P-445 Upchurch Scientific). This set-up allows very precise and efficient control of the back pressure. The sample micro flow is injected in the evaporation chamber (T2, stainless steel Valco ZT1M) where temperature is controlled at 180°C for an instantaneous vaporization. Upon evaporation of the liquid sample, mixing with dry air takes place, forming a gas sample with the desired water vapour concentration. The dry air is obtained by drying atmospheric ambient air through a Drierite Canister CaSO4. Typical water vapour levels for the dry gas are below 100ppmv water concentration. During its transfer to the spectrometer (6cm long 1/16" stainless steel tube), the sample flow is kept at 90°C to avoid any recondensation, and thus fractionation.

Water Isotopes performances:

To demonstrate the stability and precision of our method, we inject MilliQ water over 24 hours at a water level of ~21000ppm. The experiment presents a standard deviation of 213ppm for the water vapor level and 0.105 ‰ and 0.310‰ for δ18O and δD, respectively. In Figure 4, a) an investigation of the water vapor concentration dependency of our measurements is shown. This investigation has been realized by injecting our blank in the cavity during injection steps of 10min at different level covering a scale from 3000 to 30000 ppm, with averaged results for the last 2 minutes. We found a linear response area between 17000 and 23000 ppm, with optimum performances at 20000 ppm for the both isotopes. Also, in the linear response area, the variations of δ18O are within the standard deviation of our measurement. Therefore, contrary to (8), we find that a weekly calibration at 20000ppm is necessary for only δD. Thus the following water vapor level calibration is applied weekly for δD:

$$\delta_{calibrated} = \delta_{raw} - \alpha_{slope} \times ([H2O]_{raw} - 20000) \quad (1)$$

Where $\delta_{calibrated}$ the corrected value at 20000 ppm, δ_{raw} the raw isotope data, α_{slope} the slope of the δ_{raw} function of water level, and $[H2O]_{raw}$ the water level of the data.

Also shown in Figure 4, b) is a result from an isotopic step to the system. We thus evaluate the memory effect of the method by comparing to the fitted lognormal distribution function (2), fitted to our measurements:

$$\delta_{model}(t) = \frac{K_1}{2}\left[1 + erf\left(\frac{\ln t - t_{impuls}}{\sqrt{2}}\right)\right] + K_2 \quad (2)$$

The values of K1, K2 are estimated by means of a least square optimization and used accordingly to normalize the length scale and the isotopic values of the step. It appears that 40sec after the isotopic change the reported difference between the fit and the actual measurements are less than 10%. Thus a smoothing larger than 40s should be used on the isotopic signal.

To calibrate the data to the international isotopic scale, we perform at the beginning and end of each sample measurement day, a set of our 3 internal laboratory standards injections. A typical calibration data set is shown in Figure 4, c). The 3 standards are injected for 10 minutes each. The stable last few minutes of each isotopic step are averaged to determine the linear calibration.

$$\delta_{VSMOW} = \alpha_{VSMOW} \times \delta_{measured} + \beta_{SMOW} \quad (3)$$

System Conductivity (σ)

Conductivity is, as previously mentioned, determined at several points in the continuous flow system. Due to its proximity to the manifold avoiding smoothing and its position after the debubbler avoiding the effect of air bubbles, the synchronization device for the inner channel Fraction Collector has been chosen to give the CFA system conductivity measurement.

We evaluated the response time of the conductivity (C2) by switching between milliQ blank and 3 different conductivities standards. The results are presented in Figure 5. We find the response times (durations between 10% above the baseline and 90% of the peak height) independent of both concentration and the duration of the switch. The temporal resolution was determined after normalizing peaks (amplitude scaled to one) and we find the response time going up to a standard is 29s, while the return takes longer (50s). These response times relate to the response right before introduction to the detection units and thus do not take into account the potential dispersion effects between the melt head and the injection valve. The total combined dispersion was investigated by injecting the same switch of streams on the melt head. We find that the melthead add a dispersion effect of only 2 seconds on the temporal resolution. When melting the ice sample at 1.6 cm/min, the temporal resolution for conductivity converts to a depth resolution of 0.82 cm for an increase and 1.38 cm for a decrease as a σ depth resolution. The difference between increase and decrease may show also the sticky effect of the PFA tubing.

Inner channel Fraction Collector

The inner channel fraction collector flow rate is set to 2mL/min via a Reglo Digital Ismatec peristaltic with the variable depth resolution of collection. The inner channel fraction collector is maintained in a clean area with HEPA (High Efficiency Particles Arresting) filtered air to avoid contamination from the laboratory. Samples are collected in 30mL Polypropylene vials, frozen down and saved for detection on systems such as ion chromatography (IC).

- Control, data acquisition and processing.

We developed a software on Labview 2010 (National Instrument) that allows a global control of the CFA system. All devices (melting unit, pumps and valves, degassing unit, analytical systems) are connected to the CPU by Ethernet connections (Picarro l-2130), serial connections (NI USB-232/4, National Instruments), analogical/digital connections via DAQ devices (USB-6211, USB-6212, National Instruments). The drivers are either provided by manufacturers (Ismatec Reglo pump), or developed to suit the purpose (Gilson pumps, Keyence laser, Mettler-Toledo mass balance, actuated valves, conductivity meters, Picarro l-2130, Fraction Collectors). One first software process consists of running the whole system in a semi-automated way by controlling independently all devices. A second process controls the devices to automatically feed the different analytical systems with predefined switches between standards. Finally, a third process consists of controlling the system to analyze the ice sample water stream. All technical signals, melting events, such as flood at the melt head, breaks in the ice, real start and end of the sample, as well as detectors signals, are recorded with an acquisition rate of 1 second to allow a better understanding of the obtained data.
To process and analyze the data, we developed a second software program, also on LabView 2010. The data processing software allows a conversion from acquisition time to local depth with high quality positioning by reporting all positions or applying a linear fit if needed between "start" and "end" of core events. It also allows a very fast and efficient data synchronization thanks to the different conductivity measurements. Melting events are displayed for the reader to easily identify and remove potential contaminated data.

- Results and discussion:

To demonstrate the performance of the NIPR-CFA system, a measurement campaign in collaboration with the Center for Ice and Climate (CIC, Copenhagen, Denmark) was performed. We melted 12 bags of the North Greenland Eemian Ice Drilling (NEEM) ice core. The samples correspond to different climate intervals (Greenland Stadial 2_1, 2_2, Greenland Stadial 5, Greenland Interstadial 5, Greenland Interstadial 7, Greenland Stadial 8). The NIPR-CFA system was set up to also determine dissolve reactive phosphorus in a continuous way as described in (18) besides the continuous detection of δO18, δD and conductivity. Samples from the inner stream was collected with a resolution up to 5cm, and used for discrete phosphate analysis by IC (18,19,20). The outer stream was also continuously collected at a 3cm depth resolution. A fraction of each of the outer samples was taken off for discrete water isotopes measurement using a Picarro L2120-i. The method of discrete water stable isotopes measurement is similar to the method used in (22). The standard deviation of discrete water isotopes measurement was 0.25‰ and 0.15‰ for deuterium and oxygen18 respectively. We focus on our results from Greenland Stadial 8. The depth and age of these samples are 1723.7 to1724.8 meters, and 35.520 to 35.636 kyr b2k (21), respectively. The ice was dated using the timescale of (21). In order to validate the NIPR CFA system, we also present the data for the same depths obtained by the high resolution Bern CFA system used during the NEEM field campaign in Northern Greenland in 2010 (2).

Sample positioning resolution

We show in the Figure 6 the accuracy and stability of positioning comparison between our system and the Bern CFA system used on the field at NEEM. The combination between low melting speed, 1 sec acquisition rate, and high accuracy laser allow us to increase significantly the local positioning resolution of an ice core. When (2,5,7,16) obtained data sets using a wire position encoder measurements with 1mm resolution positioning (16), our system provided us for the Greenland Stadial analyzed an average step of 0.27mm with a global standard deviation of 0.045 mm. Also, such precision offers a vision of the melting instability at the end of each core, when the sample becomes smaller and lighter.

Electrical conductivity σ

In Figure 7 is shown 2 synchronized conductivity signals of our system and the conductivity signal as detected in the field, 2010, for these depths. Our conductivity cell C1 is located upstream of the debubbler and C2 downstream. The comparison of these 2 signals reflects the efficiency and the smoothing effects of our debubbling unit. C1 signal shows a good segmentation of the water stream by air bubbles, while C2 signal shows the efficiency of removing all air bubbles, with a slight smoothing of the conductivity signal. The data detected on the novel NIPR-CFA system is similar to the conductivity detected on the BERN-CFA system (2,7). Further the novel NIPR-CFA system shows more detailed variations due to the lower melt rate as well as the optimizations on minimizing all volumes in the NIPR CFA system. Also, our degassed signal conductivity peaks present higher intensities, which reveals a less smoothed signal. However, the depth resolution we calculated previously doesn't allow us to discern the expected 0.94cm annual thickness at this depth (21). We count 65 distinct peaks for the 116 years interval analyzed.

Water Isotopes

Add to the continuous measurements, we decided to also analyze a part of the samples collected on the outer line. Having also leftover sidepieces of the same sample cores, we prepared samples with 3cm resolution and analyzed them following the discrete method described previously. The result is presented in Figure 8. Because of the slow response of the continuous instrument, we cut the first and last 2cm of the data which is influenced by the blank.

The 3sets of data show a very similar evolution, reflecting the efficiency of our continuous measurements, of the sample collection, as well as the smoothing effect occurring in the 1/8"OD outer line. However we notice few significant difference between discrete sidepieces samples and the 2 other data sets. The first samples of each core, and especially 1724.4 meter deep, are presenting difference clearly out of the limit. However, regarding to the similar evolution of the whole data sets, these differences are most likely reflecting a fractionation of the sidepieces samples.

A deeper investigation of our measurement quality has been done through the deuterium excess (Figure 8, bottom). Due to the high sensitivity of this parameter, the differences are more important and except a clear difference for depths between 1724.43 and 1724.48 meters, the resemblance of their evolution points on the coherence of our 3 isotopic data sets.

- Conclusions, Perspectives

In this study a CFA system was set up and tested on glacial ice from Greenland. The new CFA system differs from existing systems by the use of a laser to position the sample and a different approach to measure and regulate the mixing volume at the debubbler. The comparison to previous detections performed by the Bern CFA system (5,6) shows good characteristics in terms of the quality and a higher sample resolution. We plan to add to the bubble free water stream the continuous measurements of chemical impurities by ICP-MS (11), the dust size distribution by Abakus (Markus Klotz GmbH) (5), and black carbon (soot) in individual aerosol particles by Single Particle Soot Photometer (Droplet Measurement Technologies).

Also, in order to continuously measure the methane gas content trapped in the ice samples following the method used by (12, 13), we plan to change the melt head as well as the debubbling unit.

Reference

(1) North Greenland Ice Core Project members. High-resolution record of Northern Hemisphere climate extending into the last interglacial period. *Nature* **2004**, 431, 147-151.

(2) North Greenland Eemian Ice Drilling community members. Eemian interglacial reconstructed from a Greenland folded ice core. *Nature* **2013**, 493, .489–494.

(3) EPICA community members. Eight glacial cycles from an Antarctic ice core. *Nature* **2004**, *429* (6992), 623–628.

(4) EPICA community members. One-to-one coupling of glacial climate variability in Greenland and Antarctica. *Nature* **2006**,*444* (7116), 195–198.

(5) Bigler at al, "Optimization of High-Resolution Continuous Flow Analysis For Transient Climate Signals in Ice Cores". Environ. Sci. Technol. 2011, **45**, 4483-4489.

(6) Rothlisberger, R.; Bigler, M.; Hutterli, M.; Sommer, S.; Stauffer,B.; Junghans, H. G.; Wagenbach, D. Technique for continuous high-resolution analysis of trace substances in firn and ice cores. *Environ. Sci. Technol.* **2000**, *34* (2), 338–342.

(7) Kaufmann et al, "An Improved Continuous Flow Analysis System for High Resolution Field Measurements on Ice Cores". *Environ. Sci. Technol.* **2008**, 42, 8044-8050.

(8) Gkinis, V., T. J. Popp, T. Blunier, M. Bigler, S. Schuepbach, E. Kettner, and S. J.Johnsen (2011), Water isotopic ratios from a continuously melted ice core sample, *Atmospheric Measurement Techniques*, *4*(11), 2531-2542, doi:10.5194/amt-4-2531-2011.

(9) Gkinis, V., T. J. Popp, S. J. Johnsen and T, Blunier, 2010: A continuous stream flash evaporator for the calibration of an IR cavity ring down spectrometer for the isotopic analysis of water. *Isotopes in Environmental and Health Studies*, **46**(4), 463-475.

(10) Osterberg E., Handley M.J., Sneed S.B., Mayewski P.A. and Kreutz K.J.: Continuous Ice Core Melter System with Discrete Sampling for Major Ion, Trace Element, and Stable Isotope Analyses. *Environ. Sci. Technol.* 2006, **40**, 3355-3361

(11) McConnell et al, "Continuous ice-core chemical analyses using inductively coupled plasma mass spectrometry". *Environ. Sci. Technol.* 2002, **36**, 7-11

(12) Stowasser, C., Buizert, C., Gkinis, V., Chappellaz, J., Schüpbach, S., Bigler, M., Faïn, X., Sperlich, P., Baumgartner, M., Schilt, A., and Blunier, T.: Continuous measurements of methane mixing ratios from ice cores, *Atmos. Meas. Tech.*, 5, 999-1013.

(13) Rhodes et al, "Continuous methane measurements from a late Holocene Greenland ice core : Atmospheric and in-situ signals" *Earth and Planetary Science Letters*. 2013, **368**, 9–19
(14) Rothlisberger, R.; Bigler, M.; Hutterli, M.; Sommer, S.; Stauffer,B.; Junghans, H. G.; Wagenbach, D. Technique for continuous high-resolution analysis of trace substances in firn and ice cores. *Environ. Sci. Technol.* **2000**, *34*, 338-342.
(15) Sigg, A.; Fuhrer, K.; Anklin, M.; Steffelbach, T.; Zurmuhle, D. A continuous analysis technique for trace species in ice cores. *Environ. Sci. Technol.* **1994**, *28*, 204-209.
(16) Breton et al, "Quantifying Signal Dispersion in a Hybrid Ice Core Melting System". *Environ. Sci. Technol.* 2012, **46**, 11922−11928
(17) O. J. Maselli, D. Fritzsche, L. Layman, J. R. McConnell, H. Meyer,2013: Comparison of water isotope-ratio determinations using two cavity ring-down instruments and classical mass spectrometry in continuous ice-core analysis. *Isotopes in Environmental and Health Studies*, DOI:10.1080/10256016.2013.781598
(18) H. A. Kjær, A. Svensson, P. Vallelonga, E. Kettner, S. Schupbach, M. Bigler, J. P. Steffensen, and M. E. Hansson, First continuous phosphate record from Greenland ice cores, *Clim. Past Discuss.*, 7, 3959–3989, 2011
(19) Udisti, R.; Becagli, S.; Castellano, E.; Mulvaney, R.; Schwander,J.; Torcini, S.; Wolff, E. W. Holocene electrical and chemical measurements from the EPICA-Dome C ice core. *Ann. Glaciol.***2000**, *30* (1), 20-26.
(20) Huber, T. M.; Schwikowski, M.; Gaggeler, H. W. Continuous melting and ion chromatographic analyses of ice cores. *J.Chromatogr. A.* **2001**, *920*, 193-200.
(21) Rasmussen et al, "A first chronology for the NEEM ice core". *Climate of the Past.* 2013, **9**, 2967--3013
(22) Pol, K., Masson-Delmotte, V., Johnsen, S., Bigler, M., Cattani, O.,Durand, G., Falourd, S., Jouzel, J., Minster, B., Parrenin, F., Ritz,C., Steen-Larsen, H. C., and Stenni, B.: New MIS 19 EPICADome C high resolution deuterium data: hints for a problematic_preservation of climate variability in the "oldest ice", *EarthPlanet. Sc. Lett.*, doi:10.1016/j.epsl.2010.07.030, 2010.)

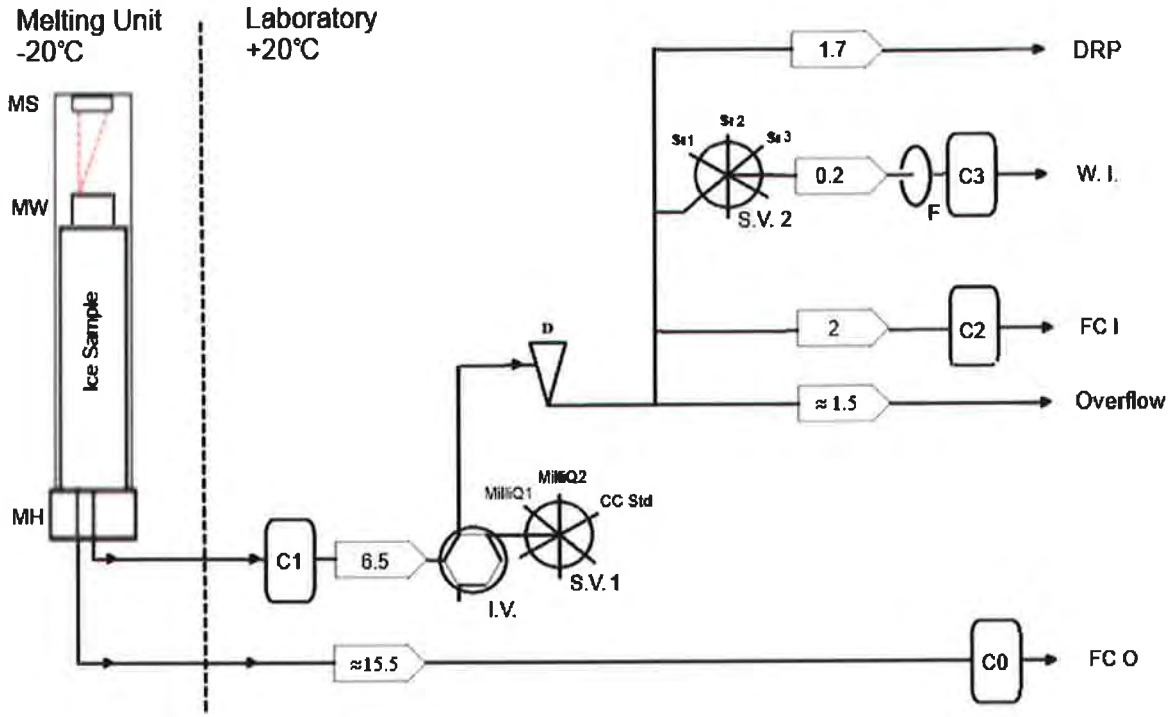

Figure 1: the setup of the NIPR CFA system. An ice core is melted on a melthead (MH) inside a freezer. The melt speed is determined by a laser positioning Melting Sensor (MS) and to stabilize flow a Melting Weight (MW) is put on top of the ice. In the laboratory, conductivity (σ) detectors (Ci), injection (IV) and a selection (SV1) valves for MilliQ or conductivity standard, Debubbler (D), water isotopes selection valve (SV2) for samples or intern laboratory isotopes standards, stainless steel frit Filter (F). Different analytical systems (DRP for dissolved reactive phosphorus, WI for Water Isotopes) and inner and outer channels Fraction collectors (respectively FC I and FC O). All flow rates of the peristaltic pumps (in ml/min) are given in the scheme.

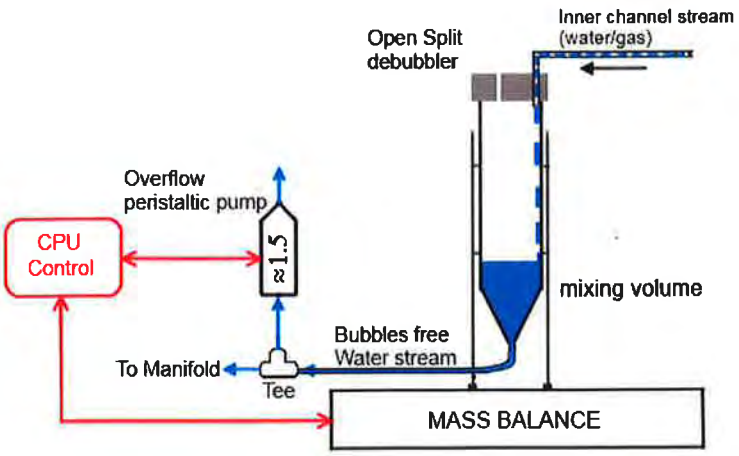

debubbler standing fixed on the mass-balance

Figure 2. Degassing unit. The scheme shows the setup of the overflow peristaltic pump rate (given in ml/min in the diagram) regulation by the CPU via the mixing volume weight. After the overflow Tee separation, the degassed water stream is separated in the manifold and sent to the different analytical systems.

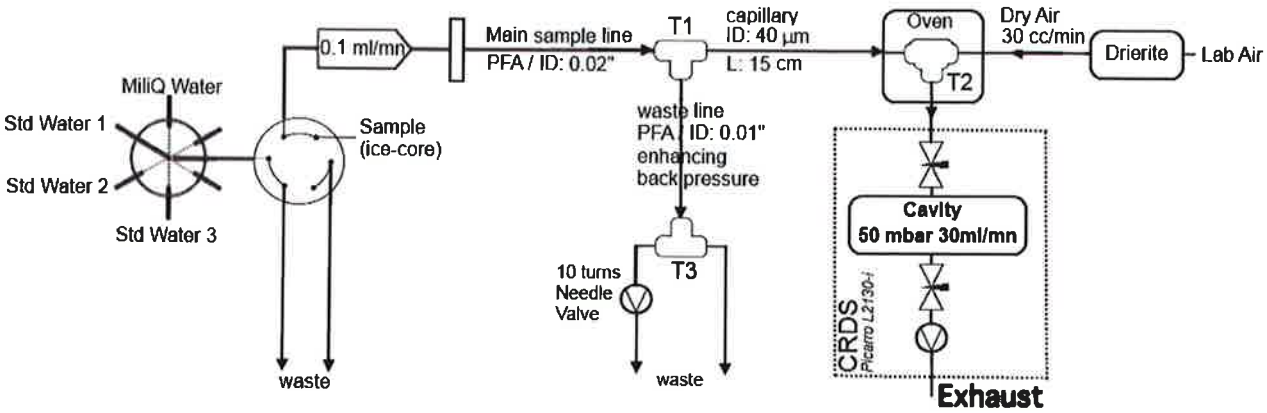

Figure 3.Bloc diagram of the continuous water isotopes system.

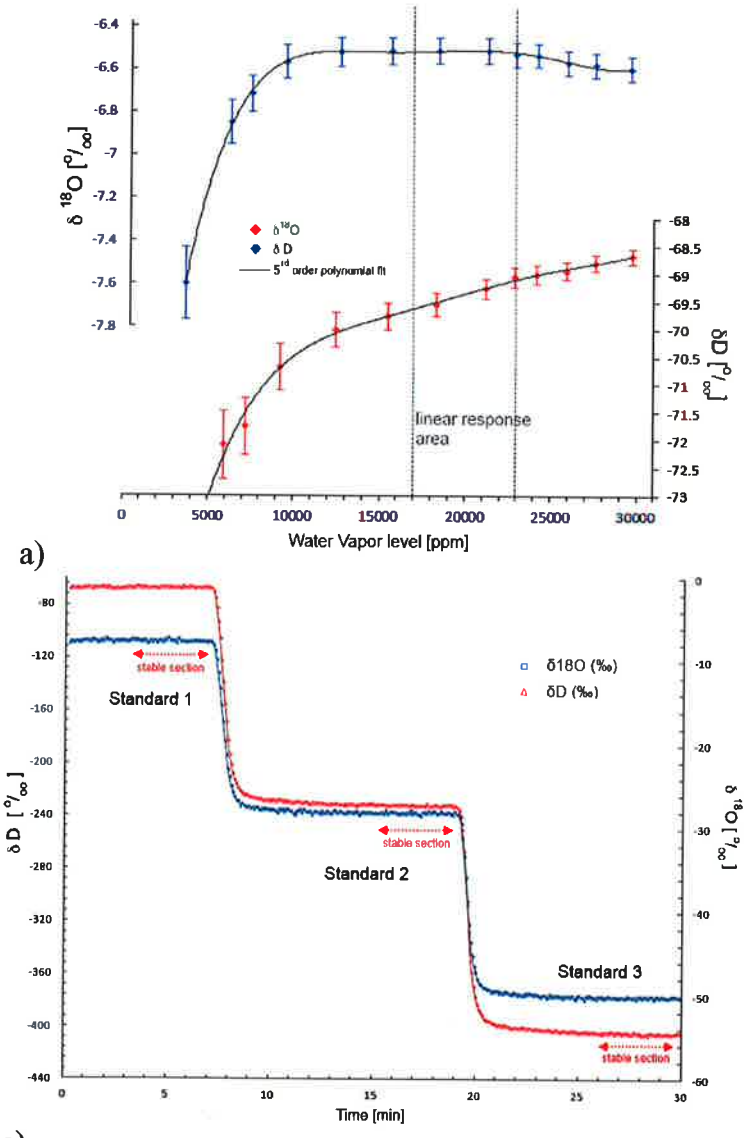

Figure 4. Water isotope system performances. In all plots, δ18O and δD are respectively the blue and red plots.

a) Response to the spectrometer to different water vapor level.
b) Memory effect performances resulting after an isotopic step.
c) VSMOW/SLAP2international isotopic scale calibration procedure.

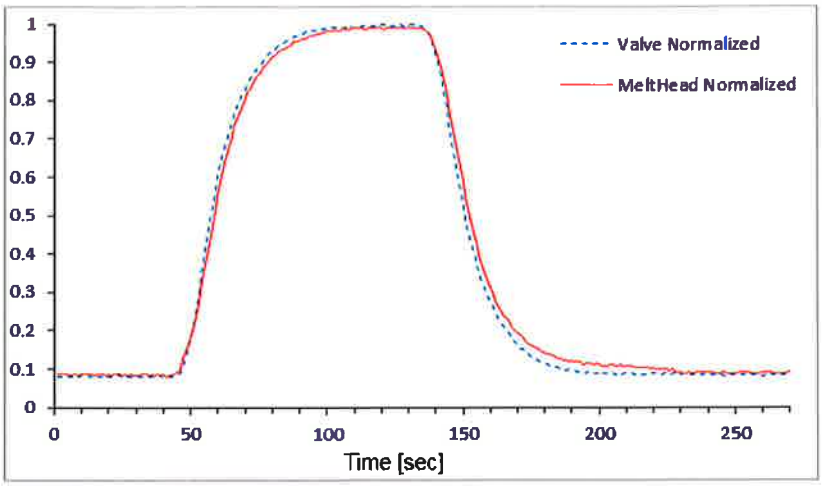

Figure 5. Response to conductivity standards. Normalized conductivity data for 90 seconds injections of standard via the injection valve (dashed blue line) or via the melt head (thick red line).

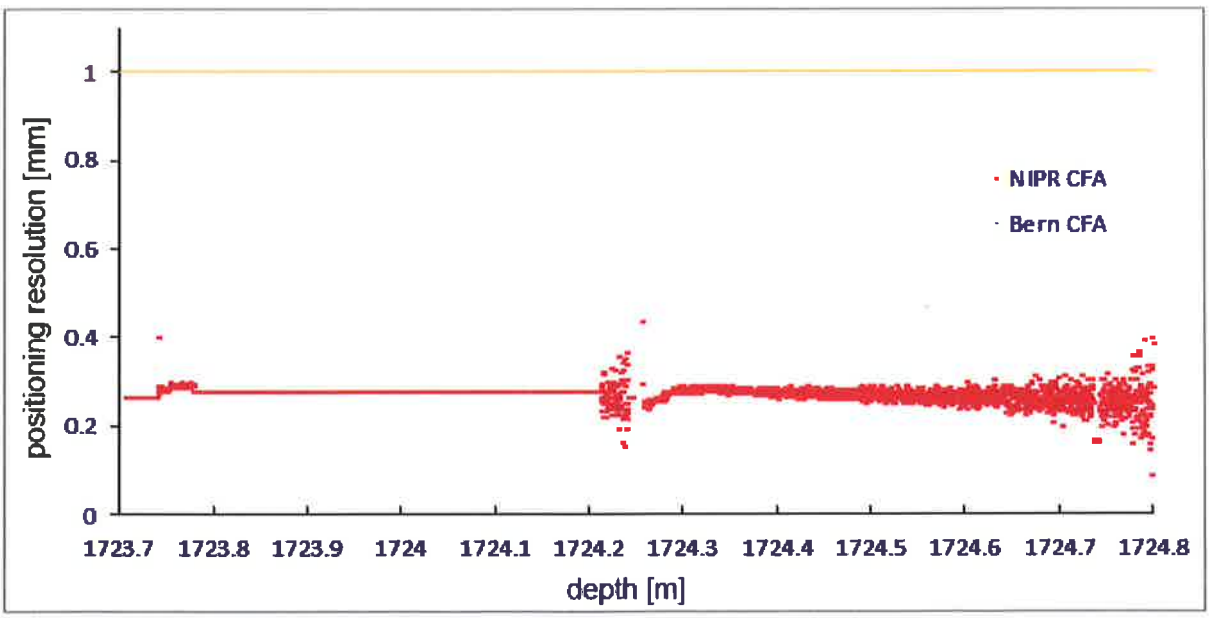

Figure 6. Comparison of the depth found for the NIPR and BERN CFA systems. Positioning resolution (distance between every acquired points) comparison between NIPR CFA system (red points) and the Bern CFA system used at NEEM (orange points) for the analyzed depths.

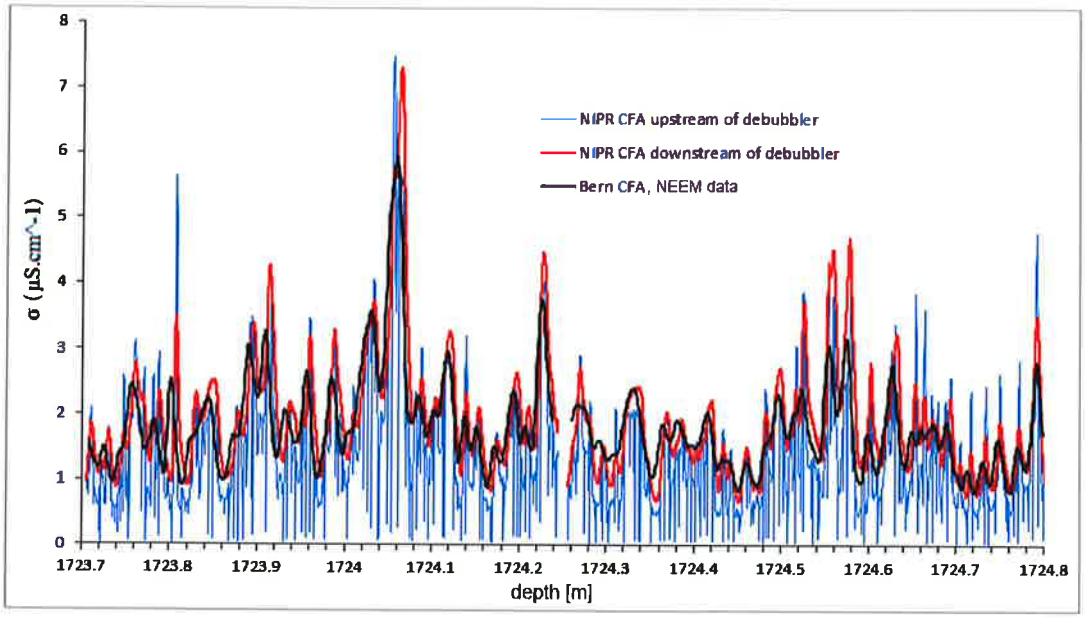

Figure 7. Comparison of the conductivity records (σ, in µS.cm^-1) upstream (blue) and downstream (red) of the debubbler, with the NEEM data obtained on the field by the Bern CFA system (black).

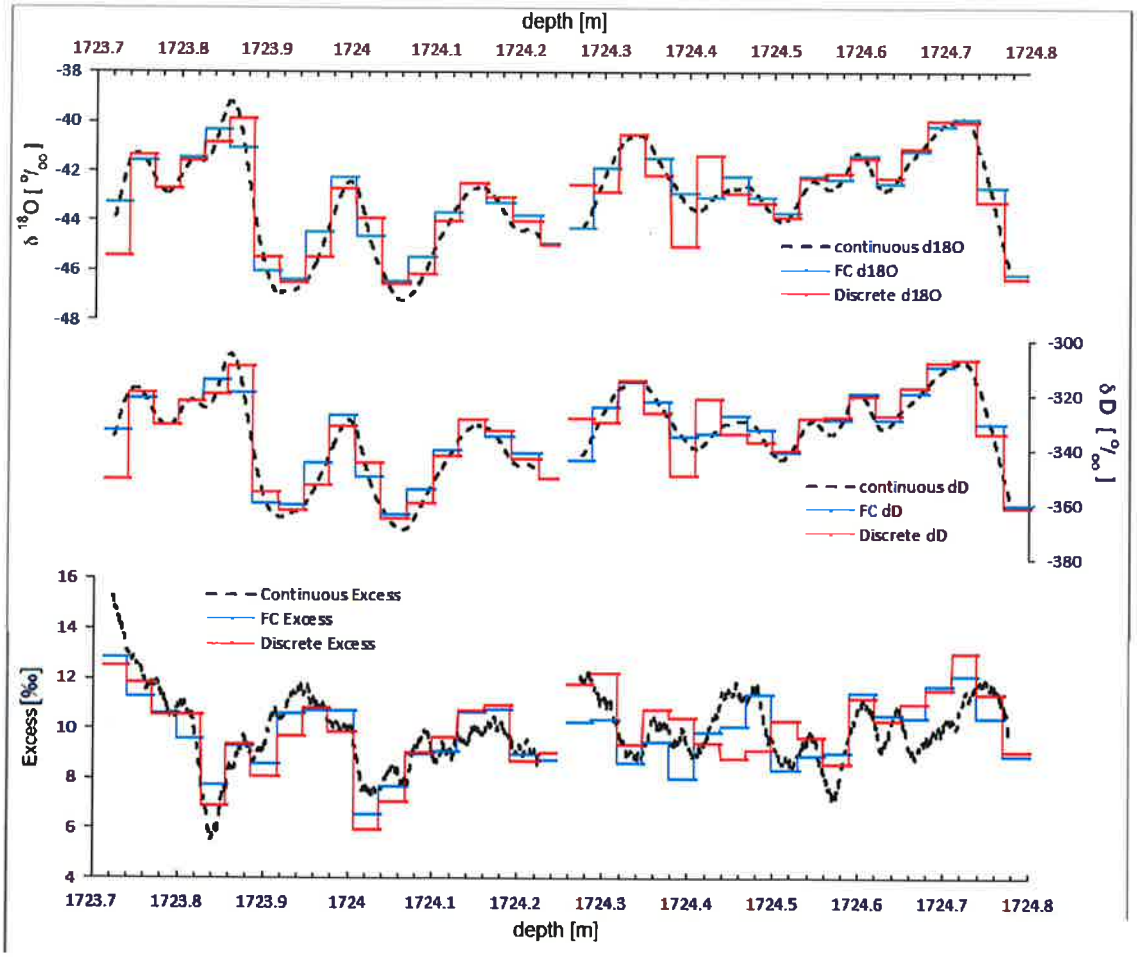

Figure 8. Comparison between 3 different isotopic results for Greenland Stadial to measure δD and δ18O. The top plot shows the oxygen 18 results, deuterium results in the middle, while the bottom plot

shows the Deuterium excess (Excess). For all plots, the continuous data correspond to the dashed black line, outer channel collected samples in blue, and discrete sidepieces samples in red.

E. ADDITIONAL RICE INFORMATION

Figure E.1 show correlations for Ca^{2+}, MWEC, indoluble dust and H^{+}. The data covers the top 130 meters and is divided into sources as explained in section 8.3.1.

A list of volcanoes identified in the RICE record is also shown.

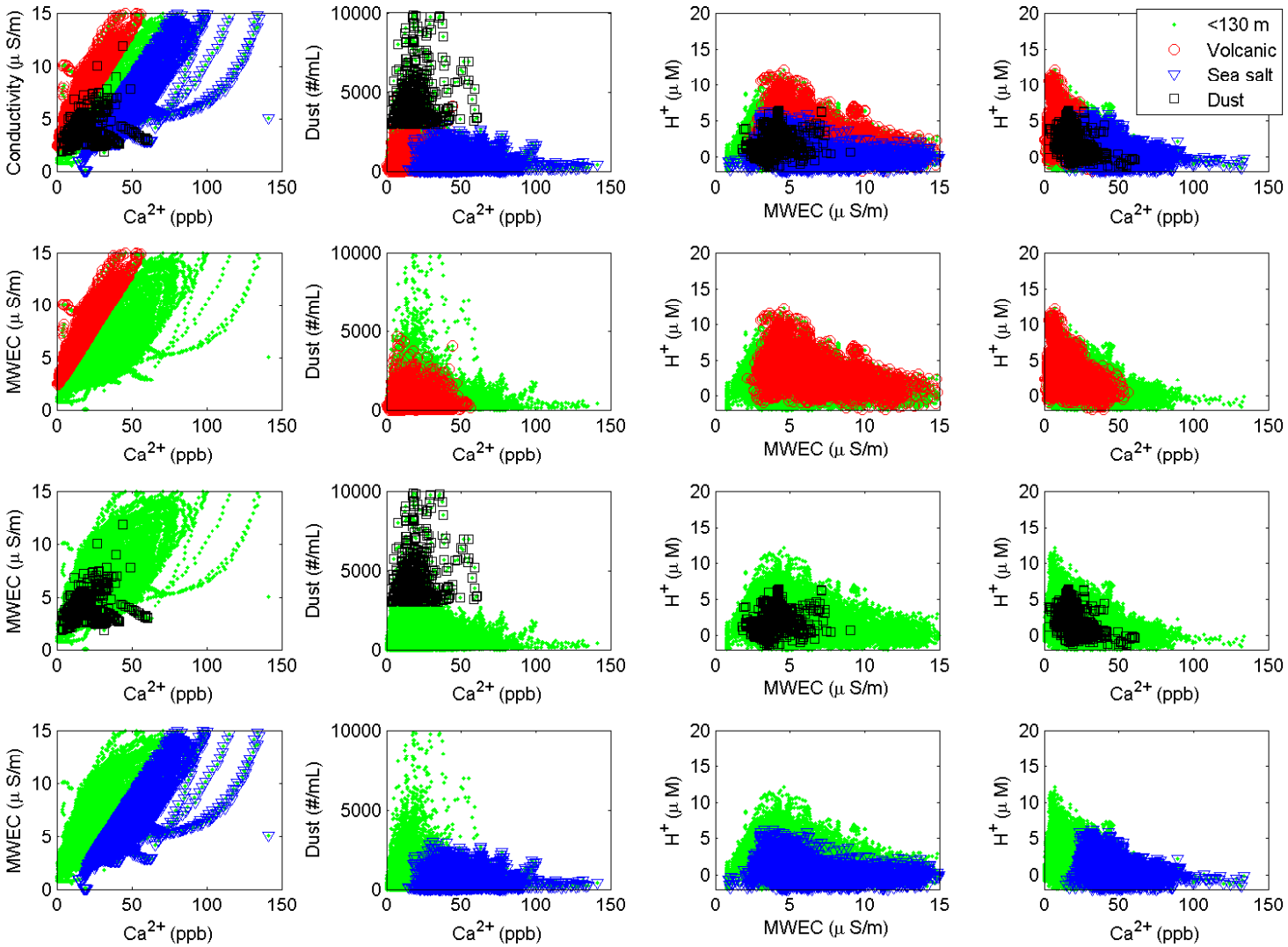

Fig. E.1: CFA determined chemistry in the RICE record plotted against each other; 1st column) MWEC and Ca^{2+}, 2nd column) Insoluble dust and Ca^{2+} 3rd colum) MWEC and H^+, 4th column) H^+ and Ca^{2+}. Colours indicate sources; all sources (green, 1st row), volcanic origin (red, 2nd row), dust sources (black, 3rd row) and sea salt derived (blue, bottom row).

Depth (metre)	H+ (uM)	Approx age from transfer of WAIS timescale
40.60	4	1892
42.30	7	1882
43.39	7	
43.72	8	1872
47.89	11	1862
53.07	6	1842
56.53	7	1822
57 -61	MISSING DATA	
64.42	8	1792
65.98	7	
66.15	7	1782
69.60	7	1762
75.16	11	1742
78-83	MISSING DATA	1702-1722
83.39	8	1702
83.75	10	1702
84.04	6	
88.86	10	1682
92.47	5	
93.07	5	1652
94.25	4	
95.40	4	
95.49	3	1642
97.11	6	1632
98.44	5	
98.76	4	1622
100.02	5	
102.78	5	1612
103.78	5	1602
104.60	5	
105-108	MISSING DATA	
108.20	6	1582
108.75	5	
110.2-115.32	missing data	
113.48	ECM!	
119.04	7	1522
119.30	8	
119.60	7	1512
120.17	6	
122.70	6	1502
125.20	7	
131.05	12	1452
131.20	9	1452
134.10	9	1442
134.40	7	
134.90	8	1432
136.10	7	1422
137.09	8	

Depth (metre)	H+ (uM)	Approx age from transfer of WAIS timescale
137.49	7	
138.60	10	1412
138.87	9	
139.07	7	
139.90	7	
140.17	8	1402
140.90	7	
141.05	7	
141.52	7	1392
143.88	5	1382
144.03	ECM!	
145.06	5	
145.14	6	1372
145.90	7	1372
146.13	5	
155.06	9	1312
158.16	6	1292
160.77	7	1282
160.94	8	1272
161.43	8	
162.17	20	
162.38	6	1262
163.89	9	1262
164.05	20	1252
164.19	7	
168.31	7	1222
169.60	7	
169.75	5	
172.05	5	1202
172.95	7	1192
173.90	6	
175.56	5	1172
177.76	5	1162
180.03	8	1132
180.80	5	
182.15	5	1132
182.68	4	1132
183.33	4	1122
183.96	5	1112
185.07	ECM!	1102
184-187	MISSING DATA	
187.43	5	1082
188.25	4	
189.41	4	1072
189.74	3	
190.14	4	1062
190.91	3	
191.28	4	1052

Depth (metre)	H+ (uM)	Approx age from transfer of WAIS timescale
193.44	4	1042
194.81	6	1032
195.24	6	
195.65	5	1022
195.83	5	
196.06	7	1012
196.44	7	
197.27	6	
197.70	6	
199.47	4	992
199.88	4	
202.20	4	972
203.34	5	962
203.45	7	962
203.63	4	
203.85	4	
204.36	5	952
204.49	7	
204.56	5	
204.86	4	
205.39	4	942
205.55	4	
205.92	4	
206.23	7	
206.83	6	932
207.10	6	
208.10	5	922
208.47	3	
308.83	5	
209.74	3	912
209.93	4	
210.94	5	902
211.39	7	892
211.83	0	
212.83	10	882
213.49	10	872
214.24	4	872
215.71	5	862
216.45	5	852
216.91	5	
217.23	4	
217.60	3	842
217.92	3	
218.18	4	
218.28	4	
218.56	4	832
218.77	3	
219.63	3	

Depth (metre)	H+ (uM)	Approx age from transfer of WAIS timescale
219.98	5	822
220.89	4	812
222.20	4	802
222.45	4	
222.50	5	
222.59	3	
222.83	3	
222.94	7	
223.17	6	
223.39	4	792
223.70	5	
223.80	6	
224.07	4	
224.24	4	
224.34	3	782
224.74	5	
225.08	5	
225.18	5	
225.61	5	772
226.20	5	
226.49	4	
226.62	5	762
227.3-228.01	MISSING DATA	
227.74	ECM!	752
228.02	6	
228.11	4	
228.70	5	
228.89	6	742
229.08	6	
229.35	7	
229.53	5	
229.77	5	
230.08	5	732
230.49	5	
230.55	6	
230.71	5	
230.94	4	
231.12	5	722
231.97	5	
232.08	5	
232.19	5	
232.48	7	712
232.66	9	712
232.93	4	
233.47	4	702
233.83	6	
234.07	6	
234.34	4	

Depth (metre)	H+ (uM)	Approx age from transfer of WAIS timescale
234.80	4	692
235.20	5	
235.35	7	692
235.54	6	
235.78	7	682
235.90	5	
236.93	7	672
237.25	9	
237.57	5	
237.69	8	
237.88	6	662
238.57	4	
239.32	6	652
239.86	7	
240.33	ECM!	642
241.33	4	632
241.50	3	
241.96	5	
242.14	4	622
242.64	5	
243.41	3	612
243.77	4	
243.84	5	
244.14	4	602
244.38	5	
244.69	4	
244.78	5	
245.64	4	592
246.15	4	
246.54	6	582
246.89	5	
247.47	6	572
248.12	5	
248.34	4	562
248.77	8	562
249.07	5	552
250.05	4	
250.82	3	542
250.93	3	
251.71	3	532
251.82	3	
252.09	5	
252.29	4	
252.37	3	
252.66	ECM	522
253.23	3	
254.80	3	502
255.61	4	492

Depth (metre)	H+ (uM)	Approx age from transfer of WAIS timescale
256.25	6	482
258.57	5	462
258.65	5	
259.08	6	
259.72	4	452
260.60	6	442
260.80	5	
261.53	4	432
261.84	5	0
262.69	4	422
263.68	4	412
264.20	4	402
265.15	4	392
265.79	4	382
266.98	7	372
267.42	8	362
267.62	5	362
269.36	4	342
269.46	4	
270.50	4	332
271.08	6	322
272.25	6	312
272.75	6	302
273.13	6	302
273.73	5	292
273.97	6	
274.11	6	282
274.97	6	272
275.06	6	
275.70	5	262
276.06	24	262
276.20	5	
277.48	3	
278.80	4	
278.94	4	
279.30	8	222
280.81	7	202
281.07	6	
281.44	4	192
282.44	5	182
282.66	5	172
283.66	4	162
285.41	3	142
285.83	5	132
286.18	5	
286.39	5	122
287.49	4	102
288.08	3	92

Depth (metre)	H+ (uM)	Approx age from transfer of WAIS timescale
289.18	4	82
290.25-291	MISSING DATA	62-52
290.49-291	ECM	
291.13	5	62
292.80	4	32
293.90	6	22
293.98-300.01	MISSING DATA	
300.87	4	-78
302.76	6	-108
303.58	5	-118
303.77	6	-118
304.12	5	-128
304.12	0	
305.08	6	-138
305.30	5	
306.24	5	-158
306.40	5	0
306.89	7	-168
307.23	4	-168
308.72	4	-188
309.12	5	-198
310.39	3	-218
311.58	4	-228
313.39	4	-258
314.02	5	-268
314.22	4	
314.39	4	-278
316.97	cond	-308
317.30	4	-318
317.51	3	
318.91	4	-328
319.48	3	-348
319.53-319.89	MISSING DATA	348-358
320.20	3	-358
320.40	4	
320.87	5	-368
320.94	4	
322.14	4	-388
322.22	4	
322.80	4	-398
323.15	4	-408
323.82	4	-418
325.26	7	-438
326.21	4	-448
327-331	MISSING DATA	468-528
331.15	6	-528
331.73	5	-538
332.13	5	-548

Depth (metre)	H+ (uM)	Approx age from transfer of WAIS timescale
332.76	4	-558
332.93	4	
333.33	4	-568
334.93	6	-588
335.15	3	-598
335.85	6	-608
336.26	5	0
337.10	3	-628
337.20	2	
337.68	3	-638
338.26	3	-648
339.36	4	-668
339.93	5	-678
340.34	6	-688
340.63	7	
341.13	10	-698
341.21	8	
341.54	7	-708
341.79	11	-718
342.54	11	
342.77	10	-728
342.94	9	
343.26-343.85	MISSING DATA	738-748
344.54	6	-748
350.11	4	-868
350.80	4	-868
350.95	4	
352.04	4	-888
352.54	5	0
354.94	2	-948
355.60	4	-958
356.83	6	-978
357.33	6	-988
358.16	4	-1008
359.16	5	1028
359.36	5	
362.55 Missing data	MISSING DATA	1038-1198
363.98-368.03	MISSING DATA	
368.06	6	-1198
368.56	3	-1208
369.11	2	-1218
370.00	4	-1238
370.31	4	
370.45	3	-1248
370.64	3	
372.55	5	-1278
373.36	4	-1298
373.67	5	

Depth (metre)	H+ (uM)	Approx age from transfer of WAIS timescale
374.89	5	-1328
377.97	4	-1378
378.10	3	
379.56	4	-1408
379.79	4	
380.97	5	-1438
383.95	5	-1488
384.46	4	-1498
386-391.46	MISSING DATA	1528-1608
391.66	6	
392.75	3	
393.67	3	
394.85	5	
395.91	3	
397.50	5	
399.38	4	
403.46	3	
404.60	3	
405.68	4	
405.90	3	
406.25	6	
406.99	4	
407.95	4	
408.68	5	
408.87	6	
409.71	3	
411.48	5	
412.11	4	
412.35	6	
413.29	4	
416.28	ECM?	
416.76	4	
417.49	4	
417.82	3	
418.32	4	
419.48	4	
420.04	ECM?	
420.29-420.79	MISSING DATA	
421.38	3	
421.80	6	
422.82	3	
423.80	4	
424-428.69	MISSING DATA	
429.02	3	
431.76	5	
432.19	4	
432.53	3	
432.87	3	

Depth (metre)	H+ (uM)	Approx age from transfer of WAIS timescale
433.83	4	
435.01	6	
435.64	4	
437.06	3	
437.19	5	
437.74	6	
438.11	3	
438.22	4	
439.40	6	
441.57	3	
441.84	4	
442.42	4	
443.24	4	
443.38	4	
445.58	4	
447.20	5	
447.98-452.02	MISSING DATA	
454.68-460.01	MISSING DATA	
460.74	13	
464.27	3	
465.37	4	
468.62-470	POOR DATA	
470.22	3	
470.90	2	
471.30	3	
471.67	3	
471.83	4	
473.10	2	
474.39	3	
477.33-477.85	MISSING DATA	
480.43	4	
480.80	4	
481.49	6	
482.11	4	
483.65	4	
483.83	3	
487.34	5	
487.41	3	
487.66	4	
488.69	4	
489.48	4	
490.14	3	
491.24	3	
497.39	3	
499.15	3	
499.78	3	

F. SUPPLEMENTARY MATERIAL FOR THE COMPUTATIONAL PYRUVIC ACID STUDY

F.0.1 Energies-supplementary

Table F.1 show the energies for structures Tc, Tt, Ct and Cc as determined using CAM-B3LYP and varying the basis set. For all six basis sets the Tc conformation was found to have the lowest energy. With increasing basis set size the energy of the Tc conformation decreases. The system shows convergence at the cc-pVQZ level.

F.0.2 Geometry in vacuo-supplementary

The geometry of Tc is shown in F.2 using CAM-B3LYP and varying basis sets. Also shown are the experimentally determined results[*Reva et al.*, 2001]. Figures F.1 and F.2 show a graphical representation of the same. Figures F.4 and F.3 show the same for various DFT methods. For Tc, for bond angles and bond lengths, the relative deviation from the experimentally determined values grows with basis set size. The Tc structure has converged at the aug-cc-pVTZ level; the methyl related bond lengths using aug-cc-pVTZ agree with the aug-cc-pVQZ to within $\leq$ 0.5% ($C_{(6)}O_{(9)}H_{(10)}$ angle) and are generally below 0.2%. The bond lengths found using aug-cc-pVQZ are short compared to the experimental values. The double bonds are least well represented (-2.19 and -1.81 %). The $C_{(1)}H_{(4)}$ (+0.93%) and $C_{(5)}C_{(6)}$(+1.38%) bonds for Tc are too long compared to experiment, and $C_{(1)}C_{(5)}$ is found to match the experimental values exactly. The angles of Tc converge at aug-cc-pVTZ. The most striking change relative to the experimental values is the change in the angles involving $C_{(6)}$ in the carboxyl group. The bond angles C-C-O_9 and C-C-C are too narrow, while the C-C=O_8 and C-O-H angles are exaggerated for Tc as compared to experiment. In the methyl group the in plane bond angle C-C-H has a slightly lower angle in experiment, while the bond angle involving the outer plane H is larger. For Tc the dihedral angles are converged at aug-cc-pVDZ.

For the remaining structures, the basis structural and energetic changes from cc-pVTZ to aug-cc-PVQZ are small. For Tt the largest change from cc-pVTZ to aug-cc-pVQZ is in the angle C-O-H in hydroxyl (0.4%), while the other changes are below 0.1%, which also holds for Ct. Conformer Cc shows a large change in the C-C-C angle (0.6%) with increasing basis set, but very small changes for all other angles. The keto bonds in the Tc and Tt conformations are long relative to experiment. This is especially true for the $C_{(5)}O_{(7)}$ bond, followed by a shortening in $C_{(1)}C_{(5)}$ for the Tc structure. The $C_{(6)}O_{(8)}$ bond length increases from Cc $\Rightarrow$ Ct $\Rightarrow$ Tc $\Rightarrow$ Tt. This can be explained by considering the parallel double bonds in the cis structures versus the opposite C=O bonds in the trans structures. For Tc the $C_{(1)}C_{(5)}$ bond is too short. For the Tc the planar $H_{(4)}$ is bent farther away from the C-C than for

the other conformers.

All the DFT methods show similar bond lengths, except for PBEPBE. Whereas the other DFT methods are all short compared to experiment, PBEPBE fits the O-H bond and the double bonds better. In the methyl group the out of plane H's are most well represented by PBEPBE, while for the in plane H the others do a better job. The C-C and the C-O bond lengths are equally well represented by CAM-B3LYP, B3PW1 and MPW1PW91.

All of the employed methods produced similar values for the angles therefore we can trust the structures. The order of how the C-C-O angles in the carboxyl are presented follow the order found for the energy difference between compounds closest to the high level CCSD(T) method (see section on energy).

F.0.3 Structures in solution-supplementary

In Table F.3 is shown the geometry for the Tc, Tt and Ct compounds in water solution using CAM-B3LYP/cc-pVQZ when using the polarizable continuum model (PCM) with self consistent reaction field (SCRF) keywords for water.

F.0.4 Vibrational frequencies-supplementary

The position of the vibrational frequencies for Tc do not change more than 6 cm^{-1} from cc-pVTZ to aug-cc-pVQZ suggesting that the calculations have converged. The intensity generally increases with basis set for all compounds, however the Tt $\nu(C_{(6)} = O)$ decreases from pVDZ to pVTZ and increases again at pVQZ, while $\nu(C_{(5)} = O)$ increases. This suggests that the basis set has higher influence on the carboxyl group than on the ketone as is also concluded from structural changes.

Comparing CAM-B3LYP to other DFT models (see Figure F.5) the picture is much less consistent than when looking at the geometry of the molecule. The variance between the models is generally about 6%. The tendency for CAM-B3LYP to perform less well at predicting vibrational frequencies than B3LYP, as found by *Biczysko et al.* [2010], is not observed in the present work. B3LYP/aug-cc-pVQZ stands out from the remaining DFT calculations using an augmented quadruple basis set by showing similar frequencies for Tc and Tt as well as between Tc and Ct's C-C asymmetric stretch and $\tau(OH)$. In Table F.4 and F.5 the results from *Reva et al.* [2001] are shown together with selected scaled vibrational frequencies obtained in this study. The vibrations causing the frequencies as determined by *Reva et al.* [2001] are shown in the right hand column. The second column from the right indicates that the vibrations found in this study are the ones ones responsible for the frequencies. The vibrational frequencies shown in Table F.4 and F.5 were selected based on differences in the analysis to the study of *Reva et al.* [2001]. All vibrational frequencies are given for compounds Tc, Tt and Ct in Tables F.6, F.7 and F.8 respectively.

It is clear that in general the frequencies obtained using CAM-B3LYP are larger than the ones obtained by *Reva et al.* [2001] using MP2, by 1% to 6%, except for the torsions which are generally lower. It is also evident that the experimentally determined frequencies are better replicated by MP2 than by CAM-B3LYP. Since the difference was so pronounced between the two models the results were tested using

a B3LYP/aug-cc-pVDZ computation to see if we could reproduce the data of *Reva et al.* [2001]. As seen in Table F.4 (columns 3 and 4), all frequencies are nicely reproduced except $\nu(C_{(5)}{=}O)$. Further comparisons between the experimental frequencies and intensities and the CAM-B3LYP/aug-cc-pVQZ calculation were performed by comparing the highest intensities, and by comparing frequencies directly and using the difference to neighbouring frequencies.

The frequencies obtained in this study using DFT/CAM-B3LYP/aug-cc-pVQZ in vacuum yield similar conclusions to the study by *Reva et al.* [2001], however, some differences remain. In the study by *Reva et al.* [2001] the observed frequencies of 124 cm^{-1} and 134 cm^{-1} are assigned to $\tau(CH_3)$ and $\tau(C-C)$ respectively (MP2: 94 cm^{-1} and 135 cm^{-1}, B3LYP 91 cm^{-1} and 127 cm^{-1}). In contrast our study suggest that $\tau(CH_3)$ occurs at 124 cm^{-1} and $\tau(C-C)$ at 115 cm^{-1}. Further Tc likely gives rise to the major part of the absorption at 258 cm^{-1}, but a minor contribution from Ct $\gamma(C-C-C)$ is not unlikely. Similarly, the 388 cm^{-1} peak is mainly due to Tc $\delta(C-C-O)$, but both Ct and Tt have a vibration at 388 cm^{-1}, however with negligible intensity.

For the absorption at 603.8 cm^{-1}, which *Reva et al.* [2001] suggest is due to Tc $\delta(C_{(5)}=O)$, we find that it is equally likely to arise from the Ct configuration, which has a dominant intensity here (87), and that the second highest intensity in that region, 602.2 cm^{-1}, is due to the Tc configuration. The calculated spacing between the experimental bands at 664.2 cm^{-1} and 762.2cm^{-1}, do not agree with the spacing between the bands for $\tau(OH)$ (710 cm^{-1}) and the next band at 743 cm^{-1}. Instead, the computationally derived 778 cm^{-1} $\nu(C-C)s$ fit the spacing. We suggest that the very weak peak at 967.1 cm^{-1} is Ct $\gamma(CH_3)s$, and that the peak at 1116.6 cm^{-1} is Ct $\nu(CO)$. This differs from the study by *Reva et al.* [2001] who assigned the 1116.6 cm^{-1} peak to Tt, even though their computational calculations did not clearly suggest this. The 967.1 cm^{-1} was not assigned in their study. The 1179.6 cm^{-1} and 1201.2 cm^{-1} peaks could be Ct's $\nu(C-C)as$ and the Tt's $\delta(COH)$, though for Ct the computed intensity seems too strong, which could suggest that only very little of the Ct compound occurs under the experimental conditions. For Tt the computed intensities are a little too low to explain the strong observed intensity. The experimentally determined peak at 1290 cm^{-1} could be due to Ct's $\delta(COH)$, and the 1364.1 cm^{-1} peak the $\delta(CH_3)s$. The vibration at 1423.7 cm^{-1} is found to be due to $\delta(CH_3)as$ for Tc as suggested by *Reva et al.* [2001]. However it is probably strengthened by the corresponding Tt vibration.

One of the stronger arguments in *Reva et al.* [2001] for assigning Tt as the second most likely conformation is that the split band arising from C=O stretching is found experimentally to be 1763.7/1761.4 cm^{-1} and 1750.8/1749.4 cm^{-1}, and thus has a difference of 13 cm^{-1}, which was replicated by the computed frequencies for Tt (MP2: 11 cm^{-1}, B3LYP: 26 cm^{-1}) in the study by *Reva et al.* [2001]. This is also the case for the CAM-B3LYP model for which the difference for Tt is 16 cm^{-1}. However the Ct difference does not stand out for the CAM-B3LYP (16 cm^{-1}) as it did for the MP2 (72 cm^{-1}) and B3LYP (57 cm^{-1}) models in the study by *Reva et al.* [2001], and thus the double bonds assigned to Tt are as likely to arise from Ct according to this study. It is worth noting that all the DFT methods show a split band for the C=O stretch below that for Ct relative to the *Reva et al.* [2001] study. The range of the

split was 16 to 12 cm^{-1} for Tt (CAM-B3LYP to B3PW91) and 25 to 16 cm^{-1} for Ct (PBEPBE to CAM-B3LYP). We tested whether the split determined by *Reva et al.* [2001] using B3LYP/aug-cc-pVDZ could be replicated, but in this study the C=O stretching split was found to be 20 and 23 cm^{-1} for Tt and Ct respectively.

Experimentally the $\nu(OH)$ stretch is a relatively broad peak. The difference in $\nu(OH)$ between the various conformers using CAM-B3LYP was found to be 112 cm^{-1} for the Tt to Tc conformers and 105 cm^{-1} for Ct and Tc, which fit well when assigning the experimental peak at 3432.3 cm^{-1} to Tc, 3556.1 cm^{-1} to Tt and 3554.1 cm^{-1} to Ct, giving relative differences of 124 cm^{-1} and 110 cm^{-1}. Intensities from the computational study suggest that Tc is the most dominant form (obs: 0.0206, CAM: 130.71), followed equally by Tt (obs: 0.040, CAM:97.54) and Ct (obs: 0.041, CAM:90.08). Thus not only the OH strech but also the overtones of the conformer Tt and Ct is higher than the similar for Tc. Finally the CAM-B3LYP model does not show the 3584.2 cm^{-1} peak clearly as arising from the Tc conformer's overtone of $\nu(C = O)$, as suggested by *Reva et al.* [2001].

Peak positions determined using the CAM-B3LYP model are generally off by 50 cm^{-1}. Despite this deviation, it does generate similar conclusions as those found in previous studies: The most stable conformer is Tc as found using the calculated energies. But whether Tt or Ct is the second most dominant form can't be determined through spectral analysis using CAM-B3LYP and comparing to experimental data. The $\nu(C = O)$ double bonds do not, as in *Reva et al.* [2001], identify Tt to be the second most likely conformer, since both Ct and Tt exhibit it in the CAM-B3LYP calculations. Further, some weak previously unassigned vibrational frequencies were found in the Ct model including 967.1, 1179.6, 1290.3 and 1364.1 cm^{-1} and the peak previously assigned to Tt at 1116.6 cm^{-1}.

Tab. F.1: Energies (atomic units) corrected for zero-point vibrational energy for the lowest energy conformer Tc and the relative instabilities in kJ mol^{-1} for Tt, Ct and Cc. Determined using the DFT/CAM-B3LYP level of theory with different basis sets and corrected for zero point energies (ZPE) for vacuo as well as for solid and liquid water using dielectric medium methods.

		cc-pVDZ	aug-cc-pVDZ	cc-pVTZ	aug-cc-pVTZ	cc-pVQZ	aug-cc-pVQZ
VACUUM	Tc / au	-342.2905070	-342.3225960	-342.4047320	-342.4111850	-342.4343780	-342.4364140
	Tt / kJ mol^{-1}	12.3083	12.1928	11.9644	12.2585	12.1692	12.2401
	Ct / kJ mol^{-1}	19.4865	19.5416	19.1294	19.3946	19.3211	19.3893
	Cc / kJ mol^{-1}	51.2393	48.1884	48.0388	47.1697	47.2065	47.0174
AQUEOUS PHASE	Tc / au	-342.298651	-342.332025	-342.413706	-342.420498	-342.443583	-342.445680
	Tt / kJ mol^{-1}	10.2920	8.8584	9.1210	8.9372	9.0081	8.9346
	Ct / kJ mol^{-1}	13.5371	10.9378	11.5496	10.2763	11.1164	10.8564
	Cc / kJ mol^{-1}	32.7741	26.4556	27.5827	25.6283	26.0896	25.5750
WATER ICE	Tc / au	-342.300715	-342.333812	-342.415596	-342.422335	-342.445424	-342.447538
	Tt / kJ mol^{-1}	11.3322	10.6895	10.6488	10.7160	10.7110	10.6923
	Ct / kJ mol^{-1}	16.4409	15.4261	15.4274	15.2620	15.3592	15.2594
	Cc / kJ mol^{-1}	40.2760	35.5288	36.0447	34.6435	34.8840	34.6671

Tab. F.2: The geometry of Tc conformers as well as experimentally determined values as in Reva (2001). Bold font indicates values that are closest to experiment. The percentage error between the experimentally determined values and the ones determined computationally using CAM-B3LYP/aug-cc-pVQZ are presented in the last column. Negative values indicate bonds or angles that were found to be too short or too narrow.

VACUUM	Exp	Tc						% deviation
		cc-pVDZ	aug-cc-pVDZ	cc-pVTZ	aug-cc-pVTZ	cc-pVQZ	aug-cc-pVQZ	(aug-cc-pVQZ)
Distances (Å)								
$C_{(1)}H_{(2)}$	1.106	**1.100**	1.098	1.090	1.089	1.089	1.089	-1.54
$C_{(1)}H_{(3)}$	1.106	**1.100**	1.098	1.090	1.089	1.089	1.089	-1.54
$C_{(1)}H_{(4)}$	1.074	1.096	1.093	1.085	**1.084**	**1.084**	**1.084**	+0.93
$C_{(1)}C_{(5)}$	1.486	1.491	1.490	**1.486**	1.487	1.487	**1.486**	0
$C_{(5)}C_{(6)}$	1.523	1.541	1.543	**1.542**	1.544	1.544	1.544	+1.38
$C_{(5)}O_{(7)}$	1.231	1.213	**1.213**	1.206	1.204	1.204	1.204	-2.19
$C_{(6)}O_{(8)}$	1.215	1.200	**1.201**	1.194	1.192	1.192	1.193	-1.81
$C_{(6)}O_{(9)}$	1.328	**1.328**	1.330	1.326	1.325	1.325	1.325	-0.23
$O_{(9)}H_{(10)}$	0.983	**0.981**	0.977	0.974	0.973	0.973	0.973	-1.02
Angles (°)								
$H_{(2)}C_{(1)}H_{(3)}$		105.9	106.1	106.0	106.1	106.1	106.1	
$H_{(2)}C_{(1)}H_{(4)}$		110.9	110.9	110.8	110.8	110.8	110.8	
$H_{(2)}C_{(1)}C_{(5)}$	109.0	**109.4**	109.4	109.5	109.5	109.5	109.5	0.46
$H_{(3)}C_{(1)}H_{(4)}$		110.9	110.9	110.8	110.8	110.8	110.8	
$H_{(3)}C_{(1)}C_{(5)}$	109.0	**109.4**	109.4	109.6	109.5	109.5	109.5	0.46
$H_{(4)}C_{(1)}C_{(5)}$	110.7	**110.3**	110.0	110.1	110.1	110.1	110.1	-0.54
$C_{(1)}C_{(5)}C_{(6)}$	118.6	117.1	**117.4**	117.1	117.1	117.1	117.1	-1.26
$C_{(1)}C_{(5)}O_{(7)}$	125.0	125.5	125.3	125.4	125.4	125.4	125.4	
$C_{(6)}C_{(5)}O_{(7)}$	117.0	117.4	**117.2**	117.5	117.5	117.5	117.5	0.43
$C_{(5)}C_{(6)}O_{(8)}$	122.0	123.0	122.9	123.0	**122.9**	**122.9**	122.9	0.74
$C_{(5)}C_{(6)}O_{(9)}$	114.5	112.0	**112.7**	112.4	112.5	112.5	112.6	-1.66
$O_{(8)}C_{(6)}O_{(9)}$		124.9	124.3	124.6	124.6	124.6	124.5	
$C_{(6)}O_{(9)}H_{(10)}$	105.2	**105.3**	106.8	106.8	107.1	107.1	107.2	1.9
Dihedral angles								
$H_{(2)}C_{(1)}C_{(5)}C_{(6)}$		-57.8	-58.0	-57.9	-58.0	-58.0	-58.0	
$H_{(2)}C_{(1)}C_{(5)}O_{(7)}$		122.2	122.0	122.1	122.0	122.0	122.0	
$H_{(3)}C_{(1)}C_{(5)}O_{(7)}$		57.8	57.8	58.0	57.9	57.9	57.9	
$H_{(3)}C_{(1)}C_{(5)}O_{(7)}$		-122.2	-122.2	-122.1	-122.1	-122.1	-122.1	
$H_{(4)}C_{(1)}C_{(5)}C_{(6)}$		180.0	-180.1	180.0	-180.0	-180.0	-180.0	
$H_{(4)}C_{(1)}C_{(6)}O_{(7)}$		0.0	-0.1	0.0	-0.1	-0.1	0.0	
$C_{(1)}C_{(5)}C_{(6)}O_{(8)}$		0.0	0.0	0.0	0.0	0.0	0.0	
$C_{(1)}C_{(5)}C_{(6)}O_{(9)}$		180.0	180.0	180.0	-180.0	-180.0	-180.0	
$O_{(7)}C_{(5)}C_{(6)}O_{(8)}$		180.0	180.0	180.0	180.0	180.0	180.0	
$O_{(7)}C_{(5)}C_{(6)}O_{(9)}$		0.0	0.0	0.0	0.0	0.0	0.0	
$C_{(5)}C_{(6)}O_{(9)}H_{(10)}$		0.0	0.0	0.0	0.0	0.0	0.0	
$O_{(8)}C_{(6)}O_{(9)}H_{(10)}$		-180.0	-180.0	-180.0	-180.0	-180.0	180.0	

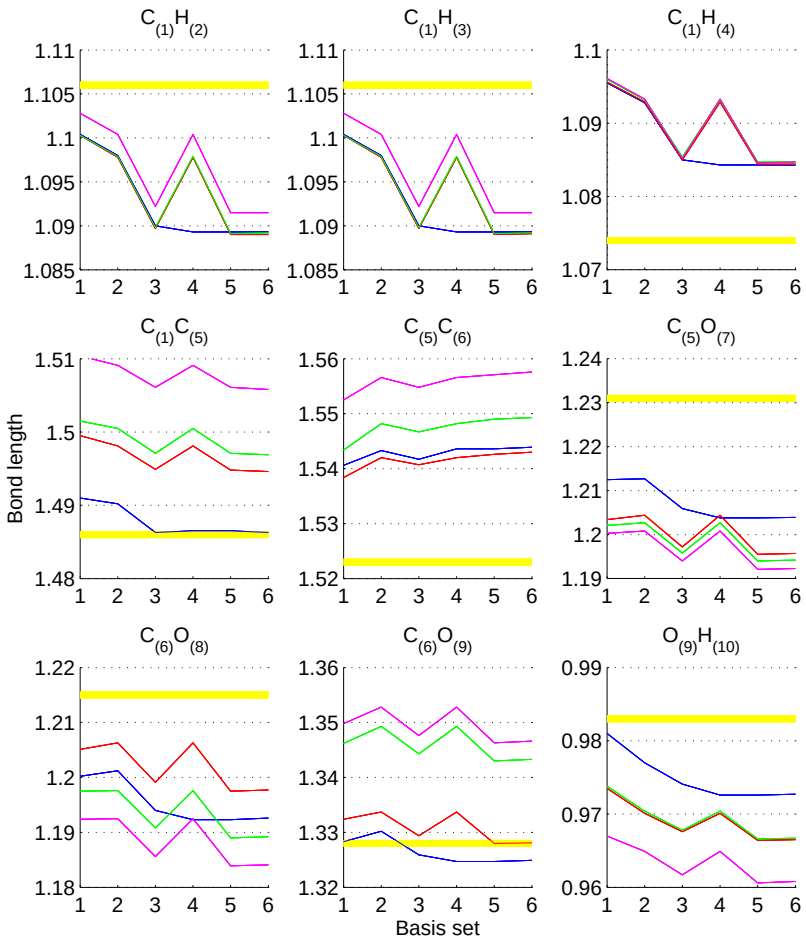

Fig. F.1: Bond lengths for Tc (blue), Tt (red), Ct (green) and Cc(purple) in the gas-phase as a function of basis set: 1 is cc-pVDZ, 2 is aug-cc-pVDZ, 3 is cc-pVTZ, 4 is aug-cc-pVTZ, 5 is cc-pVQZ and 6 is aug-cc-pVQZ. Experimental values in yellow.

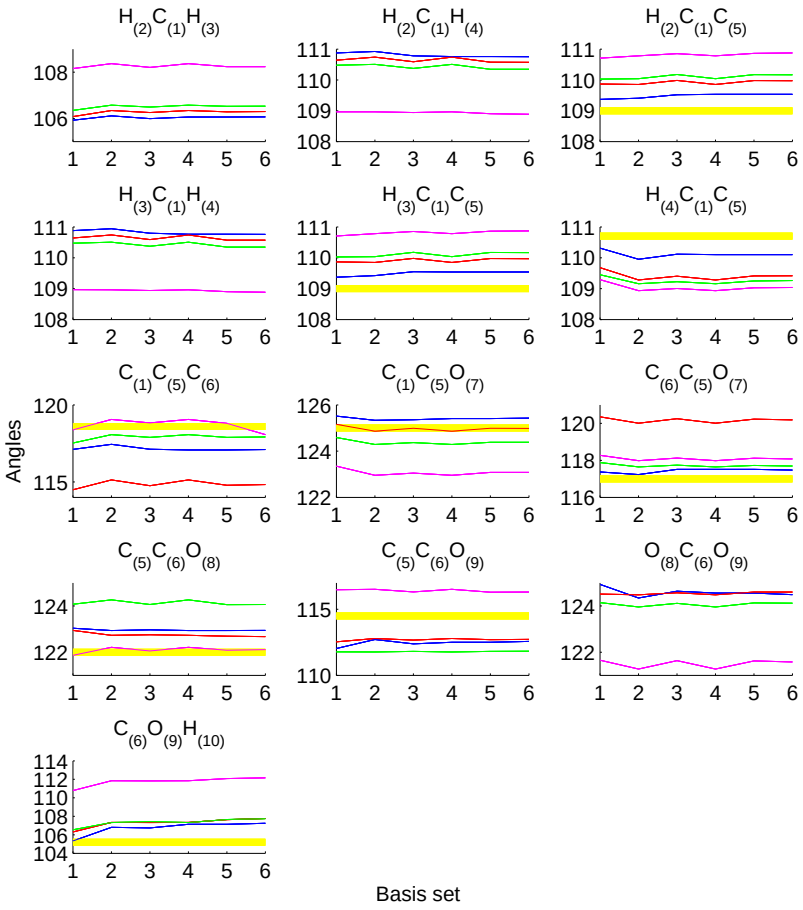

Fig. F.2: Angles for Tc (blue), Tt (red), Ct (green) and Cc(purple) in the gas-phase as a function of basis set: 1 is cc-pVDZ, 2 is aug-cc-pVDZ, 3 is cc-pVTZ, 4 is aug-cc-pVTZ, 5 is cc-pVQZ and 6 is aug-cc-pVQZ. Experimental values in yellow.

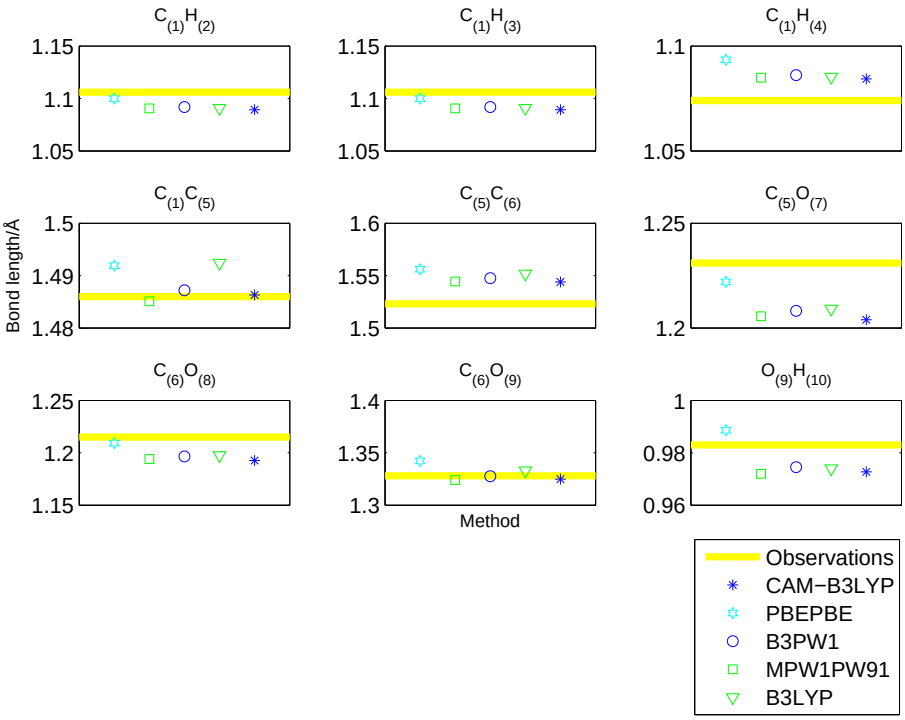

Fig. F.3: Bond lengths for Tc determined by various DFT methods using the aug-cc-pVQZ basis set. In yellow experimentally determined values. Note that y-axis differs.

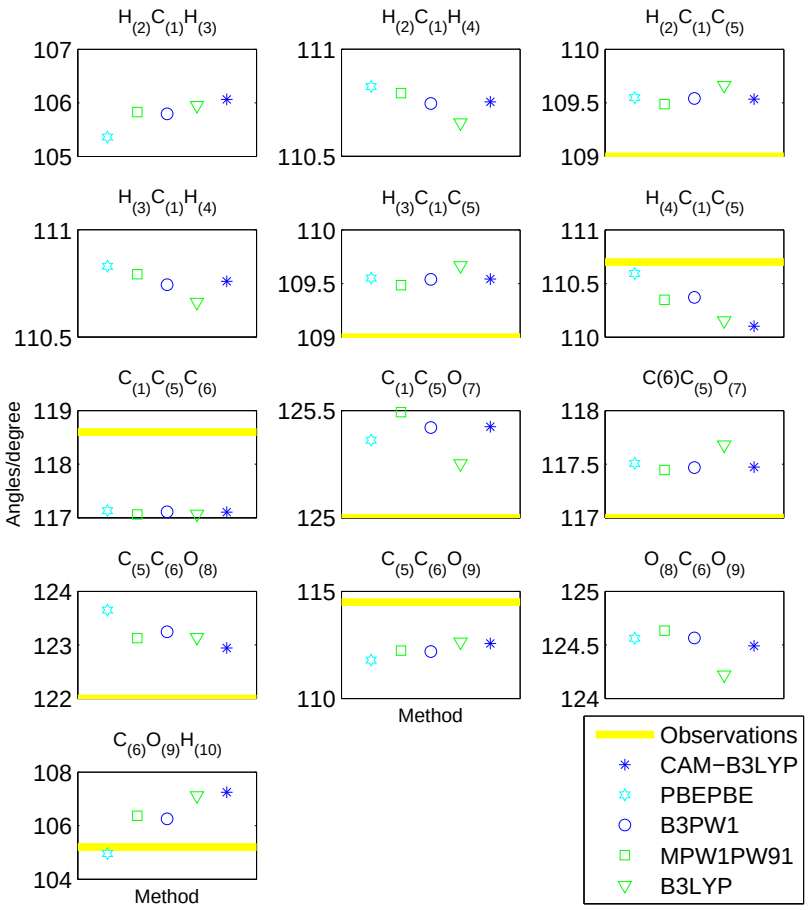

Fig. F.4: Angles for Tc determined by various DFT methods using the aug-cc-pVQZ basis set. In yellow experimentally determined values. Note that y-axis differs.

Tab. F.3: The geometry for the Tc, Tt and Ct compounds in water solution using CAM-B3LYP/cc-pVQZ when using the polarizable continuum model (PCM) with self consistent reaction field (SCRF) keywords for water. The Tc and Ct structures are shown for ice using SCRF with specified keywords.

	$\mathbf{Tc_{vacuum}}$	$\mathbf{Tc_{water}}$	$\mathbf{Tc_{ice}}$	$\mathbf{Tt_{vacuum}}$	$\mathbf{Tt_{water}}$	$\mathbf{Tt_{ice}}$	$\mathbf{Ct_{vacuum}}$	$\mathbf{Ct_{water}}$	$\mathbf{Ct_{ice}}$	$\mathbf{Cc_{vacuum}}$	$\mathbf{Cc_{water}}$	$\mathbf{Cc_{ice}}$
Distances (Å)												
$C_{(1)}H_{(2}$	1.089	1.089	1.090	1.089	1.089	1.090	1.089	1.089	1.090	1.091	1.091	1.092
$C_{(1)}H_{(3)}$	1.089	1.089	1.090	1.089	1.089	1.090	1.089	1.089	1.090	1.091	1.091	1.092
$C_{(1)}H_{(4)}$	1.084	1.084	1.085	1.084	1.084	1.085	1.085	1.084	1.085	1.085	1.084	1.085
$C_{(1)}C_{(5)}$	1.486	1.482	1.482	1.495	1.489	1.490	1.497	1.490	1.492	1.506	1.494	1.498
$C_{(5)}C_{(6)}$	1.544	1.545	1.545	1.543	1.544	1.544	1.549	1.550	1.550	1.558	1.558	1.559
$C_{(5)}O_{(7)}$	1.204	1.205	1.205	1.196	1.200	1.198	1.194	1.199	1.197	1.192	1.197	1.195
$C_{(6)}O_{(8)}$	1.193	1.197	1.195	1.198	1.199	1.199	1.189	1.196	1.192	1.184	1.193	1.189
$C_{(6)}O_{(9)}$	1.325	1.321	1.323	1.328	1.323	1.326	1.343	1.327	1.335	1.347	1.331	1.338
$O_{(9)}H_{(10)}$	0.973	0.974	0.974	0.967	0.968	0.969	0.967	0.968	0.969	0.961	0.964	0.964
Angles (°)												
$H_{(2)}C_{(1)}H_{(3)}$	106.1	106.6	106.4	106.3	106.7	106.6	106.5	106.7	106.7	108.2	108.0	108.3
$H_{(2)}C_{(1)}H_{(4)}$	110.8	110.5	110.4	110.6	110.4	110.3	110.3	110.3	110.1	108.9	109.1	108.8
$H_{(2)}C_{(1)}C_{(5)}$	109.5	109.5	109.5	110.0	109.8	110.0	110.2	109.9	110.1	110.9	110.5	110.7
$H_{(3)}C_{(1)}H_{(4)}$	110.8	110.5	110.5	110.6	110.4	110.3	110.3	110.3	110.1	108.9	109.1	108.8
$H_{(3)}C_{(1)}C_{(5)}$	109.5	109.5	109.7	110.0	109.8	110.0	110.2	109.9	110.1	110.9	110.5	110.7
$H_{(4)}C_{(1)}C_{(5)}$	110.1	110.2	110.3	109.4	109.8	109.7	109.3	109.7	109.6	109.0	109.6	109.4
$C_{(1)}C_{(5)}C_{(6)}$	117.1	117.4	117.4	114.8	115.3	115.1	117.9	118.2	118.1	118.1	118.9	118.9
$C_{(1)}C_{(5)}O_{(7)}$	125.4	125.8	125.7	125.0	125.0	125.1	124.4	124.7	124.7	123.1	124.2	123.8
$C_{(6)}C_{(5)}O_{(7)}$	117.5	116.8	116.9	120.2	119.6	119.8	117.7	117.1	117.3	118.1	117.0	117.3
$C_{(5)}C_{(6)}O_{(8)}$	122.9	123.5	123.5	122.7	122.5	122.8	124.1	122.9	123.5	122.1	121.5	121.8
$C_{(5)}C_{(6)}O_{(9)}$	112.6	113.0	112.7	112.7	112.5	112.6	111.8	112.2	112.1	116.3	117.3	116.9
$O_{(8)}C_{(6)}O_{(9)}$	124.5	123.5	123.9	124.6	125.0	124.6	124.1	124.9	124.4	121.6	121.2	121.2
$C_{(6)}O_{(9)}H_{(10)}$	107.2	107.8	107.5	107.8	109.0	108.4	107.7	109.4	108.6	112.2	113.0	112.4
Dihedral Angles (°)												
$H_{(2)}C_{(1)}C_{(5)}C_{(6)}$	-58.0	-58.2	-59.2	-58.4	-58.5	-58.5	-58.6	-58.5	-58.7	-60.1	-59.8	-60.1
$H_{(2)}C_{(1)}C_{(5)}O_{(7)}$	122.0	121.8	120.8	121.6	121.5	121.5	121.4	121.4	121.3	119.9	120.2	119.9
$H_{(3)}C_{(1)}C_{(5)}O_{(7)}$	57.9	58.4	57.3	58.4	58.5	58.5	58.6	58.6	58.7	60.1	59.8	60.1
$H_{(3)}C_{(1)}C_{(5)}O_{(7)}$	-122.1	-121.6	-122.8	-121.6	-121.5	-121.5	-121.4	-121.4	-121.3	-119.9	-120.2	-119.9
$H_{(4)}C_{(1)}C_{(5)}C_{(6)}$	-180.0	-179.9	179.2	-180.0	-180.0	-180.0	-180.0	-180.0	-180.0	-180.0	-180.0	-180.0
$H_{(4)}C_{(1)}C_{(6)}O_{(7)}$	-0.0	0.1	-0.9	0.0	0.0	0.0	0.0	-0.0	0.0	0.0	0.0	0.0
$C_{(1)}C_{(5)}C_{(6)}O_{(8)}$	0.0	0.0	-0.4	0.0	0.0	0.0	180.0	179.9	180.0	180.0	180.0	180.0
$C_{(1)}C_{(5)}C_{(6)}O_{(9)}$	-180.0	-180.0	179.6	180.0	180.0	-180.0	-0.0	0.0	-0.0	0.0	-0.0	-0.0
$O_{(7)}C_{(5)}C_{(6)}O_{(8)}$	180.0	-180.0	179.6	180.0	180.0	-180.0	-0.0	-0.1	-0.0	-0.0	-0.0	-0.0
$O_{(7)}C_{(5)}C_{(6)}O_{(9)}$	0.0	0.0	-0.3	-0.0	-0.0	-0.0	180.0	180.1	180.0	180.0	180.0	180.0
$C_{(5)}C_{(6)}O_{(9)}H_{(10)}$	-0.0	-0.0	0.1	-180.0	-180.0	-180.0	-180.0	179.9	-180.0	0.0	-0.0	0.0
$O_{(8)}C_{(6)}O_{(9)}H_{(10)}$	180.0	180.0	-179.9	-0.0	-0.0	-0.0	0.0	0.1	0.0	-180.0	180.0	-180.0

Tab. F.4: Frequencies and intensities for the Tc conformer, determined experimentally by *Reva et al.* [2001] as well as the computational results from this study using CAM-B3LYP/aug-cc-pVQZ, and the results determined by *Reva et al.* [2001] using MP2 and B3LYP with aug-cc-pVDZ. To make sure that the calculations performed in this study use the same type of B3LYP model as *Reva et al.* [2001] the B3LYP/aug-cc-pVDZ results are also shown. Note how 1752 cm^{-1} peak shifts for the B3LYP calculation; in this study and in the one by *Reva et al.* [2001]. Interpretations are presented in the last two columns for this study and the study by *Reva et al.* [2001] respectively. Notation as follows: ν-stretching, δ-bending, γ-rocking and τ-torsion.

observed		**CAM-B3LYP** aug-cc-pVQZ		**B_3LYP_{me} aug-cc-pVDZ**	**B_3LYP_{Reva} aug-cc-pVDZ**		**MP_{2Reva} aug-cc-pVDZ**		**calculated**	
									this study	**Reva(2001)**
ϑ	I	ϑ	I	ϑ	ϑ	I	ϑ	I		
3584.2	0.009								(2*$C_{(6)}$=$O_{(8)}$)	(2*$C_{(6)}$=$O_{(8)}$)
3432.3	0.0206	3518.75	130.71	3467.55	3467	111.9	3477	117.9	ν(OH)	ν(OH)
1799.5	0.646	1864.27	271.93	1811.40	1811	246.2	1791	193.2	$\nu(C_{(6)}{=}O)$	$\nu(C_{(6)}{=}O)$
1727.9	0.212	1808.67	136.26	1752.64	1732	114.4	1715	65.3	$\nu(C_{(5)}{=}O)$	$\nu(C_{(5)}{=}O)$
1423.7	0.051	1451.59	12.11	1418.03	1418	10.9	1439	10.2	$\delta(CH_3)$ as+Tt	$\delta(CH_3)$ as
1364.1	0.087								Ct	
1290.3	0.032								Ct	
1201.2	0.091								Tt	
1179.6	0.004								Ct	
967.1	0.05								Ct	
788.0	vw				757	8.8	762	12.0		ν(C−C) s
762.2	0.045	778.19	9.39	757.39	735	31.4	730	27.0	ν(C−C) s	$\gamma(C_{(5)}{=}O)$
		743.27	14.42	734.46						
664.2	0.490	710.46	87.80	694.87	695	64.2	686	65.9	τ(OH)	τ(OH)
603.8	0.118				599	17.7	596	16.4	Ct	$\delta(C_{(5)}{=}O)$
602.2	0.042	613.06	18.61	599.21					$\delta(C_{(5)}{=}O)$	
388.4		393.21	11.46	383.04	383	10.2	384	9.4	δ(C−C−O) and Tt	δ(C−C−O)
258.0		253.13	26.26	247.20	247	26.4	246	24.3	Ct	δ(C−C−C)
134					127	0.3	135	0.1		$\tau(CH_3)$
124		122.79	0.67	126.67	91	8.1	94	7.0	$\tau(CH_3)$ or Tt	τ(C−C)
115		91.64	7.89	90.70					τ(C−C)	

Tab. F.5: The frequencies for Tt and Ct. Bold indicates peaks not clearly assigned in the study by *Reva et al.* [2001]. Single parenthesis denotes frequencies which were given as comformer Tc and double parenthesis denotes frequencies which were given as conformer Tt in the study by *Reva et al.* [2001].

observed		**CAM-B3LYP** aug-cc-pVQZ		**B_3LYP_{Reva} aug-cc-pVDZ**		**MP_{2Reva} aug-cc-pVDZ**		**calculated**	
								Tt	**Ct**
ϑ	I	ϑ	I	ϑ	I	ϑ	I		
3556.1	0.040	3630.31	97.54	3588.00	77.10	3582.00	89.70	ν(OH)	
3554.1	**0.041**	3623.94	90.08	3579	67.3	3576	83.5		ν(OH)
1763.7	0.126	1836.58	103.96	1781.00	295.20	1756.00	209.40	$\nu(C_{(5)}{=}O)$	
((1763.7))	((0.126))	1857.81	202.80	1808	150.3	1788	167.7		$\nu(C_{(6)}{=}O)$
((1761.4))	((0.039))	1857.81	202.80	1808	150.3	1788	167.7		$\nu(C_{(6)}{=}O)$
1750.8	0.138	1820.21	346.91	1770.00	118.50	1730.00	102.80	$\nu(C_{(6)}{=}O)$	
((1750.8))	((0.138))	1841.00	203.93	1736	227.9	1731	110.6		$\nu(C_{(5)}{=}O)$
((1749.9))	((sh))	1841.00	203.93	1736	227.9	1731	110.6		$\nu(C_{(5)}{=}O)$
(1423.7)	(0.051)	1450.88	14.74	1415.00	13.30	1432.00	12.00	$\delta(CH_3)$ as	
1364.1	**0.087**	1396.27	47.65	1357	46.0	1366	51.1		$\delta(CH_3)$ s
1290.3	**0.032**	1347.91	28.36	1323	10.7	1336	16.7		δ(COH)
1201.2	**0.091**	1222.66	31.44	1211.00	37.70	1221.00	26.30	δ(COH)	
1179.6	**0.004**	1195.27	103.91	1177	109.7	1192	84.5		ν(C−C) as
((1116.6))	((0.069))	1150.27	227.77	1119	218.5	1112	234.2		ν(C−O)
967.1	**0.05**	983.42	19.58	964	19.2	971	13.8		$\gamma(CH_3)$
(603.8)	0.118	614.97	40.38	601	38.4	600	35.8		$\delta(C_{(5)}{=}O)$
(388.4)		389.35	0.88	382.00	1.00	383.00	0.90	δ(CCO)	
(388.4)		388.75	0.00	384	0.0	377	0.0		$\gamma(C_{(6)}{=}O)$
(258.0)		256.08	1.25	251	1.2	253	1.2		δ(C−C−C)
(124)		127.61	0.00	129.00	0.00	143.00	0.00	$\tau(CH_3)$	

Tab. F.6: Frequencies and intensities for the Tc conformer, determined experimentally by Reva et al. (2001) as well as the computational results from this study using CAM-B3LYP/aug-cc-pVQZ, and the results determined by Reva et al. (2001) using MP2 and B3LYP with aug-cc-pVDZ. To ensure that the calculations performed in this study use the same type of B3LYP model as Reva et al. (2001), the B3LYP/aug-cc-pVDZ results are also shown. Note how the 1752 cm^{-1} peak shifts for the B3LYP calculation in this study and in the one by Reva et al. (2001). Interpretations are presented in the last two columns for this study and the study by Reva et al. (2001) respectively. Notation as follows: ν-stretching, δ-bending, γ-rocking and τ-torsion.

observed		**CAM-B3LYP** aug-cc-pVQZ		**B_3LYP_{me} aug-cc-pVDZ**	**B_3LYP_{Reva} aug-cc-pVDZ**		**MP_{2Reva} aug-cc-pVDZ**		**calculated**	
									this study	**Reva(2001)**
ϑ	I	ϑ	I	ϑ	ϑ	I	ϑ	I		
3584.2	0.009								$(2*C_{(6)}=O_{(8)})$?	$(2*C_{(6)}=O_{(8)})$
3446.7	0.020									
3439.5	0.0058									
3432.3	0.0206	3518.75	130.71	3467.55	3467	111.9	3477	117.9	ν(OH)	ν(OH)
3032.3	0.004	3052.66	3.38	3041.11	3041	4.9	3085	3.8	$\nu(CH_3)$as	$\nu(CH_3)$as
		3002.52	0.12	2982.54	2982	0.6	3037	0.4	$\nu(CH_3)$as	$\nu(CH_3)$as
2936.0	0.005	2946.12	0.91	2923.74	2924	0.5	2955	0.4	$\nu(CH_3)$s	$\nu(CH_3)$s
1821.6	0.010									
1818.2	0.006									
1804.7	0.270									
1799.5	0.646	1864.27	271.93	1811.40	1811	246.2	1791	193.2	$\nu(C_{(6)}=O)$	$\nu(C_{(6)}=O)$
1797.6	0.268									
1795.7	0.248									
1791.7	0.022								Ct?	
1730.2	0.183									
1727.9	0.212	1808.67	136.26	1752.64	1732	114.4	1715	65.3		$\nu(C_{(5)}=O)$
1423.7	0.051	1451.59	12.11	1418.03	1418	10.9	1439	10.2	$\delta(CH_3)$ as+Tt	$\delta(CH_3)$ as
1408.3	0.014	1448.09	15.17	1413.49	1413	13.2	1431	11.7		$\delta(CH_3)$ as
1406.1	0.010									
1403.4	0.017									
1401.2	0.025									
1389.5	0.065									
1384.5	0.162	1412.53	49.69	1382.95	1383	128.3	1397	92.8	ν(C−C) as	ν(C−C) as
1364.1	0.087								Ct?	
1359.3	0.067									
1354.6	0.946	1383.25	305.74	1352.48	1353	231.0	1357	221.8	$\delta(CH_3)$s	$\delta(CH_3)$s
1290.3	0.032								Ct	
1214.4	0.496	1249.70	112.58	1231.42	1232	86.8	1245	105.0	δ(COH)	δ(COH)
1213.0	0.317									
1203.6	0.325									
1201.2	0.091								Tt	
1179.6	0.004								Ct	
1136.8	0.143	1167.73	56.18	1138.38	1139	58.1	1139	55.4	ν(C−O)	ν(C−O)
1133.0	0.086									
1017.8	0.027	1042.34	1.87	1014.83	1015	1.6	1015	1.0	$\gamma(CH_3)$	$\gamma(CH_3)$
968.4	0.121	984.81	15.81	965.84	966	15.3	969	13.8	$\gamma(CH_3)$	$\gamma(CH_3)$
967.1	0.05								Ct	
788.0	vw				757	8.8	762	12.0		ν(C−C) s
762.2	0.045	778.19	9.39	757.39	735	31.4	730	27.0	ν(C−C) s	$\gamma(C_{(5)}=O)$
758.9	0.025									
		743.27	14.42	734.46						
664.2	0.490	710.46	87.80	694.87	695	64.2	686	65.9	τ(OH)	τ(OH)
653.2	0.021									
603.8	0.118				599	17.7	596	16.4	Ct	$\delta(C_{(5)}=O)$
602.2	0.042	613.06	18.61	599.21					$\delta(C_{(5)}=O)$	
534.9	vw	530.57	3.24	518.57	519	3.3	521	3.0		$\delta(C_{(6)}=O)$
395.4		401.12	17.63	393.55	394	16.6	386	15.7	$\gamma(C_{(5)}=O)$	$\gamma(C_{(5)}=O)$
393.4										
388.4		393.21	11.46	383.04	383	10.2	384	9.4	δ(C−C−O) and Tt?	δ(C−C−O)
258.0		253.13	26.26	247.20	247	26.4	246	24.3	Ct?	δ(C−C−C)
134					127	0.3	135	0.1		$\tau(CH_3)$
124		122.79	0.67	126.67	91	8.1	94	7.0	$\tau(CH_3)$ or Tt?	τ(C−C)
115		91.64	7.89	90.70					τ(C−C)	

Tab. F.7: The frequencies for Tt. Bold indicates peaks not clearly assigned in the study by Reva et al. (2001). Single parenthesis denotes frequencies which were given as comformer Tc in the study by Reva et al. (2001).

observed		**CAM-B3LYP** aug-cc-pVQZ		**B_3LYP_{Reva} aug-cc-pVDZ**		**MP_{2Reva} aug-cc-pVDZ**		**calculated**	
								this study	**Reva(2001)**
ϑ	I	ϑ	I	ϑ	I	ϑ	I		
3556.1	0.040	3630.31	97.54	3588.00	77.10	3582.00	89.70	ν(OH)	ν(OH)
3554.1	0.041							Ct?	
		3051.30	3.75	3040.00	5.50	3083.00	4.20		$\nu(CH_3)$ as
		3003.63	1.05	2983.00	2.10	3037.00	1.60		$\nu(CH_3)$ as
		2946.25	0.09	2923.00	0.00	2954.00	0.20		$\nu(CH_3)$ s
1763.7	0.126	1836.58	103.96	1781.00	295.20	1756.00	209.40	$\nu(C_{(5)}{=}O)$ or Ct?	$\nu(C_{(5)}{=}O)$
1761.4	0.039								
1750.8	0.138	1820.21	346.91	1770.00	118.50	1730.00	102.80	$\nu(C_{(6)}{=}O)$ or Ct?	$\nu(C_{(6)}{=}O)$
1749.4	sh								
		1455.32	11.30	1420.00	10.10	1442.00	9.50		$\delta(CH_3)$ as
(1423.7)	(0.051)	1450.88	14.74	1415.00	13.30	1432.00	12.00	$\delta(CH_3)$ as	$\delta(CH_3)$ as
		1409.50	0.05	1375.00	0.20	1397.00	4.30		ν(C−C) as
		1381.96	64.77	1347.00	47.50	1355.00	46.00		$\delta(CH_3)$ s
1201.2	**0.091**	1222.66	31.44	1211.00	37.70	1221.00	26.30	δ(COH)	δ(COH)
1118.8	0.077	1152.34	237.88	1126.00	227.20	1124.00	236.40	ν(C−O)	ν(C−O)
1116.6	0.069							Ct	
1111.0	0.023								
		1044.14	1.50	1015.00	1.30	1015.00	1.00		$\gamma(CH_3)$
961.9	0.023	977.17	33.92	957.00	35.80	963.00	33.90	$\gamma(CH_3)$	$\gamma(CH_3)$
957.9	0.006								
		748.37	13.04	731.00	9.40	741.00	4.60		ν(C−C) s
722.7	vw	740.12	41.76	719.00	42.30	714.00	39.10	$\gamma(C_{(6)}{=}O)$+Ct?	$\gamma(C_{(6)}{=}O)$
716.4	vw								
588.2	0.088	616.62	94.94	623.00	86.50	627.00	86.20		τ(OH)
592.1	0.062	597.71	79.97	585.00	75.90	582.00	75.50	$\delta(C_{(5)}{=}O)$	$\delta(C_{(5)}{=}O)$
		519.24	1.92	507.00	1.80	511.00	1.90		$\delta(C_{(6)}{=}O)$
(388.4)		389.35	0.88	382.00	1.00	383.00	0.90		δ(CCO)
		383.46	0.00	379.00	0.10	375.00	0.20		$\gamma(C_{(5)}{=}O)$
		249.06	10.40	244.00	10.10	243.00	9.10		δ(C−C−C)
(124)		127.61	0.00	129.00	0.00	143.00	0.00		$\tau(CH_3)$
		36.77	7.88	34.00	7.60	41.00	6.60		τ(C−C)

Tab. F.8: The frequencies for Ct. Bold was not clearly assigned in the study by Reva et al. (2001). Single parenthesis denotes frequencies which were given as comformer Tc in the study by Reva et al. (2001) and double parenthesis denotes frequencies which were given as conformer Tt in the study by Reva et al. (2001).

observed		**CAM-B3LYP** aug-cc-pVQZ		**B_3LYP_{Reva} aug-cc-pVDZ**		**MP_{2Reva} aug-cc-pVDZ**		**calculated**	
ϑ	I	ϑ	I	ϑ	I	ϑ	I	**this study**	**Reva(2001)**
3554.1	**0.041**	3623.94	90.08	3579	67.3	3576	83.5		ν(OH)
		3047.16	4.68	3034	7.2	3078	5.3		$\nu(CH_3)$ as
		3002.46	1.50	2982	2.7	3036	2.0		$\nu(CH_3)$ as
		2943.90	0.00	2921	0.1	2952	0.3		$\nu(CH_3)$ s
((1763.7))	((0.126))	1857.81	202.80	1808	150.3	1788	167.7		$\nu(C_{(6)}{=}O)$
((1761.4))	((0.039))								
((1750.8))	((0.138))	1841.00	203.93	1736	227.9	1731	110.6		$\nu(C_{(5)}{=}O)$
((1749.9))	((sh))								
		1460.11	11.55	1425	10.3	1445	9.7		$\delta(CH_3)$as
		1454.40	27.39	1418	24.6	1436	26.5		$\delta(CH_3)$ as
1364.1	**0.087**	1396.27	47.65	1357	46.0	1366	51.1		$\delta(CH_3)$ s
1290.3	**0.032**	1347.91	28.36	1323	10.7	1336	16.7		δ(COH)
1179.6	**0.004**	1195.27	103.91	1177	109.7	1192	84.5		ν(C−C) as
((1116.6))	((0.069))	1150.27	227.77	1119	218.5	1112	234.2		ν(C−O)
		1046.49	1.66	1019	1.5	1017	1.2		$\gamma(CH_3)$
967.1	**0.05**	983.42	19.58	964	19.2	971	13.8		$\gamma(CH_3)$
		740.24	12.48	722	8.8	730	4.0		ν(C−C)s
		739.87	47.29	721	49.3	714	45.8		$\gamma(C_{(5)}{=}O)$
		615.99	87.10	619	77.4	619	78.5		τ(OH)
(603.8)	0.118	614.97	40.38	601	38.4	600	35.8		$\delta(C_{(5)}{=}O)$
		485.07	8.80	475	8.4	477	11.1		δ(CCO)
		401.31	3.60	393	3.5	395	3.3		$\delta(C_{(6)}{=}O)$
(388.4)		388.75	0.00	384	0.0	377	0.0		$\gamma(C_{(6)}{=}O)$
(258.0)		256.08	1.25	251	1.2	253	1.2		δ(C−C−C)
		149.89	0.05	153	0.1	169	0.0		$\tau(CH_3)$
		20.37	0.27	22	0.3	27	0.3		τ(C−C)

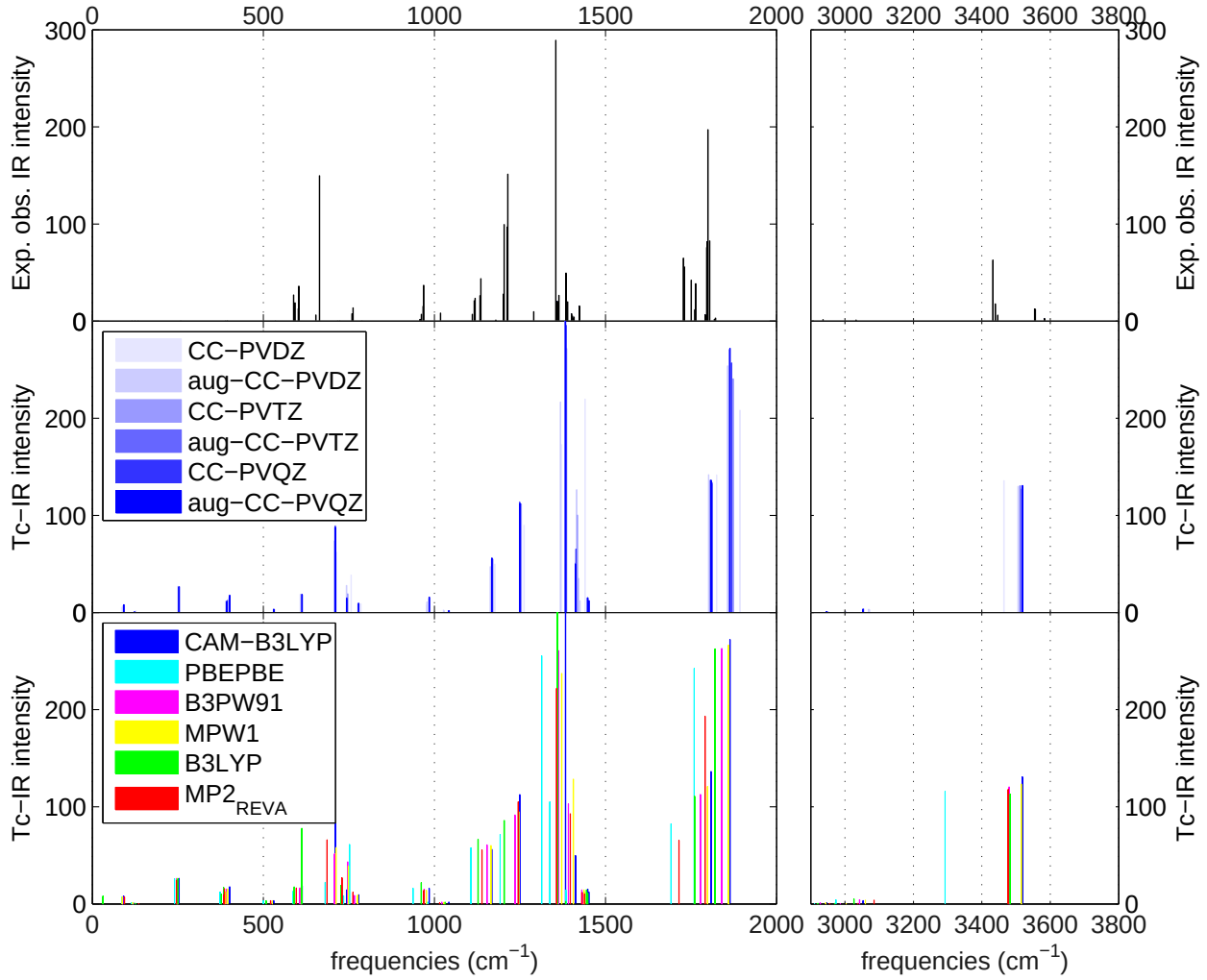

Fig. F.5: Vibrational frequencies for pyruvic acid. The top panel shows experimental results by *Reva et al.* [2001]. The middle frame shows Tc computed using CAM-B3LYP with different basis sets. The bottom graph shows the computed Tc values for different DFT methods using the aug-cc-pVQZ basis set. The experimentally determined intensities were scaled according to the maximum IR intensity found with the CAM-B3LYP method. The computed frequencies are scaled by 0.96 for the OH and CH stretching vibrations and 0.99 for all other vibrations.

G. LIST OF PUBLICATIONS

G.1 Published

- Kjær, H. A., P. Vallelonga, A. Svensson, M. E. L. Kristensen, C. Tibuleac and M. Bigler, Continuous Flow Analysis Method for Determination of Dissolved Reactive Phosphorus in Ice Cores, *Environmental science & technology*, 47 (21), pp. 12325–12332, 2013

- NEEM community members, Eemian interglacial reconstructed from a Greenland folded ice core *Nature*, 493 (7433), pp 489-494, 2013

- Vallelonga, P., G. Bertagna, T. Blunier, H. A. Kjær, T. J. Popp, S. O. Rasmussen, J. P. Steffensen, C. Stowasser, A. S. Svensson, E. Warming, M. Winstrup, M. Bigler and S. Kipfstuhl, Duration of Greenland Stadial 22 and ice-gas Δage from counting of annual layers in Greenland NGRIP ice core, *Climate of the Past*, 8 (6), pp. 1839-1847, 2012

G.2 Accepted for publication

- Spolaor, A., P. Vallelonga, J. Gabrieli, T. Martma, M. P. Björkman, E. Isaksson, G. Cozzi, C. Turetta, H. A. Kjær, M. A. J. Curran, A. D. Moy, A. Schönhardt, A.-M. Blechschmidt, J. P. Burrows, J. M. C. Plane and C. Barbante, Seasonality of halogen deposition in polar snow and ice, *Atmospheric Chemistry and Physics Discussions*, 14 (6), pp. 8185-8207, 2014

- Vallelonga, P., K. Christianson, R. B. Alley, S. Anandakrishnan, J. E. M. Christian, D. Dahl-Jensen, V. Gkinis, C. Holme, R. W. Jacobel, N. Karlsson, B. A. Keisling, S. Kipfstuhl, H. A. Kjær, M. E. L. Kristensen, A. Muto, L. E. Peters, T. Popp, K. L. Riverman, A. M. Svensson, C. Tibuleac, B. M. Vinther, Y. Weng, and M. Winstrup, Initial results from geophysical surveys and shallow coring of the Northeast Greenland Ice Stream (NEGIS), *The Cryosphere Discussions*, 8, pp. 691-719, 2014

G.3 Popular publications

- Kjær, H. A. and D. Balslev-Clausen, Iskerner-et indblik i fortidens klimaforandringer Aspekter af Dansk kemi i det 20. og 21. århundrede, Kemiforaget, pp. 65-70, 2012